frontiers | Research Topics

Tectono-magmatism, metallogenesis, and sedimentation at convergent margins

Edited by
Di Li, Peng Wang, Jiyuan Yin, Meng Wang and Richard M. Palin

Published in
Frontiers in Earth Science

ISSN 1664-8714
ISBN 978-2-8325-3769-5
DOI 10.3389/978-2-8325-3769-5

About Frontiers

Frontiers is more than just an open access publisher of scholarly articles: it is a pioneering approach to the world of academia, radically improving the way scholarly research is managed. The grand vision of Frontiers is a world where all people have an equal opportunity to seek, share and generate knowledge. Frontiers provides immediate and permanent online open access to all its publications, but this alone is not enough to realize our grand goals.

Frontiers journal series

The Frontiers journal series is a multi-tier and interdisciplinary set of open-access, online journals, promising a paradigm shift from the current review, selection and dissemination processes in academic publishing. All Frontiers journals are driven by researchers for researchers; therefore, they constitute a service to the scholarly community. At the same time, the *Frontiers journal series* operates on a revolutionary invention, the tiered publishing system, initially addressing specific communities of scholars, and gradually climbing up to broader public understanding, thus serving the interests of the lay society, too.

Dedication to quality

Each Frontiers article is a landmark of the highest quality, thanks to genuinely collaborative interactions between authors and review editors, who include some of the world's best academicians. Research must be certified by peers before entering a stream of knowledge that may eventually reach the public - and shape society; therefore, Frontiers only applies the most rigorous and unbiased reviews. Frontiers revolutionizes research publishing by freely delivering the most outstanding research, evaluated with no bias from both the academic and social point of view. By applying the most advanced information technologies, Frontiers is catapulting scholarly publishing into a new generation.

What are Frontiers Research Topics?

Frontiers Research Topics are very popular trademarks of the *Frontiers journals series*: they are collections of at least ten articles, all centered on a particular subject. With their unique mix of varied contributions from Original Research to Review Articles, Frontiers Research Topics unify the most influential researchers, the latest key findings and historical advances in a hot research area.

Find out more on how to host your own Frontiers Research Topic or contribute to one as an author by contacting the Frontiers editorial office: frontiersin.org/about/contact

Tectono-magmatism, metallogenesis, and sedimentation at convergent margins

Topic editors

Di Li — China University of Geosciences, China
Peng Wang — The University of Queensland, Australia
Jiyuan Yin — Institute of Geology, Chinese Academy of Geological Sciences (CAGS), China
Meng Wang — Chang'an University, China
Richard M. Palin — University of Oxford, United Kingdom

Citation

Li, D., Wang, P., Yin, J., Wang, M., Palin, R. M., eds. (2023). *Tectono-magmatism, metallogenesis, and sedimentation at convergent margins*.
Lausanne: Frontiers Media SA. doi: 10.3389/978-2-8325-3769-5

Table of contents

frontiers | Frontiers in Earth Science

TYPE Editorial
PUBLISHED 09 October 2023
DOI 10.3389/feart.2023.1303820

OPEN ACCESS

EDITED AND REVIEWED BY
Michel Grégoire,
UMR5563 Géosciences Environnement Toulouse (GET), France

*CORRESPONDENCE
Meng Wang,
wangmeng@chd.edu.cn

RECEIVED 28 September 2023
ACCEPTED 02 October 2023
PUBLISHED 09 October 2023

CITATION
Wang M, Palin RM, Li D, Yin J and Wang P (2023), Editorial: Tectono-magmatism, metallogenesis, and sedimentation at convergent margins.
Front. Earth Sci. 11:1303820.
doi: 10.3389/feart.2023.1303820

Editorial: Tectono-magmatism, metallogenesis, and sedimentation at convergent margins

Meng Wang[1]*, Richard M. Palin[2], Di Li[3], Jiyuan Yin[4] and Peng Wang[5]

[1]School of Earth Science and Resources, Chang'an University, Xi'an, China, [2]Department of Earth Sciences, University of Oxford, Oxford, United Kingdom, [3]The Key Laboratory of Marine Reservoir Evolution and Hydrocarbon Accumulation Mechanism, The Ministry of Education, China University of Geosciences, Beijing, China, [4]Institute of Geology, Chinese Academy of Geological Sciences, Beijing, China, [5]School of Earth and Environmental Science, University of Queensland, Brisbane, QLD, Australia

KEYWORDS

convergent margins, magmatism, sedimentation, subduction initiation, sedimentary basins

Editorial on the Research Topic
Tectono-magmatism, metallogenesis, and sedimentation at convergent margins

Convergent plate margins are key regions for material and energy recycling between surface and interior Earth reservoirs, and are major sites for continental growth, reworking, and destruction. The type, geometry, and thermal structure of subduction zones have critical impacts on subduction processes and the nature of magmatic products that formed in the overlying arc, which produces a wide range lithologies and associated ore deposits at convergent margins. Identification and characterization of the physical and chemical processes that occur at convergent margins, alongside correlating these effects with specific subduction types and stages, are crucial to understand spatiotemporal interactions between the crust, lithosphere, and asthenosphere in orogenic belts.

The geodynamic evolution of crustal and mantle components at convergent margins involves multiple processes that operate over discrete time and length scales. Recent advances in computational and analytical capability have allowed a growing body of new techniques to emerge that can unveil these geological processes in new and unprecedented detail. This Research Topic aims to bring together multi-disciplinary and state-of-the-art studies on the applications of geochronology, geochemistry, isotopic analysis, numerical modeling, machine learning, and big data to scrutinize the dynamics and effects of all stages of the Wilson Cycle, including subduction initiation, subduction zone processes, and continental collision.

Subduction initiation at continental margins

The geological mechanism that promote subduction initiation remain uncertain, despite decades of study. Numerical modelling is fast-becoming a critical tool that can be used to

study this process. Candioti et al. focused on horizontally forced subduction zone initiation at passive margins and quantify the horizontal force required for subduction zone initiation with two-dimensional petrological-thermomechanical numerical models. Interestingly, the modelling shows a causal link between subduction zone initiation and slab detachment. If forces required for subduction zone initiation are smaller, then the lithosphere is weaker and then slab detachment occurs at shallower levels and corresponding slabs are shorter.

In a separate study, Li et al. evaluated the influence of strike-slip motion on the effective strength of incipient margins and the ease of subduction initiation using computational models. Models suggest that subduction initiation can be triggered when margins become progressively weakened to the point that the resisting forces become smaller than the driving forces. Despite not being a governing factor, strike-slip velocity can still dramatically lower the force required to induce formation of a new plate margin, thereby providing a favorable condition for subduction initiation.

Magmatism at convergent margins

Teng et al. investigated a series of plutonic rocks that formed in Huatugou, situated in the inner part of the Qaidam Block. These intrusions were formed in two stages: early granodiorites formed at 451 Ma and display geochemical features of adakitic rocks, and thus were likely generated by partial melting of the thickened lower mafic crust, and were followed by later S-type muscovite granites (410 Ma) and A_2-type monzogranites (400 Ma). These authors infer that the Qaidam Block was composed of thickened continental crust during subduction, until the detachment of subducted crust during the continental collision.

Tian et al. presented a comprehensive analysis of the geochronology, whole-rock geochemistry, clinopyroxene mineral geochemistry, zircon Ti crystallization temperature, and gabbro magma temperature and pressure in the Yushigou ophiolite of the North Qilian orogenic belt. New data shows that the gabbro in the Yushigou ophiolites has zircon U-Pb ages of 519 to 495 Ma, and exhibits dual characteristics of MORB and IAT, suggesting that it may have formed in a back-arc basin environment.

Yogibekov et al. reports the petrography, geochronology, and geochemistry of Cretaceous granites and diabase dikes that intrude into the Pshart complex. The granites are highly fractionated, strongly peraluminous S-type granites with zircon U-Pb ages of 124–118 Ma. The diabase dikes contain low SiO_2, high MgO, and negative Nb and Ta anomalies, which were interpreted to record partial melting in an extensional environment. These units formed in a post-collisional environment after the final closure of the Rushan–Pshart Meso-Tethys Ocean.

Sedimentation at convergent margins

Mao et al. conducted structural mapping, geochemistry and geochronology on various lithologies within the Kanguer subduction complex, Haluo, eastern Tianshan. New analytical data from Upper Permian (257 Ma) basaltic blocks emplaced in a sandstone matrix in the northern Haluo area show N-MORB signatures, and geochronological results indicate that the sandstone matrices display two different provenance. All mélanges and coherent units in the north of the study area belong to an accretionary complex of the Dananhu intraoceanic arc, and those in the south belong to an accretionary complex of the Yamansu-central Tianshan arc.

Yang et al. performed stratigraphic and geochronologic studies to establish a chronostratigraphic framework of the western Junggar Basin, in order to better understand the evolution of the Juggar Ocean. The southern West Junggar region experienced three stages of an extended tectonic-sedimentary evolution: oceanic subduction, slab roll-back and intra-continental setting. This new model constrains closure of the Junggar Ocean during the Late Carboniferous.

Wakabayashi performed restoration of post-subduction dextral faulting to evaluate the spatial distribution of units of the Franciscan subduction complex of California. The Franciscan subduction complex exhibits significant along-strike variation, reflecting along-strike differences in the history of accretion, non-accretion, and subduction erosion, and likely slab dip. Two segments 830 km apart record subduction erosion associated with low-angle subduction events that took place at ca. 120 Ma and ca. 80–70 Ma in the north and south. Between these segments the subduction complex records net accretion from ca.175–12 Ma, but includes horizons recording non-accretion. These new results demonstrate the strong variations that may occur along strike in a single subduction zone.

Wang et al. propose a biomarker method using C_{20}-C_{21}-C_{23} tricyclic terpanes (TTs) as a tracer, and developed a discrimination diagram for environmental identification. Based on the analysis of 271 C_{20}-C_{21}-C_{23}TT data from 32 basins in 18 countries, a relationship between C_{20}-C_{21}-C_{23}TT abundance patterns and depositional environments were observed. This relationship was attributed to the control of depositional environments on the input proportions of plankton and terrigenous plants. The validity of this C_{20}-C_{21}-C_{23}TT biomarker method is well demonstrated by the rock samples with typical environmental indicators.

Deformation at subduction margins

Ninis et al. investigated tectonic uplift across the southern Hikurangi subduction margin, Aotearoa New Zealand, during the past ~200 ka, in order to understand the mechanisms driving permanent vertical displacement. Using shore platform elevation data and corresponding attitudes, together with the formation age of these shore platforms, uplift rates have been calculated across the southern Hikurangi subduction margin–since the Late Pleistocene. These results highlight the complex processes that drive uplift in subduction settings, and demonstrate the important contribution that upper-plate faults can make to such uplift.

Other papers in this Research Topic

Domel et al. examined the short-duration events (SDEs) over a 10-month period at an active seepage site on Vestnesa Ridge, a continental margin located in West Svalbard. The results indicate

that both tremors and SDEs in such geological settings show a periodic behavior. Signal periodograms show that SDEs have periodic patterns related to solar and lunar cycles, while the periodicity analysis of tremors shows a different pattern, likely caused by the effect of tidally controlled underwater currents on the instrumentation.

Yang et al. provided a method with combined use of in-reservoir geological records to rapidly identify oil-reservoir destruction, using the Yanchang Formation in the Ordos Basin as an example. Petrological and geochemical of sandstones from the Yanchang Formation were studied. They proposed that the oil-reservoir destruction was likely caused by the uplift-induced erosion and the fault activities after oil accumulation during the Late Early Cretaceous.

Author contributions

MW: Writing–original draft. RP: Writing–review and editing. DL: Writing–review and editing. JY: Writing–review and editing. PW: Writing–review and editing.

Funding

The author(s) declare financial support was received for the research, authorship, and/or publication of this article. This Research Topic was jointly supported by the National Natural Science Foundation of China (42072267), the West light Foundation of the Chinese Academy of Sciences (XAB2020YW03), the Fundamental Research Funds for the Central Universities, CHD (300102272103 and 211427230085), and the Youth Innovation Team of Shaanxi Universities.

Acknowledgments

We thank the authors for their contributions and the reviewers and editorial staff for their efforts to pull together this article Research Topic. The author also thanks the Editorial Office of Frontiers in Earth Science for the kind invitation to edit this Research Topic and the editor-in chief VA for their support.

Conflict of interest

The authors declare that the research was conducted in the absence of any commercial or financial relationships that could be construed as a potential conflict of interest.

Publisher's note

frontiers in Earth Science

ORIGINAL RESEARCH
published: 15 February 2022
doi: 10.3389/feart.2022.818171

Along-Strike Variation in Accretion, Non-accretion, and Subduction Erosion Recorded in Rocks of the Jurassic-Neogene Convergent Plate Margin of California

John Wakabayashi *

Department of Earth and Environmental Sciences, California State University, Fresno, United States

Post-subduction dextral faulting was restored to evaluate the spatial distribution of units of the Franciscan subduction complex of California that formed as a result of subduction accretion. The Franciscan and related rocks of western California exhibit significant along-strike variation in its recording of subduction-accretion processes. Most notably, two segments 830 km apart record subduction erosion associated with low-angle subduction events that took place at ca. 120 Ma and ca. 80–70 Ma in the north and south, respectively. This spatial relationship is not affected by restoration of post-subduction dextral slip because none of the slip passes between the two inboard tectonic windows. Between these segments the subduction complex records net accretion from ca.175 Ma to 12 Ma, but includes horizons recording non-accretion. None of the accreted units of the subduction complex are preserved over the entire length of the subduction complex. One unit, however, correlated on the basis of its structural level in the subduction complex and distinctive detrital zircon age spectra, accreted at about 80–83 Ma extends a strike length of 580 km, an amount increased to 850 km with restoration of post-subduction dextral faulting. The long-strike length of accretion of this unit demonstrates that detrital zircon age populations of subduction complex clastic rocks are poor indicators of strike-slip displacement. Some reaches of the subduction complex include schistose blueschist facies rocks (most Franciscan blueschist facies rocks are not schistose), whereas others do not, and some reaches lack blueschist facies rocks altogether. The significant along-strike variation in the Franciscan and related rock units reflects temporal and spatial differences in history of accretion, non-accretion, subduction erosion, and probably subduction dip. Similar time and space variation in processes and resultant geologic record should be expected for other subduction complexes of the world.

Keywords: subduction accretion, subduction erosion, along-strike variation, subduction tectonics, post-subduction deformation restoration

OPEN ACCESS

Edited by:
Andrea Festa,
University of Turin, Italy

Reviewed by:
Andrea Zanchi,
University of Milano-Bicocca, Italy
Edoardo Barbero,
University of Ferrara, Italy

***Correspondence:**
John Wakabayashi
jwakabayashi@csufresno.edu

Specialty section:
This article was submitted to Structural Geology and Tectonics, a section of the journal Frontiers in Earth Science

Received: *19 November 2021*
Accepted: *24 January 2022*
Published: *15 February 2022*

Citation:
Wakabayashi J (2022) Along-Strike Variation in Accretion, Non-accretion, and Subduction Erosion Recorded in Rocks of the Jurassic-Neogene Convergent Plate Margin of California. Front. Earth Sci. 10:818171. doi: 10.3389/feart.2022.818171

INTRODUCTION

Modern subduction zones exhibit along-strike variation from subduction-accretion (subduction fault slices into downgoing plate; referred to as "accretion" in this paper), non-accretion (subduction fault does not cut into either upper plate or downgoing plate), and subduction erosion (subduction fault cuts into upper plate) (e.g., von Huene, 1986; von Huene and Scholl, 1991; Clift and Vannucchi, 2004). Recognizing the details of along-strike variation of accretion, non-accretion, and

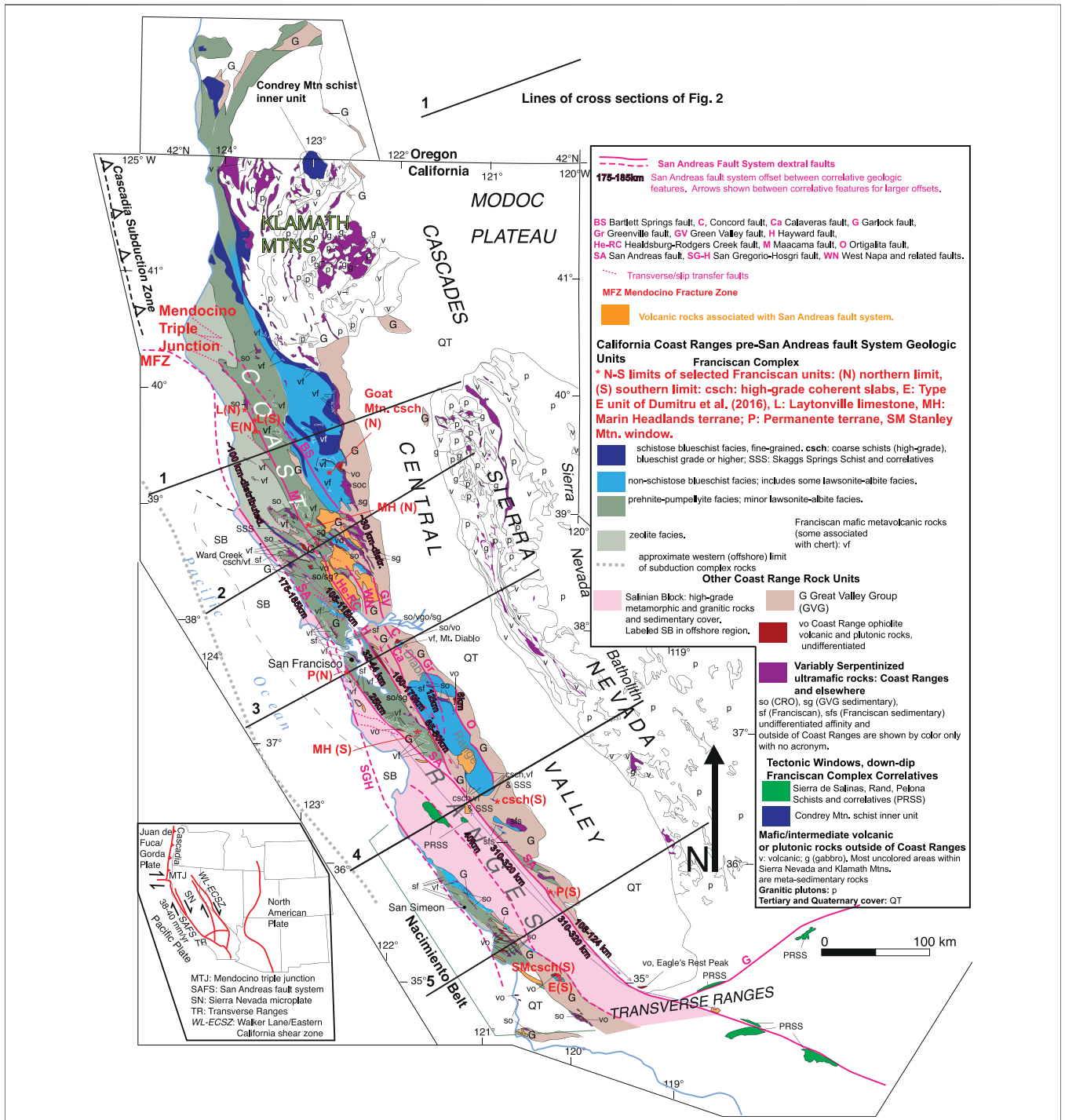

FIGURE 1 | Map showing the Franciscan Complex and related rocks in coastal California as well post-subduction dextral faults of the San Andreas fault system, post-subduction volcanic rocks, and some details of pre-Franciscan and upper plate rocks. Revised from Wakabayashi (2015), Chapman et al. (2016), Kuiper and Wakabayashi (2018) and Chapman et al. (2021). Post-subduction dextral fault offsets (revised from Wakabayashi, 1999) used in the restoration are shown.

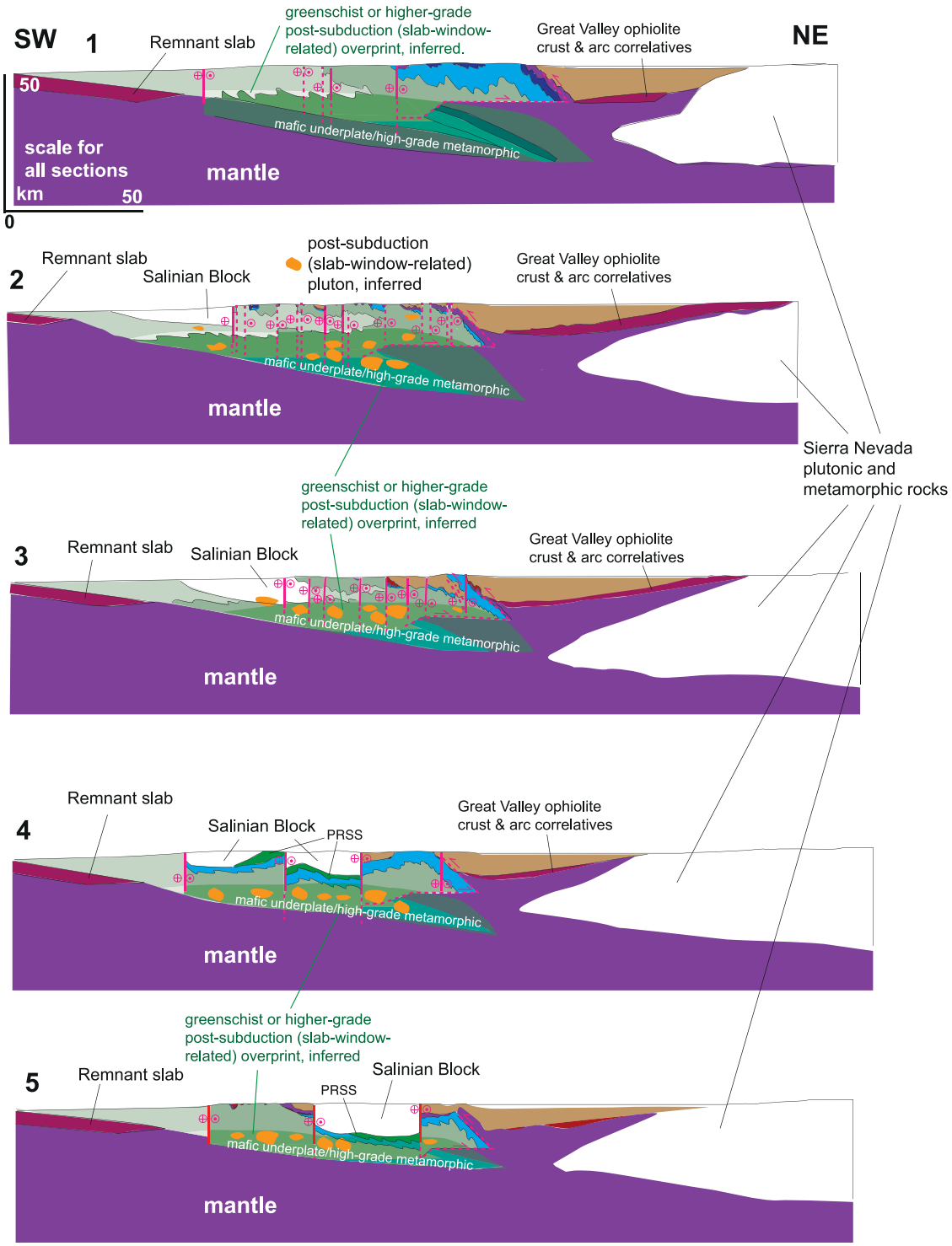

FIGURE 2 | Cross sections of present-day geologic relationships. Subsurface interpretations are partly based on Godfrey et al. (1997), Langenheim et al. (2013), and Wakabayashi (2015). Colors are the same as those used in **Figure 1** except where specifically noted. Note that arc and ophiolitic rocks correlative to the Great Valley ophiolite that may crop out in the western Sierra Nevada are not colored in **Figure 1**, but are shown with the same color as Coast Range ophiolite volcanic and plutonic rocks on **Figure 2**.

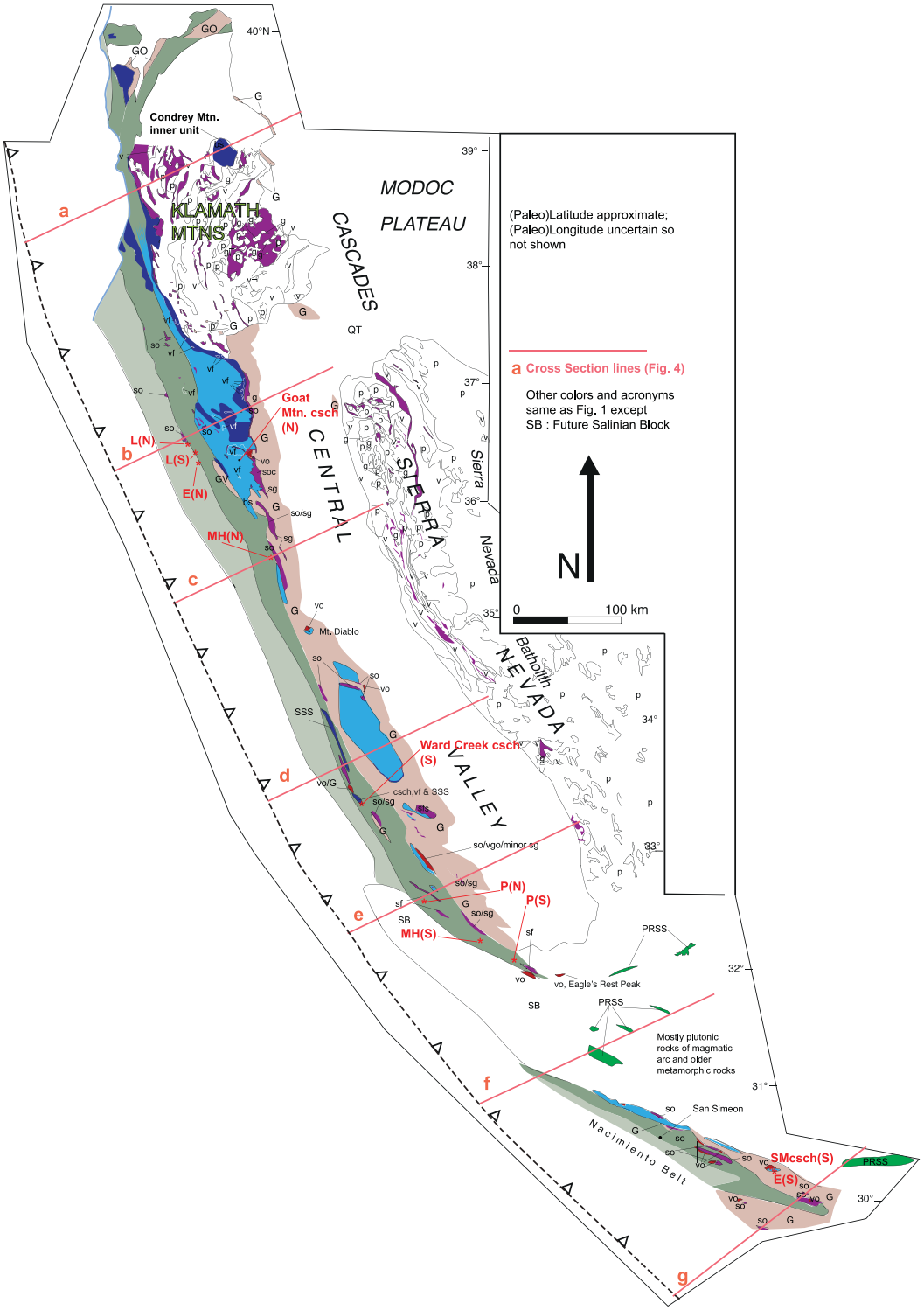

FIGURE 3 | Map showing Franciscan Complex rocks restoring dextral faulting of the San Andreas fault system largely following Wakabayashi (1999) and Chapman et al. (2016) for the southern areas. See text for details of the restoration method.

subduction erosion along exhumed paleo subduction zones is difficult because of the need to restore post-subduction deformation and the challenges posed in identifying subduction erosion and non-accretionary horizons along paleo-subduction interfaces exhumed from depth ranges that are commonly >10 km beneath the sea floor (e.g.,

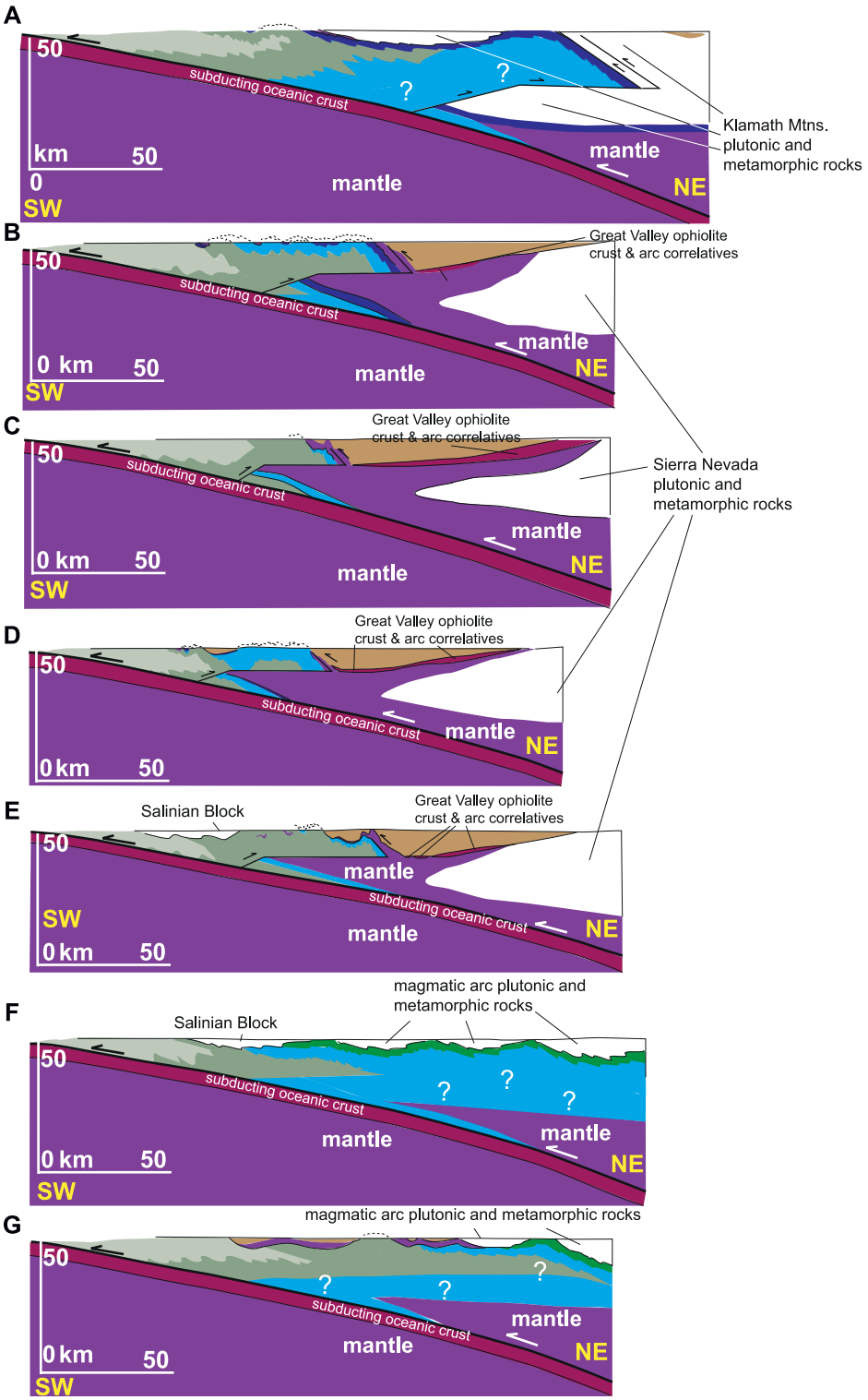

FIGURE 4 | Cross sections of Franciscan Complex and related rocks with post-subduction dextral faulting restored. See text for details. Colors are the same as those used in **Figures 1–3** except where directly labeled.

Dumitru et al., 2010; Wakabayashi, 2015, Wakabayashi, 2021a; Chapman et al., 2016). The difficulty in recognizing non-accretionary or eroding paleo subduction interfaces in such exhumed rocks is because the depth of exposure/exhumation is well below that directly observed in sea floor studies, including drilling.

This paper restores post-subduction strike-slip and related faulting to examine the spatial relationships of subduction complex rocks of the Franciscan Complex of California that formed by sporadic subduction-accretion from ca. 175 to 12 Ma prior to disruption by the post-subduction San Andreas fault system (Hamilton, 1969; Ernst, 1970; Maxwell, 1974; Blake et al., 1988; McLaughlin et al., 1996; Ernst et al., 2009; Dumitru et al., 2010; Snow et al., 2010; Dumitru et al., 2013; Dumitru et al., 2015; Dumitru et al., 2018; Raymond, 2015; Raymond and Bero, 2015; Wakabayashi, 2015; Mulcahy et al., 2018; Raymond, 2018; Apen et al., 2021; Wakabayashi, 2021a) (**Figure 1** current map view, **Figure 2** current cross sections, restored map view **Figure 3**, cross sections of restored geology **Figure 4**; lists current compared to restored spatial relationships). *The map view and inferred cross sectional relationships of Franciscan Complex units are then* evaluated in the context of the history of accretion, non-accretion, and subduction erosion in space and time. This paper presents a largely descriptive view of the three-dimensional relationship of Franciscan rocks and does not attempt to speculate on mechanisms that caused the along-strike variation recorded in the subduction complex.

FRANCISCAN AND RELATED ROCKS: BASIC ARCHITECTURE

Western California includes outcrops of the Franciscan subduction complex, as well as the components of the "upper plate" of the subduction system (never part of downgoing plate) that comprises the Coast Range ophiolite and the Great Valley Group forearc basin deposits that depositionally overlie the ophiolite (**Figures 1**, **2**) (e.g., Hamilton, 1969; Ernst, 1970, Dickinson, 1970, Hopson et al., 1981; Hopson et al., 2008). The upper plate rocks structurally overlie the Franciscan subduction complex (Hamilton, 1969; Dickinson, 1970; Ernst, 1970) along a fault known as the Coast Range fault, which records differential exhumation of the Franciscan relative to the upper plate (e.g., Suppe, 1973; Platt, 1986; Jayko et al., 1987; Harms et al., 1992; Ring and Brandon, 1994; Unruh et al., 2007). The upper plate rocks display neglible burial metamorphism and record comparatively little deformation compared to the Franciscan (Dickinson et al., 1969; Hopson et al., 1981; Evarts and Schiffman, 1983; Dumitru, 1988; Hopson et al., 2008; Ring, 2008).

Franciscan rocks consist primarily of clastic sedimentary rocks with volumetrically smaller amounts of mafic volcanic rocks, chert, serpentinite, and very rare limestone (e.g., Berkland et al., 1972; Maxwell, 1974; Blake et al., 1988; Wakabayashi, 2015; Raymond, 2018). Note that on **Figure 1** areas rich in mafic volcanic rocks with chert or limestone are delimited by "vf" but even in those areas have a significant fraction of clastic sedimentary rocks (see detailed maps two of the most volcanic and chert rich areas in the Franciscan: the Marin Headlands of Wahrhaftig, 1984, and Mt. Diablo of Wakabayashi, 2021b). The Franciscan is well-known for having high-pressure/low-temperature (HP-LT) metamorphic rocks that resulted from subduction (Ernst, 1970) but HP-LT metamorphic rocks of lawsonite-albite or blueschist facies or higher grade (blue and dark blue on **Figure 1**) make up only about a fourth of Franciscan rocks (Blake et al., 1984; Blake et al., 1988; Ernst, 1993, Terabayashi and Maruyama, 1998; Ernst and McLaughlin, 2012). A relatively small fraction of these HP-LT rocks (dark blue on **Figure 1**) are schistose and completely or nearly completely recrystallized (Blake et al., 1988; Wakabayashi, 2015). The Franciscan consists of block-in-matrix mélange and non-mélange "coherent" horizons, with the proportion of mélange varying significantly from one area to another (Berkland et al., 1972; Blake et al., 1984; Blake et al., 1988; Cloos and Shreve, 1988a; Cloos and Shreve, 1988b; Wakabayashi, 2015; Raymond, 2018).

Different researchers define Franciscan units differently (e.g., Blake et al., 1982, 1984, 1988; Raymond, 2015; Wakabayashi, 2015; Ernst, 2017; Wakabayashi, 2021a; Raymond et al., 2019; Apen et al., 2021) so it is useful to specify how units are defined in this paper. This paper follows the approach of Wakabayashi, 2015; Wakabayashi, 2021a). Units are delimited by age of accretion, estimated by radioisotopic ages of metamorphism, or by depositional age of clastic rocks, constrained by biostratigraphy and/or maximum depositional ages from U-Pb age determinations of detrital zircons and/or specific age-probability distributions of detrital zircon ages. Many individual outcrops lack geochronologic data, so for such rocks correlations are made to dated rocks on the basis of similarity in relative structural position within the Franciscan and similarities in lithologic character. It is beyond the scope of this paper to debate merits of alternative unit nomenclature schemes. The pronounced along-strike variation in the subduction complex is apparent regardless of the unit definitions used.

A slice of continental magmatic arc rocks, called the Salinian block, correlative to rocks of the southern Sierra Nevada magmatic arc and the related rocks to the south, crops out west of the main belt of Franciscan Complex exposures and east of the subduction complex rocks known as the Nacimiento belt (**Figure 1**) (Chapman et al., 2016). The rocks associated the paleo trench-forearc system (Franciscan, Coast Range ophiolite, Great Valley Group) are unconformably overlain by post-subduction volcanic and sedimentary deposits associated with the post-subduction dextral plate boundary, represented by the San Andreas fault system (only post-subduction volcanic deposits shown on **Figure 1**) (e.g., Page, 1981).

Although Franciscan, Great Valley Group and Coast Range ophiolite units dip steeply in most outcrops, the regional dips of unit boundaries are low-angle, as demonstrated by the traces of contacts over topography, so that the general architecture is that of folded low-angle sheets (Langenheim et al., 2013; Wakabayashi, 2015). Most regional-scale folds of the Franciscan are west-vergent and overturned, so easterly dips predominate (Wakabayashi, 2015) (shown somewhat schematically in **Figure 2**). Where post-subduction deposits overlap Franciscan and related rocks, most of the folding of the Franciscan rocks appears to predate this overlap, whereas some older folds have been tightened by post-subduction shortening (examples in Figures 7, 8 of Wakabayashi, 2021a).

The Coast Range fault and overlying Great Valley Group has also experienced folding prior to subduction termination, as illustrated by the overlap of this fault by deposits that date from early in the post-subduction regime (for example, see maps of Blake et al., 2000; 2002). Internal imbrication of Franciscan units as well as some of their folding predates syn-subduction movement along the Coast Range fault as illustrated by the truncation of internal Franciscan structure by the fault (Wakabayashi, 2021b) (**Figure 2**).

Post-subduction dextral faulting has significantly impacted the map-view spatial relationships of Franciscan units (e.g., Page, 1981; McLaughlin et al., 1996; Wakabayashi, 1999). In contrast, the amount of post-exhumation has been <3 km for most of exposed Franciscan rocks, so post-subduction metamorphic overprinting is lacking (Dumitru, 1989; Unruh et al., 2007). At deeper levels in the California Coast Ranges metamorphic overprinted and intrusion of post-subduction plutons is expected (**Figure 2**) from post-subduction increase in geothermal gradients and magmatism related to slab window development (Furlong, 1984; Liu and Furlong, 1992; Wakabayashi, 1996; Kuiper and Wakabayashi, 2018). This post-subduction metamorphism is recorded in some xenoliths in post-subduction volcanic rocks (Stimac, 1993; Metzger et al., 2005) but not in exposed rocks, owing to the lack of sufficient exhumation.

RESTORATION OF POST-SUBDUCTION DEFORMATION AND FAULTING

The deformation associated with the dextral San Andreas fault system that has replaced east-dipping subduction associated with Franciscan subduction has been primarily accommodated by dextral faults, with subordinate local shortening or extension (Atwater, 1970; Argus and Gordon, 1991; Atwater and Stock, 1998; Argus and Gordon, 2001). In addition to slight discordance between the azimuth of relative plate motion and the Pacific-North American plate boundary that may have been recorded by small convergent or divergent components along the otherwise dextral plate margin (e.g., Argus and Gordon, 1991; Atwater and Stock, 1998; Argus and Gordon, 2001), local transpression and transtension has been associated with the development of step-overs and bends along the dextral faults (Aydin and Page, 1984; Wakabayashi et al., 2004; Wakabayashi, 2007; Unruh et al., 2007).

Transform fault system deformation and slip has been restored by the following procedure: First, displacements along the various dextral faults of the San Andreas fault system were restored following the slip assignments of Wakabayashi (1999) (main displacements shown on **Figure 1**). Because many of the faults have bends and step-overs, gaps and minor overlaps result from dextral fault restoration. In addition, there are many faults that cut Franciscan rocks that have been proposed to be slip-transfer faults associated with fault step-overs (e.g., Wakabayashi et al., 2004; Wakabayashi, 2007; Kuiper and Wakabayashi, 2018). Accordingly, Franciscan units have been restored across various mapped dextral faults of the San Andreas fault system, but with additional smaller-scale slivering. The areas labeled with "distributed" deformation on **Figure 1** (between 38° and 39.5°N latitude) are examples. Other areas restored with distributed slip include region NW of the northern tip of the West Napa fault, and the region between the Healdsburg-Rodgers Creek-Hayward faults and the San Andreas fault. Gaps and overlaps are removed in the restored map relationships.

Surface erosion since the termination of subduction has changed the outcrop pattern, but the details of this erosion are poorly known. Because of the uncertainty in restoring erosion, and the qualitative nature of accommodation of distributed deformation and step-overs and bends (removing gaps and overlaps), the restored Franciscan geology is shown with much less detail in **Figure 3** compared that of the present-day **Figure 1**. For the southernmost part of the Franciscan Complex, represented by the Nacimiento Belt, the restoration of inboard interpreted tectonic windows (including the Sierra de Salinas, Rand, and Pelona schists) largely follows Chapman et al. (2016) with the minor adjustment of including ~55 km of sinistral slip on the Garlock Fault (Hatem and Dolan, 2018).

The restoration leaves the northern end of the Salinian block projecting about 175 km northwest of the southernmost inboard Franciscan exposures (**Figure 3**). This may reflect 175 km of syn-subduction dextral slip along a "proto San Andreas fault" (e.g., Page, 1981) or the west-directed low-angle faulting of a relatively thin crystalline sheets or sheets derived from the southernmost Sierra Nevada and regions to the south by west-directed low-angle faulting associated with earliest Paleogene thrusting (Hall, 1991) or latest Cretaceous extensional collapse (Chapman et al., 2012). If the eastern contact of the northern Salinian block is a syn-subduction dextral fault (Page 1981), Nacimiento Belt exposures restore an additional 175 km further southeastward relative to the inboard main Franciscan outcrop belt than the position shown in **Figure 3**. The cross sections of **Figures 2**, **4** have been constructed following a model of a thin Salinian block originally emplaced by westward-directed low-angle faulting (e.g., Hall, 1991; Chapman et al., 2012) whereas the model of Page (1981) would result in a thicker Salinian block bounded by a high-angle fault on its east. It is beyond the scope of this paper to discuss the relative strengths of the two types of proposals for Salinian block emplacement, and these different models to not impact the interpretations of this study about along-strike variation of Franciscan rocks with the exception of the relative position between the Nacimiento Belt and inboard main Franciscan outcrop belt.

There have been alternative schemes presented for slip distribution on the San Andreas fault system, such as Powell (1993) and McLaughlin et al., 1982; for the eastern part of the fault system). Units east of all of the strands of San Andreas fault system are unaffected by different models of slip distribution on the various dextral strands. The unaffected units include the relative position tectonic windows of the Condrey Mtn. inner unit and Rand schists (830 km between them), as well as various features along the eastern margin of the Coast Ranges such as the South Fork Mtn. schist and related units.

The positions of other Franciscan units relative to one another are also largely unaffected by the choice of slip distribution between the two alternatives noted above and Wakabayashi

(1999). The primary difference is that Powell (1993) and McLaughlin et al., 1996 restore the southernmost limit of Franciscan exposures east of the Salinian block to a position more than 100 km north of the position proposed by Wakabayashi (1999). Accordingly, the general pattern of along-strike variation of Franciscan rocks is not significantly different between different restoration schemes.

RESTORED POSITIONS OF FRANCISCAN COMPLEX UNITS

The restoration of San Andreas fault slip lengthens Franciscan Complex main exposure belt (excluding Nacimiento Belt) from 830 km to a restored length of about 980 km (**Figures 1**, **3**). If the Nacimiento Belt is included, the outcrop belt currently has a total length of 980 km and a restored length of about 1,300 km.

The amount of post-subduction dextral slip cutting Franciscan exposures decreases northward, reflecting the progressive northward lengthening of the transform fault system and progressive propagation of the eastern faults of the system (e.g., Wakabayashi, 1999; Wakabayashi et al., 2004; Wakabayashi 2007). For this reason, the Franciscan units of the northern (north of ~39°N on **Figure 1**) Coast Ranges (Fig. 4ab) are relatively unaffected by restoration of such dextral faulting (**Figures 1**, **3**). As apparent in past analyses of Franciscan accreted units, such as those of Wakabayashi (2015), there are significant differences in the tectonic stack of units along strike, with no single unit extending the length of the belt (**Figure 3**).

The most extensive unit in the Franciscan in terms of along-strike extent occupies one of the lowest structural positions among prehnite-pumpellyite facies units in the main Franciscan outcrop belt, as well as constituting part of the Nacimiento Belt, has distinctive detrital zircon age spectra, and apparently was deposited and accreted about 80–83 Ma (Type E unit of Dumitru et al., 2016 in the Franciscan and Nacimiento Belt; Wakabayashi, 2015 for structural context). This clastic-dominated unit crops out along a strike distance of 580 km in present-day exposures and 830 km with restoration of post-subduction dextral faulting (northern and southern limits labeled as E(N) and E(S) respectively on **Figures 1**, **3**). Although mapping and sampling to confirm correlations of this unit are far from exhaustive, published mapping and field observations suggest that this unit forms a reasonably continuous belt of exposures with the exception of the gap between the Nacimiento Belt and main Franciscan exposure belt (Wakabayashi, 2015; Dumitru et al., 2016). Structural thickness of the unit within the main Franciscan exposure belt reaches 3 km (Wakabayashi, 2015; Wakabayashi, 2021a).

The next most extensive unit that forms a close to continuous belt of outcrops is that of the South Fork Mtn. schist and correlative units (Blake et al., 1988; Dumitru et al., 2010; Chapman et al., 2021). This unit of schistose blueschist and greenschist facies rocks was subducted, accreted, and metamorphosed at about 121 Ma (Ar-Ar phengite, Dumitru et al., 2010), and makes up the dark blue units on **Figure 1** in the northern Coast Ranges north of ~39°N but exclusive of the Condrey Mtn schist inner unit. These rocks crop out over a distance of about 420 km and a restored distance of about 450 km (**Figures 1**, **3**), and attain a structural thickness of up to about 5 km (Worrall, 1981; Schmidt and Platt, 2018).

The comparative continuity of the extensive ca. 80–83 Ma unit and the South Fork Mtn. schist contrasts markedly with the high-grade (amphibolite, garnet-amphibolite, eclogite, with varying degrees of blueschist overprint) coherent sheets that locally make up the structurally highest and oldest units in the Franciscan and have the same metamorphic ages and metamorphic assemblages as blocks-in-mélange (commonly referred to as "high-grade blocks") (e.g., Ernst et al., 1970; Raymond, 1973; Suppe and Foland, 1978; Wakabayashi et al., 2010; Wakabayashi, 2015). Peak metamorphic ages of the high-grade Franciscan rocks, that are interpreted to reflect subduction and accretion range from about 155 to 176 Ma (Ross and Sharp, 1988; Ancziewicz et al., 2004; Wakabayashi and Dumitru 2007; Mulcahy et al., 2018; Rutte et al., 2020). The coherent high-grade sheets crop out over a distance of 330 km along the eastern margin of the Coast Ranges (Goat Mtn at the northern limit and "csch (S)" the southern limit on **Figure 1**, but "Ward Creek csch (S)" for the southern limit on **Figure 3**), and possibly 500 km if a structurally high amphibolite body in the Stanley Mtn window of the Nacimiento Belt is a coherent slab instead of a block-in-mélange (Brown, 1968) ("SMcsch(S)" on **Figures 1**, **3**). These sheets are small (all but two <2 km in long dimension, with thicknesses of hundreds of m) and rare (widely scattered). If the Stanley Mtn window exposure is such a slab then the restored along-strike distance of high-grade slab outcrops is about 800 km, whereas without the Stanley Mtn area exposure, whereas the other restored outcrops span an along strike distance of about 350 km (**Figure 3**).

The Marin Headlands terrane, a unit rich in basalt and chert that includes the oldest oceanic crust preserved in Franciscan units (e.g., Murchey and Jones, 1984) currently extends a distance of about 220 km, and this distance is increased to 420 km with restoration of post-subduction faulting ("MH(N)" and "MH(S)" on **Figures 1**, **3**). The remnants of the Marin Headlands terrane do not form a continuous belt of outcrops whereas they are more voluminous and less scattered than the high-grade coherent sheets; locally the unit attains a maximum structural thickness of about 2.5 km (Wahrhaftig, 1984).

Some units, such as the limestone-bearing, basalt-rich Permanente terrane (Blake et al., 1984; McLaughlin et al., 1996) are reduced in outcrop length by restoration ("P(N)" and "P(S)" on **Figures 1**, **3**). The current outcrop length of Permanente terrane is 260 km, and this collapses to about 110 km with restoration of dextral faults; the Permanente terrane forms a fairly continuous belt of exposures with a structural thickness of up to about 3 km (Wakabayashi, 2015; Wakabayashi, 2021a).

The Skaggs Springs, a completely recrystallized (in most exposures) glaucophane-lawsonite-quartz metaclastic schist (Wakabayashi, 1999) that has yielded phengite Ar-Ar ages of ca. 132 Ma (Wakabayashi and Dumitru, 2007), also forms a fairly continuous belt of exposures. This unit attains a structural thickness of up to 2 km (Wakabayashi, 2021a) and spans a

distance of 330 km currently, but only about 100 km with restoration of dextral faulting ("SSS" thin Dark blue unit between ~38.5 and 39°N and parts of very small remnants between ~36.5 and 37°N on **Figure 1**).

Whereas the Permanente terrane limestones and Laytonville limestone of the Franciscan are of approximately the same age (e.g, Sliter, 1984; Sliter and McGann, 1992), their paleolatitude of deposition in the open ocean differs with the Permanente terrane limestones apparently having formed north of the equator (Tarduno et al., 1985), whereas the Laytonville limestone ("L(N)" and "L(S)" on **Figures 1**, **3**) formed south of the equator (Alvarez et al., 1980; Tarduno et al., 1990). It may be potentially useful, however, to examine the along strike extent of these units collectively as they reflect accretion of possible oceanic highs (seamounts, oceanic plateau) of about the same age. They crop out over a distance of 500 km currently and 670 km with dextral faulting restored (From "L(N)" to "P(S)" on **Figures 1**, **3**).

Note that whereas the Franciscan is well known for its high-pressure/low-temperature blueschist facies and lawsonite-albite facies metamorphic rocks (e.g., Ernst 1970; 1975), some restored reaches lack such rocks (**Figure 3**). Schistose blueschist facies units of regional extent, the Skaggs Springs schist and the South Fork Mtn. schist are absent over larger reaches of the restored subduction complex.

As noted previously, the low-angle regional contacts between various Franciscan units are unaffected by restoration of post-subduction dextral faulting. Because of this, the general pattern of accretionary ages that young structurally downward (Ernst et al., 2009; Dumitru et al., 2010; Snow et al., 2010; Wakabayashi, 2015; Wakabayashi, 2021b) is also unchanged by restoration of post-subduction faulting.

DISCUSSION: TIME AND SPACE VARIATIONS IN ACCRETION, NON-ACCRETION, SUBDUCTION EROSION RECORDED BY FRANCISCAN COMPLEX ROCKS

Unaffected by Restoration of San Andreas Fault System Slip: Distinct Segments Recording Low-Angle Subduction and Subduction Erosion

FEART_feart-2022-818171_wc_f1The most significant along-strike variation in the Franciscan and related rocks, the distance between subduction complex units and coeval arc plutons, is not impacted by restoration of post-subduction dextral slip. The distance between Franciscan units and coeval arc plutons is especially short adjacent to the Klamath Mtns and to the south (Transverse Ranges and southward) and it associated with correlative inboard tectonic windows of high-pressure metamorphic rocks (Chapman et al., 2016; Chapman et al., 2021) (**Figures 1**, **3**). These relationships reflect low-angle subduction and subduction erosion that took place at ca. 121 Ma to the north (Chapman et al., 2021) and ca. 80–70 Ma to the south (Chapman et al., 2016) with about 800 km between the two reaches (**Figures 1**, **3**). The length of subduction zone associated with the southern subduction erosion reach may be estimated by the 500 km along-strike extent of the restored position of the tectonic windows (Chapman et al., 2016; note the southernmost windows restore well south of the limit of **Figure 3**). The length of the northern reach that accommodated subduction erosion is difficult to evaluate because only one tectonic window into subduction complex rocks has been found; it is possible that other tectonic windows are buried beneath Cenozoic volcanic rocks of the Cascade arc (Chapman et al., 2021).

In addition to the different time of subduction and metamorphism for the two apparent low-angle subduction segments, there are other differences in spatial relationships and metamorphism that may reflect different tectonic mechanisms. The South Fork Mtn. schist is about 75 km across-strike from the correlative inner Condrey Mtn schist unit. By comparison, the most proximal windows of the Schist de Salinas-Rand and related schists are about 40 km from the correlative outboard subduction complex rocks. The blueschist and greenschist facies metamorphism of the outboard South Fork Mtn schist and related units is reasonably similar to the blueschist and greenschist facies metamorphism of the Inner Condrey Mtn schist (Chapman et al., 2021). In contrast, the outboard (Nacimiento Belt), zeolite, prehnite-pumpellyite, and lawsonite-albite rocks have correlative rocks in various windows metamorphosed at amphibolite grade (Chapman et al., 2016).

Partly Dependent on Reconstruction: Variations in Accretion History Along Strike

Although accretion took place along both the northern and southern reaches described above, beginning with the rocks now exposed in the windows and including rocks structurally below outboard correlatives, these reaches of the paleosubduction system record net subduction erosion in contrast to the net accretion of the 800 km reach between that records sporadic accretion from ca. 175 Ma to 12 Ma (McLaughlin et al., 1998; Mulcahy et al., 2014; Wakabayashi, 2015; 2021a). Non-accretion is recorded by gaps in time of accretion between adjacent units (Dumitru et al., 2010; Wakabayashi 2021a). The reach of net accretion includes at least one horizon that records prolonged non-accretion of tens of My (Dumitru et al., 2010), but without net subduction erosion, owing to the preservation of the rare high-grade sheets above this horizon that are interpreted to have had limited original structural thickness (≤500 m) (Wakabayashi, 2015). Other horizons may reflect varying periods of non-accretion and the possibility of subduction erosion of previously accreted material (Wakabayashi, 2015; Wakabayashi, 2021a).

Details of accretion, accretion history, and possibly exhumation are reflected in the smaller-scale differences between the subduction complex tectonic stack at various positions along the restored paleo convergent margin (**Figures 3**, **4**). These differences reflect the fact that no accreted unit has

been preserved along the entire length of the restored subduction complex, including high-pressure metamorphic units.

Whereas no unit accreted or was preserved from along the entire length of the subduction complex, some accreted along distances of several hundred km. The most extensive such unit is the 80–82 Ma Type E unit of (Dumitru et al., 2016) that accreted over a strike length of about 830 km (restored length) (**Figure 3**). Such a strike length apparently reflects a long distance of trench-parallel clastic sediment transport (Dumitru et al., 2016). This unit is the most extreme example of other Franciscan units (all of which contain clastic components) of hundreds of km in along-strike extent, illustrating that detrital zircon age populations of subduction complex rocks are poor piercing points for estimating along-strike post-depositional tectonic transport. The Franciscan units with this detrital zircon age population appear to represent trench deposition and accretion at ca. 80–82 Ma, whereas forearc basin (Great Valley Group and correlatives) rocks with this detrital zircon age population appear to represent two separate depositional events (80–82 Ma and 71–75 Ma) (Surpless, 2015; Dumitru et al., 2016). Taken collectively, the Great Valley Group and correlative rocks and Franciscan rocks with this detrital zircon age population crop out over an along-strike distance of about 1,130 km (restored; present distance is about 860 km). Along strike distances between zircon sources and deposits may be further increased if fluvial or aeolian transport of zircon-bearing sediment had a significant along-strike component; the additional along-strike distance between zircon sources and deposits may exceed 500 km (e.g., Dumitru et al., 2013; 2016).

Cross-Sectional Relationships

The deeper parts of the cross sections of **Figures 2**, **4** are speculative owing to the comparative lack of subsurface information. Whereas the low-angle nature of regional contacts and steep local dips, apparent in present-day map-view contact geometry, is retained in the restored relationships, the deeper subsurface geology is poorly constrained. For those sections in the net accreting reach of the paleo subduction system (**Figures 4B–E**), the deeper subsurface interpretations are based partly on seismic and potential field data interpretations of Godfrey et al. (1997), as well as interpretations presented in Wakabayashi and Unruh (1995) and Wakabayashi (2015).

The sections with the inboard tectonic windows associated with net tectonic erosion (**Figures 4A,F,G**) present particularly daunting cross-sectional reference frame issues associated with the apparent steepening of subduction dip that took place after the subduction erosion events. This steepening of subduction dip was reflected by the westward migration of arc magmatism to a position similar to where it was prior to shut off of Sierra Nevada arc magmatism associated with the shallow slab/subduction erosion event (Busby et al., 2008). The steepening dip of the subducting slab resulted in a large vertical distance between inboard accreted units and the position of the subducted slab. Whereas an alternative is to fill this volume with accreted material, this is an immense thickness of accreted material (>50 km) and this is well in excess of the structural thickness of any exhumed subduction complex exposed in orogenic belts of the world. Steepening of slab dip is essentially slab rollback and this may have resulted in the trenchward flow of upper plate mantle beneath previously-accreted rocks of the tectonic windows. However, no examples exist in orogenic belts of large slabs of mantle (kms to tens of km thick) structurally intermediate between subduction complex rocks or below subduction complex rocks. On the other hand, such mantle material beneath subduction complexes may not have been exhumed in any of the world's orogenic belts and the density of such mantle material may preclude exhumation.

In an attempt to address the structural-tectonic condundrum posed above, I have tentatively proposed arc-vergent thrusting, associated with "tectonic wedging", as has been interpreted for the net-accretionary reach in the past (Wentworth et al., 1984; Unruh et al., 1991: Wakabayashi and Unruh, 1995), for the northern window (Condrey Mtn. schist inner unit) (**Figure 4A**). This east-vergent thrusting is interpreted to have taken place after syn-subduction extensional exhumation of the tectonic windows, similar to the scenario for the net-accretionary reaches as proposed by Wakabayashi and Unruh (1995). A potential problem with the tectonic wedging mechanism for the northern tectonic window is that it requires a far greater amount of shortening than that proposed for the net accretionary reach (**Figure 4A** compared to **Figures 4B–E**). Some researchers argued against the presence of syn-subduction tectonic wedge structures along the net accretionary reach (e.g., Costenius et al., 2000; Dickinson, 2002), whereas seismically-active tectonic wedge structures are not disputed (e.g., Wentworth et al., 1984; Namson and Davis, 1988; Unruh and Moores, 1992) (**Figure 2**).

The potential amount of shortening associated with hypothetical wedge structures would be even greater for the southern California tectonic windows (**Figures 4F,G**) that would require hundreds of km of shortening by tectonic wedging to place the most inboard windows (east of those shown in the cross sections) on the upper plate of such a thrust system. Accordingly, a compromise solution was attempted for the southern California cross sections that interprets significant accretion (30 km thick) before steepening of the slab and flow of mantle westward. This is a far higher rate of accretion than any exposed Franciscan section, so this may be unrealistic. Thus, the tentative cross sectional interpretations presented for the tectonic window reaches (**Figures 4A,F,G**) should be considered speculative, likely unrealistic, and they point to the need for detailed subsurface (seismic and potential field) data.

CONCLUSION

The Franciscan subduction complex exhibits significant along-strike variation, reflecting along-strike differences in the history of accretion, non-accretion, and subduction erosion, and likely slab dip. This along-strike difference is apparent, whether examining present-day relationships or those with post-subduction dextral faulting restored. Whereas different models have been presented for the distribution of post-subduction dextral slip, the use of these models to restore dextral slip has a minimal impact on the apparent along-strike variation in subduction complex rocks.

DATA AVAILABILITY STATEMENT

The original contributions presented in the study are included in the article/Supplementary Material, further inquiries can be directed to the corresponding author.

AUTHOR CONTRIBUTIONS

JW conducted the research and wrote the paper.

FUNDING

Some of the foundational research for this paper was supported by National Science Foundation Grants EAR-0635767, EAR-0948676, EAR-1032156.

ACKNOWLEDGMENTS

I thank reviewers for their thorough and thoughtful comments on the manuscript.

REFERENCES

Alvarez, W., Kent, D. V., Premoli Silva, I., Schweickert, R. A., and Larson, R. A. (1980). Franciscan Complex limestone Deposited at 17° South Paleolatitude. *Geol. Soc. America Bull.* 91, 476–484. doi:10.1130/0016-7606(1980)91<476:fcldas>2.0.co;2

Anczkiewicz, R., Platt, J. P., Thirlwall, M. F., and Wakabayashi, J. (2004). Franciscan Subduction off to a Slow Start: Evidence from High-Precision Lu-Hf Garnet Ages on High Grade-Blocks. *Earth Planet. Sci. Lett.* 225, 147–161. doi:10.1016/j.epsl.2004.06.003

Apen, F., Wakabayashi, J., Day, H., Roeske, S., Souders, A. K., and Dumitru, T. (2021). Regional-scale Correlations of Accreted Units in the Franciscan Complex: A Record of Long-Lived, Episodic Subduction Accretion. *Geol. Soc. America* 552. doi:10.1130/2021.2552(11)

Argus, D. F., and Gordon, R. G. (1991). Current Sierra Nevada-North America Motion from Very Long Baseline interferometry:Implications for the Kinematics of the Western United States. *Geol* 19, 1085–1088. doi:10.1130/0091-7613(1991)019<1085:csnnam>2.3.co;2

Argus, D. F., and Gordon, R. G. (2001). Present Tectonic Motion across the Coast Ranges and San Andreas Fault System in central California. *Geol. Soc. America Bull.* 113, 1580–1592. doi:10.1130/0016-7606(2001)113<1580:ptmatc>2.0.co;2

Atwater, T. (1970). Implications of Plate Tectonics for the Cenozoic Tectonic Evolution of Western North America. *Geol. Soc. America Bull.* 81, 3513–3536. doi:10.1130/0016-7606(1970)81[3513:ioptft]2.0.co;2

Atwater, T., and Stock, J. (1998). Pacific-North America Plate Tectonics of the Neogene Southwestern United States: An Update. *Int. Geology. Rev.* 40, 375–402. doi:10.1080/00206819809465216

Aydin, A., and Page, B. M. (1984). Diverse Pliocene-Quaternary Tectonics in a Transform Environment, San Francisco Bay Region, California. *Geol. Soc. America Bull.* 95, 303–1317. doi:10.1130/0016-7606(1984)95<1303:dptiat>2.0.co;2

Berkland, J. O., Raymond, L. A., Kramer, J. C., Moores, E. M., and O'Day, M. (1972). What Is Franciscan. *Am. Assoc. Pet. Geologists Bull.* 56, 2295–2302. doi:10.1306/819a421a-16c5-11d7-8645000102c1865d

Blake, M. C., Jr., Graymer, R. W., and Jones, D. L. (2000). *Geologic Map and Database of Parts of Marin, San Francisco, Contra Costa, and Sonoma Counties*, 2337. California: U.S. Geological Survey Miscellaneous Field Studies Map MF.

Blake, M. C., Jr., Graymer, R. W., and Stamski, R. E. (2002). *Geologic Map and Map Database of Western Sonoma, Northernmost Marin and Southernmost Mendocino Counties*. California: US Geological Survey Miscellaneous Field Studies Map MF, 2402.

Blake, M. C., Jr., Howell, D. G., and Jayko, A. S. (1984). Tectonostratigraphic Terranes of the San Francisco Bay Region. *Soc. Econ. Paleontologists Mineralogists* 43, 5–22.

Blake, M. C., Jr., Howell, D. G., and Jones, D. L. (1982). *Preliminary Tectonostratigraphic Terrane Map of California*, U.S.A: Geological Survey Open File Report, 82–593.

Blake, M. C., Jr., Jayko, A. S., McLaughlin, R. J., and Underwood, M. B. (1988). "Metamorphic and Tectonic Evolution of the Franciscan Complex, Northern California," in *Metamorphism and Crustal Evolution of the Western United States*. Editor W. G. Ernst (Englewood Cliffs, New Jersey: Prentice-Hall. Rubey Volume VII), 1035–1060.

Brown, J. A.. (1968)*Thrust Contact Between Franciscan Group and Great Valley Sequence*. Northeast Santa Maria, CA: Ph.D. Dissertation, Los Angeles, University of Southern California, 234.

Busby, C. J., Hagan, J. C., Putirka, K., Pluhar, C. J., Gans, P. B., Wagner, D. L., et al. (2008). The Ancestral Cascades Arc: Cenozoic Evolution of the central Sierra Nevada (California) and the Birth of the New Plate boundaryThe Ancestral Cascades Arc: Implications for the Development of the Sierran Microplate and Tectonic Significance of High K2O Volcanism. *Geol. Soc. America Spec. Paper* 438, 331–378. doi:10.1130/2008.2438(12)

Chapman, A. D., Jacobson, C. E., Ernst, W. G., Grove, M., Dumitru, T., Hourigan, J., et al. (2016). Assembling the World's Type Shallow Subduction Complex: Detrital Zircon Geochronologic Constraints on the Origin of the Nacimiento Block, central California Coast Ranges. *Geosphere* 12, 533–557. doi:10.1130/GES01257.1

Chapman, A. D., Saleeby, J. B., Wood, D. J., Piasecki, A., Kidder, S., Ducea, M. N., et al. (2012). Late Cretaceous Gravitational Collapse of the Southern Sierra Nevada Batholith, California. *Geosphere* 8 (2), 314–341.doi:10.1130/GES00740.1

Chapman*, A. D., Yule, D., Schmidt, W., and LaMaskin, T. (2021). Middle Jurassic to Early Cretaceous Tectonic Evolution of the Western Klamath Mountains and Outboard Franciscan Assemblages, Northern California-southern Oregon, USA. *Geol. Soc. America Field Guide* 62, 73–130. doi:10.1130/2021.0062(04)

Clift, P., and Vannucchi, P. (2004). Controls on Tectonic Accretion versus Erosion in Subduction Zones: Implications for the Origin and Recycling of the continental Crust. *Rev. Geophys.* 42, RG2001. doi:10.1029/2003RG000127

Cloos, M., and Shreve, R. L. (1988a). Subduction-channel Model of Prism Accretion, Melange Formation, Sediment Subduction, and Subduction Erosion at Convergent Plate Margins: 1. Background and Description. *Pageoph* 128, 455–500. doi:10.1007/bf00874548

Cloos, M., and Shreve, R. L. (1988b). Subduction-channel Model of Prism Accretion, Melange Formation, Sediment Subduction, and Subduction Erosion at Convergent Plate Margins: 2. Implications and Discussion. *Pageoph* 128, 501–545. doi:10.1007/bf00874549

Costenius, K. N., Johnson, R. A., Dickinson, W. R., and Williams, T. A. (2000). Tectonic Evolution of the Jurassic-Cretaceous Great Valley Forearc, California: Implications for the Franciscan Thrust-Wedge Hypothesis. *Geol. Soc. America Bull.* 112, 1703–1723. doi:10.1130/0016-7606(2000)112<1703:TEOTJC>2.0.CO;2

Dickinson, W. R., Ojakangas, R. W., and Stewart, R. J. (1969). Burial Metamorphism of the Late Mesozoic Great Valley Sequence, Cache Creek, California. *Geol. Soc. America Bull.* 80, 519–526. doi:10.1130/0016-7606(1969)80[519:bmotlm]2.0.co;2

Dickinson, W. R. (2002). Reappraisal of Hypothetical Franciscan Thrust Wedging at Coalinga: Implications for Tectonic Relations along the Great Valley Flank of the California Coast Ranges. *Tectonics* 21, 1039. doi:10.1029/2001/TC00131510.1029/2001tc001315

Dickinson, W. R. (1970). Relations of Andesites, Granites, and Derivative Sandstones to Arc-Trench Tectonics. *Rev. Geophys.* 8, 813–860. doi:10.1029/rg008i004p00813

Dumitru, T. A. (1989). Constraints on Uplift in the Franciscan Subduction Complex from Apatite Fission Track Analysis. *Tectonics* 8, 197–220. doi:10.1029/tc008i002p00197

Dumitru, T. A., Elder, W. P., Hourigan, J. K., Chapman, A. D., Graham, S. A., and Wakabayashi, J. (2016). Four Cordilleran Paleorivers that Connected Sevier

Thrust Zones in Idaho to Depocenters in California, Washington, Wyoming, and, Indirectly, Alaska. *Geology* 44, 75–78. doi:10.1130/g37286.1

Dumitru, T. A., Ernst, W. G., Hourigan, J. K., and McLaughlin, R. J. (2015). Detrital Zircon U-Pb Reconnaissance of the Franciscan Subduction Complex in Northwestern California. *Int. Geology. Rev.* 57, 767–800. doi:10.1080/00206814.2015.1008060

Dumitru, T. A., Ernst, W. G., Wright, J. E., Wooden, J. L., Wells, R. E., Farmer, L. P., et al. (2013). Eocene Extension in Idaho Generated Massive Sediment Floods into the Franciscan Trench and into the Tyee, Great Valley, and Green River Basins. *Green. River Basins: Geology.* 41, 187–190. doi:10.1130/G33746.1

Dumitru, T. A., Hourigan, J. K., Elder, W. P., Ernst, W. G., and Joesten, R. (2018). New, Much Younger Ages for the Yolla Bolly Terrane and a Revised Time Line for Accretion in the Franciscan Subduction Complex, California, *Geol. Soc. America Spec. Paper* 540, 339–366. doi:10.1130/2018.2540(15)

Dumitru, T. A. (1988). Subnormal Geothermal Gradients in the Great Valley Forearc basin, California, during Franciscan Subduction: A Fission Track Study. *Tectonics* 7, 1201–1221. doi:10.1029/tc007i006p01201

Dumitru, T. A., Wakabayashi, J., Wright, J. E., and Wooden, J. L. (2010). Early Cretaceous Transition from Nonaccretionary Behavior to Strongly Accretionary Behavior within the Franciscan Subduction Complex. *Tectonics* 29, a–n. doi:10.1029/2009TC002542

Ernst, W. G. (2017). Geologic Evolution of a Cretaceous Tectonometamorphic Unit in the Franciscan Complex, Western California. *Int. Geology. Rev.* 59, 563–576. doi:10.1080/00206814.2016.1201440

Ernst, W. G., Martens, U., and Valencia, V. (2009). U-pb Ages of Detrital Zircons in Pacheco Pass Metagraywackes: Sierran-Klamath Source of Mid-cretaceous and Late Cretaceous Franciscan Deposition and Underplating. *Tectonics* 28, TC6011. doi:10.2019/2008TC00235210.1029/2008tc002352

Ernst, W. G., and McLaughlin, R. J. (2012). Mineral Parageneses, Regional Architecture, and Tectonic Evolution of Franciscan Metagraywackes, Cape Mendocino-Garberville-Covelo 30′ × 60′ Quadrangles, Northwest California. *Tectonics* 31, a–n. doi:10.1029/2011TC002987

Ernst, W. G. (1993). Metamorphism of Franciscan Tectonostratigraphic Assemblage, Pacheco Pass Area, East-central Diablo Range, California Coast Ranges. *Geol. Soc. America Bull.* 105, 618–636. doi:10.1130/0016-7606(1993)105<0618:moftap>2.3.co;2

Ernst, W. G., Seki, Y., Onuki, H., and Gilbert, M. C. (1970). Comparative Study of Low-Grade Metamorphism in the California Coast Ranges and the Outer Metamorphic belt of Japan. *Geol. Soc. America Memoir* 124, 276.

Ernst, W. G. (1975). Systematics of Large-Scale Tectonics and Age Progressions in Alpine and Circum-Pacific Blueschist Belts. *Tectonophysics* 26, 229–246. doi:10.1016/0040-1951(75)90092-x

Ernst, W. G. (1970). Tectonic Contact between the Franciscan Mélange and the Great Valley Sequence-Crustal Expression of a Late Mesozoic Benioff Zone. *J. Geophys. Res.* 75, 886–901. doi:10.1029/jb075i005p00886

Evarts, R. C., and Schiffman, P. (1983). Submarine Hydrothermal Metamorphism of the Del Puerto Ophiolite, California. *Am. J. Sci.* 283, 289–340. doi:10.2475/ajs.283.4.289

Furlong, K. P. (1984). Lithospheric Behavior with Triple junction Migration: An Example Based on the Mendocino Triple junction. *Phys. Earth Planet. Interiors* 36, 213–223. doi:10.1016/0031-9201(84)90047-5

Godfrey, N. J., Beaudoin, B. C., and Klemperer, S. L. (1997). Ophiolitic Basement to the Great Valley Forearc basin, California, from Seismic and Gravity Data: Implications for Crustal Growth at the North American continental Margin. *Geol. Soc. America Bull.* 108 (12), 1536–2156. doi:10.1130/0016-7606(1997)109<1536:OBTTGV>2.3.CO;2

Hall, C. A., Jr. (1991). Geology of the Point Sur-Lopez Point Region, Coast Ranges, California: A Part of the Southern California Allochthon. *Geol. Soc. America Spec. Paper* 266, 40.

Hamilton, W. (1969). Mesozoic California and the Underflow of Pacific Mantle. *Geol. Soc. America Bull.* 80, 2409–2430. doi:10.1130/0016-7606(1969)80[2409:mcatuo]2.0.co;2

Harms, T. A., Jayko, A. S., and Blake, M. C., Jr. (1992). Kinematic Evidence for Extensional Unroofing of the Franciscan Complex along the Coast Range Fault, Northern Diablo Range, California. *Tectonics* 11, 228–241. doi:10.1029/91tc01880

Hatem, A. E., and Dolan, J. F. (2018). A Model for the Initiation, Evolution, and Controls on Seismic Behavior of the Garlock Fault, California. *Geochem. Geophys. Geosyst.* 19, 2166–2178. doi:10.1029/2017gc007349

Hopson, C. A., Mattinson, J. M., and Pessagno, E. A., Jr. (1981). "Coast Range Ophiolite, Western California," in *Geotectonic Development of California. Rubey*. (Englewood Cliffs, New Jersey: Prentice-Hall), Volume I 418–510.

Hopson, C. A., Mattinson, J. M., Pessagno, E. A., Jr., and Luyendyk, B. P. (2008). California Coast Range Ophiolite: Composite Middle and Late Jurassic Oceanic Lithosphere. *Geol. Soc. America Spec. Paper* 483, 1–101. doi:10.1130/2008.2438(01)

Jayko, A. S., Blake, M. C., Jr., and Harms, T. (1987). Attenuation of the Coast Range Ophiolite by Extensional Faulting, and Nature of the Coast Range "Thrust," California. *Tectonics* 6, 475–488. doi:10.1029/tc006i004p00475

Kuiper, Y. D., and Wakabayashi, J. (2018). A Comparison between Mid-paleozoic New England, USA, and the Modern Western USA: Subduction of an Oceanic ridge-transform Fault System. *Tectonophysics* 745, 278–292. doi:10.1016/j.tecto.2018.08.020

Langenheim, V. E., Jachens, R. C., Wentworth, C. M., and McLaughlin, R. J. (2013). Previously Unrecognized Regional Structure of the Coastal Belt of the Franciscan Complex, Northern California, Revealed by Magnetic Data. *Geosphere* 9 (6), 1514–1529. doi:10.1130/GES00942.1

Liu, M., and Furlong, K. P. (1992). Cenozoic Volcanism in the California Coast Ranges: Numerical Solutions. *J. Geophys. Res.* 97, 4941–4951. doi:10.1029/92jb00193

Maxwell, J. C. (1974). Anatomy of an Orogen. *Geol. Soc. America Bull.* 85, 1195–1204. doi:10.1130/0016-7606(1974)85<1195:aoao>2.0.co;2

McLaughlin, R. J., Blake, M. C., Jr., Griscom, A., Blome, C. D., and Murchey, B. (1988). Tectonics of Formation, Translation, and Dispersal of the Coast Range Ophiolite of California. *Tectonics* 7, 1033–1056. doi:10.1029/tc007i005p01033

McLaughlin, R. J., Kling, S. A., Poore, R. Z., McDougall, K., and Beutner, E. C. (1982). Post-middle Miocene Accretion of Franciscan Rocks, Northwestern California. *Geol. Soc. America Bull.* 93, 595–605. doi:10.1130/0016-7606(1982)93<595:pmaofr>2.0.co;2

McLaughlin, R. J., Sliter, W. V., Sorg, D. H., Russell, P. C., and Sarna-Wojcicki, A. M. (1996). Large-scale Right-Slip Displacement on the East San Francisco Bay Region Fault System, California: Implications for Location of Late Miocene to Pliocene Pacific Plate Boundary. *Tectonics* 15, 1–18. doi:10.1029/95tc02347

Metzger, E. P., Ernst, W. G., and Sorg, D. (2005). Aluminous Xenoliths in Miocene Andesite, Central California Coast Ranges: Magma-Crust Interaction in a Subduction-Transform Transitional Setting. *Int. Geology. Rev.* 47, 573–590. doi:10.2747/0020-6814.47.6.573

Mulcahy, S. R., Starnes, J. K., Day, H. W., Coble, M. A., and Vervoort, J. D. (2018). Early Onset of Franciscan Subduction. *Tectonics* 37, 1194–1209. doi:10.1029/2017TC004753

Mulcahy, S. R., Vervoort, J. D., and Renne, P. R. (2014). Dating Subduction-Zone Metamorphism with Combined Garnet and Lawsonite Lu-Hf Geochronology. *J. Meta. Geol.* 32, 515–533. doi:10.1111/jmg.12092

Murchey, B. M., and Jones, D. L. (1984). Age and Significance of Chert in the Franciscan Complex of the San Francisco Bay Region. Franciscan Geology of Northern California. *Pac. Section Soc. Econ. Paleontologists Mineralogists (Sepm)* 43, 23–30.

Namsom, J. S., and Davis, T. L. (1988). Seismically Active Fold and Thrust belt in the San Joaquin Valley, California. *Geol. Soc. America Bull.* 100, 257–273. doi:10.1130/0016-7606(1988)100<0257:SAFATB>2.3.CO;2

Page, B. M. (1981). "The Southern Coast Ranges," in *The Geotectonic Development of California, Rubey Volume I*. Editor W. G. Ernst (Englewood Cliffs, New Jersey: Prentice-Hall), 329–417.

Platt, J. P. (1986). Dynamics of Orogenic Wedges and the Uplift of High-Pressure Metamorphic Rocks. *Geol. Soc. America Bull.* 97, 1037–1053. doi:10.1130/0016-7606(1986)97<1037:doowat>2.0.co;2

Powell, R. E. (1993). Chapter 1: Balanced Palinspastic Reconstruction of Pre-late Cenozoic Paleogeology, Southern California: Geologic and Kinematic Constraints on Evolution of the San Andreas Fault System. *Geol. Soc. America Memoir* 178, 1–106. doi:10.1130/mem178-p1

Raymond, L. A., and Bero, D. A. (2015). Sandstone-matrix Mélanges, Architectural Subdivision, and Geologic History of Accretionary Complexes: A Sedimentological and Structural Perspective from the Franciscan Complex

of Sonoma and Marin Counties, California, USA. *Geosphere* 11, 1077–1110. doi:10.1130/GES01137.1

Raymond, L. A. (2015). Designating Tectonostratigraphic Terranesversusmapping Rock Units in Subduction Complexes: Perspectives from the Franciscan Complex of California, USA. *Int. Geology. Rev.* 57, 801–823. doi:10.1080/00206814.2014.911124

Raymond, L. A. (1973). *Franciscan Geology of the Mount Oso Area*. CaliforniaDavis: University of California, 180. Ph.D. dissertation.

Raymond, L. A., Ogawa, Y., and Maddock, M. E. (2019). Accretionary Unit Formats in Subduction Complexes: Examples from the Miura-Bosa and Franciscan Complexes. *Int. Geology. Rev.* 62, 1581–1609. doi:10.1080/00206814.2019.1667881

Raymond, L. A. (2018). What Is Franciscan?: Revisited. *Int. Geology. Rev.* 60, 1968–2030. doi:10.1080/00206814.2017.1396933

Ring, U., and Brandon, M. T. (1994). Kinematic Data for the Coast Range Fault and Implications for Exhumation of the Franciscan Subduction Complex. *Geol* 22, 735–738. doi:10.1130/0091-7613(1994)022<0735:kdftcr>2.3.co;2

Ring, U. (2008). *Deformation and Exhumation at Convergent Margins: The Franciscan Subduction Complex*. Boulder, CO: Geological Society of America Special Paper 445, 61.

Ross, J. A., and Sharp, W. D. (1988) The Effects of Sub-Blocking Temperature Metamorphism on the K/Ar Systematics of Hornblendes: 40Ar/39Ar Dating of Polymetamorphic Garnet Amphibolite From the Franciscan Complex, California, *Contributions to Mineralogy and Petrology*. 100, 213–221

Rutte, D., Garber, J., Kylander-Clark, A., and Renne, P. R. (2020) An Exhumation Pulse From the Nascent Franciscan Subduction Zone (California, USA), *Tectonics*. 39 (10), e2020TC006305. doi:10.1029/2020TC006305

Schmidt, W. L., and Platt, J. P. (2018) Subduction, Accretion, and Exhumation of Coherent Franciscan Blueschist-Facies Rocks, Northern Coast Ranges, California, *Lithosphere*. 10, 301–326. doi:10.1130/l697.1

Sliter, R. V., and McGann, M. L. (1992). *Age and Correlation of the Calera Limestone in the Permanente Terrane of Northern California: U.S.* Washington, D.C: United States Government Printing Office, 27p.

Sliter, W. V. (1984). "Foraminifers from Cretaceous limestone of the Franciscan Complex, Northern California, *Pac. Section Soc. Econ. Paleontologists Mineral.* 43, 5–22.

Snow, C. A., Wakabayashi, J., Ernst, W. G., and Wooden, J. L. (2010). Detrital Zircon Evidence for Progressive Underthrusting in Franciscan Metagraywackes, West-central California. *Geol. Soc. America Bull.* 122, 282–291. doi:10.1130/b26399.1

Stimac, J. A. (1993). The Origin and Significance of High-Grade Metamorphic Xenoliths, Clear Lake Volcanics, California. *Soc. Econ. Paleontologists Mineralogists Guidebook* 16, 171–189.

Suppe, J., and Foland, K. A. (1978). "The Goat Mountain Schists and Pacific Ridge Complex: A Redeformed but Still-Intact Late Mesozoic Franciscan Schuppen Complex," in *Mesozoic Paleogeography of the Western United States. Pacific Coast Paleogeography Symposium 2*. Editors D. G. Howell and K. A. McDougall (Los Angeles, California: Society of Economic Paleontologists and Mineralogists, Pacific Section), 431–451.

Suppe, J. (1973). *Geology of the Leech Lake Mountain-Ball Mountain Region*, California. University of California Publications Geological Sciences, 107, 1–81.

Surpless, K. D. (2015). Hornbrook Formation, Oregon and California: A Sedimentary Record of the Late Cretaceous Sierran Magmatic Flare-Up Event. *Geosphere* 11, 1770–1789. doi:10.1130/GES01186.1

Tarduno, J. A., McWillams, M., and Sleep, N. (1990). Fast Instantaneous Oceanic Plate Velocities Recorded by the Cretaceous Laytonville limestone: Paleomagnetic Analysis and Kinematic Implications. *J. Geophys. Res.* 95, 15503–15527. doi:10.1029/jb095ib10p15503

Tarduno, J. A., McWilliams, M., Debiche, M. G., Sliter, W. V., and Blake, M. C., Jr. (1985). Franciscan Complex Calera Limestones: Accreted Remnants of Farallon Plate Oceanic Plateaus. *Nature* 317, 345–347. doi:10.1038/317345a0

Terabayashi, M., and Maruyama, S. (1998). Large Pressure Gap Between the Coastal and Central Belts, Northern and Central California. *Tectonophysics* 285, 87–101.

Unruh, J. R., Dumitru, T. A., and Sawyer, T. L. (2007). Coupling of Early Tertiary Extension in the Great Valley Forearc basin with Blueschist Exhumation in the Underlying Franciscan Accretionary Wedge at Mount Diablo, California. *Geol. Soc. America Bull.* 119, 1347–1367. doi:10.1130/b26057.1

Unruh, J. R., and Moores, E. M. (1992). Quaternary Blind Thrusting in the Southwestern Sacramento Valley, California. *Tectonics* 11, 192–203. doi:10.1029/91tc02494

Unruh, J. R., Ramirez, V. R., Phipps, S. P., and Moores, E. M. (1991). Tectonic Wedging beneath Forearc Basins: Ancient and Modern Examples from California and the Lesser Antilles. *GSA Today* 1, 185–190.

von Huene, R., and Scholl, D. W. (1991). Observations at Convergent Margins Concerning Sediment Subduction, Subduction Erosion, and the Growth of continental Crust. *Rev. Geophys.* 29, 279–316. doi:10.1029/91rg00969

von Huene, R. (1986). To Accrete or Not Accrete, that Is the Question. *Geol. Rundsch* 75, 1–15. doi:10.1007/bf01770175

Wahrhaftig, C. W. (1984). Structure of the Marin Headlands Block, California: A Progress Report. *Pac. Section Soc. Econ. Paleontologists Mineralogists (Sepm)* 43, 31–50.

Wakabayashi, J. (2015). Anatomy of a Subduction Complex: Architecture of the Franciscan Complex, California, at Multiple Length and Time Scales. *Int. Geology. Rev.* 57, 669–746. doi:10.1080/00206814.2014.998728

Wakabayashi, J. (1999). Distribution of Displacement on and Evolution of a Young Transform Fault System: The Northern San Andreas Fault System, California. *Tectonics* 18, 1245–1274. doi:10.1029/1999tc900049

Wakabayashi, J., and Dumitru, T. A. (2007). 40Ar/39Ar Ages from Coherent, High-Pressure Metamorphic Rocks of the Franciscan Complex, California: Revisiting the Timing of Metamorphism of the World's Type Subduction Complex. *Int. Geology. Rev.* 49, 873–906. doi:10.2747/0020-6814.49.10.873

Wakabayashi, J. (2021b). Field and Petrographic Reconnaissance of Franciscan Complex Rocks of Mount Diablo, California: Imbricated Ocean Floor Stratigraphy with a Roof Exhumation Fault System. *Geol. Soc. America Memoir* 217, 155–178. doi:10.1130/2021.1217(09)

Wakabayashi, J., Ghatak, A., and Basu, A. R. (2010). Suprasubduction-zone Ophiolite Generation, Emplacement, and Initiation of Subduction: A Perspective from Geochemistry, Metamorphism, Geochronology, and Regional Geology. *Geol. Soc. America Bull.* 122, 1548–1568. doi:10.1130/b30017.1

Wakabayashi, J., Hengesh, J. V., and Sawyer, T. L. (2004). Four-dimensional Transform Fault Processes: Progressive Evolution of Step-Overs and Bends. *Tectonophysics* 392, 279–301. doi:10.1016/j.tecto.2004.04.013

Wakabayashi, J. (2007). Stepovers that Migrate with Respect to Affected Deposits: Field Characteristics and Speculation on Some Details of Their Evolution. *Geol. Soc. Lond. Spec. Publications* 290, 169–188. doi:10.1144/sp290.4

Wakabayashi, J. (2021a). "Subduction and Exhumation Slip Accommodation at Depths of 10-80 Km Inferred from Field Geology of Exhumed Rocks: Evidence for Temporal-Spatial Localization of Slip, *Geol. Soc. America Spec. Paper* 552, 257–296. doi:10.1130/2021.2552(12)

Wakabayashi, J. (1996). Tectono-metamorphic Impact of a Subduction-Transform Transition and Implications for Interpretation of Orogenic Belts. *Int. Geology. Rev.* 38, 979–994. doi:10.1080/00206819709465376

Wakabayashi, J., and Unruh, J. R. (1995). Tectonic Wedging, Blueschist Metamorphism, and Exposure of Blueschists: Are They Compatible. *Geol* 23, 85–88. doi:10.1130/0091-7613(1995)023<0085:twbmae>2.3.co;2

Wentworth, C. M., Blake, M. C., Jr., Jones, D. L., Walter, A. W., and Zoback, M. D. (1984). Tectonic Wedging Associated with Emplacement of the Franciscan Assemblage, California Coast Ranges. *Soc. Econ. Paleontologists Mineralogists* 43, 163–173.

Worrall, D. M. (1981). Imbricate Low-Angle Faulting in Uppermost Franciscan Rocks, South Yolla Bolly Area, Northern California. *Geol. Soc. America Bull.* 92, 703–729. doi:10.1130/0016-7606(1981)92<703:ilfiuf>2.0.co;2

Conflict of Interest: The author declares that the research was conducted in the absence of any commercial or financial relationships that could be construed as a potential conflict of interest.

frontiers in Earth Science

ORIGINAL RESEARCH
published: 02 March 2022
doi: 10.3389/feart.2022.831526

Origin and Periodic Behavior of Short Duration Signals Recorded by Seismometers at Vestnesa Ridge, an Active Seepage Site on the West-Svalbard Continental Margin

P. Domel[1]*, *S. Singhroha*[1], *A. Plaza-Faverola*[1], *V. Schlindwein*[2,3], *H. Ramachandran*[1] and *S. Bünz*[1]

[1]CAGE—Centre for Arctic Gas Hydrate, Environment and Climate, Department of Geosciences, UiT The Arctic University of Norway, Tromsø, Norway, [2]Alfred Wegener Institute, Helmholtz Centre for Polar and Marine Research, Bremerhaven, Germany, [3]University of Bremen, Faculty of Geosciences, Bremen, Germany

OPEN ACCESS

Edited by:
Mourad Bezzeghoud, Universidade de Évora, Portugal

Reviewed by:
Kimihiro Mochizuki, The University of Tokyo, Japan
Christopher Schmidt, Helmholtz Association of German Research Centres (HZ), Germany

***Correspondence:**
P. Domel
przemyslaw.domel@uit.no

Specialty section:
This article was submitted to Solid Earth Geophysics, a section of the journal Frontiers in Earth Science

Received: *08 December 2021*
Accepted: *02 February 2022*
Published: *02 March 2022*

Citation:
Domel P, Singhroha S, Plaza-Faverola A, Schlindwein V, Ramachandran H and Bünz S (2022) Origin and Periodic Behavior of Short Duration Signals Recorded by Seismometers at Vestnesa Ridge, an Active Seepage Site on the West-Svalbard Continental Margin. Front. Earth Sci. 10:831526. doi: 10.3389/feart.2022.831526

Short duration events (SDEs) are reported worldwide from ocean-bottom seismometers (OBSs). Due to their high frequency (4–30 Hz) and short duration, they are commonly attributed to aseismic sources, such as fluid migration related processes from cold seeps, biological signals, or noise. We present the results of a passive seismic experiment that deployed an OBS network for 10-month (October 2015–July 2016) at an active seepage site on Vestnesa Ridge, West Svalbard continental margin. We characterize SDEs and their temporal occurrence using the conventional short-time-average over long-time-average approach. Signal periodograms show that SDEs have periodic patterns related to solar and lunar cycles. A monthly correlation between SDE occurrences and modelled tides for the area indicates that tides have a partial control on SDEs recorded over 10 months. The numbers of SDEs increase close to the tidal minima and maxima, although a correlation with tidal highs appears more robust. Large bursts of SDEs are separated by interim quiet cycles. In contrast, the periodicity analysis of tremors shows a different pattern, likely caused by the effect of tidally controlled underwater currents on the instrumentation. We suggest that SDEs at Vestnesa Ridge may be related to the dynamics of the methane seepage system which is characterized by a complex interaction between migration of deep sourced fluids, gas hydrate formation and seafloor gas advection through cracks. Our observation from this investigated area offshore west-Svalbard, is in line with the documentation of SDEs from other continental margins, where micro-seismicity and gas release into the water column are seemingly connected.

Keywords: ocean-bottom seismometer, micro-seismicity, short duration events, methane seepage, gas hydrates, tidal cycle

1 INTRODUCTION

Ocean-bottom seismometers (OBSs) are usually deployed in marine settings to investigate local seismicity of an area by monitoring earthquakes (e.g., Grevemeyer et al., 2015; Meier et al., 2021) or long-duration tremors (e.g., Monigle et al., 2009; Hsu et al., 2013; Franek et al., 2014).

In addition to earthquakes and tremors, OBSs often record signals commonly referred to as short duration events (SDEs) (e.g., Díaz et al., 2007; Tary et al., 2012; Franek et al., 2017). SDEs are characterized by a single pulse of a short (usually <1 s) duration with no discernible P and S phases, a relatively high (at least 4–30 Hz) frequency content, and a strong signal/noise ratio (Batsi et al., 2019). Although the general frequency range lies between 4–30 Hz, higher upper limits (reaching Nyquist frequency of the specific record—50 Hz), has been reported (Sgroi et al., 2014). Recorded SDEs also have variations in their signal characteristics, duration, periodicity and directionality, but similar types of signals have been recorded in different geological settings (Tary et al., 2012). The underlying mechanisms for variations in SDEs are not yet completely understood (e.g., Ugalde et al., 2019).

Recent experiments show the potential of using OBS recordings as a tool to study the long-term variability of the gas seepage and fluid movements through the analysis of SDEs (e.g., Franek et al., 2017; Batsi et al., 2019; Tsang-Hin-Sun et al., 2019). It is believed that there is a strong link between SDEs and fracture-controlled fluid migration. Laboratory experiments (Batsi et al., 2019), as well as several field studies (Sultan et al., 2011; Tary et al., 2012; Hsu et al., 2013; Embriaco et al., 2014; Franek et al., 2014; Liu et al., 2018; Ugalde et al., 2019), link SDEs in recorded signals to fluid movements in the subsurface.

Other existing and proposed origins of SDEs in marine environments include hydraulic fracturing and pressure transients in hydrothermal systems (Sohn et al., 1995; Bowman and Wilcock, 2013), pressure fluctuations in fluid pathways (Díaz et al., 2007), underwater currents (Chang et al., 2016; Ugalde et al., 2019), and fracture opening due to strong local earthquakes (Tsang-Hin-Sun et al., 2019). Some studies also hypothesize about biological sources of SDEs (e.g., fish and marine mammals) (Buskirk et al., 1981; Bowman and Wilcock, 2013; Batsi et al., 2019). In few cases, when SDE occurrences coincide with the initial stage of long-term experiments, mechanical coupling of the OBS at the sea bottom has been proposed as the source of SDEs (Ostrovsky, 1989).

The natural release of hydrocarbon gases from the seafloor at continental margins is widespread (e.g., Judd and Hovland, 2007; Römer et al., 2014; Mau et al., 2017). Factors such as changes in ice sheet thickness (Cremiere et al., 2016; Wallmann et al., 2018; Himmler et al., 2019), geological processes in the subsurface and local tectonic activity (Himmler et al., 2019; Plaza-Faverola and Keiding, 2019; Ciotoli et al., 2020), variations in the gas hydrate stability zone (Taylor et al., 2000; Crutchley et al., 2014; Mishra et al., 2020), changes in sea water temperature over geological times (Thomsen et al., 2012; Berndt et al., 2014; Cremiere et al., 2016) and sedimentation (Horozal et al., 2017; Karstens et al., 2018) create changes in seepage intensity and distribution over geological timescales (Etiope, 2015). Some studies attribute fluctuations in the seepage intensity to seasonal changes in the seawater temperature (Berndt et al., 2014; Embriaco et al., 2014; Ferré et al., 2020). Other studies link small diurnal-scale variations in gas seepage to tides (Boles et al., 2001; Hsu et al., 2013; Römer et al., 2016; Riedel et al., 2018; Sultan et al., 2020).

Seasonal and diurnal variations in the seepage activity have been primarily studied using backscattering from gas bubbles observed in sonar data (e.g., Veloso et al., 2015), direct *in-situ* observations using underwater cameras (e.g., Beccari et al., 2020; Di et al., 2020), and with sensors mounted at ocean-bottom observatories (e.g., Boles et al., 2001; Kvenvolden et al., 2001). Observations of the seepage periodicity using ship-mounted sonar data are dependent on the cruise time availability and therefore short-term and infrequent. Remotely operated vehicles (ROVs) for direct imaging are costly and not suitable for monitoring seepage activity for several hours. In contrast, long term OBS experiments can last more than a year and provide a continuous record of seismicity, allowing the investigation of the periodicity of SDE occurrences and their potential correlation to seepage activity.

In this study, we report on SDE occurrences in 10-month-long OBS recordings from an actively seeping pockmark on Vestnesa Ridge, a sedimentary ridge located offshore west-Svalbard. We study patterns of occurrence and intensity of SDEs in a deep marine Arctic geological setting and discuss their potential link with gas seepage dynamics.

1.1 Geological Setting

Vestnesa Ridge is a ca. 60 km long contourite drift located on west-Svalbard continental margin between North Atlantic mid-ocean ridge and Svalbard Archipelago (Eiken and Hinz, 1993; Howe et al., 2007; Hustoft et al., 2009) (**Figure 1A**). Molloy and Spitsbergen transform faults bound the ridge to the south and the north, respectively. The ridge consists of turbidites, hemipelagic and glaciomarine sediments (Eiken and Hinz, 1993; Ottesen et al., 2005) distributed along a northwest-southeast orientated eastern segment and an east-west orientated western segment (Vogt and Crane, 1994; Ritzmann et al., 2004; Plaza-Faverola et al., 2014).

Vestnesa Ridge hosts a broadly investigated gas hydrate system (Hustoft et al., 2009; Panieri et al., 2017; Pape et al., 2020; Plaza-Faverola et al., 2017). The presence of a bottom simulating reflection, a seismic boundary created by acoustic impedance contrast at the base of the gas hydrate stability zone (Shipley et al., 1979), establishes and constrains the gas hydrate system along the entire ridge (Bünz et al., 2012; Plaza-Faverola et al., 2017). Hydrocarbon gases seep through selected pockmarks in the eastern segment of the ridge (Bünz et al., 2012; Plaza-Faverola et al., 2015; Singhroha et al., 2019; Smith et al., 2014). Gas hydrate is not the main controller of the seepage at the site, however. Systems of faults and fractures control the underlying fluid migration pathways and chimneys, and thus, the distribution of pockmarks (**Figure 1C**) (Plaza-Faverola et al., 2015; Singhroha et al., 2019, 2020). The spatial and temporal distribution of seepage features along the sedimentary ridge has been linked to dynamic forcing from mid-ocean ridge spreading and from glacial isostatic rebound (Schneider et al., 2018; Himmler et al., 2019; Plaza-Faverola and Keiding, 2019). Studies based on sediment proxies suggest that there is a link

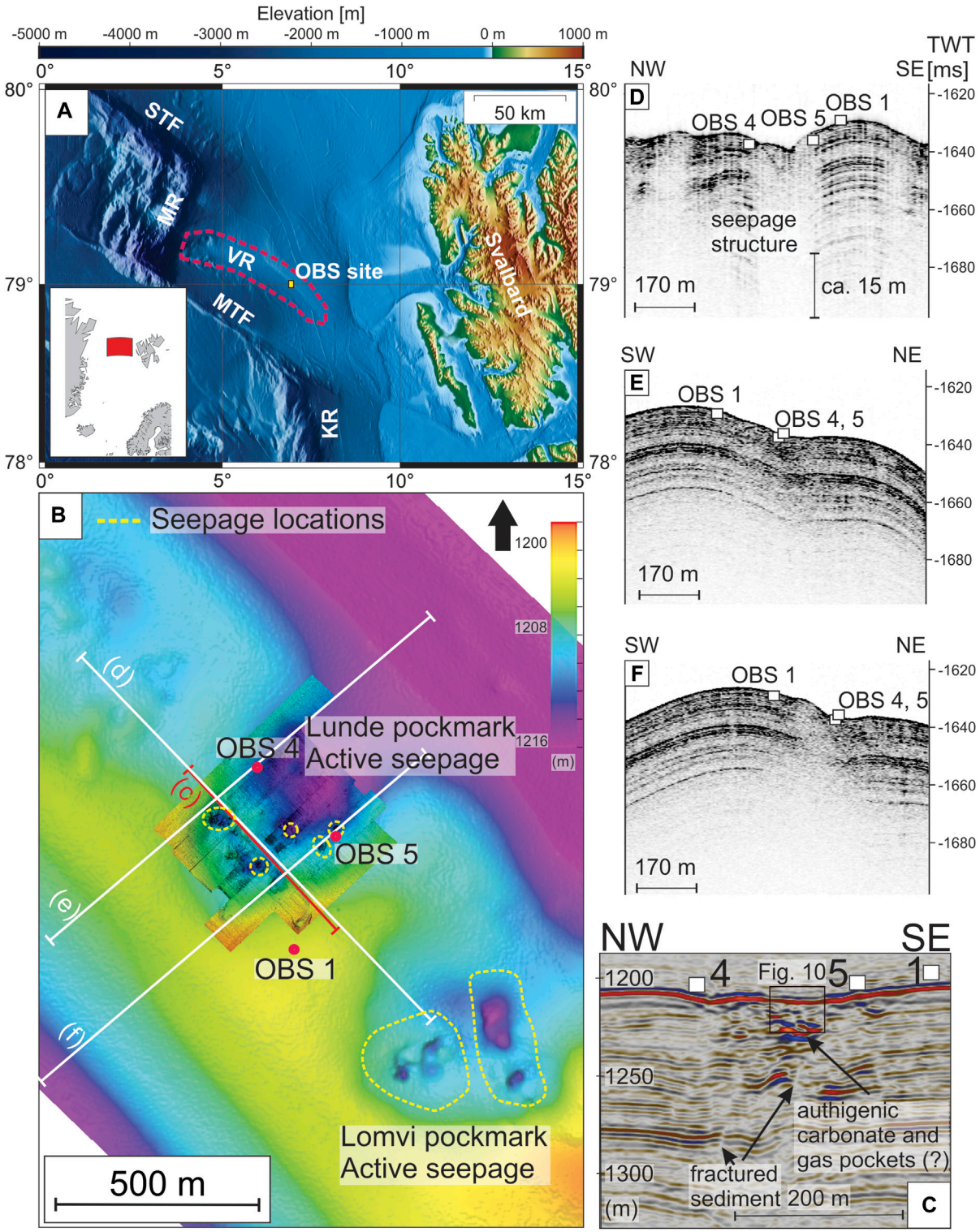

FIGURE 1 | (A) Regional map showing the study area. VR-Vestnesa Ridge, MR-Molloy Ridge, MTF—Molloy Transform Fault, STF—Spitsbergen Transform Fault and KR—Knipovich Ridge; **(B)** OBS deployment locations around Lunde pockmark, projected over the seafloor bathymetry from depth converted 3D seismic data (e.g., Singhroha et al., 2019), with the micro-bathymetry at the pockmark (Himmler et al., 2019; Hong et al., 2021); approximate seepage locations marked by yellow outlines; **(C)** Seismic transect highlighting the seepage structure beneath Lunde; **(D–F)** Sub-bottom profiles illustrating the location of the OBSs with respect to near-surface fluid migration features.

between seepage episodes and glacial cycles during the latest glaciations (Schneider et al., 2018; Himmler et al., 2019).

Annual multi-beam and single-beam sonar surveys show that acoustic flares in the water column (i.e., reaching heights of up to ~800 m) are restricted to the eastern Vestnesa Ridge segment (Bünz et al., 2012; Smith et al., 2014). The presence of seemingly dormant pockmarks on the ridge crest, especially towards the western segment, where there is no evidence of present-day advective seepage, suggests paleo-seepage at many locations along the ridge (Vogt and Crane, 1994; Petersen et al., 2010; Consolaro et al., 2015). Radio isotopic dating of authigenic carbonates extracted from shallow sediments shows three methane seepage episodes around ~160 to 133 ka, ~50 to 40 ka, and ~20 to 5 ka, that directly correspond to the episodes of glaciation and de-glaciation in the area (Himmler et al., 2019). Based on this information, it is suggested that glacial tectonics is one of the dominant forces driving the seepage on geological time scales.

Sonar data collected during numerous expeditions to the area show the presence of gas flares only from six pockmarks on the eastern side of the ridge (Smith et al., 2014). Pockmark Lunde is the one with the largest acoustic flare observed and it is in the near vicinity (<1 km) of another active pockmark (i.e., Lomvi (Panieri et al., 2017)). These pockmarks are ~300–400 m wide complex structures, containing both small-scale (<1 m) features and depressions up to 50 m in diameter (**Figure 1B**) that focus most of the seepage (Panieri et al., 2017). Diffusive gas release is likely to take place as well within the pockmarks, outside the pits. The presence of acoustic flares in the water column has been documented from three such pits at each pockmark (Panieri et al., 2017). Biological markers obtained from gravity cores indicate periodic variations in seepage on a scale of 1 ka years, possibly due to fault reactivation (Ambrose et al., 2015). Sampling of authigenic carbonate (Himmler et al., 2019) inside Lunde provided ground truth data for the widespread inference of past methane seepage events based on high resolution 3D seismic data (Plaza-Faverola et al., 2015).

2 DATA AND METHODS

2.1 Data

We deployed five LOBSTER type OBSs (Stähler et al., 2018) around the Lunde pockmark (**Figure 1**) to study the potential link between seismicity and seepage. Upon recovery of the OBSs we have lost one data unit to the sea and discovered that another unit has not recorded any data, leaving only 3 instruments for further study (OBSs 1, 4 and 5; **Figure 1**). The entire experiment lasted from October 2015 to July 2016. All OBSs were equipped with a three-component short-period seismometer (with 4.5 Hz corner frequency), and a hydrophone attached to the OBS frame at a ~0.5-m height from the sea bottom. Each seismometer was attached to a metal rod extending from the OBS frame, mechanically uncoupled and dropped directly onto the seafloor after approximately 1 h. By using this approach, we achieved direct contact with sediments and improved coupling of the seismometers.

The OBSs were deployed in with the free-fall approach at a water depth of ca. 1,200 m. Seismic lines were shot over the OBSs with the intention to precisely relocate the OBSs at the seafloor using times of direct wave arrivals (e.g., Plaza-Faverola et al., 2010). However, problems with the time records for the shots hampered improved relocation efforts. Thus, in this study, we used OBS positions registered during deployment. Since we did not attempt event location, the OBS position accuracy was not critical.

The instruments recorded with 20 ms (OBS-1) and 5 ms (OBS-4 and OBS-5) sampling intervals. This corresponds to the Nyquist frequency of 25 Hz for OBS-1 and 100 Hz for OBS-4 and OBS-5. All these data cover roughly the duration of the deployment (10.2015–07.2016), excluding the first two weeks of October 2015, when OBSs were settling on the sediment. Data quality of OBS-1 and OBS-4 is better than OBS-5. OBS-1 shows a consistent recorded signal throughout the entire deployment period. OBS-4 and OBS-5 have some periods (~up to week-long at times), where the recorded signal quality is unsatisfactory for analysis. During the first month of operation, OBS-5 recorded almost no signals of any kind, possibly due to poor coupling between the seismometer and the seafloor.

2.2 Preprocessing

We converted the whole dataset into day-long mseed-format files and visually inspected the overall quality of the data. Subsequently we verified that known earthquakes (i.e., recorded by the nearby land stations at Svalbard) are present in the recording, that the signal quality is satisfactory and that most of the strong earthquakes have been recorded on all three stations.

2.3 Visual Recognition of Recorded Signals

By manual inspection of the datasets, we identify four dominant types of signals: SDEs, earthquakes, harmonic tremors and whale calls.

2.3.1 SDEs

From visual inspection of the data set, we noticed prominent signals (**Figure 2A**) that usually have amplitudes similar, if not stronger, than local earthquakes (**Figure 2B**). Their spectra cover almost the entire frequency range (up to 20 Hz in OBS-1 and 60–80 Hz in OBS-4 and OBS-5). Whereas the amplitude of these signals is highly variable, the frequency content between events remains more stable. Their average duration is between 1–2 s. On corresponding spectrograms, these signals appear as narrow "stripes" covering a large frequency band from 3–4 Hz to 20–25 Hz (OBS-1) or 60–65 Hz (OBS-4 and OBS-5), with similar energy levels for all frequencies they contain. We classify these signals as SDEs (**Figure 2A**). SDEs are usually observed on all channels of a seismometer, and sporadically, on a hydrophone record. One common characteristic they share is a lack of separate P and S wave arrivals, which clearly distinguishes them from local earthquakes (**Figures 2A,B**). The SDEs we document here follow the characteristics of SDEs described at Western Svalbard Shelf by Franek et al. (2017), and Sea of Marmara by Batsi et al. (2019).

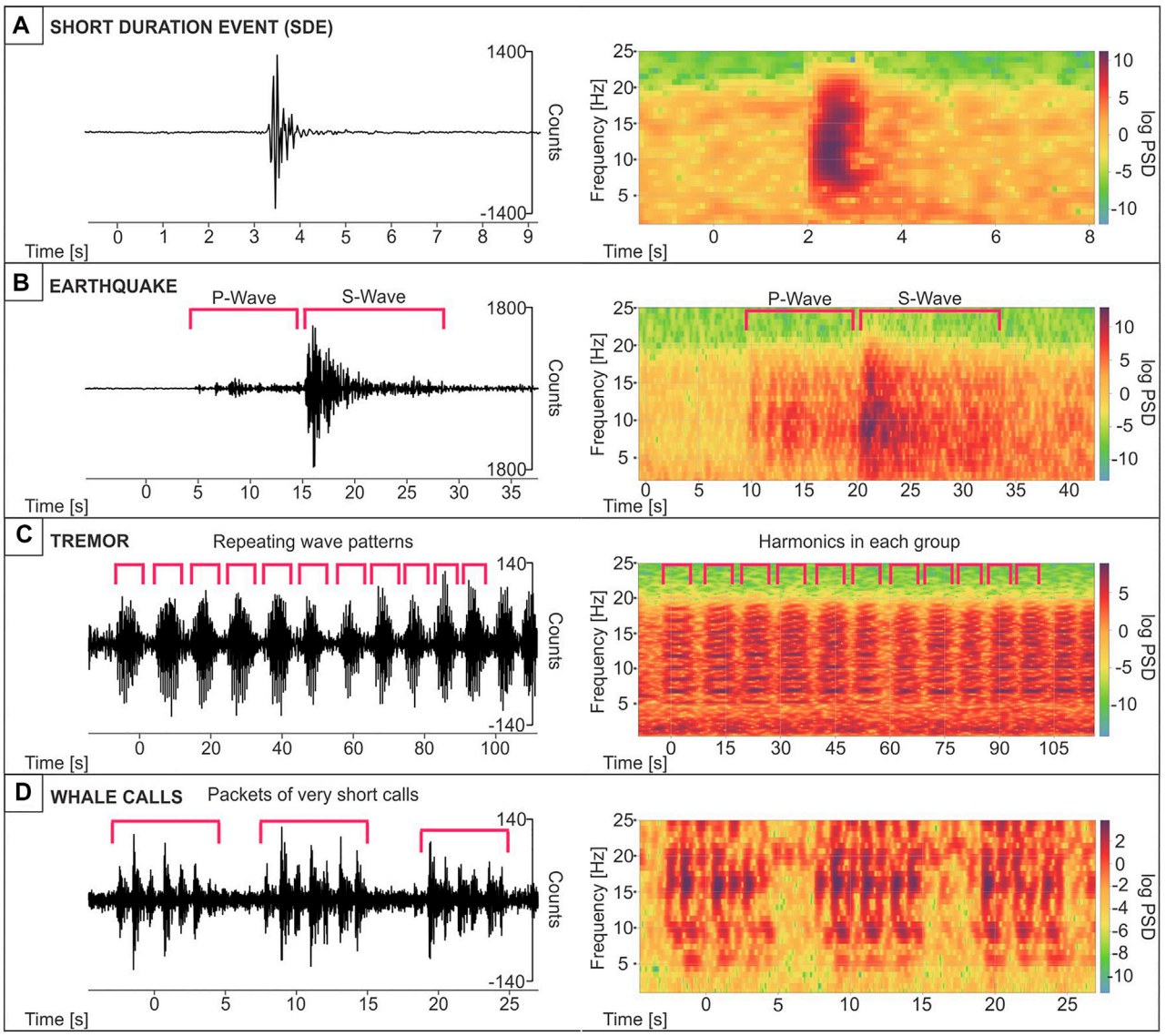

FIGURE 2 | Individual examples of types of events observed on the vertical channel of the seismometer, with spectrograms showing how each type of observed signals can be differentiated by their spectra. Events presented: SDEs **(A)**, earthquakes **(B)**, harmonic tremors **(C)**, and whale calls **(D)**. Spectrograms calculated using Fast Fourier Transform (window length 1 s, except tremors—5 s used there instead; overlap—90%; Hanning taper).

2.3.2 Earthquakes

The dominant sources of earthquakes in this dataset are ultra-slow spreading oceanic ridges (e.g., Molloy Ridge and Knipovich Ridge), that have been successfully studied by OBS deployments (e.g., Meier et al., 2021; Schlindwein et al., 2013). Earthquakes can be clearly distinguished from other signals by independent P and S waves arrivals and their overall length (**Figure 2B**). Usually, an individual earthquake is recorded on all three OBSs and on all channels of the seismometer. After an earthquake, a seismic wavefield propagating from the hypocenter reaches the seafloor and undergoes conversion at the water-sediment boundary. This process leads to the generation of acoustic waves in the water column that we have observed in our hydrophone data, for particularly large earthquakes in the region with known, independently determined magnitudes. In this study, we observe events with the total duration of 8–10 s or more, for the most part, since our short-period seismometers (with a useful frequency range of 1 Hz upwards) are mainly suitable for studies of local and regional seismicity (Sutton et al., 1965; Webb, 1998).

2.3.3 Harmonic Tremors

A tremor is defined as a continuous signal of sustained amplitude recorded at frequencies within limited bandwidth (Chouet, 1992). By harmonic tremor, we refer to signals which beside the fundamental frequency contain one or more harmonics of this

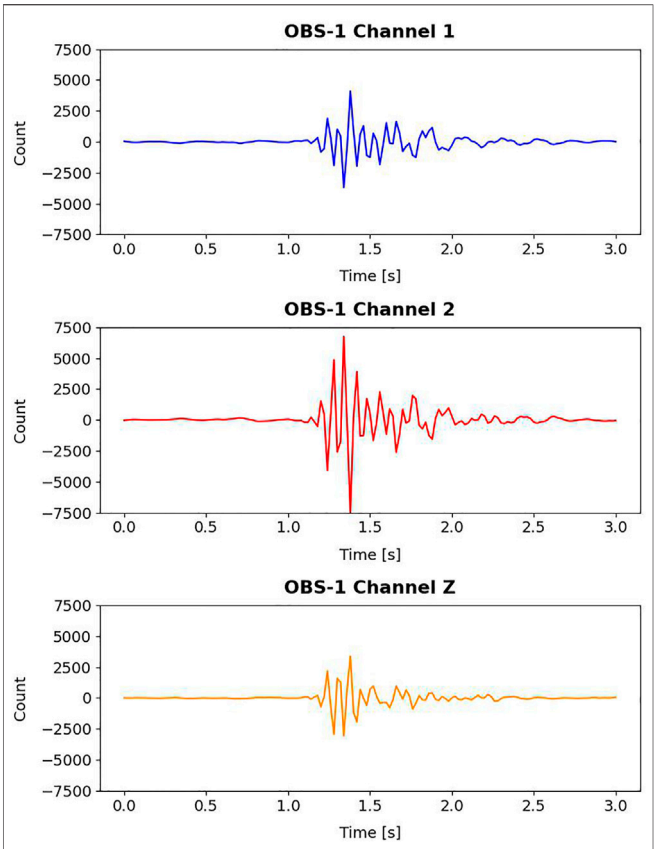

FIGURE 3 | An example of short duration event recorded on three channels of OBS-1 station seismometer. Horizontal channels marked as 1 and 2 due to lack of orientation with regards to geographic coordinates.

frequency, as defined e.g., in Essing et al. (2021). This can be clearly seen on their spectra, with an energy pick for the fundamental frequency and subsequent energy levels for integer multiples of this frequency. We observe tremor on all seismometer channels, but not on the hydrophones. Tremors have ~1–5 Hz dominant frequency with at least one or more harmonics present (**Figure 2C**), and harmonic frequencies going up to 15–20 Hz in the case of strong tremors. Tremor events usually start with only the dominant frequency and one, sometimes two harmonics visible, but they increase in intensity quickly and the number of harmonics visible becomes larger. The opposite process is occurring towards the end of the tremor "window," with number of harmonics decreasing, until only energy of the dominant frequency can be visible before tremor disappears completely. The usual duration of continuous presence of a tremor is counted in hours, but throughout these longer intervals, shorter (from few minutes upwards), "patchy" breaks can be randomly seen during the tremor events. They are observed on nearby instrumentation simultaneously, but there are small time differences between the start and the disappearance of tremor bursts between OBSs, with the variation between the onset and the disappearance time.

Approximately half of the dataset from each OBS is contaminated with the tremor noise of uniform characteristics (**Figure 2C**). Instead of short, strong impulses, it consists of repeating patterns of a longer duration (few seconds and upwards) signal. Its amplitude is also much weaker in comparison to SDEs and most of the recorded earthquakes, which means that the signal to noise ratio is generally much lower. Unlike many whale calls, sporadic SDEs and stronger earthquakes, tremors are not present in the data of the hydrophone channel. These differences in signal's strength over noise and individual packet duration allow for a distinction of tremor from other observed phenomena. However, due to its prevalence, tremors often coincide with SDEs and earthquakes. Owing to their frequency content up to 60 Hz and high amplitudes, SDEs are still recognizable during times of tremor (cf. **Figure 4A**).

Harmonic tremors are often interpreted as an effect of OBS instrumentation interacting with the deployment environment. Radio antenna used in OBS recovery has been suggested as a vibrating source of tremor controlled by underwater currents (Duennebier et al., 1981). Underwater currents can excite the rope holding the head buoy used for post-deployment retrieval in LOBSTER design OBS instruments (Stähler et al., 2018). This excitation can give rise to a tremor-like signal with a fundamental frequency close to 1 Hz, in a process known as Karman vortex shedding. Tremor characteristics, similar to the ones discussed here, were also observed near Canary Islands and were attributed to underwater currents exciting the seismometers (Ugalde et al., 2019). This type of a harmonic noise exhibits strong correlation with tidal cycles (Ramakrushana Reddy et al., 2020; Essing et al., 2021). We therefore suggest that the observed harmonic tremor signals are likely caused by seafloor currents acting on the OBSs.

2.3.4 Whale Calls

We found numerous examples of fin whale calls in the sensitive frequency range of seismometers and hydrophones. They produce a repeating sequence of short (~1 s), down-sweeping pulses within the range of 5–40 Hz, with highest energy around 18 Hz (**Figure 2D**). The overall duration of an individual animal call lasts usually for more than 200 s (Gaspa Rebull et al., 2006). The duration of recorded calls is highly dependent on whether we observe a group of animals or just a single whale. Since the source of the signal is in the water column, it is predominantly recorded by the hydrophones, and depending on the distance, may also be seen on seismometer channels.

Many different marine mammal species produce vocalizations that can be recorded with a high frequency hydrophone, but numerous studies have shown it is possible to record fin and blue whale calls also on seismometers due to the low frequency of their calls (e.g., McDonald et al., 1995; Morano et al., 2012; Soule and Wilcock, 2013). Both species are seasonally present west of Svalbard (Edwards et al., 2015; Storrie et al., 2018; Løviknes et al., 2021). Blue whales' songs have frequencies that also overlap with the bandwidth of OBS recordings, however their sounds are longer in duration (~8 s) and narrower in frequency (~20 Hz) for groups observed in North Atlantic (McDonald et al., 2006).

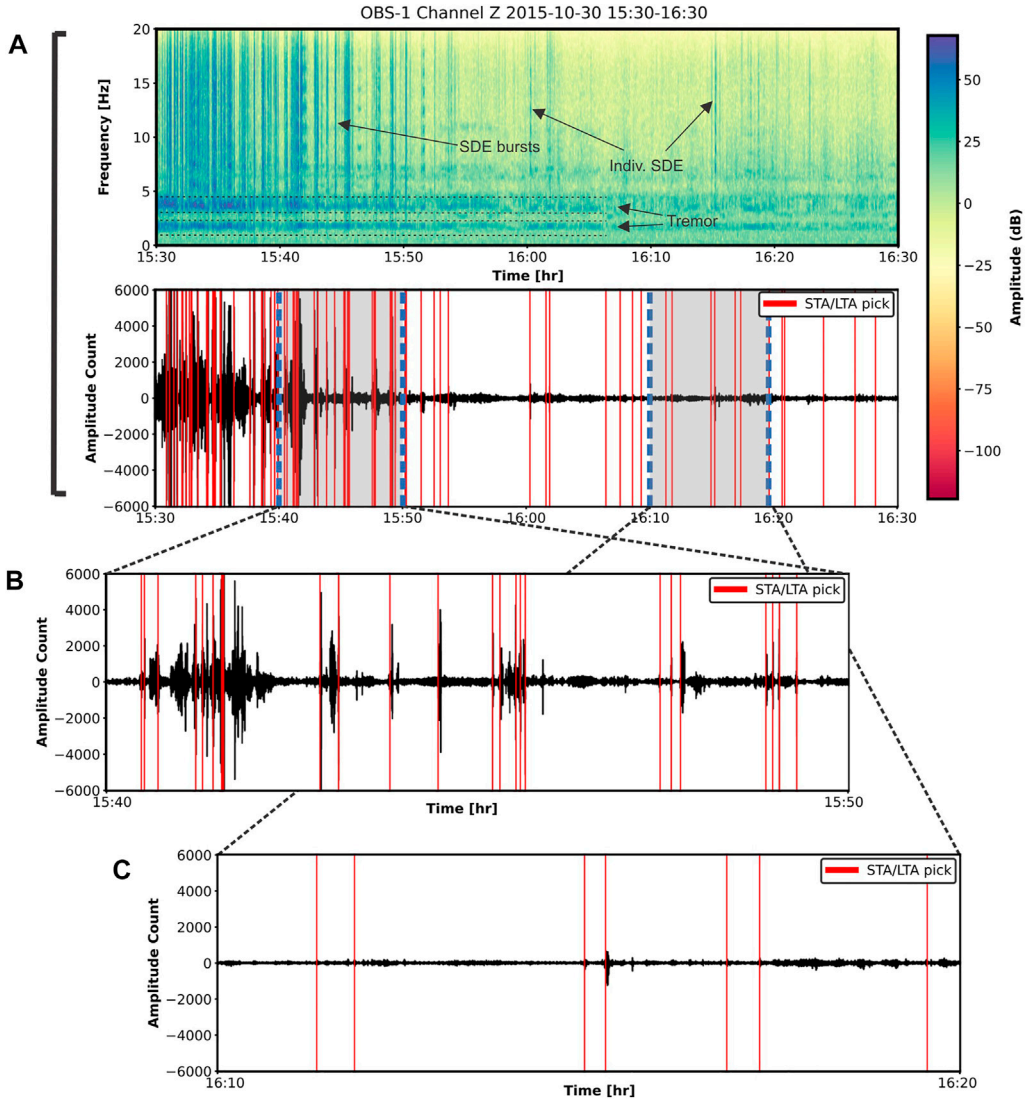

FIGURE 4 | Spectrogram of the hour-long subset of the vertical seismometer channel data from OBS-1 **(A)** containing examples of tremor (horizontal spectral lines below about 5 Hz) and SDEs (thin vertical lines) with the automatic picks of STA/LTA algorithm presented on the corresponding seismograms. Accuracy of the picking in the interval of high number of SDEs **(B)** and the period of relative quietness **(C)** are presented below. Parameters used to calculate the spectrogram: window length—10 s, overlap of windows—90%, taper function—Hanning.

They can also produce a different type of call (D call), possibly related to feeding, that can resemble a fin whale down-sweeping pulse, but a single event is lasting several seconds, longer than a fin whale call (Mellinger and Clark, 2003; Rice et al., 2021).

Call patterns of any of these species can clearly be distinguished from SDEs which lack down-sweep character and rhythmic sequences, they also have a longer duration.

Earthquakes, tremors and whale calls are beyond the scope of our study and will not be further discussed.

2.4 Automatic SDE Detection

We automatically extracted SDEs using the routine STA/LTA (short-term average/long-term average) algorithm implemented in ObsPy toolbox (Beyreuther et al., 2010) following an approach adopted for several studies of SDEs (e.g., Tary et al., 2012; Embriaco et al., 2014; Franek et al., 2014; Franek et al., 2017; Batsi et al., 2019). First, we visually identified a large number of SDEs present in the data to gain an idea of the best search parameters for the STA/LTA detector, based on their signal characteristics (**Figure 3**). We conducted the search on vertical channels of all seismometers, because only the strongest SDEs were present on all channels of a seismometer (**Figure 3**). We have chosen arbitrary two-week long period of data and tested different detection parameters until we obtained satisfactory result. After a careful analysis and testing of STA/LTA trigger sensitivity, we set the following parameters: length of short-term window 0.35 s, length of long-term window 8 s, trigger threshold

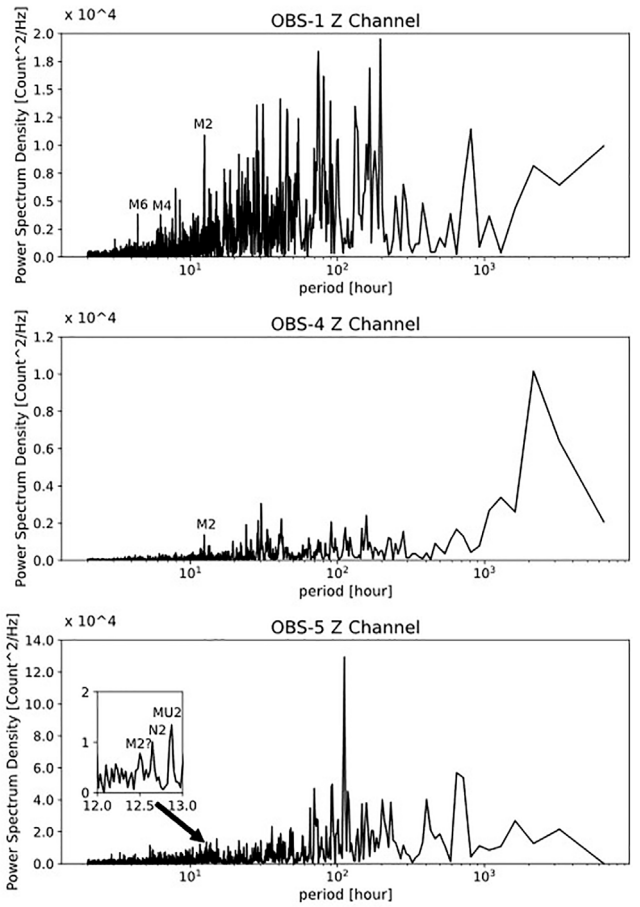

FIGURE 5 | Power spectrum density (periodogram) functions for hourly count of SDEs detected on vertical channels of OBS-1, OBS-4, and OBS-5. Labels for corresponding tidal components are as follows: M2—principal lunar semidiurnal, M4—shallow water overtides of principal lunar semidiurnal (first overtide of principal lunar semidiurnal), M6—second overtide of principal lunar semidiurnal, N2—larger lunar elliptic semidiurnal, MU2 – variational.

ratio 5 and de-trigger threshold 2. We restricted the event duration to less than 2.5 s to make sure that local earthquakes from oceanic ridges and whale calls would not be included in the resulting dataset. The final output contained each picked SDE start time and its duration (defined as the difference between trigger and de-trigger time).

Overall, the STA/LTA automatic extraction is highly effective for periods with limited SDE activity (**Figure 4C**). However, in periods of intensive SDEs we notice that the STA/LTA identifies fewer SDEs than observed by visual inspection during the selected period (**Figure 4B**). Specifically, it fails to trigger detection more than once during longer periods of SDEs activity with practically no low-amplitude intervals in between. Therefore, the number of SDEs during phases of high activity is likely underestimated. Nevertheless, the presence of harmonic tremors does not affect the trigger sensitivity and SDEs are also detected during phases of intense tremor (15:30–15:50, **Figure 4A**). The use of the vertical seismometer channel for SDE detection further avoided triggering on whale calls.

3 RESULTS

3.1 Occurrence and Periodicity of Observed SDEs

We detected more than 300,000 events using STA/LTA detector and more than 90,000 on OBS-1 alone throughout the deployment period. They occur as a single event or in bursts of dozens, sometimes hundreds, lasting several hours (**Figure 4**). We operated the STA/LTA detector on the vertical seismometer channel. However, SDEs are generally visible on all channels of a seismometer, and sometimes also on a hydrophone channel. We observe that the number of SDE occurrences varies with time along the records and these variations are not regular. Also, the observed bursts of SDEs do not occur simultaneously on the neighboring stations, despite their estimated distance of only 250–300 m. This indicates that the origin of the signal is very local, otherwise we would expect simultaneous detection on nearby stations. This is in line with other reports about their occurrence (e.g., Tary et al., 2012; Embriaco et al., 2014; Sgroi et al., 2021).

Periodogram plots reveal a periodic pattern of occurrence of SDEs that can be correlated with major tidal cycles. The SDE occurrence peaks in cycles of about 12.4 h (M2 in **Figure 5**) on OBSs 1 and 4, and to a lesser extent on OBS-5. There are also spectral peaks at 4.39 h (M6 in **Figure 5**) and 6.28 h (M4 in **Figure 5**) on OBS-1. M2, M4 and M6 correspond to the principal lunar semi-diurnal constituent and the first and the second overtide of principal lunar semi-diurnal constituent, respectively (Lopes and Tenreiro Machado, 2017). It can be argued that there are three small peaks related to M2 and other tidal constituents present on OBS-5 (M2? N2 and MU2 in **Figure 5**). In general, we also observe many more periodicity peaks greater than full-day on the spectra that cannot be assigned to the tides in a direct manner.

We conducted similar analysis of periodicity for the tremors to compare the strength of the tidal influence on both processes. We utilized the detection approach of Roman (2017) to obtain an hourly-binned dataset of tremor occurrence. This method uses the pitch detection approach from speech and music processing, due to their similar characteristics to harmonic tremors. It initially assumes that each individual sample has the tremor present. It first determines the fundamental frequency of a signal by consecutively decimating the Fourier transform of a signal and designating a frequency with the highest power as the fundamental one. Then, for the integer multiples of this frequency (harmonics), it measures the relative power ratios between the windows containing the fundamental frequency and its potential harmonics. If this ratio exceeds a predefined value, we can assume that the signal contains tremor, with a given fundamental frequency. We can also decide for how many harmonics the ratio has to be checked and met for a signal to be declared as a tremor.

In the resulting plots, we also observed clear spectral peaks corresponding to tidal cycles on OBS-1 and OBS-4 (**Supplementary Figure S1**), with the M2 peak more pronounced than in the SDE periodogram. In addition, longer

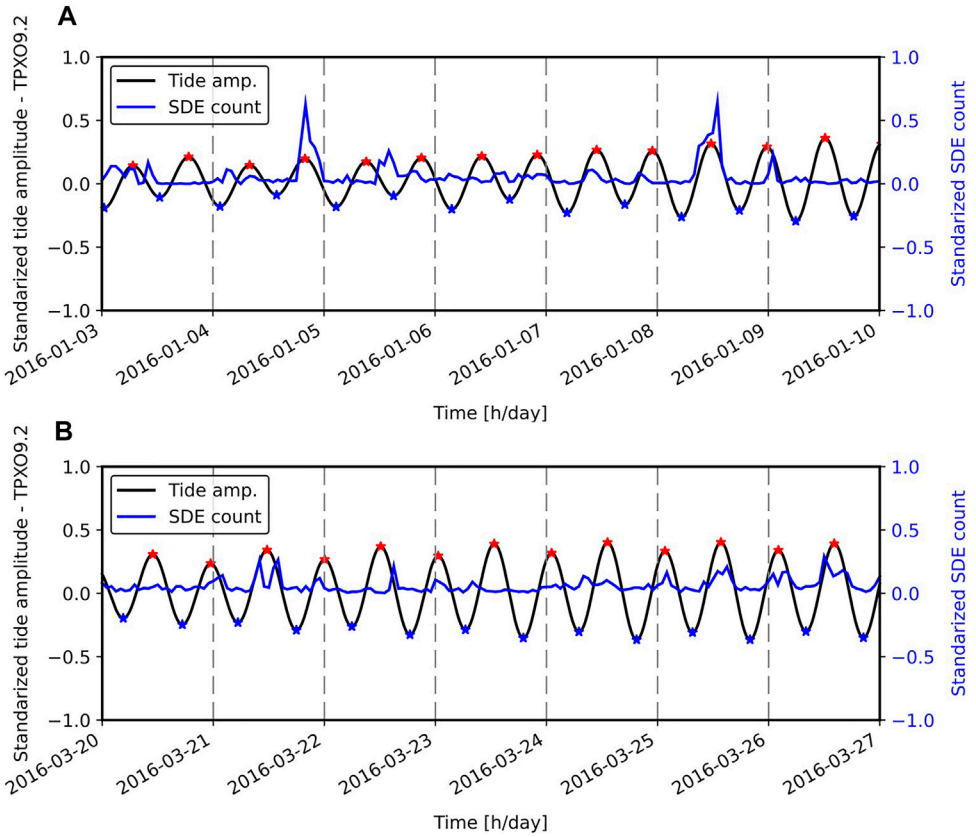

FIGURE 6 | Standardized plots of the mean sea level amplitude change due to tides (black line) superimposed on the SDEs hourly count from vertical channel of OBS-1 (blue line) for a week 03.01-09.01.2016 **(A)** and a week 13.03-19.03.2016 **(B)**. Small red and blue stars indicate moment of high/low tide, respectively. Each day is separated by a dashed vertical line.

period tidal constituents (K1 and longer periods) are present in the tremor cyclicity. This underlines two points: that we could successfully discriminate SDE events and tremor signals with SDE occurrence patterns differing from tremor occurrence patterns; secondly, that different source mechanisms are responsible for producing tremors and SDEs.

3.2 Periodicity of SDEs and Comparison With Tidal Cycles

To further compare the observed periodicity of SDEs with the periodicity of diurnal tides, we used the models of expected mean sea level height changes for the months of the experiment using pyTMD (Sutterley et al., 2019). We calculated these values for the location of OBS-1 (6°54′30″E, 79°00′17″N) using TPXO 9.2 model (Egbert and Erofeeva, 2002). For this site, we obtained the maximum mean sea level height difference due to tides of about 1.2 m. We then compared the normalized modelled tidal response time series with normalized SDEs time series (**Figure 6**). Subsequently, we also noticed that occurrence of SDEs matches, albeit in not a consistent way, the pattern represented by tidal cycles calculated for Vestnesa Ridge. It appears that increased numbers of SDEs are usually visible near the peaks of sea level change, but SDEs are not present in every consecutive diurnal tide cycle. More examples of observed SDEs intensity can be found in the supporting material (**Supplementary Figures S2–S40**). We performed manual picking of the SDEs on a smaller subset of the data and confirmed that the similar periodic pattern is present (**Figure 7**). Therefore, we can exclude those artefacts caused by the relative insensitivity of the STA/LTA detector in times of SDE bursts affect the SDE periodicity.

In general, these plots show that the observed relationship between tides and SDE occurrence is not very strong. This agrees with what is observed on periodograms, where peaks of spectral amplitude at the frequencies corresponding to tides are visible, but other, stronger periods are also present. Likewise, a prominent increase in SDE numbers is rarely observed on subsequent tidal cycles. We observe instead that at least a few days can pass with a lesser amount of SDEs. This pattern occurs through the entire dataset, with additional longer quiet periods (on a scale of weeks), where clear increases in SDEs are not observed (**Supplementary Figures S2–S40**).

3.3 Phase Relationship Between SDE Bursts and Tides

In order to quantify the strength of the relationship between SDEs and tides, we use cross-correlations (**Appendix A**) of the

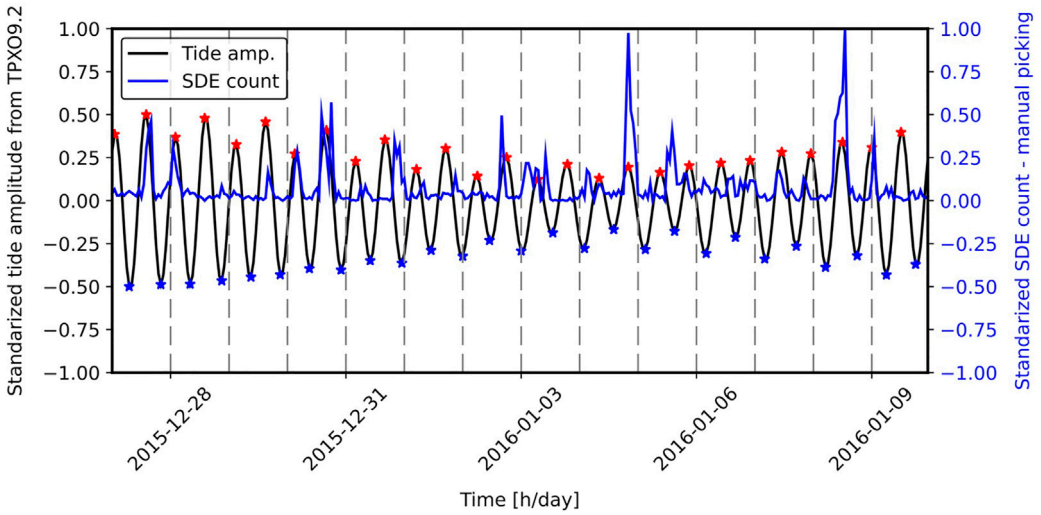

FIGURE 7 | Standardized plot of manually picked and subsequently binned hourly count of SDEs observed at vertical channel of OBS-1 vs. relative mean sea level change caused by tides (from TPXO 9.2 model), for arbitrarily selected two-week-long period.

normalized mean sea level change with the normalized SDE hourly count function as a quantitative measure of similarity. The cross-correlation allows calculation of the lag (i.e., the phase difference between the input time series), at which the relationship is potentially strongest. Since one of the functions used in the calculation has a clear periodic pattern (i.e., roughly 12-h periodicity in the case of the tides), we looked at the cross-correlation lag values only between −12 and 12 h (**Figure 8**). We detrended the time series prior to the correlation. In the next step, we split the data into monthly intervals and evaluated the relationship of SDE counts to both rising and falling tides. We then generated monthly plots for each OBS using the same approach, with the omission of July 2016, since we only had 5 full days of the record for this month (**Figure 9**).

The cross-correlation between the tidal time series and hourly SDE count time series shows a peak correlation in all three OBS stations between 0–1 h time lag. This indicates that rising tides close to the tidal maximum correspond to the highest likelihood of occurrence of SDEs (**Figure 8**). Additionally, each correlation peak has a corresponding minimum at roughly 6 h before and after the peak. This is a consequence of the periodic nature of one of the input functions (mean sea level change) for the correlation process, but it also indicates a weaker connection between SDEs and low tides. Shifting the tidal dataset back and forth by an arbitrary number of hours produces a cross correlation function with the maxima and minima shifted by the same number of hours, respectively.

We then study 27 individual samples representing correlation results for month-long subsets of SDE data for each of three OBSs (**Table 1**). In most (17/27) of the cases, the peak correlation occurs either at 0 h lag or at 1 h lag. Since the input dataset is binned into hour-long intervals, this means that the actual peak occurs at the value between 0 and 1 h. In these cases, a maximum correlation value equal ~0.1–0.5 (**Figure 9**). This indicates a stronger relationship between times of a rising tide and peaks in SDEs occurrence rather than between falling tides and peaks in SDE occurrence. The average correlation value for these periods is 0.17. For months where the correlation peak occurs at a time lag other than 0 h or 1 h, the correlation value is much lower (usually <0.05, mean value 0.06), indicating weaker correlation/relationship between SDEs and relative wave height change due to tides. Additionally, among these 10 results with the correlation peak outside of 0–1 h range, only one correlation value is greater than 0.1 (i.e., for 2 h correlation lag in October for OBS-1), so the reliability of these 10 correlation results is poor. In general, the resultant correlation values are low, but there is a clear separation between values observed at lag 0–1 h in most of the months and the correlation results when peak is at different lag or barely recognizable.

It is worth remembering however, that the resulting coefficients are neither robust nor resistant (Wilks, 2011). This means that cross correlation may not recognize strong, but non-linear relationships (robustness), or its outcome value can be extremely sensitive to one or a few outlying points pars (resistance). Relatively low coefficient values are caused partially by a high variance in the SDE dataset, where most of the observed counts during tide changes have relatively low value compared to extreme SDEs bursts that we observe sporadically in the data (median value of the normalized SDE occurrence is just 0.0259, 0.0185, and 0.0684 for OBS-1, OBS-4, and OBS-5, respectively). The aforementioned issues with the data quality for OBS-5 are likely the reason behind generally weak correlation for most of the months (with notable distinction of June (0.45), where the correlation is the strongest for the entire dataset from all recorders). In summary the results suggest that SDE peaks are more likely to happen at high and low tide but not at every tidal cycle and only sporadically. There is a stronger

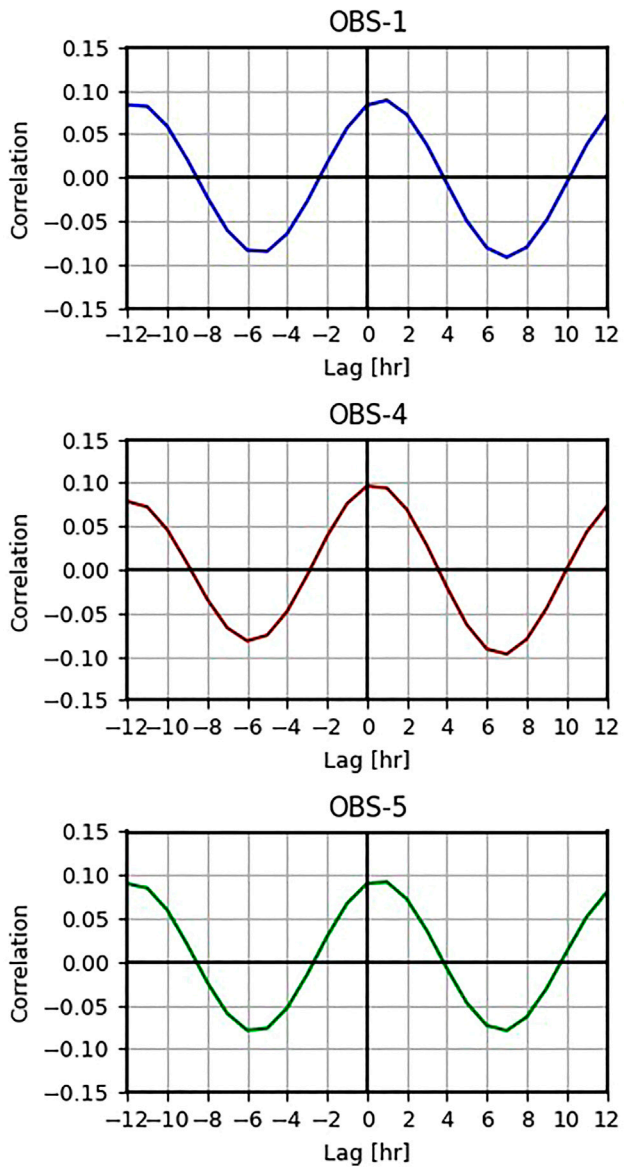

FIGURE 8 | Correlation of standardized SDEs hourly count (calculated for vertical channel of seismometer), with standardized tide amplitude for OBS-1, OBS-4, and OBS-5. For each plot the maximum positive correlation occurs at around +1 h (and repeat with periodicity of 12 h)—SDEs peak precedes the point of high tide by 1 h.

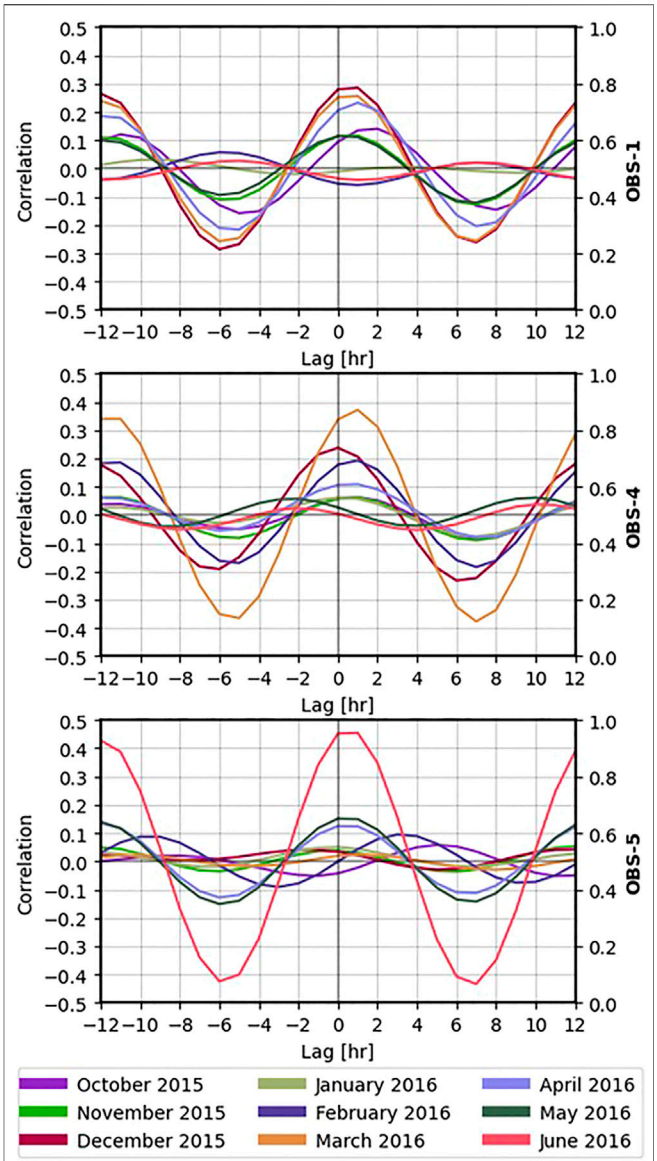

FIGURE 9 | Monthly correlation between standardized SDEs hourly count from vertical channels of OBS-1, OBS-4 and OBS-5, and standardized relative sea level change from TPXO 9.2 model.

connection between high tides and peaks in SDE occurrence than between low tides and peaks in SDE occurrence.

4 DISCUSSION

4.1 Tidal Control on SDEs

The analyses above indicate that:

- SDEs at the investigated site on Vestnesa Ridge have a periodic pattern of distribution
- SDEs can be correlated with diurnal and longer-term periodicity sea level changes to some extent
- The correlation between SDE occurrences and tides is in average low, with a stronger connection between their increase at maximum sea level periods. In such an instance, increase in SDEs does not necessarily occur within each tidal cycle, but with the periods of lower activity in between

Our results reveal that although SDEs are not strongly correlated with sea level changes associated to ocean tides, observing their variability on a month-by-month basis still shows partial effect of tidal sea level oscillations on the intensity of SDE bursts.

TABLE 1 | Maximum peak correlation lag time (in h) and corresponding correlation coefficient values for every month of deployment of each OBS. For all peaks occurring outside of the lag window 0–2 h we observe very low, close to 0, values of correlation coefficient.

Month	Lag of peak [hr]			Correlation value		
	OBS-1	OBS-4	OBS-5	OBS-1	OBS-4	OBS-5
October	2	1	5	0.14	0.06	0.05
November	1	4	12	0.11	0.06	0.05
December	1	0	12	0.29	0.23	0.04
January	–9	0	0	0.03	0.06	0.05
February	–6	1	3	0.05	0.19	0.09
March	1	1	1	0.26	0.37	0.02
April	1	1	0	0.23	0.1	0.12
May	0	10	0	0.11	0.06	0.15
June	1	10	1	0.12	0.03	0.45

While tremor periodicity indicates tidally modulated underwater currents (**Supplementary Figure S1**; Stähler et al., 2018; Ramakrushana Reddy et al., 2020; Essing et al., 2021), SDEs show a different periodic pattern, suggesting that their link to the sea level changes is via more complex near-seafloor processes.

Mean sea level changes represent pressure difference that impact near-surface geological processes. There are global observations that document a strong link between SDEs (i.e., micro-seismicity), and fluid movement through near seafloor sediments (Sultan et al., 2011; Tary et al., 2012; Embriaco et al., 2014; Franek et al., 2014; Franek et al., 2017; Batsi et al., 2019). Batsi et al. (2019) recreated in the lab (i.e., using a small amount of air and water injected into the sediments within a meter from the geophone) a signal characterized by high frequency content, strong amplitude and short duration that has a remarkable resemblance with SDEs.

All three SDE measurements documented here are concentrated near (<500 m) pockmark with proven gas hydrates and fracture-related seafloor seepage (**Figure 1**; Bünz et al., 2012; Panieri et al., 2017). The fact that SDEs are not recognized simultaneously on the three OBSs, together with strong relative amplitudes and no clear separation between the P and S wave signals (as in earthquakes), indicate local sources of SDEs that lose energy rapidly.

Discussions on the link between SDEs, tides and seepage dynamics at continental margins have gained significant attention following observations from various margins and geological settings. Several studies document tidal modulated seepage activity at continental margins (e.g., Boles et al., 2001; Torres et al., 2002; Hsu et al., 2013) and hydrothermal systems (e.g., Schultz et al., 1992; Plant et al., 2010). Along west-Svalbard continental margin, a potential effect of tides on the seepage intensity has been inferred from analyses of gas signatures on sonar (Veloso-Alarcon et al., 2019) and *in-situ* pore fluid pressure data (Sultan et al., 2020). Other studies document temporal relations between SDEs and enhanced methane release to the water column (e.g., Sea of Marmara; Embriaco et al., 2014). Bayrakci et al. (2014) noted a strong increase in the number of SDEs recorded on an OBS deployed directly at a seep location compared to other nearby devices. The polarization of SDEs observed by Hsu et al. (2013) at a mud volcano off Taiwan indicated a source in the shallow subsurface. In their case, the tidal pattern in SDE occurrence matched the periodicity of the gas flux in the water column giving further direct evidence of a link between tidally controlled fluid flow systems and SDE generation.

Very few studies discuss simultaneously mechanisms by which tides may affect seafloor seepage periodicity, which in turn may control the pattern of distribution of micro-seismic signals. Moreover, while a link between temporal modulation of gas release and occurrence of SDE events has been established based on data from various continental margins, the physical process behind this link is still the subject of the debate. We discuss hereafter physical mechanisms that can explain the link between SDE occurrences, sea level changes and seepage dynamics at Vestnesa Ridge gas hydrates and associated seepage system.

4.2 SDEs From a Fracture-controlled Gas Hydrate and Seepage System

Documented SDEs occurrences on Vestnesa Ridge are in line with observations from other margins, possibly reflecting sea level controlled dynamic changes on the seepage system from one or several of the surrounding pockmarks (**Figure 1**).

Soft, unconsolidated sediments create temporary pathways for migrating gas that undergo closure after the gas release (Boudreau et al., 2005). It has been suggested that SDEs could be the manifestation of opening new fractures allowing for gas expulsion or pockets of gas travelling upwards in the shallow sediment (Tary et al., 2012). Both modeling (Tary et al., 2012) and test in a sediment tank (Batsi et al., 2019), have shown that gas release from the surface would produce signals that resemble the SDEs recorded in the field.

Seepage over the monitored pockmark on Vestnesa Ridge has been documented over multiple yearly surveys since 2009 (e.g., Smith et al., 2014; Panieri et al., 2017). The pockmark is associated with one, among several, vertical fluid migration conduits along Vestnesa Ridge. These conduits are known as gas chimneys or gas pipes and are thought to be formed due to overpressured gas at the base of the gas hydrate stability zone (GHSZ) (Hustoft et al., 2009; Singhroha et al., 2016). The source of gas is both microbial and thermogenic (Pape et al., 2020) and seepage at the seafloor is sustained by pulses of gas migrating though fractured strata (**Figures 1C,D**) (Bünz et al., 2012; Plaza-Faverola et al., 2015; Singhroha et al., 2016). Buried authigenic carbonate accumulations within the pipes, characterized by high amplitude anomalies in 3D seismic data, indicate periods of enhanced methane release in the past (Himmler et al., 2019; Plaza-Faverola et al., 2015; Schneider et al., 2018). These shallow authigenic carbonate concentrations and gas hydrates promote the entrapment of gas within the upper few meters below the seafloor (**Figure 1C**) (Plaza-Faverola et al., 2015; Himmler et al., 2019). Over time, trapped gas bypasses local seals and continue through shallow fractures to sustain seafloor seepage at present day (Hong et al., 2021). Such fluid flow systems are known as self-sealed (Hovland et al., 2002).

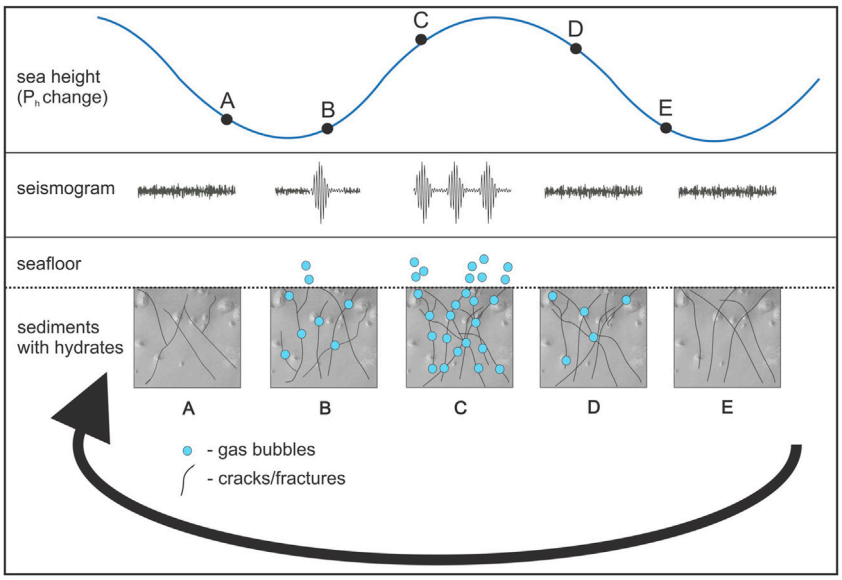

FIGURE 10 | Conceptual model for a potential explanation of micro-seismicity generation from a near-surface gas hydrate system, driven by solubility changes. **(A)** Initial conditions. **(B)** Increase in tidal pressure leads to gas exsolution and bubble formation which reopens fractures. **(C)** Maximum number of bubbles is being generated when the pressure difference from tides is approaching highest value, consequently the largest amount of short duration events is observed. **(D)** During the falling tide, pressure decrease leads to closing of existing fractures and bubble formation. **(E)** For the next tidal cycle, smaller amounts of gas in pore fluids prohibit from immediate repetition of the process, consequently this pattern is observed only after few more tidal cycles.

The physical mechanism usually invoked to explain the modulation of seepage by tides is the forcing exerted by increasing and decreasing hydrostatic pressure on gas (i.e., a compressible fluid) present in the pore-fluids (Römer et al., 2016; Sultan et al., 2020). This change in pore-fluid pressure would also lead to changes in the state of pre-existing fractures in the subsurface, which would lead to enhanced or hindered gas migration. Such mechanical changes generate micro-seismicity (Hsu et al., 2013).

Observations of gas emissions into the water column (Boles et al., 2001; Torres et al., 2002; Plant et al., 2010; Römer et al., 2016; Riedel et al., 2018) at Cascadia margin and inferred from pore fluid pressure changes (Sultan et al., 2020) at Vestnesa Ridge point to the highest seepage activity during low tides, which would then lead to the largest number of SDEs also during low tides (i.e., assuming that the three processes: fracture opening, gas seepage, and generation of SDEs, occur simultaneously). This is not entirely consistent with the seismological SDE pattern we observe. We suggest that the key to understanding this apparent discrepancy is in the dynamics of the fluid migration system. The system monitored on Vestnesa Ridge has a constant supply of gas from the deeper sediments (e.g., Knies et al., 2018; Daszinnies et al., 2021) and seafloor seepage is continuous (Smith et al., 2014). Thus, it is possible that changes in pressure due to tides only modulate but do not control the seepage activity.

A constant input of gas (e.g., from the base of the gas hydrate stability zone; Singhroha et al., 2016) into the shallow sediment may result in overpressure-driven pulses of gas migration upwards (Hustoft et al., 2009). Micro-seismicity generation can happen both during high and low tides, provided there is enough gas present, and an effective stress of sediments is overcome (Hsu et al., 2013). Hsu et al. (2013) points out, that for a specific location, the vertical stress of a rock stays more or less constant throughout the tidal cycle, leading to a greater pressure difference between gas-filled sediments and the water column at a high tide compared to at a low tide. This leads to larger observed micro-seismicity response during a tidal peak than during a tidal low, which is what they observed, and what we also have noticed during tidal cycles with micro-seismic activity present. In their case, the micro-seismic pattern is directly matched with the gas emission intensity measurement in the water column. Furthermore, in this study it is postulated that in a case of an insufficient methane replenishment (occurring on a scale larger than a single tidal cycle), there is a smaller gas charge, not strong enough to overcome the pressure difference when the influence of tides is largest (high tide). This mechanism can explain observations of increased gas emissions during low tide (e.g., Römer et al., 2016; Riedel et al., 2018; Sultan et al., 2020). Slower replenishment of the gas (on a scale of at least few tidal cycles), could also lead to gaps in the micro-seismic activity, which is what we have observed.

Complex thermodynamic behaviors of gas hydrates may be having an effect on the response of the seepage system to sea level changes and subsequently on the pattern of micro-seismicity generated in response to fluid migration. Normally, solubility of the methane in the pore water increases with the increase in pressure, but in a system supporting stable conditions for methane hydrate to form, the opposite situation is possible (Handa, 1990; Tishchenko et al., 2005; Sun and Duan, 2007; Liu and Flemings, 2011). This is especially true at low temperatures encountered at deep (>1200 m) seafloors. Specific pressure and

temperature conditions may favor exsolution of methane from the aqueous phase during high tides, leading to either formation of gas hydrate or generation of methane bubbles that fracture very shallow sediments and release in the form of bubbles. While the change in solubility will be very small, it has been shown that for shallow, unconsolidated sediments reopening of previously existing fractures and bubble generation is possible at a pressure difference provided by tides (Boudreau, 2012). This will not lead to a large change in the amount of methane seeping, but actually, the smaller the bubbles generated, the easier they move to the seafloor, either by initiating minor fractures (assuming linear elastic fracture mechanics) or through pre-existing fluid-filled cracks/pathways (Johnson et al., 2002; Boudreau et al., 2005; Algar et al., 2011a; Algar et al., 2011b; Boudreau, 2012). A conceptual model of such a cycle is presented in **Figure 10**. Such a change of release would probably not produce an observable difference in the acoustic flares observed in sonar data.

How gas hydrate thermodynamics affect seepage periodicity at continental margins is a largely understudied, yet highly relevant problem that deserves broader investigation.

5 CONCLUSION

Seismological data from three ocean bottom seismometers (OBS) obtained at Vestnesa Ridge reveals, in addition to information about local seismicity, continuous records of tremor-like signals and a large number of short duration events (SDEs). In line with observations from other margins, the tremors documented here are likely caused by the effect of tidal currents on the OBS instrumentation. These currents exhibit strong variability that can be linked to semi-diurnal tides and observed patterns of tremor occurrence match the periodicity of modelled tides for the site.

Comparably to other studies reporting SDEs, our analysis support local, near-surface origin of the observed events. Lack of simultaneous detections of SDEs on closely-spaced OBSs and no observations of SDEs in hydrophone channels point to shallow, subsurface SDE origin.

Our results indicate that both tremors and SDEs occurrences in the investigated setting have a periodic behavior, and their periodicity is comparable to tidal cycles. While the relationship between tides and tremors is through tide-generated currents at the sea-bottom, the relation between tides and SDEs reveals different periodic pattern, in addition to a clear tidal component. SDE bursts generally correlate better with local tide maxima.

SDE distribution, periodic behavior and signal characteristics from Vestnesa Ridge compare to reports from other seepage sites worldwide. A potential connection between SDEs, sea-level changes and seepage dynamics in this deep marine gas hydrate system is explained by:

- Sediment fracturing and gas release caused by small pressure changes due to tides
- Insufficient gas charge unable to overcome pressure difference at a high tide, leading to emission only during periods of low tide, whilst also explaining gaps between the tidal cycles with increased SDE bursts
- Alternatively, complex thermodynamic behavior of gas hydrate under pressure changes due to tides likely affects seepage periodicity and near-surface deformation. This is under-investigated, yet highly relevant problem for quantifying seafloor seepage at continental margins

More quantitative modelling of the gas hydrate behavior in the sediments influenced by tidal pressure variations is necessary to verify how it affects the seepage and shallow sediments.

DATA AVAILABILITY STATEMENT

The datasets presented in this study can be found at UiT's open research data repository (DataverseNO): https://doi.org/10.18710/TCWUQN.

AUTHOR CONTRIBUTIONS

SB, APF, and PF (former colleague at the Center) designed and conducted the ocean bottom seismic (OBS) experiment. PD conducted the processing and analysis of OBS records. SS and PD worked on the cross correlation with modelled tides. PD prepared the manuscript with significant contributions from APF, VS, and SS. HR contributed to the conceptualization of the proposed model and discussion.

FUNDING

This work is part of the SEAMSTRESS project, supported by the Tromsø Research Foundation (TFS) and the Research Council of Norway (grant nr. 287865). The work is also supported by the Research Council of Norway through its Centers of Excellence funding scheme grant 223259 (Centre for Arctic Gas Hydrate, Environment and Climate—CAGE).

ACKNOWLEDGMENTS

We thank the crew of R/V *Helmer Hanssen* for their help with deployment and recovery of OBSs. We also thank Peter Franek for his initial work with the datasets and valuable assistance at an early stage of data processing. We thank the Reviewers Kimihiro Mochizuki and Christopher Schmidt for the constructive feedback that helped to improve the final publication. We also thank the Associate Editor Mourad Bezzeghoud. Regional map was created using GMT (Wessel et al., 2019). Plotting waveforms and spectrograms was done using Pyrocko (Heimann et al., 2017).

SUPPLEMENTARY MATERIAL

The Supplementary Material for this article can be found online at: https://www.frontiersin.org/articles/10.3389/feart.2022.831526/full#supplementary-material

REFERENCES

Algar, C. K., Boudreau, B. P., and Barry, M. A. (2011a). Initial Rise of Bubbles in Cohesive Sediments by a Process of Viscoelastic Fracture. *J. Geophys. Res.* 116 (B4). doi:10.1029/2010jb008133

Algar, C. K., Boudreau, B. P., and Barry, M. A. (2011b). Release of Multiple Bubbles from Cohesive Sediments. *Geophys. Res. Lett.* 38 (8). doi:10.1029/2011gl046870

Ambrose, W. G., Panieri, G., Schneider, A., Plaza-Faverola, A., Carroll, M. L., Åström, E. K. L., et al. (2015). Bivalve Shell Horizons in Seafloor Pockmarks of the Last Glacial-interglacial Transition: a Thousand Years of Methane Emissions in the A Rctic O Cean. *Geochem. Geophys. Geosyst.* 16 (12), 4108–4129. doi:10.1002/2015gc005980

Batsi, E., Tsang-Hin-Sun, E., Klingelhoefer, F., Bayrakci, G., Chang, E. T. Y., Lin, J. Y., et al. (2019). Nonseismic Signals in the Ocean: Indicators of Deep Sea and Seafloor Processes on Ocean-Bottom Seismometer Data. *Geochem. Geophys. Geosyst.* 20 (8), 3882–3900. doi:10.1029/2019gc008349

Bayrakci, G., Scalabrin, C., Dupré, S., Leblond, I., Tary, J.-B., Lanteri, N., et al. (2014). Acoustic Monitoring of Gas Emissions from the Seafloor. Part II: a Case Study from the Sea of Marmara. *Mar. Geophys. Res.* 35 (3), 211–229. doi:10.1007/s11001-014-9227-7

Beccari, V., Basso, D., Spezzaferri, S., Rüggeberg, A., Neuman, A., and Makovsky, Y. (2020). Preliminary Video-Spatial Analysis of Cold Seep Bivalve Beds at the Base of the continental Slope of Israel (Palmahim Disturbance). *Deep Sea Res. Part Topical Stud. Oceanography* 171, 104664. doi:10.1016/j.dsr2.2019.104664

Berndt, C., Feseker, T., Treude, T., Krastel, S., Liebetrau, V., Niemann, H., et al. (2014). Temporal Constraints on Hydrate-Controlled Methane Seepage off Svalbard. *Science* 343 (6168), 284–287. doi:10.1126/science.1246298

Beyreuther, M., Barsch, R., Krischer, L., Megies, T., Behr, Y., and Wassermann, J. (2010). ObsPy: A Python Toolbox for Seismology. *Seismological Res. Lett.* 81 (3), 530–533. doi:10.1785/gssrl.81.3.530

Boles, J. R., Clark, J. F., Leifer, I., and Washburn, L. (2001). Temporal Variation in Natural Methane Seep Rate Due to Tides, Coal Oil Point Area, California. *J. Geophys. Res.* 106 (C11), 27077–27086. doi:10.1029/2000jc000774

Boudreau, B. P., Algar, C., Johnson, B. D., Croudace, I., Reed, A., and Furukawa, Y. (2005). Bubble Growth and Rise in Soft Sediments. *Geology* 33 (6). doi:10.1130/g21259.1

Boudreau, B. P. (2012). The Physics of Bubbles in Surficial, Soft, Cohesive Sediments. *Mar. Pet. Geology.* 38 (1), 1–18. doi:10.1016/j.marpetgeo.2012.07.002

Bowman, D. C., and Wilcock, W. S. D. (2013). Unusual Signals Recorded by Ocean Bottom Seismometers in the Flooded Caldera of Deception Island Volcano: Volcanic Gases or Biological Activity? *Antartic Sci.* 26 (3), 267–275. doi:10.1017/s0954102013000758

Bünz, S., Polyanov, S., Vadakkepuliyambatta, S., Consolaro, C., and Mienert, J. (2012). Active Gas Venting through Hydrate-Bearing Sediments on the Vestnesa Ridge, Offshore W-Svalbard. *Mar. Geology.* 332-334, 189–197. doi:10.1016/j.margeo.2012.09.012

Buskirk, R. E., Frohlich, C., Latham, G. V., Chen, A. T., and Lawton, J. (1981). Evidence that Biological Activity Affects Ocean Bottom Seismograph Recordings. *Mar. Geophys. Researches* 5 (2), 189–205.

Chang, E. T. Y., Chao, B. F., Chen, G. Y., and Liau, J. M. (2016). Internal Tides Recorded at Ocean Bottom off the Coast of Southeast Taiwan. *J. Geophys. Res. Oceans* 121 (5), 3381–3394. doi:10.1002/2015jc011370

Chouet, B. (1992). "A Seismic Model for the Source of Long-Period Events and Harmonic Tremor." in *Volcanic Seismology*. Berlin, Heidelberg: Springer, 133–156. doi:10.1007/978-3-642-77008-1_11

Ciotoli, G., Procesi, M., Etiope, G., Fracassi, U., and Ventura, G. (2020). Influence of Tectonics on Global Scale Distribution of Geological Methane Emissions. *Nat. Commun.* 11 (1), 2305. doi:10.1038/s41467-020-16229-1

Consolaro, C., Rasmussen, T. L., Panieri, G., Mienert, J., Bünz, S., and Sztybor, K. (2015). Carbon Isotope (δ13C) Excursions Suggest Times of Major Methane Release during the Last 14 Kyr in Fram Strait, the Deep-Water Gateway to the Arctic. *Clim. Past* 11 (4), 669–685. doi:10.5194/cp-11-669-2015

Crémière, A., Lepland, A., Chand, S., Sahy, D., Condon, D. J., Noble, S. R., et al. (2016). Timescales of Methane Seepage on the Norwegian Margin Following Collapse of the Scandinavian Ice Sheet. *Nat. Commun.* 7, 11509. doi:10.1038/ncomms11509

Crockett, R. (2019). *A Primer on Fourier Analysis for the Geosciences*. Cambridge: Cambridge University Press.

Crutchley, G. J., Klaeschen, D., Planert, L., Bialas, J., Berndt, C., Papenberg, C., et al. (2014). The Impact of Fluid Advection on Gas Hydrate Stability: Investigations at Sites of Methane Seepage Offshore Costa Rica. *Earth Planet. Sci. Lett.* 401, 95–109. doi:10.1016/j.epsl.2014.05.045

Daszinnies, M., Plaza-Faverola, A., Sylta, Ø., Bünz, S., Mattingsdal, R., Tømmerås, A., et al. (2021). The Plio-Pleistocene Seepage History off Western Svalbard Inferred from 3D Petroleum Systems Modelling. *Mar. Pet. Geology.* 128, 105023. doi:10.1016/j.marpetgeo.2021.105023

Di, P., Feng, D., Tao, J., and Chen, D. (2020). Using Time-Series Videos to Quantify Methane Bubbles Flux from Natural Cold Seeps in the South China Sea. *Minerals* 10 (3), 216. doi:10.3390/min10030216

Díaz, J., Gallart, J., and Gaspà, O. (2007). Atypical Seismic Signals at the Galicia Margin, North Atlantic Ocean, Related to the Resonance of Subsurface Fluid-Filled Cracks. *Tectonophysics* 433 (1-4), 1–13. doi:10.1016/j.tecto.2007.01.004

Duennebier, F. K., Blackinton, G., and Sutton, G. H. (1981). Current-generated Noise Recorded on Ocean Bottom Seismometers. *Mar. Geophys. Res.* 5 (1), 109–115. doi:10.1007/bf00310316

Edwards, E. F., Hall, C., Moore, T. J., Sheredy, C., and Redfern, J. V. (2015). Global Distribution of Fin Whales B Alaenoptera Physalus in the post-whaling Era (1980-2012). *Mammal Rev.* 45 (4), 197–214. doi:10.1111/mam.12048

Egbert, G. D., and Erofeeva, S. Y. (2002). Efficient Inverse Modeling of Barotropic Ocean Tides. *J. Atmos. Oceanic Technol.* 19 (2), 183–204. doi:10.1175/1520-0426(2002)019<0183:eimobo>2.0.co;2

Eiken, O., and Hinz, K. (1993). Contourites in the Fram Strait. *Sediment. Geology.* 82 (1-4), 15–32. doi:10.1016/0037-0738(93)90110-q

Embriaco, D., Marinaro, G., Frugoni, F., Monna, S., Etiope, G., Gasperini, L., et al. (2014). Monitoring of Gas and Seismic Energy Release by Multiparametric Benthic Observatory along the North Anatolian Fault in the Sea of Marmara (NW Turkey). *Geophys. J. Int.* 196 (2), 850–866. doi:10.1093/gji/ggt436

Essing, D., Schlindwein, V., Schmidt-Aursch, M. C., Hadziioannou, C., and Stähler, S. C. (2021). Characteristics of Current-Induced Harmonic Tremor Signals in Ocean-Bottom Seismometer Records. *Seismological Res. Lett.* doi:10.1785/0220200397

Etiope, G. (2015). "Gas Seepage and Past Climate Change," in *Natural Gas Seepage: The Earth's Hydrocarbon Degassing* (Cham: Springer International Publishing), 165–182. doi:10.1007/978-3-319-14601-0_8

Ferré, B., Jansson, P. G., Moser, M., Serov, P., Portnov, A., Graves, C. A., et al. (2020). Reduced Methane Seepage from Arctic Sediments during Cold Bottom-Water Conditions. *Nat. Geosci.* 13 (2), 144–148. doi:10.1038/s41561-019-0515-3

Franek, P., Mienert, J., Buenz, S., and Géli, L. (2014). Character of Seismic Motion at a Location of a Gas Hydrate-bearing Mud Volcano on the SW Barents Sea Margin. *J. Geophys. Res. Solid Earth* 119 (8), 6159–6177. doi:10.1002/2014jb010990

Franek, P., Plaza-Faverola, A., Mienert, J., Buenz, S., Ferré, B., and Hubbard, A. (2017). Microseismicity Linked to Gas Migration and Leakage on the Western Svalbard Shelf. *Geochem. Geophys. Geosyst.* 18 (12), 4623–4645. doi:10.1002/2017gc007107

Gaspà Rebull, O., Cusí, J. D., Ruiz Fernández, M., and Muset, J. G. (2006). Tracking Fin Whale Calls Offshore the Galicia Margin, North East Atlantic Ocean. *The J. Acoust. Soc. America* 120 (4), 2077–2085. doi:10.1121/1.2336751

Grevemeyer, I., Gràcia, E., Villaseñor, A., Leuchters, W., and Watts, A. B. (2015). Seismicity and Active Tectonics in the Alboran Sea, Western Mediterranean: Constraints from an Offshore-onshore Seismological Network and Swath Bathymetry Data. *J. Geophys. Res. Solid Earth* 120 (12), 8348–8365. doi:10.1002/2015jb012073

Handa, Y. P. (1990). Effect of Hydrostatic Pressure and Salinity on the Stability of Gas Hydrates. *J. Phys. Chem.* 94 (6), 2652–2657. doi:10.1021/j100369a077

Heimann, S., Kriegerowski, M., Isken, M., Cesca, S., Daout, S., Grigoli, F., et al. (2017). Pyrocko - an Open-Source Seismology Toolbox and Library. V. 0.3. *GFZ Data Serv.*

Himmler, T., Sahy, D., Martma, T., Bohrmann, G., Plaza-Faverola, A., Bünz, S., et al. (2019). A 160,000-Year-Old History of Tectonically Controlled Methane Seepage in the Arctic. *Sci. Adv.* 5 (8), eaaw1450. doi:10.1126/sciadv.aaw1450

Hong, W. L., Pape, T., Schmidt, C., Yao, H., Wallmann, K., and Plaza-Faverola, A. (2021). Interactions between Deep Formation Fluid and Gas Hydrate Dynamics Inferred from Pore Fluid Geochemistry at Active Pockmarks of the Vestnesa Ridge, West Svalbard Margin. *Mar. Pet. Geology.* 127. doi:10.1016/j.marpetgeo.2021.104957

Horozal, S., Bahk, J.-J., Urgeles, R., Kim, G. Y., Cukur, D., Kim, S.-P., et al. (2017). Mapping Gas Hydrate and Fluid Flow Indicators and Modeling Gas Hydrate Stability Zone (GHSZ) in the Ulleung Basin, East (Japan) Sea: Potential Linkage between the Occurrence of Mass Failures and Gas Hydrate Dissociation. *Mar. Pet. Geology.* 80, 171–191. doi:10.1016/j.marpetgeo.2016.12.001

Hovland, M., Gardner, J. V., and Judd, A. G. (2002). The Significance of Pockmarks to Understanding Fluid Flow Processes and Geohazards. *Geofluids* 2, 127–136. doi:10.1046/j.1468-8123.2002.00028.x

Howe, J. A., Shimmield, T. M., Harland, R. E. X., and Eyles, N. (2007). Late Quaternary Contourites and Glaciomarine Sedimentation in the Fram Strait. *Sedimentology* 55 (1), 179–200. doi:10.1111/j.1365-3091.2007.00897.x

Hsu, S.-K., Wang, S.-Y., Liao, Y.-C., Yang, T. F., Jan, S., Lin, J.-Y., et al. (2013). Tide-modulated Gas Emissions and Tremors off SW Taiwan. *Earth Planet. Sci. Lett.* 369-370, 98–107. doi:10.1016/j.epsl.2013.03.013

Hustoft, S., Bünz, S., Mienert, J., and Chand, S. (2009). Gas Hydrate Reservoir and Active Methane-Venting Province in Sediments on < 20 Ma Young Oceanic Crust in the Fram Strait, Offshore NW-Svalbard. *Earth Planet. Sci. Lett.* 284 (1-2), 12–24. doi:10.1016/j.epsl.2009.03.038

Johnson, B. D., Boudreau, B. P., Gardiner, B. S., and Maass, R. (2002). Mechanical Response of Sediments to Bubble Growth. *Mar. Geology.* 187 (3-4), 347–363. doi:10.1016/s0025-3227(02)00383-3

Judd, A., and Hovland, M. (2007). *Seabed Fluid Flow : The Impact on Geology, Biology, and the marine Environment*. Cambridge: Cambridge University Press.

Karstens, J., Haflidason, H., Becker, L. W. M., Berndt, C., Rüpke, L., Planke, S., et al. (2018). Glacigenic Sedimentation Pulses Triggered post-glacial Gas Hydrate Dissociation. *Nat. Commun.* 9 (1), 635. doi:10.1038/s41467-018-03043-z

Knies, J., Daszinnies, M., Plaza-Faverola, A., Chand, S., Sylta, Ø., Bünz, S., et al. (2018). Modelling Persistent Methane Seepage Offshore Western Svalbard since Early Pleistocene. *Mar. Pet. Geology.* 91, 800–811. doi:10.1016/j.marpetgeo.2018.01.020

Kvenvolden, K. A., Lorenson, T. D., and Reeburgh, W. S. (2001). Attention Turns to Naturally Occurring Methane Seepage. *Eos Trans. AGU* 82 (40), 457. doi:10.1029/01eo00275

Liu, X., and Flemings, P. B. (2011). Capillary Effects on Hydrate Stability in marine Sediments. *J. Geophys. Res. Solid Earth* 116 (B7). doi:10.1029/2010jb008143

Liu, Y., Tao, C., Liu, C., Qiu, L., Schlindwein, V., Zhang, H., et al. (2018). Seismic Activity Recorded by a Single OBS/H Near the Active Longqi Hydrothermal Vent at the Ultraslow Spreading Southwest Indian Ridge (49°39′ E). *Mar. Georesources Geotechnology* 37 (2), 201–211. doi:10.1080/1064119x.2017.1420114

Lopes, M. A., and Tenreiro Machado, J. (2017). Tidal Analysis Using Time–Frequency Signal Processing and Information Clustering. *Entropy* 19 (8). e19080390. doi:10.3390/e19080390

Løviknes, S., Jensen, K. H., Krafft, B. A., Anthonypillai, V., and Nøttestad, L. (2021). Feeding Hotspots and Distribution of Fin and Humpback Whales in the Norwegian Sea from 2013 to 2018. *Front. Mar. Sci.* 8.

Mau, S., Römer, M., Torres, M. E., Bussmann, I., Pape, T., Damm, E., et al. (2017). Widespread Methane Seepage along the continental Margin off Svalbard - from Bjørnøya to Kongsfjorden. *Sci. Rep.* 7, 42997. doi:10.1038/srep42997

McDonald, M. A., Hildebrand, J. A., and Webb, S. C. (1995). Blue and Fin Whales Observed on a Seafloor Array in the Northeast pacific. *J. Acoust. Soc. Am.* 98 (2 Pt 1), 712–721. doi:10.1121/1.413565

McDonald, M. A., Mesnick, S. L., and Hildebrand, J. A. (2006). Biogeographic Characterization of Blue Whale Song Worldwide: Using Song to Identify Populations. *J. Cetacean Res. Manage.* 8 (1), 55–65.

Meier, M., Schlindwein, V., Scholz, J. R., Geils, J., Schmidt-Aursch, M. C., and Kruger, F. (2021). Segment-Scale Seismicity of the Ultraslow Spreading Knipovich Ridge. *Geochem. Geophys. Geosystems* 22 (2), e2020GC009375. doi:10.1029/2020gc009375

Mellinger, D. K., and Clark, C. W. (2003). Blue Whale (Balaenoptera Musculus) Sounds from the North Atlantic. *J. Acoust. Soc. America* 114 (2), 1108–1119. doi:10.1121/1.1593066

Mishra, C. K., Dewangan, P., Sriram, G., Kumar, A., and Dakara, G. (2020). Spatial Distribution of Gas Hydrate Deposits in Krishna-Godavari Offshore basin, Bay of Bengal. *Mar. Pet. Geology.* 112. doi:10.1016/j.marpetgeo.2019.104037

Monigle, P. W., Bohnenstiehl, D. R., Tolstoy, M., and Waldhauser, F. (2009). Seismic Tremor at the 9°50′N East Pacific Rise Eruption Site. *Geochem. Geophys. Geosystems* 10 (11). doi:10.1029/2009gc002561

Morano, J. L., Salisbury, D. P., Rice, A. N., Conklin, K. L., Falk, K. L., and Clark, C. W. (2012). Seasonal and Geographical Patterns of Fin Whale Song in the Western North Atlantic Ocean. *J. Acoust. Soc. America* 132 (2), 1207–1212. doi:10.1121/1.4730890

Ostrovsky, A. A. (1989). On the Nature of Microshocks Recorded by Ocean Bottom Seismographs. *Mar. Geophys. Res.* 11 (2), 113–118. doi:10.1007/bf00285662

Ottesen, D., Dowdeswell, J. A., and Rise, L. (2005). Submarine Landforms and the Reconstruction of Fast-Flowing Ice Streams within a Large Quaternary Ice Sheet: The 2500-Km-Long Norwegian-Svalbard Margin (57°–80°N). *GSA Bull.* 117 (7-8), 1033–1050. doi:10.1130/b25577.1

Panieri, G., Bünz, S., Fornari, D. J., Escartin, J., Serov, P., Jansson, P., et al. (2017). An Integrated View of the Methane System in the Pockmarks at Vestnesa Ridge, 79°N. *Mar. Geology.* 390, 282–300. doi:10.1016/j.margeo.2017.06.006

Pape, T., Bünz, S., Hong, W. L., Torres, M. E., Riedel, M., and Panieri, G. (2020). Origin and Transformation of Light Hydrocarbons Ascending at an Active Pockmark on Vestnesa Ridge, Arctic Ocean. *J. Geophys. Res. Solid Earth* 125 (1). doi:10.1029/2018jb016679

Petersen, C. J., Bünz, S., Hustoft, S., Mienert, J., and Klaeschen, D. (2010). High-resolution P-Cable 3D Seismic Imaging of Gas Chimney Structures in Gas Hydrated Sediments of an Arctic Sediment Drift. *Mar. Pet. Geology.* 27 (9), 1981–1994. doi:10.1016/j.marpetgeo.2010.06.006

Plant, J. N., Johnson, K. S., Fitzwater, S. E., Sakamoto, C. M., Coletti, L. J., and Jannasch, H. W. (2010). Tidally Oscillating Bisulfide Fluxes and Fluid Flow Rates Observed with *In Situ* Chemical Sensors at a Warm spring in Monterey Bay, California. *Deep Sea Res. Oceanographic Res. Pap.* 57 (12), 1585–1595. doi:10.1016/j.dsr.2010.10.001

Plaza-Faverola, A., Bünz, S., Johnson, J. E., Chand, S., Knies, J., Mienert, J., et al. (2015). Role of Tectonic Stress in Seepage Evolution along the Gas Hydrate-Charged Vestnesa Ridge, Fram Strait. *Geophys. Res. Lett.* 42 (3), 733–742. doi:10.1002/2014gl062474

Plaza-Faverola, A., Bünz, S., and Mienert, J. (2010). Fluid Distributions Inferred from P-Wave Velocity and Reflection Seismic Amplitude Anomalies beneath the Nyegga Pockmark Field of the Mid-Norwegian Margin. *Mar. Pet. Geology.* 27 (1), 46–60. doi:10.1016/j.marpetgeo.2009.07.007

Plaza-Faverola, A., and Keiding, M. (2019). Correlation between Tectonic Stress Regimes and Methane Seepage on the Western Svalbard Margin. *Solid Earth* 10 (1), 79–94. doi:10.5194/se-10-79-2019

Plaza-Faverola, A., Pecher, I., Crutchley, G., Barnes, P. M., Bünz, S., Golding, T., et al. (2014). Submarine Gas Seepage in a Mixed Contractional and Shear Deformation Regime: Cases from the Hikurangi Oblique-Subduction Margin. *Geochem. Geophys. Geosyst.* 15 (2), 416–433. doi:10.1002/2013gc005082

Plaza-Faverola, A., Vadakkepuliyambatta, S., Hong, W.-L., Mienert, J., Bünz, S., Chand, S., et al. (2017). Bottom-simulating Reflector Dynamics at Arctic Thermogenic Gas Provinces: An Example from Vestnesa Ridge, Offshore West Svalbard. *J. Geophys. Res. Solid Earth* 122 (6), 4089–4105. doi:10.1002/2016jb013761

Ramakrushana Reddy, T., Dewangan, P., Arya, L., Singha, P., and Raju, K. A. (2020). Tidal Triggering of the Harmonic Noise in Ocean-Bottom Seismometers. *Seismological Res. Lett.* 91 (2A), 803–813. doi:10.1785/0220190080

Rice, A., Širović, A., Trickey, J. S., Debich, A. J., Gottlieb, R. S., and Wiggins, S. M. (2021). Cetacean Occurrence in the Gulf of Alaska from Long-Term Passive Acoustic Monitoring. *Mar. Biol.* 168 (5). doi:10.1007/s00227-021-03884-1

Riedel, M., Scherwath, M., Römer, M., Veloso, M., Heesemann, M., and Spence, G. D. (2018). Distributed Natural Gas Venting Offshore along the Cascadia Margin. *Nat. Commun.* 9 (1), 3264. doi:10.1038/s41467-018-05736-x

Ritzmann, O., Jokat, W., Czuba, W., Guterch, A., Mjelde, R., and Nishimura, Y. (2004). A Deep Seismic Transect from Hovgård Ridge to Northwestern Svalbard across the continental-ocean Transition: A Sheared Margin Study. *Geophys. J. Int.* 157 (2), 683–702. doi:10.1111/j.1365-246x.2004.02204.x

Roman, D. C. (2017). Automated Detection and Characterization of Harmonic Tremor in Continuous Seismic Data. *Geophys. Res. Lett.* 44 (12), 6065–6073. doi:10.1002/2017gl073715

Römer, M., Riedel, M., Scherwath, M., Heesemann, M., and Spence, G. D. (2016). Tidally Controlled Gas Bubble Emissions: A Comprehensive Study Using Long-Term Monitoring Data from the NEPTUNE Cabled Observatory Offshore Vancouver Island. *Geochem. Geophys. Geosyst.* 17 (9), 3797–3814. doi:10.1002/2016gc006528

Römer, M., Torres, M., Kasten, S., Kuhn, G., Graham, A. G. C., Mau, S., et al. (2014). First Evidence of Widespread Active Methane Seepage in the Southern Ocean, off the Sub-antarctic Island of South Georgia. *Earth Planet. Sci. Lett.* 403, 166–177. doi:10.1016/j.epsl.2014.06.036

Schlindwein, V., Demuth, A., Geissler, W. H., and Jokat, W. (2013). Seismic gap beneath Logachev Seamount: Indicator for Melt Focusing at an Ultraslow Mid-ocean ridge? *Geophys. Res. Lett.* 40 (9), 1703–1707. doi:10.1002/grl.50329

Schneider, A., Panieri, G., Lepland, A., Consolaro, C., Crémière, A., Forwick, M., et al. (2018). Methane Seepage at Vestnesa Ridge (NW Svalbard) since the Last Glacial Maximum. *Quat. Sci. Rev.* 193, 98–117. doi:10.1016/j.quascirev.2018.06.006

Schultz, A., Delaney, J. R., and McDuff, R. E. (1992). On the Partitioning of Heat Flux between Diffuse and point Source Seafloor Venting. *J. Geophys. Res.* 97 (B9). doi:10.1029/92jb00889

Sgroi, T., Monna, S., Embriaco, D., Giovanetti, G., Marinaro, G., and Favali, P. (2014). Geohazards in the Western Ionian Sea: Insights from Non-earthquake Signals Recorded by the NEMO-SN1 Seafloor Observatory. *Oceanog* 27 (2), 154–166. doi:10.5670/oceanog.2014.51

Sgroi, T., Polonia, A., Beranzoli, L., Billi, A., Bosman, A., Costanza, A., et al. (2021). One Year of Seismicity Recorded through Ocean Bottom Seismometers Illuminates Active Tectonic Structures in the Ionian Sea (Central Mediterranean). *Front. Earth Sci.* 9, 643. doi:10.3389/feart.2021.661311

Shipley, T. H., Houston, M. H., Buffler, R. T., Shaub, F. J., McMillen, K. J., Laod, J. W., et al. (1979). Seismic Evidence for Widespread Possible Gas Hydrate Horizons on Continental Slopes and Rises1. *AAPG Bull.* 63 (12), 2204–2213. doi:10.1306/2f91890a-16ce-11d7-8645000102c1865d

Singhroha, S., Bünz, S., Plaza-Faverola, A., and Chand, S. (2020). Detection of Gas Hydrates in Faults Using Azimuthal Seismic Velocity Analysis, Vestnesa Ridge, W-Svalbard Margin. *J. Geophys. Res. Solid Earth* 125 (2). doi:10.1029/2019jb017949

Singhroha, S., Bünz, S., Plaza-Faverola, A., and Chand, S. (2016). Gas Hydrate and Free Gas Detection Using Seismic Quality Factor Estimates from High-Resolution P-cable 3D Seismic Data. *Interpretation* 4 (1), SA39–SA54. doi:10.1190/int-2015-0023.1

Singhroha, S., Chand, S., and Bünz, S. (2019). Constraints on Gas Hydrate Distribution and Morphology in Vestnesa Ridge, Western Svalbard Margin, Using Multicomponent Ocean-Bottom Seismic Data. *J. Geophys. Res. Solid Earth* 124 (5), 4343–4364. doi:10.1029/2018jb016574

Smith, A. J., Mienert, J., Bünz, S., and Greinert, J. (2014). Thermogenic Methane Injection via Bubble Transport into the Upper Arctic Ocean from the Hydrate-Charged Vestnesa Ridge, Svalbard. *Geochem. Geophys. Geosyst.* 15 (5), 1945–1959. doi:10.1002/2013gc005179

Sohn, R. A., Hildebrand, J. A., Webb, S. C., and Fox, C. G. (1995). Hydrothermal microseismicity at the megaplume site on the southern Juan de Fuca Ridge. *Bull. Seismological Soc. America* 85 (3), 775–786.

Soule, D. C., and Wilcock, W. S. D. (2013). Fin whale tracks recorded by a seismic network on the Juan de Fuca Ridge, Northeast Pacific Ocean. *J. Acoust. Soc. America* 133 (3), 1751–1761. doi:10.1121/1.4774275

Stähler, S. C., Schmidt-Aursch, M. C., Hein, G., and Mars, R. (2018). A Self-Noise Model for the German DEPAS OBS Pool. *Seismological Res. Lett.* 89 (5), 1838–1845. doi:10.1785/0220180056

Storrie, L., Lydersen, C., Andersen, M., Wynn, R. B., and Kovacs, K. M. (2018). Determining the Species Assemblage and Habitat Use of Cetaceans in the Svalbard Archipelago, Based on Observations from 2002 to 2014. *Polar Res.* 37 (1). doi:10.1080/17518369.2018.1463065

Sultan, N., Plaza-Faverola, A., Vadakkepuliyambatta, S., Buenz, S., and Knies, J. (2020). Impact of Tides and Sea-Level on Deep-Sea Arctic Methane Emissions. *Nat. Commun.* 11 (1), 5087. doi:10.1038/s41467-020-18899-3

Sultan, N., Riboulot, V., Ker, S., Marsset, B., Géli, L., and Tary, J. B. (2011). Dynamics of Fault-Fluid-Hydrate System Around a Shale-Cored Anticline in deepwater Nigeria. *J. Geophys. Res.* 116 (B12). doi:10.1029/2011jb008218

Sun, R., and Duan, Z. (2007). An Accurate Model to Predict the Thermodynamic Stability of Methane Hydrate and Methane Solubility in marine Environments. *Chem. Geology.* 244 (1-2), 248–262. doi:10.1016/j.chemgeo.2007.06.021

Sutterley, T. C., Markus, T., Neumann, T. A., van den Broeke, M., van Wessem, J. M., and Ligtenberg, S. R. M. (2019). Antarctic Ice Shelf Thickness Change from Multimission Lidar Mapping. *The Cryosphere* 13 (7), 1801–1817. doi:10.5194/tc-13-1801-2019

Sutton, G. H., McDonald, W. G., Prentiss, D. D., and Thanos, S. N. (1965). Ocean-bottom Seismic Observatories. *Proc. IEEE* 53 (12), 1909–1921. doi:10.1109/proc.1965.4468

Tary, J. B., Géli, L., Guennou, C., Henry, P., Sultan, N., Çağatay, N., et al. (2012). Microevents Produced by Gas Migration and Expulsion at the Seabed: a Study Based on Sea Bottom Recordings from the Sea of Marmara. *Geophys. J. Int.* 190 (2), 993–1007. doi:10.1111/j.1365-246x.2012.05533.x

Taylor, M. H., Dillon, W. P., and Pecher, I. A. (2000). Trapping and Migration of Methane Associated with the Gas Hydrate Stability Zone at the Blake Ridge Diapir: New Insights from Seismic Data. *Mar. Geology.* 164 (1), 79–89. doi:10.1016/s0025-3227(99)00128-0

Thomsen, L., Barnes, C., Best, M., Chapman, R., Pirenne, B., Thomson, R., et al. (2012). Ocean Circulation Promotes Methane Release from Gas Hydrate Outcrops at the NEPTUNE Canada Barkley Canyon Node. *Geophys. Res. Lett.* 39 (16). doi:10.1029/2012gl052462

Tishchenko, P., Hensen, C., Wallmann, K., and Wong, C. S. (2005). Calculation of the Stability and Solubility of Methane Hydrate in Seawater. *Chem. Geology.* 219 (1-4), 37–52. doi:10.1016/j.chemgeo.2005.02.008

Torres, M. E., McManus, J., Hammond, D., De Angelis, M., Heeschen, K., and Colbert, S. (2002). Fluid and Chemical Fluxes in and Out of Sediments Hosting Methane Hydrate Deposits on Hydrate Ridge, OR, I: Hydrological Provinces. *Earth Planet. Sci. Lett.* 201 (3-4), 525–540. doi:10.1016/s0012-821x(02)00733-1

Tsang-Hin-Sun, E., Batsi, E., Klingelhoefer, F., and Géli, L. (2019). Spatial and Temporal Dynamics of Gas-Related Processes in the Sea of Marmara Monitored with Ocean Bottom Seismometers. *Geophys. J. Int.* 216 (3), 1989–2003. doi:10.1093/gji/ggy535

Ugalde, A., Gaite, B., Ruiz, M., Villaseñor, A., and Ranero, C. R. (2019). Seismicity and Noise Recorded by Passive Seismic Monitoring of Drilling Operations Offshore the Eastern Canary Islands. *Seismological Res. Lett.* doi:10.1785/0220180353

Veloso, M., Greinert, J., Mienert, J., and De Batist, M. (2015). A New Methodology for Quantifying Bubble Flow Rates in Deep Water Using Splitbeam Echosounders: Examples from the A Rctic Offshore NW- S Valbard. *Limnol. Oceanogr. Methods* 13 (6), 267–287. doi:10.1002/lom3.10024

Veloso-Alarcon, M. E., Janson, P., De Batist, M., Minshull, T. A., Westbrook, G. K., and Palikes, H. (2019). Variability of Acoustically Evidenced Methane Bubble Emissions Offshore Western Svalbard. *Geophys. Res. Lett.* 46 (15), 9072–9081.

Vogt, P. R., and Crane, K. (1994). Methane-generated( ) Pockmarks on Young, Thickly Sedimented Oceanic Crust in the Arctic. Vestnesa ridge, Fram Strait. *Geology* 22 (3). doi:10.1130/0091-7613(1994)022<0255:mgpoyt>2.3.co;2

Wallmann, K., Riedel, M., Hong, W. L., Patton, H., Hubbard, A., Pape, T., et al. (2018). Gas Hydrate Dissociation off Svalbard Induced by Isostatic Rebound rather Than Global Warming. *Nat. Commun.* 9 (1), 83. doi:10.1038/s41467-017-02550-9

Webb, S. C. (1998). Broadband Seismology and Noise under the Ocean. *Rev. Geophys.* 36 (1), 105–142. doi:10.1029/97rg02287

Wessel, P., Luis, J. F., Uieda, L., Scharroo, R., Wobbe, F., Smith, W. H. F., et al. (2019). The Generic Mapping Tools Version 6. *Geochem. Geophys. Geosyst.* 20, 5556–5564. doi:10.1029/2019gc008515

Wilks, D. S. (2011). *Statistical Methods in the Atmospheric Sciences (Vol. 100)*. San Diego, CA: Academic Press.

Conflict of Interest: The authors declare that the research was conducted in the absence of any commercial or financial relationships that could be construed as a potential conflict of interest.

Publisher's Note: All claims expressed in this article are solely those of the authors and do not necessarily represent those of their affiliated organizations, or those of the publisher, the editors and the reviewers. Any product that may be evaluated in this article, or claim that may be made by its manufacturer, is not guaranteed or endorsed by the publisher.

APPENDIX A CROSS-CORRELATION

For two N-element equal-interval (1 h) time series SDE(t) = {SDE(t_n)} and Tide(t) = {Tide(t_n)}) with the lag value k such as -max_lag <= k <= max_lag, lagged cross-correlation coefficient (Pearson product-moment coefficient of linear correlation) is given by (Crockett, 2019):

$$R_{xy}(k) = \frac{cov(SDE_{k'}, Tide_k)}{\sigma(SDE_{k'}), \sigma(Tide_k)}$$

where the covariance and standard deviations (σ) apply to the segments $SDE_{k'}$ and $Tide_k$ that overlap at lag k and -1 <= $R_{xy}(k)$ <= 1. Covariance (joint variance) between two N-element discrete variables SDE(n) = {SDE_n} and Tide(n) = {$Tide_n$}, where n = 0, 1, . . ., N-1 is defined as:

$$cov(SDE, Tide) = \frac{1}{N}\sum_{n=0}^{N-1}\left(SDE_n - \overline{SDE}\right)\left(Tide_n| - \overline{Tide}\right)$$

where $\overline{SDE}$, $\overline{Tide}$ are arithmetic means of normalized SDEs counts and normalized tidal height values, respectively. Lastly, the standard deviation of discrete variable SDE(n) is defined as (definition for Tide is analogous):

$$\sigma(SDE) = \sqrt{\frac{1}{N}\sum_{i=1}^{N}\left(SDE_i - \overline{SDE}\right)^2}$$

frontiers | Frontiers in Earth Science

ORIGINAL RESEARCH
published: 04 May 2022
doi: 10.3389/feart.2022.785418

Horizontal Force Required for Subduction Initiation at Passive Margins With Constraints From Slab Detachment

Lorenzo G. Candioti[1]*, *Thibault Duretz*[2] and *Stefan M. Schmalholz*[1]

[1]*Institut des Sciences de la Terre, Université de Lausanne, Lausanne, Switzerland,* [2]*Institut für Geowissenschaften, Goethe-Universität Frankfurt, Frankfurt, Germany*

Subduction zones are essential drivers of plate tectonics. However, the processes causing subduction zone initiation (SZI), involving the formation of a new plate boundary, and the forces required remain disputed. Here, we focus on horizontally forced SZI at passive margins and quantify the horizontal force required for SZI with two-dimensional petrological-thermomechanical numerical models. The initial configuration, involving two passive margins bounding a 400 km wide basin with exhumed mantle, is calculated by a numerical rifting simulation to guarantee thermomechanical feasibility and isostatic equilibrium. SZI occurs at one passive margin during convergence of the basin-margin system. SZI is caused by thermal softening due to local shear heating. A local temperature increase of only ca. 50°C is sufficient to cause SZI. Corresponding simulations without shear heating do not show SZI, showing unequivocally that thermal softening controls SZI. We systematically limit the lithospheric deviatoric stress to determine the minimum force required for SZI. A minimum force (per unit length) of ca. 14 TN m^{-1} is required for SZI; a force magnitude that agrees with independent estimates from mantle convection models. However, for the associated stress limit of 200 MPa the lithosphere is so weak that slab detachment (SD) already occurs at the onset of basin closure in the horizontal, non-subducted region of the subducting plate. Only for stress limits > =300 MPa (yielding a force of ca. 15 TN m^{-1}) subduction of continental crust occurs and SD occurs in the subducted slab. The force required for SZI is a proxy for the effective compressive lithospheric strength. This strength also controls subsequent SD due to tensile slab pull, which increases during subduction, also since our models include the olivine–wadsleyite phase change. Our simulations show a causal link betweeen SZI and subsequent SD: If forces required for SZI are smaller, then the lithosphere is weaker and then SD occurs at shallower levels and corresponding slabs are shorter. Concerning the European Alps, our results imply that if there was no SD since the Europe–Adria collision some 30 Myr ago (as proposed by some studies), then the subducted lithosphere must be considerably strong.

Keywords: Convergent plate boundary formation, subduction zone initiation, thermal softening, shear heating, slab detachment, lithospheric strength, plate driving force, Alps

OPEN ACCESS

Edited by:
Fabio Crameri, Undertone.design, Switzerland

Reviewed by:
Elvira Mulyukova, Northwestern University, United States
Carmen Gaina, Queensland University of Technology, Australia

***Correspondence:**
Lorenzo G. Candioti
lorenzo.candioti@unil.ch

Specialty section:
This article was submitted to Structural Geology and Tectonics, a section of the journal Frontiers in Earth Science

Received: *29 September 2021*
Accepted: *25 March 2022*
Published: *04 May 2022*

Citation:
Candioti LG, Duretz T and Schmalholz SM (2022) Horizontal Force Required for Subduction Initiation at Passive Margins With Constraints From Slab Detachment. Front. Earth Sci. 10:785418. doi: 10.3389/feart.2022.785418

1 INTRODUCTION

Earth is the only planet in our Solar System known to have currently active plate tectonics. Subduction zones, where old lithosphere is recycled back into the mantle, are major drivers of plate motion. However, the mechanisms that form convergent plate boundaries and create new subduction zones remain elusive (Stern, 2004; Stern and Gerya, 2018; Crameri et al., 2020). Two conceptual endmember scenarios for subduction zone initiation (SZI) have been proposed in the past decades: spontaneous, or vertically-forced, and induced, or horizontally-forced SZI (Stern, 2004; Stern and Gerya, 2018; Crameri et al., 2020). Vertically-forced SZI is supposedly driven by the increasing density, and therefore buoyancy, contrast between cooling oceanic lithosphere moving away from mid-ocean ridges and the underlying mantle. The feasibility of this scenario is disputed (e.g., Mueller and Phillips, 1991), particularly for SZI at passive margins. Cloetingh et al. (1989) already estimated that if SZI is not successful by ca. 20 Myr after continental break-up, the body force arising from density contrasts is likely insufficient to break the oceanic lithosphere. In fact, old ages of ocean floor (e.g., Müller et al., 2008) and various data collected from recent and ancient subduction zones (Crameri et al., 2020; Lallemand and Arcay, 2021) indicate that vertically-forced SZI was unlikely the dominant scenario during the last ca. 100 Myr. Instead, an additional horizontal compressive force, i.e., horizontally-forced SZI (McKenzie, 1977; Crameri et al., 2020), is required to overcome the increasing strength of cooling oceanic lithosphere. Recent geophysical observations of the Puysegur plate boundary south of New Zealand suggest that horizontal forces initially dominate at the site of SZI, but with time, vertical forces can accelerate, propagate along strike and facilitate the development of self-sustaining subduction (Shuck et al., 2022). However, both the horizontal force required for SZI as well as the processes causing strain localization and creating a new plate boundary remain poorly constrained.

Due to the large time and spatial scales, the complex petrological-thermomechanical feedbacks and the sparsity of geological evidence for SZI on present-day Earth (e.g., Crameri et al., 2020), a suitable method to study SZI is numerical geodynamic modelling. Published numerical models of SZI can be classified in two categories: 1) Models that investigate SZI at already existing, weak plate boundaries, which are prescribed as weak zones in the initial model configuration. These studies focus on the onset of sinking of a lithospheric plate and sometimes on the subduction of one plate below another plate (e.g., Malatesta et al., 2013; Zhong and Li, 2020; Zhou et al., 2020; Zhou and Wada, 2021). These studies do not investigate the formation of a new convergent plate boundary associated with SZI. 2) Models that investigate both SZI and the associated formation of a new convergent plate boundary, without *a priori* prescribing an already existing weak plate boundary in the initial model configuration (e.g., Thielmann and Kaus, 2012; Auzemery et al., 2020; Kiss et al., 2020; Candioti et al., 2021). The plate boundary formation must be numerically simulated in these models and, hence, these models can be used to determine the horizontal force required for SZI at, for example, passive margins. SZI involving the formation of a new plate boundary at a passive margin, so-called newly destructive SZI after Crameri et al. (2020), requires most likely a mechanism that mechanically softens, or weakens, the lithosphere while compressive horizontal forces build up. Several softening mechanisms have been proposed that can facilitate strain localisation of a compressed lithosphere during SZI, such as reaction-induced softening (e.g., White and Knipe, 1978), fluid-induced softening (e.g., Regenauer-Lieb et al., 2001; Dymkova and Gerya, 2013), evolution of fabric and anisotropy (e.g., Montési, 2013) or grain damage (e.g., Bercovici and Ricard, 2012; Mulyukova and Bercovici, 2018). All these mechanisms require knowledge of microscale (i.e., mineral grain scale) or two-phase (solid-fluid) pore-scale processes, which remain poorly constrained and are challenging to upscale for lithosphere models having typically numerical resolutions in the order of a kilometer. A softening mechanism that does not require assumptions of microscale and two-phase processes and that results only from the fundamental law of conservation of energy and the well established temperature dependence of viscous creep of rocks is thermal softening (e.g., Yuen et al., 1978; Regenauer-Lieb and Yuen, 1998). The conversion of dissipative work into heat, so called shear or strain heating, is inherent in all inelastic deformation such as viscous, or rate-dependent, and plastic, or rate-independent deformation. Hence, since viscous creep is thermally activated (e.g., Turcotte and Schubert, 2014), thermal softening may effectively reduce the strength of the viscously deforming regions of the lithosphere and yield to spontaneous formation of shear zones (e.g., Yuen et al., 1978; Regenauer-Lieb and Yuen, 1998; Leloup et al., 1999; Takeuchi and Fialko, 2012; Kiss et al., 2019). Furthermore, all physical processes proposed to explain high-velocity weakening of frictional faults are essentially related to shear heating (e.g., Aharonov and Scholz, 2018). Therefore, we consider here shear heating and associated thermal softening of viscous creep as main softening mechanism during SZI on the lithospheric scale, as has been done in several previous studies (Thielmann and Kaus, 2012; Jaquet and Schmalholz, 2018; Kiss et al., 2020; Auzemery et al., 2020, 2021).

Models for SZI at passive margins consider frequently an initial model configuration with an idealized, ad hoc designed passive margin geometry and associated temperature field (e.g., Auzemery et al., 2020; Kiss et al., 2020). At an idealized passive margin with homogeneous crustal and mantle material properties, Kiss et al. (2020) reported a required horizontal force per unit length of ca. 37 TN m^{-1}, indicating that high driving forces are required for shear heating to cause SZI. Such large driving forces, and associated locally high deviatoric stresses, have been used as argument against thermal softening being a feasible mechanism for shear localization (e.g., Platt, 2015). An important step to reduce the driving force necessary for SZI by thermal softening is to consider more realistic passive margin architectures. Including mechanical heterogeneities and numerically modelling the architecture of passive margins prior to convergence, instead of designing these margins ad hoc, Candioti et al. (2020) and Candioti et al. (2021) report significantly smaller force magnitudes between 15 and 18 TN m^{-1} for thermal softening induced SZI. Although the plate

driving force magnitudes in these models are significantly reduced, a minimum value for horizontal forces required for SZI *via* thermal softening has not been quantified yet in a systematic way. Here, we generate the passive margin architecture with a numerical lithosphere rifting simulation and apply this architecture as initial configuration for convergence simulations to investigate SZI at passive margins (see also Candioti et al., 2020, 2021, for detailed discussion). Advantages of using a numerically calculated passive margin architecture as initial configuration are that 1) such architecture is thermomechanically feasible and consistent with the applied convergence model, 2) it is isostatically stable and 3) the initial temperature field, including thermal convection in the upper mantle, is consistent with the architecture and applied thermal parameters.

Here, we present two-dimensional (2D) petrological–thermomechanical numerical models that predict SZI at hyperextended passive continental margins. We aim to quantify the minimum horizontal force required for SZI at a passive continental margin *via* thermal softening. Hence, we quantify the resistance to failure of the lithosphere around passive margins under compressive forces during SZI. After SZI we continue modelling convergence and progressive subduction until slab detachment (SD) occurs. Therefore, we also quantify tensile forces, arising due to increasing slab pull, required to fail the lithosphere by SD. With our model we want to test the following hypothesis: The magnitude of the horizontal force required for SZI also controls the force required for detachment of the slab generated by SZI. Therefore, the smaller the force required for SZI, the shorter the slab for which SD occurs. In other words, if the force required for SZI is small, then the initiated subduction zone cannot generate a slab of significant length. To this end, we systematically limit the stresses in the load-bearing layers of the lithosphere (lower crust and mantle lithosphere), because the strength of these layers is a key parameter for successful SZI. Unfortunately, the strength of the lithosphere is difficult to constrain (e.g., Burov and Watts, 2006; Baumann et al., 2014) and often determined by laboratory experiments on olivine, an abundant mineral in the upper mantle, conducted under accelerated deformation conditions and then extrapolated over many orders of magnitude to geological time and deformation scales. In consequence, the actual strength of olivine deforming under geological conditions is currently actively debated (e.g., Demouchy et al., 2013; Idrissi et al., 2016; Hansen et al., 2019; Furstoss et al., 2021). Many recent rock deformation experiments suggest that the strength of olivine is mainly controlled by dislocation glide, or low-temperature plasticity, and is significantly lower than determined in previous laboratory experiments (e.g., Demouchy et al., 2013; Idrissi et al., 2016). However, other studies recently showed that although olivine might be initially weaker than previously thought, strain hardening during increasing rate-dependent plastic deformation might increase its overall strength significantly (e.g., Hansen et al., 2019). Knowledge of the strength of the lithosphere is important because it controls essentially all deformation processes of the lithosphere, such as lithosphere flexure at subduction zones or around seamounts, and of course SZI and SD as studied here. One aim of our modelling study is, therefore, also to evaluate whether our combined SZI and SD simulations can help in assessing the effective strength of the lithosphere.

Furthermore, we discuss potential implications of our results for the closure and subduction of the Piemonte–Liguria ocean during the formation of the European Alps and potential slab detachment associated with the Alpine continental collision (**Figure 1**). For the Western Alpine orogeny, a wealth of data exists that allowed constraining the tectonic and petrological evolution from SZI at the Adriatic margin, through the closure of the Piemont-Liguria ocean to the Alpine continental collision potentially involving slab detachment. Thus, the configuration of our numerical models is motivated by tectonic reconstructions for the Alpine orogeny.

2 MODEL

2.1 The Alpine Orogeny as Motivation for Our Model Configuration

Here we focus on SZI at magma-poor passive margins that bound embryonic oceans. We define embryonic oceans as marine basins that are small in extent (ca. ≤ 600 km) and mainly floored by exhumed mantle and hyperextended continental crust rather than mature oceanic crust (Chenin et al., 2017). Ancient and recent examples of embryonic oceans are, for example, the Piemonte–Liguria ocean (e.g., McCarthy et al., 2020), the present day Ligurian Basin (e.g., Dannowski et al., 2020) and Red Sea (e.g., Chenin et al., 2017). These ocean basins result from slow-to-ultra-slow spreading rift systems, and the architecture and extent of these oceans is similar (Chenin et al., 2017). Mesozoic rifting separated Europe from Adria and terminated at ca. 145 Ma (e.g., Le Breton et al., 2021). This rifting generated the Piemonte-Liguria ocean basin and the two magma-poor passive margins of Europe and Adria (e.g., Handy et al., 2010; McCarthy et al., 2020; Le Breton et al., 2021). The European and Adriatic passive margins were likely hyperextended and bounded the embryonic Piemonte–Liguria ocean (see **Figure 1A**). At ca. 85–80 Ma subduction was presumably initiated within the Adriatic continental margin leading to subduction of the Sesia–Dent Blanche unit (e.g., Manzotti et al., 2014, see **Figure 1B**). Remnants of the Piemonte–Liguria ocean have been incorpated in the Alpine orogenic wedge (e.g., Schmid et al., 2017, see **Figure 1C**). Whether the European slab is detached or still attached to the European plate is currently disputed (e.g., Kästle et al., 2019).

2.2 Modelling Approach Involving Geodynamic Cycles

In this study we build upon our previous work presented in Candioti et al. (2021). Candioti et al. (2021) presented two-dimensional (2D) petrological-thermomechanical numerical models that simulate several, subsequent geodynamic processes in a single and continuous simulation, including thermal convection in the upper mantle. They modelled 1) the

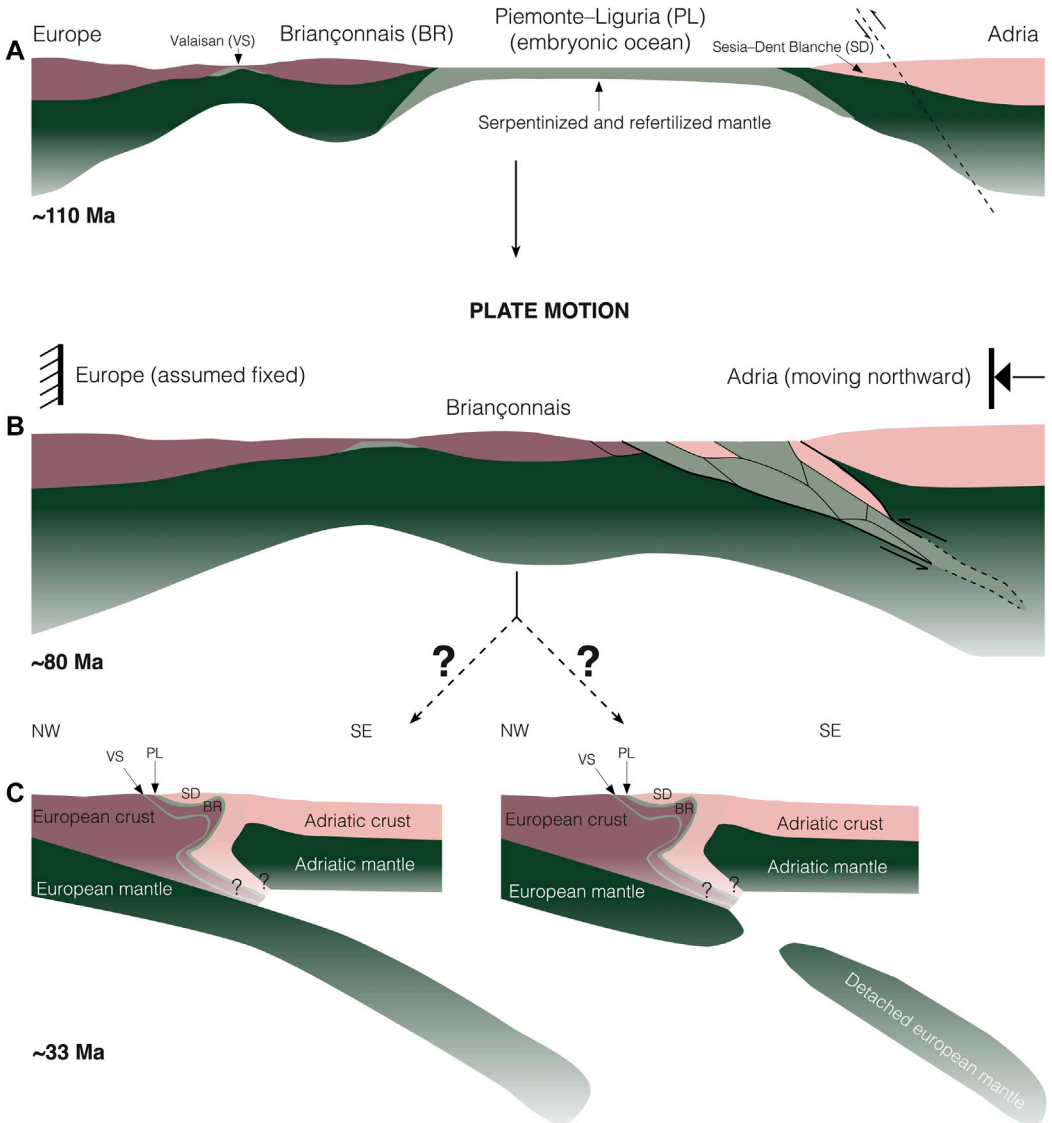

FIGURE 1 | Simplified conceptual geodynamic sketch of the Alpine orogeny. **(A)** Passive margin geometry and embryonic oceans after the rifting stage. **(B)** Horizontally-forced SZI at the Adriatic passive margin and subduction of the Sesia–Dent Blanche unit. **(C)** Possible scenarios for the collisional stage of the Alpine orogeny with a continuously subducting slab (left) or detached slab (right). Geological units are simplified and taken from Schmid et al. (2017) and McCarthy et al. (2020).

formation of hyperextended passive continental margins bounding an embryonic ocean, 2) SZI *via* thermal softening during convergence of the ocean-margin system, 3) subduction and closure of an embryonic ocean, 4) formation of a collisional orogen and 5) SD of subducted lithosphere. This Wilson-type cycle of embryonic ocean basins comprised 1) a 50 Myr extension period, 2) a 60 Myr cooling period between the extension and convergence phase and 3) a ca. 70 Myr convergence period. Candioti et al. (2021) applied this cycle to the opening and closure of the Piemonte–Liguria ocean and the subsequent formation of the European western Alps (e.g., McCarthy et al., 2020). They mainly focused on the competition between buoyancy and shear forces during the collisional stage of the orogen. When shear forces dominate the collisional stage of the orogen, wedge formation without deep subduction of continental crustal material occured. When buoyancy forces were equally important as shear forces, Candioti et al. (2021) observed deep subduction and exhumation of continental units. The mechanical boundary velocities and the duration of the deformation periods they applied were motivated by plate motion reconstructions from the European and Adriatic plate during the past ca. 180 Myr (e.g., Le Breton et al., 2021). Complementary to their results, we here focus on the subduction stage. Especially, we aim at quantifying the minimum force required for SZI and the role of lithospheric strength in the kind of models presented by Candioti et al. (2021). Note, that we refer to time as the

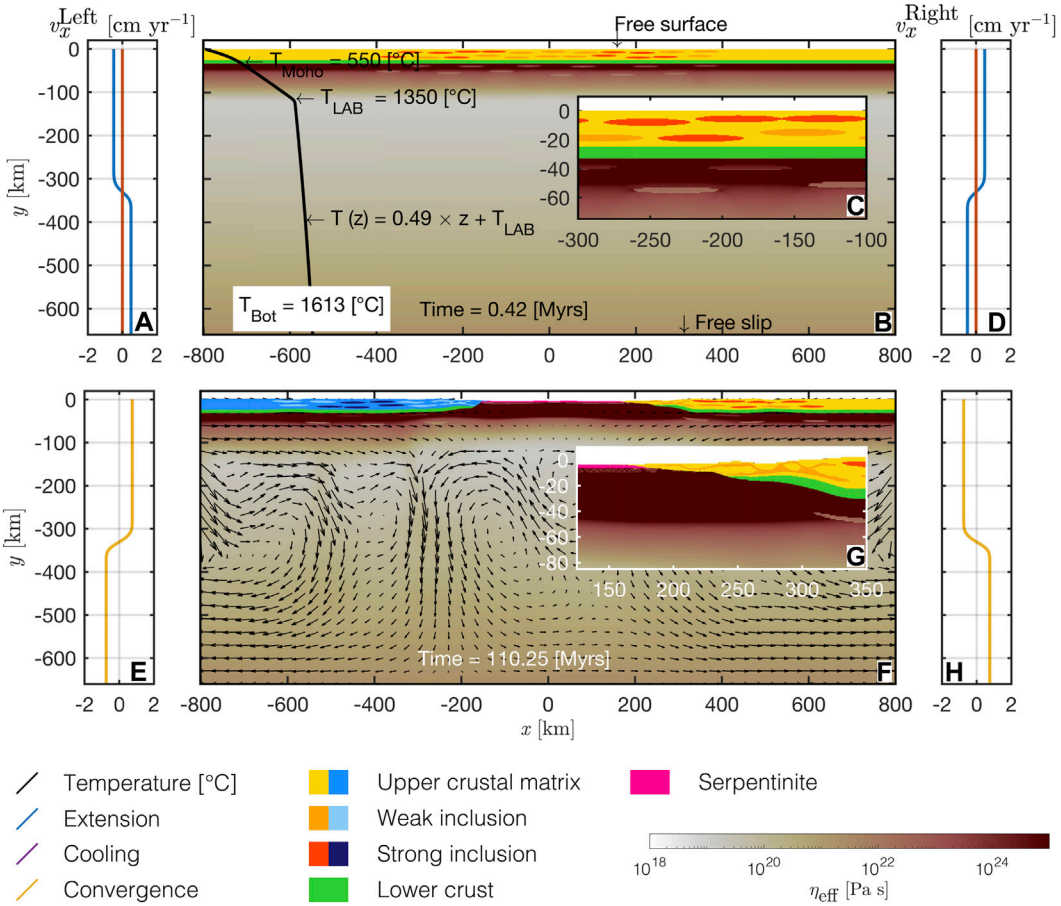

FIGURE 2 | Initial model configuration. Numerical resolution is 1 km by 1 km everywhere in the domain. **(A–D)** From the onset of rifting as modelled in detail by Candioti et al. (2021) and **(E–H)** from the onset of convergence as investigated in this study. **(A,E)**: vertical profile of horizontal boundary velocity applied along the left boundary. **(D,H)**: vertical profile of horizontal velocity applied along the right model boundary. **(B,F)** show the entire model domain. White to red indicates the effective viscosity calculated by numerical algorithm, black solid line is the initial temperature profile, light to dark orange are upper crustal lithologies of the right plate, light to dark blue are the lithologies of the left plate, green is the lower crust of both plates and magenta is a serpentinite layer, initially 3 km thin. **(C)**: enlargement of the domain center and **(G)** shows an enlargement of the right margin. Glyphs in **(F)** show the velocity field calculated by the numerical algorithm.

simulated physical time and its unit is Myr. Whenever we refer to actual geological time, we use the unit Ma. **Figures 2A-D** shows the initial configuration used by Candioti et al. (2021) to model this type of Wilson cycle. A detailed justification of the initial conditions, a full description of the entire model evolution as well as in depth information on the implementation of boundary conditions, petrological-thermomechanical coupling and surface processes (i.e., sedimentation and erosion) is given in the open-access article of Candioti et al. (2021). The models we present here start from the configuration predicted at 110 Myr (end of cooling period) in model history by the reference model of Candioti et al. (2021) (see **Figures 2E-H**). Similar to the study of Candioti et al. (2021), we parameterize a serpentinisation front propagating across the top 3 km of exhumed mantle material in the embryonic oceanic basin before the onset of convergence. Because of ultra-slow spreading rates, no significant mid-ocean ridge with active magmatism is formed. Therefore, embryonic oceans often lack a mature Penrose-type oceanic crust (e.g., McCarthy et al., 2020). Instead, the subcontinental mantle is exhumed to the surface and in contact with the sea-water. Thus, serpentinisation is likely significant in embryonic ocean basins and presumably plays an important role during subduction of embryonic oceans (e.g., McCarthy et al., 2020). In our models, convergence is induced by applying a constant absolute boundary horizontal velocity of 1.5 cm yr^{-1}. To quantify the minimum driving force and assess the strength of embryonic oceanic lithosphere, we employ a parameterized stress limiter in the mantle lithosphere and the lower crust. In addition to the applied pressure-sensitive Drucker-Prager plastic stress limiter function, this stress limiter is independent on pressure and is used here as a controlling parameter for the plate strength. We systematically tested stress limits of 10, 50, 100, 150, 200, 300, 500 MPa, and 500 GPa. Employing a value of 500 GPa deactivates the stress limiter in the reference model, named NOSLIM hereafter. In addition to the reference model, we here report results for models employing stress limits of 100, 200 and

300 MPa, named SLIM100, SLIM200 and SLIM300 hereafter. These models predict end-member dynamics for subduction initiation and the evolving subduction zone. To test the impact of shear heating and associated thermal softening on SZI we also performed the two simulations SLIM300 and NOSLIM without shear heating.

2.3 Governing Equations

We consider incompressible materials that slowly creep (no inertia) under gravity and boundary tractions. The applied numerical algorithm solves the continuity equation, the equation for the conservation of momentum and the heat transfer equation in a two-dimensional Cartesian coordinate system, which are given by:

$$\frac{\partial v_i}{\partial x_i} = 0 \tag{1}$$

$$\frac{\partial \sigma_{ij}}{\partial x_j} = -\rho\ g_i \tag{2}$$

$$\rho\ c_{\mathrm{P}}\ \frac{\mathcal{D}T}{\mathcal{D}t} = \frac{\partial}{\partial x_i}\left(k\ \frac{\partial T}{\partial x_i}\right) + H_{\mathrm{A}} + H_{\mathrm{D}} + H_{\mathrm{R}}\ , \tag{3}$$

where i and j are spatial indices and repeated indices are summed, v is velocity and x is the spatial coordinate, σ is the total stress tensor, ρ is density and g = [0; −9.81] is a vector including the gravitational acceleration. The density is a function of temperature, T, pressure, P, and a given bulk rock composition, C, which is precomputed using a thermodynamic software package (Perple_X Connolly, 2005, 2009). We, thus, include large density variations resulting from mineral phase transitions. For example, at a lithostatic pressure and a temperature corresponding to a depth of ca. 410 km, the olivine–wadsleyite phase transition results in a density increase of ca. 150 kg m^{-3} (see Candioti et al., 2020, **Figures 2B,E**). Such an increase might significantly impact on the subduction dynamics. A detailed description of the implementation of petrological-thermomechanically coupled processes and the applied chemical composition of the model units is given in the two open-access publications Candioti et al. (2020) and Candioti et al. (2021). In **Eq. 3**, c_P is heat capacity at constant P, $\mathcal{D}/\mathcal{D}t$ is the material time derivative, k is thermal conductivity and H_{R} comprise source terms resulting from radiogenic heat production. We include source terms resulting from adiabatic processes (Extended Boussinesq Approximation, e.g., Candioti et al., 2020, for detailed justification), $H_{\mathrm{A}} = T\alpha v_y g\rho$, where α is the coefficient of thermal expansion and v_y is the vertical component of velocity. Further, we consider contributions from the conversion of rate-dependent and rate-independent mechanical processes into heat, $H_{\mathrm{D}} = \tau_{ij}\,(\dot{\varepsilon}_{ij} - \dot{\varepsilon}_{ij}^{\mathrm{ela}})$, where $\dot{\varepsilon}$ is the total deviatoric strain rate tensor and $\dot{\varepsilon}^{\mathrm{ela}}$ denotes the strain rate resulting from elastic deformation. The total stress tensor is decomposed into a pressure and a deviatoric part as

$$\sigma_{ij} = -P\delta_{ij} + 2\ \eta^{\mathrm{eff}}\ \dot{\varepsilon}_{ij}^{\mathrm{eff}} \tag{4}$$

$$\delta_{ij} = \begin{cases} 0 & ,\ i \neq j \\ 1 & ,\ i = j, \end{cases} \tag{5}$$

where δ_{ij} is the Kronecker-Delta, η^{eff} is the effective viscosity, $\dot{\varepsilon}^{\mathrm{eff}}$ is the effective deviatoric strain rate tensor,

$$\dot{\varepsilon}_{ij}^{\mathrm{eff}} = \left(\dot{\varepsilon}_{ij} + \frac{\tau_{ij}^{o}}{2G\Delta t}\right), \tag{6}$$

where G is shear modulus, Δt is the time step, τ^o are the deviatoric stress tensor components of the preceding time step. We consider visco-elasto-plastic deformation and additively decompose (so-called Maxwell model) the total deviatoric strain rate tensor into contributions from rate-dependent plastic deformation (i.e., effectively viscous behaviour by dislocation, diffusion and Peierls creep), elastic and rate-independent (brittle) plastic deformation as

$$\dot{\varepsilon}_{ij} = \dot{\varepsilon}_{ij}^{\mathrm{ela}} + \dot{\varepsilon}_{ij}^{\mathrm{pla}} + \dot{\varepsilon}_{ij}^{\mathrm{dis}} + \dot{\varepsilon}_{ij}^{\mathrm{dif}} + \dot{\varepsilon}_{ij}^{\mathrm{Pei}}\ . \tag{7}$$

The viscosity for dislocation, diffusion and Peierls creep are a function of the respective second strain rate tensor invariant, $\dot{\varepsilon}_{\mathrm{II}}^{\mathrm{dis,\,dif,Pei}} = \sqrt{\frac{1}{2}(\dot{\varepsilon}_{ij}^{\mathrm{dis,\,dif,Pei}})^2}$. The dislocation and diffusion creep viscosity are computed as

$$\eta^{\mathrm{dis,\,dif}} = \frac{2^{\frac{1-n}{n}}}{3^{\frac{1+n}{2n}}}\ A^{-\frac{1}{n}}\ \left(\dot{\varepsilon}_{\mathrm{II}}^{\mathrm{dis,\,dif}}\right)^{\frac{1}{n}-1}\ d^{m}\ \exp\!\left(\frac{Q+PV}{nRT}\right)\ \left(f_{\mathrm{H_2O}}\right)^{-\frac{r}{n}}, \tag{8}$$

where d is grain size and the ratio in front of the prefactor A results from the conversion of experimentally derived flow laws into a tensor formulation of these flow laws (e.g., Schmalholz and Fletcher, 2011). The quantities A, n, m, Q, V, $f_{\mathrm{H_2O}}$ and r are experimentally determined material parameters which are characteristic for each creep law (see **Table 1**). To increase the readability we have omitted the superscripts "dif/dis" for these parameters. Note that for diffusion creep the n = 1 and for dislocation creep m = 0. Hence, dislocation and diffusion creep are essentially insensitive to grain size and strain rate, respectively. We further include the experimentally derived Peierls flow law by Goetze and Evans (1979) expressed in the regularized form of Kameyama et al. (1999) and calculate the Peierls viscosity as

$$\eta^{\mathrm{Pei}} = \frac{2^{\frac{1-s}{s}}}{3^{\frac{1+s}{2s}}}\ \hat{A}\ \left(\dot{\varepsilon}_{\mathrm{II}}^{\mathrm{Pei}}\right)^{\frac{1}{s}-1}\ , \tag{9}$$

employing an effective stress exponent

$$s = 2\ \gamma\ \frac{Q}{RT}\left(1-\gamma\right). \tag{10}$$

$\hat{A}$ in **Eq. 9** is calculated as

$$\hat{A} = \left[A^{\mathrm{Pei}}\ \exp\!\left(-\frac{Q(1-\gamma)^2}{RT}\right)\right]^{-\frac{1}{s}}\ \gamma\sigma^{\mathrm{Pei}}\ , \tag{11}$$

where A^{Pei}, γ and σ^{Pei} are material parameters. We control rate-independent (brittle) plastic deformation by a deviatoric stress limiter function

$$F = \tau_{\mathrm{II}} - \tau^{\mathrm{eq}} \tag{12}$$

$$\tau^{\mathrm{eq}} = \begin{cases} P\ \sin\varphi + C\ \cos\varphi & ,\ P\ \sin\varphi + C\ \cos\varphi < S \\ S & ,\ P\ \sin\varphi + C\ \cos\varphi \geq S, \end{cases} \tag{13}$$

TABLE 1 | Physical parameters used in the numerical simulations.

Model Unit	Rheology (reference)	k [W m^{-1} K^{-1}]	H_R [W m^{-3}]	C [Pa]	φ [°]
Crustal matrix [a]	Westerly Granite Hansen and Carter (1983)	2.25	1.0200×10^{-6}	1×10^{7}	30
Weak inclusion[a]	Wet Quartzite Ranalli (1995)	2.25	1.0200×10^{-6}	1×10^{6}	5
Strong inclusion[a]	Maryland Diabase Mackwell et al. (1998)	2.25	1.0200×10^{-6}	1×10^{7}	30
Calcite[a]	Calcite Schmid et al. (1977)	2.37	0.5600×10^{-6}	1×10^{7}	30
Mica[a]	Mica Kronenberg et al. (1990)	2.55	2.9000×10^{-6}	1×10^{7}	15
Lower crust[b]	Wet Anorthite Rybacki and Dresen (2004)	2.25	0.2600×10^{-6}	1×10^{7}	30
Strong mantle[c]	Dry Olivine Hirth and Kohlstedt (2003)	2.75	2.1139×10^{-8}	1×10^{7}	30
Weak mantle[c]	Wet Olivine Hirth and Kohlstedt (2003)	2.75	2.1139×10^{-8}	1×10^{7}	30
Serpentinite[d]	Antigorite Hilairet et al. (2007)	2.75	2.1139×10^{-8}	1×10^{7}	25

Dislocation creep	A [Pa^{-n-r} m^{m} s^{-1}]	m [ ]	n [ ]	Q [J mol^{-1}]	V [m^3 mol^{-1}]	r [ ]
Crustal matrix	3.1623×10^{-26}	0.0	3.3	186.5×10^{3}	0.00×10^{-6}	0.0
Weak inclusion	5.0717×10^{-18}	0.0	2.3	154×10^{3}	0.00×10^{-6}	0.0
Strong inclusion	5.0477×10^{-28}	0.0	4.7	485×10^{3}	0.00×10^{-6}	0.0
Calcite	1.5849×10^{-25}	0.0	4.7	297×10^{3}	0.00×10^{-6}	0.0
Mica	1.0000×10^{-138}	0.0	18.0	51.0×10^{3}	0.00×10^{-6}	0.0
Lower crust	3.9811×10^{-16}	0.0	3.0	356×10^{3}	0.00×10^{-6}	0.0
Strong mantle	1.1000×10^{-16}	0.0	3.5	530×10^{3}	14.0×10^{-6}	0.0
Weak mantle[e]	5.6786×10^{-27}	0.0	3.5	480×10^{3}	11.0×10^{-6}	1.2
Serpentinite	4.4738×10^{-38}	0.0	3.8	8.90×10^{3}	3.20×10^{-6}	0.0

Diffusion creep[f]	A [Pa^{-n-r} m^{m} s^{-1}]	m [ ]	n [ ]	Q [J mol^{-1}]	V [m^3 mol^{-1}]	r [ ]
Strong mantle	1.5000×10^{-15}	3.0	1.0	375×10^{3}	7.5×10^{-6}	0.0
Weak mantle[e]	2.5000×10^{-23}	3.0	1.0	375×10^{3}	7.0×10^{-6}	1.0

Peierls creep	A^{Pei} [s^{-1}]	Q [J mol^{-1}]	V [m^3 mol^{-1}]	σ^{Pei} [Pa]	γ [ ]
Mantle[g]	5.7000×10^{11}	540×10^{3}	0.0×10^{-6}	8.5×10^{9}	0.1

Constant parameters: A heat capacity c_P *= 1,050 [J kg^{-1} K^{-1}] is employed for all phases.*
[a,b,c]*A constant shear modulus* G *= 2 × 10^{10} [Pa] is used.*
[d]*A constant shear modulus* G *= 1.81 × 10^{10} [Pa] is used.*
[e]*A water fugacity* f_{H_2O} *= 1.0 × 10^{9} [Pa] is used. For all other phases* f_{H_2O}*= 0.0 [Pa].*
[f]*A constant grain size* d *= 1 × 10^{-3} [m] is used.*
[g]*Reference: Goetze and Evans (1979) regularized by kameyama1999thermal. These parameters are used for both strong and weak mantle rheology.*

where, $\tau_{II} = \sqrt{\frac{1}{2}(\tau_{ij})^2}$ is the second invariant of the deviatoric stress tensor, φ is the internal angle of friction, C is the cohesion and S is a stress limiter which is a parameter that is not experimentally derived but a variable used to control the material strength. The plastic viscosity at the equivalent deviatoric stress, τ^{eq}, is computed as

$$\eta^{vep} = \frac{\tau^{eq}}{2\dot{\varepsilon}_{II}^{eff}} , \tag{14}$$

where $\dot{\varepsilon}_{II}^{eff} = \sqrt{\frac{1}{2}\dot{\varepsilon}_{ij}^{eff}\dot{\varepsilon}_{ij}^{eff}}$. In **Eq. 4**, the effective viscosity is either the quasi-harmonic average of the visco-elastic contributions

$$\eta^{eff} = \begin{cases} \left(\frac{1}{G\Delta t} + \frac{1}{\eta^{dis}} + \frac{1}{\eta^{dif}} + \frac{1}{\eta^{Pei}}\right)^{-1} & , F < 0 \\ \eta^{vep} & , F \geq 0 \end{cases} \tag{15}$$

or is equal to η^{vep}. Advection of material is performed using a marker-and-cell technique (Gerya and Yuen, 2003) and we compute rigid body rotation of stresses analytically (see also Candioti et al., 2021, for a more detailed description of the algorithm). A marker chain and a stabilisation algorithm (Duretz et al., 2011b, 2016) is employed to allow for dynamic evolution of topography. Surface processes, namely erosion and sedimentation, are parameterized in the model. In case, the newly computed topography falls below a sedimentation level of $z = -5$ km it is corrected back to the sedimentation level. The resulting gap between the newly computed topographic level and the sedimentation level is filled instantaneously with markers describing a calcite or a mica rheology. The rheology of the sediment markers alternates every 2 Myr. In case the newly computed topography rises above an erosion level of $z = 2$ km, the topographic level is corrected downward. The distance of correction is calculated by multiplying the current time increment, Δt, by a constant erosion velocity of 0.5 mm yr^{-1}. All material parameters used in the models presented here are listed in **Table 1**.

2.4 Calculation of Plate Driving Forces and Slab-Pull-Force Estimate

Here, $F_D = 2 \times \bar{\tau}_{II}^{avg}$ is used as a representative value for the horizontal driving force per unit length. Close to the lateral model boundaries, where F_D is calculated, the smallest principal stress is vertical and is close to the lithostatic pressure, and the maximal principal stress is approximately horizontal. Therefore, F_D is a representative estimate for the plate driving force (e.g., Schmalholz et al., 2014, 2019). First, the vertical integral of $\tau_{II}(x, y)$ is calculated at the different horizontal positions of the numerical grid as

$$\bar{\tau}_{\mathrm{II}}(x) = \int_{b}^{a} \tau_{\mathrm{II}}(x, y)\, \mathrm{d}y\ , \tag{16}$$

where a is the topographic level at each horizontal grid point and b = −660 km is the bottom coordinate of the model domain. The values of $\bar{\tau}_{\mathrm{II}}(x)$ are then averaged horizontally inside two regions of 100 km width located at the two lateral model sides. This horizontally averaged, vertically integrated stress is termed $\bar{\tau}_{\mathrm{II}}^{\mathrm{avg}}$. The reader is referred to Candioti et al. (2020) for further detail.

We further estimate the slab-pull force per unit length by calculating the effective body force of the subducting slab. This body force, F_{SP}, is computed as the difference between densities of all material that is 1) enclosed horizontally within $-700 \le x \le 700$ km of the domain, 2) colder than $T \le 1{,}300$°C and 3) subducted below y = −160 km and a vertical reference density profile. This reference profile is obtained from the last time step of the cooling period of model NOSLIM by averaging horizontally all material densities at each vertical grid level below y = −160 km over the entire horizontal domain. This reference density is also used to compute the density difference, $\Delta\rho$, induced by a phase transition. The body force is then calculated as follows:

$$F_{\mathrm{SP}} = \int_{\Omega} \Delta\rho g\ \mathrm{d}\Omega\ , \tag{17}$$

where $\Delta\rho$ is the aforementioned density difference integrated over the area Ω covered by material matching the three criteria defined above. This is a maximum estimate for the slab-pull force, because the surrounding mantle material exerts shear stresses on the slab surface which resist subduction. Assuming shear stress magnitudes of 1–10 MPa along the bottom and top of a ca. 500 km long slab results in force magnitudes between 1 and 10 TN m^{-1}, respectively, acting against the slab pull force due to buoyancy only. Therefore, the natural, effective slab pull force magnitudes including the shear resistance from the surrounding mantle are likely lower than the ones reported here (see also Turcotte and Schubert, 2014). However, the relative evolution of F_{SP} likely remains as reported here.

3 RESULTS

In this section we first report the results of the reference model without stress limiter, termed NOSLIM, and compare them to the models with different stress limits afterwards. We compare the stage of SZI, the evolution of plate driving and approximated slab pull forces as well as the dynamics of SD. We refer to the model passive margins on the left and right side of the model as left and right margin from here onward.

3.1 Geodynamic Evolution of the Reference Model NOSLIM

Convergence is started at 110 Myr in model history. Subduction initiates at ca. 113 Myr at the transition zone between the proximal and the necking domain within the mantle lithosphere of the right margin (**Figures 3A,E**). SZI occurs at a region where no serpentinite is present which indicates that the initially horizontal serpentinite layer is not important for SZI. This conclusion is also supported by the findings of Candioti et al. (2021), who report successful SZI with and without a serpentinite layer in similar numerical models. Maximal bending stresses within the lithosphere of the subducting and overriding plate are ca. 500–700 MPa and limited to a 10–25 km thin layer (**Figure 3E**). Until ca. 129 Myr, large portions of the serpentinite are sheared off the subducting slab (**Figure 3B**). The values for stresses decrease below ca. 100 MPa within the overriding plate and remain at ca. 250–400 MPa where the subducting plate is bent below the overriding plate (**Figures 3F,G**). This stage marks the successful SZI in this simulation. The embryonic ocean basin is closed at ca. 140 Myr in model history. At this stage, the serpentinite material has largely been sheared off the subducting plate and reorganized along the plate interface (**Figure 3C**). A thrust wedge has formed at ca. 160 Myr and a large part of the subducting slab has been detached from the subducting plate (**Figure 3D**). The values of deviatoric stresses within the thrust wedge remain between ca. 100–250 MPa (e.g., $-200 \le x \le -100$ km and $y > -30$ km in **Figure 3H**).

3.2 Subduction Initiation at Hyperextended Continental Margins

Figure 4 shows the stage of SZI in the different models. In the reference model, NOSLIM, and in SLIM300 a shear zone forms below the right margin (blue region in right column of **Figures 4A,B**). Values for dissipative heating inside the shear zone are above 10^{-5} W m^{-3} (red contour line in **Figures 4A,B**) and the temperature inside the evolving shear zone increases compared to the surrounding ambient mantle temperature. This temperature increase is indicated by the geometry of the isotherms which are in shallower depth inside the shear zone compared to the corresponding isotherms to the left and right side of the shear zone. By comparing the vertical position of the grey isotherms in **Figures 4A,B**, one can estimate the temperature rise inside the shear zone assuming that before shear zone formation the isotherms were approximately horizontal, like in the corresponding left margins. For example, at the right margin of model NOSLIM, the isotherm for 727°C inside the shear zone is in approximately the same depth as the horizontal isotherm for 637°C to the left of the shear zone. Therefore, in NOSLIM the temperature rises by ca. 90°C and in SLIM300 by ca. 50°C, using the same estimate based on isotherm geometries. Kiss et al. (2019) showed that a small temperature increase of only ca. 50°C already can cause strain localization by thermal softening. Compared to models NOSLIM and SLIM300, less dissipative heat is generated by the shear zone forming in model SLIM200. The temperature rise inside the shear zone of model SLIM200 is still ca. 50°C, which is comparable to model SLIM300. In SLIM100 the heat generated by the conversion of mechanical work into heat is insignificant and the temperature inside the shear zone rises by less than 10°C (compare **Figures 4A,B** to **Figures 4C,D**). **Figure 5**

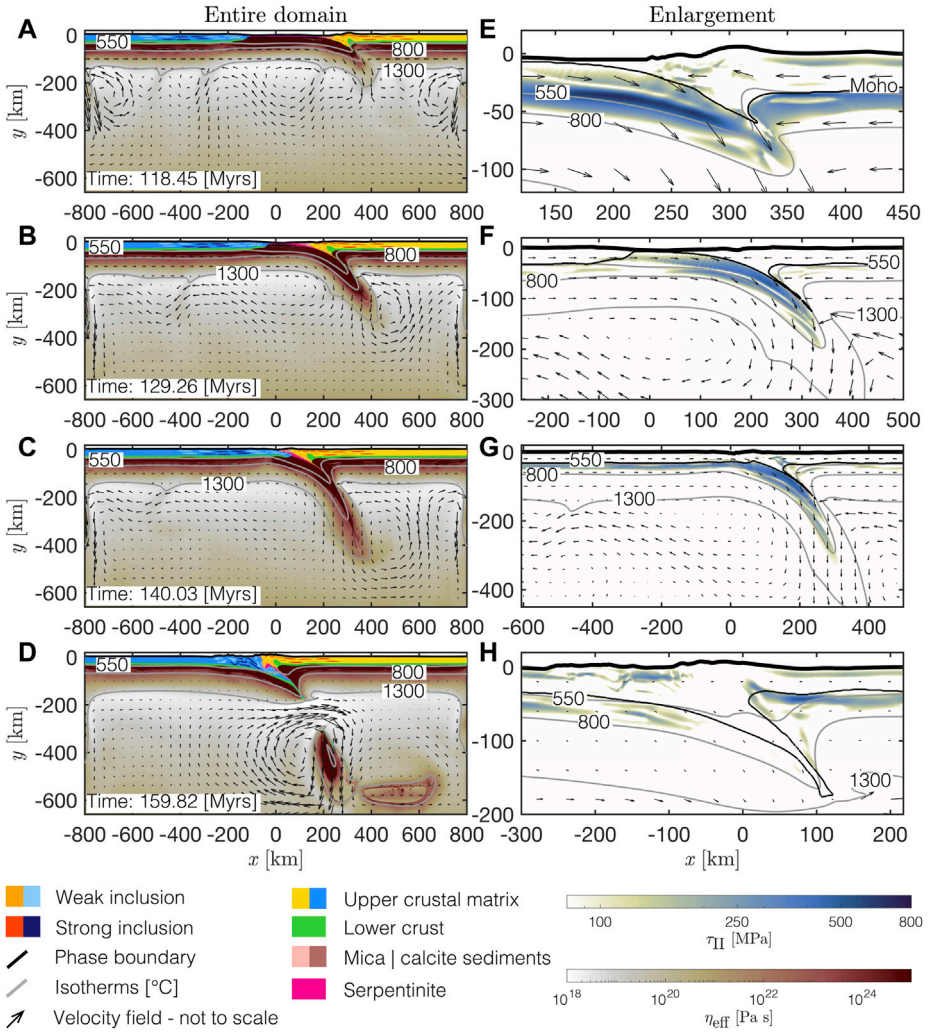

FIGURE 3 | Geodynamic evolution of the reference model NOSLIM (no additional applied stress limit). **(A–D)**: Entire domain. White to red is the effective viscosity calculated by the numerical algorithm. Colouring of lithologies as indicated in the legend. **(E–H)**: White to blue is the second invariant of the deviatoric stress tensor as calculated by the numerical algorithm. Glyphs in all panels show the velocity field and grey solid lines are several isotherms predicted by the numerical algorithm.

shows which regions in the model exhibit only rate–independent plastic, or brittle, deformation (highlighted in blue) and which regions exhibit elastic or rate–dependent plastic, or ductile, deformation (highlighted in white, see **Section 2.3** for calculation). In contrast to the ductile (white regions in **Figures 5A,B**) shear zones formed in NOSLIM and SLIM300, the shear zones in SLIM200 and SLIM100 are mainly formed due to brittle deformation (blue regions in **Figures 5C,D**). The reason is that in SLIM200 and SLIM100 the stress limits are lower and, hence, the regions in which stresses exceed the stress limit (i.e., here the brittle region) become larger. Further, brittle shear zones also form below the left margin in SLIM100 (**Figure 4D** and **Figure 5D**). In consequence, the subduction zone in SLIM100 evolves completely different compared to the subduction zone in SLIM300. Subduction in SLIM100 is initiated below the opposite margin (**Figures 6A,B**) and the slab is subducted much slower (compare depth of slab tip in the left and right column of **Figure 6C**). The detachment of the slab occurs approximately at the same depth in SLIM100 and SLIM300, but much later in SLIM100 compared to SLIM300 (156 and 150 Myr, respectively, **Figure 6D**). We consider the slab as detached when the distance between the 1,300°C isotherms bounding the slab is less than 10 km. The slab in model SLIM300 is much longer than it is thick, thus resembling the typical rectangular cross-sectional shape of a slab. In contrast, the shape of the slab in SLIM100 resembles more the cross-sectional shape of a lithospheric droplet rather than a subducting slab (compare left and right panel **Figure 6D**). The deformation behaviour observed in SLIM100 is very similar to the so-called drip-off mode described in the numerical simulations of Thielmann and Kaus (2012). This deformation behaviour does not correspond to the subduction of a coherent plate-like slab.

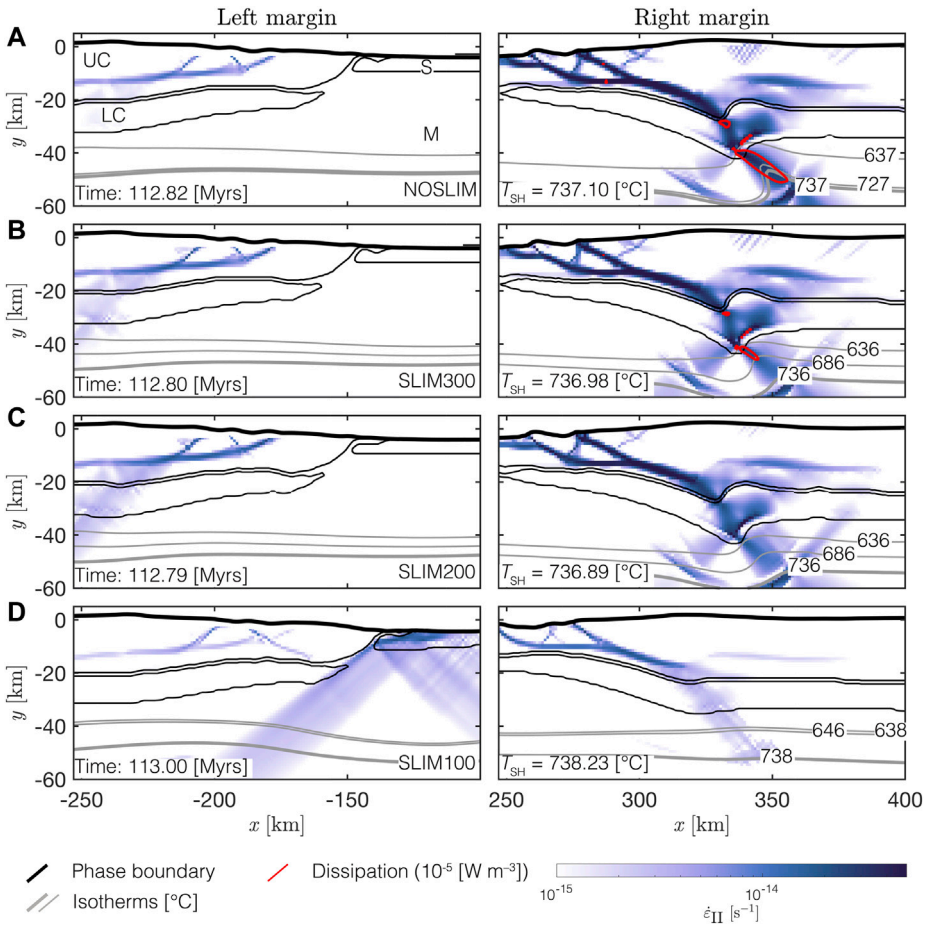

FIGURE 4 | Subduction initiation via thermal softening for models with different applied stress limits: **(A)** no stress limit, **(B)** 300 MPa, **(C)** 200 MPa and **(D)** 100 MPa. White to dark blue is the second invariant of the deviatoric strain rate tensor, solid grey lines are several isotherms used to estimate the temperature rise inside the shear zone based on their vertical position, the red contour indicates the dissipation and black solid lines are material phase boundaries. The left column shows the left margin and the right column shows the right margin. For decreasing stress limits, the dissipation inside the evolving shear zone is significantly reduced and the T_{SH} (an analytically predicted temperature; see text for details) isotherm is less deflected upward indicating that thermal softening (shear heating) becomes less important for shear localization and, thus, for subduction initiation at the passive margin.

As shown above, the maximum temperature increase associated with the formation of shear zones is less than 100°C. It is, therefore, difficult to isolate the temperature increase exclusively caused by shear heating because of the simultaneously ongoing temperature advection and conduction. To clearly show that the shear zones, causing SZI in our models, are due to shear heating and associated thermal softening, we have performed two additional simulations of NOSLIM and SLIM300 in which we have deactivated the shear heating (**Figure 7**). This deactivation was done by setting the term H_D in **Eq. 3** to zero. When shear heating is deactivated (see right column in **Figure 7**) SZI is not successful. Instead, buckling and thickening in the regions of the two margins is the dominant deformation behaviour of the lithosphere. Therefore, the four simulations NOSLIM and SLIM300 with and without shear heating clearly show that shear heating is causing SZI in our models. Consequently, other model features such as the mechanical heterogeneities, mimicked by initial elliptical heterogeneities, or the serpentinite layer are not able to cause SZI.

3.3 Evolution of Horizontal Driving Force and Approximate Slab Pull Force

In **Figure 8** we report the evolution of the plate driving forces per unit length, F_D, and an approximate estimate for the slab pull force per unit length, F_{SP}, over time. The magnitude of F_D increases to ca. 18 TN m^{-1} in NOSLIM, ca. 15 TN m^{-1} in SLIM300 and ca. 12 TN m^{-1} in SLIM200 between the onset of convergence and ca. 113 Myr (**Figure 8A**). A maximum F_D = 14 TN m^{-1} is reached at ca. 122 Myr in SLIM200. Between ca. 113 and 114 Myr, values for F_D decrease in NOSLIM and SLIM300 and remain relatively constant in SLIM200. In NOSLIM, SLIM300 and SLIM200, the values for F_D overall decrease to ca. 10 TN m^{-1} between ca. 130 Myr and ca. 135 Myr. In SLIM100 the magnitude of F_D

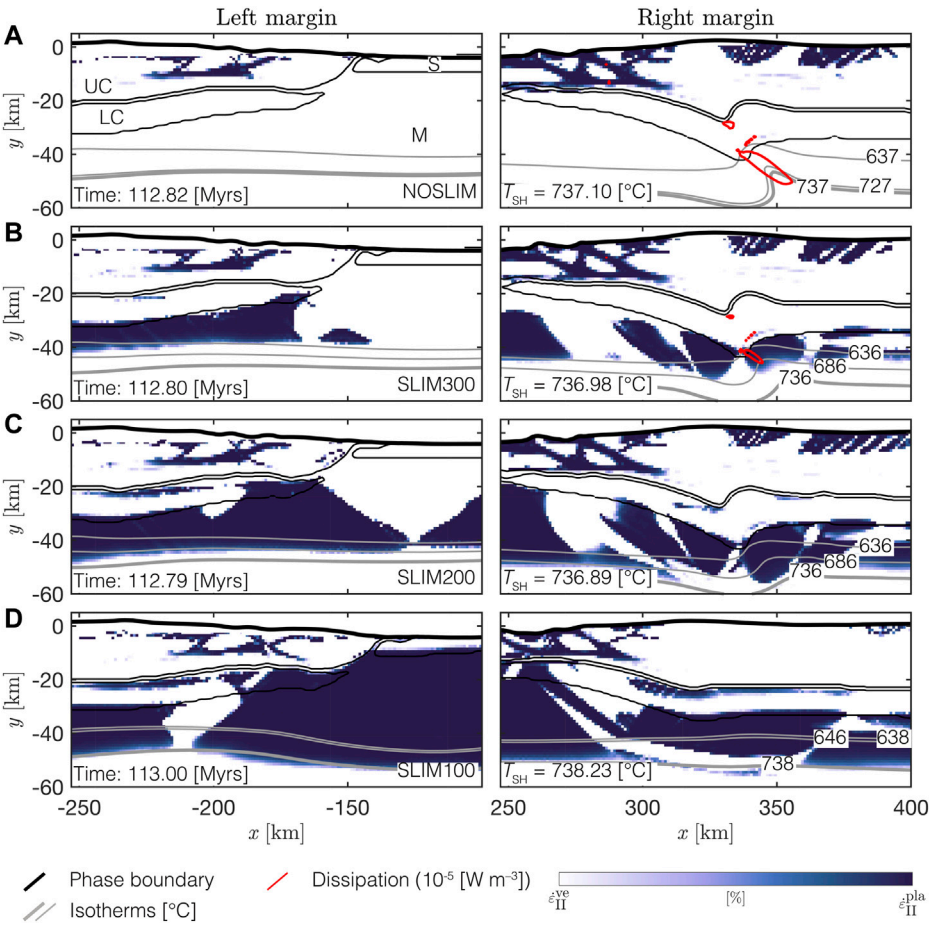

FIGURE 5 | Subduction initiation via thermal softening for models with different applied stress limits: **(A)** no stress limit, **(B)** 300 MPa, **(C)** 200 MPa and **(D)** 100 MPa. White to dark blue mark the model region that undergo rate-dependent (viscoelastic, white) or rate-independent (brittle, blue) plastic deformation. Solid grey lines are several isotherms used to estimate the temperature rise inside the shear zone based on their vertical position, the red contour indicates the dissipation and black lines are material phase boundaries. The left column shows the left margin and the right column shows the right margin. When no stress limit is applied (NOSLIM) the emerging shear zone and large parts of the plate deform ductilly. With decreasing stress limit, large portions of the plate deform brittle-plastically.

continuously increases to ca. 10 TN m^{-1} until ca. 122 Myr in model history (blue solid line in **Figure 8A**).

The density within the subducting slab increases by up to 150 kg m^{-3} compared to the ambient mantle density structure when it transects y = −410 km (**Figures 8D–F**). The reason for this increase in density is the olivine–wadsleyite phase transition. Due to a positive Clapeyron slope (i.e., the change in temperature–pressure space), this phase transition occurs at shallower depths for cold material than for hot material. Therefore, the phase transition is deflected upward inside the cold subducting slabs (see **Figures 8D–F**) and induces an additional pull force. A gradual increase in F_{SP} until the onset of necking in the subducting slab (left edge of grey rectangles in **Figure 8B**, see also stages in **Figures 8D–F**) is observed in all models. This stage is reached after ca. 141 Myr in SLIM200, ca. 150 Myr in SLIM300 and ca. 158 Myr in NOSLIM. The corresponding magnitudes are $F_{SP} \approx 15$ TN m^{-1} in SLIM200, $F_{SP} \approx 25$ TN m^{-1} in SLIM300 and $F_{SP} \approx 35$ TN m^{-1} in NOSLIM. When the slab detaches and sinks into the mantle, magnitudes of F_{SP} increase rapidly to ca. 40 TN m^{-1} in SLIM200, ca. 42 TN m^{-1} in SLIM300 and again ca. 40 TN m^{-1} in NOSLIM. This rapid increase of F_{SP} occurs ca. 4, 13 and 21 Myr after the slab has transected y = −410 km in SLIM200, SLIM300 and NOSLIM, respectively. The depths of slab detachment also vary from $y \approx -200$ km in NOSLIM, $y \approx -150$ km in SLIM300 to $y \approx -30$ km in SLIM200 (**Figure 9**). In SLIM100 the magnitude of F_{SP} increases slowly to ca. 30 TN m^{-1} until ca. 156 Myr. At this stage, drip-off of the lithosphere occurs in this model (**Figure 6D**).

4 DISCUSSION

4.1 Subduction Initiation *via* Thermal Softening

In combination with temperature-dependent rheologies, shear heating is potentially a feasible mechanism to form a shear zone transecting the lithosphere (Yuen et al., 1978; Thielmann and Kaus, 2012; Jaquet and Schmalholz, 2018) and initiate subduction at a hyperextended continental

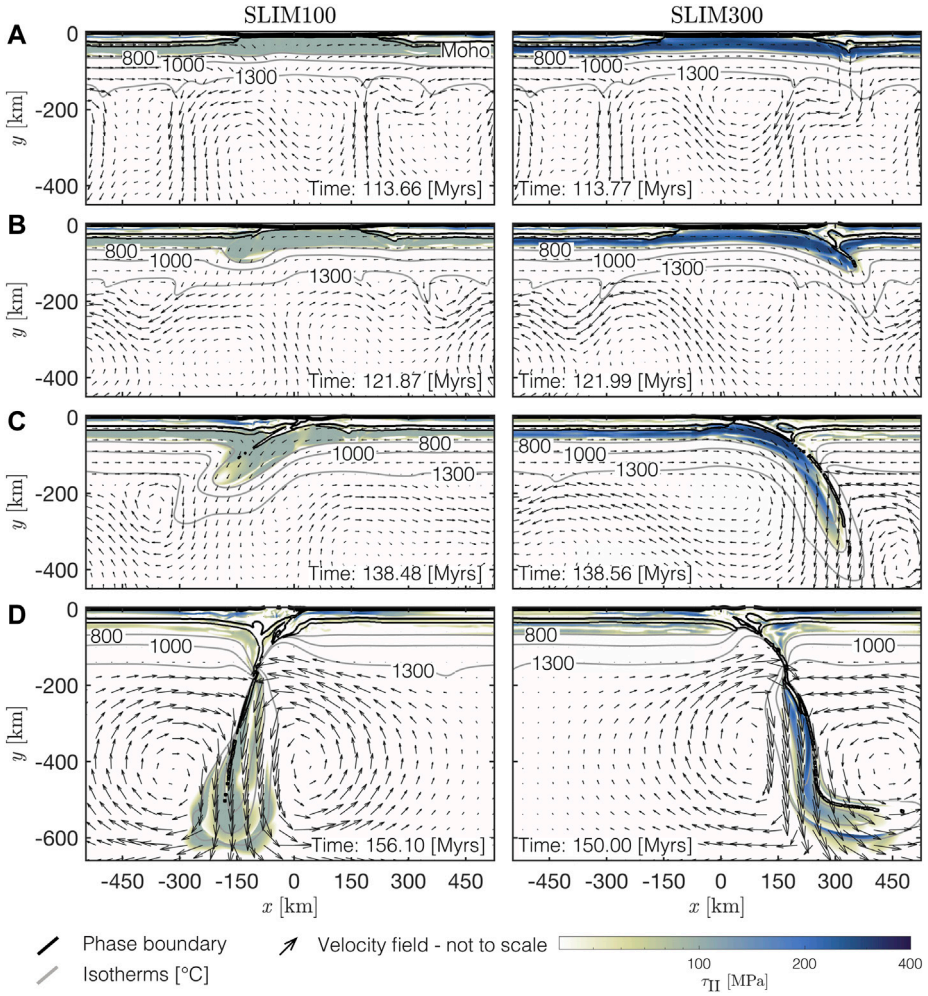

FIGURE 6 | Comparing the evolution of the subduction zone in SLIM100 (left column) and SLIM300 (right column). Black solid lines are phase boundaries and grey solid lines are several isotherms. White to blue colors are the second invariant of the deviatoric stress tensor and glyphs indicate the velocity field calculated by the numerical algorithm at various stages:**(A)** Subduction initiation, **(B)** embryonic subduction zone, **(C)** mature subduction zone and **(D)** slab detachment. Note that subduction is initiated below the opposite margin in SLIM100.

margin (Candioti et al., 2021). Kiss et al. (2019) derived an equation to predict the maximum temperature rise inside a shear zone, T_{SH} (Eq. 22 in Kiss et al., 2019), that is formed *via* shear heating. This prediction relies only on material parameters and the applied absolute horizontal velocity difference, and has already been applied to SZI at homogeneous hyperextended continental margins (Kiss et al., 2020). According to their prediction, a temperature rise by 50°C is sufficient for spontaneous shear localisation *via* shear heating and the associated thermal softening. In our models, the dissipation created by the conversion of mechanical work into heat is ca. 10^{-5} W m^{-3}. Consequently, the temperature increases by 50–90°C in models SLIM200, SLIM300 and NOSLIM. Due to thermal diffusion such a moderate temperature increase is likely not detectable in natural shear zones having a thickness in the order of a few kilometers (e.g., Kiss et al., 2019). The temperature inside the evolving shear zone can be predicted by the equation of Kiss et al. (2019) (deflection of grey solid lines in **Figures 4A,B**). Therefore, shear heating is efficient for stresses inside the lithospheric mantle that are as low as ca. 200 MPa in our models. This stress magnitude represents the maximum stress during the onset of the formation of a shear zone and stresses are decreasing during progressive shear zone formation (Kiss et al., 2019). This observation is crucial as shear heating is often critized for requiring too high stresses to be an efficient mechanism for ductile shear zone localization (e.g., Platt, 2015). Furthermore, Kiss et al. (2019) reported that shear heating is already efficient for stresses as low as 200 MPa. The predicted temperature inside the shear zone forming in SLIM200 is still accurate, although the deformation inside and around the shear zone is mainly occurring in the brittle-plastic field due to the low stress limit (**Figure 5C**). Although the generated dissipation is relatively lower compared to higher stress limiters, the temperature increase in SLIM200 and SLIM300 are comparable (compare isotherms in **Figures 4B,C**). The estimated temperature increase of ca. 50°C in SLIM200 is the limit for shear heating causing spontaneous shear localisation predicted by Kiss et al. (2019). This indicates that likely ductile and brittle-plastic processes are equally

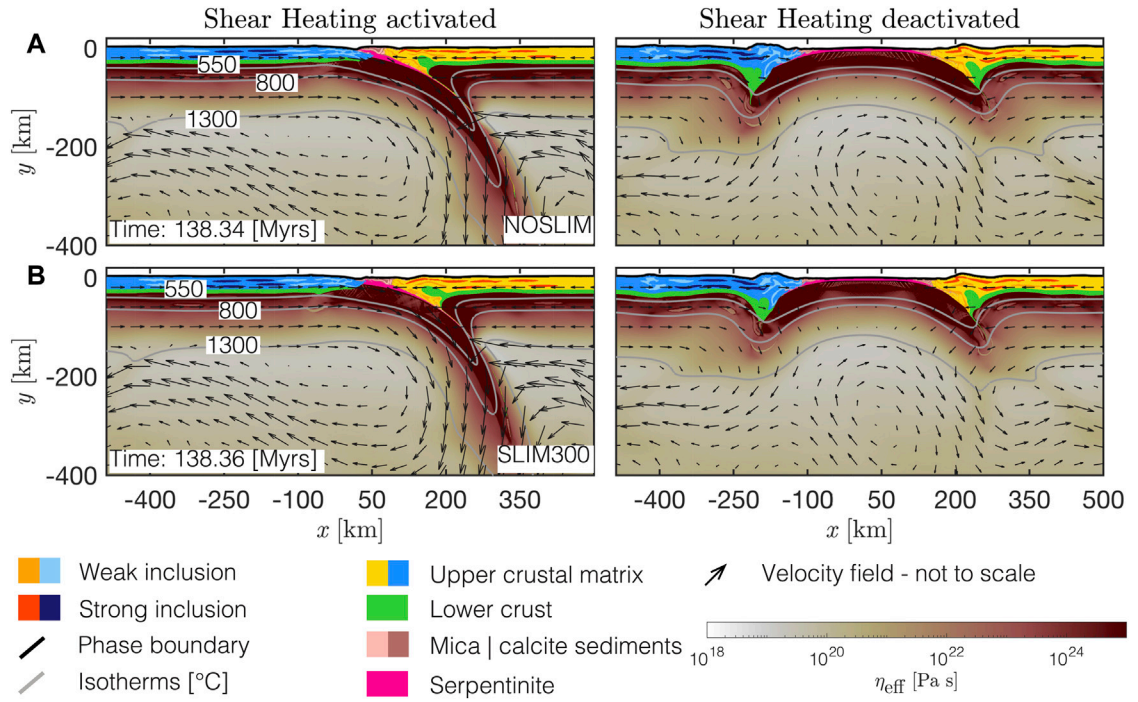

FIGURE 7 | Comparison of NOSLIM **(A)** and SLIM300 **(B)** with activated (left column) and deactivated shear heating (right column). While SZI at the right passive margin evolves into a mature subduction zone when shear heating is activated, buckling and thickening dominates the lithospheric deformation at both passive margins when shear heating is deactivated. Subduction is not initiated in models without shear heating. Colours as indicated in the legend.

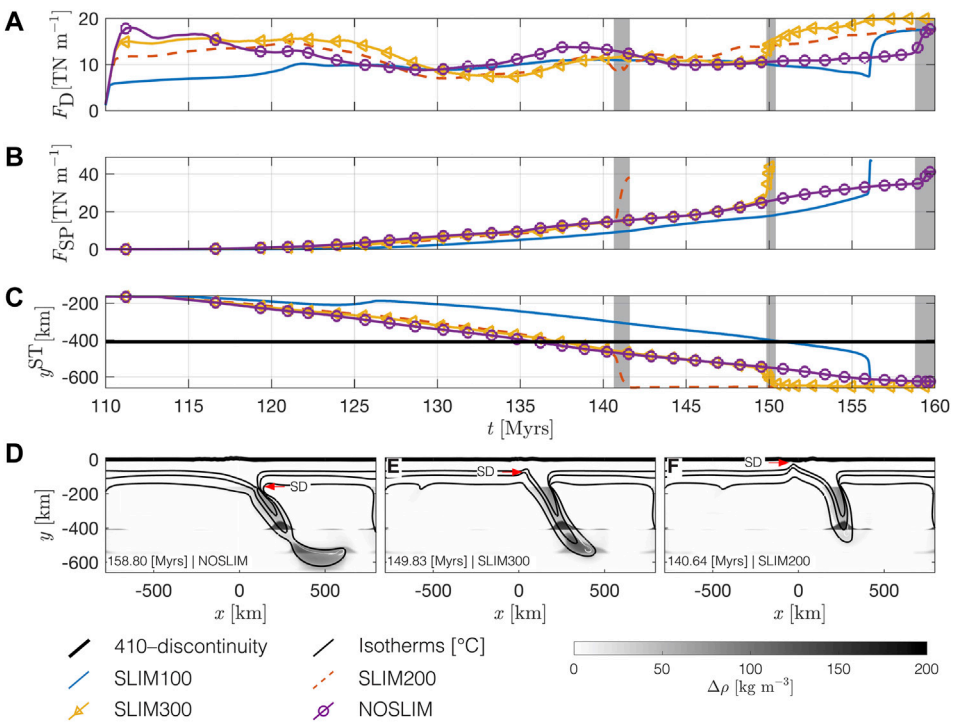

FIGURE 8 | Evolution of **(A)** horizontal driving forces, F_D, and **(B)** the slab pull force, F_{SP}. Panel **(C)** shows the depth of the slab tip over time and panels **(D–F)** show the difference between the local mantle density and an average vertical mantle density profile, $\Delta\rho$, at the onset of necking in the subducting slab for three different stress limiters. Grey rectangles in panels **(A–C)** mark the period from necking of the subducting slab to its detachment. Compared to a strong plate [no stress limit, **(D)**], necking is induced soon after the slab tip transects the 410-discontinuity [see panel **(C)**] for a weak plate [low stress limit, **(F)**].

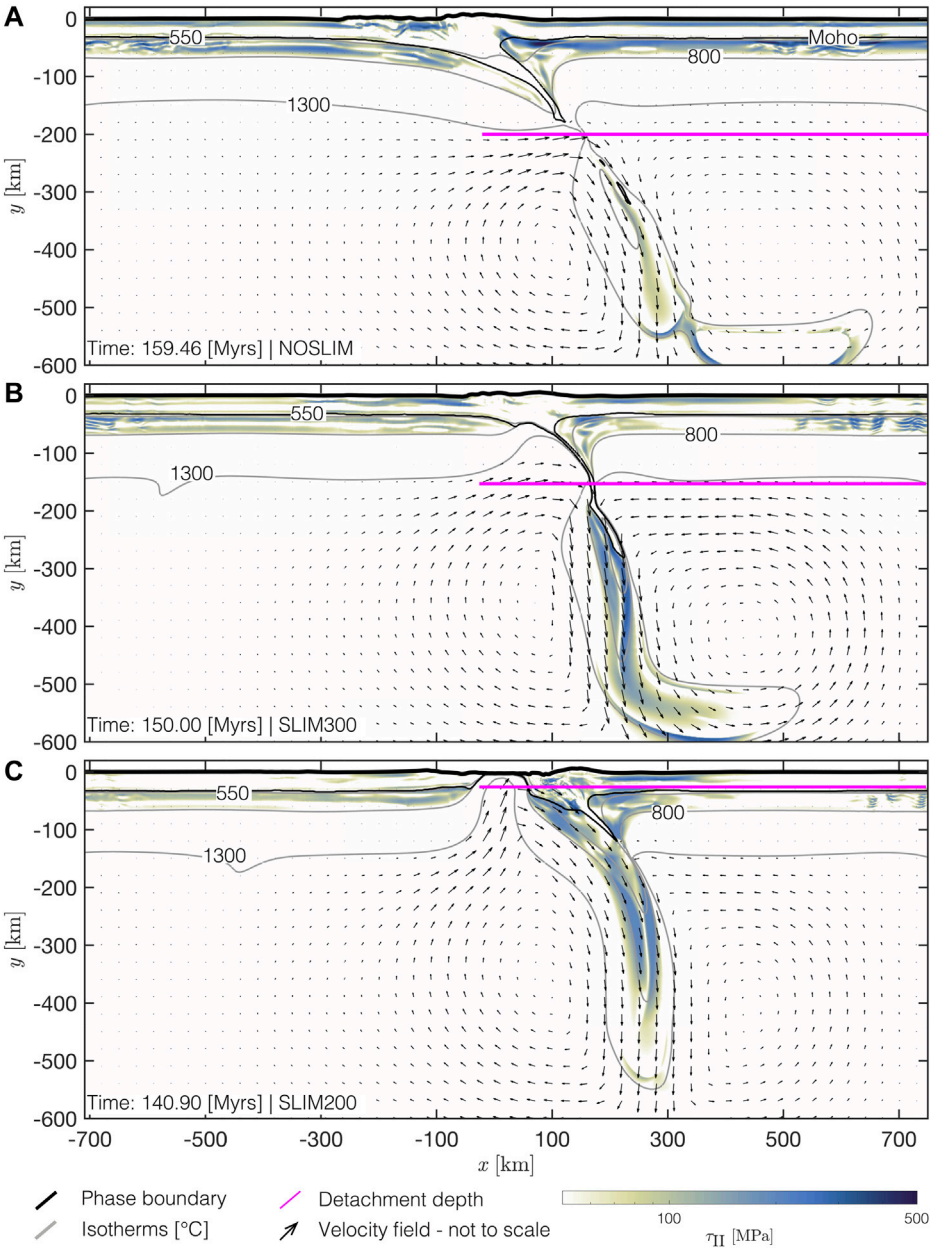

FIGURE 9 | Depth of slab detachments for models with different applied stress limits. White to dark blue is the second invariant of deviatoric stress tensor, solid grey lines are several isotherms, glyphs show the velocity field calculated by the numerical algorithm, solid black lines indicate the crustal phase boundary and the solid magenta line marks the approximate depth of slab detachment. For a weak plate [low stress limit, **(B,C)**], the slab detachment occurs earlier in model history and at shallower depth compared to a strong plate [no stress limit, **(A)**].

important for shear zone localization in model SLIM200. In case stresses are lower than 200 MPa, brittle-plastic processes dominate the deformation inside the lithospheric mantle and shear heating is likely inefficient (flat grey isotherm in **Figure 5D**). Thielmann and Kaus (2012), Jaquet and Schmalholz (2018) and Kiss et al. (2020) already showed that in absence of other softening mechanisms, thermal softening is required for convergent plate boundary formation and successful SZI in lithospheric-scale geodynamic models. We here confirm these results. In the models we present, thermal softening is indeed the responsible mechanism that causes SZI (see **Figure 7**).

4.2 Horizontal and Slab-Pull Forces

We report a minimum magnitude of ca. 14–15 TN m^{-1} for horizontal plate driving forces required for SZI *via* shear heating (SLIM200 and SLIM300, **Figure 8A**). While a magnitude of ca. 30–37 TN m^{-1} for plate driving forces was required to initiate subduction at a homogeneous continental

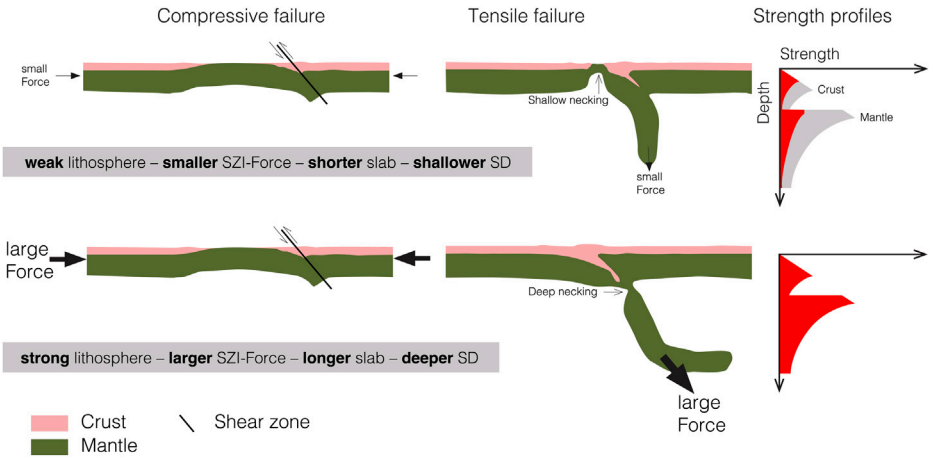

FIGURE 10 | Simplified sketch illustrating the causal link between plate strength, forces required for subduction zone initiation (SZI) and slab detachment (SD) depth. Pink colours indicate the crust, olive green colours the mantle, the red colour in the strength profiles represents a schematic yield strength envelope of the crust and the mantle for a given depth and the black solid lines represent shear zones. Compared to a weak plate, a strong plate requires higher forces for SZI, yields a longer slab and slab detachments at larger depth.

margin in the models of Kiss et al. (2020) and Auzemery et al. (2021), we here report a maximum value of ca. 18 TN m^{-1} for a continental margin that includes elliptical mechanical heterogeneities. Subduction initiation at ca. 10 TN m^{-1} is observed in SLIM100. However, subduction initiation in this model is controlled by brittle-plastic deformation rather than by shear heating. In our model SLIM100, the lithospheric deformation style changes from a subduction (**Figure 6C**) into a delamination, or drip-off, style with ongoing convergence (**Figure 6D**). Such drip-off deformation behaviour is consistent with earlier studies on subduction initiation within mechanically weak lithospheric plates (e.g., Thielmann and Kaus, 2012). We therefore propose that the minimum driving force magnitude predicted by SLIM200 and SLIM300 of 14–15 TN m^{-1} are likely more meaningful estimates for SZI at natural geodynamic settings than the magnitude predicted by SLIM100. This magnitude could likely be further reduced by modulating, for example, the olivine dislocation and Peierls flow law parameters.

The density difference between the slab and the surrounding mantle due to the uplift of the olivine–wadsleyite phase transition (at y = −410 km) in our models is between ca. 150–200 kg m^{-3}. This petrological-thermomechanically coupled density prediction is slightly lower but overall in good agreement with previous estimates (275 kg m^{-3}, Turcotte and Schubert, 2014). This increase in density causes an increase in slab pull force magnitude of ca. 16 TN m^{-1} (Turcotte and Schubert, 2014). Although this estimate is based on buoyancy only and does not consider shear forces along the subducting slab, it is meaningful as these shear forces already act on the slab before the phase change. Our model SLIM200 confirms this estimate. A sharp increase in slab pull force occurs when a magnitude of ca. 17 TN m^{-1} is reached at ca. 141 Myr (**Figure 8B**). In SLIM200, SD begins immediately after the slab has transited a depth of 410 km (**Figures 8C,F**). This observation indicates that slabs must at least be strong enough to support the additional pull force induced by the phase transition in order to penetrate further into the mantle without detaching immediately after the olivine–wadsleyite phase transition occurs within the slab.

In our models we observe the following correlation between the slab strength and the timing of slab detachment: The weaker the slab, the earlier it detaches after transiting the olivine–wadsleyite phase transition. We further observe a correlation between the strength of the slab and the depth of the detachment: weak slabs detach already in the horizontal region of the subducting plate, whereas strong slabs detach in ca. 100–200 km depth (**Figure 10**). In all models, the slab detaches within ca. 1 Myr from the onset of necking. These observations are consistent with earlier studies of slab detachment (e.g., Andrews and Billen, 2009; Baumann et al., 2010; Duretz et al., 2011a; Schmalholz, 2011; van Hunen and Allen, 2011; Thielmann and Schmalholz, 2020). The estimates for slab pull forces we report here are between ca. 18 and 35 TN m^{-1}. These magnitudes are lower than previous calculations (e.g., Forsyth and Uyeda, 1975). However, these magnitudes only consider forces arising from buoyancy contrasts between the subducting slab and the surrounding mantle and do not include viscous tractions along the slab. Such tractions reduce the effective slab pull force (e.g., Schellart, 2004).

4.3 Implications for Natural Subduction Zone Initiation and Slab Detachment

Natural orogens like the Variscides, the Pyrenees or the European Alps may have resulted from the closure of narrow oceanic basins (e.g., Chenin et al., 2019). These immature extensional systems are characterized by insignificant production of new, mature oceanic lithosphere and subduction of these embryonic oceans

produce insignificant amounts of volcanic arc–basalts (e.g., McCarthy et al., 2020). In absence of a significant active mid–ocean ridge, such embryonic basin–margin system is likely more laterally homogeneous (due to lack of a ridge) compared to an ocean basin including a significant spreading ridge. Consequently, embryonic ocean basins likely lack significant lateral variation in temperature and, therefore, strength. Hence, the closure of such basins from SZI to SD may be considered as, respectively, natural compressive and tensile failure tests of the lithosphere. The models we present have significant implications for these natural systems. For example, subduction in the Western Alpine-Tethys presumably initiated below the hyperextended continental margin of the Adriatic plate at ca. 85 Ma (e.g., Manzotti et al., 2014) and lead to closure of the embryonic Piemonte–Liguria ocean (e.g., McCarthy et al., 2020). Our models predict that, compared to a weak subducting lithosphere, a strong lithosphere requires higher forces to fail under compression and yield SZI and plate boundary formation. However, under tension, which develops due to increasing pull forces induced by the subducting slab, the same strong lithosphere may be able to hold a continuous subducting slab down to 660 km depth over more than 20 Myr after basin closure. In contrast, a weak lithosphere fails immediately under tension and exhibits shallow SD early after closure of the embryonic ocean basin. This result may help explaining the strong east–west variability of slab geometries observed in tomographic images from the present-day European Alps (e.g., Lippitsch et al., 2003; Hua et al., 2017; Kästle et al., 2019).

Our models NOSLIM and SLIM300 (**Figures 9A,B**) suggest that the embryonic Piemonte–Liguria ocean might have been weaker in the east compared to the centre which lead to early and shallow slab break-off in the eastern Alps (slab gap, Lippitsch et al., 2003) whereas the slab remained more or less intact in the central region (Zhao et al., 2016). The resulting asthenospheric window in the slab (see glyphs in **Figure 9B**) below the eastern Alps might have induced a heat pulse in the crustal units (e.g., Davies and von Blanckenburg, 1995). For example, in simulation SLIM300 the 1,300°C isotherm is uplifted towards shallower depth in the region of SD (**Figure 9B**). The 1,300°C isotherm is uplifted to approximately the same depth as that of the horizontal 800°C isotherm to the left and right side of the region with SD. Therefore, the temperature can be locally increased by ca. 500°C with respect to temperatures in an undeformed lithosphere. Such local temperature increase due to SD might contribute to magmatism associated with the Bergell intrusion, which has been explained by SD (e.g., Davies and von Blanckenburg, 1995). Certainly, the Alps have a distinct 3D architecture and our models are only two-dimensional. Previous three-dimensional modelling studies have studied the impact of along-strike variations on the process of slab detachment (van Hunen and Allen, 2011; von Tscharner et al., 2014; Duretz et al., 2014). Because of their two-dimensional nature, our models do not capture along-strike propagation of slab detachment. Nevertheless, they successfully account for the physics of necking which is the underlying physical process governing slab detachment (e.g., Schmalholz, 2011; Duretz et al., 2012). Moreover, lateral propagation of slab detachment is triggered by asymmetries in the lateral structure of collision zones (van Hunen and Allen, 2011), which remain difficult to constrain through the course of the Alpine history. We hence suggest that our models remain applicable, at first order, to the study of slab detachment in the Alps.

Slab detachment is a short-lived process and we just mention also briefly two regions in which SD is presumably occurring at present day. In the Vrancea area (e.g., Wenzel et al., 1998) a nearly vertically hanging slab which is still attached to the overlying plate induces earthquakes at an intermediate depth between 70 and 180 km. However, the maximum depth of the slab might be much deeper (Sperner et al., 2001; Ferrand and Manea, 2021). Also, recent seismic data from the Hindu Kush indicates a potential onset of slab detachment or delamination at depths of ca. 200 km (e.g., Kufner et al., 2021). Such detachment depths are well predicted by our models (**Figures 8D–F**).

4.4 Constraining the Lithospheric Strength With Numerical Models

Three-dimensional numerical models of global mantle convection have been used to constrain the effective strength of the lithosphere. Mallard et al. (2016), for example, applied a constant von-Mises stress limiter function in their models (similar to this study) and showed that stress magnitudes between 150 and 200 MPa in the lithosphere result in the most realistic plate-like behaviour. The model results of SLIM200 confirm the results reported by Mallard et al. (2016). However, our models predict plate-like behaviour also for stresses higher than 200 MPa in the lithosphere (see for example model NOSLIM), likely because of the higher numerical resolution. In our models, high stresses in the lithosphere are limited to a 10–25 km thin, load-bearing layer (see f.e. **Figures 3E–H**). Such thin layers cannot be resolved numerically in most global mantle convection models. In comparison, dividing, for example, F_D = 18 TN m^{-1}, which was necessary to overcome the plate strength in NOSLIM and initiate subduction, by a ca. 50 km thick lithosphere yields an average deviatoric stress of ca. 180 MPa which agrees with the equivalent von-Mises shear stress between 150 and 200 MPa of Mallard et al. (2016), which is required to generate a plate size–frequency distribution observed for Earth. Therefore, the magnitude of the horizontal driving forces in our numerical simulations agree with horizontal forces predicted by recent global mantle convection models.

Because of the high numerical resolution, our models can test first the resistance of plates to failure under variable applied compressive stresses (during SZI) and subsequently under variable tensile stresses (during SD). Therefore, models as presented here may represent a complementary method to classical laboratory experiments, inversion from geophysical data and global mantle convection models and help to better constrain the effective strength of the lithosphere.

5 CONCLUSION

We presented 2D petrological-thermomechanical models for the convergence of embryonic ocean basins bounded by passive margins to quantify the minimum horizontal force required for subduction zone initiation (SZI) at passive margins. Although we also include an initially horizontal weak serpentinite layer in the ocean basin, our results show that this layer has no impact on SZI. In our models, plate boundary formation and SZI is controlled by thermal softening caused by shear heating. Simulations in which shear heating only is deactivated do not show SZI which clearly shows that shear heating and associated thermal softening controls SZI in our models. A temperature increase due to shear heating inside a shear zone of only ca. 50°C is sufficient for successful SZI. The minimum horizontal force (per unit length) required for such SZI is between 14 and 15 TN m^{-1}. Dividing 15 TN m^{-1} by a lithosphere thickness of 50 km (representing the region with significant strength) yields a shear stress of 150 MPa. Such shear stress magnitude is consistent with average lithospheric yield stress estimates based on 3D spherical models of mantle convection in order to self-consistently produce the plate size–frequency distribution observed for Earth. Consequently, we conclude that 1) shear heating and associated thermal softening is a feasible mechanism for horizontally-forced SZI at passive margins and 2) the required horizontal force magnitudes for such SZI are realistic and in agreement with independent estimates from global mantle convection models.

The convergence and closure of ocean basins bounded by passive margins involves two geodynamic processes that are controlled by the effective strength of the lithosphere: SZI, controlled by the compressive strength of the lithosphere, and subsequent slab detachment (SD), controlled by the tensile strength. Therefore, the compressive force magnitude required to "break" the lithosphere during horizontally forced SZI is linked to the tensile force required to "break" the lithosphere during SD. Our results show that the smaller the horizontal force required for SZI, the earlier and shallower SD occurs during basin closure and the shorter is the length of the slab. We presented one simulation with a stress limit in the lithosphere of 200 MPa (corresponding to a horizontal force during SZI of 14 TN m^{-1}) which showed a successful SZI. However, the lithosphere was so weak that the subducting lithosphere detached already in the horizontal, non-subducted region of the lithospheric plate shortly before basin closure. Such horizontal slab detachment is most likely unrealistic for most natural settings such as for the closure of the Piemonte-Liguria ocean during Alpine orogeny. In the Alps, the slab geometries are still contentious with some studies proposing slab detachment linked to the Europe-Adria collision some 30 Myrs ago while other studies argue that there was no slab detachment. Our results imply that if there was no slab detachment since the Europe-Asia collision, as suggested by some studies, then the corresponding slab must have a large effective strength to prohibit SD.

We propose that the closure of ocean basins involving both SZI and SD can be considered as a natural "experiment" that tests both the effective compressive and tensile strength of the lithosphere. Consequently, we propose that numerical studies on horizontally-forced SZI also should test whether their models can generate a significant slab which can support realistic slab pull forces in order to avoid that SZI is studied for an unrealistically weak lithosphere.

DATA AVAILABILITY STATEMENT

The raw data supporting the conclusion of this article will be made available by the authors, without undue reservation.

AUTHOR CONTRIBUTIONS

LC conducted the numerical simulations, interpreted the results and wrote the manuscript. TD developed the applied numerical algorithm, helped interpreting the results and writing the manuscript. SS conceptualized and supervised the study, helped interpreting the results and writing the manuscript.

FUNDING

This study was supported by SNSF grant No. 200020 163169.

REFERENCES

Aharonov, E., and Scholz, C. H. (2018). A Physics-Based Rock Friction Constitutive Law: Steady State Friction. *J. Geophys. Res. Solid Earth* 123, 1591–1614. doi:10.1002/2016jb013829

Andrews, E. R., and Billen, M. I. (2009). Rheologic Controls on the Dynamics of Slab Detachment. *Tectonophysics* 464, 60–69. doi:10.1016/j.tecto.2007.09.004

Auzemery, A., Willingshofer, E., Yamato, P., Duretz, T., and Beekman, F. (2021). Kinematic Boundary Conditions Favouring Subduction Initiation at Passive Margins over Subduction at Mid-oceanic Ridges. *Front. Earth Sci.* 9. doi:10.3389/feart.2021.765893

Auzemery, A., Willingshofer, E., Yamato, P., Duretz, T., and Sokoutis, D. (2020). Strain Localization Mechanisms for Subduction Initiation at Passive Margins. *Glob. Planet. Change* 195, 103323. doi:10.1016/j.gloplacha.2020.103323

Baumann, C., Gerya, T. V., and Connolly, J. A. D. (2010). Numerical Modelling of Spontaneous Slab Breakoff Dynamics during continental Collision. *Geol. Soc. Lond. Spec. Publications* 332, 99–114. doi:10.1144/sp332.7

Baumann, T. S., Kaus, B. J. P., and Popov, A. A. (2014). Constraining Effective Rheology through Parallel Joint Geodynamic Inversion. *Tectonophysics* 631, 197–211. doi:10.1016/j.tecto.2014.04.037

Bercovici, D., and Ricard, Y. (2012). Mechanisms for the Generation of Plate Tectonics by Two-phase Grain-Damage and Pinning. *Phys. Earth Planet. Interiors* 202-203, 27–55. doi:10.1016/j.pepi.2012.05.003

Burov, E. B., and Watts, A. B. (2006). The Long-Term Strength of continental Lithosphere: "jelly sandwich" or "crème Brûlée"? *GSA today* 16, 4. doi:10.1130/1052-5173(2006)016<4:tltsoc>2.0.co;2

Candioti, L. G., Duretz, T., Moulas, E., and Schmalholz, S. M. (2021). Buoyancy versus Shear Forces in Building Orogenic Wedges. *Solid Earth* 12, 1749–1775. doi:10.5194/se-12-1749-2021

Candioti, L. G., Schmalholz, S. M., and Duretz, T. (2020). Impact of Upper Mantle Convection on Lithosphere Hyperextension and Subsequent Horizontally

Forced Subduction Initiation. *Solid Earth* 11, 2327–2357. doi:10.5194/se-11-2327-2020

Chenin, P., Manatschal, G., Picazo, S., Müntener, O., Karner, G., Johnson, C., et al. (2017). Influence of the Architecture of Magma-Poor Hyperextended Rifted Margins on Orogens Produced by the Closure of Narrow versus Wide Oceans. *Geosphere* 13, 559–576. doi:10.1130/ges01363.1

Chenin, P., Picazo, S., Jammes, S., Manatschal, G., Müntener, O., and Karner, G. (2019). Potential Role of Lithospheric Mantle Composition in the wilson Cycle: a north atlantic Perspective. *Geol. Soc. Lond. Spec. Publications* 470, 157–172. doi:10.1144/sp470.10

Cloetingh, S., Wortel, R., and Vlaar, N. J. (1989). "On the Initiation of Subduction Zones," in *Subduction Zones Part II* (Berlin, Germany: Springer), 7–25. doi:10.1007/978-3-0348-9140-0_2

Connolly, J. A. D. (2005). Computation of Phase Equilibria by Linear Programming: a Tool for Geodynamic Modeling and its Application to Subduction Zone Decarbonation. *Earth Planet. Sci. Lett.* 236, 524–541. doi:10.1016/j.epsl.2005.04.033

Connolly, J. (2009). The Geodynamic Equation of State: what and How. *Geochem. Geophys. Geosystems* 10. doi:10.1029/2009gc002540

Crameri, F., Magni, V., Domeier, M., Shephard, G. E., Chotalia, K., Cooper, G., et al. (2020). A Transdisciplinary and Community-Driven Database to Unravel Subduction Zone Initiation. *Nat. Commun.* 11, 3750. doi:10.1038/s41467-020-17522-9

Dannowski, A., Kopp, H., Grevemeyer, I., Lange, D., Thorwart, M., Bialas, J., et al. (2020). Seismic Evidence for Failed Rifting in the Ligurian basin, Western alpine Domain. *Solid Earth* 11, 873–887. doi:10.5194/se-11-873-2020

Demouchy, S., Tommasi, A., Boffa Ballaran, T., and Cordier, P. (2013). Low Strength of Earth's Uppermost Mantle Inferred from Tri-axial Deformation Experiments on Dry Olivine Crystals. *Phys. Earth Planet. Interiors* 220, 37–49. doi:10.1016/j.pepi.2013.04.008

Duretz, T., Gerya, T. V., and May, D. A. (2011a). Numerical Modelling of Spontaneous Slab Breakoff and Subsequent Topographic Response. *Tectonophysics* 502, 244–256. doi:10.1016/j.tecto.2010.05.024

Duretz, T., Gerya, T. V., and Spakman, W. (2014). Slab Detachment in Laterally Varying Subduction Zones: 3-d Numerical Modeling. *Geophys. Res. Lett.* 41, 1951–1956. doi:10.1002/2014GL059472

Duretz, T., May, D. A., Gerya, T., and Tackley, P. (2011b). Discretization Errors and Free Surface Stabilization in the Finite Difference and Marker-In-Cell Method for Applied Geodynamics: A Numerical Study. *Geochem. Geophys. Geosystems* 12. doi:10.1029/2011gc003567

Duretz, T., May, D. A., and Yamato, P. (2016). A Free Surface Capturing Discretization for the Staggered Grid Finite Difference Scheme. *Geophys. J. Int.* 204, 1518–1530. doi:10.1093/gji/ggv526

Duretz, T., Schmalholz, S., and Gerya, T. (2012). Dynamics of Slab Detachment. *Geochem. Geophys. Geosystems* 13. doi:10.1029/2011gc004024

Dymkova, D., and Gerya, T. (2013). Porous Fluid Flow Enables Oceanic Subduction Initiation on Earth. *Geophys. Res. Lett.* 40, 5671–5676. doi:10.1002/2013gl057798

Ferrand, T. P., and Manea, E. F. (2021). Dehydration-induced Earthquakes Identified in a Subducted Oceanic Slab beneath Vrancea, romania. *Sci. Rep.* 11, 10315–10319. doi:10.1038/s41598-021-89601-w

Forsyth, D., and Uyeda, S. (1975). On the Relative Importance of the Driving Forces of Plate Motion. *Geophys. J. Int.* 43, 163–200. doi:10.1111/j.1365-246x.1975.tb00631.x

Furstoss, J., Petit, C., Tommasi, A., Ganino, C., Muñoz, D. P., and Bernacki, M. (2021). On the Role of Solute Drag in Reconciling Laboratory and Natural Constraints on Olivine Grain Growth Kinetics. *Geophys. J. Int.* 224, 1360–1370.

Gerya, T. V., and Yuen, D. A. (2003). Characteristics-based Marker-In-Cell Method with Conservative Finite-Differences Schemes for Modeling Geological Flows with Strongly Variable Transport Properties. *Phys. Earth Planet. Interiors* 140, 293–318. doi:10.1016/j.pepi.2003.09.006

Goetze, C., and Evans, B. (1979). Stress and Temperature in the Bending Lithosphere as Constrained by Experimental Rock Mechanics. *Geophys. J. Int.* 59, 463–478. doi:10.1111/j.1365-246x.1979.tb02567.x

Handy, M. R., M. Schmid, S., Bousquet, R., Kissling, E., and Bernoulli, D. (2010). Reconciling Plate-Tectonic Reconstructions of Alpine Tethys with the Geological-Geophysical Record of Spreading and Subduction in the Alps. *Earth-Science Rev.* 102, 121–158. doi:10.1016/j.earscirev.2010.06.002

Hansen, F., and Carter, N. (1983). "Semibrittle Creep of Dry and Wet Westerly Granite at 1000 MPa," in The 24th US Symposium on Rock Mechanics (USRMS).

Hansen, L. N., Kumamoto, K. M., Thom, C. A., Wallis, D., Durham, W. B., Goldsby, D. L., et al. (2019). Low-Temperature Plasticity in Olivine: Grain Size, Strain Hardening, and the Strength of the Lithosphere. *J. Geophys. Res. Solid Earth* 124, 5427–5449. doi:10.1029/2018jb016736

Hilairet, N., Reynard, B., Wang, Y., Daniel, I., Merkel, S., Nishiyama, N., et al. (2007). High-pressure Creep of Serpentine, Interseismic Deformation, and Initiation of Subduction. *Science* 318, 1910–1913. doi:10.1126/science.1148494

Hirth, G., and Kohlstedt, D. (2003). Rheology of the Upper Mantle and the Mantle Wedge: A View from the Experimentalists. *Geophys. Monograph-American Geophys. Union* 138, 83–105. doi:10.1029/138gm06

Hua, Y., Zhao, D., and Xu, Y. (2017). P Wave Anisotropic Tomography of the Alps. *J. Geophys. Res. Solid Earth* 122, 4509–4528. doi:10.1002/2016jb013831

Huw Davies, J., and von Blanckenburg, F. (1995). Slab Breakoff: a Model of Lithosphere Detachment and its Test in the Magmatism and Deformation of Collisional Orogens. *Earth Planet. Sci. Lett.* 129, 85–102. doi:10.1016/0012-821x(94)00237-s

Idrissi, H., Bollinger, C., Boioli, F., Schryvers, D., and Cordier, P. (2016). Low-temperature Plasticity of Olivine Revisited with *In Situ* Tem Nanomechanical Testing. *Sci. Adv.* 2, e1501671. doi:10.1126/sciadv.1501671

Jaquet, Y., and Schmalholz, S. M. (2018). Spontaneous Ductile Crustal Shear Zone Formation by thermal Softening and Related Stress, Temperature and Strain Rate Evolution. *Tectonophysics* 746, 384–397. doi:10.1016/j.tecto.2017.01.012

Kameyama, M., Yuen, D. A., and Karato, S.-I. (1999). Thermal-mechanical Effects of Low-Temperature Plasticity (The Peierls Mechanism) on the Deformation of a Viscoelastic Shear Zone. *Earth Planet. Sci. Lett.* 168, 159–172. doi:10.1016/s0012-821x(99)00040-0

Kästle, E. D., Rosenberg, C., Boschi, L., Bellahsen, N., Meier, T., and El-Sharkawy, A. (2019). Slab Break-Offs in the alpine Subduction Zone. *Solid Earth Discuss.* 2019, 1–19.

Kiss, D., Candioti, L. G., Duretz, T., and Schmalholz, S. M. (2020). Thermal Softening Induced Subduction Initiation at a Passive Margin. *Geophys. J. Int.* 220, 2068–2073. doi:10.1093/gji/ggz572

Kiss, D., Podladchikov, Y., Duretz, T., and Schmalholz, S. M. (2019). Spontaneous Generation of Ductile Shear Zones by thermal Softening: Localization Criterion, 1D to 3D Modelling and Application to the Lithosphere. *Earth Planet. Sci. Lett.* 519, 284–296. doi:10.1016/j.epsl.2019.05.026

Kronenberg, A. K., Kirby, S. H., and Pinkston, J. (1990). Basal Slip and Mechanical Anisotropy of Biotite. *J. Geophys. Res.* 95, 19257–19278. doi:10.1029/jb095ib12p19257

Kufner, S. K., Kakar, N., Bezada, M., Bloch, W., Metzger, S., Yuan, X., et al. (2021). The Hindu Kush Slab Break-Off as Revealed by Deep Structure and Crustal Deformation. *Nat. Commun.* 12, 1685. doi:10.1038/s41467-021-21760-w

Lallemand, S., and Arcay, D. (2021). Subduction Initiation from the Earliest Stages to Self-Sustained Subduction: Insights from the Analysis of 70 Cenozoic Sites. *Earth-Science Rev.* 221, 103779. doi:10.1016/j.earscirev.2021.103779

Le Breton, E., Brune, S., Ustaszewski, K., Zahirovic, S., Seton, M., and Müller, R. D. (2021). Kinematics and Extent of the Piemont-Liguria Basin - Implications for Subduction Processes in the Alps. *Solid Earth* 12, 885–913. doi:10.5194/se-12-885-2021

Leloup, P. H., Ricard, Y., Battaglia, J., and Lacassin, R. (1999). Shear Heating in continental Strike-Slip Shear Zones:model and Field Examples. *Geophys. J. Int.* 136, 19–40. doi:10.1046/j.1365-246x.1999.00683.x

Lippitsch, R., Kissling, E., and Ansorge, J. (2003). Upper Mantle Structure beneath the alpine Orogen from High-Resolution Teleseismic Tomography. *J. Geophys. Res. Solid Earth* 108. doi:10.1029/2002jb002016

Mackwell, S. J., Zimmerman, M. E., and Kohlstedt, D. L. (1998). High-temperature Deformation of Dry Diabase with Application to Tectonics on Venus. *J. Geophys. Res.* 103, 975–984. doi:10.1029/97jb02671

Malatesta, C., Gerya, T., Crispini, L., Federico, L., and Capponi, G. (2013). Oblique Subduction Modelling Indicates Along-Trench Tectonic Transport of Sediments. *Nat. Commun.* 4, 2456–6. doi:10.1038/ncomms3456

Mallard, C., Coltice, N., Seton, M., Müller, R. D., and Tackley, P. J. (2016). Subduction Controls the Distribution and Fragmentation of Earth's Tectonic Plates. *Nature* 535, 140–143. doi:10.1038/nature17992

Manzotti, P., Ballèvre, M., Zucali, M., Robyr, M., and Engi, M. (2014). The Tectonometamorphic Evolution of the Sesia-Dent Blanche Nappes (Internal Western Alps): Review and Synthesis. *Swiss J. Geosci.* 107, 309–336. doi:10.1007/s00015-014-0172-x

McCarthy, A., Tugend, J., Mohn, G., Candioti, L., Chelle-Michou, C., Arculus, R., et al. (2020). A Case of Ampferer-type Subduction and Consequences for the Alps and the Pyrenees. *Am. J. Sci.* 320, 313–372. doi:10.2475/04.2020.01

McKenzie, D. P. (1977). The Initiation of Trenches: a Finite Amplitude Instability. *Isl. arcs, deep sea trenches back-arc basins* 1, 57–61. doi:10.1029/me001p0057

Montési, L. G. (2013). Fabric Development as the Key for Forming Ductile Shear Zones and Enabling Plate Tectonics. *J. Struct. Geology.* 50, 254–266.

Mueller, S., and Phillips, R. J. (1991). On the Initiation of Subduction. *J. Geophys. Res.* 96, 651–665. doi:10.1029/90jb02237

Müller, R. D., Sdrolias, M., Gaina, C., and Roest, W. R. (2008). Age, Spreading Rates, and Spreading Asymmetry of the World's Ocean Crust. *Geochem. Geophys. Geosystems* 9.

Mulyukova, E., and Bercovici, D. (2018). Collapse of Passive Margins by Lithospheric Damage and Plunging Grain Size. *Earth Planet. Sci. Lett.* 484, 341–352. doi:10.1016/j.epsl.2017.12.022

Platt, J. P. (2015). Influence of Shear Heating on Microstructurally Defined Plate Boundary Shear Zones. *J. Struct. Geology.* 79, 80–89. doi:10.1016/j.jsg.2015.07.009

Ranalli, G. (1995). *Rheology of the Earth*. Berlin, Germany: Springer Science & Business Media.

Regenauer-Lieb, K., Yuen, D. A., and Branlund, J. (2001). The Initiation of Subduction: Criticality by Addition of Water? *science* 294, 578–580. doi:10.1126/science.1063891

Regenauer-Lieb, K., and Yuen, D. A. (1998). Rapid Conversion of Elastic Energy into Plastic Shear Heating during Incipient Necking of the Lithosphere. *Geophys. Res. Lett.* 25, 2737–2740. doi:10.1029/98gl02056

Rybacki, E., and Dresen, G. (2004). Deformation Mechanism Maps for Feldspar Rocks. *Tectonophysics* 382, 173–187. doi:10.1016/j.tecto.2004.01.006

Schellart, W. (2004). Quantifying the Net Slab Pull Force as a Driving Mechanism for Plate Tectonics. *Geophys. Res. Lett.* 31. doi:10.1029/2004gl019528

Schmalholz, S. M. (2011). A Simple Analytical Solution for Slab Detachment. *Earth Planet. Sci. Lett.* 304, 45–54. doi:10.1016/j.epsl.2011.01.011

Schmalholz, S. M., Duretz, T., Hetényi, G., and Medvedev, S. (2019). Distribution and Magnitude of Stress Due to Lateral Variation of Gravitational Potential Energy between Indian lowland and Tibetan Plateau. *Geophys. J. Int.* 216, 1313–1333. doi:10.1093/gji/ggy463

Schmalholz, S. M., and Fletcher, R. C. (2011). The Exponential Flow Law Applied to Necking and Folding of a Ductile Layer. *Geophys. J. Int.* 184, 83–89. doi:10.1111/j.1365-246x.2010.04846.x

Schmalholz, S. M., Medvedev, S., Lechmann, S. M., and Podladchikov, Y. (2014). Relationship between Tectonic Overpressure, Deviatoric Stress, Driving Force, Isostasy and Gravitational Potential Energy. *Geophys. J. Int.* 197, 680–696. doi:10.1093/gji/ggu040

Schmid, S. M., Boland, J. N., and Paterson, M. S. (1977). Superplastic Flow in Finegrained limestone. *Tectonophysics* 43, 257–291. doi:10.1016/0040-1951(77)90120-2

Schmid, S. M., Kissling, E., Diehl, T., van Hinsbergen, D. J. J., and Molli, G. (2017). Ivrea Mantle Wedge, Arc of the Western Alps, and Kinematic Evolution of the Alps-Apennines Orogenic System. *Swiss J. Geosci.* 110, 581–612. doi:10.1007/s00015-016-0237-0

Shuck, B., Gulick, S. P. S., Van Avendonk, H. J. A., Gurnis, M., Sutherland, R., Stock, J., et al. (2022). Stress Transition from Horizontal to Vertical Forces during Subduction Initiation. *Nat. Geosci.* 15, 149–155. doi:10.1038/s41561-021-00880-4

Sperner, B., Lorenz, F., Bonjer, K., Hettel, S., Muller, B., and Wenzel, F. (2001). Slab Break-Off - Abrupt Cut or Gradual Detachment? New Insights from the Vrancea Region (SE Carpathians, Romania). *Terra Nova* 13, 172–179. doi:10.1046/j.1365-3121.2001.00335.x

Stern, R. J., and Gerya, T. (2018). Subduction Initiation in Nature and Models: A Review. *Tectonophysics* 746, 173–198. doi:10.1016/j.tecto.2017.10.014

Stern, R. (2004). Subduction Initiation: Spontaneous and Induced. *Earth Planet. Sci. Lett.* 226, 275–292. doi:10.1016/s0012-821x(04)00498-4

Takeuchi, C. S., and Fialko, Y. (2012). Dynamic Models of Interseismic Deformation and Stress Transfer from Plate Motion to continental Transform Faults. *J. Geophys. Res. Solid Earth* 117. doi:10.1029/2011jb009056

Thielmann, M., and Kaus, B. J. P. (2012). Shear Heating Induced Lithospheric-Scale Localization: Does it Result in Subduction? *Earth Planet. Sci. Lett.* 359-360, 1–13. doi:10.1016/j.epsl.2012.10.002

Thielmann, M., and Schmalholz, S. M. (2020). Contributions of Grain Damage, thermal Weakening, and Necking to Slab Detachment. *Front. Earth Sci.* 8, 254. doi:10.3389/feart.2020.00254

Turcotte, D., and Schubert, G. (2014). *Geodynamics*. Cambridge: Cambridge University Press.

van Hunen, J., and Allen, M. B. (2011). Continental Collision and Slab Break-Off: A Comparison of 3-d Numerical Models with Observations. *Earth Planet. Sci. Lett.* 302, 27–37. doi:10.1016/j.epsl.2010.11.035

von Tscharner, M., Schmalholz, S. M., and Duretz, T. (2014). Three-dimensional Necking during Viscous Slab Detachment. *Geophys. Res. Lett.* 41, 4194–4200. doi:10.1002/2014GL060075

Wenzel, F., Achauer, U., Enescu, D., Kissling, E., Russo, R., Mocanu, V., et al. (1998). Detailed Look at Final Stage of Plate Break-Off Is Target of Study in romania. *Eos Trans. AGU* 79, 589–594. doi:10.1029/98eo00427

White, S. H., and Knipe, R. J. (1978). Transformation- and Reaction-Enhanced Ductility in Rocks. *J. Geol. Soc.* 135, 513–516. doi:10.1144/gsjgs.135.5.0513

Yuen, D. A., Fleitout, L., Schubert, G., and Froidevaux, C. (1978). Shear Deformation Zones along Major Transform Faults and Subducting Slabs. *Geophys. J. Int.* 54, 93–119. doi:10.1111/j.1365-246x.1978.tb06758.x

Zhao, L., Paul, A., Malusà, M. G., Xu, X., Zheng, T., Solarino, S., et al. (2016). Continuity of the alpine Slab Unraveled by High-Resolution P Wave Tomography. *J. Geophys. Res. Solid Earth* 121, 8720–8737. doi:10.1002/2016jb013310

Zhong, X., and Li, Z.-H. (2020). Subduction Initiation during Collision-Induced Subduction Transference: Numerical Modeling and Implications for the Tethyan Evolution. *J. Geophys. Res. Solid Earth* 125, e2019JB019288. doi:10.1029/2019jb019288

Zhou, X., Li, Z. H., Gerya, T. V., and Stern, R. J. (2020). Lateral Propagation-Induced Subduction Initiation at Passive continental Margins Controlled by Preexisting Lithospheric Weakness. *Sci. Adv.* 6, eaaz1048. doi:10.1126/sciadv.aaz1048

Zhou, X., and Wada, I. (2021). Differentiating Induced versus Spontaneous Subduction Initiation Using Thermomechanical Models and Metamorphic Soles. *Nat. Commun.* 12, 1–10. doi:10.1038/s41467-021-24896-x

Conflict of Interest: The authors declare that the research was conducted in the absence of any commercial or financial relationships that could be construed as a potential conflict of interest.

frontiers | Frontiers in Earth Science

TYPE Original Research
PUBLISHED 12 January 2023
DOI 10.3389/feart.2022.1089700

OPEN ACCESS

EDITED BY
Jiyuan Yin,
Chinese Academy of Geological Sciences (CAGS), China

REVIEWED BY
Xijun Liu,
Guilin University of Technology, China
Yongjiang Liu,
Ocean University of China, China

*CORRESPONDENCE
Qigui Mao,
qg-mao@ms.xjb.ac.cn
Wenjiao Xiao,
wj–xiao@mail.iggcas.ac.cn
Miao Sang,
sangmiao@ms.xjb.ac.cn

SPECIALTY SECTION
This article was submitted to Petrology, a section of the journal Frontiers in Earth Science

RECEIVED 04 November 2022
ACCEPTED 16 November 2022
PUBLISHED 12 January 2023

CITATION
Mao Q, Xiao W, Sang M, Ao S, Song D, Tan Z, Wang H and Li R (2023), Two different types of provenances and the amalgamation of subduction complexes in the Eastern Tianshan of the Southern Altaids.
Front. Earth Sci. 10:1089700.
doi: 10.3389/feart.2022.1089700

Two different types of provenances and the amalgamation of subduction complexes in the Eastern Tianshan of the Southern Altaids

Qigui Mao[1,2,3]*, Wenjiao Xiao[1,2,4,5]*, Miao Sang[1,2]*, Songjian Ao[4,5,6], Dongfang Song[4,5,6], Zhou Tan[1,2], Hao Wang[1,2] and Rui Li[1,2]

[1]State Key Laboratory of Desert and Oasis Ecology, Xinjiang Institute of Ecology and Geography, Chinese Academy of Sciences, Urumqi, China, [2]Xinjiang Research Center for Mineral Resources, Xinjiang Institute of Ecology and Geography, Chinese Academy of Sciences, Urumqi, China, [3]Redrock Mining Co. Ltd., Hami, China, [4]Innovation Academy for Earth Science, Chinese Academy of Sciences, Beijing, China, [5]College of Earth and Planetary Sciences, University of Chinese Academy of Sciences, Beijing, China, [6]State Key Laboratory of Lithospheric Evolution, Institute of Geology and Geophysics, Chinese Academy of Sciences, Beijing, China

The nature and final closure of the northern Tianshan Ocean have been debated in regard to the eastern Tianshan orogen, southern Altaids. The Kanguer subduction complex of the eastern Tianshan is the key to addressing these issues. In this study, we report new mapping, geochemical and geochronological results on the Kanguer subduction complex in the Haluo area. Our new results show that upper Permian (257 Ma) basaltic blocks emplaced in a sandstone matrix in the northern HL area are fragments of normal-mid-ocean-ridge-basalt (N-MORB)-type oceanic crust. The geochronological results indicate that the sandstone matrices display two different types of provenances. The first type in the northern part of the cross-section (till Sample YY12) has maximum depositional ages ranging from 316 Ma to 238 Ma. Their depositional settings varied from intraoceanic island arcs to continental Andean arcs after ca. 244 Ma, their detrital zircon age patterns vary from a single peak to multiple peaks, and their zircon $\varepsilon_{Hf}(t)$ values vary from uniquely high positive to some negative values. The second type is in the southern part of the cross-section with Samples YY12 to 21Kg05, which have the geochemical signatures of continental island arc sandstone, multiple-peak detrital zircon-age patterns, and positive to negative zircon $\varepsilon_{Hf}(t)$ values. The youngest sandstone sample has a maximum depositional age of 241 Ma. The above provenance results indicate that all mélanges and coherent units north of Sample YY12 belong to an accretionary complex of the Dananhu intraoceanic arc, and those south of Sample YY12 belong to an accretionary complex of the Yamansu-central Tianshan arc. According to the youngest components in both accretionary complexes, which suggest the latest subduction events, we conclude that the final amalgamation timing was after 238 Ma and that the Paleo-Asian Ocean closed during the Middle to Late Triassic.

KEYWORDS
detrital zircon, U-Pb ages, mélange, suture zone, Altaids

1 Introduction

The ophiolitic mélange in an accretionary complex is a set of tectonic complexes that are formed by long-term, complicated subduction and are scraped and stacked in the subduction zone. In general, the mélange consists of fragments of oceanic crust, oceanic islands, oceanic mountains, flysch, and different types of sedimentary rocks (Hsü, 1968; Isozaki et al., 1990; Zhang et al., 2012; Kusky et al., 2013; Xiao et al., 2015). The ophiolitic mélange is a significant unit of orogens and sedimentary records and can provide important information on the evolutionary processes of paleo-oceans and the tectonic patterns of paleo-plates. However, the amalgamation processes of different blocks are complicated, and the suture line and the final collisional time are usually difficult to constrain (Isozaki et al., 1990; Wakabayashi, 2015; Wakita, 2015).

The Altaids or the southern Central Asian Orogenic Belt, which is one of the largest accretionary orogens in the world (Figure 1A), accreted around and southward from the Siberian craton with many arcs, accretionary complexes and microcontinents in the Paleo-Asian Ocean (PAO, Bazhenov et al., 2003; Buchan et al., 2002; Coleman, 1989; Dobretsov et al., 1995; Şengör and Natal'in, 1996; Şengör et al., 1993; Wilhem et al., 2012; Windley et al., 2007; Xiao et al., 2018). The PAO had a paleogeography similar to that of the present SW Pacific, with multiple oceans, islands and subduction zones (Windley et al., 2007; Xiao et al., 2010). The Kanguer subduction complex (KGSC) occurs between the Dananhu intraoceanic arc and the Yamansu-central Tianshan (CTS) continental arc in the eastern Tianshan. It represents the subduction zone of the northern Tianshan Ocean which is a southern branch of the Paleo-Asian Ocean remnants (Xiao et al., 2004; Li et al., 2005; Chen et al., 2019; Ao et al., 2021). Therefore, the provenances of the sedimentary matrix in the accretionary complex of the Dananhu and Yamansu-CTS arcs may be significantly different (Maynard et al., 1982; Floyd and Leveridge, 1987; Floyd et al., 1991; Mader and Neubauer, 2004; Yan et al., 2016). Therefore, in regard to this critical accretionary complex, this study determines the constraints on the subduction tectonic processes of this ancient ocean and on the accretionary history and final amalgamation of the southern Altaids.

Several models have been proposed for the tectonics of the KGSC; however, the composition and tectonic nature of the subduction complex and the subduction polarity of the paleo-ocean are controversial and can be summarized as 1) the accretionary complex of the Dananhu (Li, 2004; Xiao et al., 2004; Li et al., 2005; Ao et al., 2021), 2) the accretionary complex of the Yamansu arc (Chen et al., 2019), and 3) the mixing of the forearc mélange between the Dananhu and Yamansu arcs (Muhetaer et al., 2010). The proposals for the time of final accretion and amalgamation vary from the Devonian (Xia et al., 2004; Wang et al., 2006) to the Carboniferous (Gao and Klemd, 2003; Zhou et al., 2004; Qin et al., 2011; Han and Zhao, 2018) to the latest Carboniferous-early Permian (Xiao et al., 2004; Zhang et al., 2018; Du et al., 2020) to the Middle-Late Triassic (Chen et al., 2020; Ao et al., 2021; Mao et al., 2022a; Mao et al., 2022b).

In this paper, we report our new lithological and structural mapping results of the KGSC in the Haluo (HL) area in eastern Tianshan (NW China), new geochronological and isotopic data of the sandstone matrix, and new geochemical data of basaltic blocks in the mélange, aiming to constrain the tectonics of the northern Tianshan Ocean and the final amalgamation processes of the southern Altaids.

2 Geological background

The eastern Tianshan occupies the southernmost Altaids (Figure 1A) and comprises E/W-trending continental margin arcs, microcontinents, island arcs, ophiolites, and accretionary wedges (Xiao et al., 2004; Li et al., 2006). The internal tectonic units of the orogen are as follows from north to south (Figure 1B): the Dannanhu arc, the Kanguer subduction complex, the Yamansu arc, the Central Tianshan (CTS) block, and the southern Tianshan accretionary complex. These tectonic units were accreted and amalgamated from Ordovician to Triassic and docked together during the closure of the Paleo-Asian Ocean in the Permian to the Triassic (Ma et al., 1997; Xiao et al., 2004; Li et al., 2006; Zhang et al., 2018).

The Dannanhu arc, which is an intraoceanic arc, is mainly composed of Ordovician to Permian tholeiitic basalts, calc-alkaline andesites, pyroclastic rocks, sedimentary rocks and granitoids (Xiao et al., 2004; Wang et al., 2018; Zhang et al., 2018; Mao Q. G. et al., 2021; Du et al., 2021). These magmatic rocks have subduction-related geochemical features with positive whole-rock $\varepsilon_{Nd}(t)$ (+0.6– +10.2) (Qin et al., 2011; Mao et al., 2014b; Du et al., 2018a; Wang et al., 2018; Zhang et al., 2018; Mao et al., 2019; Mao Q. G. et al., 2021) and zircon $\varepsilon_{Hf}(t)$ (+0.3– +19.6) values. The Yamansu arc consists of Devonian-Permian tholeiitic to calc-alkaline volcanic and intrusive rocks interbedded with sedimentary rocks with relatively low whole-rock $\varepsilon_{Nd}(t)$ (ca. −1.1– +7.1) and zircon $\varepsilon_{Hf}(t)$ values (ca. −3.4– +17.0) (Luo et al., 2016; Du et al., 2019; Long et al., 2020), which were interpreted as a continental arc built on the northern margin of the CTS Arc during the Devonian-Permian (Hou et al., 2014; Du et al., 2018b; Chen et al., 2019; Han et al., 2019; Zhao et al., 2019). The CTS comprises Paleozoic calc-alkaline basaltic andesites, volcaniclastic rocks, minor I-type granites, and

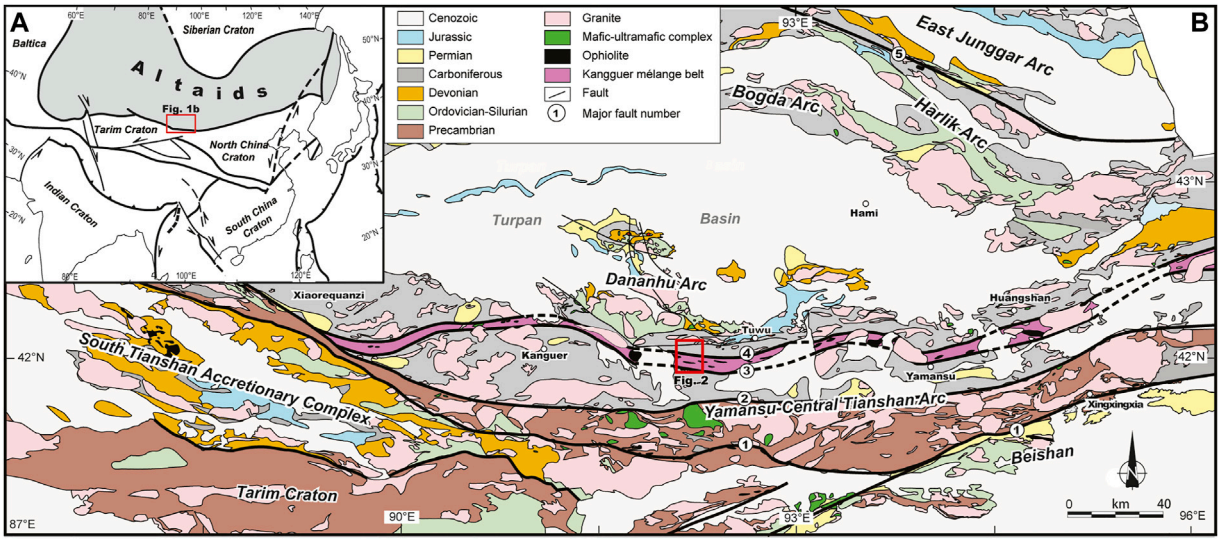

FIGURE 1
(A) Schematic tectonic map of Central Asia (Şengör et al., 1993; Xiao et al., 2018) showing the position of the eastern Tianshan in Figure 1B. **(B)** Geological map of the eastern Tianshan showing the distribution of the main tectonic units (modified after Xiao et al. (2004)). The locations of Figure 2 are marked. ① Kawabulake-Xingxingxia fault, ② Aqikekuduke-Shaquanzi fault, ③ Yamansu-Kushui fault, ④ Kanguer fault, and ⑤ Kalameili fault.

a Precambrian basement (Hu et al., 2000; Liu et al., 2004; Li et al., 2009; Mao et al., 2014a; Ma et al., 2014; Luo et al., 2016). The arc-related volcanic rocks and granitoids with relatively low whole-rock $\varepsilon_{Nd}(t)$ (ca. −5.7– +2.2) (Li et al., 2016; Lu et al., 2017; Mao et al., 2022a) and zircon $\varepsilon_{Hf}(t)$ values (ca. −15.4– +17.0) (Figure 8).

The Southern Tianshan accretionary complex contains discontinuous slices of Middle Devonian to early Carboniferous ophiolites (Gao and Klemd, 2003; Ao et al., 2020; Sang et al., 2020). The KGSC is located between the Dananhu arc in the north and the Yamansu-CTS arc in the south (Figure 1C). It was formed by long-lived northward subduction of the north Tianshan Ocean (a branch of the Paleo-Asian Ocean) and is composed of thrust-imbricated and dismembered serpentinite, ultramafic rocks, gabbro, basalt, limestone, and chert in a meta/deformed sandstone matrix. The gabbro and basalt blocks contain supra subduction zone (SSZ), normal-mid-ocean-ridge-basalt (N-MORB) and enriched mid-ocean ridge basalts (E-MORB) type ophiolite fragments (Xiao et al., 2004; Li et al., 2005; Li et al., 2006; Li et al., 2008; Chen et al., 2019; Ao et al., 2021).

3 Field geology of the Haluo area and sampling

The mélange in the Haluo (HL) area, which is located in the middle section of the KGSC, has a block-in-matrix structure with strong, nearly E–W-trending vertical cleavages. The blocks of sandstone and basalt belong to top-to-the-south thrust duplexes. The thrusts and cleavages of the KGSC in the entire HL area were displaced by late NW/SE-trending dextral strike-slip faults (Figure 2). At the map scale, the blocks of gabbro, massive basalt, diabase dikes, chert, limestone, and sandstone/siltstone are embedded and imbricated in a matrix of chlorite-phyllite schist and cleaved sandstone (Figures 2, 3A), and at the field scale, the oceanic and sedimentary rocks form a mutual matrix, e.g., the sedimentary rocks are the matrix, as shown in Figure 3A, and the strongly deformed basalts are the matrix as well (Figure 3B). The gabbro, basalt and chert blocks are highly cleaved (Figure 3C) and crop out in discontinuous lenses or ribbons ranging in length from several centimeters to several hundred meters (Figures 2A, 3C,D). The blocks of gabbro and basalt are elongated with their long axes aligned subparallel to the nearly E–W-trending faults in the mélange. The cherts generally crop out as lenses ranging in length from several meters to a kilometer with aspect ratios from 1:1 to 1:10 with their long axes parallel to the adjacent cleavage. The limestones crop out as discontinuous structural lenses or ribbon beds in the continuous sedimentary units. The matrix sandstones and chlorite-phyllite blocks display tectonic lenses and continuous bedding units and range in width from several meters to several kilometers and are tens of kilometers long. Most of them are highly cleaved and were intruded by volumes of quartz veins, indicating the movement of hydrothermal fluids during shearing (Figure 2A). The E–W-trending, subvertical cleavages in the matrix are penetrative and

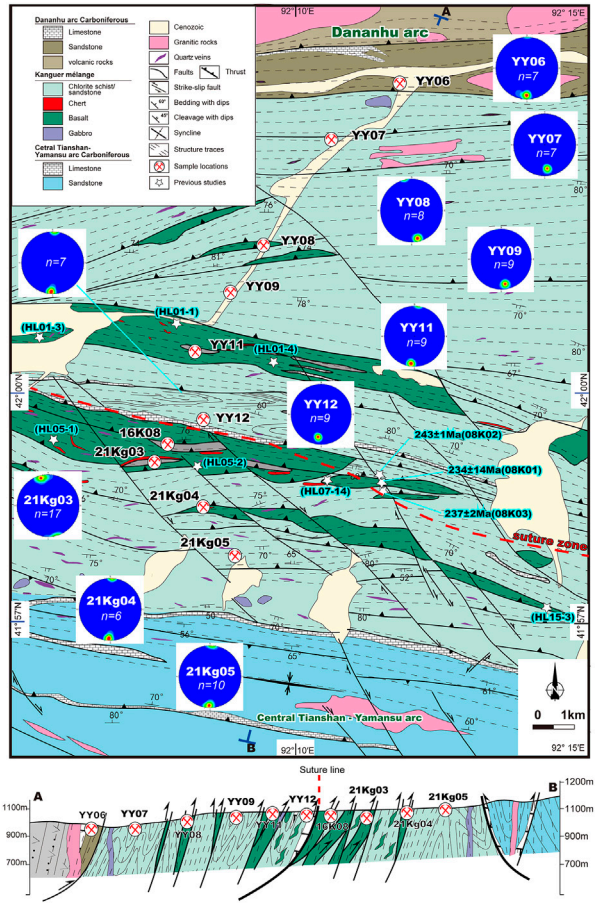

FIGURE 2
A geological map of the Kanguer subduction complex in the HL area showing the block-in-matrix structure. The sample locations and cross-section are marked. Stereographic projections of cleavages in the mélange matrix along the sections.

have overprinted the bedding so strongly that the primary depositional structures are mostly difficult to observe (Figure 2A). Some places have primary sedimentary bedding that can be distinguished, such as in the northern, central and southern continuous units of the mélange.

The KGSC in the HL area was thrusted southward; most of the blown sandstones, white limestone, red cherts, and massive green basalt blocks were thrusted to the south (Figures 2, 3A,B), but in some places, they also display northward thrusting, as shown in Figures 3C,D. Both the basalt and chert blocks are more strongly cleaved close to their whole bordering thrust planes (Figures 2, 3A–C). Some folds can be distinguished in the continuous sandstone blocks in the northern, central and southern parts of the HL area. Folded bedding planes parallel to the NE-trending cleavage indicate tight to isoclinal subvertical folds in the sandstone (Figure 2). Some elongated granitoid and gabbro dikes/intrusions intrude the mélange in the northern and southernmost HL area and are weakly cleaved; the long axes of the granitoid intrusions are parallel to the regional cleavage. Overall, these structures indicate regional N–S compression. All these compositions and structures indicate that the blocks of basalt, diabase, gabbro, limestone, sandstones and chert probably formed in different environments and were intermixed during subduction processes.

Two basalt samples (YY08-3 and YY08-6) were collected at location YY08 to analyze the zircon U–Pb ages, Hf isotopes and whole-rock geochemistry. The basalt is highly chloritized and epidotized, and consists of plagioclase, pyroxene, magnetite, ilmenite, minor olivine and clinopyroxene phenocrysts (Figures 4A,B). Eight sandstone samples in the NS-trending cross-section were collected for detrital zircon U–Pb dating and Hf isotope analysis. Most of them have deformed (Figure 4). The coarse-grained sandstone comprises angular plagioclase, quartz and lithic fragments (e.g., Samples 16K08 and 21Kg05, Figures 4C,D). The sandstones are composed of directionally arranged quartz, plagioclase and minor lithic fragments (e.g., Samples YY07, YY09, and YY12, Figures 4E,F,G). The tuffaceous siltstone consists of quartz and tuff/clay (Samples YY11 and 21Kg04, Figures 4H,I).

4 Zircon U–Pb age and Hf isotopes

4.1 Basalt

Zircons from basalt Sample YY08 in the northern part of the Kanguer accretionary complex are 50–120 μm long and have length/width ratios of 1.0–1.5, with magmatic oscillatory zones in cathodoluminescence (CL) images (Figure 5B), and they have variable Th/U values of 0.33–0.91. Fifteen zircon grains were analyzed, and fourteen of them yielded concordant ages with $^{206}Pb/^{238}U$ ages scattered from 361 Ma to 254 Ma (Figure 5A). There are three groups of grains that have mean weight ages of 257 ± 15 Ma (MSWD = 10, n = 3), 296.6 ± 6.4 Ma (MSWD = 6.6, n = 9) and 359.4 ± 6.0 Ma (MSWD = 0.29, n = 2). The older zircon grains were the precursor or xenocrysts of early magmatic events with $\varepsilon_{Hf}(t)$ values of +6.2 to +15.2, while the youngest three grains were the products of crystallization of the magma with high positive $\varepsilon_{Hf}(t)$ values of +7.3 to +11.1.

4.2 Sedimentary matrix sandstone

A total of 771 analyzed grains from nine sandstone matrix samples were collected along the NS-trending cross-section of the KGSC in the HL area (Figure 2). Seven hundred and ten analyzed grains yielded concordant ages (concordance % > 90% or <110%). All U–Pb and Lu–Hf isotopic data are shown in Supplementary Tables S1, S2, respectively. Only concordant ages are described and discussed below from north to south.

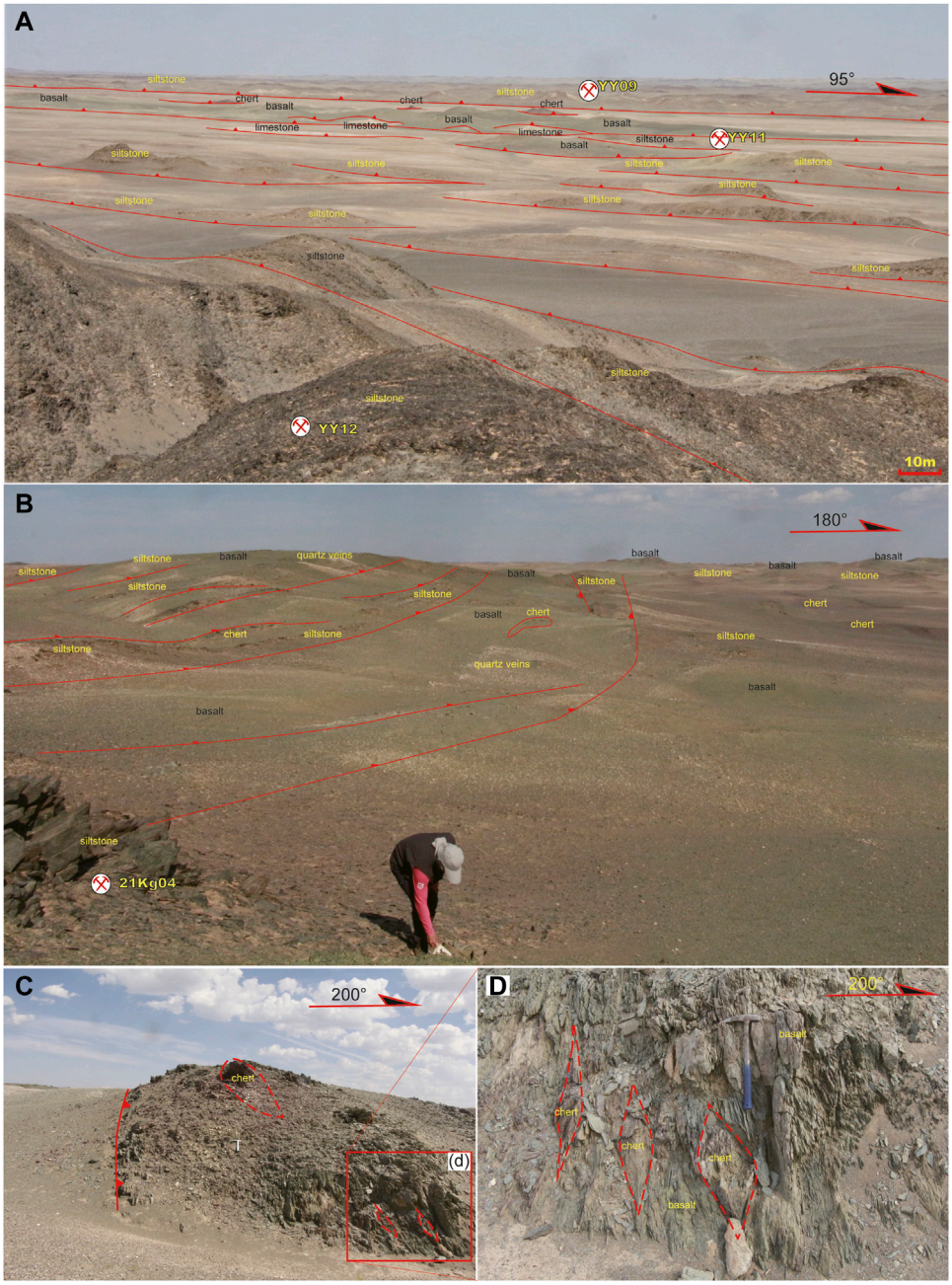

FIGURE 3
(A) Field photograph of the northern part of the HL area showing the block-in-matrix structure. **(B)** Field photograph of the southern part of the HL area showing the sedimentary blocks in the basalt matrix. **(C)** and **(D)** Photographs of strongly deformed basalt–chert blocks in the cleaved sedimentary rocks.

Several methods can calculate the maximum depositional age (MDA) of sedimentary rocks from their detrital zircon U–Pb ages, e.g., the youngest grain, the youngest three grains and the youngest peak (Coutts et al., 2019). Here, we use the weighted average ages of the youngest three grains if they overlap with a 2σ uncertainty or the youngest grain if the ages of the youngest three zircons far exceed a 2σ uncertainty [or the mean squared weighted deviation (MWSD) is poor].

4.2.1 Sample YY07

The zircons have grain sizes of 80–120 μm with length/width ratios of 1.2–1.8 and clear oscillatory zones in CL images. The

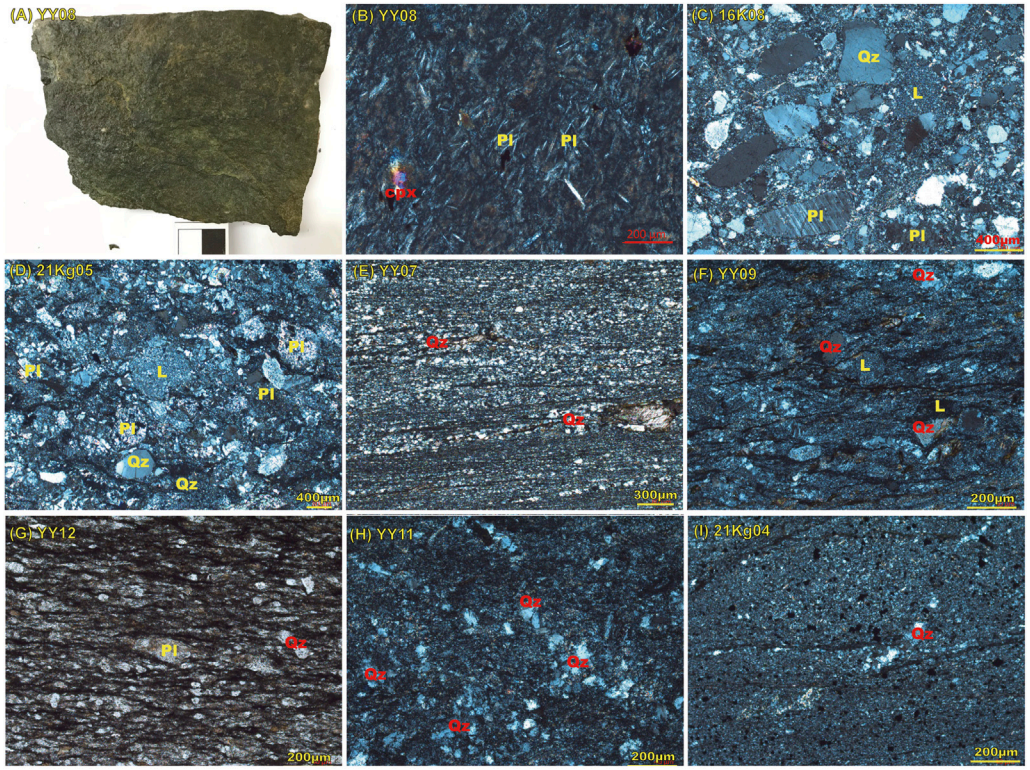

FIGURE 4
Photographs and Microphotographs of dated the samples. **(A)** Photographs of the basaltic sample YY08, **(B)** Microphotographs of the basaltic sample YY08, showing it comprises the clinopyroxene phenocrysts and plagioclase. **(C,D)** Microphotographs of coarse-grained sandstones (16K08 and 21Kg05), showing directionally, poor sorting and high proportions of detrital altered matrix. Grains are angular and subrounded. **(E–G)** Microphotographs of sandstones, showing directionally and poor sorting, high proportions of detrital and diagenetically altered matrix and a mix of quartz, feldspar and lithic framework fine grains. **(H,I)** Microphotographs of tuffaceous siltstones (YY11 and 21Kg04) consists of quartz and tuff/clay.

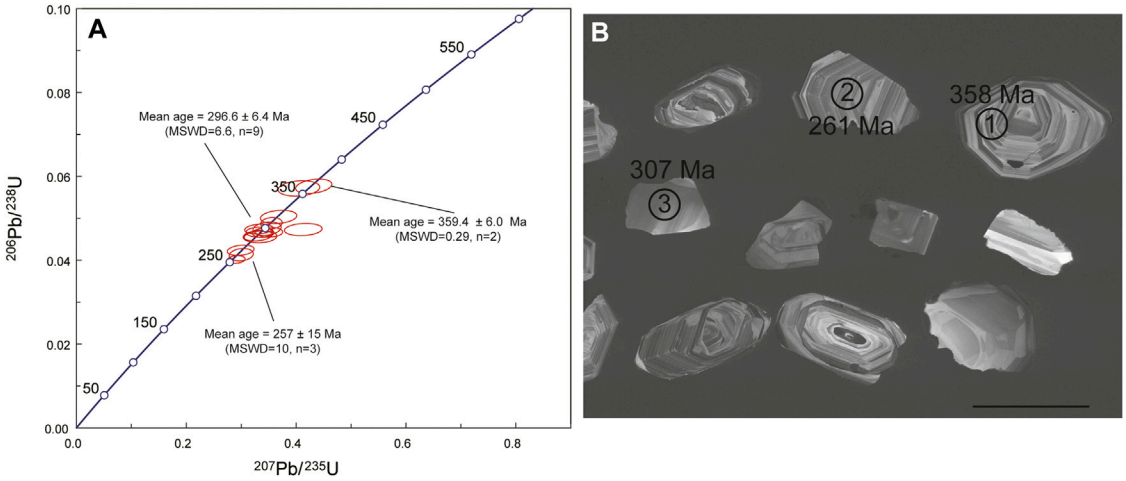

FIGURE 5
Concordia U–Pb diagrams **(A)** and CL images **(B)** for the zircons of the basalt fromf the north HL area.

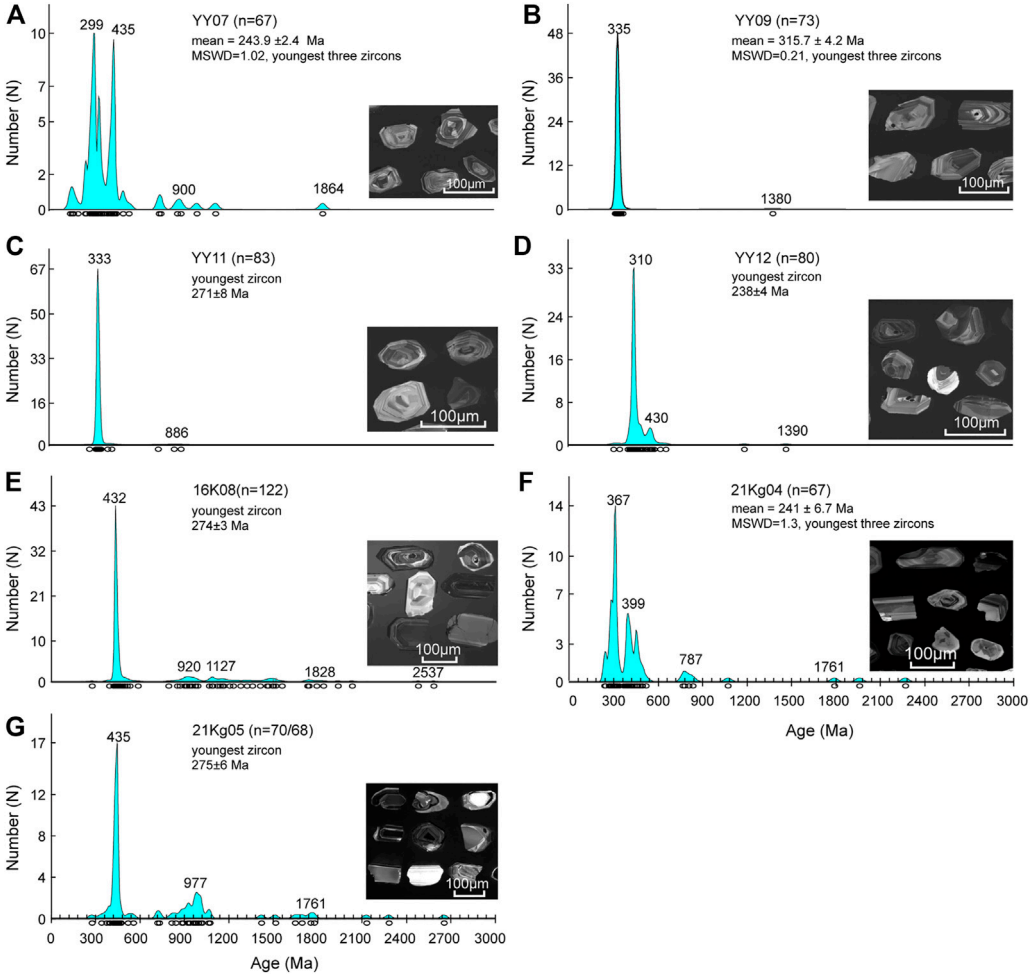

FIGURE 6
Histograms for the detrital zircons of the sandstones in the HL area (see Figure 2 for sample locations and supporting information and Supplementary Table S3 for data sources). **(A)** Sample YY07 of the north HL area shows multiple peaks detrital zircon age pattern. **(B), (C)**, and **(D)** Samples YY09, YY11 and YY12 of the north HL area show single peaks detrital zircon age patterns. **(E), (F)**, and **(G)** Samples 16K08, 21Kg04 and 21Kg05 of the south HL area show multiple peaks detrital zircon age patterns. Ages of 206Pb/238U and 1σ, with concordance % > 90% or < 110%, were used for density plots using DensityPlotter software Version 8.5 (Vermeesch, 2012).

concordant zircons have variable Th/U values of 0.25–2.04. Sixty-seven of the ninety-three analyzed grains yielded concordant ages ranging from 244–1,861 Ma. They have two main peaks at 299 and 435 Ma and three subordinate peaks at 240, 900, and 1,864 Ma (Figure 6A). The three younger ages yielded a weighted mean age of 243.9 ± 2.4 Ma (MSWD = 1.02). The $\varepsilon_{Hf}(t)$ values of the detrital zircons range from −18.0 to +15.6 (Figure 7C) and have 28% (18 grains in 65 analyzed grains) analyzed grains have negative $\varepsilon_{Hf}(t)$ values.

4.2.2 Sample YY09

The zircon grains are 100 μm long, and they have length/width ratios of 1–2.0 and prominent oscillatory zones in CL images (Figure 6B). Furthermore, they have variable contents of Th (56–910 ppm) and U (55–738 ppm) and Th/U values of 0.43–1.71. Of the ninety analyzed zircon grains, seventy-three grains yielded concordant ages with major concordant age peaks at 335 Ma (99% of the total), and only one grain has a Precambrian age of 1,380 ± 31 Ma (Figure 6B). The youngest three zircons yielded a weighted mean age of 315.7 ± 4.2 Ma (MSWD = 0.21). Lu–Hf isotope analyses of the concordant zircons yielded $\varepsilon_{Hf}(t)$ values ranging from +4.1 to +16.7 (Figure 7B).

4.2.3 Sample YY11

The zircons are 50–120 μm long and have length/width ratios of 1.0–2.0, with oscillatory zones in CL images. They have variable Th/U values of 0.22–1.37. Of the ninety analyzed zircon grains, eighty-three grains yielded concordant ages with major concordant age peaks at 333 Ma (91.6% of the total), and

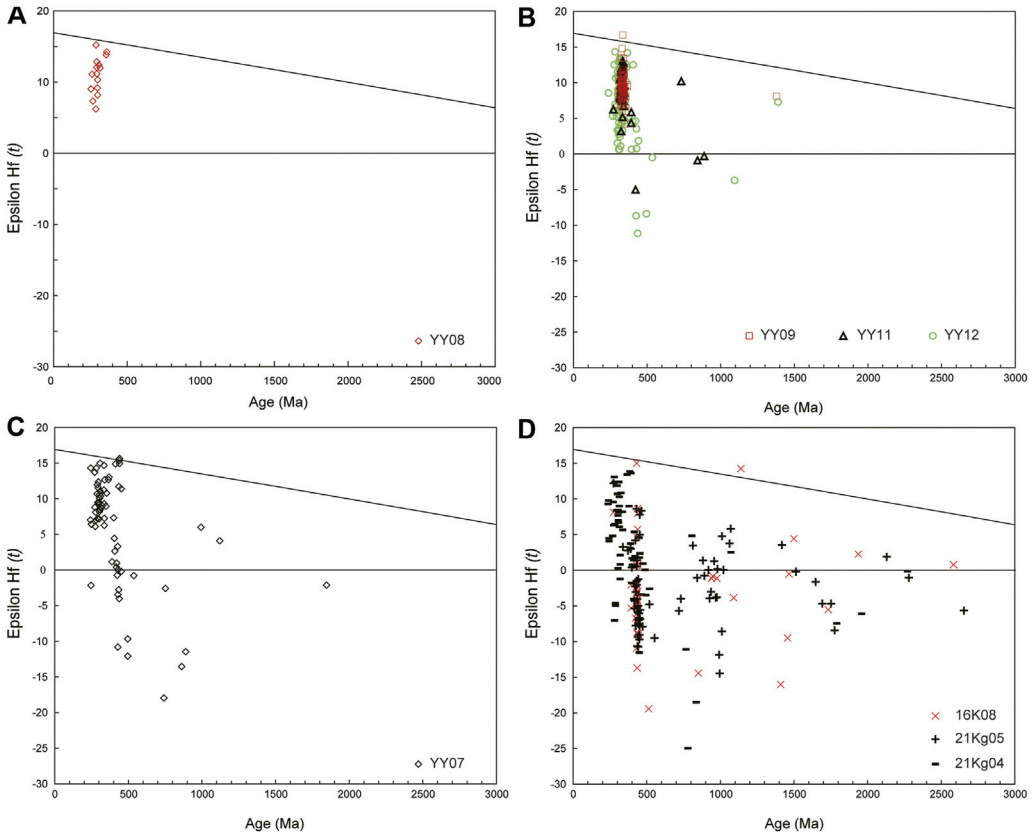

FIGURE 7
Hf isotope diagrams of dated samples. **(A)** Basalt from the northern HL area. **(B)** Samples YY09 and YY11 in the northern HL area showing that the sandstone samples were probably derived from the Dananhu intraoceanic arc to the north. **(C)** Samples YY07 and YY12 in the northern HL area show a small amount of material sourced from the Yamansu-central Tianshan arc to the south. **(D)** Samples 16K08, 21Kg04 and 21Kg05 in the southern HL area showing that the sandstones were probably derived from the Yamansu-central Tianshan arc to the south. The age data after Supplementary Table S3.

only three grains yielded Precambrian ages at 886, 843, and 733 Ma. The youngest zircon has an age of 271 ± 8 Ma, which is interpreted as the MDA of the sandstone (Figure 6C). Lu–Hf isotope analyses of the detrital zircons yielded $\varepsilon_{Hf}(t)$ values ranging from −5.1 to +13.1 (Figure 7B) and only three grains in 83 ananlyzed grains (ca. 4%) have negative $\varepsilon_{Hf}(t)$ values.

4.2.4 Sample YY12

Ninety zircon grains were analyzed, and seventy-nine grains yielded concordant ages with variable Th/U values of 0.08–1.06. Most of them have oscillatory zones in CL images. They have a major concordant age peak at 310 Ma and a second age peak at 430 Ma; only two grains yielded Precambrian ages at 1,095 and 1,390 Ma (Figure 6D). The youngest zircon has an age of 238 ± 4 Ma, which is interpreted as the MDA of the sandstone. Lu–Hf isotope analyses of the detrital zircons yielded $\varepsilon_{Hf}(t)$ values ranging from −11.2 to +14.3 (Figure 7C) and only six grains in 79 analyzed grains (ca. 8%) have negative $\varepsilon_{Hf}(t)$ values.

4.2.5 Sample 16K08

One hundred and twenty-nine zircon grains from Sample 16K08 were analyzed. One hundred and twenty-four zircon grains yielded concordant ages with variable Th/U values of 0.01–2.23. Most of them have oscillatory zones in CL images. These detrital zircons have multiple concordant age major peaks at 432 Ma and small peaks at 920, 1,127, 1,828, and 2,500 Ma (Figure 6E). The youngest zircon yielded a concordant age of 274 ± 3 Ma, which we interpret as the MDA of the sandstone. The detrital zircons have relatively variable $\varepsilon_{Hf}(t)$ values ranging from −19.4 to +15.0 (Figure 7D) and ca. 78% of 58 analyzed grains have negative the $\varepsilon_{Hf}(t)$ values.

4.2.6 Sample 21Kg04

All seventy analyzed zircon grains yielded concordant ages with variable Th/U values of 0.07–2.02. Most of them have oscillatory zones in CL images. The zircons display three major concordant age peaks at 367, 399, and 787 Ma, and

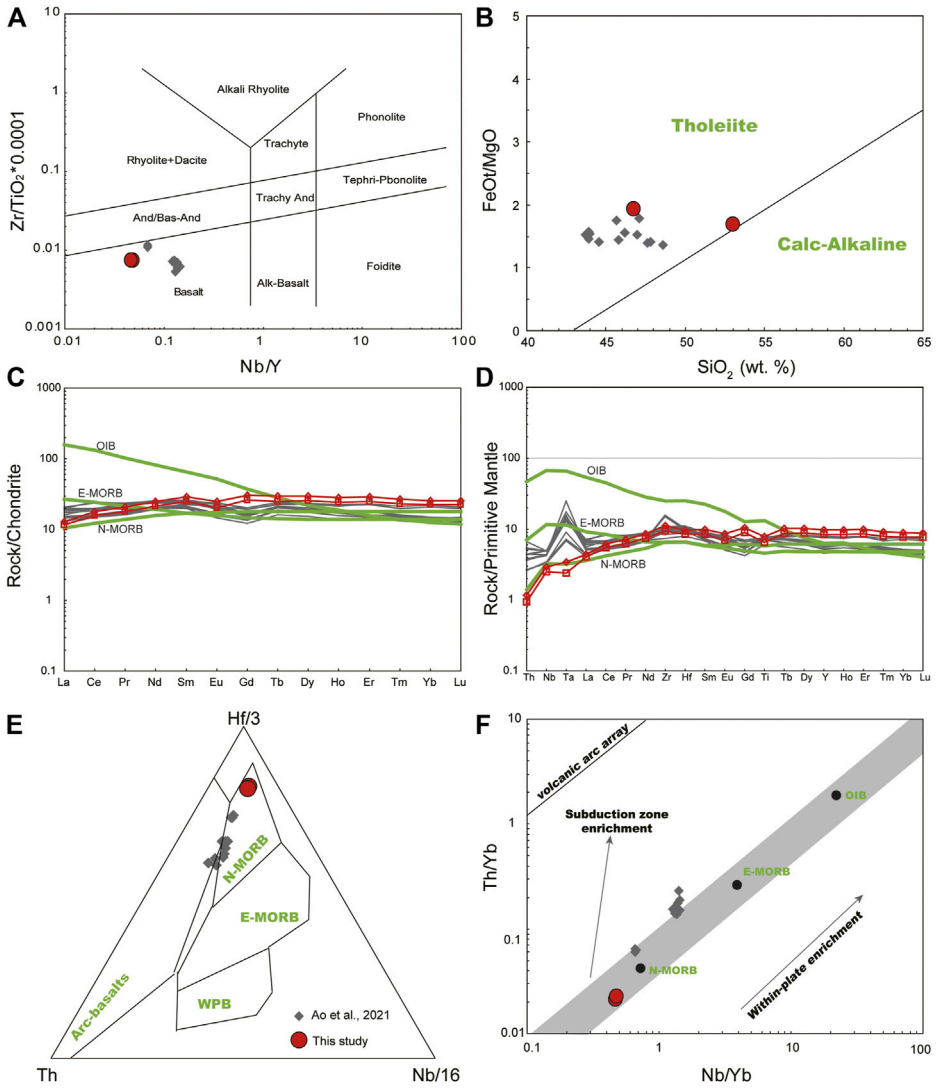

FIGURE 8
Geochemical diagrams of the basalt in the northern HL area of the KGSC. **(A)** Zr/Ti vs. Nb/Y diagram (Winchester & Floyd, 1977) and **(B)** FeO_t/MgO vs. SiO_2 diagram (Myashiro, 1974), **(C)** Chondrite-normalized REE and **(D)** primitive mantle normalized multielement diagrams. Chondrite values are from a previous study (Boynton, 1984). The PM values are from a previous study (Sun and McDonough, 1989). **(E)** Hf-Th-Ta diagram (Hawkins, 2003; Wood, 1980) and **(F)** Nb/Yb vs. Th/Yb diagram (Pearce, 2008). The fields of the Tofua Arc, Lau Basin and Mariana Trough are from Hawkins (2003). The basaltic fragments in the northern HL area are similar to those of N-MORBs. The dark diamonds and lines are after Ao et al. (2021).

the other four Precambrian zircon grains yielded ages of 1,073, 1,791, 1,960, and 2,302 Ma (Figure 6F). The youngest three zircon weight average ages are 241 ± 6.7 Ma (MSWD = 1.3), which we interpret as the MDA of the sandstone. The detrital zircons have relatively high $\varepsilon_{Hf}(t)$ values ranging from −35.6 to +13.9 (Figure 7D) and ca. 33% of 66 analyzed grains have negative the $\varepsilon_{Hf}(t)$ values.

4.2.7 Sample 21Kg05

The zircons have grain sizes of 80–120 μm with length/width ratios of 1.0–1.5 and clear oscillatory zones in CL images. Sixty-eight of the seventy analyzed zircon grains yielded concordant ages with variable Th/U values of 0.31–1.70. They have three major concordant age peaks at 435, 977, and 1,761 Ma, and three Paleoproterozoic to Neoarchean zircon grains yielded ages of 2,130, 2,281, and 2,655 Ma (Figure 6G). The youngest zircon has a concordant age of 275 ± 6 Ma, which is interpreted as the MDA of the sandstone. The detrital zircons have widely variable $\varepsilon_{Hf}(t)$ values ranging from −14.5 to +12.2 (Figure 7D) and ca. 66% of 68 analyzed grains have negative the $\varepsilon_{Hf}(t)$ values.

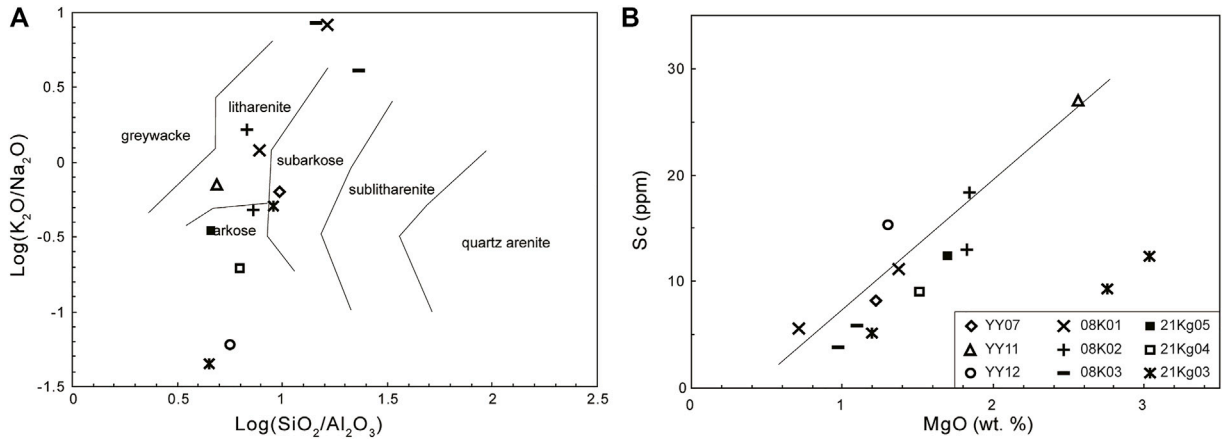

FIGURE 9
Chemical classification diagrams discriminating sedimentary rocks. **(A)** SiO_2/Al_2O_3 vs. Na_2O/K_2O (Pettijohn et al., 1972) and **(B)** MgO vs. Sc diagrams.

5 Geochemistry

5.1 Basalt

Two alternating basalt samples from the KGSC are the tholeiite basalts in the northern HL area (Figures 8A,B), which have moderate TiO_2 (1.4–1.7 wt.%) and relatively narrow elemental ratios with SiO_2 = 46.8–53.0 wt.%, Al_2O_3 = 12.3–13.3 wt.%, and CaO = 6.1–10.1 wt.%. They have high MgO (6.0–6.6 wt.%) contents and Mg# values of 52–55. The samples are altered and thus have variable loss on ignition (LOI) contents ranging from 4.8 to 5.9 wt.%. Their Na_2O concentrations vary from 0.78 to 3.71 wt.%, likely reflecting seawater alteration. They have right-obliquely depleted rare earth element (REE) patterns ($(La/Yb)_N$ = 0.4–0.53) that are similar to those of N-MORBs (Figure 8C) and slightly negative Eu anomalies (Eu* = 0.80–0.84). They also display right-oblique trace patterns ($(Nb/La)_{PM}$ = 0.67 $(Th/Nb)_{PM}$ = 0.40) and are slightly depleted in Ti on a primitive mantle-normalized spider diagram (Figure 8D).

5.2 Sedimentary matrix sandstone

The whole-rock geochemical data of these sandstones are listed in Supplementary Table S2. The SiO_2 contents (65.8–76.7 wt.%) and K_2O/Na_2O ratios (0.06–0.71) of sandstone in the northern HL area are lower than those in the southern HL area (74.1–88.7 wt.% and 0.48–8.39, respectively), but the Al_2O_3 contents of the sandstone in the northern HL area are higher (7.95–13.56 wt.%) than those in the southern HL area (3.82–10.88 wt.%). The SiO_2/Al_2O_3 ratios of the northern sandstones (4.86–9.46) are lower than those of the southern sandstones (6.81–23.24), indicating low clay and feldspar contents but high quartz contents in the protolith of the southern sandstone (Potter, 1978). On the SiO_2/Al_2O_3 vs. K_2O/Na_2O diagram (Figure 9A), the northern analyzed samples plot within the subarkose and litharenite fields, and the southern samples mainly plot as litharenite. All samples have a good positive Sc-MgO correlation (Figure 9B), indicating that abundant mafic clasts were contained within their protolith, which is supported by their petrological results.

The samples from the northern and southern HL areas have variable concentrations of REEs (64.9–141.1 ppm and 39.9–104.5 ppm, respectively) with similar chondrite-normalized REE patterns (Figures 10A,C). They are enriched in light rare earth elements (LREEs) with $(La/Yb)_N$ values of 3.18–5.95 and 4.82–11.0 and distinct Eu anomalies with Eu/Eu* values of 0.65–0.74 and 0.65–1.10, respectively. In comparison with the average upper continental crust (UCC), all samples show distinct negative Nb, Ta and Ba anomalies but higher enrichments in V, Cr, Ni, Sc, Cs, Ti and Y and negative to positive Sr (Figures 10B,D). This pattern is similar to that of the sandstones in the continental arc and active margin (Floyd et al., 1991).

6 Discussion

6.1 Nature of the northern Tianshan Ocean

Several competing models have been proposed for the northern Tianshan Ocean and can be summarized as follows: 1) an interarc basin between the Dannanhu and Yamansu arcs (Li, 2004; Xiao et al., 2004; Han and Zhao, 2018), 2) a short-lived limited ocean or back-arc basin in the Carboniferous (Ma et al., 1997; Wang et al., 2006; Wang et al., 2019), 3) a branch of the

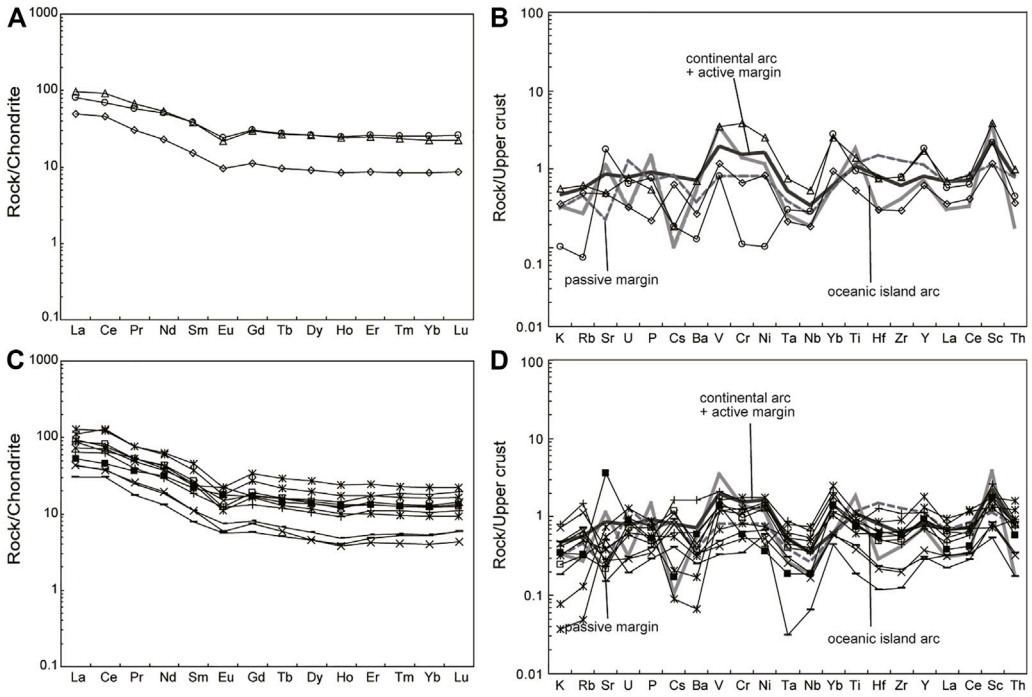

FIGURE 10
Chondrite-normalized REE diagram and multielement diagrams normalized to average upper continental crustal values (Floyd et al., 1991). **(A)** and **(B)** are the sandstone samples of the north KGSC in HL area, **(C)** and **(D)** are the sandstone samples of the south KGSC in HL area. The chondrite values are from a previous study (Boynton, 1984). The cited passive margin, oceanic island arc and continental arc island arc+ active continental margin values are from Floyd et al. (1991). The symbols used are the same as those used in Figure 9.

Paleo-Asian Ocean that separated the Siberian craton to the north and the Tarim craton to the south (Li et al., 2005; Li et al., 2008; Chen et al., 2019; Mao et al., 2019; Ao et al., 2021), and 4) a short-lived, limited-rifted ocean on the accretionary wedge in the Carboniferous to Permian (Wang et al., 2006; Wang et al., 2019).

Our zircon LA-ICP–MS U–Pb dating reveals that the basaltic rocks have crystallization ages of 257 Ma. In addition, Li et al. (2008) reported that the gabbro of the Kanguertage ophiolite yielded a zircon SHRIMP U–Pb age of 494 ± 10 Ma. Therefore, direct geochronological studies of oceanic crust fragments suggest that the northern Tianshan Ocean was a long-lived ocean with an age of >ca. 494 Ma to <ca. 257 Ma. The zircon U–Pb dating of the sedimentary matrix in the KGSC reveals MDAs ranging from 384 to 234 Ma (Chen et al., 2019; Ao et al., 2021) and arc-related magmatism ages from the Ordovician to Triassic in the Dananhu arc (ca. 453 Ma to 234 Ma) and Yamansu-CTS arc (ca. 481 Ma to 234 Ma) (Xiao et al., 2004; Zhang et al., 2018; Chen et al., 2019; Du et al., 2019; Long et al., 2020; Mao Q. et al., 2021; Mao Q. G. et al., 2021; Du et al., 2021; Mao et al., 2022a). All of these data suggest that the northern Tianshan Ocean was a long-lived ocean (494 Ma to ca. 234 Ma).

The KGSC in the map area is characterized by "block-in-matrix" structures and was thrust-imbricated (Ao et al., 2021, this study). The field relationships and structural characteristics indicate that the HL area is a classic ophiolitic-bearing tectonic mélange that formed at a convergent margin and was created by subduction–accretion processes (Wakabayashi, 2015; Xiao et al., 2015; Kusky et al., 2020; Ao et al., 2021). Basalt, diabase, gabbro, limestone, and chert represent fragments of oceanic crust that can provide information on the nature and history of the oceanic plate (Xiao et al., 2015; Festa et al., 2019; Raymond, 2019; Wakabayashi, 2019; Kusky et al., 2020). Our studies reveal that the basaltic fragments from the northern parts of the HL area are tholeiitic rocks and have typical N-MORB geochemical signatures with right-oblique depleted REE patterns ($(La/Yb)_N$ = 0.4–0.53) and trace patterns (Figures 8C,D) and high zircon Hf isotope values (+9.0–+14.4). They have relatively high Zr/Nb (59.0–59.7) and La/Nb (1.44–1.57) and higher Th/Nb (0.04–0.05) ratios, which are similar to those of N-type MORB basalts (>30, 1.07 and 0.05) (Sun and McDonough, 1989; Wilson, 2001). On Hf-Th-Nd and Th/Yb-Nb/Yb diagrams (Figures 8E,F), the basalts plot in the N-MORB field. Thus, all geochemical and Hf isotope features demonstrate that these basalts were probably generated in a mid-ocean ridge, where erupted lavas were influenced by seawater penetration. This conclusion is consistent with the ophiolitic fragments in the southern part of the map area, which have N-MORB to SSZ ophiolitic fragments (Figures 8E,F), suggesting that the northern Tianshan Ocean contained typical N-MORB oceanic crust (Ao

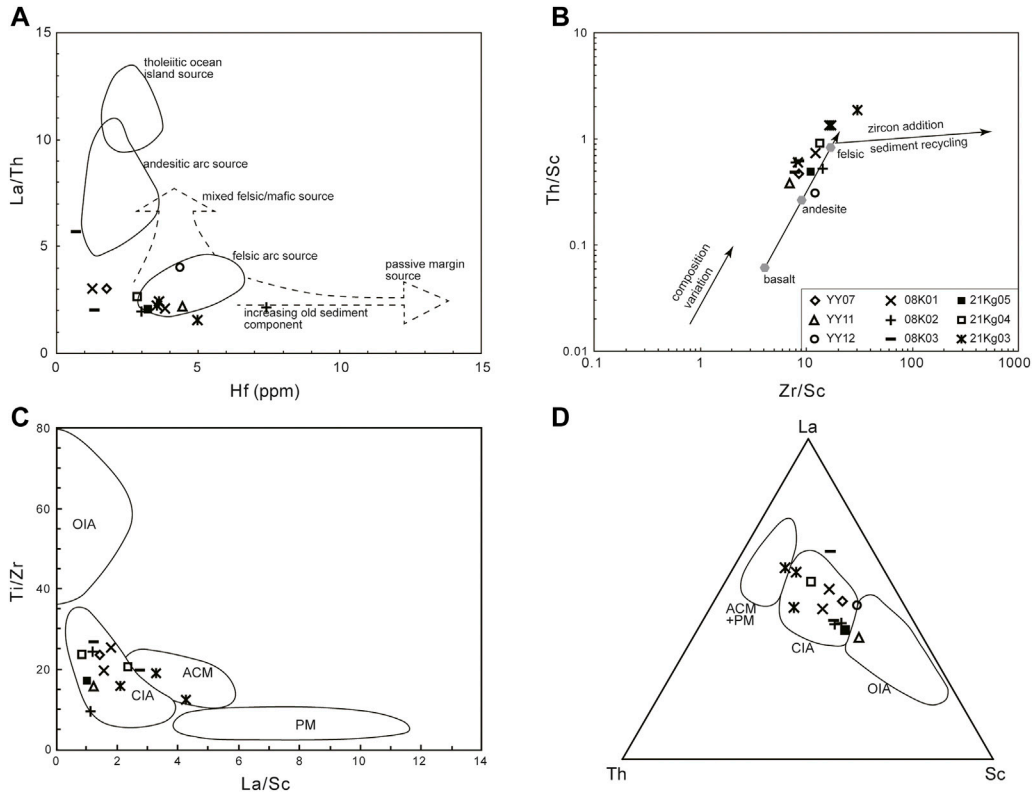

FIGURE 11
Tectonic setting discrimination diagrams for the sandstone matrix in the KGSC in the HL area. **(A)** Hf vs. La/Th diagram (Floyd and Leveridge, 1987), **(B)** Th/Sc vs. Zr/Sc diagram (McLennan et al., 1993), **(C)** La/Sc vs. Ti/Zr, **(B)** Th-Co-Zr/10 and **(D)** La–Th–Sc plots (Bhatia and Crook, 1986). ACM, active continental margin; PM, passive continental margin; CIA, continental island arc; and OIA, oceanic island arc.

et al., 2021). Previous studies have also suggested that the KGSC contains SSZ-, N-MORB- and E-MORB-type oceanic fragments, e.g., 1) some basalt fragments in the middle part of the map area have SSZ and N-MORB ophiolitic geochemical characteristics (Ao et al., 2021); 2) the E-MORB- and N-MORB-type ophiolitic blocks in the Yamansu area (Chen et al., 2019); and 3) the SSZ-type ophiolitic blocks in the Kanguertage area in the western section of the KGSC (Li et al., 2005; Li et al., 2008). These geochemical signatures of the ophiolitic fragments of the KGSC indicate that the northern Tianshan oceanic crust was as complicated as the Pacific oceanic crust.

In summary, the geological, geochemical and geochronological features of the ophiolitic fragments of the KGSC, together with data from the Dananhu arc and Yamansu-CTS arc, suggest that the northern Tianshan Ocean was a branch of the Paleo-Asian Ocean. The northern Tianshan Ocean born before 497 Ma, and N-MORB and E-MORB type ophiolites were formed by the normal middle oceanic-ridge and hotspot, respectively. The subduction formed the SSZ-type ophiolite and caused the different oceanic crust to be accreted in the Kanguer subduction complex during Cambrian to Triassic.

6.2 Two types of provenances for the sedimentary matrix in the Kanguer subduction complex

The matrix of the accretionary complex originates from arcs and/or forearcs sedimentary rocks. Therefore, the provenance variations in the matrix can provide detailed information on the spatiotemporal framework of the arcs, the subduction polarity and the evolution of the subduction. Therefore, the two arcs were the main potential provenance for the sandstone matrix of the KGSC.

Basalt and rhyolite detrital fragments in the sandstone indicate a mixed origin (Figure 4). The angular clastic and euhedral detrital zircon grains (Figures 4, 6) indicate that they had a proximal source and were deposited on an active margin (Floyd and Leveridge, 1987). The significant enrichment of LREEs and the flat HREE patterns (Figures 10A,C) also imply a felsic source, which is also attested by a plot of La/Th against Hf (Figure 11A). On the Th/Sc vs. Zr/Sc diagrams (McLennan et al., 1993), the samples plot along the compositional variation line from the area of felsic volcanic rocks to the

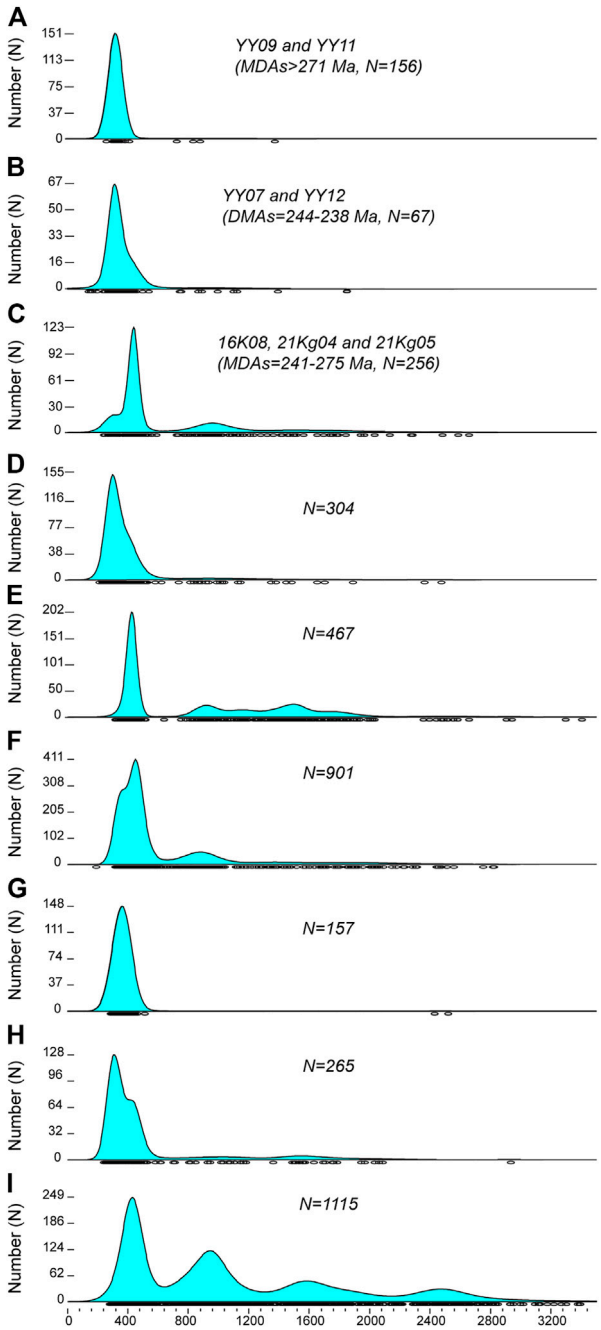

FIGURE 12
Comparison of probability plots for zircon U–Pb ages of sedimentary rocks around the KGSC. **(A)** The sandstone matrix (MDAs > ca. 244 Ma, Samples YY09 and YY11) in the KGSC in the northern HL area. **(B)** The sandstone matrix (MDAs ≤ ca. 244 Ma, Samples YY07 and YY12) in the KGSC in the northern HL area. **(C)** The sandstone matrix in the KGSC in the southern HL area. **(D)** The sandstone matrix (MDAs = 243–243 Ma) in the KGSC in the northern HL area (Ao et al., 2021). **(E)** The sandstone matrix (MDAs = 384–315 Ma) in the KGSC in the Yamansu area (Chen et al., 2019). **(F)** Sedimentary rocks in the Harlik arc. **(G)** Devonian-Permian sedimentary rocks of the Dananhu arc (Chen et al., 2019). **(H)** Late Permian–Triassic sedimentary rocks (MDAs ≤ 258 Ma) of the Dananhu arc (Chen et al., 2019). **(I)** Sedimentary rocks of the (*Continued*)

FIGURE 12 (Continued)
Yamansu-CTS arc. Ages of $^{206}Pb/^{238}U$ and 1σ values, having concordance % >90% or <110%, which are used for density plots using DensityPlotter Version 8.5 software (Vermeesch, 2012). The age data after Supplementary Table S4.

andesitic arc field (Figure 11B), also suggesting that the sandstones were derived from a mixed source of intermediate and felsic components with a low degree of weathering, sorting and/or sedimentary rock recycling. On the plots of La/Sc vs. Ti/Zr (Figure 11C), all samples plot within the CIA field. On the La–Th–Sc diagrams, except for Sample YY11-2 (with a MDA of 271 Ma) from the northern HL area, which plots in the OIA fields, all other samples plot within the CIA field (Figure 11D).

The detrital zircon U–Pb age spectra of the sandstone matrix of the KGSC in the HL area show that the sources mainly contained Triassic, Permian-Ordovician and minor Neoproterozoic zircons, also indicating a mixed source. According to the spatiotemporal relationship of the detrital zircon age spectra, Hf isotopes and whole-rock geochemical characteristics, the sandstone samples in the N–S-trending cross-sections can be subdivided into two types of provenances:

6.2.1 Type I: Provenances of the northern Haluo area

The provenances of the sandstone matrix samples from the northern HL area changed after ca. 244 Ma. Sandstone matrix Samples YY09 and YY11 with MDAs of 316 Ma to 271 Ma were deposited in an OIA setting. They have similar spectra of zircon ages with a single age peak pattern and most analyzed grains show high positive $\varepsilon_{Hf}(t)$ values (only ca. 4% and ca. 8% analyzed grains have negative $\varepsilon_{Hf}(t)$ values), indicating that they were sourced from intraoceanic arcs. Their age and Hf isotope patterns are similar to those of the Devonian to Permian sedimentary rocks of the Dananhu arc (Figures 12G, 13A) (Chen et al., 2020) but are different from those of the Triassic sedimentary rocks of the Dananhu arc and the southern part of the HL area (Figures 12H, 13A,C) and the sedimentary rocks in the KGSC in the Yamansu area (Figures 12E, 13D), Harlik arc (Figure 12F) and Yamansu-CTS arc (Figure 12I). All of these facts indicate that these sandstone matrices (MDAs > ca. 244 Ma) were most likely sourced from the Dananhu arc.

However, the geochemical, detrital zircon age and isotope data of the sandstone matrix samples whose MDAs are younger than 244 Ma are proven to be from a continental arc. First, their geochemical signatures suggest that they were deposited in a CIA setting. Second, the zircon age spectrum of Sample YY07 has multiple peaks and a percentage of Precambrian zircon grains. They have positive to negative zircon $\varepsilon_{Hf}(t)$ values (−18.0 to +15.6) and have ca. 28% analyzed grains have negative $\varepsilon_{Hf}(t)$ values. Although Sample YY12 has a single age peak pattern

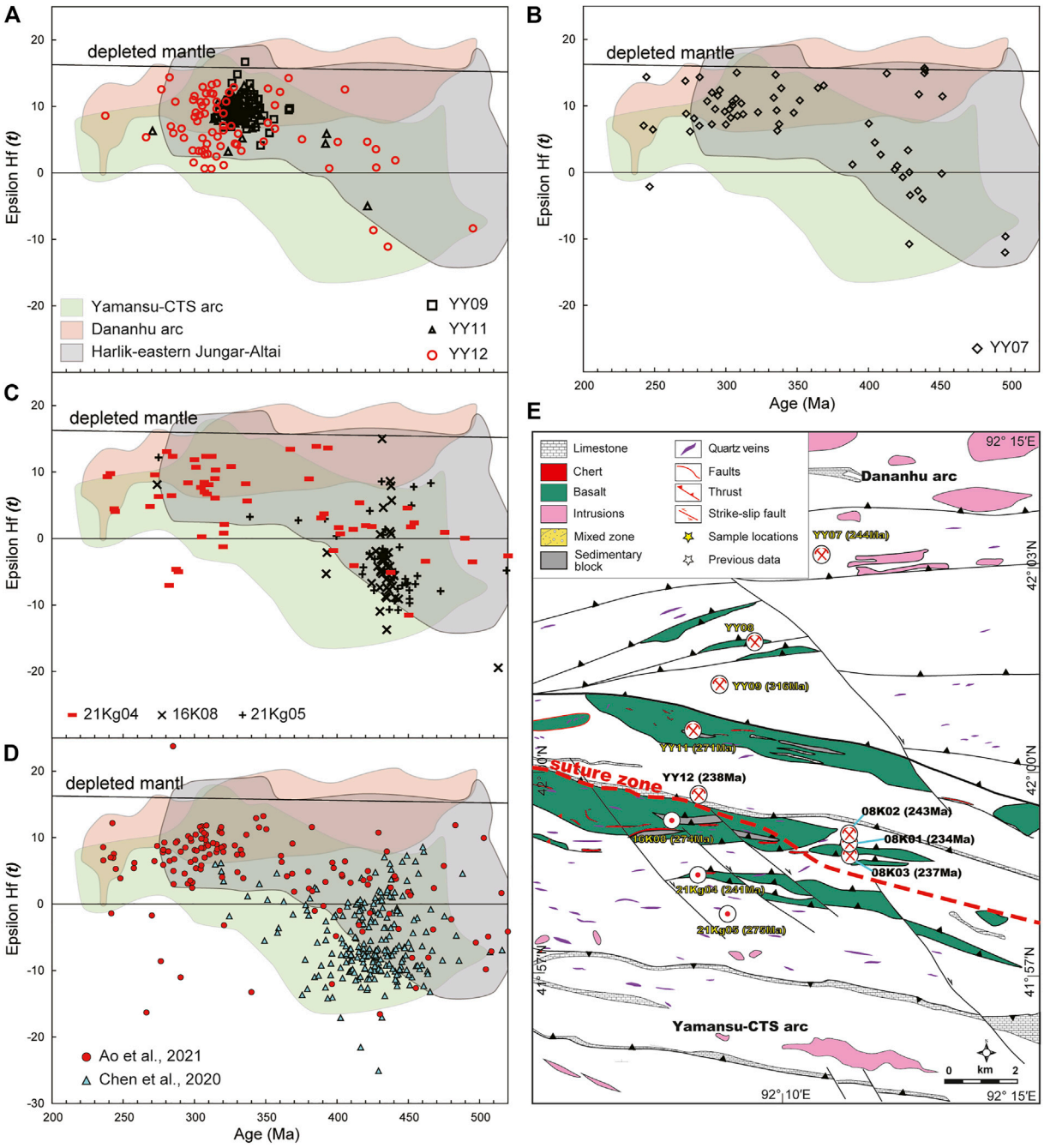

FIGURE 13
Hf isotope diagram of dated sandstones from the KGSC. **(A)** Shows that the sandstone matrix (Samples YY09 and 11) was probably derived from the Dananhu intraoceanic arc to the north. **(B)** Shows that the sandstone matrix (Samples YY07 and 12) was probably derived from the southern South Mongolian-Dananhu Andean arc to the north in the Triassic. **(C)** Shows that the sandstone matrix (Samples 16K08, 21Kg04 and 05) was probably derived from the Yamansu-CTS arc. **(D)** The Hf isotopes of the sandstone matrix samples from the KGSC in the Yamansu area (Chen et al., 2019) and the HL area (Ao et al., 2021). **(E)** Suture line between Samples YY12 and 16K08 in the N–S-trending cross-section in the HL area. The Hf isotopic data are provided in Supplementary Table S5.

similar to Samples YY07 and YY11 (Figure 12A), it displays positive to negative zircon $\varepsilon_{Hf}(t)$ values (−11.2 to +14.3) with few grains with negative zircon $\varepsilon_{Hf}(t)$ values (ca. 8%). The sample has percentages of Precambrian zircon grains but no 25Ga zircon grains, which is distinct from the detrital patterns of the Yamansu-CTS arc (Figure 12I). It also has different zircon Hf

isotope patterns to the late Paleozoic magmatic rocks of Yamansu-CTS arc (Figure 13B) and sedimentary rocks of the KGSC in south HL area (Figure 13C). In contrast, its detrital zircon age and isotopic characteristics are similar to those of Triassic sedimentary rocks in the Dananhu arc (Figure 12H) (Chen et al., 2020), the sedimentary rocks of the Harlik arc (Figure 12F) and the magmatic rocks of the South Mongolian collage (Altai, eastern Jungar and Harlik) (Figure 13B), suggesting that a small number of zircons may have been sourced from the South Mongolian collage Andean arc. These study data are consistent with our previous age and isotopic results of the sandstone matrix (with MDAs of 243 to 234 Ma) of the northern KGSC in the HL area (Figures 12D, 13D) (Ao et al., 2021).

In summary, the provenances of the sandstone matrix in the northern HL area of the KGSC were deposited and emplaced in the forearc of the Dananhu arc, and their depositional settings varied from an intraoceanic island arc to a continental Andean arc after ca. 244 Ma.

6.2.2 Type II: Continental arc provenance of the southern area

Samples 16K08, 21Kg04 and 21Kg05 were collected from the southern part of the HL area. Their MDAs are 274, 241, and 275 Ma, respectively. They have similar multiple age peak patterns with volumes of Precambrian ages similar to those of the Yamansu-CTS arc (Figures 12E,J). The high percent of analyzed grains have negative $\varepsilon_{Hf}(t)$ values (ca. 68%, 33% and 66%, respectively) are similar to those of magmatic rocks in the Yamansu-CTS arc (Figure 13C) and the KGSC in the Yamansu area (Figure 13D), suggesting that they were mainly sourced from the Yamansu-CTS continental arc.

Based on these characteristics, we can conclude that the first type of provenance for the sedimentary matrix of the KGSC in the northern HL area was mainly sourced from the Dananhu intraoceanic arc to the Andean arc after ca. 244 Ma. These results are consistent with the interpretation that the Triassic sedimentary rocks (<258 Ma) in the Dananhu arc were partly sourced from the southern South Mongolian Andean arc (Altai, eastern Junggar and Harlik) (Chen et al., 2020). However, the other type of sandstone matrix of the KGSC in the southern HL area was mainly sourced from the Yamansu-central Tianshan arc, which was similar to the KGSC in the Yamansu area (Chen et al., 2019). In summary, our study suggests that the KGSC in the HL area had a mixed provenance between the Dananhu and Yamansu-CTS arcs.

6.3 Suture zone and closure time of the Kanguer subduction complex in the Haluo area

The nature and composition of the KGSC have been widely discussed and remains controversial (Ma et al., 1997; Li, 2004; Li et al., 2008; Muhetaer et al., 2010; Chen et al., 2019; Ao et al., 2021). To date, three competing models have been proposed by previous studies and have been interpreted an the accretionary complex of the Dananhu (Li, 2004; Xiao et al., 2004; Li et al., 2005; Li et al., 2008; Ao et al., 2021), the Yamansu arc (Ma et al., 1997; Chen et al., 2019) and a mixture of the Dananhu and Yamansu arcs (Muhetaer et al., 2010; Mao Q. et al., 2021; Mao et al., 2022b).

As discussed above, our geochemical, geocryological and isotopic studies reveal that the KGSC in the HL area represents mixing of the forearc subduction mélanges which consist of the N-MORB, E-MORB and SZZ type ophiolite fragments (including gabbro, basalt, and chert) and sedimentary matrix and limestones between the Dananhu and Yamansu-CTS arcs formed by double subduction. Our study reveals that the matrices (Samples YY07, 09, 11 and 12) in the northern HL area are mainly proven to be from the Dananhu arc. However, the matrices in the southern HL area, which are represented by Samples 16K08, 21Kg 04 and 05, were mainly proven to be from the Yamansu-CTS arc. All of these data indicate that the suture line of the KGSC in the HL area is located between Samples YY12 and 16K08 in the N–S-trending section. Combined with the previous data from Ao et al. (2021), which suggest that the sedimentary matrix rocks in the middle HL area were sourced from the Triassic Dananhu Andean arc (Figure 13D), we suggest that the final suture line was located in the middle part of the HL area, as shown in Figure 10E.

As discussed above, the petrological and geochemical characteristics of the sandstone matrix together reveal that they were deposited on a convergence margin; therefore, the MDA of the detrital zircons can represent the time of deposition of these sedimentary matrix rocks (Cawood et al., 2012). In this study, the youngest sandstone matrix has a MDA of 238 Ma, and Ao et al. (2021) reported that the sandstone matrix of the KGSC in the HL area has MDAs of 243–234 Ma, suggesting that the northern Tianshan Ocean closed later than ca. 234 Ma. In addition, the mid-Late Triassic peak metamorphic ages of the eclogites in the western Tianshan (Zhang et al., 2007; Sang et al., 2017; Sang et al., 2020) and the 243–234 Ma thickened lower crust-derived adakites in the Dananhu arc (Mao Q. et al., 2021) also suggest that subduction continued in the mid-Late Triassic. Thus, we conclude that the Paleo-Asian Ocean closed later than ca. 234 Ma.

6.4 Tectonic implications

Our new detrital zircon U–Pb ages and zircon $\varepsilon_{Hf}(t)$ values of the matrix sandstone reveal that the KGSC experienced double-directional subduction and that the suture line is located in the middle of the KGSC in the HL area. The northern samples of the Kanguer subduction in the HL area were deposited in an oceanic-island-arc setting before ca. 244 Ma and changed to an Andean-type arc setting after ca. 244 Ma. Furthermore, the southern samples were deposited in a continental-island-arc setting

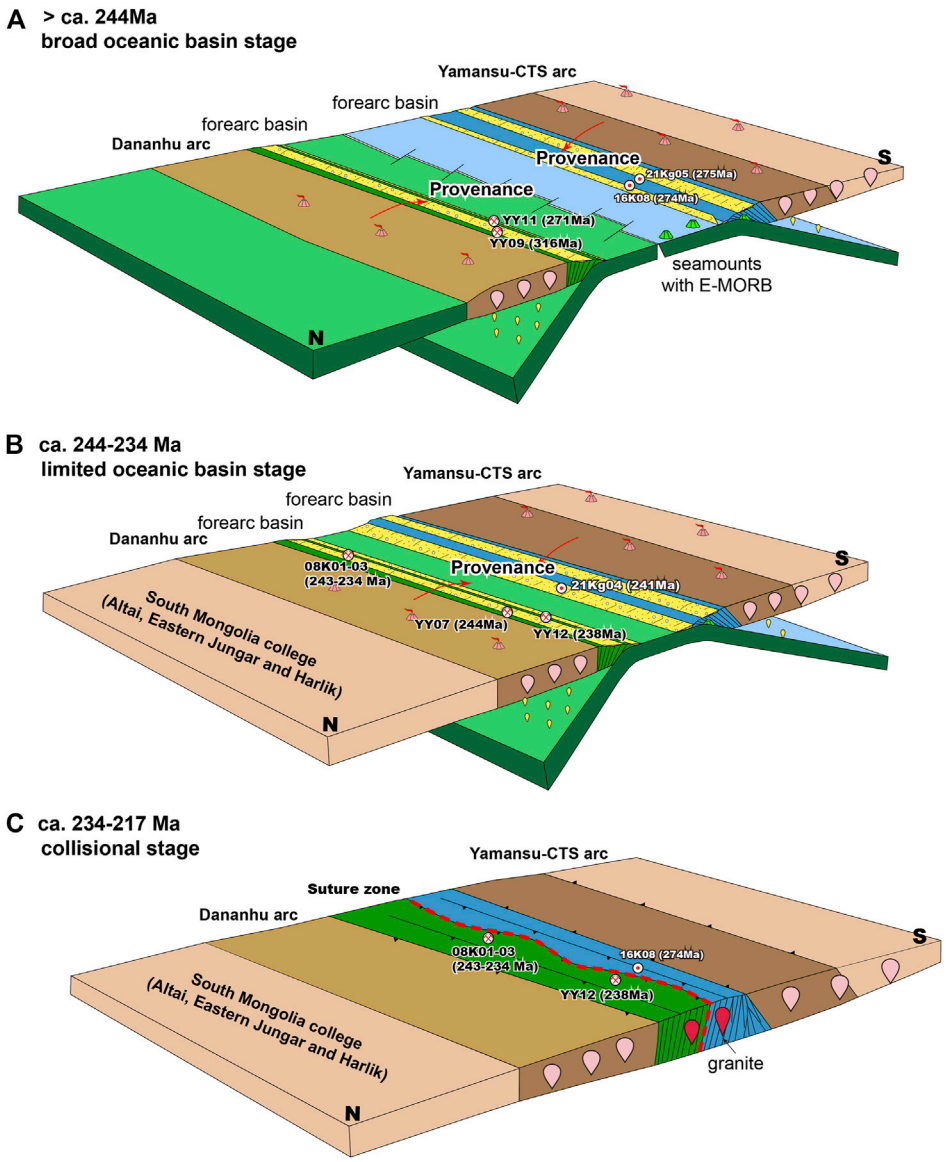

FIGURE 14
Tectonic model showing two stages of evolution in the eastern Tianshan. **(A)** Before the Middle Triassic (>ca. 244 Ma), the northern Tianshan Ocean, a branch of the Paleo-Asian Ocean, remained open preventing material exchanges on both sides and was doubly subducting. Blocks of N-MORB, SSZ-affinity oceanic crust, limestone, and chert were accreted to the forearc of the Dananhu arc and N-MORB, E-MORB-affinity oceanic crust, limestone, and chert accreted to the forearc of Yamansu-CTS arcs of the growing Kanguer accretionary complex. **(B)** In the Middle to Late Triassic (244–234 Ma), the northern Tianshan Ocean remained open and was subducted on both sides, and the sandstone matrices on both sides of the accretionary complexes have MDAs of 244 to 234 Ma. The convergence between the Dananhu Arc and South Mongolian collage (Altai, eastern Jungar and Harlik Arc) led to Precambrian zircon input in the sandstone matrix of the AC of the Dananhu Arc. **(C)** In the Late Triassic (234–217 Ma), the northern Tianshan Ocean closed by double subduction, and the Dananhu Andean arc was amalgamated with the Yamansu-CTS continental arc. Large syncollisional granodiorite plutons intruded the two arcs and their accretionary complexes.

(Figures 11A,B). Therefore, we updated our tectonic model of the eastern Tianshan in the southern Altaids (Figure 14).

The northern Tianshan ocean basin was a broad ocean prevented material exchanges between the Dananhu and Yamansu arcs before ca. 244 Ma (Figure 14A), the sandstone matrices in the northern HL area have simple detrital U–Pb ages and zircon Hf isotope patterns (Figures 6, 12B, 13A). This interpretation is consistent with the detrital zircon age and isotopic studies of the sedimentary rocks of the Dananhu and Yamansu-CTS arcs (Chen et al., 2020) and the sandstone matrix in the KGSC in the Yamansu area (Chen et al., 2019). From ca. 244 Ma to 234 Ma (Figure 14B), the northern Tianshan Ocean was

a limited oceanic basin and was still subducting on both sides. The Dananhu arc converged with the South Mongolian collage (Altai, eastern Jungar and Harlik arc systems) and formed an Andean continental arc. The Precambrian zircons of the South Mongolian collage were deposited into the sedimentary matrix of the accretionary complex of the Dananhu arc (Chen et al., 2019; Ao et al., 2021), such as Sample YY07. These tectonic processes also induced the Dananhu arc crust to thicken and to form volumes of 243–234 Ma thickened lower crust-derived adakites in the Dananhu arc (Mao Q. et al., 2021). Combined with large-scale syncollisional granites intruded in the eastern Tianshan in the Late Triassic (232–217 Ma) (Li et al., 2012; Wang et al., 2016; Wu et al., 2016; Mao et al., 2022a) and the rapid and strong regional uplift and denudation of the Tianshan orogen in the Late Triassic (Gong et al., 2021), we suggest that the closure time of the northern Tianshan Ocean was most likely during the Late Triassic (Ao et al., 2021; Mao et al., 2022a) (Figure 14C). The KGSC was thrust southward during the final amalgamated processes.

7 Conclusion

(1) The KGSC in the HL area was thrusted top-to-the-south and is characterized by a block-in-matrix structure among the different oceanic fragments and sedimentary rocks. The basaltic blocks of the northern HL area yielded a zircon U–Pb age of 257 Ma and have N-MORB geochemical signatures.
(2) The geochemistry and composition of the sandstone matrix of the northern Kanguer subduction complex in the HL area suggest that the Dananhu arc has varied from an OIA to a CIA setting since ca. 244 Ma. However, the sandstone matrix of the southern Kanguer subduction complex in the HL area was always deposited in a CIA setting during the late Paleozoic.
(3) The northern Tianshan Ocean experienced double subduction, and the suture line is located between Samples YY12 and 16K08 in the middle of the HL area. The MDAs of the KGSC matrix sandstones in the HL area have an age range of 316 Ma to 238 Ma, which indicates that the northern Tianshan Ocean was still open at 238 Ma, and the final collision occurred during 234–217 Ma.

Data availability statement

The original contributions presented in the study are included in the article/Supplementary Material, further inquiries can be directed to the corresponding authors.

Author contributions

QM and WX initiated the idea and designed the studies. QM, MS, and SA finished the field, petrology, and geochemical experiments. DS and RL performed the zircon dating and Hf isotopic analysis. HW and ZT processed the geochemical data. QM and MS write the original manuscript. WX works with the geological model and finalized the manuscript. All authors have been involved in the study.

Funding

This study was financially supported by the National Natural Science Foundation of China (41888101, 41822204), One Hundred Talent Program of the Chinese Academy of Sciences (E2250403), Science and Technology Major Project of Xinjiang Uygur Autonomous Region, China (2021A03001&4), the Chinese Ministry of Land and Resources for the Public Welfare Industry Research (201411026-1), the "Light of West China" Program of the CAS (2017-XBQNXZ-B-013, 2018-XBYJRC-003), and the Project of China-Pakistan Joint Research Center on Earth Sciences of the CAS (131551KYSB20200021). This is a contribution to IGCP 662 and IGCP 710.

Conflict of interest

Author QM was employed by the company Redrock Mining Co. Ltd.

The remaining authors declare that the research was conducted in the absence of any commercial or financial relationships that could be construed as a potential conflict of interest.

Publisher's note

Supplementary material

The Supplementary Material for this article can be found online at: https://www.frontiersin.org/articles/10.3389/feart.2022.1089700/full#supplementary-material

SUPPLEMENTARY TABLE S1
U–Pb ages of detrital zircons of sedimentary rocks from the KGSC in the Haluo area. HigHLy discordant analyses (concord% <90% or >110%) are considered unusable, displayed in strikethrough text, and were not included in the concordia diagrams. Concord% = 100*(^{207}Pb/^{206}Pb) age/(^{206}Pb/^{238}U) age for age >1,500 Ma, or 100*(^{207}Pb/^{235}U) age/(^{206}Pb/^{238}U) age for age <1,500 Ma.

SUPPLEMENTARY TABLE S2
Lu–Hf isotope data of zircons from the sedimentary matrix rocks in the KGSC in the Haluo area.

SUPPLEMENTARY TABLE S3
Whole-rock major and trace element data of basalts and sandstone matrix from the KGSC in the Haluo area.

SUPPLEMENTARY TABLE S4
Zircon U–Pb ages of the sedimentary rocks around the KGSC in the eastern Tianshan.

SUPPLEMENTARY TABLE S5
Zircon Hf isotope data of the magmatic rocks of the Dananhu arc, Yanmansu-CTS arc and South Mongolian collage (Altai, eastern Junggar and Harlik arcs).

References

Ao, S. J., Mao, Q. G., Windley, B. F., Song, D. F., Zhang, Z. Y., Zhang, J. E., et al. (2021). The youngest matrix of 234Ma of the kanguer accretionary mélange containing blocks of N-MORB basalts: Constraints on the northward subduction of the paleo-asian kanguer Ocean in the eastern tianshan of the southern Altaids. *Int. J. Earth Sci.* 110, 791–808. doi:10.1007/s00531-021-01990-5

Ao, S. J., Xiao, W. J., Windley, B. F., Mao, Q. G., Zhang, J. E., and Zhang, Z. Y. (2020). Ordovician to Early Permian accretionary tectonics of Eastern Tianshan: Insights from Kawabulak ophiolitic melange, granitoid, and granitic gneiss. *Geol. J.* 55 (1), 280–298. doi:10.1002/gj.3371

Bazhenov, M. L., Collins, A. Q., Degtyarev, K. E., Levashova, N. M., Mikolaichuk, A. V., Pavlov, V. E., et al. (2003). Paleozoic northward drift of the north tien Shan (central Asia) as revealed by ordovician and carboniferous paleomagnetism. *Tectonophysics* 366 (1), 113–141. doi:10.1016/s0040-1951(03)00075-1

Bhatia, M., and Crook, K. W. (1986). Trace element characteristics of graywackes and tectonic setting discrimination of sedimentary basins. *Contr. Mineral. Pet.* 92, 181–193. doi:10.1007/bf00375292

Boynton, W. V. (1984). "Geochemistry of the rare Earth elements: Meteorite study," in *Rare Earth element geochemistry*. Editor P. Henderson (Amsterdam: Elsevier), 63–114.

Buchan, C., Pfänder, J., Kröner, A., Brewer, T. S., Tomurtogoo, O., Tomurhuu, D., et al. (2002). Timing of accretion and collisional deformation in the central asian orogenic belt: Implications of granite geochronology in the bayankhongor ophiolite zone. *Chem. Geol.* 192, 23–45. doi:10.1016/s0009-2541(02)00138-9

Cawood, P. A., Hawkesworth, C. J., and Dhuime, B. (2012). Detrital zircon record and tectonic setting. *Geology* 40 (10), 875–878. doi:10.1130/g32945.1

Chen, Z., Xiao, W., Windley, B. F., Schulmann, K., Mao, Q., Zhang, Z., et al. (2019). Composition, provenance, and tectonic setting of the southern kangurtag accretionary complex in the eastern tianshan, NW China: Implications for the late paleozoic evolution of the north Tianshan ocean. *Tectonics* 38 (8), 2779–2802. doi:10.1029/2018tc005385

Chen, Z., Xiao, W., Windley, B. F., Schulmann, K., Mao, Q., Zhang, Z., et al. (2020). Latest permian–early triassic arc amalgamation of the eastern tianshan (NW China): Constraints from detrital zircons and Hf isotopes of devonian–triassic sediments. *Geol. J.* 55, 1708–1727. doi:10.1002/gj.3540

Coleman, R. G. (1989). Continental growth of northwest China. *Tectonics* 8, 621–635. doi:10.1029/tc008i003p00621

Coutts, D. S., Matthews, W. A., and Hubbard, S. M. (2019). Assessment of widely used methods to derive depositional ages from detrital zircon populations. *Geosci. Front.* 10 (4), 1421–1435. doi:10.1016/j.gsf.2018.11.002

Dobretsov, N. L., Berzin, N. A., and Buslov, M. M. (1995). Opening and tectonic evolution of the paleo-Asian ocean. *Int. Geol. Rev.* 35, 335–360. doi:10.1080/00206819509465407

Du, L., Long, X., Yuan, C., Zhang, Y., Huang, Z., Sun, M., et al. (2018a). Petrogenesis of Late Paleozoic diorites and A-type granites in the central Eastern Tianshan, NW China: Response to post-collisional extension triggered by slab breakoff. *Lithos* 318-319, 47–59. doi:10.1016/j.lithos.2018.08.006

Du, L., Long, X., Yuan, C., Zhang, Y., Huang, Z., Wang, X., et al. (2018b). Mantle contribution and tectonic transition in the aqishan-yamansu belt, eastern tianshan, NW China: Insights from geochronology and geochemistry of early carboniferous to early permian felsic intrusions. *Lithos* 304-307, 230–244. doi:10.1016/j.lithos.2018.02.010

Du, L., Zhang, Y., Huang, Z., Li, X.-P., Yuan, C., Wu, B., et al. (2019). Devonian to carboniferous tectonic evolution of the Kangguer Ocean in the Eastern Tianshan, NW China: Insights from three episodes of granitoids. *Lithos* 350-351, 105243. doi:10.1016/j.lithos.2019.105243

Du, L., Zhu, H., Yuan, C., Zhang, Y., Huang, Z., Li, X.-P., et al. (2021). Paleozoic crustal evolution and tectonic switching in the northeastern tianshan: Insights from zircon Hf isotopes of granitoids. *J. Geol. Soc. Lond.* 178 (2), jgs2020–035. doi:10.1144/jgs2020-035

Du, L., Zhu, H., Yuan, C., Zhang, Y., Long, X., Li, X. P., et al. (2020). Paleozoic crustal evolution and tectonic switching in the northeastern tianshan: Insights from zircon Hf isotopes of granitoids. *J. Geol. Soc. Lond.* 178, jgs2020–035. doi:10.1144/jgs2020-035

Festa, A., Pini, G. A., Ogata, K., and Dilek, Y. (2019). Diagnostic features and field-criteria in recognition of tectonic, sedimentary and diapiric mélanges in orogenic belts and exhumed subduction-accretion complexes. *Gondwana Res.* 74, 7–30. doi:10.1016/j.gr.2019.01.003

Floyd, P. A., and Leveridge, B. E. (1987)., 144. London, 531–542. doi:10.1144/gsjgs.144.4.0531Tectonic environment of the devonian gramscatho basin, south cornwall: Framework mode and geochemical evidence from turbiditic sandstones*J. Geol. Soc. Lond.*

Floyd, P. A., Shail, R., Leveridge, B., and Franke, W. (1991). Geochemistry and provenance of Rhenohercynian synorogenic sandstones: Implications for tectonic environment discrimination. *Geol. Soc. Lond. Spec. Publ.* 57, 173–188. doi:10.1144/gsl.sp.1991.057.01.14

Gao, J., and Klemd, R. (2003). Formation of HP-lt rocks and their tectonic implications in the Western tianshan orogen, NW China: Geochemical and age constraints. *Lithos* 66 (1-2), 1–22. doi:10.1016/s0024-4937(02)00153-6

Gong, L., Kohn, B. P., Zhang, Z., Xiao, B., Wu, L., and Chen, H. (2021). Exhumation and preservation of Paleozoic porphyry Cu deposits: Insights from the Yandong deposit, southern Central Asian orogenic belt. *Econ. Geol.* 116 (3), 607–628. doi:10.5382/econgeo.4812

Han, J., Chen, H., Jiang, H., Zhao, L., Zhang, W., and Lai, C. K. (2019). Genesis of the paleozoic aqishan-yamansu arc-basin system and Fe (-Cu) mineralization in the eastern tianshan, NW China. *Ore Geol. Rev.* 105, 55–70. doi:10.1016/j.oregeorev.2018.12.012

Han, Y., and Zhao, G. (2018). Final amalgamation of the tianshan and junggar orogenic collage in the southwestern central asian orogenic belt: Constraints on the closure of the paleo-Asian ocean. *Earth-Science Rev.* 186, 129–152. doi:10.1016/j.earscirev.2017.09.012

Hou, T., Zhang, Z., Santosh, M., Encarnacion, J., Zhu, J., and Luo, W. (2014). Geochronology and geochemistry of submarine volcanic rocks in the Yamansu iron deposit, Eastern Tianshan Mountains, NW China: Constraints on the metallogenesis. *Ore Geol. Rev.* 56, 487–502. doi:10.1016/j.oregeorev.2013.03.008

Hawkins, J. W. (2003). Geology of supra-subduction zones-Implications for the origin of ophiolites. *Geol. Soc. Am. Spec. Pap.* 373, 227–268. doi:10.1130/0-8137-2373-6.227

Hsü, K. (1968). Principles of mélanges and their bearing on the Franciscan-Knoxville Paradox. *Geol. Soc. Am. Bull.* 78, 1063–1174. doi:10.1130/0016-7606(1968)79[1063:pomatb]2.0.co;2

Hu, A., Jahn, B. M., Zhang, G., Chen, Y., and Zhang, Q. (2000). Crustal evolution and phanerozoic crustal growth in northern Xinjiang: Nd isotopic evidence, Part I. Isotopic characterization of basement rocks. *Tectonophysics* 328, 15–51. doi:10.1016/s0040-1951(00)00176-1

Isozaki, Y., Maruyama, S., and Furuoka, F. (1990). Accreted oceanic materials in Japan. *Tectonophysics* 181 (1-4), 179–205. doi:10.1016/0040-1951(90)90016-2

Kusky, T. M., Windley, B. F., Safonova, I., Wakita, K., Wakabayashi, J., Polat, A., et al. (2013). Recognition of ocean plate stratigraphy in accretionary orogens through Earth history: A record of 3.8 billion years of sea floor spreading, subduction, and accretion. *Gondwana Res.* 24 (2), 501–547. doi:10.1016/j.gr.2013.01.004

Kusky, T., Wang, J., Wang, L., Huang, B., Ning, W., Fu, D., et al. (2020). Mélanges through time: Life cycle of the world's largest Archean mélange compared with Mesozoic and Paleozoic subduction-accretion-collision mélanges. *Earth-Science Rev.* 209, 103303. doi:10.1016/j.earscirev.2020.103303

Li, D.-F., Zhang, L., Chen, H.-Y., Hollings, P., Cao, M.-J., Fang, J., et al. (2016). Geochronology and geochemistry of the high Mg dioritic dikes in Eastern Tianshan, NW China: Geochemical features, petrogenesis and tectonic implications. *J. Asian Earth Sci.* 115, 442–454. doi:10.1016/j.jseaes.2015.10.018

Li, J. Y., He, G. Q., Xu, X., Li, H. Q., Sun, G. H., Yang, T. N., et al. (2006). Crustal tectonic framework of northern Xinjiang and adjacent and its formation. *Acta Geol. Sin.* 80, 149–168. (in Chinese with English abstract).

Li, J. Y. (2004). Late neoproterozoic and paleozoic tectonic framework and evolution of eastern Xinjiang, NW China. *Geol. Rev.* 50, 304–322.

Li, Q. G., Liu, S. W., Song, B., Wang, Y. B., and Chen, Y. (2009). Late mesoproterozoic to paleozoic tectonothermal events in the eastern segment of the central tianshan tectonic zone of northwestern China: Constraints from SHRIMP zircon geochronology. *Earth Sci. Front.* 16, 175–184. doi:10.1016/S1874-8651(10)60080-4

Li, S., Wang, T., Wilde, S. A., Tong, Y., Hong, D., and Guo, Q. (2012). Geochronology, petrogenesis and tectonic implications of Triassic granitoids from Beishan, NW China. *Lithos* 134-135, 123–145. doi:10.1016/j.lithos.2011.12.005

Li, W. Q., Ma, H., Wang, R., and Xia, B. (2008). SHRIMP dating and Nd-Sr isotopic Tracing of Kangguertage ophiolite in eastern Tianshan, Xinjiang. *Acta Petrol. Sin.* 24 (4), 773–780. (in Chinese with English abstract).

Li, W. Q., Xia, B., Wu, G. G., Wang, H., and Wang, R. (2005). Kangguertage ophiolite and tectonic significance, Shanshan, Xinjiang China. *Acta Petrol. Sin.* 21, 1617–1632. (in Chinese with English abstract).

Liu, S., Guo, Z., Zhang, Z., Qiugen, L. I., and Zheng, H. (2004). Nature of the Precambrian metamorphic blocks in the eastern segment of Central Tianshan: Constraint from geochronology and Nd isotopic geochemistry. *Sci. China Ser. D-Earth. Sci.* 47 (12), 1085–1094. doi:10.1360/03yd0177

Long, X., Wu, B., Sun, M., Yuan, C., Xiao, W., and Zuo, R. (2020). Geochronology and geochemistry of Late Carboniferous dykes in the Aqishan–Yamansu belt, eastern Tianshan: Evidence for a post-collisional slab breakoff. *Geosci. Front.* 11 (1), 347–362. doi:10.1016/j.gsf.2019.06.003

Lu, W. J., Chen, H. Y., Zhang, L., Han, J. S., Xiao, B., Li, D. F., et al. (2017). Age and geochemistry of the intrusive rocks from the Shaquanzi-Hongyuan Pb–Zn mineral district: Implications for the Late Carboniferous tectonic setting and Pb–Zn mineralization in the Eastern Tianshan, NW China. *Lithos* 294-295, 97–111. doi:10.1016/j.lithos.2017.10.009

Luo, T., Liao, Q.-A., Zhang, X.-H., Chen, J.-P., Wang, G.-C., and Huang, X. (2016). Geochronology and geochemistry of carboniferous metabasalts in eastern tianshan, central Asia: Evidence of a back-arc basin. *Int. Geol. Rev.* 58 (6), 756–772. doi:10.1080/00206814.2015.1114433

Ma, R. S., Shu, L. S., and Sun, J. (1997). *Tectonic evolution and metalogeny of eastern tianshan mountains*. Beijing: Geological Publishing House.

Ma, X., Shu, L., Meert, J. G., and Li, J. (2014). The paleozoic evolution of central tianshan: Geochemical and geochronological evidence. *Gondwana Res.* 25 (2), 797–819. doi:10.1016/j.gr.2013.05.015

Mader, D., and Neubauer, F. (2004). Provenance of palaeozoic sandstones from the carnic alps (Austria): Petrographic and geochemical indicators. *Int. J. Earth Sci.* 93 (2), 262–281. doi:10.1007/s00531-004-0391-x

Mao, Q., Ao, S., Windley, B. F., Wang, J., Li, Y., and Xiao, W. (2021a). Middle Triassic lower crust-derived adakitic magmatism: Thickening of the Dananhu intra-oceanic arc and its implications for arc–arc amalgamation in the Eastern Tianshan (NW China). *Geol. J.* 56 (6), 3137–3154. doi:10.1002/gj.4095

Mao, Q., Ao, S., Windley, B. F., Zhang, Z., Sang, M., Tan, Z., et al. (2022a). Middle-late triassic southward-younging granitoids: Tectonic transition from subduction to collision in the eastern tianshan-beishan orogen, NW China. *GSA Bull.* 134, 2206–2224. doi:10.1130/b36172.1

Mao, Q. G., Wang, J. B., Xiao, W. J., Fang, T. H., Wang, N., and Yu, M. J. (2014a). The deiscovery of low-Carboniferous arc volcanic rocks and its tectonic signifance at the Kalatage area in the central Tianshan, eastern Tianshan Mountans, Xinjiang, NW China. *Acta Geol. Sin.* 88, 1790–1799. (in Chinese with English abstract).

Mao, Q. G., Wang, J. B., Xiao, W. J., Windley, B. F., Schulmann, K., Ao, S. J., et al. (2021b). From ordovician nascent to early permian mature arc in the southern Altaids: Insights from the kalatage inlier in the eastern tianshan, NW China. *Geosphere* 17, 647–683. doi:10.1130/ges02232.1

Mao, Q. G., Wang, J. B., Xiao, W. J., Windley, B. F., Schulmann, K., Yu, M. J., et al. (2019). Mineralization of an intra-oceanic arc in an accretionary orogen: Insights from the Early Silurian Honghai volcanogenic massive sulfide Cu-Zn deposit and associated adakites of the Eastern Tianshan (NW China). *GSA Bull.* 131, 803–830. doi:10.1130/b31986.1

Mao, Q. G., Xiao, W. J., Fang, T. H., Windley, B. F., Sun, M., Ao, S. J., et al. (2014b). Geochronology, geochemistry and petrogenesis of early permian alkaline magmatism in the eastern tianshan: Implications for tectonics of the southern Altaids. *Lithos* 190-191, 37–51. doi:10.1016/j.lithos.2013.11.011

Mao, Q., Xiao, W., Huang, P., Ao, S., Song, D. F., Zhang, J. E., et al. (2022b). Deformational history of the kanguer subduction complex in the eastern tianshan (NW China): Implications for paleozoic-triassic multiple accretionary tectonics of the southern Altaids. *Tectonics* 41, e2022TC007527. In press. doi:10.1029/2022tc007527

Maynard, J., Valloni, R., and Yu, H.-S. (1982). Composition of modern deep-sea sands from arc-related basins. *Geol. Soc. Lond. Spec. Publ.* 10, 551–561. doi:10.1144/gsl.sp.1982.010.01.36

McLennan, S. M., Hemming, S., McDaniel, D. K., Hanson, G. N., Johnsson, M. J., and Basu, A. (1993). "Geochemical approaches to sedimentation, provenance, and tectonics," in *Processes controlling the composition of clastic sediments* (United States: Geological Society of America), 0.

Muhetaer, Z., Wu, Z., and Parati, A. (2010). Relationship between tectonic evolution and polymetallic mineralization of the east tianshan plate suture zone. *Earth Sci.* 30 (2), 245–253. (in Chinese with English abstract).

Myashiro, A. (1974). Volcanic series in island arc and active continental margins. *Am. J. Sci.* 274, 321–355. doi:10.2475/ajs.274.4.321

Pearce, J. A. (2008). Geochemical fingerprinting of oceanic basalts with applications to ophiolite classification and the search for Archean oceanic crust. *Lithos* 100, 14–48. doi:10.1016/j.lithos.2007.06.016

Pettijohn, F. J., Potter, P. E., and Siever, R. (1972). *Sand and sandstone*. New York: Springer-Verlag.

Potter, P. E. (1978). Petrology and chemistry of modern big river sands. *J. Geol.* 86, 423–449. doi:10.1086/649711

Qin, K. Z., Su, B. X., Sakyi, P. A., Tang, D. M., Li, X. H., Sun, H., et al. (2011). SIMS zircon U-Pb geochronology and Sr-Nd isotopes of Ni-Cu-Bearing Mafic-Ultramafic Intrusions in Eastern Tianshan and Beishan in correlation with flood basalts in Tarim Basin (NW China): Constraints on a ca. 280 Ma mantle plume. *Am. J. Sci.* 311, 237–260. doi:10.2475/03.2011.03

Raymond, L. A. (2019). Perspectives on the roles of melanges in subduction accretionary complexes: A review. *Gondwana Res.* 74, 68–89. doi:10.1016/j.gr.2019.03.005

Sang, M., Xiao, W., Bakirov, A., Orozbaev, R., Sakiev, K., and Zhou, K. (2017). Oblique wedge extrusion of UHP/HP complexes in the late triassic: Structural analysis and zircon ages of the atbashi complex, south tianshan, Kyrgyzstan. *Int. Geol. Rev.* 59, 1369–1389. doi:10.1080/00206814.2016.1241163

Sang, M., Xiao, W., and Windley, B. F. (2020). Unravelling a Devonian–Triassic seamount chain in the South Tianshan high-pressure/ultrahigh-pressure accretionary complex in the Atbashi area (Kyrgyzstan). *Geol. J.* 55 (3), 2300–2317. doi:10.1002/gj.3776

Şengör, A. M. C., Natal'in, B. A., and Burtman, U. S. (1993). Evolution of the Altaid tectonic collage and Paleozoic crustal growth in Eurasia. *Nature* 364, 209–304. doi:10.1038/364299a0

Şengör, A. M. C., and Natal'in, B. (1996). Turkic-type orogeny and its role in the making of the continental crust. *Annu. Rev. Earth Planet. Sci.* 24, 263–337. doi:10.1146/annurev.earth.24.1.263

Sun, S. S., and McDonough, W. F. (1989). "Chemical and isotopic systematic of oceanic basalts: Implicattions for mantle composition and process," in *Magmatism in the ocean basins*. Editors A. D. Sauders and M. J. Norry (London: Geological Society Special Publication), 3l3–345.

Vermeesch, P. (2012). On the visualisation of detrital age distributions. *Chem. Geol.* 312-313, 190–194. doi:10.1016/j.chemgeo.2012.04.021

Wakabayashi, J. (2015). Anatomy of a subduction complex: Architecture of the franciscan complex, California, at multiple length and time scales. *Int. Geol. Rev.* 57 (5-8), 669–746. doi:10.1080/00206814.2014.998728

Wakabayashi, J. (2019). Sedimentary compared to tectonically-deformed serpentinites and tectonic serpentinite mélanges at outcrop to petrographic scales: Unambiguous and disputed examples from California. *Gondwana Res.* 74, 51–67. doi:10.1016/j.gr.2019.04.005

Wakita, K. (2015). OPS mélange: A new term for mélanges of convergent margins of the world. *Int. Geol. Rev.* 57 (5-8), 529–539. doi:10.1080/00206814.2014.949312

Wang, G. C., Zhang, M., Feng, J. L., Liao, Q. A., Zhang, X. H., Kang, L., et al. (2019). New understanding of the tectonic framework and evolution during the Neoproterozoic-Paleozoic era in the East Tianshan mountains. *Joural Geomechanics* 25 (5), 798–819. doi:10.12090/j.issn.1006-6616.2019.25.05.066

Wang, J. B., Wang, Y. W., and He, Z. J. (2006). Ore deposits as a guide to the tectonic evolution in the East Tianshan Mountains, NW China. *Geol. China* 33, 461–469. (in Chinese with English abstract).

Wang, Y., Chen, H., Han, J., Chen, S., Huang, B., Li, C., et al. (2018). Paleozoic tectonic evolution of the Dananhu-Tousuquan island arc belt, Eastern Tianshan: Constraints from the magmatism of the Yuhai porphyry Cu deposit, Xinjiang, NW China. *J. Asian Earth Sci.* 153, 282–306. doi:10.1016/j.jseaes.2017.05.022

Wang, Y. H., Xue, C. J., Liu, J. J., and Zhang, F. F. (2016). Geological, geochronological, geochemical, and Sr-Nd-O-Hf isotopic constraints on origins

of intrusions associated with the Baishan porphyry Mo deposit in eastern Tianshan, NW China. *Min. Depos.* 51, 953–969. doi:10.1007/s00126-016-0646-z

Wilhem, C., Windley, B. F., and Stampfli, G. M. (2012). The Altaids of central Asia: A tectonic and evolutionary innovative review. *Earth-Science Rev.* 113 (3-4), 303–341. doi:10.1016/j.earscirev.2012.04.001

Wilson, M. (2001). *Igneous petrogenesis: A global tectonic approach*. Amsterdam: Kuwer Academic, 245–285.

Windley, B. F., Alexeiev, D., Xiao, W., Kröner, A., and Badarch, G. (2007)., 164. London, 31–47. doi:10.1144/0016-76492006-022Tectonic models for accretion of the central asian orogenic belt*J. Geol. Soc. Lond.*

Wood, D. A. (1980). The application of a Th-Hf-Ta diagram to problems of tectonomagmatic classification and to establishing the nature of crustal contamination of basaltic lavas of the British Tertiary volcanic province. *Earth & Planet. Sci. Lett.* 50, 11–30. doi:10.1016/0012-821x(80)90116-8

Wu, Y. S., Zhou, K. F., Li, N., and Chen, Y. J. (2016). Zircon U–Pb dating and Sr–Nd–Pb–Hf isotopes of the ore-associated porphyry at the giant Donggebi Mo deposit, Eastern Tianshan, NW China. *Ore Geol. Rev.* 2 (2), 794–807. doi:10.1016/j.oregeorev.2016.02.007

Xia, L. Q., Xu, X. Y., Xia, Z. C., Li, X. M., Ma, Z. P., and Wang, L. S. (2004). Petrogenesis of Carboniferous rift-related volcanic rocks in the Tianshan, northwestern China. *Geol. Soc. Am. Bull.* 116, 419–433. doi:10.1130/b25243.1

Xiao, W. J., Mao, Q. G., Windley, B. F., Qu, J. F., Zhang, J. E., Ao, S. J., et al. (2010). Paleozoic multiple accretionary and collisional processes of the Beishan orogenic collage. *Am. J. Sci.* 310, 1553–1594. doi:10.2475/10.2010.12

Xiao, W. J., Windley, B. F., Han, C. M., Liu, W., Wan, B., Zhang, J. E., et al. (2018). Late Paleozoic to early Triassic multiple roll-back and oroclinal bending of the Mongolia collage in Central Asia. *Earth-Science Rev.* 186, 94–128. doi:10.1016/j.earscirev.2017.09.020

Xiao, W. J., Windley, B. F., Sun, S., Li, J. L., Huang, B. C., Han, C. M., et al. (2015). A tale of amalgamation of three permo-triassic collage systems in central Asia: Oroclines, sutures, and terminal accretion. *Annu. Rev. Earth Planet. Sci.* 43 (1), 477–507. doi:10.1146/annurev-earth-060614-105254

Xiao, W. J., Zhang, L. C., Qin, K. Z., Sun, S., and Li, J. L. (2004). Paleozoic accretionary and collisional tectonics of the Eastern Tianshan (China): Implications for the continental growth of central Asia. *Am. J. Sci.* 304, 370–395. doi:10.2475/ajs.304.4.370

Yan, Z., Fu, C., Wang, Z., Yan, Q., Chen, L., and Chen, J. (2016). Late Paleozoic subduction–accretion along the southern margin of the North Qinling terrane, central China: Evidence from zircon U-Pb dating and geochemistry of the Wuguan Complex. *Gondwana Res.* 30, 97–111. doi:10.1016/j.gr.2015.05.005

Zhang, J., Xiao, W., Han, C., Ao, S., Chao, Y., Min, S., et al. (2012). Kinematics and age constraints of deformation in a Late Carboniferous accretionary complex in Western Junggar, NW China. *Gondwana Res.* 19, 958–974. doi:10.1016/j.gr.2010.10.003

Zhang, L., Ai, Y., Li, X., Rubatto, D., Song, B., Williams, S., et al. (2007). Triassic collision of Western Tianshan orogenic belt, China: Evidence from SHRIMP U–Pb dating of zircon from HP/UHP eclogitic rocks. *Lithos* 96 (1-2), 266–280. doi:10.1016/j.lithos.2006.09.012

Zhang, Y., Sun, M., Yuan, C., Long, X., Jiang, Y., Li, P., et al. (2018). Alternating trench advance and retreat: Insights from paleozoic magmatism in the eastern tianshan, central asian orogenic belt. *Tectonics* 37, 2142–2164. doi:10.1029/2018tc005051

Zhao, L., Chen, H., Hollings, P., and Han, J. (2019). Late paleozoic magmatism and metallogenesis in the aqishan-yamansu belt, eastern tianshan: Constraints from the bailingshan intrusive complex. *Gondwana Res.* 65, 68–85. doi:10.1016/j.gr.2018.08.004

Zhou, M. F., Lesher, C. M., Yang, Z. X., Li, J. W., and Sun, M. (2004). Geochemistry and petrogenesis of 270 Ma Ni-Cu-(PGE) sulfide-bearing mafic intrusions in the huangshan district, eastern Xinjiang, northwest China: Implications for the tectonic evolution of the central asian orogenic belt. *Chem. Geol.* 209, 233–257. doi:10.1016/j.chemgeo.2004.05.005

frontiers | Frontiers in Earth Science

TYPE Original Research
PUBLISHED 16 January 2023
DOI 10.3389/feart.2022.1090952

OPEN ACCESS

EDITED BY
Jiyuan Yin,
Chinese Academy of Geological Sciences (CAGS), China

REVIEWED BY
Xijun Liu,
Guilin University of Technology, China
Zhonghua Tian,
Chinese Academy of Geological Science, China

*CORRESPONDENCE
Miao Sang,
sangmiao@ms.xjb.ac.cn
Wenjiao Xiao,
wj-xiao@mail.iggcas.ac.cn

SPECIALTY SECTION
This article was submitted to Petrology, a section of the journal *Frontiers in Earth Science*

RECEIVED 06 November 2022
ACCEPTED 15 November 2022
PUBLISHED 16 January 2023

CITATION
Yogibekov D, Sang M, Xiao W, Mamadjonov Y, Zhou C, Yang H, Mao Q, Aminov J, Khalimov G and Ashuraliev S (2023), Post-collisional magmatism associated with the final closure of the Rushan-Pshart Meso-Tethys Ocean in Pamir, Tajikistan: Inference from Cretaceous igneous rocks of the Pshart accretionary complex.
Front. Earth Sci. 10:1090952.
doi: 10.3389/feart.2022.1090952

Post-collisional magmatism associated with the final closure of the Rushan-Pshart Meso-Tethys Ocean in Pamir, Tajikistan: Inference from Cretaceous igneous rocks of the Pshart accretionary complex

Dzhovid Yogibekov[1,2,3], Miao Sang[1]*, Wenjiao Xiao[1,2]*, Yunus Mamadjonov[3,4], Chuanming Zhou[5], He Yang[1], Qigui Mao[1], Jovid Aminov[6], Gufron Khalimov[1,3] and Sohibnazar Ashuraliev[1,3]

[1]Xinjiang Key Laboratory of Mineral Resources and Digital Geology, Xinjiang Institute of Geology and Geography, Chinese Academy of Science, Urumqi, China, [2]Collage of Earth and Planetary Sciences, University of Chinese Academy of Sciences, Beijing, China, [3]Institute of Geology, Earthquake Engineering and Seismology, Academy of Sciences of the Republic of Tajikistan, Dushanbe, Tajikistan, [4]Research Center for Ecology and Environment of Central Asia, Chinese Academy of Sciences, Dushanbe, Tajikistan, [5]Research Institute of Petroleum Exploration and Development, China National Petroleum Corporation, Beijing, China, [6]University of Central Asia, Khorog, Tajikistan

The Pamir orogen was formed by the subducted accretion and amalgamation of Cimmerian terranes from the northern margin of Gondwana with the southern margin of Eurasia. The Mesozoic magmatic rocks are widespread in Pamir and record the tectonic evolution in different stages. The Rushan–Pshart suture zone represents an ancient ocean between Central and Southern Pamir. This paper reports the petrography, geochronology, and geochemistry of Cretaceous granites and diabase dikes that intrude into the Pshart complex. The granites were emplaced between 124 and 118 Ma, based on their zircon U-Pb ages. These granites are characterized by high-K calc-alkaline, low magnesian, and high SiO_2, A/CNK, and K_2O+Na_2O values. They also display strong depletion of Ba, Sr, Eu, and Ti and comparatively weak negative Nb anomalies in spidergrams. Thus, we proposed in this study that these are highly fractionated, strongly peraluminous S-type granites. They were generated by the partial melting of the metasedimentary rocks in the plagioclase stability field and underwent subsequent fractional crystallization during their ascent. The diabase dikes contain low SiO_2, and high MgO levels and negative Nb and Ta anomalies, which were interpreted to form in an extensional environment. Late Jurassic–Early Cretaceous closure of the Rushan–Pshart Ocean and subsequent foundering of its oceanic lithosphere caused local extension and upwelling of the asthenospheric mantle. The underplating of mafic magma provided a heat source to melt the metasedimentary-derived granitic that formed in the initial post-collisional

environment. The subsequent local extension caused the emplacement of diabase dikes. Based on our new data and combined with data from previous studies, we concluded that the Rushan–Pshart suture zone is the remnant of the Meso-Tethys Ocean and may represent the western continuation of the Bangong–Nujiang suture of the Tibetan Plateau.

KEYWORDS

Meso-Tethys, Pshart AC, igneous rocks, geochronology, geochemistry

1 Introduction

The Pamir orogenic belt, located west to the Himalayan–Tibet orogen, was formed by the closure of the Paleo and Meso-Tethyan Oceans and the amalgamation of microcontinents derived from Gondwana supercontinent (Central Pamir, South Pamir, Karakoram terrane, and the Cimmerian blocks) to the southern margin of Eurasia during the early Mesozoic (Burtman and Molnar, 1993; Zanchi et al., 2000, 2009; Burtman, 2010; Zanchi and Gaetani, 2011). The Rushan–Pshart suture zone (RPSZ) lies in the Pamir orogen; it represents the tectonic boundary separating the Central and Southern Pamir terranes (Figure 1) and preserves the remnants of consumed Rushan–Pshart Ocean (Shvol'man, 1978; Pashkov and Shvol'man, 1979; Burtman and Molnar, 1993; Leven, 1995; Burtman, 2010; Yogibekov et al., 2020).

Two controversial hypotheses/models have been proposed regarding the evolution and closure timing of the Rushan–Pshart Ocean. One group of studies reported a Late Triassic–Early Jurassic closure time for the Rushan–Pshart Ocean (Angiolini

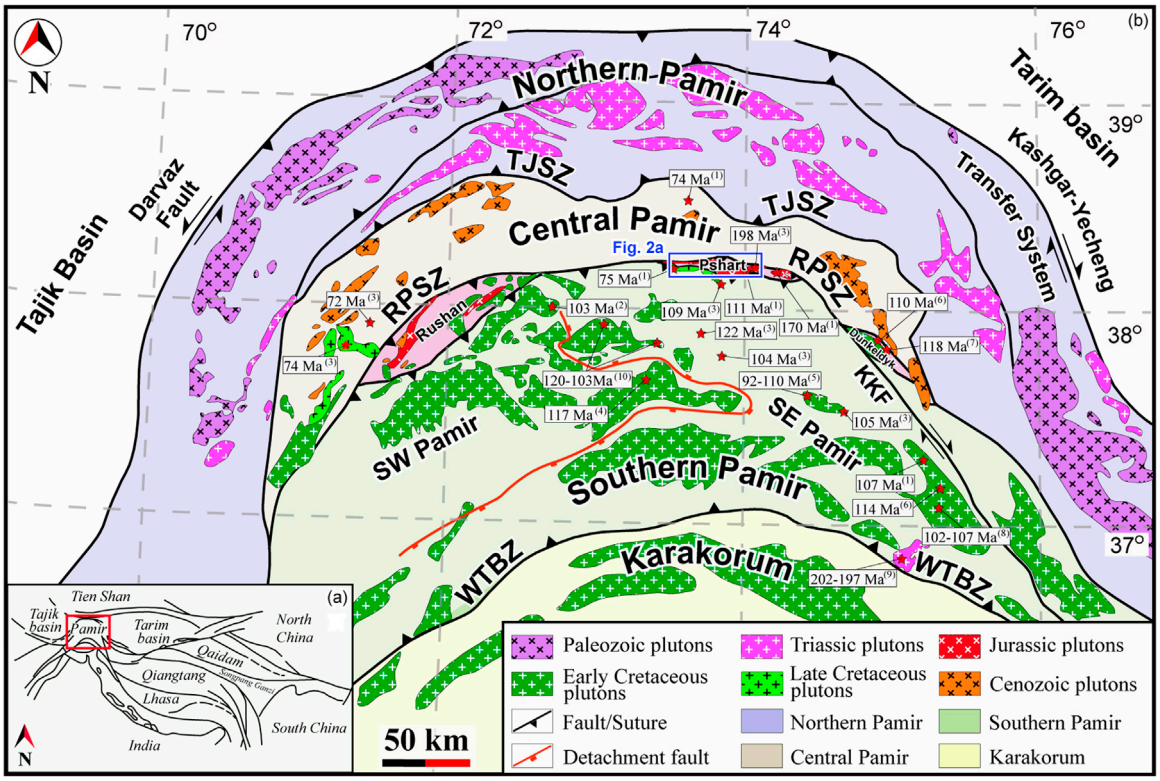

FIGURE 1
(A) Tectonic scheme of Central Asia and Tibet area showing the main sutures and regional scale. **(B)** Geologic map of the Pamir Mountains, with the distributions of igneous rocks of different ages shown in different colors. TJSZ, Tanymas–Jingsha Suture Zone; RPSZ, Rushan–Pshart Suture Zone; WTSZ, Wakhan–Tirich Boundary Zone; KKF, Karakoram fault. The ages and locations of the Jurassic–Cretaceous igneous rocks were adopted from (1) Schwab et al. (2004); (2) Stearns et al. (2015); (3) Chapman et al. (2018b); (4) Zanchetta et al. (2018); (5) Aminov et al. (2017); (6) Jiang et al. (2014); (7) (Li R. H. et al., 2019) (8) Liu et al. (2020b); (9) (Liu et al., 2020c); (10) Worthington et al. (2020). Modified from Angiolini et al. (2015), Robinson (2015), and Zanchetta et al. (2018).

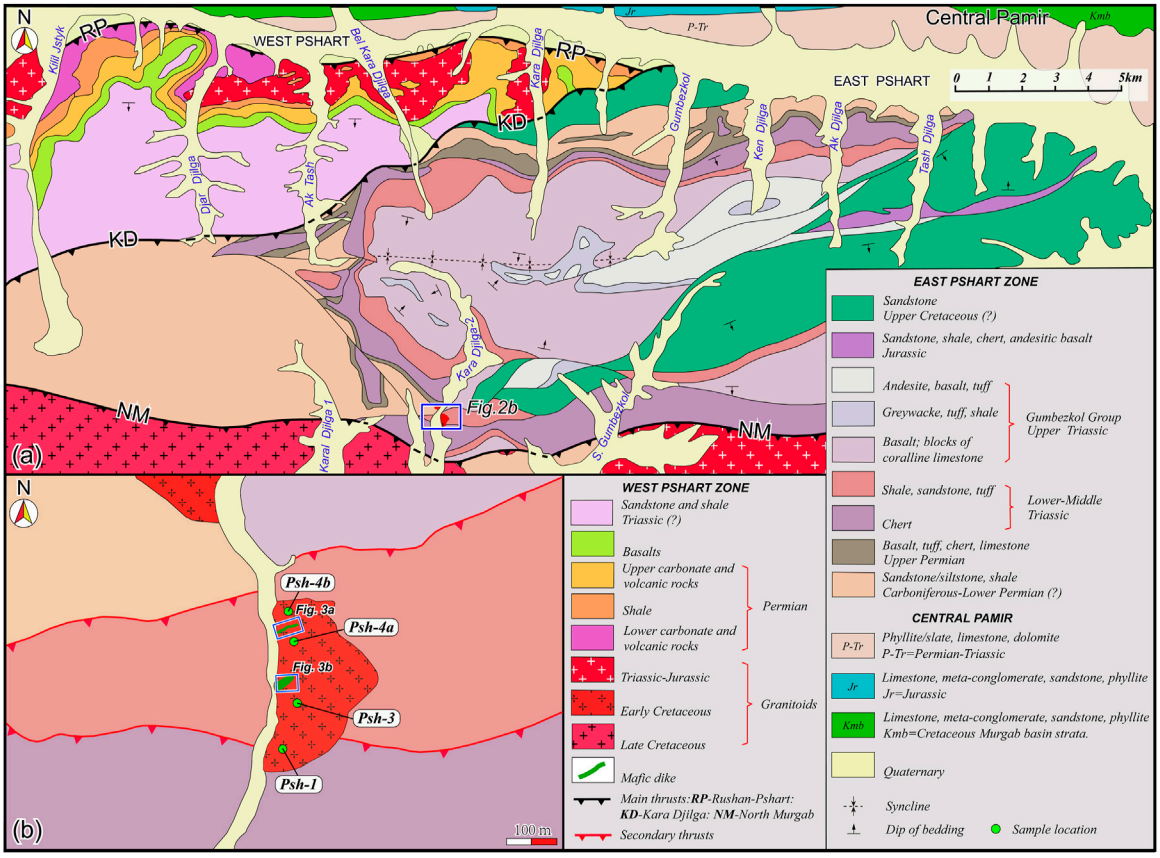

FIGURE 2
(A) Geological map of the Pshart zones showing the Kara Djilga fault, which is the boundary between the East and West Pshart zone. **(B)** Investigation area. The location of **(B)** is shown in **(A)** (red square). The map was modified after Leven (1995).

et al., 2013, 2015; Robinson, 2015; Zanchetta et al., 2018; Wang S. et al., 2020; Villarreal et al., 2020). However, another group argues for the Late Jurassic to Early Cretaceous closure time of the Rushan–Pshart Ocean (Shvol'man, 1978; Pashkov and Shvol'man, 1979; Burtman and Molnar, 1993; Leven, 1995; Schwab et al., 2004; Li R. H. et al., 2019; He et al., 2019; Fan B. et al., 2021). The eastward and westward continuation of the RPSZ also remains uncertain and controversial. Burtman and Samygin (2001); Burtman (2010); Angiolini et al. (2013); Villarreal et al. (2020) and Wang S. et al. (2020) correlated the RPSZ to the Longmu Co-Shuanghu suture zone, which is defined as the boundary between the Northern and Southern Qiantang terrane (Liang et al., 2012; Zhao et al., 2015; Zhai et al., 2016). However, other scholars correlated the RPSZ to the Bangong–Nujiang suture of Tibet (Lacassin et al., 2004; Schwab et al., 2004; Valli et al., 2008; Li R. H. et al., 2019), which separates the Southern Qiantang from Lhasa terrane (Liu et al., 2017; Hu et al., 2019; Wang W. et al., 2020).

Granitic rocks form in different geodynamic settings (Floyd and Winchester, 1975; Pearce and Norry, 1979; Petro et al., 1979; Pitcher, 1983; Maniar and Piccoli, 1989; Förster et al., 1997), and their proper classification, precise dating, and neat interpretation can be used as a geodynamic indicator of switch in the geodynamic environment (Barbarin, 1999; Dong et al., 2011; Zheng and Gao, 2021). The RPSZ is invaded by the Triassic–Jurassic and Cretaceous granites (the Cretaceous granites are invaded by diabase dikes (Figure 3) (Schwab et al. (2004) and this study)). The relationship of the granites and diabase dikes with the country rocks and their distinct characteristics may reveal the tectonic significance and particular stage of the tectonic evolution of the Pamir Orogen. The mechanism, emplacement timing, nature/protolith, provenance source, and geodynamic significance of the granites and their genetic relationship with diabase dikes and surrounding rocks remain unresolved. This paper, presents the petrographical description, geochronological and geochemical results of Early Cretaceous granites, and geochemistry of diabase dikes along the Kara Djilga-2 valley of the eastern Pshart zone (Figure 2) to reveal their geodynamic significance, nature, and provenance. Based on our observation/results in integration with

previous studies on Pamir, we propose a new model for the tectonic evolution of the Rushan–Pshart Meso-Tethys Ocean during the Mesozoic and its tentative correlations to the eastern and western extensions in the Tibetan Plateau.

2 Geological background

The Pamir orogen is in the western part of the Tibetan Plateau and comprises three extensive E–W-trending suture zones. From north to south, these sutures are the Tanymas Suture Zone (TSZ), the Rushan–Pshart Suture Zone (RPSZ), and the Wakhan–Tirich Boundary Zone (WTSZ) (Figure 1) (Burtman and Molnar, 1993; Zanchi et al., 2000; Burtman, 2010; Zanchi and Gaetani, 2011; Robinson, 2015). These suture zones subdivide the Pamir Plateau, from north to south, into the Northern Pamir/Karakul Mazar (Asian affinity), the Central Pamir, the Southern Pamir, and the Karakoram terranes (Cimmerian blocks) (Burtman and Molnar, 1993; Schwab et al., 2004). To the east and west, it is bounded by the transpressional Karakoram (dextral) and Darvaz (sinistral) faults respectively (Figure 1) (Burtman and Molnar, 1993; Robinson, 2009). The Northern Pamir is a part of the Kunlun Orogen that developed in response to subduction–accretion processes and the consumption of the Tethyan Oceans (Xiao et al., 2002; Robinson et al., 2012; Robinson, 2015; Li Y et al., 2018; Imrecke et al., 2019; Chen et al., 2021). Widespread intermediate granitoids of Triassic age (230–210 Ma) extensively intrude into the meta-sedimentary and meta-igneous mélange of the Karakul–Mazar accretionary complex (Schwab et al., 2004; Robinson et al., 2007). The exposed Late Triassic to Early Jurassic metamorphic rocks along the Karakul–Mazar arc-accretionary complex record the amalgamation process of the Northern and Central Pamir (Qu et al., 2007; Robinson et al., 2007, 2012; Yang et al., 2010; Li Y. P. et al., 2020; Rembe et al., 2021). The Northern Pamir (Karakul–Mazar arc accretionary complex) is considered the western extension (along-strike equivalent) of the Songpan–Ganzi terrane (Yin and Harrison, 2000; Schwab et al., 2004; Robinson et al., 2012; Robinson, 2015; Groppo et al., 2019; He et al., 2019; Imrecke et al., 2019). The structural analysis and proposed models suggest that, before its complete consumption, the Paleo-Tethys started to subduct southward beneath the Central Pamir (Robinson et al., 2012; Robinson, 2015; Imrecke et al., 2019). However, recent studies in the Muztaghata dome contradict this interpretation, assuming that the Gondwana affinity Central Pamir terrane juxtaposed above the Asian affinity Karakul–Mazar terrane during the exhumation of the lower crust in the Miocene, rather than during its southward subduction beneath Central Pamir (Li Y.-P. et al., 2020). The Central Pamir comprises metamorphic domes that mainly consist of marbles and siliciclastic rocks ranging in age from Paleozoic to Mesozoic, which are strongly folded and subjected to ductile deformation (Schwab et al., 2004; Stearns et al., 2015; Rutte et al., 2017a; 2017b). In the northeastern part of the Central Pamir, Triassic rocks (flysch and sedimentary mélange) of the Karakul–Mazar terrane were thrust to the Central Pamir along the Akbaital–Kalaktash thrust and unconformably overlay the Proterozoic to Cenozoic rocks (He et al., 2019). In the southeastern part, Late Triassic granitoids (206–201 Ma) intruded due to the northward subduction of the Rushan–Pshart Ocean beneath the Central Pamir (Wang S. et al., 2020). The youngest documented Mesozoic igneous rock in the Central Pamir is the Late Cretaceous (74–72 Ma; Figure 1) (Schwab et al., 2004; Chapman et al., 2018b). Chapman et al. (2018b) associated the Late Cretaceous mafic magmatism with the slab rollback of the Neo-Tethyan oceanic lithosphere, causing limited extension in Pamir. The Rushan–Pshart suture zone marks the boundary between the Central and Southern Pamir terranes (Figure 1) (Leven, 1995; Yogibekov et al., 2020), considered to be the western equivalent of the greater Qiantang terrane of the Tibetan Plateau (Burtman and Samygin, 2001; Robinson et al., 2012; Angiolini et al., 2013; Robinson, 2015; Wang S. et al., 2020; Villarreal et al., 2020). The Southern Pamir is divided into the Southeast (SE) and Southwest (SW) Pamirs, based on their different rock assemblages and metamorphic degrees of the exposed rocks.

The SE Pamir comprises non or slightly-metamorphosed mostly sedimentary and igneous rocks that record the tectonic evolution of the SE Pamir from its drifting from Gondwana until its accretion to the southern margin of Eurasia (rift to drift history) (Angiolini et al., 2013, 2015). The SW Pamir comprises the Neogene Alichur and Shakhdara gneiss dome complex, which was exhumed from a depth of 10–15 km (Alichur dome) and 30–55 km (Shakhdara dome) along the Alichur–Gunt and South Pamir sear zones, respectively (Schmidt et al., 2011; Stübner et al., 2013a; 2013b; Stearns et al., 2015; Worthington et al., 2020). The boundary between the Southern Pamir and Karakoram terrane is defined by the WTBZ, along which serpentinized mantle peridotites are exposed (Zanchi et al., 2000; Zanchi and Gaetani, 2011). Within the Southern Pamir, the exposed ophiolites in the hanging wall of the Alichur dome have been interpreted as the obducted fragment of the Rushan–Pshart oceanic lithosphere (north Alichur and Bashgumbaz ophiolites) (Shvol'man, 1980). However, a recent study on the Bashgumbaz complex revealed that the ophiolites formed in a supra-subduction setting during the initial southward subduction of the Rushan–Pshart Ocean beneath the Southern Pamir (Zanchetta et al., 2018). Liu et al. (2020c) first documented the Late Triassic–Early Jurassic monzogranite of 202–197 Ma (Turuke pluton) in the Southern Pamir. The Early and Late Cretaceous rocks intruded into the basement of the southern Pamir. To the south, the Shyok suture may have formed as a result of an amalgamation of the Kohistan–Ladakh intra-

oceanic arc and Karakoram terrane by the Late Cretaceous (Ravikant et al., 2009; Pundir et al., 2020; Saktura et al., 2021).

2.1 The geology of the Pshart zones

The Rushan–Pshart suture zone was considered a separate zone from the Central and Southern Pamirs by Dronov (1964). This zone comprises three distinct lens-shaped blocks (Rushan, Pshart, and Dunkeldyk) (Figure 1). Two distinct zones were distinguished within the Pshart zone and the Eastern and Western Pshart zones, which are separated by the Kara–Djilga fault (Figure 2A) (Pashkov and Shvol′man, 1979; Leven, 1995). The geology of the Rushan and Dunkeldyk blocks was briefly described by Leven (1995) and Zanchetta et al. (2018). The Pshart complex is the focus of the present study.

2.1.1 Western Pshart

The Western Pshart zone starts with the massive succession of the carbonate, shale, and interlayer volcanic rocks Permian in age, which were locally intruded by Late Triassic–Jurassic granitoids. The lithology is locally strongly metamorphosed and deformed by multiple faults. The presence of the alkaline picritic basalt was interpreted to be associated with the initial stage of the rifting and opening of the Rushan–Pshart Ocean (Pashkov and Shvol′man, 1979; Leven, 1995). Basalt, andesitic basalt, and basic effusive rocks with subordinating basic and acidic tuffs and local thin layers of clayey-shale and embedded fragments of the limestone occur in the intermediate part of the succession. The upper section mostly consists of volcaniclastic sandstone, shale, and siltstone, with distinctive layers of altered basalt and intermediate to acidic tuffs (about 10 m) of undetermined ages (Pashkov and Shvol′man, 1979; Leven, 1995). For more detailed information, refer to Leven (1995).

2.1.2 Eastern Pshart

The Eastern Pshart zone is characterized by Carboniferous to Permian clastic rocks, followed upward by volcaniclastic limestones and basalt of Upper Permian age (Leven, 1995). However, recent investigations revealed that it is a sedimentary mélange, comprising incorporated fragments of the upper portion of oceanic plate stratigraphy (OPS), with Upper Triassic (212 Ma) maximum deposition age (MDA), rather than Carboniferous or Permian (Yogibekov et al., 2020). Following upward, the Triassic interval is represented by Upper Triassic volcanic and sedimentary deposits (Gumbezkol Group; up to 1000 m) overlying chert, shale, and sandstone with layers of andesite and basalt of Lower to Middle Triassic age. The Upper Triassic Gumbezkol group comprises basalt and embedded blocks of limestone in the lower part, passing upward to clastic rocks such as greywacke, alternating with andesitic tuff, silicious shale, conglomerate, and breccia. The upper portion comprises andesite, andesitic basalt, and tuff. Small amounts of spilite, basalt, and diabase with thin layers of chert, limestone, shale, and tuffitic sandstone also occur. Late Triassic age was tentatively inferred for the section based on its stratigraphic position and poorly dated fossils (Leven, 1995). The Upper Jurassic and Cretaceous rocks (Etchki Tushar Formation) are composed of andesite, andesitic basalt and tuff, limestone, and sandstone, together with chert and/or cherty-shale (Pashkov and Shvol'man, 1979; Leven, 1995). The non-conforming overlying sandstone was tentatively dated as the Late Cretaceous (Leven, 1995).

3 Sampling and petrography

We collected four granite (Figure 2B) and two diabase (Figures 3A,B) samples, which cropped out in the southern part of the eastern Pshart zone, along the Kara Djilga-2 River (Figure 2B). The granitic rocks intruded into Early–Middle Triassic rocks, composed of shale, sandstone, tuff (Figures 2A,B), and cherty units, showing sharp intrusive contact (Figure 3C). The basic rocks occurred as diabase dikes (ranging in size from 50 cm up to 10 m), which invaded the granitic rocks (Figures 3A,B). Thin sections were made by Beijing GeoAnalysis Technology Co., Ltd. We classified the granitic rocks as two-mica monzogranite based on our microscopic observation. The granitic rocks were medium-to-fine-grained and contained plagioclase (40%), K-feldspar (30%), quartz (25%), biotite, and muscovite (≤5%), as well small amounts of garnet and accessory minerals, such as apatite and zircon (Figures 3E,F). The plagioclase was semi-automorphic in shape, with twining crystal development, and moderately subjected to sericitization. Occasionally, the plagioclase fractured, and quartz veins filled the cracks. The K-feldspar was slightly muddy with a striped feldspar structure. The diabase was represented by samples Psh-6 and Psh-7, which predominantly consisted of plagioclase (50%), pyroxene (35%), amphibole (10%), and olivine (5%) (Figure 3D). Apatite, magnetite, and titanomagnetite were present as accessory minerals. Disordered plagioclase was distributed within the rock and slightly altered to kaolinite and sericite, representing the matrix within the rocks. Micro-fissures were also observed in the diabase. The interstices were filled with carbonate and quartz veins.

4 Results

4.1 Geochronology

The detailed analytical methods are provided in Supplementary Material. Zircon grains from the granitic rocks including samples Psh-1, Psh-3, Psh-4a, and Psh-4b from the Kara Djilga-2 section were subjected to LA-ICP-MS U-Pb zircon

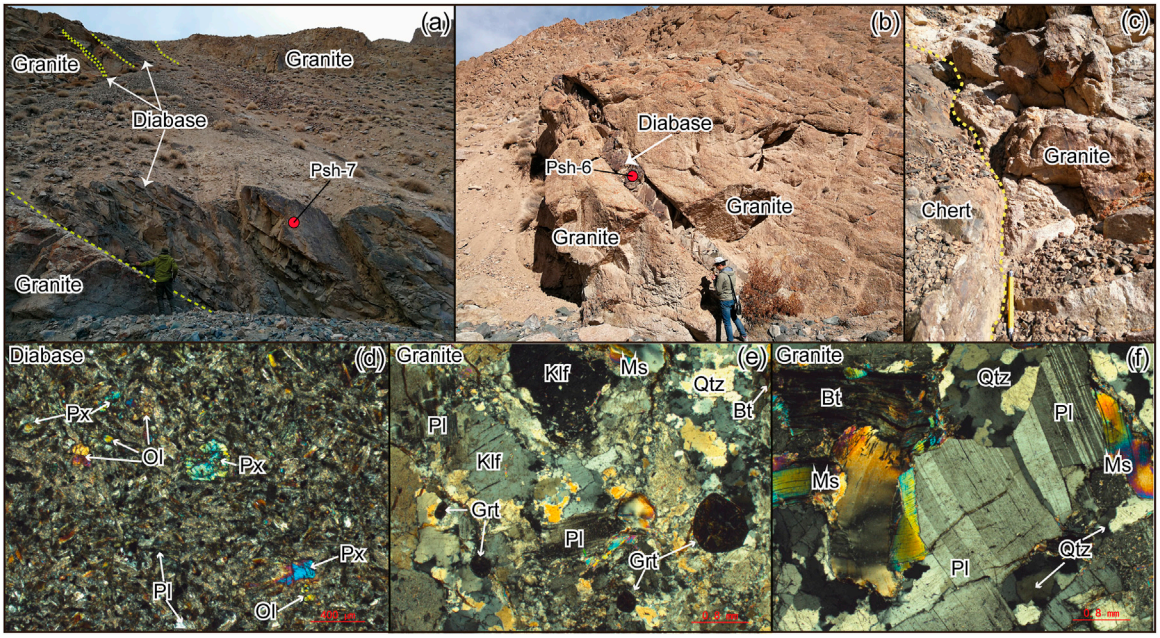

FIGURE 3
(A,B) Variably sized diabase dikes intruding into the granitic rocks. Their location is shown in Figure 2B. Scientists for scale. **(C)** Intrusion contacts between chert and invaded granite. **(D)** Photomicrograph of diabase rocks, the location of which is shown in Figure 2B. **(E,F)** Photomicrographs of granites. Px, pyroxene; Ol, olivine; Pl, plagioclase; Kfl, K-feldspar; Ms, muscovite; Bt, biotite; Qtz, quartz; Grt, garnet.

dating to determine the crystallization age and intrusion time of the granitic magma. We utilized the Th/U ratio (Corfu et al., 2003) to distinguish the genetic origins of the zircons as either metamorphic or igneous growth. The zircon crystals from the samples varied in color from colorless, deep black, and grayish. They were euhedral, subhedral, and tabular in shape. Most of the zircons showed well-developed oscillatory zoning with a lack of core and rim structure in cathodoluminescent images (Figure 4F). The zircon grains ranged in length from 60 to 190 μm, with variable concentrations of Th (51–1439) and U (87–4053) that yielded Th/U values of 0.16–0.97 (only a few spots yielded ratios of 0.06–0.07), consistent with a magmatic origin (Corfu et al., 2003). The U-Pb systematics are provided in Supplementary Table S1.

The data from Psh-1 yielded $^{206}Pb/^{238}U$ ages ranging from 116 to 130 Ma and a weighted mean age of 121.9 ± 2.6 Ma (MSWD=4.3, n=12; Figure 4A). Three grains yielded older ages, ranging from 136 to 137 Ma, with a weighted mean age of 135.9 ± 24 (Figure 4A). However, these zircons were slightly discordant; thus, we did not consider them in the crystallization aging.

Eleven analyses from sample Psh-3 showed $^{206}Pb/^{238}U$ ages ranging from 107 to 123, with a weighted mean age of 118.0 ± 2.5 Ma (MSWD = 3.6, n = 11; Figure 4B). Three zircons from sample Psh-4a yielded ages ranging from 113 to 128 Ma with a weighted mean $^{206}Pb/^{238}U$ age of 122.9 ± 4.8 Ma (MSWD = 11, n = 10; Figure 4C). Two inherited zircon crystals showed ages of 180 ± 2 and 877 ± 4 Ma from the same sample, with Th concentrations of 51–85 ppm, U concentrations of 87–921ppm, and Th/U of 0.05–0.87 (Figure 4C).

Zircon crystals from sample Psh-4b ranged in age from 112 to 131 Ma, with a weighted mean $^{206}Pb/^{238}U$ age of 124.5 ± 2.0 Ma (MSWD = 3.6, n = 16; Figure 4D). A single inherited zircon grain of 924 ± 5 Ma was obtained from the sample. The weighted mean ages were interpreted as the crystallization age for each sample.

Zircons from the diabase sample Psh-7 yielded only Precambrian concordant ages and were not further considered (Supplementary Table S1). Similarly, the diabase Psh-6 yielded mostly inherited Precambrian ages, with single concordia age of 121 Ma with a Th/U ratio of 0.49, indicating the magmatic origin of the zircon (Figure 4E).

4.2 Geochemistry

4.2.1 Geochemistry of the granites

The major and trace element compositions of the granite samples are shown in Supplementary Table S2. The granitic rocks showed loss on ignition (LOI) values of 1.03 wt.% to 1.42 wt.%, while those of diabases were 1.14 wt.% and 8 wt.%, indicating the relative freshness of the samples except for Psh-7, which showed a high LOI. The granites were characterized by high SiO_2

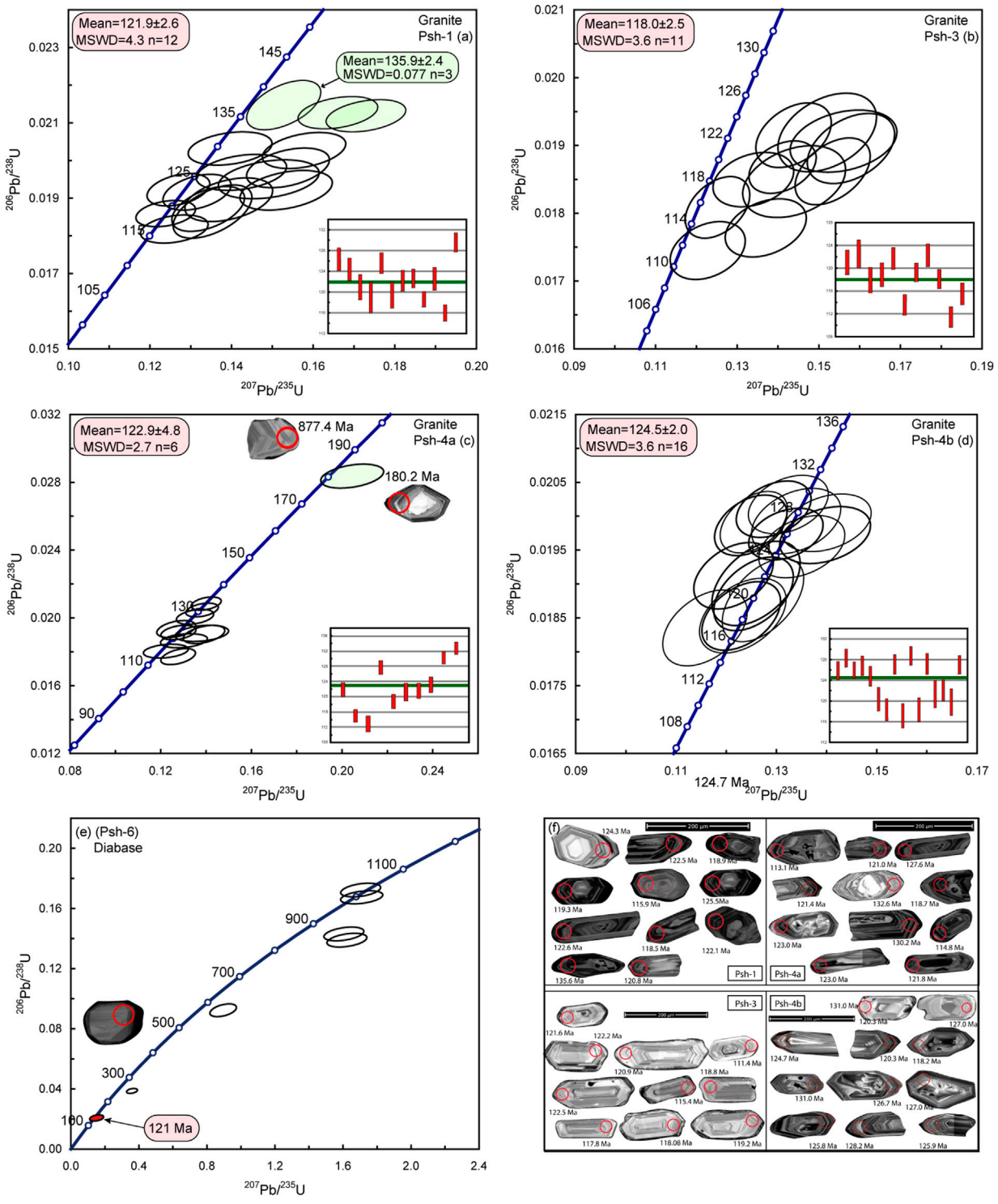

FIGURE 4
(A–D) U–Pb Concordia diagrams of zircons from granites. **(E)** Diabase dike and **(F)** CL images of dated granite zircons. MSWD, mean square of the weighted deviation.

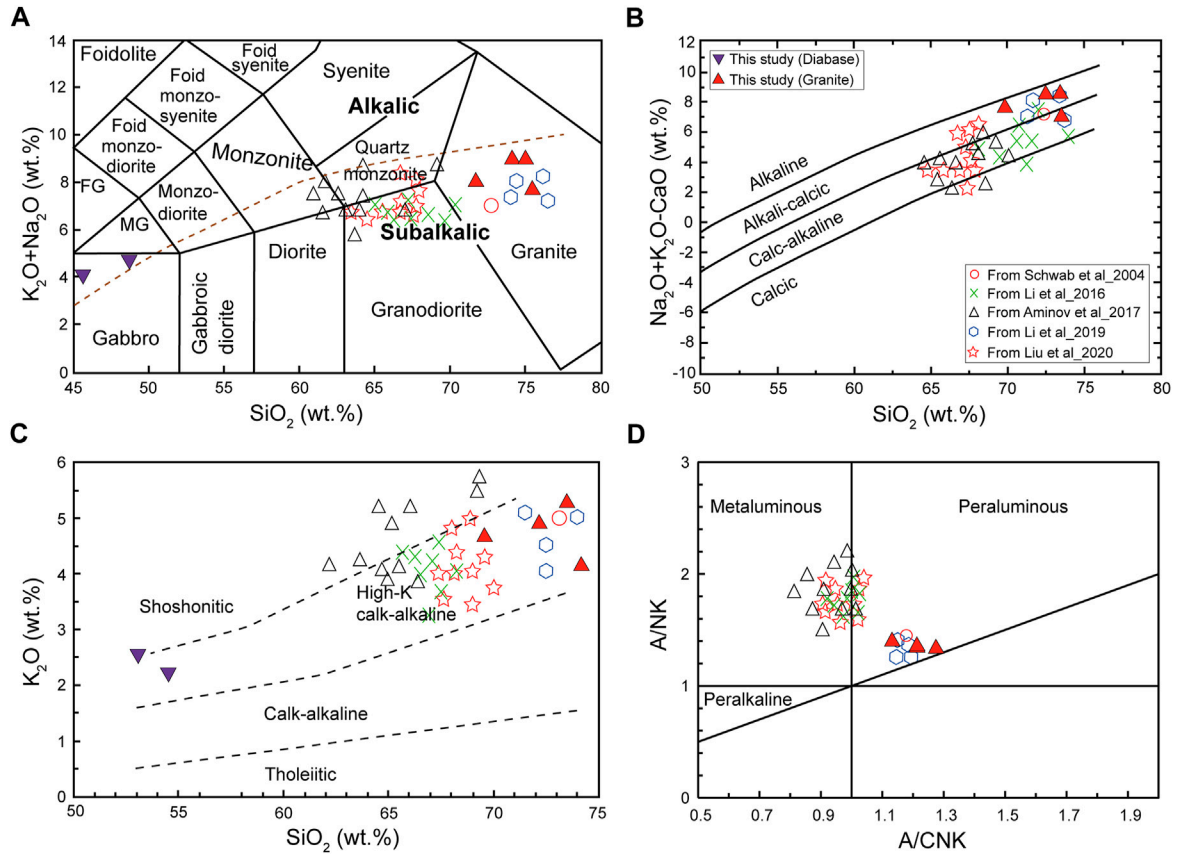

FIGURE 5
(A) K_2O+ Na_2O vs. SiO_2 (after Le Bas et al. (1986)); **(B)** SiO_2 vs. Na_2O+K_2O-CaO (Frost et al., 2001); **(C)** SiO_2 vs. K_2O referenced from Roberts and Clemens (1993); **(D)** A/NK versus A/CNK (after Maniar and Piccoli (1989)). Diagrams of igneous rocks from Kara Djilga-2 valley, Pshart complex, and other published Cretaceous plutons from Pamir.

concentrations ranging from 70.32 to 74.40 (wt.%), with total alkali (Na_2O+K_2O) ranging from 7.69 wt.% to 8.96 wt.%. In the SiO_2 vs. K_2O+Na_2O diagram of Le Bas et al. (1986), the samples were classified as granitic rocks, consistent with our microscopic observations (Figure 5A).

K_2O ranged from 4.21 wt.% to 5.79 wt.%, CaO from 8.54 wt.% to 8.55 wt.%, and Na_2O from 3.17 wt.% to 3.95 wt.%, with K_2O/Na_2O ratios of 1.21–1.83 and CaO/Na_2O ratios of 0.03–0.44. In the SiO_2 vs. Na_2O+K_2O-CaO (wt.%) and SiO_2 vs. K_2O classification diagrams, the granites plotted in the field of calc-alkaline to alkali-calcic and high-K calc-alkaline series, respectively (Figures 5B,C). The granitic rocks were similar to S-type granitoids, with strongly peraluminous features (Figure 5D) and high alumina saturated indexes (ASI) of A/CNK ($Al_2O_3/(CaO+Na_2O+K_2O)_{mol.}$) and A/NK ($Al/Na_2O+K_2O)_{mol.}$), ranging from 1.13 to 1.28 and 1.21 to 1.83, respectively. The samples showed moderate concentrations of Al_2O_3, ranging from 13.49 to 15.53, and low TiO_2 content, ranging from 0.05–0.47, with Al_2O_3/TiO_2 ratios ranging from 31.43 to 310.06. They were also characterized by varying content of $Fe_2O_3^T$ (0.48–2.81) and CaO (0.12–1.42) and low MgO (0.13–0.87), with Mg# between 26.3 and 46.4.

In the chondrite-normalized patterns, the granitic samples showed light rare earth element (LREE) enrichment relative to heavy rare earth elements (HREE, La_N/Yb_N = 3.73–32.58) with strong depletion of Eu (Eu/Eu* = 0.22–0.41; (Figure 6A)). In the primitive normalized spidergram, the samples showed strong depletion of Ba, Sr, Eu, and Ti and a comparatively weak negative Nb anomaly. The samples showed variable enrichment on Th, U, and K and strong enrichment of Rb (Figure 6B). The depletion of Sr and Eu likely reflected plagioclase fractionation or accumulation, consistent with our petrographical observations (Figures 3E,F).

4.2.2 Geochemistry of the diabase dikes

The diabase dike samples (Psh-6 and Psh-7) showed relatively low SiO_2 content, ranging from 49.77 to 50.71. The K_2O content ranged from 1.66 wt.% to 1.80 wt.%, while Na_2O ranged from 2.84 wt.% to 3.22 wt.%, with the K_2O/Na_2O ratios ranging from 0.51 to 0.63. The Al_2O_3 content ranged from

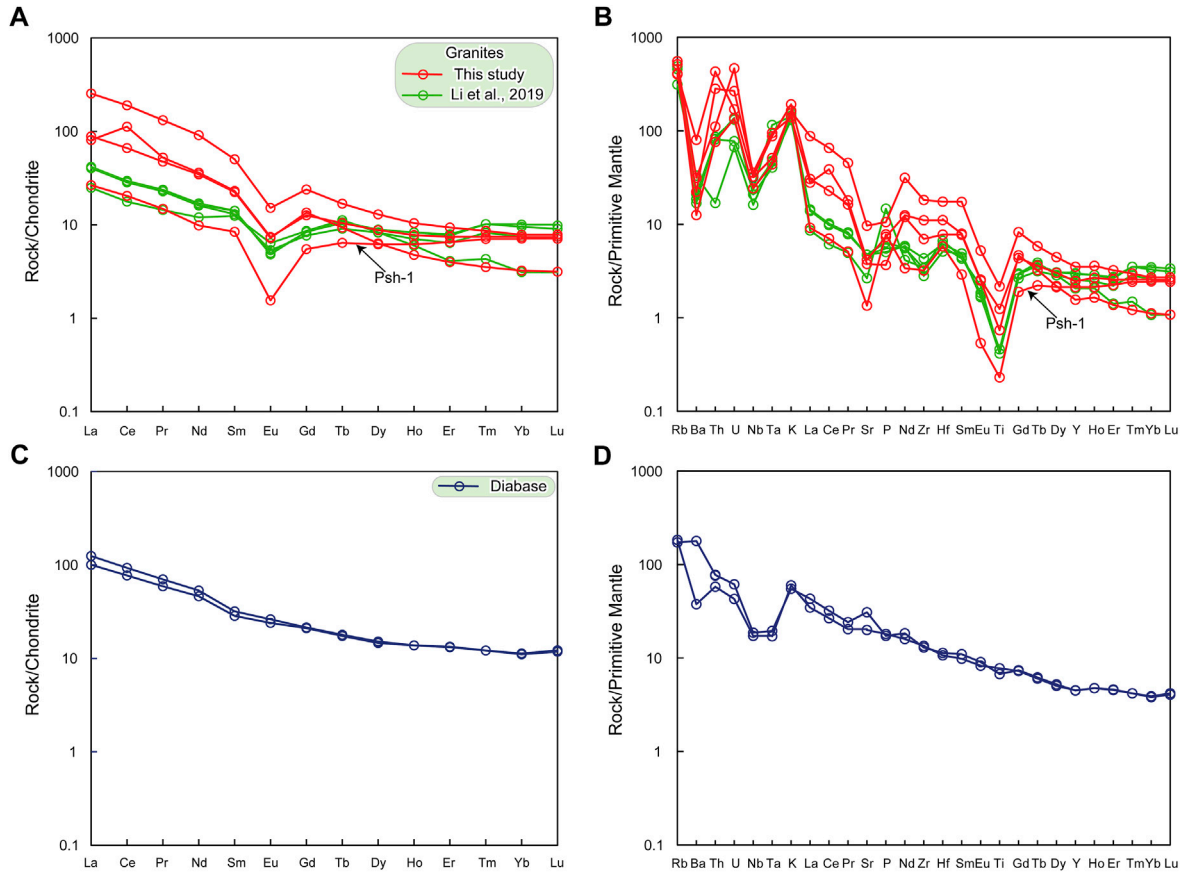

FIGURE 6
Chondrite-normalized REE and primitive-mantle normalized trace element multi-variation diagrams of granitic **(A,B)** and diabase **(C,D)** rocks. The mantle-normalization and chondrite values are from Sun and McDonough (1989).

16.15 wt.% to 16.95 wt.%. The TiO_2 content was slightly high (1.46 wt.% to 1.48 wt.%). The Fe_2O_3 content was 8.73–9.48 wt.%, and high MgO content was also observed, ranging between 7.93 and 8.58 wt.%, with Mg# between 62.4 and 66.1. The samples plotted in the gabbroic field and showed alkaline affinity in the TAS diagram (Figure 5A). In the SiO_2 vs. Na_2O+K_2O diagram, the samples plotted in the alkaline series field (Supplementary Figure S2B). In the SiO_2 vs. K_2O classification diagram, the samples fell in the high-K calc-alkaline and shoshonitic rock series (Figure 5C). The Nb, Yb, and Th content ranged from 12.3–13.3 ppm, 1.88–1.92 ppm, and 4.92–6.59 ppm, respectively, with Nb/Yb and Th/Yb ratios of 6.54–6.93 to 3.43–2.6.

In the chondrite-normalized REE diagrams (Sun and McDonough, 1989) the samples were characterized by LREE enrichment compared to HREEs, which displayed relatively flat patterns without Eu anomalies (Figure 6C). In the multi-elemental spidergram (Sun and McDonough, 1989), the samples showed depletion of high-field strength elements (Nb and Ta), with negligible positive Sr and Ti anomalies. Slightly positive and negative Ba anomalies were also observed (Figure 6D).

5 Discussion

5.1 Petrogenesis

5.1.1 Granite

The granites were high-K calc-alkaline with high SiO_2 content [70.32–74.40 (wt.%)], strongly peraluminous (A/CNK=1.13–1.28), with K_2O/Na_2O ratios ranging from 1.21 to 1.83, suggesting that they were strongly peraluminous S-type granites (Chappell and White, 1992; Patiño Douce and Harris, 1998; Chappell, 1999; Clemens, 2003; Clarke, 2019; Liu X. et al., 2021). These findings are also supported by the A/CNK vs. SiO_2 diagram (Figure 7A). The results of multi-experimental studies revealed that most of the S-type granites formed from the partial melting of metasedimentary rocks (Chappell and White, 1974; Beard et al., 1993; Clemens, 2003; Stevens et al., 2007; Wang et al.,

2007; Villaros et al., 2009b; Bartoli et al., 2013; Champion and Bultitude, 2013; Wang et al., 2014; Gao et al., 2016b; Gao et al., 2017; Zhu et al., 2018; Clemens et al., 2020; Zhu et al., 2020). The A/CNK ratio can be used to define the boundary between S and I-type granite (Chappell and White, 1974). The A/CNK ratios of S and I-type granites range from 1.044–1.248 and 0.902–1.092, respectively (Chappell, 1999). Our petrographic observations showed the presence of biotite, muscovite, and garnet and the absence of mafic phase minerals, suggesting its S-type nature (Chappell and White, 1992; Villaros et al., 2009a). The high K_2O (4.21–5.79) content relative to Na_2O (3.17–3.95), with K_2O/Na_2O values of 1.21–1.83 (Supplementary Table S2), also confirmed that the granites from this study were S-type in nature (Chappell and White, 2001). In the K_2O/MgO vs. 10000*Ga/Al and FeO^T/MgO vs. 10000*Ga/Al diagrams, the samples clearly plotted in the A-type granite field (Figures 7C,E). However, in the K_2O+Na_2O, FeO^T/MgO, (K_2O+Na_2O)/CaO vs. Zr+Nb+Ce+Y diagrams, the samples plotted in the highly fractionated S-type to A-type, highly fractionated S-type to unfractionated I-S-type and highly fractionated S-type, and unfractionated I-S-type, respectively (Figures 7B,D,F). The 10000*Ga/Al value of the samples ranged from 2.79 to 3.52 and Zr+Nb+Ce+Y are 76–359 ppm, which was nearly identical to those of A-type granites, which are characterized by an average 10000 Ga/Al value >2.6 and Zr+Nb+Ce+Y >350 ppm. However, Whalen et al. (1987) reported that some strongly fractionated S-and I-type granites also show high Ga/Al ratios, thus showing similar characteristics to those of A-type granites. This ambiguity is controlled by the entrainment of xenocrystic/or peritectic and accessory minerals and their constituent element concentrations in the melt. In combination with our data, we used the data from 118 Ma granitoids reported by Li R. H. et al. (2019) (from the Taxkorgan region (Figure 1)), which plotted in the same fields as our samples (Figure 7D). Garnet containing elements such as Zr, Ce, Ga, Y, and others can be concentrated within refractory minerals such as zircon (Zr, Hf, Y, and Yb) and monazite (Ce and La) (Villaros et al., 2009b). Thus, the zircon, monazite, and garnet and their constituent elements may have provided the A-type characteristics in the granite samples in this study. The lack of monazite may be due to its full dissolution and equilibration within the melt, thus changing the compositional variation of the melt (Villaros et al., 2009b; Clemens and Stevens, 2012). These findings imply that the assent of the melt was not rapid after partial melting and segregation of the melt from the magma source rocks and that entrained peritectic and accessory minerals had enough time to dissolve and equilibrate within the melt. The process was well-described by Villaros et al. (2009b). Thus, the dissolution of the peritectic and accessory minerals (equilibrium melting) may have modified the trace element composition of the studied granites. Extremally negative Eu anomalies (Eu/Eu*<0.30) were interpreted to be characteristic of A-type granite (Zhang Q. et al., 2012). However, our samples displayed comparatively high Eu/Eu* values (0.40–0.42), characterizing them as S-type granite. An exception was sample Psh-1 which showed a slightly lower Eu/Eu* value (0.22). Metasedimentary-derived, highly fractionated S-type granites with geochemical characteristics overlapping those of A-type granites have been reported worldwide (Whalen et al., 1987; Huang and Jiang, 2014; Zhu et al., 2020). The overlap of geochemical characteristics is attributed to the entrainment of peritectic and accessory minerals and their constituent elements, which is in good agreement and can be attributed to our samples. A-type granites are ferroan/and or alkaline in nature (Whalen et al., 1987; Gao et al., 2016b); however, our samples tend to be magnesian and sub-alkaline in the SiO_2 vs. ^{T}FeO/(^{T}FeO+MgO) and SiO_2 vs. Na_2O+K_2O diagrams, respectively (Supplementary Figure S2A,B). The negative Eu and Sr anomalies may have been related to the separation of plagioclase from the melt during fractional crystallization or may indicate that the granitic melt was generated in the plagioclase stability field (Figures 6A,B). K-feldspar fractionation was also reflected by the negative Ba and Eu anomalies (Figures 6A,B). The strong negative Ti anomaly reflected the fractionation of ilmenite (Fe–Ti oxides) or mica fractionation during magma evolution. However, the samples showed low Sr/Y and relatively high La/Yb, indicating that the melt was forming in the plagioclase stability field, with residues of garnet and plagioclase (Figures 3E,F), similar to those documented in Jurassic (160 Ma) Maofengshan (South China Block) metasedimentary-derived highly fractionated S-type granites that originated in the middle crust (16.5–20 km) (Liu X. et al., 2021). The chondrite-normalized and spidergram patterns showed that our samples were slightly evolved compared to those reported by Li R. H. et al. (2019) from the Taxkorgan region. The exception was sample Psh-1 which displayed an identical pattern to those for the Taxkorgan granites (Figures 6A,B). Thus, the samples in this study were highly fractionated, strongly peraluminous S-type granites.

The strongly fractionated peraluminous I-type granites showed a nearly identical geochemical signature to those of peraluminous S-type granites (with some overlap) (Miller, 1985; Gao et al., 2016a). We aimed to identify the source protolith of the granites by using their major and trace elements to discriminate between metasedimentary or metaigneous-derived granitic melt. The Th/Sm vs. Th/Yb, Th/Ce vs. Y, and SiO_2 vs. Rb diagrams showed the sediment-derived trends for the melt (Figures 8A–D). Furthermore, the samples showed variable Rb/Ba (0.46–3.73), Rb/Sr (1.3–11.5), CaO/Na_2O (0.04–0.45), and Al_2O_3/TiO_2 (31.43–310.60) ratios and fell within the fields of pelite-derived magmas. The exception was sample Psh-3, which showed a psammite-derived magma source (Figures 9A,B).

Another convincing argument for the metasedimentary-derived melt is the major oxide element magma source discrimination diagrams of Al_2O_3/(FeO^T+Mg+TiO_2) vs. Al_2O_3+FeO^T+MgO+TiO_2 (wt.%) and CaO/

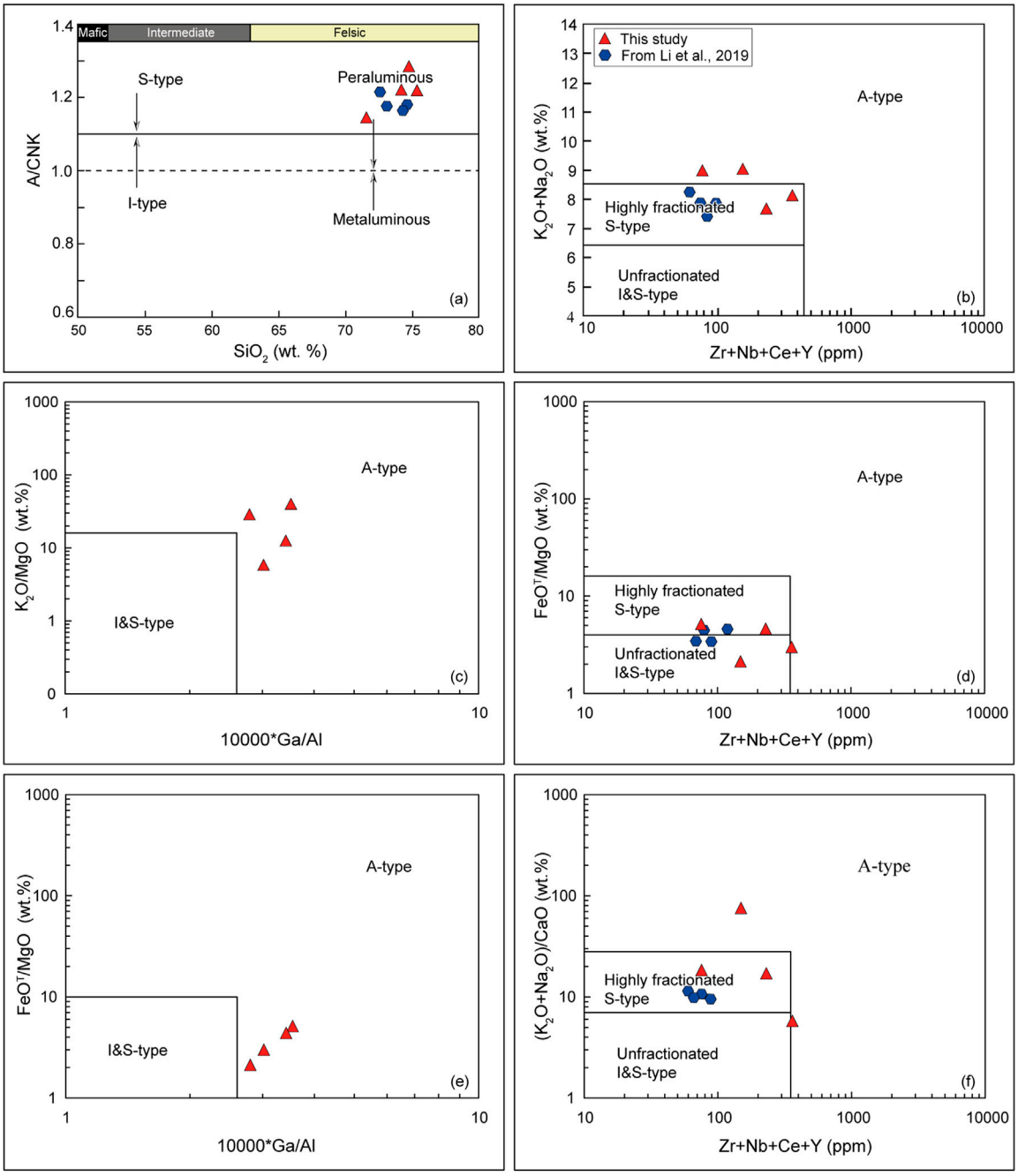

FIGURE 7
(A) A/CNK (molar $Al_2O_3/(CaO+Na_2O+K_2O)$) versus Si_2O (after Maniar and Piccoli (1989)). **(C,E)** K_2O/MgO and FeOT/MgO vs. 10000*Ga/Al. **(B,D,F)** K_2O+Na_2O, FeO^T/MgO and $(K_2O+Na_2O)/CaO$ vs. Zr+Nb+Ce+Y (Whalen et al., 1987).

$(MgO+FeO^T+TiO_2)$ vs. $CaO+MgO+FeO^T+TiO_2$ (wt.%) (Figures 9C,D). The samples fell in the field of the pelite-derived melt, except for sample Psh-3, which fell in the greywacke field (Figures 9C,D). Based on the major and trace element concentrations, we concluded that the granites originated from the partial melting of metasedimentary rocks [predominantly from pelite with a minor contribution from psammite (sample Psh-3)] in the plagioclase stability field (middle crust; ±20 km), underwent subsequent fractional crystallization during magma ascent, and were emplaced to the upper crust. We have also compiled available data on Early Cretaceous arc-related and S-type granites and plotted them in

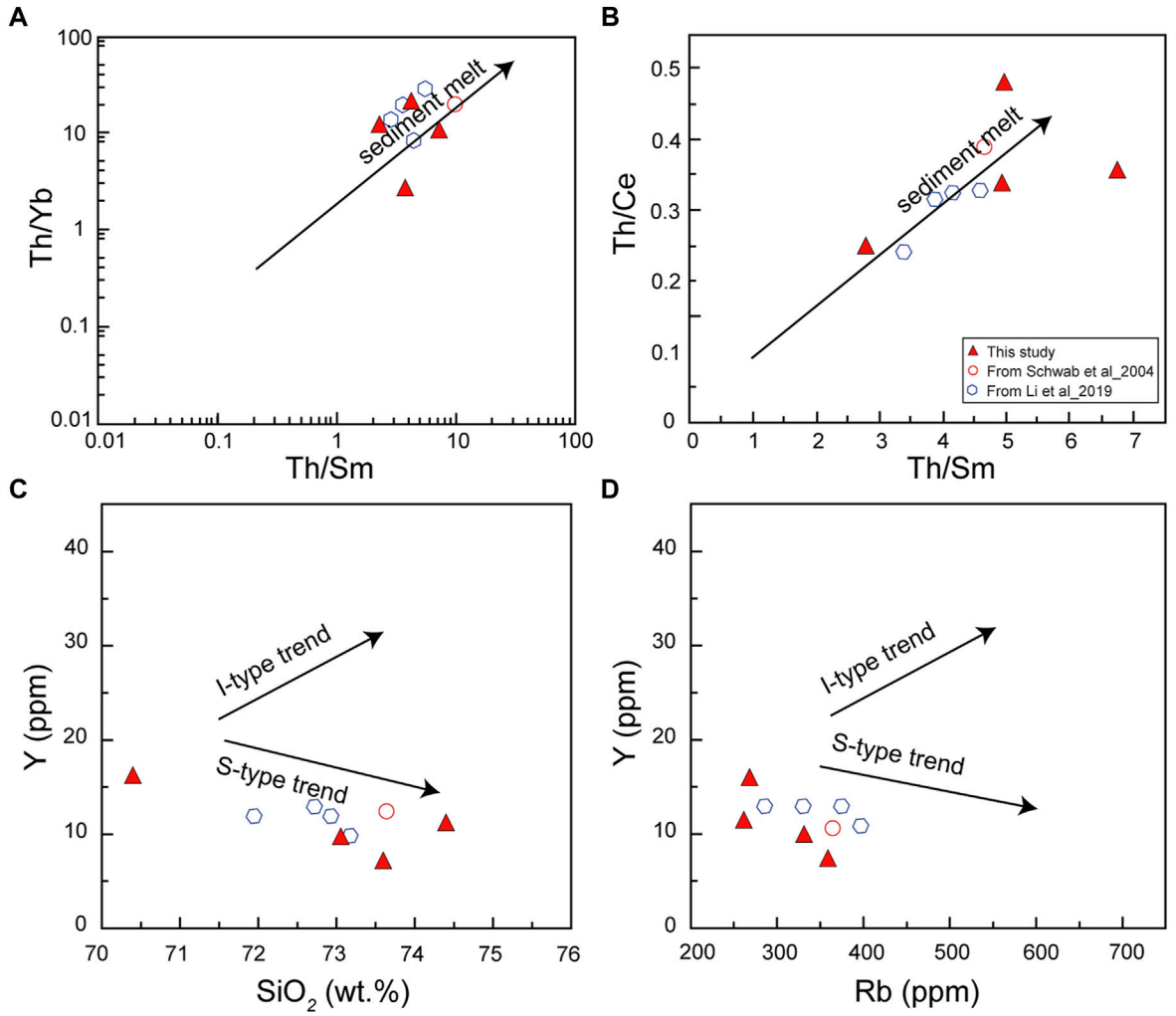

FIGURE 8
(A) Th/Yb vs. Th/Sm, **(B)** Th/Ce vs. Th/Sm, **(C)** Y vs. SiO_2, and **(D)** Y vs. Rb (Chappell, 1999). The data are from this study, Schwab et al. (2004), and Li R. H. et al. (2019).

combination with our samples (Figures 5, 8, 9). The arc-related igneous rocks show an obviously different trend.

5.1.2 Mafic dikes

The diabase samples showed a low SiO_2 content (49.77–50.71 wt. %) and high MgO (7.93–8.58), $Fe_2O_3^T$, Cr (220–300), and Mg# (62.4–66.1) contents, indicating that the mantle-derived parental melt was not evolved, as also suggested by their trace element concentration in the primitive mantle and chondrite-normalized multi-elemental diagram (Figures 6C,D). The moderate-to-high loss on ignition (LOI) value (1.14–8 wt.%) indicated that the samples had undergone variable degrees of alteration. The samples showed a large range in TiO_2 content (1.46–1.68 wt.%), which was interpreted as a typical feature of ocean island basalt (OIB)/or oceanic plateau and continental flood basalt (CFB), associated with the hot-spot zone/or plume activity. However, they are typically hump-shaped in pattern with positive Nb and Ta anomalies in trace element spidergrams (Safonova et al., 2009; Xia, 2014; Xia and Li, 2019). The depletion of Nb and Ta resulted in a continental crust or arc-like signature to the mafic dikes, reflecting the metasomatism of the source region (Donnely et al., 2004). Their crustal or arc-like signature was inherited from the foundering of the Rushan–Pshart oceanic lithospheric crust, which released the fluid-like component and fertilized the overlying mantle (Figure 10). Contamination by crustal rocks may also imprint such a signature. The inherited Precambrian zircons (Figure 4E and Supplementary Figure S1) support crustal contamination. Both crustal contamination and metasomatism can cause Nb and Ta negative anomalies. A simple way to explain the slightly high TiO_2 concentration of

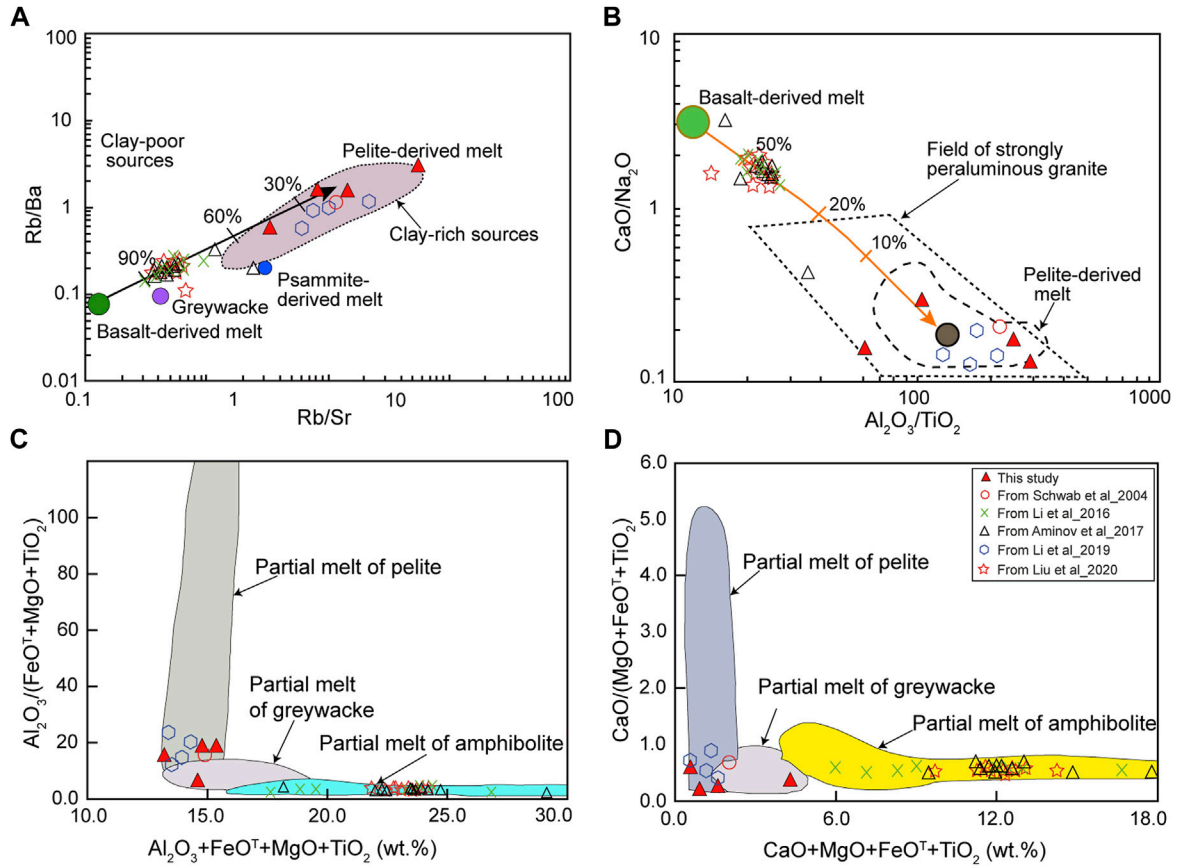

FIGURE 9
(A) Rb/Sr vs. Rb/Ba, **(B)** CaO/Na_2O vs. Al_2O_3/TiO_2, **(C)** $Al_2O_3/(MgO+FeO^T+TiO_2)$ vs. $Al_2O_3+MgO+FeO^T+TiO_2$, **(D)** $CaO+MgO+FeO^T+TiO_2$ vs. $CaO/(MgO+FeO^T+TiO_2)$ plots. Fields are from Patiño Douce and Beard (1995); Sylvester (1998) and Wang et al. (2007), respectively. The data of Early Cretaceous igneous rocks from Pamir are as previously reported.

the diabase dikes is that it was inherited and coupled with the opening of the Rushan–Pshart Ocean in the Permian, which has been interpreted to be associated with the plume-related magmatism, as evidenced by high TiO_2 content of the basaltic rock of the West Pshart and SE Pamir (Pashkov and Shvol'man, 1979; Tadjidinov, 1988; Leven, 1995; Angiolini et al., 2015). Thus, the upwelling of mafic magmatism and melting of the former TiO_2-rich subcontinental lithospheric mantle or crust caused TiO_2 enrichment of the diabase dikes. Fractional crystallization/or accumulation of plagioclase causes strong depletion of melt on Sr and Eu. However, in the primitive mantle-normalized trace-element diagram, the samples did not show any Eu anomaly, with a slightly positive Sr anomaly (Figure 6C). Thus, the lack of Eu anomaly was ascribed to plagioclase-free assemblage at >40 km depth of the lower crust source (Girardi et al., 2012). The slightly positive and negative Ba anomaly was probably the effect of the continental crust contamination/or alteration, which is also supported by the high LOI and inherited zircons in the samples (Supplementary Table S1). Based on the geochemical data, we proposed that the parental magma of the diabase dikes possibly originated from depleted mantle sources, which may have been metasomatized by fluids released from the detached Rushan–Pshart oceanic lithospheric slab and its foundering in the Late Jurassic–Early Cretaceous. This interpretation is also supported by the U/Th and Th/Nb diagrams, which showed the involvement of fluid-like components in the generation of the parental magma of the diabase dikes (Figure 10).

5.2 Geodynamic settings

5.2.1 Granites

Peraluminous granitoids might form during crustal thickening following the final ocean closure in the continent–continent collisional phase, along shear zones (or along strike–slip faults). In addition, the delamination of the lower crust/of former oceanic crust can cause upwelling of the asthenospheric mantle and its underplating, which serves as a

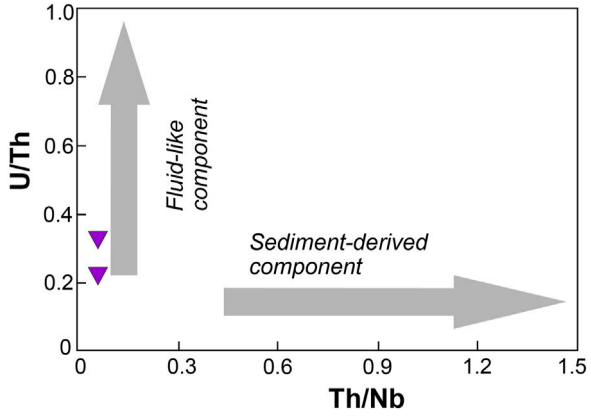

FIGURE 10
Th/Nb versus U/Th diagram showing that the mantle source of the diabase dikes was metasomatized by slab-released aqueous fluids.

heat source to generate granitic melt by partial melting of infracrustal and supracrustal rocks (Harris et al., 1986; Barbarin, 1996, 1999; Sylvester, 1998; Reichardt and Weinberg, 2012; Huang et al., 2015; Chen Y.-X. et al., 2017; Liu X. et al., 2021; Zheng and Gao, 2021). Based on the aforementioned discussion, we defined the granites as high-K calc-alkaline, highly fractionated, and strongly peraluminous S-type granites produced by partial melting of metasedimentary rocks (pelite/psammite-derived melts).

To identify the tectonic settings of granitic magmatism and provide a geodynamic explanation for the generation of S-type granitoids in the present study, we used several tectonic discrimination diagrams. We compiled available data on Early Cretaceous igneous rocks of active continental margins from Li et al. (2016), Aminov et al. (2017) and Liu et al. (2020b) from the Southern Pamir, and Early Cretaceous S-type granite data from the Rushan-Pshart zone, which we plotted in combination with our data (Figure 11). The continental arc rocks were distinctive from the S-type granites and plots in the volcanic arc and syn-to post-collisional fields (Figure 11). We aimed to define whether the granites from this study belonged to volcanic arc, within-plate, oceanic ridge, or collisional granites by utilizing the Ta vs. Yb diagram, the results of which clearly showed that the granites were collisional-related (Figure 11A). In the triangle tectonic discrimination diagram (Hf vs. Ta*3 vs. Rb/13) of Harris et al. (1986), the samples plotted within the syn to post-collisional fields (Figure 11C). However, in the Rb vs. Y+Nb plot by Pearce (1996) and Rb vs. Yb+Ta diagrams, the samples fell within the post-collisional fields (Figures 11A,C).

The sample from Schwab et al. (2004) (111 Ma; S-type granite) similarly fell in syn-collisional to the post-collisional fields (Figures 11B–D). The samples from Li R. H. et al. (2019) (118 Ma) fell into the syn to post-collisional or syn-collisional fields (Figures 11A–D). S-type granites can form in both syn and post-collisional settings (Barbarin, 1996). However, the early Cretaceous granites are highly fractionated S-type granites, which suggests that they formed in an extensional environment. This is inconsistent with the tectonic setting discrimination diagram, which shows a post-collisional setting. Furthermore, the granites had high zircon saturation temperatures (T_{Zr} = 746–813), except for sample Psh-1, which showed a lower temperature (T_{Zr} = 682), consistent with characteristics of post-collisional granites (Liu X. et al., 2021). S-type granites contain abundant inherited zircons; however, our samples showed little inheritance of zircons. This suggests that the samples were dry granites that may have been produced through dehydration (heat fluxed) melting at high temperatures, thus containing small amounts of zircons, compared to wet granites (hydrate melting) that form at lower temperatures and contain abundant inherited zircons (Bea et al., 2021). This implies that the granites were produced in high-temperature dehydration melting conditions with a thermal supply underneath.

Sample Psh-1 had a lower zircon saturation temperature (T_{Zr} = 682); however, Clemens et al. (2020) suggested that lower zircon saturation temperatures do not necessarily indicate that the granitic melt was generated in a low-temperature environment. Clemens et al. (2020) and Zheng and Gao (2021) concluded that most crustal-derived melt (S-type granite) was produced in high-temperature conditions through dehydration (fluid absent) melting in an extensional environment. The mafic magma underplating serves as a driven force/or heat source that causes melting of the supracrustal metasedimentary rocks (Sylvester, 1998; Gao et al., 2016b; Clemens et al., 2020). Therefore, we attributed this concept to our studied granites, which were formed and emplaced in the same way, as shown in the petrogenesis and discrimination diagrams. We concluded that the granitic rocks in the present study formed in an initial post-collisional setting in an extensional environment. Our conclusion is consistent with those reported highly fractionated S-type granites, which were interpreted to form in an extensional environment (Huang and Jiang, 2014; Zhu et al., 2020; Liu X. et al., 2021).

5.2.2 Mafic dikes

We did not obtain a precise age (only a single-zircon age of 121 Ma; Figure 4E) to constrain the exact emplacement time of the diabase dikes (samples of Psh-6; 7). The dikes intruded the Early Cretaceous granitic pluton of 124–118 Ma, suggesting a younger age than 124 Ma (Figures 3A,B). Thus, we tentatively interpreted them to have formed in the late Early Cretaceous, nearly contemporaneous with granitic rocks from this study. Hydrothermal alteration and post-emplacement metamorphism can change/or modify the concentration of mobile elements such as Na, K, R, B, Sr, and Pb (Hart and Staudigel, 1982; Photiades et al., 2003). It is generally accepted that the high-field strength

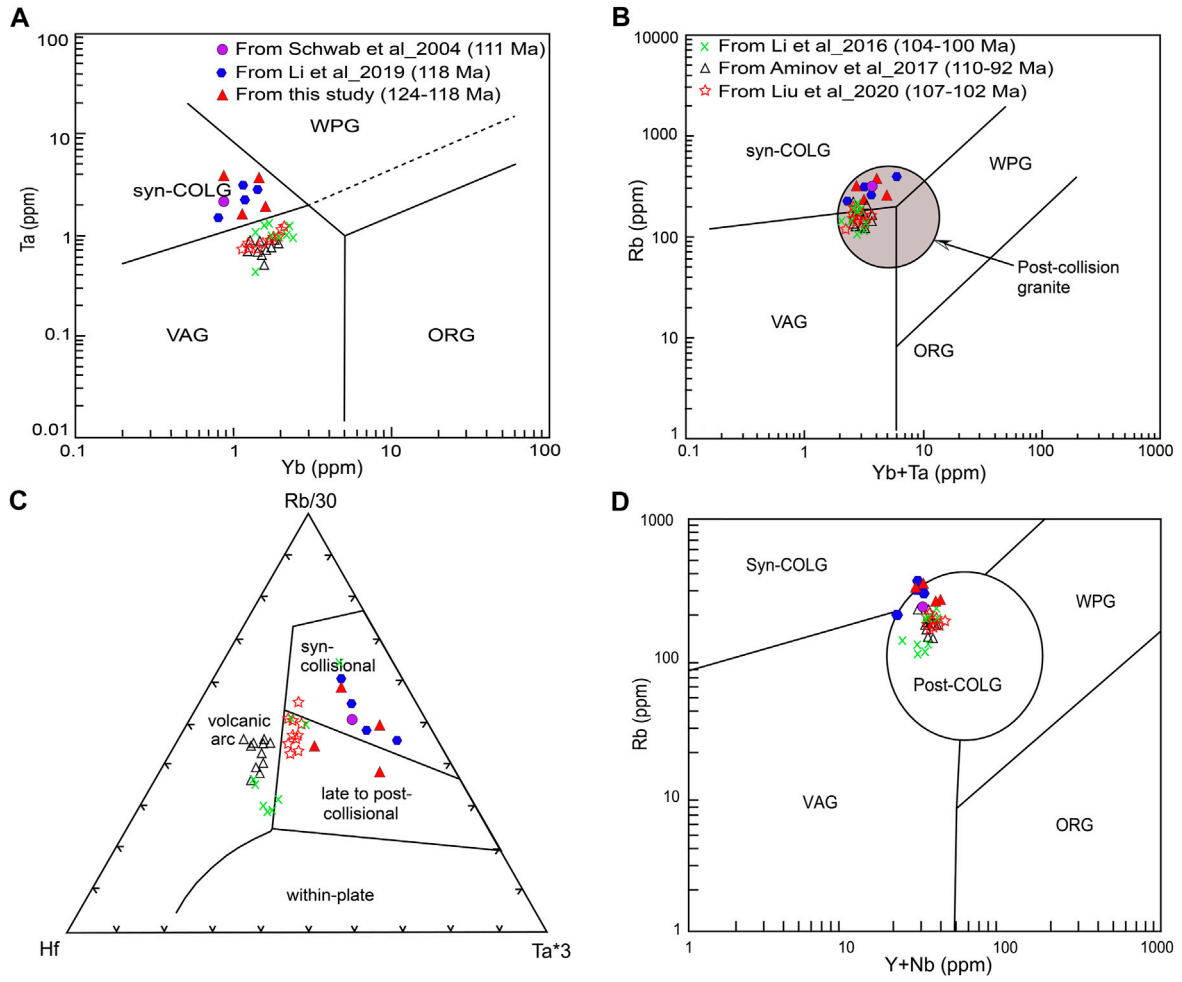

FIGURE 11
Trace element geotectonic discrimination diagrams. **(A)** Ta vs. Yb, **(B)** Rb vs. (Yb+Ta), **(C)** Hf-Ta*3-Rb/30, and **(D)** Rb vs. (Y+Nb) (after Pearce (1996) and Harris et al. (1986)). Abbreviations: WPG, within-plate granites; syn COLG, syn-collisional granites; VAG, volcanic arc granites; ORG, ocean ridge granites. The reference data are compiled from Schwab et al. (2004); Li et al. (2016); Aminov et al. (2017); Li R. H. et al. (2019) and Liu et al. (2020b).

elements (HFSEs) are less susceptible to alteration (Floyd and Winchester, 1975). Therefore, we used HFSEs (Zr, Y, Nb, Th, Ta, and Hf) to decipher the tectonic setting of the mafic dikes.

The samples showed alkaline affinity (Figure 5A; Supplementary Table S2B) but plotted within the field of within-plate tholeiite rocks on Th-Ta-Hf/3 (Figure 12B). In the Zr vs. Zr/Y and Zr-Y*3-Ti/100 diagrams, the samples plotted in the within-plate basalt field (Figures 12A,D). Thus, the geochemical data favor that the diabase dikes that intruded the Early Cretaceous granites formed in an extensional tectonic setting immediately after the Early Cretaceous granites. However, the samples plotted within the field of the island arc calk-alkaline basalt in the Th-Ta-Hf/3 diagram, suggesting that the mantle sources were metasomatized (giving an arc-related signature to the diabase dikes) by slab-released components, which is consistent with the Th/Nb and U/Th diagrams (Figure 10). Therefore, the mafic diabase dikes were derived from a metasomatized mantle source in an extensional environment.

5.3 Closure timing and post-collisional magmatism

The Central and Southern Pamir (Cimmerides) are the detached fragments/blocks of Gondwana, which drifted northward during the opening of the Neo-Tethys Ocean and amalgamated to the southern margin of Eurasia in the Mesozoic (Sengör, 1979; Burtman and Molnar, 1993; Schwab et al., 2004; Burtman, 2010; Robinson et al., 2012; Angiolini et al., 2013, 2015; Villarreal et al., 2020). Nowadays, the RPSZ marks the site where

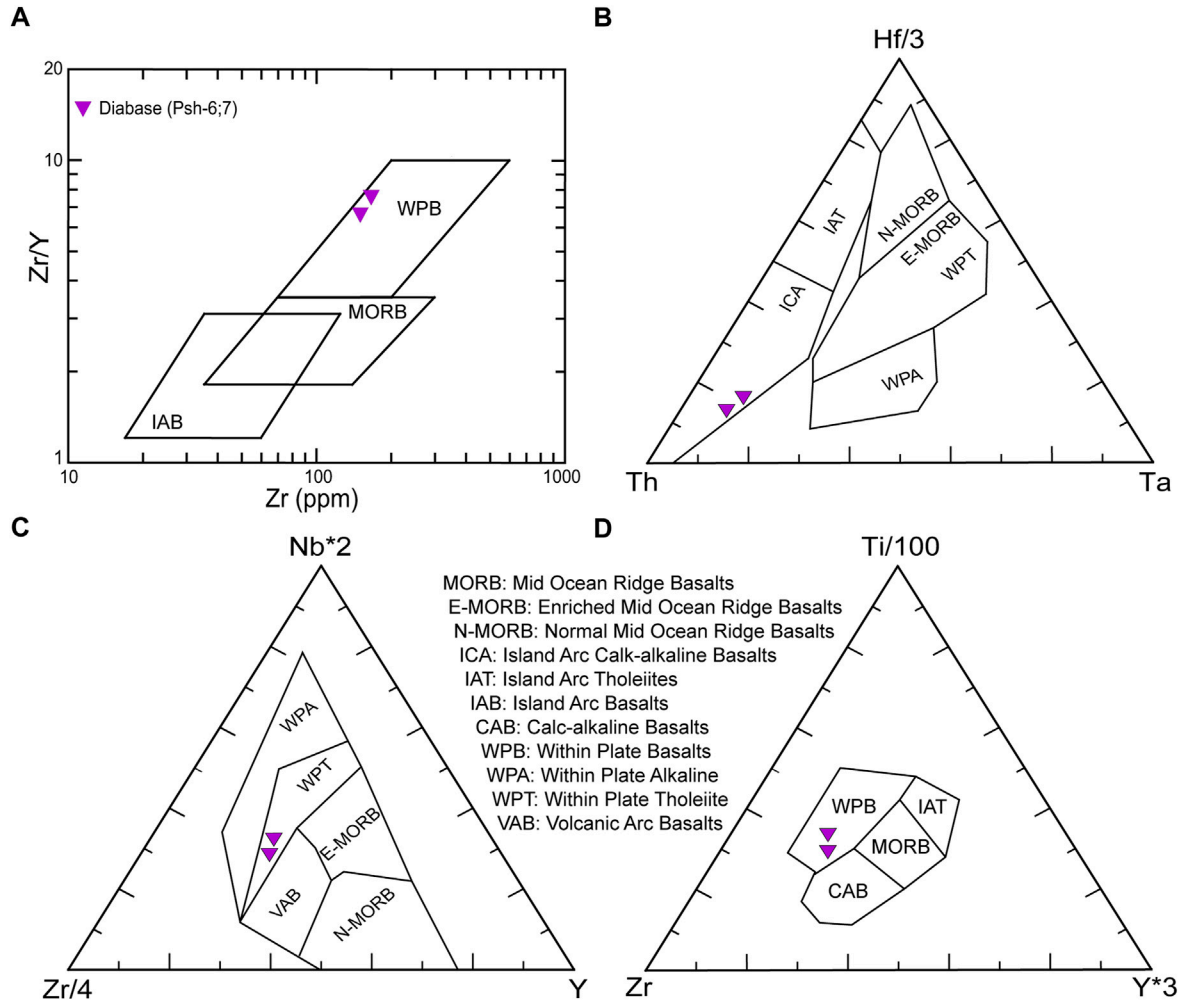

FIGURE 12
Tectonic setting discrimination diagrams for the diabase dikes from Kara-Djilga 2 valley, Pshart complex. **(A)** Zr/Y vs. Zr (ppm) (Pearce and Norry, 1979); **(B)** Th-Ta- Hf/3 (Wood, 1980); **(C)** Nb*2- Zr/4-Y (Meschede, 1986); and **(D)** Zr-Y*3-Ti/100 (Pearce and Cann, 1973).

the Central and Southern Pamir terranes collided after the complete consumption of the Rushan–Pshart Ocean. Generally, the rifting time between the Central and Southern Pamir has been interpreted as the Early Permian to Middle Triassic, based on the Lower Permian basaltic rocks within the western Pshart zone and SE Pamir (Shindy Formation) (Pashkov and Shvol′man, 1979; Leven, 1995; Angiolini et al., 2015). However, it remains unclear whether the Rushan–Pshart Ocean was completely consumed by the Late Triassic–Early Jurassic or later. Several studies suggested the Late Triassic–Early Jurassic coalescence of the Central and Southern Pamir based on the Cimmerian nonconformity in the Southern Pamir (Angiolini et al., 2013; Robinson, 2015; Chapman et al., 2018a; Villarreal et al., 2020). The presence of Late Triassic I-type arc-related granitoids (206-201Ma; U-Pb dating) on the southern edge of the Central Pamir led Wang S. et al. (2020) to the same conclusion.

However, several lines of evidence contradict these interpretations:

1) The presence of 198–170 Ma arc-related granitic intrusions in the southernmost part of the Pshart complex (Schwab et al., 2004; Chapman et al., 2018b) and the Late Jurassic cooling age (Schwab et al., 2004). Schwab et al. (2004) also reported the 151 Ma ($^{40}Ar/^{39}Ar$ of muscovite) monzogranite pebble (sample 96P4e) from the conglomerate of possibly Miocene ages within the western Pshart intermontane valley.
2) The presence of andesite, andesitic basalt, and tuff in combination with limestone and sandstone and deep marine rocks, including chert and cherty-shale, of Late

Jurassic age (Etchki–Tushar Formation) (Pashkov and Shvol′man, 1979; Leven, 1995), suggests magmatic activity and presence of the oceanic basin by that time.

3) The presence of a 118-Ma two-mica monzogranite with strongly peraluminous S-type granite characteristics in the south-western part of the Central Pamir has been interpreted to form in a syn-collisional setting during the final closure of the Rushan–Pshart Ocean (Li R. H. et al., 2019). A slightly younger two-mica monzogranite of 111 Ma (Rb-Sr age; sample P7) from the Pshart complex was interpreted as being syn-collisional (Schwab et al., 2004) (Figure 1).
4) The presence of strongly deformed carbonate rocks of the Central and Southern Pamir, with a non-conforming overlay of sandstones and conglomerates of Cretaceous age, reported by Shvol'man (1978) and Ruzhentsev and Shvol'man (1981), was associated with the closure timing of the Rushan–Pshart Ocean.

Therefore, the closure timing of the Rushan–Pshart Ocean may have been younger than the Late Triassic–Early Jurassic. The volcaniclastic sandstone in the southernmost Central Pamir (111 Ma) bears a strong similarity to the Cretaceous sedimentary and volcanic rocks of the Bangong–Nujiang zone and northern Lhasa terrane (He et al., 2019). We agree with He et al. (2019) that the proposed Cimmerian nonconformity (Permian–Triassic strata composed of quartzite, slate, and carbonate) possibly formed in retro-arc deformation during the subduction of the Rushan–Pshart oceanic lithosphere rather than the collision of the Central and Southern Pamir.

Our petrological, geochemical, and geochronological data revealed that the 124–118 Ma granites were highly fractionated, strongly peraluminous S-type granite generated from the partial melting of metasedimentary rocks in an initial post-collisional stage (Figure 13A). These findings were deduced from mostly well-studied regions such as the Himalayas, Alps, and other orogens in which the post-collisional granites were emplaced after 5–20 Ma (maximum 26 Ma), following the main collisional events (Sylvester, 1998; Zheng and Gao, 2021). If the Late Triassic to Early Jurassic collision of the Central and Southern Pamir were the case (Villarreal et al., 2020), it would take ca. 75 Ma for the emplacement of post-collisional granitoids in this study, which is unlikely. This is also not consistent with the four facts and/or arguments aforementioned. Therefore, it is likely that the granites were emplaced immediately after the final closure of the Rushan–Pshart Ocean in the Late Jurassic–Early Cretaceous. This view is supported by the presence of the volcanic rocks and cherts of the Late Jurassic and the absence of younger ages (as described in the previous section). The minimum U-Pb age for the inherited zircon from the granites is the late Lower Jurassic (180 Ma; Figure 4C), indicating active sedimentation by that time. The Late Jurassic to Early Cretaceous compressional tectonic switched to an extensional regime, as indicated by the post-collisional, highly fractionated peraluminous S-type granites. The mafic dikes were emplaced in an extensional setting (Figures 12A,C,D). In the Th-Ta-Hf/3 diagram, the samples plot in the island arc calk-alkaline basalt field (Figure 12B), implying that the slab-released fluids of the foundered Rushan–Pshart oceanic lithosphere compositionally modified the upwelling asthenospheric mantle (Figure 10).

After the Late Jurassic–Early Cretaceous closure and collision of the Central and Southern Pamir, the oceanic lithosphere sank after detachment, which caused an upwelling of mafic magma and its underplating, which constituted the heat source for the partial melting of metasedimentary rocks. Furthermore, the partially melted and segregated granitic magma underwent fractional crystallization during its ascent and emplacement. Continuous local extension, asthenospheric mantle upwelling, and lithospheric thinning caused the emplacement of the diabase dikes (Figure 13C).

5.4 Implications for the suture/terrane correlations associated with the closure of Meso-Tethys Ocean

The Cenozoic India–Asia collision and the northward translation of Pamir relative to the Tibetan Plateau make the current terranes and suture correlations very complicated (Figure 1) (Burtman and Molnar, 1993; Sobel and Dumitru, 1997; Lacassin et al., 2004; Robinson, 2009; Cowgill, 2010). It is not clear whether the Rushan–Pshart Ocean is the Meso-Tethys or Paleo-Tethys Ocean. One group of scholars correlated the RPSZ to the Longmu Co-Shuanghu suture zone (Burtman and Samygin, 2001; Burtman, 2010; Angiolini et al., 2013; Wang S. et al., 2020; Liu et al., 2020c), which bisects the Northern and Southern Qiantang terranes (Liu et al., 2011; Liang et al., 2012; Zhao et al., 2015). Another group of scholars directly connected the RPSZ to the Bangong–Nujiang suture (Lacassin et al., 2004; Schwab et al., 2004; Valli et al., 2008; Li R. H. et al., 2019), thus considering it to preserve the remnant of the Meso-Tethys Ocean (Shvol′man, 1978; Burtman and Molnar, 1993; Burtman, 1994). To the west in Afghanistan, the Farah-Rud zone likely represents the extension of the RPSZ (Tapponnier et al., 1981; Montenat, 2009). Zanchetta et al. (2018) considered the RPSZ to be an independent suture that was not correlated to any of the aforementioned sutures.

Several lines of similarities and arguments between the RPSZ-Southern Pamir and Bangong–Nujiang and Lhasa terrane are discussed below.

The deformation and thrusting of Cretaceous strata in the Southern Pamir and Central Pamir (Chapman et al., 2018a; He et al., 2019) resemble those of the Cretaceous non-marine strata (southward propagation) of the Bangong–Nujiang suture and northern Lhasa terrane (Kapp et al., 2007; Volkmer et al., 2014; Sun et al., 2015).

Regarding the evolution and subduction polarity of the Bangong–Nujiang Ocean, a northward (Yin and Harrison,

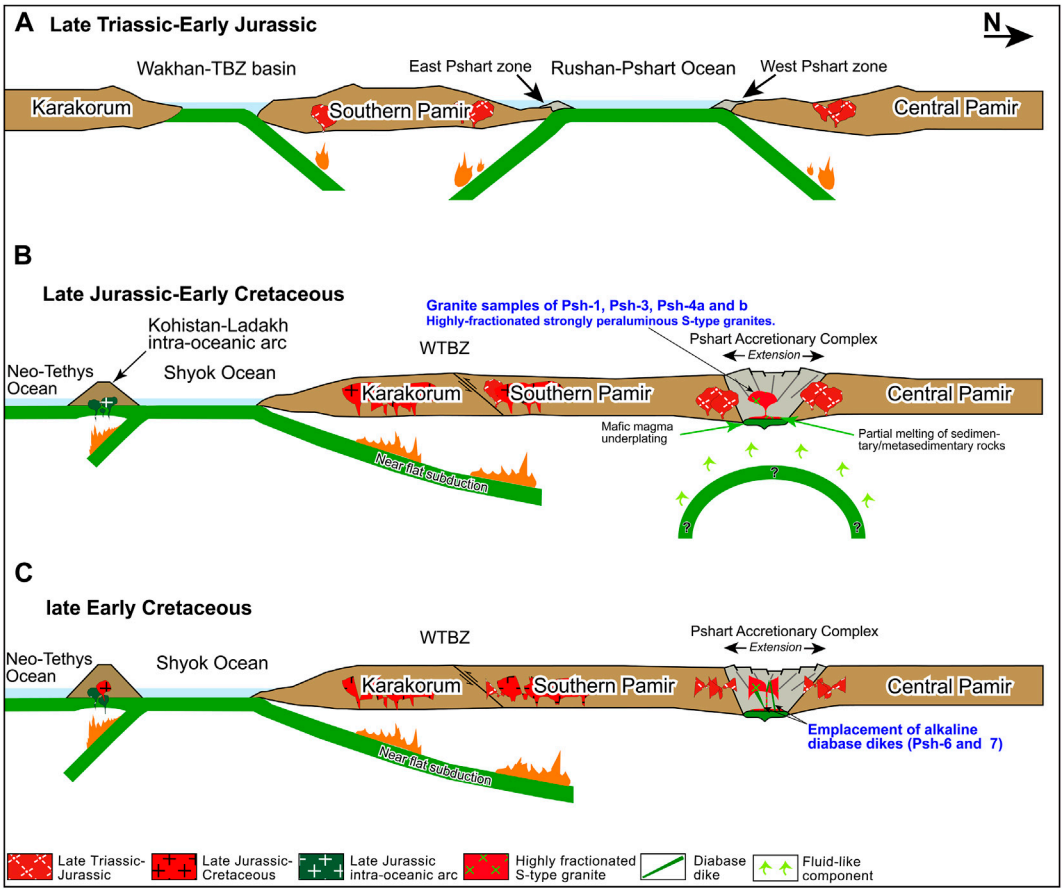

FIGURE 13
Schematic illustration of the Mesozoic evolution of Pamir: **(A)** Initiation of double-sided subduction of the Rushan–Pshart oceanic lithosphere, initial growth of accretionary complexes (East and West Pshart zones), and generation of the Late Triassic–Early Jurassic arc granitoids in the Central and Southern Pamir; **(B)** Late Jurassic–Early Cretaceous collision of the Central and Southern Pamir, underplating of the mafic magma and partial melting of the sedimentary/metasedimentary rocks, and emplacement of highly fractionated, strongly peraluminous S-type granite in the initial post-collisional setting. **(C)** Subsequent extension and emplacement of diabase dikes. The northward subduction is adapted from Wang S. et al. (2020). The southward subduction of the Shyok oceanic lithosphere and formation of the Kohistan–Ladakh intra-oceanic arc were adapted from Saktura et al. (2021).

2000; Li et al., 2014; Liu et al., 2017), southward (Zhu et al., 2013; Li S M et al., 2018; Ma et al., 2020), or double-sided subduction and subsequent "soft collision" have been proposed (Fan et al., 2014a; 2014b; Wang et al., 2016; Zhu et al., 2016; Tang et al., 2018; Li S. et al., 2019; Liu H. et al., 2020). For the Rushan–Pshart Ocean, the southward (Angiolini et al., 2013; Robinson, 2015; Zanchetta et al., 2018; Yogibekov et al., 2020), northward (Schwab et al., 2004; Wang S. et al., 2020), and possibly double-sided subduction (Robinson et al., 2012; Robinson, 2015; Li R. H. et al., 2019) have been proposed. The Upper Triassic–Jurassic plutons are pervasively intruded to either side of the RPSZ (Figures 1, 2A), which were formed during the double-sided subduction. The Eastern and Western Pshart zones developed in different subduction zones (Leven, 1995; Zanchetta et al., 2018). The lithology of the Eastern Pshart zone greatly differs from that of the Western Pshart zone, with only basalts common between zones. However, the basaltic rocks from the West Pshart are Early Permian, while those of the East Pshart are Late Permian to Triassic (Pashkov and Shvol'man, 1979; Leven, 1995). In this context, we depict the double-sided subduction for the Rushan–Pshart Ocean (Figure 13A). No high-grade metamorphic rocks have been documented along the RPSZ and the Bangong–Nujiang suture likely does not preserve Cretaceous high-grade metamorphic rocks, which reflects a soft collision (arc–arc collision) (Zhu et al., 2016). Conversely, the Longmu Cu-Shuanghu suture is defined by an exposed high-pressure metamorphic belt from the Triassic. The Longmu Co-Shuanghu Paleo-Tethys Ocean opened in the Early Ordovician to Silurian (480–428 Ma) and closed by the Middle Triassic (220 Ma) (Zhai et al., 2013b, 2016, 2011; Hu et al., 2014; Metcalfe, 2021). The newly discovered Silurian subduction-related rocks in the northern margin of the South Qiangtang

terrane (Xiangtaohu intrusive complex; 430–437 Ma) are evidence for the southward subduction of the Proto-Tethys Longmu Co-Shuanghu Ocean by that time (Liu H. et al., 2021). In contrast, the opening time of the Rushan–Pshart Ocean has been interpreted as the Late Carboniferous–Early Permian to the Middle Triassic (Pashkov and Shvol′man, 1979; Burtman and Molnar, 1993; Leven, 1995; Angiolini et al., 2015). Similarly, the opening time of the Bangong–Nujiang Meso-Tethys Ocean is considered to be the Late Carboniferous–Early Permian (Pan et al., 2006; Zhai et al., 2013a; Chen S. S. et al., 2017; Fan et al., 2021c), with a close timing of the Late Jurassic–Early Cretaceous (Li S. et al., 2020; Li et al., 2019 S.; Hu et al., 2019; Wang W. et al., 2020; Ma et al., 2020; Fan et al., 2021b). In this study, we concluded that the Rushan–Pshart Ocean closed in the Late Jurassic–Early Cretaceous (section 5.3; Figure 13B). The Late Carboniferous–Early Permian opening of the Rushan–Pshart and Bangong–Nujiang Oceans was associated with mantle plume activity (Pashkov and Shvol′man, 1979; Leven, 1995; Angiolini et al., 2013; Fan et al., 2021c). However, the formation of the Longmu-Co Shuanghu Ocean was induced with a back-arc basin opening in response to the southward subduction of the Proto-Tethys oceanic lithosphere (Xu et al., 2020; Metcalfe, 2021).

The Early Cretaceous arc-related igneous rocks are widespread in the Southern Pamir (105 Ma high flux event) and represent the product of a northward subduction of the Neo-Tethyan (Shyok) oceanic lithosphere (Schwab et al., 2004; Aminov et al., 2017; Chapman et al., 2018b; Liu et al., 2020b). In the Tibetan Plateau, Cretaceous magmatism with high a flux event occurring 110 Ma is widely distributed in the Lhasa terrane, which is interpreted to have formed in response to the near-flat northward subduction of the Neo-Tethys oceanic lithosphere (Zhang et al., 2010; Zhang K.-J. et al., 2012; Kang et al., 2014; Zheng et al., 2019), southward subduction of the Bangong-Nujiang Ocean, or a combination of both (Du et al., 2011; Zhu et al., 2013; Li Y et al., 2018; Ma et al., 2020). Jurassic arc-related granitoids of 198–170 Ma have been reported from the southern edge of the Pshart complex (Schwab et al., 2004; Chapman et al., 2018b), which are identical to the arc-related granitoids (185–170 Ma) of the Amdo region (Guynn et al., 2006). A systematic study of sedimentary rocks in the Garze area of the Bangong–Nujiang suture revealed that the sediments were sourced from the Early Jurassic arc of the Southern Qiantang terrane, which may have been completely eroded (Li S. et al., 2019). These findings fit well and record a similar pre-Cenozoic history of the Southern Pamir–RPSZ and Bangong–Nujiang suture and Lhasa terrane and differ greatly from that of the Longmu Co-Shuanghu zone.

However, the relative movement along the Karakoram fault hampered the correlations of the RPSZ and Bangong–Nujiang suture, which requires a displacement of up to 300 km. Seismological and receiver functions studies revealed 300 km of subducted Asian crust beneath Pamir, thus assuming the same amount for the northward translation of Pamir relative to the major part of the Tibetan Plateau (Burtman and Molnar, 1993; Schneider et al., 2019; Bloch et al., 2021; Xu et al., 2021). Robinson (2009) reported a displacement of approximately 167 km along the Karakoram fault based on the results of the analysis of satellite images of the Upper Triassic–Lower Jurassic carbonates of the Aghil Formation. A recent study in the northeastern Pamir proposed that the present curvature shape of the Pamir orogen is inherited from Late Paleozoic embayment with negligible left-lateral displacement along the Darvaz fault, rather than due to a Cenozoic northward translation (Li Y.-P. et al., 2020). All these facts support the complicated geological structure of the Pamir, thus making it difficult to precisely define the amount of its displacement relative to the adjacent regions. Additional undocumented displacements may also exist along the Karakoram fault and its branches. More broadly, it is noteworthy that the RPSZ–Bangong-Nujiang and Southern Pamir-Lhasa terrane have similar pre-Cenozoic tectono-magmatic histories (as aforementioned), as well as the opening and closure timings of the oceans.

Thus, based on our observations and the aforementioned discussion, we tentatively propose that the Bangong–Nujiang zone may represent the eastern extension of the RPSZ and that the Farah–Rud zone is the possible western "time-correlative"/continuation of the given suture. However, we cannot preclude the possibility that the Rushan–Pshart Ocean evolved separately without a direct connection to the east, as proposed by Zanchetta et al. (2018). We consider the Rushan–Pshart Ocean to be the Meso-Tethys Ocean.

6 Conclusion

The data on granites and diabase dikes newly acquired in the present study, combined with previously published data, suggest the following conclusions.

1) The Early Cretaceous granites from the Pshart complex were emplaced during 124–118 Ma and are interpreted here as highly fractionated, strongly peraluminous S-type granite.
2) The underplating of mafic magma served as a heat source for the partial melting of metasedimentary rocks. The granitic melt formed in a plagioclase stability field and underwent subsequent fractional crystallization during its ascent.
3) The diabase dikes were derived from a metasomatized source and were emplaced within an extensional tectonic setting.
4) The Early Cretaceous, highly fractionated, and strongly peraluminous S-type granites of the Pshart complex represent the product of metasedimentary-derived melt, which were formed in the post-collisional environment after the final closure of the Rushan–Pshart Meso-Tethys Ocean. Thus, the studied rocks record the change in

geodynamic regime from compressional to extensional. The diabase dikes were emplaced during subsequent continued local extension.

5) The RPSZ may represent the western continuation of the Bangong–Nujiang suture of the Tibetan Plateau and it is "time-correlative" to the Farah-Rud zone in Afghanistan.

Data availability statement

The original contributions presented in the study are included in the article/Supplementary Material; further inquiries can be directed to the corresponding authors.

Author contributions

DY and MS wrote the article. WX, YM, CZ, HY, and QM revised the manuscript, conceived the experiments, and contributed to the data interpretation. The fieldwork and preliminary study of samples were carried out by JA, GK, and SA. HY conducted the geochemical analyses. All authors have read and agreed to the published version of the manuscript.

Funding

This study was financially supported by the National Natural Science Foundation of China (42072269), the Science and Technology Major Project of Xinjiang Uygur Autonomous Region, China (2021A03001), the Project of China-Pakistan Joint Research Center on Earth Sciences of the CAS (131551KYSB20200021), and the PetroChina Science and Technology Project (2021DJ0301) from the Research Institute of Petroleum Exploration and Development, China National Petroleum Corporation, Beijing, China.

Acknowledgments

This study was conducted in Tajikistan. We thank the staff at the Research Center for Ecology and Environment of Central Asia (Dushanbe subcenter) for their assistance. Our special to the Alliance of International Science Organization (ANSO) under the Chinese Academy of Sciences (CAS) for the scholarship award to conduct the doctoral studies (PhD) of which this study is a part. We are grateful to Zhixin Zhang and Jilin Wang for their assistance during the fieldwork in Pamir (Tajikistan). We also thank the *Journal*'s formal reviewers and editors for providing thoughtful and constructive reviews of our manuscript.

Conflict of interest

The authors declare that the research was conducted in the absence of any commercial or financial relationships that could be construed as a potential conflict of interest.

Publisher's note

Supplementary material

The Supplementary Material for this article can be found online at: https://www.frontiersin.org/articles/10.3389/feart.2022.1090952/full#supplementary-material

References

Aminov, J., Ding, L., Mamadjonov, Y., Dupont-Nivet, G., Aminov, J., Zhang, L.-Y., et al. (2017). Pamir Plateau formation and crustal thickening before the India-Asia collision inferred from dating and petrology of the 110–92 Ma Southern Pamir volcanic sequence. *Gondwana Res.* 51, 310–326. doi:10.1016/j.gr.2017.08.003

Angiolini, L., Zanchi, A., Zanchetta, S., Nicora, A., and Vezzoli, G. (2013). The cimmerian geopuzzle: New data from South Pamir. *Terra* 25, 352–360. doi:10.1111/ter.12042

Angiolini, L., Zanchi, A., Zanchetta, S., Nicora, A., Vuolo, I., Berra, F., et al. (2015). From rift to drift in South Pamir (Tajikistan): Permian evolution of a Cimmerian terrane. *J. Asian Earth Sci.* 102, 146–169. doi:10.1016/j.jseaes.2014.08.001

Barbarin, B. (1999). A review of the relationships between granitoid types, their origins and their geodynamic environments. *Lithos* 46, 605–626. doi:10.1016/s0024-4937(98)00085-1

Barbarin, B. (1996). Genesis of the two main types of peraluminous granitoids. *Geol.* 24, 295–298. doi:10.1130/0091-7613(1996)024<0295:gottmt>2.3.co;2

Bartoli, O., Cesare, B., Poli, S., Bodnar, R. J., Acosta-Vigil, A., Frezzotti, M. L., et al. (2013). Recovering the composition of melt and the fluid regime at the onset of crustal anatexis and S-type granite formation. *Geology* 41, 115–118. doi:10.1130/G33455.1

Bea, F., Morales, I., Molina, J. F., Montero, P., and Cambeses, A. (2021). Zircon stability grids in crustal partial melts: Implications for zircon inheritance. *Contrib. Mineral.* . 176, 18–13. doi:10.1007/s00410-021-01772-x

Beard, J. S., Abitz, R. J., and Lofgren, G. E. (1993). Experimental melting of crustal xenoliths from Kilbourne Hole, New Mexico and implications for the contamination and Genesis of magmas. *Contr. Mineral.* . 115, 88–102. doi:10.1007/BF00712981

Bloch, W., Schurr, B., Yuan, X., Ratschbacher, L., Reuter, S., Kufner, S. K., et al. (2021). Structure and stress field of the lithosphere between Pamir and tarim. *Geophys. Res. Lett.* doi:10.31223/X5N60C

Burtman, V., and Samygin, S. (2001). Tectonic evolution of high Asia in the paleozoic and mesozoic. *Geotectonics* 35, 276–294.

Burtman, V. S. (1994). Meso-Tethyan oceanic sutures and their deformation. *Tectonophysics* 234, 305–327. doi:10.1016/0040-1951(94)90230-5

Burtman, V. S., and Molnar, P. H. (1993). Geological and geophysical evidence for deep subduction of continental crust beneath the Pamir. *Geol. Soc. Am. Special Pap.* 281, 1–76. doi:10.1130/SPE281-p1

Burtman, V. S. (2010). Tien Shan, Pamir, and Tibet: History and geodynamics of phanerozoic oceanic basins. *Geotecton.* 44, 388–404. doi:10.1134/S001685211005002X

Champion, D. C., and Bultitude, R. J. (2013). The geochemical and Sr-Nd isotopic characteristics of Paleozoic fractionated S-types granites of north Queensland: Implications for S-type granite petrogenesis. *Lithos* 162, 37–56. doi:10.1016/j.lithos.2012.11.022

Chapman, J. B., Robinson, A. C., Carrapa, B., Villarreal, D., Worthington, J., DeCelles, P. G., et al. (2018a). Cretaceous shortening and exhumation history of the South Pamir terrane. *Lithosphere* 10, 494–511. doi:10.1130/L691.1

Chapman, J. B., Scoggin, S. H., Kapp, P., Carrapa, B., Ducea, M. N., Worthington, J., et al. (2018b). Mesozoic to cenozoic magmatic history of the Pamir. *Earth Planet. Sci. Lett.* 482, 181–192. doi:10.1016/j.epsl.2017.10.041

Chappell, B. (1999). Aluminium saturation in I-and S-type granites and the characterization of fractionated haplogranites. *Lithos* 46, 535–551. doi:10.1016/S0024-4937(98)00086-3

Chappell, B., and White, A. (1992). I-And S-type granites in the lachlan fold belt. *Trans. R. Soc. Edinb. Earth Sci.* 83, 1–26. doi:10.1130/SPE272-p1

Chappell, B., and White, A. (1974). Two contrasting granite types. Pacif. *Geology* 8, 173–174.

Chappell, B. W., and White, A. J. (2001). Two contrasting granite types: 25 years later. *Aust. J. earth Sci.* 48, 489–499. doi:10.1046/j.1440-0952.2001.00882.x

Chen, S., Chen, H., Zhu, K., and Tao, Y. (2021). Petrogenesis of the middle–late triassic S-and I-type granitoids in the eastern Pamir and implications for the tanymas–jinshajiang Paleo-Tethys Ocean. *Int. J. Earth Sci.* 110, 1213–1232. doi:10.1007/s00531-021-02013-z

Chen, S. S., Shi, R. D., Fan, W. M., Gong, X. H., and Wu, K. (2017a). Early Permian mafic dikes in the Nagqu area, central Tibet, China, associated with embryonic oceanic crust of the Meso-Tethys Ocean. *J. Geophys. Res. Solid Earth* 122, 4172–4190. doi:10.1002/2016JB013693

Chen, Y.-X., Zhou, K., and Gao, X.-Y. (2017b). Partial melting of ultrahigh-pressure metamorphic rocks during continental collision: Evidence, time, mechanism, and effect. *J. Asian Earth Sci.* 145, 177–191. doi:10.1016/j.jseaes.2017.03.020

Clarke, D. B. (2019). The origins of strongly peraluminous granitoid rocks. *Can. Mineralogist* 57, 529–550. doi:10.3749/canmin.1800075

Clemens, J. D., Stevens, G., and Bryan, S. E. (2020). Conditions during the formation of granitic magmas by crustal melting–hot or cold; drenched, damp or dry? *Earth-Science Rev.* 200, 102982. doi:10.1016/j.earscirev.2019.102982

Clemens, J. (2003). S-Type granitic magmas—Petrogenetic issues, models and evidence. *Earth-Science Rev.* 61, 1–18. doi:10.1016/S0012-8252(02)00107-1

Clemens, J., and Stevens, G. (2012). What controls chemical variation in granitic magmas? *Lithos* 134, 317–329. doi:10.1016/j.lithos.2012.01.001

Corfu, F., Hanchar, J. M., Hoskin, P. W., and Kinny, P. (2003). Atlas of zircon textures. *Rev. Mineral. Geochem.* 53, 469–500. doi:10.2113/0530469

Cowgill, E. (2010). Cenozoic right-slip faulting along the eastern margin of the Pamir salient, northwestern China. *Geol. Soc. Am. Bull.* 122, 145–161. doi:10.1130/B26520.1

Dong, Y., Zhang, G., Neubauer, F., Liu, X., Hauzenberger, C., Zhou, D., et al. (2011). Syn-and post-collisional granitoids in the central tianshan orogen: Geochemistry, geochronology and implications for tectonic evolution. *Gondwana Res.* 20, 568–581. doi:10.1016/j.gr.2011.01.013

Donnely, K. E., Goldstain, S. L., Langmuir, C. H., and Spiegelman, M. (2004). Origin of enriched ocean ridge basalts and implications for mantle dynamics. *Earth Planet. Sci. Lett.* 226, 347–366. doi:10.1016/j.epsl.2004.07.019

Dronov, V. I. (1964). On the south boundary of Central Pamir. Dushanbe (in Russia). *Mater. po Geol. Pamira* 2, 133–137.

Du, D., Qu, X., Wang, G., Xin, H., and Liu, Z. (2011). Bidirectional subduction of the middle tethys oceanic basin in the west segment of bangonghu-nujiang suture, Tibet: Evidence from zircon U-Pb LAICPMS dating and petrogeochemistry of arc granites. *Acta Petrol. Sin.* 27, 1993–2002.

Fan, B., Liu, M., He, Z., Meng, G., Ma, Z., and Li, L. (2021a). Mesozoic-cenozoic tectonic evolution and uplift in Pamir: Application of fission track thermochronology. *Acta Geol. sinica-. Engl. Ed.* 95, 780–793. doi:10.1111/1755-6724.14671

Fan, J.-J., Li, C., Xie, C.-M., and Wang, M. (2014a). Petrology, geochemistry, and geochronology of the zhonggang ocean island, northern Tibet: Implications for the evolution of the banggongco–nujiang oceanic arm of the neo-tethys. *Int. Geol. Rev.* 56, 1504–1520. doi:10.1080/00206814.2014.947639

Fan, J.-J., Li, C., Xu, J.-X., and Wang, M. (2014b). Petrology, geochemistry, and geological significance of the Nadong ocean island, Banggongco–Nujiang suture, Tibetan plateau. *Int. Geol. Rev.* 56, 915–928. doi:10.1080/00206814.2014.900651

Fan, J.-J., Niu, Y., Liu, Y.-M., and Hao, Y.-J. (2021b). Timing of closure of the Meso-Tethys Ocean: Constraints from remnants of a 141– 135 Ma ocean island within the Bangong– nujiang suture zone, Tibetan plateau. *GSA Bull.* 133, 1875–1889. doi:10.1130/B35896.1

Fan, J.-J., Niu, Y., Luo, A.-B., Xie, C.-M., Hao, Y.-J., and Liu, H.-Y. (2021c). Timing of the Meso-Tethys Ocean opening: Evidence from permian sedimentary provenance changes in the South Qiangtang terrane, Tibetan plateau. *Palaeogeogr. Palaeoclimatol. Palaeoecol.* 567, 110265. doi:10.1016/j.palaeo.2021.110265

Floyd, P. A., and Winchester, J. (1975). Magma type and tectonic setting discrimination using immobile elements. *Earth Planet. Sci. Lett.* 27, 211–218. doi:10.1016/0012-821X(75)90031-X

Förster, H. J., Tischendorf, G., and Trumbull, R. B. (1997). An evaluation of the Rb vs.(Y+ Nb) discrimination diagram to infer tectonic setting of silicic igneous rocks. *Lithos* 40, 261–293. doi:10.1016/S0024-4937(97)00032-7

Frost, B. R., Barnes, C. G., Collins, W. J., Arculus, R. J., Ellis, D. J., and Frost, C. D. (2001). A geochemical classification for granitic rocks. *J. petrology* 42, 2033–2048. doi:10.1093/petrology/42.11.2033

Gao, L.-E., Zeng, L., and Asimow, P. D. (2017). Contrasting geochemical signatures of fluid-absent versus fluid-fluxed melting of muscovite in metasedimentary sources: The Himalayan leucogranites. *Geology* 45, 39–42. doi:10.1130/G38336.1

Gao, P., Zheng, Y.-F., and Zhao, Z.-F. (2016a). Distinction between S-type and peraluminous I-type granites: Zircon versus whole-rock geochemistry. *Lithos* 258, 77–91. doi:10.1016/j.lithos.2016.04.019

Gao, P., Zheng, Y. F., and Zhao, Z. F. (2016b). Experimental melts from crustal rocks: A lithochemical constraint on granite petrogenesis. *Lithos* 266, 133–157. doi:10.1016/j.lithos.2016.10.005

Girardi, J. D., Patchett, P. J., Ducea, M. N., Gehrels, G. E., Cecil, M. R., Rusmore, M. E., et al. (2012). Elemental and isotopic evidence for granitoid Genesis from deep-seated sources in the Coast Mountains Batholith, British Columbia. *J. petrology* 53, 1505–1536. doi:10.1093/petrology/egs024

Groppo, C., Rolfo, F., McClelland, W. C., and Coble, M. A. (2019). Pre-cenozoic evolution of the Aghil range (Western Tibetan plateau): A missing piece of the tibet-pamir-karakorum geopuzzle. *Gondwana Res.* 69, 122–143. doi:10.1016/j.gr.2018.12.006

Guynn, J. H., Kapp, P., Pullen, A., Heizler, M., Gehrels, G., and Ding, L. (2006). Tibetan basement rocks near Amdo reveal "missing" Mesozoic tectonism along the Bangong suture, central Tibet. *Geol.* 34, 505–508. doi:10.1130/G22453.1

Harris, N. B., Pearce, J. A., and Tindle, A. G. (1986). Geochemical characteristics of collision-zone magmatism. *Geol. Soc. Lond. Spec. Publ.* 19, 67–81. doi:10.1144/gsl.sp.1986.019.01.04

Hart, S. R., and Staudigel, H. (1982). The control of alkalies and uranium in seawater by ocean crust alteration. *Earth Planet. Sci. Lett.* 58, 202–212. doi:10.1016/0012-821X(82)90194-7

He, J., Kapp, P., Chapman, J. B., DeCelles, P. G., and Carrapa, B. J. G. S. (2019). Structural setting and detrital zircon U–Pb geochronology of Triassic–Cenozoic strata in the eastern Central Pamir, Tajikistan. *Geol. Soc. Lond. Spec. Publ.* 483, 605–630. doi:10.1144/SP483.11

Hu, P., Li, C., Wu, Y., Xie, C., Wang, M., and Li, J. (2014). Opening of the Longmu Co–Shuanghu–Lancangjiang ocean: Constraints from plagiogranites. *Chin. Sci. Bull.* 59, 3188–3199. doi:10.1007/s11434-014-0434-z

Hu, W.-L., Wang, Q., Yang, J.-H., Zhang, C., Tang, G.-J., Ma, L., et al. (2019). Late early Cretaceous peraluminous biotite granites along the Bangong–Nujiang suture zone, Central Tibet: Products derived by partial melting of metasedimentary rocks? *Lithos* 344, 147–158. doi:10.1016/j.lithos.2019.06.005

Huang, H.-Q., Li, X.-H., Li, Z.-X., and Li, W.-X. (2015). formation of the jurassic south China large granitic province: Insights from the Genesis of the jiufeng pluton. *Chem. Geol.* 401, 43–58. doi:10.1016/j.chemgeo.2015.02.019

Huang, L.-C., and Jiang, S.-Y. (2014). Highly fractionated S-type granites from the giant dahutang tungsten deposit in jiangnan orogen, Southeast China: Geochronology, petrogenesis and their relationship with W-mineralization. *Lithos* 202, 207–226. doi:10.1016/j.lithos.2014.05.030

Imrecke, D. B., Robinson, A. C., Owen, L. A., Chen, J., Schoenbohm, L. M., Hedrick, K. A., et al. (2019). Mesozoic evolution of the eastern Pamir. *Lithosphere* 11, 560–580. doi:10.1130/l1017.1

Jiang, Z.-Q., Wang, Q., Wyman, D. A., Li, Z.-X., Yang, J.-H., Shi, X.-B., et al. (2014). Transition from oceanic to continental lithosphere subduction in southern Tibet: Evidence from the late cretaceous–early oligocene (~ 91–30 Ma) intrusive rocks in the chanang–zedong area, southern gangdese. *Lithos* 196, 213–231. doi:10.1016/j.lithos.2014.03.001

Kang, Z.-Q., Xu, J.-F., Wilde, S. A., Feng, Z.-H., Chen, J.-L., Wang, B.-D., et al. (2014). Geochronology and geochemistry of the sangri group volcanic rocks, southern Lhasa terrane: Implications for the early subduction history of the neo-tethys and gangdese magmatic arc. *Lithos* 200, 157–168. doi:10.1016/j.lithos.2014.04.019

Kapp, P., DeCelles, P. G., Gehrels, G. E., Heizler, M., and Ding, L. (2007). Geological records of the lhasa-qiangtang and indo-asian collisions in the nima area of central Tibet. *Geol. Soc. Am. Bull.* 119, 917–933. doi:10.1130/B26033.1

Lacassin, R., Valli, F., Arnaud, N., Leloup, P. H., Paquette, J. L., Haibing, L., et al. (2004). Large-scale geometry, offset and kinematic evolution of the Karakorum fault, Tibet. *Earth Planet. Sci. Lett.* 219, 255–269. doi:10.1016/S0012-821X(04)00006-8

Le Bas, M., Le Maitre, R., Streckeisen, A., and Zanettin, B. (1986). A chemical classification of volcanic rocks based on the total alkali-silica diagram. *J. petrology* 27, 745–750. doi:10.1093/petrology/27.3.745

Leven, E. J. (1995). Permian and triassic of the rushan-pshart zone (Pamir). *Riv. Ital. Paleontol. Stratigr.* 101, 3–16.

Li, J., Niu, Y., Hu, Y., Chen, S., Zhang, Y., Duan, M., et al. (2016). Origin of the late early cretaceous granodiorite and associated dioritic dikes in the hongqilafu pluton, northwestern Tibetan plateau: A case for crust–mantle interaction. *Lithos* 260, 300–314. doi:10.1016/j.lithos.2016.05.028

Li, R. H., Peng, B., Zhao, C. S., Yu, M., Song, L. S., and Zhang, H. (2019a). Origin of early creceouscalc-alkaline granite, taxkorgan: Implications for evolution of tethys evolution in central Pamir. *J. Cent. South Univ.* 26, 3470–3487. doi:10.1007/s11771-019-4267-4

Li, S.-M., Zhu, D.-C., Wang, Q., Zhao, Z.-D., Sui, Q.-L., Liu, S.-A., et al. (2014). Northward subduction of bangong–nujiang tethys: Insight from late jurassic intrusive rocks from Bangong tso in Western Tibet. *Lithos* 205, 284–297. doi:10.1016/j.lithos.2014.07.010

Li, S. M., Wang, Q., Zhu, D. C., Stern, R. J., Cawood, P. A., Sui, Q. L., et al. (2018). One or two early Cretaceous arc systems in the Lhasa terrane, southern Tibet. *J. Geophys. Res. Solid Earth* 123, 3391–3413. doi:10.1002/2018JB015582

Li, S., Yin, C., Guilmette, C., and Ding, L. (2020a). Reply to comment by LZ Shi et al. on "Birth and demise of the Bangong–Nujiang Tethyan Ocean: A review from the Gerze area of central Tibet". *Earth-Science Rev.* 208, 103213. doi:10.1016/j.earscirev.2020.103213

Li, S., Yin, C., Guilmette, C., Ding, L., and Zhang, J. (2019b). Birth and demise of the bangong-nujiang tethyan ocean: A review from the gerze area of central Tibet. *Earth-Science Rev.* 198, 102907. doi:10.1016/j.earscirev.2019.102907

Li, Y.-P., Robinson, A. C., Gadoev, M., and Oimuhammadzoda, I. (2020b). Was the Pamir salient built along a Late Paleozoic embayment on the southern Asian margin? *Earth Planet. Sci. Lett.* 550, 116554. doi:10.1016/j.epsl.2020.116554

Li, Y. P., Robinson, A. C., Lapen, T. J., Righter, M., and Stevens, M. K. (2020c). Muztaghata dome Miocene eclogite facies metamorphism: A record of lower crustal evolution of the ne Pamir. *Tectonics* 39, e2019TC005917. doi:10.1029/2019TC005917

Li, Y., Xiao, W., and Tian, Zh. (2018). Early palaeozoic accretionary tectonics of west Kunlun orogen: Insights from datong granitoids, mafic–ultramafic complexes, and silurian–devonian sandstones, Xinjiang, NW China. *Geol. J.* 54, 1505–1517. doi:10.1002/gj.3246

Liang, X., Wang, G., Yuan, G., and Liu, Y. (2012). Structural sequence and geochronology of the qomo ri accretionary complex, central Qiangtang, Tibet: Implications for the late triassic subduction of the Paleo-Tethys Ocean. *Gondwana Res.* 22, 470–481. doi:10.1016/j.gr.2011.11.012

Liu, D., Shi, R., Ding, L., Huang, Q., Zhang, X., Yue, Y., et al. (2017). Zircon U–Pb age and Hf isotopic compositions of mesozoic granitoids in southern Qiangtang, Tibet: Implications for the subduction of the bangong–nujiang tethyan ocean. *Gondwana Res.* 41, 157–172. doi:10.1016/j.gr.2015.04.007

Liu, H., Chen, L., Huang, F., Zeng, Y.-C., and Wang, L.-Q. (2021a). Silurian intermediate–felsic complex in the Xiangtaohu area of central Qiangtang, northern Tibet: Evidence for southward subduction of the Longmuco–Shuanghu Prototethys oceanic plate. *Lithos* 404, 106465–107405. doi:10.1016/j.lithos.2021.106465

Liu, H., Huang, Q., Uysal, I. T., Cai, Z., Wan, Z., Xia, B., et al. (2020a). Geodynamics of the divergent double subduction along the Bangong-Nujiang tethyan suture zone: Insights from late mesozoic intermediate-mafic rocks in central Tibet. *Gondwana Res.* 79, 233–247. doi:10.1016/j.gr.2019.09.018

Liu, X.-Q., Zhang, C.-L., Hao, X.-S., Zou, H., Zhao, H.-X., and Ye, X.-T. (2020b). Early cretaceous granitoids in the southern Pamir: Implications for the meso-tethys evolution of the Pamir Plateau. *Lithos* 362, 105492. doi:10.1016/j.lithos.2020.105492

Liu, X.-Q., Zhang, C.-L., Zou, H., Wang, Q., Hao, X.-S., Zhao, H.-X., et al. (2020c). Triassic-jurassic granitoids and pegmatites from western kunlun-pamir syntax: Implications for the paleo-tethys evolution at the northern margin of the Tibetan plateau. *Lithosphere* 2020, 7282037. doi:10.2113/2020/7282037

Liu, X., Wang, Q., Ma, L., Gou, G.-N., Ou, Q., and Wang, J. (2021b). Late jurassic maofengshan two-mica granites in Guangzhou, south China: Fractional crystallization products of metasedimentary-rock-derived magmas. *Mineral.* . 115, 323–341. doi:10.1007/s00710-020-00733-9

Liu, Y., Santosh, M., Zhao, Z. B., Niu, W. C., and Wang, G. H. (2011). Evidence for palaeo-Tethyan oceanic subduction within central Qiangtang, northern Tibet. *Lithos* 127, 39–53. doi:10.1016/j.lithos.2011.07.023

Ma, X., Song, Y., Tang, J., and Chen, W. (2020). Newly identified rhyolite-biotite monzogranite (A2-type granite)-norite belt from the Bangong-Nujiang collision zone in Tibet Plateau: Evidence for the slab break-off beneath the Lhasa Terrane. *Lithos* 366, 105565. doi:10.1016/j.lithos.2020.105565

Maniar, P. D., and Piccoli, P. M. (1989). Tectonic discrimination of granitoids. *Geol. Soc. Am. Bull.* 101, 635–643. doi:10.1130/0016-7606(1989)101<0635:tdog>2.3.co;2

Meschede, M. (1986). A method of discriminating between different types of mid-ocean ridge basalts and continental tholeiites with the Nb-1bZr-1bY diagram. *Chem. Geol.* 56, 207–218. doi:10.1016/0009-2541(86)90004-5

Metcalfe, I. (2021). Multiple Tethyan ocean basins and orogenic belts in Asia. *Gondwana Res.* 100, 87–130. doi:10.1016/j.gr.2021.01.012

Miller, C. F. (1985). Are strongly peraluminous magmas derived from pelitic sedimentary sources? *J. Geol.* 93, 673–689. doi:10.1086/628995

Montenat, C. (2009). The mesozoic of Afghanistan. *GeoArabia* 14, 147–210. doi:10.2113/geoarabia1401147

Pan, G. T., Mo, X. X., Hou, Z. Q., Zhu, D. C., Wang, L. Q., Li, G. M., et al. (2006). Spatial–temporal framework of the Lhasa orogenic belt and its evolution. *Acta Petrol. Sin.* 22, 521–533.

Pashkov, B. R., and Shvol'man, V. A. (1979). Rift margins of tethys in the pamirs. *Geotectonics* 13, 447–456.

Patiño Douce, A. E., and Beard, J. S. (1995). Dehydration-melting of biotite gneiss and quartz amphibolite from 3 to 15 kbar. *J. petrology* 36, 707–738. doi:10.1093/petrology/36.3.707

Patiño Douce, A. E., and Harris, N. (1998). Experimental constraints on Himalayan anatexis. *J. petrology* 39, 689–710. doi:10.1093/petroj/39.4.689

Pearce, J. A., and Cann, J. R. (1973). Tectonic setting of basic volcanic rocks determined using trace element analyses. *Earth Planet. Sci. Lett.* 19, 290–300. doi:10.1016/0012-821X(73)90129-5

Pearce, J. A., and Norry, M. J. (1979). Petrogenetic implications of Ti, Zr, Y, and Nb variations in volcanic rocks. *Contr. Mineral. Pet.* 69, 33–47. doi:10.1007/bf00375192

Pearce, J. (1996). Sources and settings of granitic rocks. *Episodes* 19, 120–125. doi:10.18814/epiiugs/1996/v19i4/005

Petro, W. L., Vogel, T. A., and Wilband, J. T. (1979). Major-element chemistry of plutonic rock suites from compressional and extensional plate boundaries. *Chem. Geol.* 26, 217–235. doi:10.1016/0009-2541(79)90047-0

Photiades, A., Saccani, E., and Tassinari, R. (2003). Petrogenesis and tectonic setting of volcanic rocks from the Subpelagonian ophiolitic mélange in the Agoriani area (Othrys, Greece). *Ofioliti* 28, 121–135. doi:10.4454/ofioliti.v28i2.200

Pitcher, W. (1983). *Granite type and tectonic environment,* Symposium on mountain building, 19–40.

Pundir, S., Adlakha, V., Kumar, S., and Singhal, S. (2020). Closure of India–Asia collision margin along the Shyok suture zone in the eastern Karakoram: New geochemical and zircon U–Pb geochronological observations. *Geol. Mag.* 157, 1451–1472. doi:10.1017/S0016756819001547

Qu, J., Zhang, L., Ai, Y., Lü, Z., Wang, J., Zhou, H., et al. (2007). High-pressure granulite from Western Kunlun, northwestern China: Its metamorphic evolution, zircon SHRIMP U-Pb ages and tectonic implication. *Sci. China Ser. D Earth Sci.* 50, 961–971. doi:10.1007/s11430-007-0065-1

Ravikant, V., Wu, F.-Y., and Ji, W.-Q. (2009). Zircon U–Pb and Hf isotopic constraints on petrogenesis of the Cretaceous–Tertiary granites in eastern Karakoram and Ladakh, India. *Lithos* 110, 153–166. doi:10.1016/j.lithos.2008.12.013

Reichardt, H., and Weinberg, R. F. (2012). The dike swarm of the Karakoram shear zone, Ladakh, NW India: Linking granite source to batholith. *Geol. Soc. Am. Bull.* 124, 89–103. doi:10.1130/B30394.1

Rembe, J., Sobel, E. R., Kley, J., Zhou, R., Thiede, R., and Chen, J. (2021). The carboniferous arc of the north Pamir. *Lithosphere* 2021. doi:10.2113/2021/6697858

Roberts, M. P., and Clemens, J. D. (1993). Origin of high-potassium, talc-alkaline, I-type granitoids. *Geol.* 21, 825–828. doi:10.1130/0091-7613(1993)021<0825:oohpta>2.3.co;2

Robinson, A. C., Ducea, M., and Lapen, T. J. (2012). Detrital zircon and isotopic constraints on the crustal architecture and tectonic evolution of the northeastern Pamir. *Tectonics* 31, 1–16. doi:10.1029/2011TC003013

Robinson, A. C. (2009). Geologic offsets across the northern Karakorum fault: Implications for its role and terrane correlations in the Western Himalayan-Tibetan orogen. *Earth Planet. Sci. Lett.* 279, 123–130. doi:10.1016/j.epsl.2008.12.039

Robinson, A. C. (2015). Mesozoic tectonics of the Gondwanan terranes of the Pamir plateau. *J. Asian Earth Sci.* 102, 170–179. doi:10.1016/j.jseaes.2014.09.012

Robinson, A. C., Yin, A., Manning, C. E., Harrison, T. M., Zhang, S.-H., and Wang, X.-F. (2007). Cenozoic evolution of the eastern Pamir: Implications for strain-accommodation mechanisms at the Western end of the Himalayan-Tibetan orogen. *Geol. Soc. Am. Bull.* 119, 882–896. doi:10.1130/B25981.1

Rutte, D., Ratschbacher, L., Khan, J., Stübner, K., Hacker, B. R., Stearns, M. A., et al. (2017a). Building the Pamir-Tibetan plateau—crustal stacking, extensional collapse, and lateral extrusion in the central Pamir: 2. Timing and rates. *Tectonics* 36, 385–419. doi:10.1002/2016TC004294

Rutte, D., Ratschbacher, L., Schneider, S., Stübner, K., Stearns, M. A., Gulzar, M. A., et al. (2017b). Building the Pamir-Tibetan plateau—crustal stacking, extensional collapse, and lateral extrusion in the central Pamir: 1. Geometry and kinematics. *Tectonics* 36, 342–384. doi:10.1002/2016TC004293

Ruzhentsev, S. V., and Shvol'man, V. A. (1981). Tectonic zoning of the pamirs and Afghanistan contemporary geoscientific researches in Himalaya: Dehradun Bishan Singh. Mahendra Pal Singh Publishers, 1, 53–59.

Safonova, I. Y., Utsunomiya, A., Kojima, S., Nakae, S., Tomurtogoo, O., Filippov, A., et al. (2009). Pacific superplume-related oceanic basalts hosted by accretionary complexes of Central Asia, Russian Far East and Japan. *Gondwana Res.* 16, 587–608. doi:10.1016/j.gr.2009.02.008

Saktura, W. M., Buckman, S., Nutman, A. P., and Bennett, V. C. (2021). Late jurassic changmar complex from the Shyok ophiolite, NW himalaya: A prelude to the ladakh arc. *Geol. Mag.* 158, 239–260. doi:10.1017/S0016756820000400

Schmidt, J., Hacker, B. R., Ratschbacher, L., Stübner, K., Stearns, M., Kylander-Clark, A., et al. (2011). Cenozoic deep crust in the Pamir. *Earth Planet. Sci. Lett.* 312, 411–421. doi:10.1016/j.epsl.2011.10.034

Schneider, F., Yuan, X., Schurr, B., Mechie, J., Sippl, C., Kufner, S. K., et al. (2019). The crust in the Pamir: Insights from receiver functions. *J. Geophys. Res. Solid Earth* 124, 9313–9331. doi:10.1029/2019JB017765

Schwab, M., Ratschbacher, L., Siebel, W., McWilliams, M., Minaev, V., Lutkov, V., et al. (2004). Assembly of the Pamirs: Age and origin of magmatic belts from the southern Tien Shan to the southern Pamirs and their relation to Tibet. *Tectonics* 23 (4). doi:10.1029/2003TC001583

Sengör, A. M. C. (1979). Mid-Mesozoic closure of permo-triassic tethys and its implications. *Nature* 279, 590–593. doi:10.1038/279590a0

Shvol'man, V. (1980). A Mesozoic ophiolite complex in the Pamirs. *Geotectonics* 14, 465–470.

Shvol'man, V. (1978). Relicts of the mesotethys in the pamirs. *Himal. Geol.* 8, 369–378.

Sobel, E. R., and Dumitru, T. A. (1997). Thrusting and exhumation around the margins of the Western Tarim basin during the India-Asia collision. *J. Geophys. Res.* 102, 5043–5063. doi:10.1029/96JB03267

Stearns, M., Hacker, B., Ratschbacher, L., Rutte, D., and Kylander-Clark, A. (2015). Titanite petrochronology of the Pamir gneiss domes: Implications for middle to deep crust exhumation and titanite closure to Pb and Zr diffusion. *Tectonics* 34, 784–802. doi:10.1002/2014TC003774

Stevens, G., Villaros, A., and Moyen, J.-F. (2007). Selective peritectic garnet entrainment as the origin of geochemical diversity in S-type granites. *Geol.* 35, 9–12. doi:10.1130/G22959A.1

Stübner, K., Ratschbacher, L., Rutte, D., Stanek, K., Minaev, V., Wiesinger, M., et al. (2013a). The giant Shakhdara migmatitic gneiss dome, Pamir, India-Asia collision zone: 1. Geometry and kinematics. *Tectonics* 32, 948–979. doi:10.1002/tect.20057

Stübner, K., Ratschbacher, L., Weise, C., Chow, J., Hofmann, J., Khan, J., et al. (2013b). The giant Shakhdara migmatitic gneiss dome, Pamir, India-Asia collision zone: 2. Timing of dome formation. *Tectonics* 32, 1404–1431. doi:10.1002/tect.20059

Sun, G., Hu, X., Sinclair, H. D., BouDagher-Fadel, M. K., and Wang, J. (2015). Late Cretaceous evolution of the Coqen Basin (Lhasa terrane) and implications for early topographic growth on the Tibetan Plateau. *Geol. Soc. Am. Bull.* 127, 1001–1020. doi:10.1130/B31137.1

Sun, S.-S., and McDonough, W. F. (1989). Chemical and isotopic systematics of oceanic basalts: Implications for mantle composition and processes. *Geol. Soc. Lond. Spec. Publ.* 42, 313–345. doi:10.1144/GSL.SP.1989.042.01.19

Sylvester, P. J. (1998). Post-collisional strongly peraluminous granites. *Lithos* 45, 29–44. doi:10.1016/S0024-4937(98)00024-3

Tadjidinov, K. S. (1988). "Paleovolcanic reconstructions and geological mapping (South Pamir)," in *Materials of the Central Asian regional petrographic meeting*. Editor L. Donish, 223–224.

Tang, Y., Zhai, Q., Hu, P., Xiao, X., and Wang, H. (2018). Petrology, geochemistry and geochronology of the zhongcang ophiolite, northern Tibet: Implications for the evolution of the Bangong-Nujiang Ocean. *Geosci. Front.* 9, 1369–1381. doi:10.1016/j.gsf.2018.05.007

Tapponnier, P., Mattauer, M., Proust, F., and Cassaigneau, C. (1981). Mesozoic ophiolites, sutures, and arge-scale tectonic movements in Afghanistan. *Earth Planet. Sci. Lett.* 52, 355–371. doi:10.1016/0012-821x(81)90189-8

Valli, F., Leloup, P. H., Paquette, J. L., Arnaud, N., Li, H., Tapponnier, P., et al. (2008). New U-Th/Pb constraints on timing of shearing and long-term slip-rate on the Karakorum fault. *Tectonics* 27. doi:10.1029/2007TC002184

Villaros, A., Stevens, G., and Buick, I. S. (2009a). Tracking S-type granite from source to emplacement: Clues from garnet in the cape granite suite. *Lithos* 112, 217–235. doi:10.1016/j.lithos.2009.02.011

Villaros, A., Stevens, G., Moyen, J.-F., and Buick, I. S. (2009b). The trace element compositions of S-type granites: Evidence for disequilibrium melting and accessory phase entrainment in the source. *Contrib. Mineral.* . 158, 543–561. doi:10.1007/s00410-009-0396-3

Villarreal, D. P., Robinson, A. C., Carrapa, B., Worthington, J., Chapman, J. B., Oimahmadov, I., et al. (2020). Evidence for late triassic crustal suturing of the central and southern Pamir. *J. Asian Earth Sci. X* 3, 100024. doi:10.1016/j.jaesx.2019.100024

Volkmer, J. E., Kapp, P., Horton, B. K., Gehrels, G. E., Minervini, J. M., and Ding, L. (2014). Northern Lhasa thrust belt of central Tibet: Evidence of cretaceous–early cenozoic shortening within a passive roof thrust system. *Geol. Soc. Am. Special Pap.* 507, 59–70. doi:10.1130/2014.2507(03

Wang, B.-D., Wang, L.-Q., Chung, S.-L., Chen, J.-L., Yin, F.-G., Liu, H., et al. (2016). Evolution of the bangong–nujiang tethyan ocean: Insights from the geochronology and geochemistry of mafic rocks within ophiolites. *Lithos* 245, 18–33. doi:10.1016/j.lithos.2015.07.016

Wang, S., Tang, W., Liu, Y., Liu, X., and Yao, X. (2020a). Rushan-Pshart Paleo-Tethyan suture deduced from geochronological, geochemical, and Sr-Nd-Hf isotopic characteristics of granitoids in Pamir. *Lithos* 364, 105549. doi:10.1016/j.lithos.2020.105549

Wang, W., Wang, M., Zhai, Q.-G., Xie, C.-M., Hu, P.-Y., Li, C., et al. (2020b). Transition from oceanic subduction to continental collision recorded in the Bangong-Nujiang suture zone: Insights from Early Cretaceous magmatic rocks in the north-central Tibet. *Gondwana Res.* 78, 77–91. doi:10.1016/j.gr.2019.09.008

Wang, Y., Fan, W., Sun, M., Liang, X., Zhang, Y., and Peng, T. (2007). Geochronological, geochemical and geothermal constraints on petrogenesis of the indosinian peraluminous granites in the South China block: A case study in the hunan province. *Lithos* 96, 475–502. doi:10.1016/j.lithos.2006.11.010

Wang, Y., Zhang, Y., Fan, W., Geng, H., Zou, H., and Bi, X. (2014). Early Neoproterozoic accretionary assemblage in the Cathaysia Block: Geochronological, Lu–Hf isotopic and geochemical evidence from granitoid gneisses. *Precambrian Res.* 249, 144–161. doi:10.1016/j.precamres.2014.05.003

Whalen, J. B., Currie, K. L., and Chappell, B. W. (1987). A-Type granites: Geochemical characteristics, discrimination and petrogenesis. *Contrib. Mineral.* . 95, 407–419. doi:10.1007/BF00402202

Wood, D. A. (1980). The application of a Th-Hf-Ta diagram to problems of tectonomagmatic classification and to establishing the nature of crustal contamination of basaltic lavas of the British Tertiary Volcanic Province. *Earth Planet. Sci. Lett.* 50, 11–30. doi:10.1016/0012-821X(80)90116-8

Worthington, J. R., Ratschbacher, L., Stübner, K., Khan, J., Malz, N., Schneider, S., et al. (2020). The Alichur dome, South Pamir, Western India–Asia collisional zone: Detailing the Neogene Shakhdara–Alichur syn-collisional gneiss-dome complex and connection to lithospheric processes. *Tectonics* 39, e2019TC005735. doi:10.1029/2019tc005735

Xia, L.-Q. (2014). The geochemical criteria to distinguish continental basalts from arc related ones. *Earth-Science Rev.* 139, 195–212. doi:10.1016/j.earscirev.2014.09.006

Xia, L., and Li, X. (2019). Basalt geochemistry as a diagnostic indicator of tectonic setting. *Gondwana Res.* 65, 43–67. doi:10.1016/j.gr.2018.08.006

Xiao, W. J., Windley, B. F., Chen, H. L., Zhang, G. C., and Li, J. L. (2002). Carboniferous-Triassic subduction and accretion in the Western Kunlun, China: Implications for the collisional and accretionary tectonics of the northern Tibetan Plateau. *Geol.* 30, 295–298. doi:10.1130/0091-7613(2002)030<0295:ctsaai>2.0.co;2

Xu, Q., Zhao, J., Yuan, X., Liu, H., Ju, C., Schurr, B., et al. (2021). Deep crustal contact between the Pamir and Tarim Basin deduced from receiver functions. *Geophys. Res. Lett.* 48. doi:10.1029/2021GL093271

Xu, W., Liu, F., and Dong, Y. (2020). Cambrian to triassic geodynamic evolution of central Qiangtang, Tibet. *Earth-Science Rev.* 201, 103083. doi:10.1016/j.earscirev.2020.103083

Yang, W., Liu, L., Cao, Y., Wang, C., He, S., Li, R., et al. (2010). Geochronological evidence of Indosinian (high-pressure) metamorphic event and its tectonic significance in Taxkorgan area of the Western Kunlun Mountains, NW China. *Sci. China Earth Sci.* 53, 1445–1459. doi:10.1007/s11430-010-4081-1

Yin, A., and Harrison, T. M. (2000). Geologic evolution of the Himalayan-Tibetan orogen. *Annu. Rev. Earth Planet. Sci.* 28, 211–280. doi:10.1146/ANNUREV.EARTH.28.1.211

Yogibekov, D., Sang, M., Xiao, W., Windley, B. F., Mamadjonov, Y., Yang, H., et al. (2020). Late Palaeozoic to Late Triassic northward accretion and incorporation of seamounts along the northern South Pamir: Insights from the anatomy of the Pshart accretionary complex. *Geol. J.* 55, 7837–7857. doi:10.1002/gj.3906

Zanchetta, S., Worthington, J., Angiolini, L., Leven, E. J., Villa, I. M., and Zanchi, A. (2018). The Bashgumbaz complex (Tajikistan): Arc obduction in the cimmerian orogeny of the Pamir. *Gondwana Res.* 57, 170–190. doi:10.1016/j.gr.2018.01.009

Zanchi, A., and Gaetani, M. (2011). The geology of the Karakoram range, Pakistan: The new 1: 100, 000 geological map of central-western Karakoram. *Italian J. Geosciences* 130, 161–264. doi:10.3301/IJG.2011.09

Zanchi, A., Poli, S., Fumagalli, P., and Gaetani, M. (2000). Mantle exhumation along the tirich mir fault zone, NW Pakistan: Pre-mid-cretaceous accretion of the Karakoram terrane to the asian margin. *Geol. Soc. Lond. Spec. Publ.* 170, 237–252. doi:10.1144/GSL.SP.2000.170.01.13

Zanchi, A., Zanchetta, S., Berra, F., Mattei, M., Garzanti, E., Molyneux, S., et al. (2009). The eo-cimmerian (late? Triassic) orogeny in north Iran. *Geol. Soc. Lond. Spec. Publ.* 312, 31–55. doi:10.1144/SP312.3

Zhai, Q.-g., Jahn, B.-m., Su, L., Ernst, R. E., Wang, K.-l., Zhang, R.-y., et al. (2013a). SHRIMP zircon U–Pb geochronology, geochemistry and Sr–Nd–Hf isotopic compositions of a mafic dyke swarm in the Qiangtang terrane, northern Tibet and geodynamic implications. *Lithos* 174, 28–43. doi:10.1016/j.lithos.2012.10.018

Zhai, Q.-g., Jahn, B.-m., Su, L., Wang, J., Mo, X.-X., Lee, H.-y., et al. (2013b). Triassic arc magmatism in the Qiangtang area, northern Tibet: Zircon U–Pb ages, geochemical and Sr–Nd–Hf isotopic characteristics, and tectonic implications. *J. Asian Earth Sci.* 63, 162–178. doi:10.1016/j.jseaes.2012.08.025

Zhai, Q.-g., Jahn, B.-m., Wang, J., Hu, P.-y., Chung, S.-l., Lee, H.-y., et al. (2016). Oldest paleo-Tethyan ophiolitic mélange in the Tibetan Plateau. *Geol. Soc. Am. Bull.* 128, 355–373. doi:10.1130/B31296.1

Zhai, Q.-G., Jahn, B.-M., Zhang, R.-Y., Wang, J., and Su, L. (2011). Triassic subduction of the paleo-tethys in northern Tibet, China: Evidence from the geochemical and isotopic characteristics of eclogites and blueschists of the Qiangtang block. *J. Asian Earth Sci.* 42, 1356–1370. doi:10.1016/j.jseaes.2011.07.023

Zhang, K.-J., Zhang, Y.-X., Tang, X.-C., and Xia, B. (2012a). Late Mesozoic tectonic evolution and growth of the Tibetan plateau prior to the Indo-Asian collision. *Earth-Science Rev.* 114, 236–249. doi:10.1016/j.earscirev.2012.06.001

Zhang, Q., Ran, H., and Li, C. (2012b). A-type granite: What is the essence? *Acta Petrologica Mineralogica* 31, 621–626. (in Chinese with English abstract).

Zhang, Z., Zhao, G., Santosh, M., Wang, J., Dong, X., and Shen, K. (2010). Late cretaceous charnockite with adakitic affinities from the gangdese batholith, southeastern Tibet: Evidence for neo-tethyan mid-ocean ridge subduction? *Gondwana Res.* 17, 615–631. doi:10.1016/j.gr.2009.10.007

Zhao, Z., Bons, P. D., Wang, G., Soesoo, A., and Liu, Y. (2015). Tectonic evolution and high-pressure rock exhumation in the Qiangtang terrane, central Tibet. *Solid* 6, 457–473. doi:10.5194/se-6-457-2015

Zheng, H., Huang, Q. T., Cai, Z. R., Zhang, K. J., Liu, H. C., Cheng, C., et al. (2019). Early Cretaceous arc granitoids from the central Lhasa subterrane: Production of the northward subduction of yarlung zangbo neo-tethyan ocean? *Geol. J.* 54, 4001–4013. doi:10.1002/gj.3399

Zheng, Y.-F., and Gao, P. (2021). The production of granitic magmas through crustal anatexis at convergent plate boundaries. *Lithos* 402403, 106232. doi:10.1016/j.lithos.2021.106232

Zhu, D.-C., Li, S.-M., Cawood, P. A., Wang, Q., Zhao, Z.-D., Liu, S.-A., et al. (2016). Assembly of the Lhasa and Qiangtang terranes in central Tibet by divergent double subduction. *Lithos* 245, 7–17. doi:10.1016/j.lithos.2015.06.023

Zhu, D.-C., Zhao, Z.-D., Niu, Y., Dilek, Y., Hou, Z.-Q., and Mo, X.-X. (2013). The origin and pre-Cenozoic evolution of the Tibetan Plateau. *Gondwana Res.* 23, 1429–1454. doi:10.1016/j.gr.2012.02.002

Zhu, R.-Z., Lai, S.-C., Qin, J.-F., Zhao, S.-W., and Santosh, M. (2018). Strongly peraluminous fractionated S-type granites in the Baoshan Block, SW China: Implications for two-stage melting of fertile continental materials following the closure of Bangong-Nujiang Tethys. *Lithos* 316, 178–198. doi:10.1016/j.lithos.2018.07.016

Zhu, Y., Lai, S.-c., Qin, J.-f., Zhu, R.-z., Zhang, F.-y., and Zhang, Z.-z. (2020). Petrogenesis and geochemical diversity of late mesoproterozoic S-type granites in the Western yangtze block, south China: Co-Entrainment of peritectic selective phases and accessory minerals. *Lithos* 352, 105326. doi:10.1016/j.lithos.2019.105326

frontiers | Frontiers in Earth Science

TYPE Original Research
PUBLISHED 19 January 2023
DOI 10.3389/feart.2023.1128692

OPEN ACCESS

EDITED BY
Jiyuan Yin,
Chinese Academy of Geological Sciences (CAGS), China

REVIEWED BY
Feng Guo,
Xi'an Shiyou University, China
Jiawang Ge,
Southwest Petroleum University, China

*CORRESPONDENCE
Aiguo Wang,
wag@nwu.edu.cn

SPECIALTY SECTION
This article was submitted to Petrology, a section of the journal Frontiers in Earth Science

RECEIVED 21 December 2022
ACCEPTED 09 January 2023
PUBLISHED 19 January 2023

CITATION
Wang A, Li C, Li L, Pu R, Yang Z, Zhu N and Guo K (2023), C_{20}-C_{21}-C_{23} tricyclic terpanes abundance patterns: Origin and application to depositional environment identification.
Front. Earth Sci. 11:1128692.
doi: 10.3389/feart.2023.1128692

C_{20}-C_{21}-C_{23} tricyclic terpanes abundance patterns: Origin and application to depositional environment identification

Aiguo Wang[1]*, Chunyu Li[1], Long Li[2], Renhai Pu[1], Zeguang Yang[1], Nan Zhu[1] and Kai Guo[1]

[1]State Key Laboratory of Continental Dynamics, Department of Geology, Northwest University, Xi'an, China, [2]Department of Earth and Atmospheric Sciences, University of Alberta, Edmonton, AB, Canada

Reconstruction of paleo-depositional environments in a sedimentary basin is often obstructed by the absence of typical environmental indicators in sedimentary rocks. Here, we propose a biomarker method using C_{20}-C_{21}-C_{23} tricyclic terpanes (TTs) as a tracer, which is simple in analysis but robust to provide reliable and detailed environmental information. Based on the analysis of 271 C_{20}-C_{21}-C_{23}TT data from 32 basins in 18 countries, we observed a relationship between C_{20}-C_{21}-C_{23}TT abundance patterns and depositional environments. This relationship was attributed to the control of depositional environments on the input proportions of plankton and terrigenous plants, which act as two end-member precursors for the TTs in a depositional system. The various mixing proportions between these two end-members result in different C_{20}-C_{21}-C_{23}TT abundance patterns associated with different depositional environments, e.g., C_{20}>C_{21}>C_{23}TT in river-lake transitional, C_{20}<C_{21}<C_{23}TT in marine or saline lacustrine environments, C_{20}<C_{21}>C_{23}TT in freshwater lacustrine and C_{20}>C_{21}<C_{23}TT in marine-continental transitional environments. In addition, the C_{23}/C_{21}TT ratio increases with elevated salinity of depositional water, and the C_{21}/C_{20}TT ratio increases with increasing water depths. Based on these observations, a discrimination diagram using C_{23}/C_{21}TT vs. C_{21}/C_{20}TT was developed for environmental identification. The validity of this C_{20}-C_{21}-C_{23}TT biomarker method is well demonstrated by the rock samples with typical environmental indicators. This method is applicable in a broad spectrum of rocks and in maturities up to 2.4%Ro. Its strength was shown by a case study of a complex depositional system in the East China Sea Basin, which has been strongly affected by eustasy.

KEYWORDS

tricyclic terpanes, depositional environment, biomarker, East China Sea Basin, environmental identification

1 Introduction

Reconstruction of paleo-depositional environment is critical in oil-gas exploration, paleoclimatic and paleoenvironmental studies. Conventional methods for environmental reconstruction mostly rely on sedimentary, petrological and/or mineralogical characterizations (e.g., Oskay et al., 2019; Pichat et al., 2021), paleontological record (e.g., Heard et al., 2020), and/or geochemical tracing (e.g., Govind et al., 2021). For example, lithology, sedimentary/biogenic structures, rock fabrics and texture in sedimentary rocks have been used to reconstruct sedimentary microfacies, which is further used to infer depositional

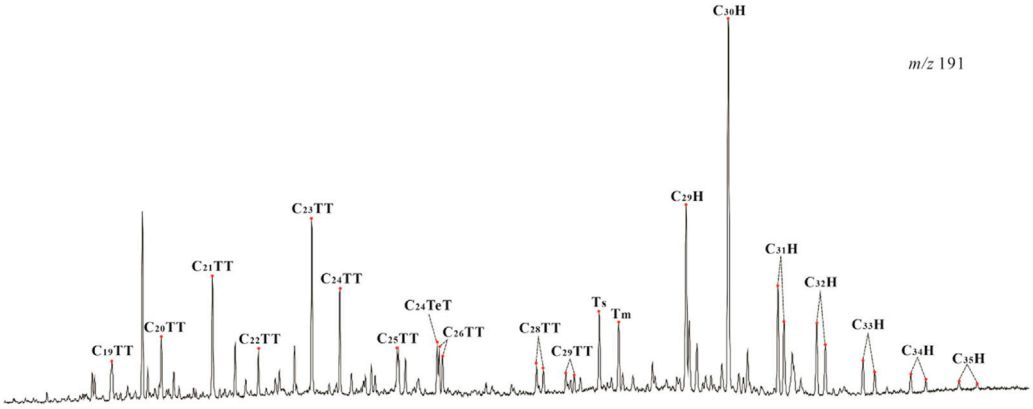

FIGURE 1
Mass chromatogram (*m/z* 191) showing the distribution of tricyclic terpanes (TTs) and hopanes (Hs) in the rock extract from C1 well in the East China Sea Basin.

environments (e.g., El-Sabbagh et al., 2017; Mtelela et al., 2017; Barrera et al., 2020). However, these sedimentological, mineralogical and petrological characterizations are sometimes limited by the availability of outcrops and drilling cores, or the lack of typical depositional indicators. Paleontological methods are highly efficient in revealing paleo-depositional environment. Fossils, bioglyphs and their assemblages have been used to classify biofacies (e.g., Laprida et al., 2007; El-Sabbagh et al., 2017; Mahfouz et al., 2021). However, well-preserved characteristic fossils are not always available in sedimentary rocks because most of organisms in sediments have been degraded during burial and diagenesis. Geochemical data are sensitive to a variety of depositional conditions, such as redox condition (e.g., V/Cr, Ni/Co, U/Th) and salinity (e.g., Sr/Ba, B/Ga, Rb/K). However, these geochemical parameters are not diagnostic to a specific depositional environment, and thus cannot be used solely for depositional environment identification. Recently, biomarkers produced from the degradation of organisms living in different environments has attracted increasing attention in depositional environment studies (e.g., Aderoju and Bend, 2018; Wendorff-Belon et al., 2021; Liu et al., 2022). Here, we demonstrate a new biomarker method using C_{20}-C_{21}-C_{23} tricyclic terpanes (TTs) as a robust tool for the identification of depositional environment.

TTs with carbon numbers range from C_{19} to C_{29} are ubiquitous in crude oils and extracts of sedimentary rocks (De Grande et al., 1993). Higher carbon TTs are also present but are often masked by hopanes in the *m/z* 191 mass chromatogram (Samuel et al., 2010) (Figure 1). TTs have been widely applied to oil-source correlation due to their high thermal stability and resistance to biodegradation (Farrimond et al., 1999; Xiao et al., 2019a). Although the exact precursors of TTs have not been identified yet (Dutta et al., 2006; Philp et al., 2021), previous studies have noticed a close relationship between TTs and depositional environments. TTs always show a predominance of C_{23}TT in marine facies and a predominance of C_{21}TT in freshwater lacustrine facies, and more abundant lower than higher carbon numbers of TTs in shallow-water environments (e.g., Zumberge, 1987; Tao et al., 2015; Atoyebi et al., 2017; Xiao et al., 2019b).

However, the exact correspondences between TTs and various depositional environments have not been clearly defined, limiting their applications to environmental identification. Here, we carried out a thorough examination of new and published C_{20}-C_{21}-C_{23}TT data from a range of known depositional environments worldwide and discovered good correspondences between C_{20}-C_{21}-C_{23}TT abundance patterns and typical depositional environments. Based on the analysis on the origin of C_{20}-C_{21}-C_{23}TT abundance patterns, a discriminating diagram of C_{20}-C_{21}-C_{23}TTs was developed for environmental identification and was then demonstrated for its validity and applicability, and was finally applied to a complex depositional system in the East China Sea Basin to show its strength.

2 Materials and methods

A total of 232 C_{20}-C_{21}-C_{23}TT data from a range of depositional environments in 30 basins across 18 countries were compiled from the literature (Table 1; Supplementary Table S1). The data were obtained from gas chromatography-mass spectrometry (GC-MS) analysis of crude oils and source-rock extracts, with rock ages mainly ranging from the Devonian to Neogene (Supplementary Table S1).

Additionally, new C_{20}-C_{21}-C_{23}TT data were acquired from four source-rock samples and 35 oil samples from three basins (the Ordos, Bohai Bay and Qaidam basins) in China (Table 1 and Supplementary Table S1). The soluble organic matter was extracted from the source rocks following the description by Philp et al. (2021). The biomarkers including C_{20}-C_{21}-C_{23}TTs in the rock extracts and oils were analyzed by GC-MS as described by Wang et al. (2019). Subsequently, the source rocks for the oils were determined by the previous oil-source correlations in these basins (e.g., Sun, 2006; Cao et al., 2008; Zhang et al., 2009). As the depositional environments of source rocks in these three basins have been well constrained by previous studies (e.g., Zhu and Jin, 2003; Sun, 2006; Cao et al., 2008; Zhang et al., 2009; Gao et al., 2014), the correspondence between C_{20}-C_{21}-C_{23}TT data and depositional environments were easily determined.

In order to verify the validity of our biomarker method and its applicability to thermal maturity, 13 core samples from 8 wells were collected from the Ordovician and Permian in the Ordos Basin (Table 2). These samples contain typical depositional environment indicators or were deposited in the well-defined depositional

TABLE 1 The ratios of $C_{21}/C_{20}TT$ and $C_{23}/C_{21}TT$ from a range of depositional environments.

Depositional environment	$C_{21}/C_{20}TT$	$C_{23}/C_{21}TT$	Sample type	Source-rock/reservoir age	Basin	Country	Data source
Marine facies	0.98–2.83	1.20–3.57	89 oils	Silurian, Devonian, Carboniferous, Permian, Triassic, Jurassic, Cretaceous, Paleogene, Neogene	Cuanza, Benguala, Neuquan, North Sea, W. Canadian, Magdalans, Gulf of Suez, Oriente, Overthrust, North Slope, Nemaha, Great, Williston, Anadarko, GOM, Barinas, Los Angeles, Ventura, Santa Maria	Angola, Argentina, Britain, Canada, Colombia, Egypt, Netherlands, Norway, Peru, United States, Venezuela	Zumberge (1987)
Saline lacustrine facies	1.00–2.08	1.15–1.52	5 oils, 9 source rocks	Permian, Paleogene	Bohai Bay, Junggar	China	This study; Yu et al. (2017)
Brackish-freshwater lacustrine facies	1.11–3.03	0.36–1.23	34 oils, 25 source rocks	Triassic, Cretaceous, Paleogene	Bohai Bay, Ordos, Sudan	China, Sudan, South Sudan	This study; Lv and Thesis, (2019); Xiao et al. (2019a)
Marine-continental transitional facies	0.24–1.03	0.96–3.01	24 oils, 6 source rocks	Cambrian, Triassic, Jurassic, Cretaceous, Paleogene, Neogene	Vulcan, Lianos, Java Sea, Niger Delta, Indus, North slope, Williston, GOM, Paradox, Maracabio, Junggar	Australia, China, Colombia, Indonesia, Nigeria, Pakistan, Thailand, United States, Venezuela	Zumberge (1987); Gao et al. (2017)
River-lake transitional facies	0.52–1.04	0.51–1.03	13 oils, 43 source rocks	Permian, Jurassic	Qaidam, Junggar	China	This study; Wang et al. (2020); Cao et al. (2008)
Terrigenous source	0.50–0.91	0.25–0.53	25 source rocks	Triassic	Junggar	China	Gao et al. (2017)

environments. All these samples are now at highly mature stages (Table 2). C_{20}-C_{21}-C_{23}TTs in these rock extracts were also analyzed by GC-MS as described by Wang et al. (2019). Two samples (i.e., L65, 4296.3 m and L41-1, 4120 m) were selected to measure vitrinite reflectance (Ro%) following the description by Kalinowski and Gurba (2020). Two thin sections (i.e., L65, 4296.3 m and L66, 4040.45 m) were prepared for the observation of petrography and fossil.

Forty-four sets of geochemical data (including total organic carbon (TOC), Rock-Eval pyrolysis, chloroform asphalt 'A', Ro and biomarkers of rock extracts) obtained from 14 wells in the Pingbei area in the East China Sea Basin (Table 3), were collected from the SINOPEC Shanghai Offshore Oil & Gas Company for a case study.

3 Results

3.1 Marine facies

The marine C_{20}-C_{21}-C_{23}TT data were compiled from 20 basins in 11 countries (Table 1). Their C_{21}/C_{20}TT and C_{23}/C_{21}TT ratios vary from 0.98 to 2.83 and 1.20 to 3.57, respectively (Figure 2). The relative abundances of C_{20}-C_{21}-C_{23}TTs display a pattern of $C_{20}<C_{21}<C_{23}$TT (e.g., Figure 3A).

3.2 Saline lacustrine facies

Saline lacustrine facies is represented by the source rocks from the Junggar Basin in Northwestern China (Bian et al., 2010; Yu et al., 2017) and the oil samples from the Bohai Bay Basin in Eastern China (Table 1). Their C_{21}/C_{20}TT and C_{23}/C_{21}TT ratios vary from 1.00 to 2.08 and 1.15 to 1.52, respectively (Figure 2), which slightly overlaps with samples classified as marine in origin (Zhu and Jin, 2003; Yu et al., 2017). The relative abundances of C_{20}-C_{21}-C_{23}TTs associated with saline lacustrine facies are similar to those of marine facies.

3.3 Brackish-freshwater lacustrine facies

Brackish-freshwater lacustrine facies is represented by the samples from the Muglad Basin (Sudan) (Xiao et al., 2019b), Bohai Bay Basin (Lv and Thesis, 2019) and Ordos Basin in Central China (this study, Table 1), which were deposited in semi-deep to deep brackish-freshwater lacustrine facies (Zhang et al., 2009; Xiao et al., 2019a; Ma et al., 2019). The C_{21}/C_{20}TT and C_{23}/C_{21}TT ratios fall into the ranges of 0.95–3.03 and 0.36 to 1.34, respectively (Figure 2). The relative abundances of C_{20}-C_{21}-C_{23}TTs display two patterns: $C_{20}<C_{21}<C_{23}$TT and $C_{20}< C_{21}>C_{21}$TT (e.g., Figure 3B).

3.4 Terrigenous source

Terrigenous organic matter can be transported by rivers and eventually deposited in lacustrine or marine environments. Terrigenous organic matter transported by rivers has been reported to be deposited in marine facies in the northern South China Sea (Li et al., 2011; Deng et al., 2019) and lacustrine facies in the Junggar Basin

TABLE 2 The ratios of $C_{21}/C_{20}TT$, $C_{23}/C_{21}TT$ and vitrinite reflectance (Ro) from the known depositional environments in the Ordos Basin.

Well	Depth(m)	Sample lithology	Environmental indicators	Period	Formation	$C_{21}/C_{20}TT$	$C_{23}/C_{21}TT$	Ro (%)	Depositional environment*	Depositional environment#
L66	4040.5	Gravel limestone	Fuzulinid fossil, Storm deposit	Early Permian	Taiyuan	0.88	1.24	2.0	Sub-tidal	Marine-continental transitional facies
CH3	3802.8	Siderite bearing mudstone	Nodular siderite, Pyrite absent			0.87	0.76	2.0	Delta	River-lake transitional facies
L65	4296.3					0.83	0.52	**2.3**		
L47-1	4120.0	Carbonaceous mudstone	Cordaites fossil			0.76	0.73	**2.4**	Swamp	River-lake transitional facies
HT7	4435.0	Pyrite bearing mudstone	Pyrite crystal			0.97	1.21	2.2	Lagoon; Tidal flat	Marine-continental transitional facies
XY1	3067.2	Dark mudstone	Thin coal interlayer	Early Permian	Shanxi	1.33	1.10	1.4	Continental facies	Brackish-freshwater lacustrine facies
	3132.0					1.28	0.95			
	3132.4					1.27	0.76			
XY2	2796.7					1.15	0.84			
MT3	2976.6	Calcareous mudstone	mudstone interlayer in carbonate rocks	Middle Ordovician	Majiagou (4th Member)	1.45	2.04	1.6	Marine facies	Marine facies
	2976.8	Massive limestone	Carbonate rocks			1.2	1.47			
	3177.7	Gypsum bearing mudstone	Depositional gypsum		Majiagou (3rd Member)	1.54	2.42		Marine facies	Marine facies
	3180.0					1.53	2.16			

(*) denotes the depositional environments identified by fossil, characteristic mineral or previous studies; (#) denotes the depositional environments identified by the C_{20}-C_{21}-$C_{23}TT$, method; **2.3** and **2.4** Ro% were measured in this study; the Ro values for the Permian were estimated according to Sun (2017); the Ro values for the Ordovician were cited from Kong et al. (2019) which was converted from asphalt reflectivity.

10.3389/feart.2023.1128692

TABLE 3 Geochemical data of sedimentary rock in the Pingbei area, East China Sea Basin.

Well	Depth (m)	Sample lithology	Formation	TOC (%)	"A" (%)	S_1+S_2 (mg/g)	Tmax (°C)	Ro (%)	$C_{21}/C_{20}TT$	$C_{23}/C_{21}TT$	Pr/Ph
A1	4167.00	Coal (cuttings)	P4	4.78	3.77	30.43	437	/	0.98	1.52	3.89
A1	4367.00	Carbonaceous mudstone (cuttings)	P3	16.40	1.40	71.89	439	/	0.82	1.34	3.80
A1	4427.50	Mudstone (sidewall core)	P2	1.14	0.17	5.69	441	/	0.75	0.93	2.36
A1	4432.00	Carbonaceous mudstone (sidewall core)	P2	19.60	3.72	88.89	451	/	0.72	0.77	3.14
A2	4345.99	Mudstone (core)	P4	0.62	0.03	0.73	444	0.78	0.26	0.97	5.78
A2	4350.84	Mudstone (core)	P4	0.29	0.01	0.21	445	0.78	0.14	1.10	3.64
A2	4351.24	Mudstone (core)	P4	0.23	0.01	0.20	443	0.78	0.13	1.31	3.14
A2	4351.64	Mudstone (core)	P4	0.38	0.01	0.33	449	0.78	0.19	1.14	2.79
A3	3569.00	Mudstone (core)	P3	0.88	0.05	3.43	440	/	0.94	0.73	1.46
A3	4043.50	Carbonaceous mudstone (core)	P1	/	/	/	/	/	0.57	0.71	6.19
A3	3962.50	Mudstone (core)	P1	/	/	/	/	/	0.80	0.66	4.86
A4	3320.50	Mudstone (core)	P2	2.18	/	4.95	439	0.68	0.73	0.79	4.69
A5	4204.36	Mudstone (core)	P3	1.35	0.04	1.96	443	0.75	1.05	0.64	4.14
A5	4609.00	Coal (core)	P1	/	/	/	/	/	0.25	0.89	5.69
A6	4344.07	Mudstone (core)	P1	0.66	0.04	0.60	443	0.76	1.17	1.07	3.68
B1	3391.00	Mudstone (core)	P4	0.60	/	0.23	392	0.51	1.82	1.30	1.08
B1	3807.50	Mudstone (core)	P1	1.66	/	2.74	444	0.68	1.03	0.73	2.07
B1	3809.14	Mudstone (core)	P1	1.77	/	1.21	442	0.70	1.26	0.94	6.34
B2	4103.00	Mudstone (sidewall core)	P2	0.37	0.05	0.86	439	0.69	1.40	1.38	3.49
B2	4239.00	Mudstone (sidewall core)	P2	0.42	0.09	0.98	439	0.73	1.00	1.09	4.69
B2	4295.00	Mudstone (sidewall core)	P2	0.81	0.23	2.22	441	0.74	1.31	0.75	5.11
B2	4405.00	Mudstone (sidewall core)	P2	0.66	0.11	3.10	449	0.81	2.27	0.29	3.45
B2	4564.80	Mudstone (core)	P1	0.38	/	0.40	484	0.78	1.82	0.46	1.14
B2	4677.00	Mudstone (sidewall core)	P1	0.32	0.06	1.94	292	0.87	1.35	1.67	2.95
B3	4186.00	Mudstone (core)	P2	0.62	/	0.43	443	0.72	0.99	1.02	4.11
B3	4188.00	Mudstone (core)	P2	0.59	/	0.42	441	0.71	0.83	0.90	4.76
B4	3842.00	Mudstone (sidewall core)	P3	0.31	0.02	0.30	434	/	1.57	1.71	0.93
B4	3878.00	Mudstone (sidewall core)	P3	0.28	0.04	0.37	435	/	2.21	1.35	1.19
C1	3273.00	Mudstone (core)	P4	1.38	/	1.58	433	0.54	1.27	1.11	1.91
C1	3275.85	Coal (core)	P4	56.49	/	217	421	0.54	0.48	1.05	7.34
C1	3398.00	Mudstone (core)	P3	0.60	/	0.37	405	0.57	1.43	1.16	0.92
C1	3442.00	Coal (core)	P2	/	/	/	/	0.65	0.02	0.78	3.32
C1	3444.81	Mudstone (core)	P2	0.64	/	0.82	436.00	0.65	1.35	0.94	5.20
C1	3627.00	Mudstone (core)	P1	0.50	/	0.20	410	0.67	1.40	1.20	0.92
C2	3652.00	Mudstone (core)	P3	0.77	/	0.66	437	/	1.18	1.05	1.66
C2	3961.00	Mudstone (core)	P1	0.72	/	0.74	446	/	1.37	1.24	1.17
C3	3753.00	Mudstone (sidewall core)	P4	0.58	0.31	2.42	430	/	1.33	2.29	1.21

(Continued on following page)

TABLE 3 (*Continued*) Geochemical data of sedimentary rock in the Pingbei area, East China Sea Basin.

Well	Depth (m)	Sample lithology	Formation	TOC (%)	"A" (%)	S_1+S_2 (mg/g)	Tmax (°C)	Ro (%)	$C_{21}/C_{20}TT$	$C_{23}/C_{21}TT$	Pr/Ph
C3	3922.00	Mudstone (sidewall core)	P3	1.00	0.21	3.03	434	/	1.66	2.09	3.41
D1	4094.50	Mudstone (core)	P3	0.36	0.01	0.76	432	0.74	0.38	1.47	2.40
D1	4095.26	Coal (core)	P3	74.52	/	167.53	437	0.74	0.29	1.19	7.85
D1	4096.00	Mudstone (core)	P3	3.68	0.03	6.03	436.00	0.72	0.15	1.51	6.39
D1	4097.00	Mudstone (core)	P3	0.89	0.04	0.91	444.00	0.73	0.26	1.55	8.02
D1	4157.00	Mudstone (core)	P3	/	/	/	/	/	0.65	0.67	4.84
D1	4658.00	Carbonaceous mudstone (core)	P1	/	/	/	/	/	0.34	0.44	3.66

Abbreviations: TOC = total organic carbon content; "A" = chloroform asphalt "A"; S_1+S_2 = sum of free hydrocarbon and pyrolytic hydrocarbon; Tmax = maximum pyrolysis temperature; Ro = vitrinite reflectance; TT = tricyclic terpane; Pr/Ph = pristane/phytane; /= missing data.

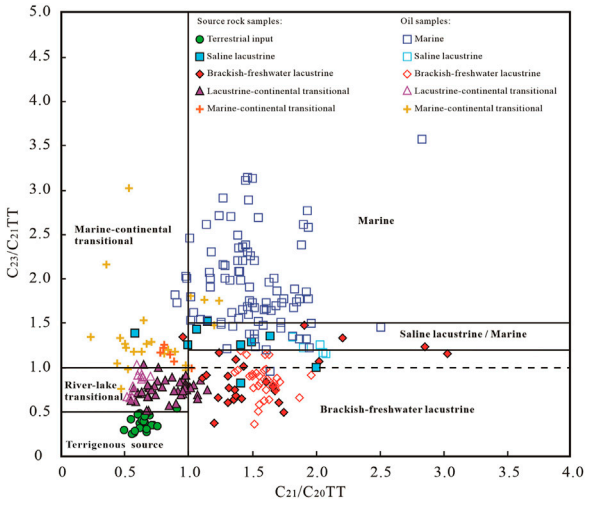

FIGURE 2
Cross-plots of C_{20}-C_{21}-C_{23} tricyclic terpane (TT) ratios in context of depositional environments. The solid boundary lines were established with confidence by the data. The dotted line is a speculated boundary between brackish and freshwater lacustrine facies.

(Gao et al., 2017). On this condition, the C_{20}-C_{21}-C_{23}TT data are strongly controlled by the source instead of depositional environment. The C_{20}-C_{21}-C_{23}TT data of terrigenous source in the Junggar Basin give C_{21}/C_{20}TT ratios of 0.50–0.91, and C_{23}/C_{21}TT ratios of 0.25–0.53 (Figure 2), with a relative abundance of C_{20}>C_{21}>C_{23}TT (e.g., Figure 3C).

3.5 Transitional facies

3.5.1 Marine-continental transitional facies

Marine-continental transitional facies is represented by the C_{20}-C_{21}-C_{23}TT data from 11 basins in nine countries collected by Zumberge (1987) and Gao et al. (2017) (Table 1). The majority of the C_{21}/C_{20}TT ratios are lower than 1.0, while the C_{23}/C_{21}TT ratios are mostly greater than 1.0 (Figure 2), showing an abundance pattern of C_{20}>C_{21}<C_{23}TT (e.g., Figure 3D).

3.5.2 River-lake transitional facies

River-lake transitional facies is represented by the C_{20}-C_{21}-C_{23}TT data from the Junggar Basin (Wang et al., 2020) and Qaidam Basin (this study and Cao et al., 2008; Table 1) in China. Their C_{21}/C_{20}TT and C_{23}/C_{21}TT ratios vary from 0.52 to 1.04 and 0.51 to 1.03, respectively (Figure 2), with a dominant C_{20}>C_{21}>C_{23}TT pattern.

4 Discussion

4.1 Origin of C_{20}-C_{21}-C_{23}TT abundance patterns

TTs have drawn broad attention in literature since Anders and Robinson (1971) and Gallegos (1971) described the lower homologs (C_{19}-C_{24}) of TTs in the bitumen and oils of the Green River Shale (e.g., Aquino Neto et al., 1982; Chicarelli et al., 1988; De Grande et al., 1993; Dutta et al., 2006; Tao et al., 2015; Philp et al., 2021). Multiple compound sources/precursors for TTs have been proposed, such as prokaryotic cell membrane (e.g., Ourisson et al., 1982), diterpenes in terrigenous plants (e.g., Ekweozor et al., 1983) and the now-extinct algal-like Tasmanites (e.g., Aquino Neto et al., 1982; Chicarelli et al., 1988; De Grande et al., 1993; Dutta et al., 2006). So far, no clear precursor-product relationship has been established, which has at least partially impeded the direct application of TTs as source indicators (Philp et al., 2021).

Here, the analysis of a large amount of C_{20}-C_{21}-C_{23}TT data from various depositional environments provides some insights into the origin of the observed C_{20}-C_{21}-C_{23}TT abundance patterns. Previous studies have shown that the organic matter in typical marine and shallow-water terrestrial facies mainly originated from plankton and terrestrial plants (e.g., Tissot and Welte, 1978). Accordingly, the C_{20}<C_{21}<C_{23}TT pattern likely corresponds to a dominant plankton input, while the C_{20}>C_{21}>C_{23}TT pattern may correspond to a dominant contribution of terrigenous plants. The former correspondence can be evidenced by the Neoproterozoic oil shale (900–873 Ma; maturity: 0.6–0.7%Ro) in North China, in which the terrigenous plant input can be ignored (Zhang et al., 2007). This oil shale contains cyanobacteria and green algae, and shows a C_{20}<C_{21}<C_{23}TT abundance pattern in the rock extracts, suggesting that planktons are the biological source for the TTs with C_{20}<C_{21}<C_{23}TT abundance pattern.

The analysis also indicates that neither plankton nor terrigenous plants alone can generate the TTs with C_{20}>C_{21}<C_{23}TT or

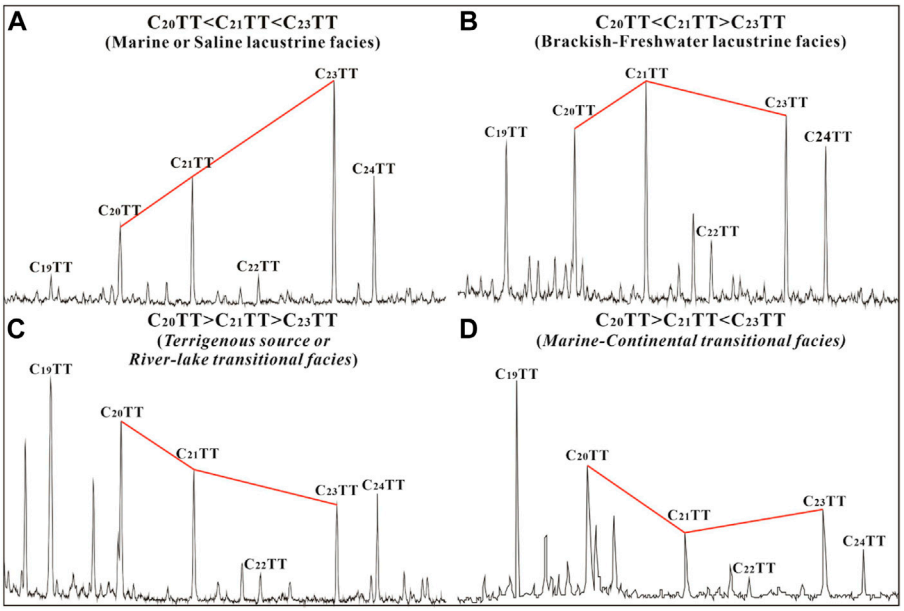

FIGURE 3
Four representative abundance patterns of C_{20}-C_{21}-C_{23} tricyclic terpanes (TTs) in six depositional environments **(A)**, Marine or Saline lacustrine facies; **(B)**, Brackish-freshwater lacustrine facies; **(C)**, Terrigenous or River-lake transitional facies; **(D)**, Marine-continental transitional facies.

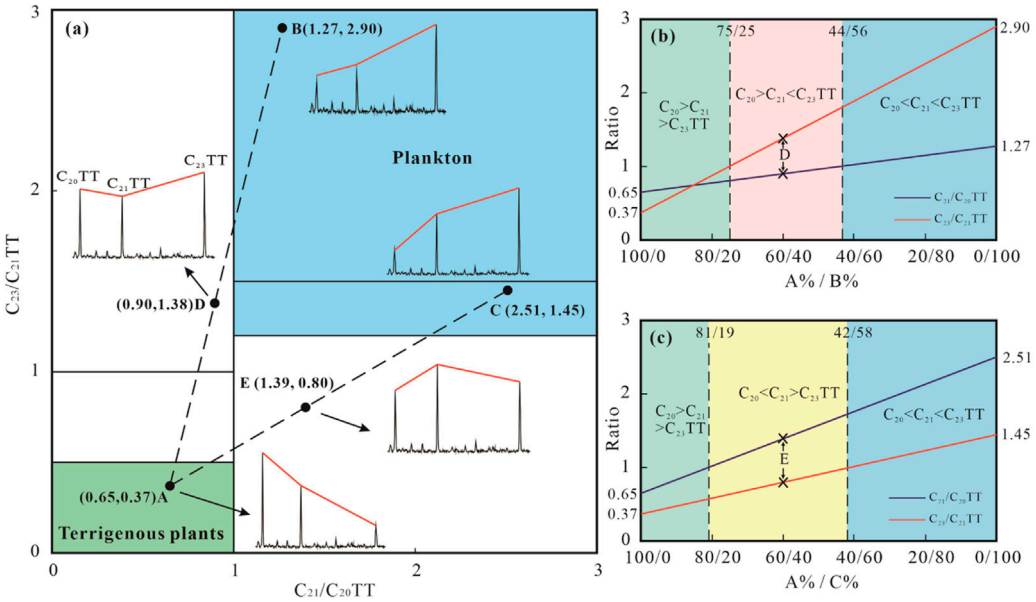

FIGURE 4
Numerical simulation for the origin of C_{20}-C_{21}-C_{23} tricyclic terpane (TT) abundance patterns by mixing plankton and terrigenous plants at various mixing ratios. Points **(A–C)** are the representative end-member C_{20}-C_{21}-C_{23}TT distributions for the mixing modeling. With the change of mixing ratios between A and B (C), the C_{20}-C_{21}-C_{23}TT abundance pattern changes along Line A-B (C). Points D and E are the representative C_{20}-C_{21}-C_{23}TT abundance patterns of A-B mixture and A-C mixture, respectively.

C_{20}<C_{21}>C_{23}TT patterns, which have been observed in marine-continental transitional and brackish-freshwater lacustrine facies, respectively. As these two depositional environments commonly receive blended input of plankton and terrigenous plants, mixing from different sources is likely the cause of the C_{20}>C_{21}<C_{23}TT and C_{20}<C_{21}>C_{23}TT patterns. This hypothesis is well supported by the numerical modeling of a mixing between plankton and terrigenous plants at various mixing ratios (Figure 4). Representative C_{20}-C_{21}-C_{23}TT abundance patterns in the terrigenous plants domain (i.e., Point A in Figure 4A) and the plankton domain (i.e., Points B or C in Figure 4A) determined by this study, were used as end-members for the mixing modeling.

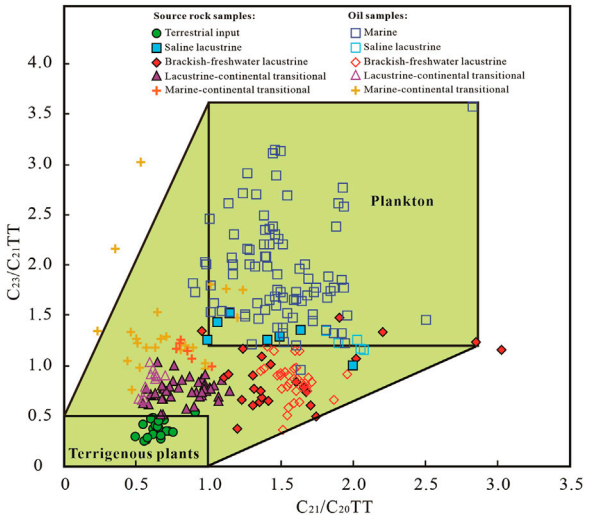

FIGURE 5
Cross-plot of C_{20}-C_{21}-C_{23} tricyclic terpane (TT) ratios with two defined end-member domains of plankton and terrigenous plants. Almost all C_{20}-C_{21}-C_{23}TT data in this study fall into a range from the terrigenous plants domain to the plankton domain.

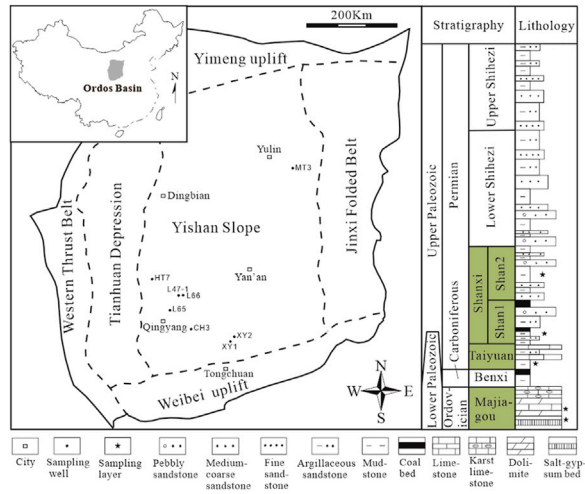

FIGURE 6
Tectonic units and composite stratigraphic columnar section of the Ordos Basin (modified from Li et al., 2021). The samples were collected from the Yishan Slope with the ages ranging from the Ordovician to Permian.

As illustrated in Figure 4, with the change of mixing ratios between A and B, the C_{20}-C_{21}-C_{23}TT abundance pattern changes from C_{20}>C_{21}>C_{23}TT to C_{20}>C_{21}<C_{23}TT (e.g., D in Figures 4A, B) when the mixing ratio (expressed as A%/B% ratio) decreases from 100/0 to 75/25, and further to C_{20}<C_{21}<C_{23}TT when the mixing ratio is lower than 44/56 (Figure 4B). Similarly, mixing between A and C can generate the C_{20}<C_{21}>C_{23}TT pattern (e.g., E in Figures 4A, C) when the mixing ratios (expressed as A%/C% ratio) are in the range of 81/19–42/58 (Figure 4C). Notably, almost all C_{20}-C_{21}-C_{23}TT data in this study fall into a range from the terrigenous plants domain to the plankton domain (Figure 5), suggesting that C_{20}-C_{21}-C_{23}TT abundance patterns are strongly controlled by the two end-member biological sources and their mixing contributions. Thus, the input mixing of plankton and terrigenous plants at different proportions should be responsible for the formation of various C_{20}-C_{21}-C_{23}TT abundance patterns.

4.2 Environmental implication of C_{20}-C_{21}-C_{23}TT abundance patterns

Depositional environments control the input proportions of plankton and terrigenous plants, which is proposed to control the C_{20}-C_{21}-C_{23}TT abundance patterns in sedimentary rocks. The analysis of available C_{20}-C_{21}-C_{23}TT data from known depositional environments clearly show that the C_{20}-C_{21}-C_{23}TT abundance patterns in different depositional environments are distinct from each other, with C_{20}<C_{21}<C_{23}TT in typical marine and saline lacustrine facies, C_{20}<C_{21}>C_{23}TT in freshwater lacustrine facies, C_{20}>C_{21}>C_{23}TT in river-lake transitional facies, and C_{20}>C_{21}<C_{23}TT in marine-continental transitional facies. As illustrated in Figure 2, the C_{23}/C_{21}TT ratio not only increases progressively from freshwater lacustrine, to saline lacustrine, to marine facies, but also increases progressively from terrigenous source, to river-lake transitional, to marine-continental transitional facies. The C_{23}/C_{21}TT ratio appears to increase gradually with elevated salinity of depositional water. The increase in salinity usually indicates a decrease in fresh-water input and therefore a decrease in terrigenous input, which results in the C_{23}/C_{21}TT ratios approaching their source signatures of halophilic plankton. Accordingly, the boundary between brackish and freshwater lacustrine facies is expected to lie around a C_{23}/C_{21}TT ratio of 1.0 (Figure 2). Furthermore, the C_{21}/C_{20}TT ratios in marine and lacustrine facies are obviously greater than those in transitional facies (Figure 2), suggesting that the C_{21}/C_{20}TT ratio seems to increase with elevated depths of depositional water. In general, the greater the depositional depth, the farther offshore, and the less terrigenous input. Thus, their C_{21}/C_{20}TT ratios approach the signatures of planktons (halophilic plankton or freshwater plankton).

Based on the good correspondences between C_{20}-C_{21}-C_{23}TT abundance patterns and typical depositional environments, the cross-plot of C_{23}/C_{21}TT vs. C_{21}/C_{20}TT in context of depositional environments (Figure 2) can be used as a discriminating diagram for environmental identification. C_{23}/C_{21}TT and C_{21}/C_{20}TT are expected to be the parameters to assess water salinity and depositional depth, respectively.

4.3 Validity of the C_{20}-C_{21}-C_{23}TT biomarker method

The Ordos Basin undergone (1) an early Paleozoic shallow oceanic-platform stage and 2) a late Paleozoic offshore-plain stage during the Paleozoic (Li, 2004). During the Middle Ordovician, the Majiagou Formation was deposited within a semi–closed epicontinental sea environment (Li et al., 2018). From the Late Ordovician to the Early Carboniferous, the basin was uplifted by the Caledonian orogeny and underwent 130 million years of erosion (Yang et al., 2012; Xu et al., 2018). The following Hercynian orogeny caused the Late Paleozoic Ordos Basin subsidence. Large scale of transgression occurred from the east and west of the basin during the Benxi period and the seawater

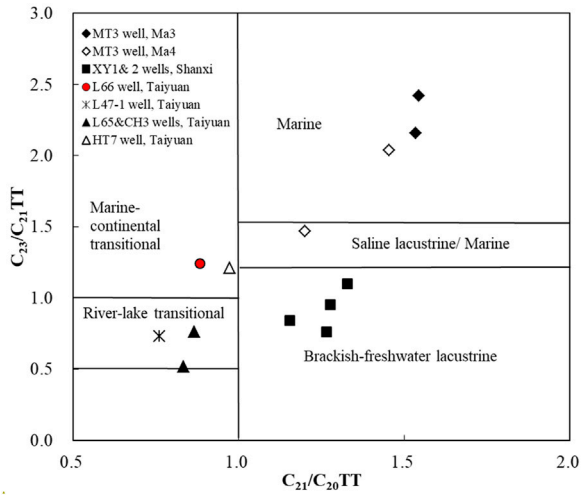

FIGURE 7
Environmental identification for the samples from the Ordovician and Permian in the Ordos Basin.

connected together during the Late Taiyuan period. With the gradual regression during the Shanxi period, continental deposition began to dominate, resulting in the development of marine-continental transitional facies, delta facies and lacustrine facies (Sun, 2017).

Thirteen core samples from the Ordovician-Permian in the Ordos Basin (Figure 6; Table 2) and ten coal or carbonaceous mudstones from the Eocene in the East China Sea Basin (Table 3) were used to verify the validity of C_{20}-C_{21}-C_{23}TT biomarker method.

4.3.1 Marine facies

The four samples including gypsum bearing mudstones, massive limestone and calcareous mudstone (Table 2) from the Majiagou Formation were all identified as marine facies (Figure 7), which is consistent with the present understanding of epicontinental sea environment (Li et al., 2018). Furthermore, the suggestion that the C_{23}/C_{21}TT ratio is a salinity indicator in this study is also evidenced by these samples. The Majiagou Formation is divided into six members, numbered from bottom to top as Ma1 to Ma6. The Ma1, Ma3 and Ma5 members were deposited with evaporite production during low sea level, while the Ma2, Ma4 and Ma6 members were deposited with carbonate production during high sea level (Xiao et al., 2019b). Thus, the depositional water salinity of Ma3 is higher than that of Ma4. It should be noted that the C_{23}/C_{21}TT ratios in Ma3 extract are indeed greater than those in Ma4 extract (Table 2; Figure 7).

4.3.2 Brackish-freshwater lacustrine facies

The depositional environments of the Permian Shanxi Formation in the southern Ordos basin have been determined by previous studies to be continental facies including delta and lacustrine facies (e.g., Wang et al., 2007; Sun, 2017; Li et al., 2021). Four dark mudstones from the Shanxi Formation in XY1 and XY2 wells (See locations in Figure 6) were extracted for environmental identification. As shown in Figure 7, the C_{21}/C_{20}TT and C_{23}/C_{21}TT ratios of these mudstones plot within the brackish-freshwater lacustrine facies, consistent with the regional depositional environments.

4.3.3 Transitional facies

4.3.3.1 Cordaitean fossil leaves

Cordaitean fossil leaves are known from early Carboniferous to early Permian deposits, representing the depositional environments including floodplains, river levees, coastal plains or swamp (Zodrow et al., 2000; Yang, 2007). The carbonaceous mudstone containing the Cordaitean fossil leaves (Figure 8A; Table 2) was identified as river-lake transitional facies by our biomarker method (Figure 7). This is consistent with the depositional environments indicated by the Cordaitean fossil leaves.

4.3.3.2 Fuzulinid fossil

The Fuzulinid fossil with 1 mm~4 mm in size and limestone gravels (Figures 8D, E) constitute a storm deposition which indicates a sub-tidal depositional environment. This sample was identified by the biomarker method to be deposited within a marine-continental transitional facies (Figure 7). As sub-tidal belongs to marine-continental transitional facies, the identification result of our biomarker method is thus correct.

4.3.3.3 Coal and carbonaceous mudstone

It is widely known that coal and carbonaceous mudstone are the indicators of shallow-water environment (e.g., swamp). The C_{20}-C_{21}-C_{23}TT biomarker method not only identified the coal and carbonaceous mudstone as shallow-water environment (i.e., transitional environments defined by C_{21}/C_{20}TT<1.0) as expected, but further determined their specific depositional environments: marine-continental transitional or river-lake transitional environments (Figure 9A).

4.3.3.4 Siderite and pyrite

Although siderite can occur in various depositional environments, layered nodular siderite without pyrite in mudstone (Figures 8F, G) was considered to be deposited in delta front, where iron oxides and terrigenous organic matter transported by river water are condensed and precipitated in a large amount (Shen et al., 2017). The two siderite bearing mudstones were identified by the biomarker method to be deposited within a river-lake transitional facies (Figure 7). According to the sedimentary model of rock series containing siderite and pyrite created by Shen et al. (2017), the mudstone containing pyrite was expected to be deposited in lagoon or tidal flat. The pyrite bearing mudstone was identified by the biomarker method to be deposited within a marine-continental transitional facies (Figure 7). It is clear that these two identification results using the biomarker method are both correct.

Compared with siderite, pyrite was considered to be precipitated in a relatively deeper environment (Figure 10). Notably, the C_{23}/C_{21}TT ratio of pyrite bearing mudstone is greater than those of siderite bearing mudstones (Table 2; Figure 7), indicating that the suggestion of C_{23}/C_{21}TT ratio as a depth indicator is reasonable. This suggestion was also evidenced by the negative correlation between pristane/phytane (Pr/Ph) and C_{21}/C_{20}TT ratios (Figure 9B). Pr/Ph ratios, which have been widely used to assess the redox of depositional environment, decrease with elevated anoxic conditions (Rashid, 1979). As shown in Figure 9B, the Pr/Ph ratios decrease along the C_{21}/C_{20}TT values. The increase in C_{21}/C_{20}TT ratios indicates an increase in depositional depths, which further indicates an increase in anoxic conditions.

FIGURE 8
Depositional environment indicators in the core samples and thin sections from the Taiyuan Formation in the Ordos Basin [**(A)**, Cordaites fossil, L47-1 well, 4120m; **(B)**, Cordaites fossil, L81 well; **(C)**, Pyrite crystal, HT7 well, 4435.0m; **(D, E)**, Fuzulinid fossil and limestone gravels, L66 well, 4040.5 m; **(F, G)**, Nodular siderite, L65 well, 4296.3 m].

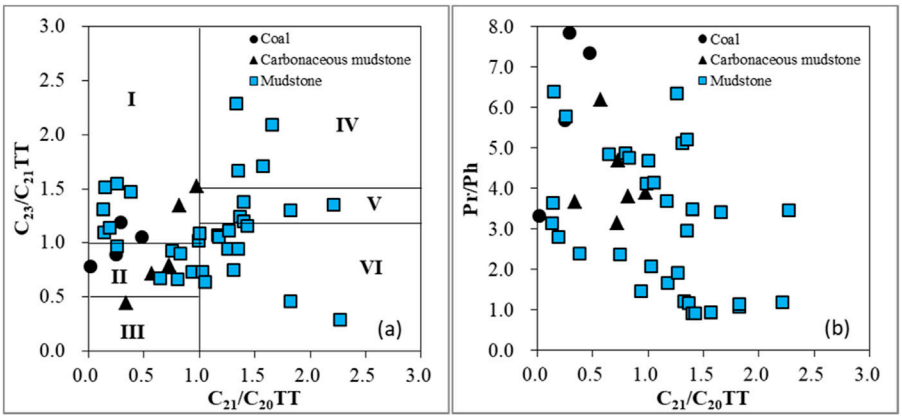

FIGURE 9
Cross-plots of C_{23}/C_{21}TT vs. C_{23}/C_{21}TT **(A)** and C_{21}/C_{20}TT vs. Pr/Ph **(B)** in the Pingbei area, East China Sea Basin. Note: TT= tricyclic terpane; Pr/Ph = pristane/phytane; I: Marine-continental transitional facies; II: River-lake transitional facies; III: Terrigenous source; IV: Marine facies; V: Saline lacustrine facies or marine facies; VI: Brackish-freshwater lacustrine facies.

4.4 Applicability of the C_{20}-C_{21}-C_{23}TT biomarker method

The C_{20}-C_{21}-C_{23}TT biomarker method only requires a small amount of rock extracts, depending on the lower limit of GC-MS analysis. At present, the rock extracts more than 10 μg is guaranteed to obtain high-quality *m/z*191 mass chromatogram. Take the mudstone samples from the Pingbei area for example, the TOC and S_1+S_2 values of mudstone samples vary from 0.23% to 3.68% and from 0.20 mg/g to 6.03 mg/g (Table 3), which were classified as “poor” to “fair” level

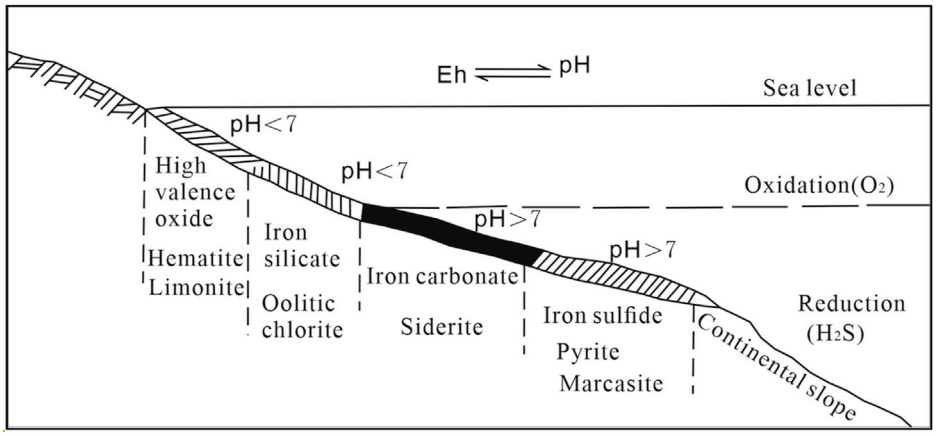

FIGURE 10
Schematic diagram of the facies change of sedimentary iron ore deposits (modified from Qiu, 1987).

source rocks. Although the chloroform asphalt 'A' extracted from the mudstones are as low as 0.01% (Table 3), the high-quality *m/z* 191 mass chromatogram with C_{20}-C_{21}-C_{23}TT signature has been obtained from every mudstone sample (e.g., Figure 1). This indicates that our method is not necessarily restricted to hydrocarbon source rocks, but can be applied to a broad spectrum of rocks.

TTs are characterized by higher thermal stability than hopanes and steroterpenes (Peters et al., 1990; Farrimond et al., 1999; Xiao et al., 2019a). Thermal evolution during maturation and high-maturation stages makes little effect on the abundance patterns of C_{20}-C_{21}-C_{23}TT (Chen et al., 2017; Xiao et al., 2019b). As shown in Table 2, although the rocks have evolved into the maturities ranging from 1.6% to 2.4%Ro, C_{20}-C_{21}-C_{23}TT biomarker method are still effective in environmental identification. Furthermore, C_{20}-C_{21}-C_{23}TT distributions are stable even in the severely biodegraded oils with 25-norhopane series, showing strong resistance to biodegradation (Xiao et al., 2019a).

5 Case study: Environmental identification for a complex depositional system in the East China Sea Basin

To test the robustness of the C_{20}-C_{21}-C_{23}TT biomarker method for environmental identification, it has been applied to a complex depositional system: the Pingbei area in the East China Sea Basin (Figure 11).

5.1 Geological background of the Pingbei area

The Pingbei area was a hinged margin of a rift basin during the Eocene (Soreghan and Cohen, 1996). The petroleum system in the area is within the upper-middle Eocene Pinghu Formation, which consists of alternate sandstone, mudstone and thin coal seams. From bottom to top, the Pinghu Formation is further divided into the P1, P2, P3 and P4 members (Figure 11A).

Due to the scarcity of wells and the lack of typical facies indicators in drill core, the depositional environments of the Pinghu Formation have been strongly debated among three possibilities: delta environment (e.g., Shen et al., 2016; Jiang et al., 2020), tidal flat environment (e.g., Zhao et al., 2008) and mixed delta and tidal flat environment (e.g., Zhang et al., 2017; Abbas et al., 2018).

5.2 Depositional environments of Pinghu Formation in the Pingbei area

The Ro values in the Pinghu Formation in the area vary from 0.51% to 0.87% (Table 3), indicating a low-mature to mature stage. The C_{20}-C_{21}-C_{23} TT abundance patterns cannot be affected by this maturity range, and are thus available to identify depositional environments. The C_{21}/C_{20}TT and C_{23}/C_{21}TT ratios were plotted in the discriminating diagram to identify the depositional environment of each member in the Pinghu Formation (Figure 12). Paleogeomorphologic map (Figure 11B) and seismic inversion data (Figures 11C–F) are also reported here as additional evidence to (1) support the environmental identification by the C_{20}-C_{21}-C_{23}TT biomarker method, and (2) help characterize the spatial distribution of depositional environment (Figures 12B, D, F, H).

5.2.1 P1 member

The depositional environments of P1 Member in zones A, B and C (see locations in Figure 11B) are identified as river-lake transitional, freshwater lacustrine and saline-lacustrine/marine facies (Figure 12A), respectively. Organic matter in the carbonaceous mudstone (Table 3) in Zone D (Figure 11B) was originated from a terrestrial source through river transportation (Figure 12A). Based on the environmental identification and paleogeomorphologic map of this period (Figure 11B), the depositional environment in Zone D is expected to be marine facies.

Notably, the spatial distribution of these facies is consistent with an environmental transition from continental facies in the

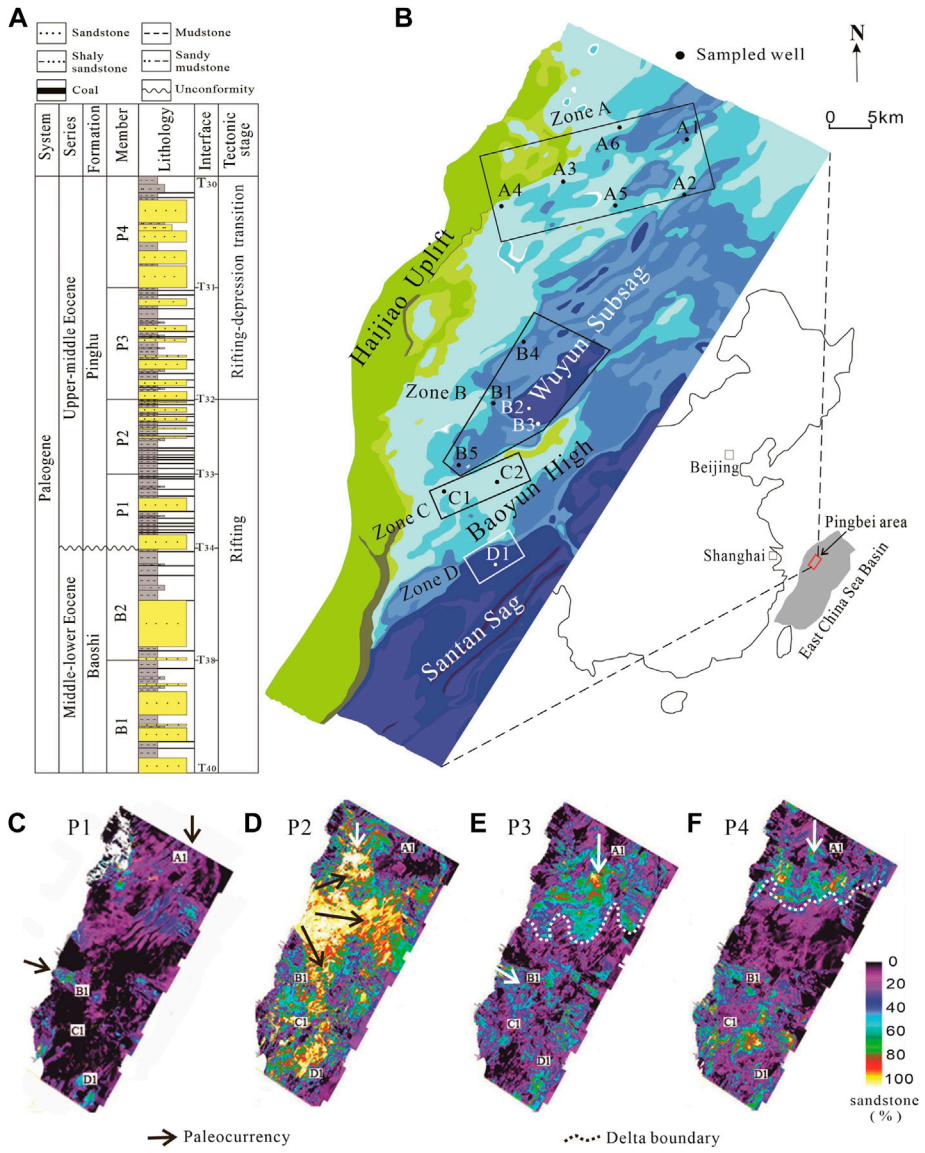

FIGURE 11
Generalized stratigraphy of the Pinghu Formation **(A)**, the paleogeomorphology at the bottom of P1 Member [**(B)**, modified from Li et al., 2019), the sandstone percentages (including siltstone, obtained by seismic inversion] in the P1 **(C)**, P 2**(D)**, P3 **(E)** and P4 **(F)** members in the Pingbei area in the East China Sea Basin.

north to marine facies in the south (Figure 12B). The Baoyun High formed in the rifting stage (Figures 11A, B) probably isolated the northern freshwater deposition and southern saline water deposition. The interpretation of a freshwater lake in Zone B is acceptable because Zone B was located at the Wuyun Subsag during the P1 period (Figure 11B).

5.2.2 P2 member

The depositional environments of P2 Member are identified as a continental depositional system including freshwater lacustrine facies in the subsag and river-lake transitional facies around the subsag (Figures 12C, D). This environmental identification is supported by the evidence from seismic sedimentology: a large-scale fluvial-induced delta with a bird-foot shaped distribution of sand bodies occurred in the study area (Figure 11D).

5.2.3 P3 member

The spatial distribution and sand body shapes revealed by seismic inversion indicate a wave-altered delta in the north and a speculative delta in the south (Figure 11E), suggesting a transitional facies dominated in the area. For comparison, the C_{20}-C_{21}-C_{23}TT biomarker method also identified a transitional facies, but provides much more detailed depositional information: river-lake transitional facies in Zone A, marine facies in Zone B, and marine-continental transitional facies in C and D zones (Figures 12E, F).

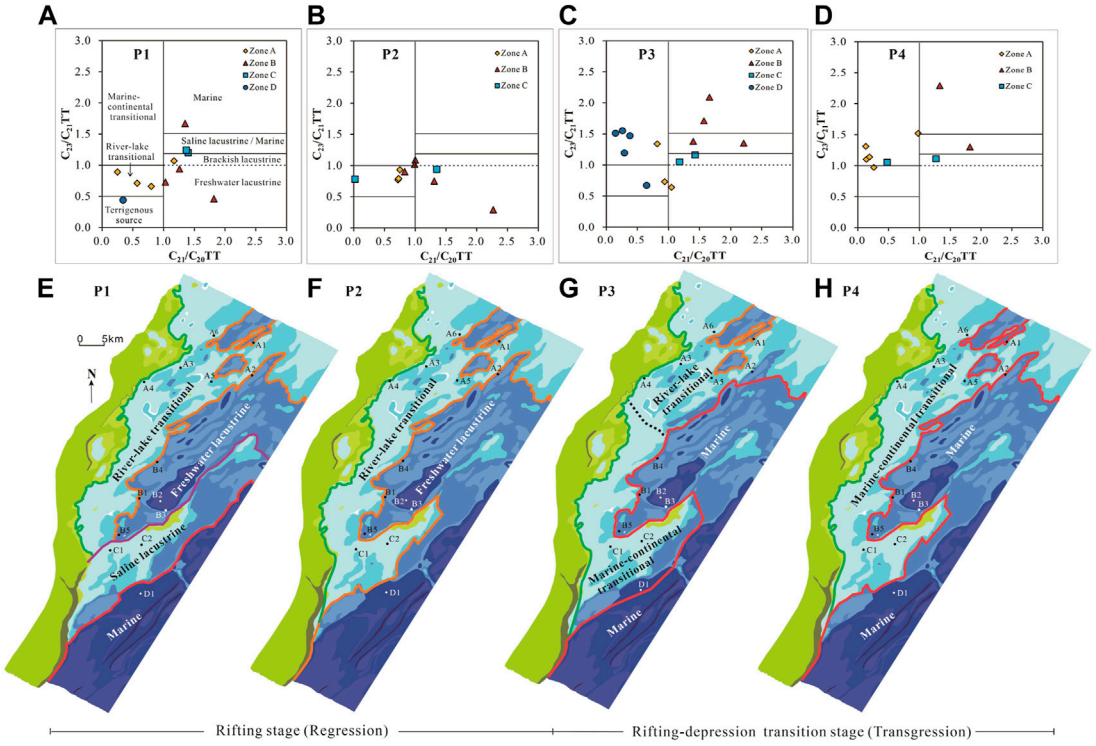

FIGURE 12
Environmental identification for the P1 **(A)**, P2 **(C)**, P3 **(E)** and P4 **(G)** members, and depositional environment distribution of the P1 **(B)**, P2 **(D)**, P3 **(F)** and P4 **(H)** members in the Pingbei area.

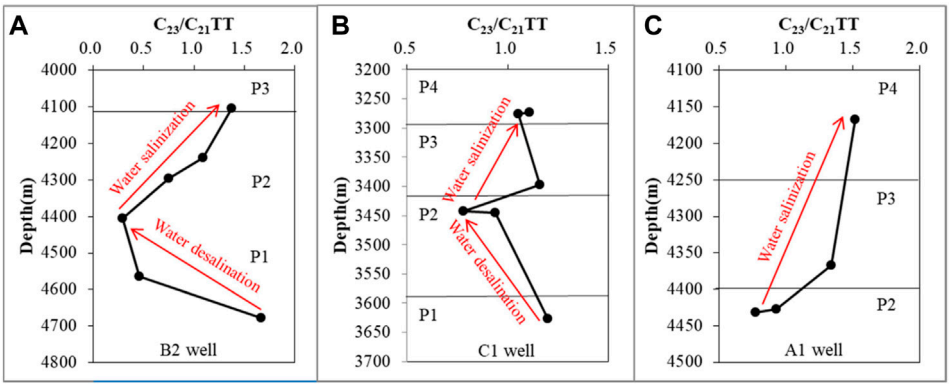

FIGURE 13
The profile of $C_{23}/C_{21}TT$ ratios along depths for the rock samples in the B2 **(A)**, C1 **(B)** and A1 **(C)** wells. The $C_{23}/C_{21}TT$ ratios in these three wells vary synchronously along stratum.

5.2.4 P4 member

The depositional environment of P4 Member in Zone A is identified as marine-continental transitional facies (Figure 12G), which is consistent with the interpretation of wave-altered deltas by seismic inversion (Figure 11F). The depositional environments in B and C zones are identified as marine/saline lacustrine and marine-continental transitional facies (Figure 12G). These environments indicate that the Pingbei area was dominated by saline-water deposition during the P4 period (Figure 12H).

5.2.5 Environment evolution of Pinghu Formation

Based on the above depositional environments identified by the C_{20}-C_{21}-C_{23}TTs, the environmental evolution process of the Pinghu Formation was reconstructed. The P1 Member in the area is characterized by a coexistence of continental system in the north and marine system in the south which were isolated by the Baoyun High (Figure 12B). During the P2 period, freshwater deposition range obviously expanded and the area was dominated by a continental depositional system (Figure 12D), suggesting a

regression has occurred since the P1 period. This regression can be characterized by a synchronous decrease of C_{23}/C_{21}TT values from the P1 to P2 members in B1 and C1 wells (Figures 13A, B). Subsequently, the depositional environments in the area gradually evolved into a marine depositional system (Figures 12F, H), suggesting a transgression occurred during the P3 and P4 periods in the area. This transgression was also characterized by a synchronous increase of C_{23}/C_{21}TT values from the P2 to P4 members (Figure 13).

In summary, the depositional environments of the Pinghu Formation in the Pingbei area were controlled by a complex marine-continental transitional system to a large extent. The C_{20}-C_{21}-C_{23}TT biomarker method not only identified the depositional environments supported by evidence from seismic sedimentology, paleogeomorphology and other conventional methods (e.g., Shen et al., 2016), but also provided much more depositional details. Take the freshwater lacustrine facies hidden in the marine-continental transitional environment for example, it has not been recognized by previous studies but was easily identified by our method. Thus, the C_{20}-C_{21}-C_{23}TT abundance patterns are robust for environmental identification even for the complex systems strongly affected by eustasy, which generally resulted in coexistence of and/or fast transition between diverse depositional environments.

6 Conclusion

Based on the analysis of a large quantity of published data and this study from a range of depositional environments worldwide, we propose that the relative abundance of C_{20}-C_{21}-C_{23}TTs in sedimentary rocks and oils are controlled by the relative contribution of plankton and terrigenous plants. The C_{20}-C_{21}-C_{23}TT abundance patterns in marine and saline lacustrine, freshwater lacustrine, shallow-water terrestrial, and marine-continental transitional facies are very distinct, characterized by $C_{20}<C_{21}<C_{23}$TT, $C_{20}<C_{21}>C_{23}$TT, $C_{20}>C_{21}>C_{23}$TT and $C_{20}>C_{21}<C_{23}$TT, respectively. The C_{23}/C_{21}TT ratio increases with increasing salinity of depositional water, while the C_{21}/C_{20}TT ratio increases with increasing depth of depositional water.

A discrimination diagram has been developed in this study for environmental identification. The C_{20}-C_{21}-C_{23}TT ratios can not only identify depositional environments, but also restore the environmental evolution through the analysis of salinity and depth variation. The effectiveness, applicability and robustness of this C_{20}-C_{21}-C_{23}TT method have been demonstrated by the samples with typical environmental indicators and a case study in a complex depositional system in the East China Sea Basin.

Data availability statement

The original contributions presented in the study are included in the article/Supplementary Material; further inquiries can be directed to the corresponding author.

Author contributions

AW: Idea, Writing; CL: Data collection, Sample testing, Writing; LL: Review, Supervision, Language polishing; RP: Seismic inversion.

Funding

This work was supported by the National Natural Science Foundation of China (No. 41402115); the Natural Science Basic Research Program of Shaanxi (2020JQ-591).

Acknowledgments

The authors sincerely thank the SINOPEC Shanghai Offshore Oil & Gas Company for contributing data. Prof. Qu Hongjun at Department of Geology, Northwest University is thanked for his informative and valuable discussions on research methods of depositional environment.

Conflict of interest

The authors declare that the research was conducted in the absence of any commercial or financial relationships that could be construed as a potential conflict of interest.

Publisher's note

Supplementary material

The Supplementary Material for this article can be found online at: https://www.frontiersin.org/articles/10.3389/feart.2023.1128692/full#supplementary-material

References

Abbas, A., Zhu, H. T., Zeng, Z. W., and Zhou, X. H. (2018). Sedimentary facies analysis using sequence stratigraphy and seismic sedimentology in the paleogene Pinghu Formation, xihu depression, east China sea shelf basin. *Mar. Petrol. Geol.* 93, 287–297. doi:10.1016/j.marpetgeo.2018.03.017

Aderoju, T., and Bend, S. (2018). Reconstructing the palaeoecosystem and palaeodepositional environment within the upper devonian–lower mississippian bakken formation: A biomarker approach. *Org. Geochem.* 119, 91–100. doi:10.1016/j.orggeochem.2018.03.003

Anders, D. E., and Robinson, W. E. (1971). Cycloalkane constituents of the bitumen from Green River Shale. *Geochim. Cosmochim. Ac.* 35 (7), 661–678. doi:10.1016/0016-7037(71)90065-2

Aquino Neto, F., Restle, A., Connan, J., Albrecht, P., and Ourisson, G. (1982). Novel tricyclic terpanes (C_{19}, C_{20}) in sediments and petroleums. *Tetrahedron Lett.* 23 (19), 2027–2030. doi:10.1016/S0040-4039(00)87251-2

Atoyebi, A. O., Adekola, S. A., and Akinlua, A. (2017). Tricyclic terpane geochemistry of source rocks from Northwestern and Central Niger Delta. *Petroleum Sci. Technol.* 35 (22), 2094–2101. doi:10.1080/10916466.2017.1381714

Barrera, I., Nogueira, A., and Bandeira, J. (2020). The Silurian glaciation in the eastern Parnaíba Basin, Brazil: Paleoenvironment, sequence stratigraphy and insights for the evolution and paleogeography of West Gondwana. *Sediment. Geol.* 406, 105714. doi:10.1016/j.sedgeo.2020.105714

Bian, W. H., Hornung, J., Liu, Z. H., Wang, P. J., and Hinderer, M. (2010). Sedimentary and palaeoenvironmental evolution of the Junggar Basin, xinjiang, northwest China. *Palaeobiodiversity Palaeoenvironments* 90 (3), 175–186. doi:10.1007/s12549-010-0038-9

Cao, J., Bian, L. Z., Hu, K., Liu, Y. T., Wang, L. Q., Yang, S. Y., et al. (2008). Biomarker features of Jurassic mudstone source rock from different sedimentary environments in the northern Qaidam basin and its applications. *Acta Geol. Sin.* 82 (8), 1121–1128. (in Chinese with English abstract).

Chen, Z., Liu, G., Wei, Y., Gao, G., Ren, J., Yang, F., et al. (2017). Distribution pattern of tricyclic terpanes and its influencing factors in the Permian source rocks from Mahu Depression in the Junggar Basin. *Oil gas Geol.* 38, 311–322. (in Chinese with English abstract). doi:10.11743/ogg20170211

Chicarelli, M. I., Neto, F., and Albrecht, P. (1988). Occurrence of four stereoisomeric tricyclic terpane series in immature Brazilian shales. *Geochim. Cosmochim. Ac.* 52 (8), 1955–1959. doi:10.1016/0016-7037(88)90176-7

De Grande, S. M. B., Neto, F. R. A., and Mello, M. R. (1993). Extended tricyclic terpanes in sediments and petroleums. *Org. Geochem.* 20 (7), 1039–1047. doi:10.1016/0146-6380(93)90112-O

Deng, Y. H., Lan, L., Li, Y. C., Liu, S. X., Tang, W., and Chen, Y. (2019). On the control effect of deltas on the distribution of marine oil and gas fields in the South China Sea. *Acta Pet. Sin.* 40 (S2), 1–12. (in Chinese with English abstract). doi:10.7623/syxb2019S2001

Dutta, S., Greenwood, P. F., Brocke, R., Schaefer, R. G., and Mann, U. (2006). New insights into the relationship between Tasmanites and tricyclic terpenoids. *Org. Geochem.* 37 (1), 117–127. doi:10.1016/j.orggeochem.2005.08.010

Ekweozor, C., Strausz, O., Albrecht, P., Cornford, C., de Groot, K., Eglinton, G., et al. (1983). "Tricyclic terpanes in the athabasca oil sands: Their geochemistry [C]//bjorøy, speers, G," in *Advances in organic geochemistry* New York (1983) 746–766.

El-Sabbagh, A. M., El-Hedeny, M. M., and Mansour, A. S. (2017). Paleoecology and paleoenvironment of the middle–upper jurassic sedimentary succession, central Saudi Arabia. *Proc. Geologists' Assoc.* 128, 340–359. doi:10.1016/j.pgeola.2017.02.001

Farrimond, P., Bevan, J. C., and Bishop, A. N. (1999). Tricyclic terpane maturity parameters: Response to heating by an igneous intrusion. *Org. Geochem.* 30 (8), 1011–1019. doi:10.1016/s0146-6380(99)00091-1

Gallegos, E., J. (1971). Identification of new steranes, terpanes, and branched paraffins in Green River shale by combined capillary gas chromatography and mass spectrometry. *Anal. Chem.* 43 (10), 1151–1160. doi:10.1021/ac60304a004

Gao, B. B., Xu, Y. H., and Li, K. W. (2014). Characteristics of jurassic source rocks in northern Qaidam Basin. *J. Yangtze Univ.* 11 (2), 21–23. (in Chinese with English abstract).

Gao, G., Titi, A., Yang, S. R., Tang, Y., Kong, Y. H., and He, W. J. (2017). Geochemistry and depositional environment of fresh lacustrine source rock: A case study from the triassic baijiantan formation shales in Junggar Basin, northwest China. *Org. Geochem.* 113, 75–89. doi:10.1016/j.orggeochem.2017.08.002

Govind, A. V., Behera, K., Dash, J. K., Balakrishnan, S., Bhutani, R., Managave, S., et al. (2021). Trace element and isotope Geochemistry of Neoarchean carbonate rocks from the Dharwar craton, southern India: Implications for depositional environments and mantle influence on ocean chemistry. *Precambrian Res.* 357, 106137. doi:10.1016/j.precamres.2021.106137

Heard, R. W., Morales-Núñez, A. G., de Lourdes Serrano-Sánchez, M., Coutiño, M. A., Barragán, R., and Vega, F. J. (2020). A new family, genus and species of Tanaidacea (Crustacea; Apseudomorpha) from the Lower Cretaceous (Aptian) of Chiapas, Mexico: Systematic revisions, including designation of two new Paleozoic families, and paleoenvironmental observations. *J. S. Am. Earth Sci.* 102, 102609. doi:10.1016/j.jsames.2020.102609

Jiang, Y. M., Shao, L. Y., Li, S., Zhao, H., Kang, S. L., Shen, W. C., et al. (2020). Deposition system and stratigraphy of pinghu formation in pinghu tectonic belt, xihu sag. *Geoscience* 34 (1), 141–153. (in Chinese with English abstract). doi:10.19657/j.geoscience.1000-8527.2020.002

Kalinowski, A. A., and Gurba, L. W. (2020). Interpretation of vitrinite reflectance–depth profiles in the northern denison trough, bowen basin, Australia. *Int. J. Coal Geol.* 219, 103367. doi:10.1016/j.coal.2019.103367

Kong, Q. F., Zhang, W. Z., Li, J. F., and Zan, C. L. (2019). Geochemical characteristice and Genesis of Ordovician natural gas under gypsolyte in Ordos Basin. *Nat. Gas. Geosci.* 30 (03), 423–432. (in Chinese with English abstract). doi:10.11764/j.issn.1672-1926.2018.12.020

Laprida, C., Chapori, N. G., Violante, R. A., and Compagnucci, R. H. (2007). Mid-Holocene evolution and paleoenvironments of the shoreface–offshore transition, north-eastern Argentina: New evidence based on benthic microfauna. *Mar. Geol.* 240 (1-4), 43–56. doi:10.1016/j.margeo.2007.02.001

Li, D. S. (2004). Return to petroleum geology of Ordos Basin. *Petrol. explor. Dev.* 31, 1–7. (in Chinese with English abstract).

Li, J., Li, J., Li, Z., Zhang, C., Cui, H., and Zhu, Z. (2018). Characteristics and genetic types of the lower Paleozoic natural gas, Ordos Basin. *Mar. Petrol. Geol.* 89, 106–119. doi:10.1016/j.marpetgeo.2017.06.046

Li, K., Zhou, X., Ding, F., Yuan, J., Shen, S., and Lv, P. (2019). Multi-factor control of sandboies distribution in the Pinghu Formation, Pingbei region of baochu slop, the xihu sag. *Mar. Geol. Quat. Geol.* 39, 115–123. (in Chinese with English abstract). doi:10.16562/j.cnki.0256-1492.2019061701

Li, Y. C., Deng, Y. H., Zhang, G. C., Fu, N., and Sun, Y. M. (2011). Tertiary marine source rocks in the northern South China Sea. *Acta Pet. Sin.* 32 (2), 219–225. (in Chinese with English abstract). doi:10.7623/syxb201102005

Li, Y., Fan, A., Yang, R., Sun, Y., and Lenhardt, N. (2021). Sedimentary facies control on sandstone reservoir properties: A case study from the permian Shanxi Formation in the southern Ordos basin, central China. *Mar. Petrol. Geol.* 129, 105083. doi:10.1016/j.marpetgeo.2021.105083

Liu, Z., Chang, X., Xu, Y., Shi, B., Zeng, Z., and Zhang, P. (2022). Depositional environment, age determination and source diagnose of oils from the Western Chepaizi Uplift (Junggar Basin) constrained by molecular biomarkers. *J. Petrol. Sci. Eng.* 110495, 110495. doi:10.1016/j.petrol.2022.110495

Lv, C. (2019). *Geochemical characteristics and oil-source correlation of paleogene source rocks in southern Dongpu Depression*. M.S. thesis. Wuhan: Yangtze University. (in Chinese with English abstract).

Ma, X. X., Yao, S. P., Zhang, B. L., Zhang, Y. X., and Peng, J. (2019). Redox conditions of paleogene paleolake and development models of high-quality source rocks in the dongpu sag, bohai bay basin. *Geol. J. China Univ.* 25 (6), 801–812. (in Chinese with English abstract).

Mahfouz, K. H., El-Sheikh, I., Obaidalla, N. A., and Shreif, A. (2021). New insights into stratigraphy and paleoenvironment of the upper cretaceous–eocene succession, farafra oasis, western desert, Egypt. *J. Afr. Earth Sci.* 175, 104096–104117. doi:10.1016/j.jafrearsci.2020.104096

Mtelela, C., Roberts, E. M., Hilbert-Wolf, H. L., Downie, R., Hendrix, M. S., Patrick, M, O., et al. (2017). Sedimentology and paleoenvironments of a new fossiliferous late Miocene-Pliocene sedimentary succession in the Rukwa Rift Basin, Tanzania. *J. Afr. Earth Sci.* 129, 260–281. doi:10.1016/j.jafrearsci.2017.01.010

Oskay, R. G., Bechtel, A., and Karayiğit, A. (2019). Mineralogy, petrography and organic geochemistry of Miocene coal seams in the Kınık coalfield (Soma Basin-Western Turkey): Insights into depositional environment and palaeovegetation. *Int. J. Coal Geol.* 210, 103205. doi:10.1016/j.coal.2019.05.012

Ourisson, G., Albrecht, P., and Rohmer, M. (1982). Predictive microbial biochemistry — From molecular fossils to procaryotic membranes. *Trends biochem. Sci.* 7 (7), 236–239. doi:10.1016/0968-0004(82)90028-7

Peters, K. E., Moldowan, J. M., and Sundararaman, P. (1990). Effects of hydrous pyrolysis on biomarker thermal maturity parameters: Monterey Phosphatic and Siliceous members. *Org. Geochem.* 15 (3), 249–265. doi:10.1016/0146-6380(90)90003-I

Philp, P., Symcox, C., Wood, M., Nguyen, T., Wang, H., and Kim, D. (2021). Possible explanations for the predominance of tricyclic terpanes over pentacyclic terpanes in oils and rock extracts. *Org. Geochem.* 155, 104220. doi:10.1016/j.orggeochem.2021.104220

Pichat, A., Hoareau, G., Lopez, M., Callot, J., and Ringenbach, J. (2021). Sedimentology and depositional environment of the Late Eocene marine siliciclastic to evaporite transition in the Sivas Basin (Turkey). *Mar. Petrol. Geol.* 131, 105151. doi:10.1016/j.marpetgeo.2021.105151

Qiu, Z. G. (1987). Metallogenetic models of sedimentary iron ore deposits. *J. Chengdu Coll. Geol.* 14 (04), 1–7. (in Chinese with English abstract).

Rashid, M. A. (1979). Pristane-phytane ratios in relation to source and diagenesis of ancient sediments from the Labrador Shelf. *Chem. Geol.* 25 (1), 109–122. doi:10.1016/0009-2541(79)90087-1

Samuel, O. J., Kildahl-Andersen, G., Nytoft, H. P., Johansen, J. E., and Jones, M. (2010). Novel tricyclic and tetracyclic terpanes in Tertiary deltaic oils: Structural identification, origin and application to petroleum correlation. *Org. Geochem.* 41 (12), 1326–1337. doi:10.1016/j.orggeochem.2010.10.002

Shen, Y. L., Qin, Y., Guo, Y. H., Zhao, Z. G., Yuan, X. X., Qu, Z. H., et al. (2016). Development characteristics of coal-measure source rocks divided on the basis of Milankovich coal accumulation cycle in Pinghu Formation, Xihu sag. *Acta Pet. Sin.* 37 (6), 706–714. (in Chinese with English abstract). doi:10.7623/syxb201606002

Shen, Y. L., Qin, Y., Li, Z. F., Jin, J., Wei, Z. H., Zheng, J., et al. (2017). The sedimentary origin and geological significance of siderite in the Longtan Formation of Western Guizhou Province. *Earth Sci. Front.* 24 (6), 152–161. (in Chinese with English abstract). doi:10.13745/j.esf.yx.2016-11-51

Soreghan, M. J., and Cohen, A. S. (1996). Textural and compositional variability across littoral segments of lake tanganyika: The effect of asymmetric basin structure on sedimentation in large rift lakes. *AAPG Bull.* 80 (3), 382–409. doi:10.1306/64ed87f0-1724-11d7-8645000102c1865d

Sun, J. P. (2017). *Research on Taiyuan Formation-Shanxi Formation sedimentary facies and potential shale gas exploration*. M.S. thesis. Beijing): China University of Geosciences. (in Chinese with English abstract).

Sun, Y. Z. (2006). Sedimentary system and oil and gas source characteristics of Shahejie Formation in Shengtuo area, Dongying Sag. *J. China Univ. Petroleum* 30 (6), 24–30. (in Chinese with English abstract).

Tao, S., Wang, C., Du, J., Liu, L., and Chen, Z. (2015). Geochemical application of tricyclic and tetracyclic terpanes biomarkers in crude oils of NW China. *Mar. Petrol. Geol.* 67, 460–467. doi:10.1016/j.marpetgeo.2015.05.030

Tissot, B. P., and Welte, D. H. (1978). *Petroleum Formation and occurrence*. 2nd ed. Berlin: Springer-Verlag, 1–699.

Wang, A., Wang, Z., Li, L., Fan, C., Zhang, K., Xiang, B., et al. (2019). Hydrocarbon migration in the multiple-sourced petroleum system in the northwestern Junggar Basin (northwestern China): Constraint from geochemical and phase fractionation analysis. *AAPG Bull.* 103 (9), 2247–2284. doi:10.1306/01211916512

Wang, C. Y., Chen, M. J., Wang, Z. C., and Guo, Y. H. (2007). Sedimentarv facies of the Shanxi Formation and member 8 of xiashihezi formation of permian in southern Ordos Basin. *J. Palaeogeogr.* 9 (04), 369–378. (in Chinese with English abstract).

Wang, Y. C., Cao, J., Tao, K. Y., Li, E., Ma, C., and Shi, C. H. (2020). Reevaluating the source and accumulation of tight oil in the middle permian lucaogou formation of the Junggar Basin, China. *Mar. Petrol. Geol.* 117, 104384. doi:10.1016/j.marpetgeo.2020.104384

Wendorff-Belon, M., Rospondek, M., and Marynowski, L. (2021). Early oligocene environment of the central paratethys revealed by biomarkers and pyrite framboids from the tarcău and vrancea nappes (eastern outer carpathians, Romania). *Mar. Petrol. Geol.* 128, 105037. doi:10.1016/j.marpetgeo.2021.105037

Xiao, H., Li, M. J., Liu, J. G., Mao, F. J., Cheng, D. S., and Yang, Z. (2019a). Oil-oil and oil-source rock correlations in the Muglad Basin, Sudan and South Sudan: New insights from molecular markers analyses. *Mar. Petrol. Geol.* 103, 351–365. doi:10.1016/j.marpetgeo.2019.03.004

Xiao, H., Li, M. J., Yang, Z., and Zhu, Z. L. (2019b). Distribution and geochemical significance of C19~C23 tricyclic terpanes in source rocks and crude oils from different environments. *Geochimica* 48 (2), 161–170. (in Chinese with English abstract).

Xu, Q. H., Shi, W. Z., Xie, X. Y., Busbeyet, A., Xu, L. T., Wu, R., et al. (2018). Inversion and propagation of the late paleozoic porjianghaizi fault (north Ordos Basin, China): Controls on sedimentation and gas accumulations. *Mar. Petrol. Geol.* 91, 706–722. doi:10.1016/j.marpetgeo.2018.02.003

Yang, H., Fu, J. H., Liu, X. S., and Meng, P. L. (2012). Accumulation conditions and exploration and development of tight gas in the Upper Paleozoic of the Ordos Basin. *Petrol. explor. Dev.* 39 (3), 315–324. doi:10.1016/S1876-3804(12)60047-0

Yang, T. (2007). *Restudy of Cordaites baodeensis Sun from lower permian Shanxi Formation of baode, Shanxi*. M.S. thesis. Changchun: Jilin University. (in Chinese with English abstract).

Yu, S., Wang, X. L., Xiang, B. L., Ren, J. L., Li, E. T., Wang, J., et al. (2017). Molecular and carbon isotopic geochemistry of crude oils and extracts from Permian source rocks in the northwestern and central Junggar Basin, China. *Org. Geochem.* 113, 27–42. doi:10.1016/j.orggeochem.2017.07.013

Zhang, S., Zhang, B., Bian, L., Jin, Z., Wang, D., and Chen, J. (2007). Xiamaling Formation oil shale: Accumulated by red algae more than 800 million years ago. *Sci. China Ser. D Earth Sci.* 37, 636–643. (in Chinese). doi:10.1360/zd2007-37-5-636

Zhang, W. Z., Yang, H., Hou, L. H., and Liu, F. (2009). Distribution and geological significance of 17α(H)-diahopanes from different hydrocarbon source rocks of Yanchang Formation in Ordos Basin. *Sci. China Ser. D-Earth Sci.* 52 (7), 965–974. (in Chinese with English abstract). doi:10.1007/s11430-009-0076-1

Zhang, X., Lin, C., Zahid, M. A., Jia, X., and Zhang, T. (2017). Paleosalinity and water body type of Eocene Pinghu Formation, xihu depression, east China Sea Basin. *J. Petrol. Sci. Eng.* 158, 469–478. doi:10.1016/j.petrol.2017.08.074

Zhao, L., Chen, J., Zhang, Y., Cheng, X., and Sha, X. (2008). Sedimentary characteristics of Pinghu Formation in pinghu structural belt of xihu depression, east China sea. *Glob. Geol.* 27, 42–47. (in Chinese with English abstract).

Zhu, G. Y., and Jin, Q. (2003). Geological and geochemical characteristics of two sets of high quality source rocks in Dongying Sag. *Acta sedimentol. Sin.* 21 (3), 506–512. (in Chinese with English abstract).

Zodrow, E. L., Mastalerz, M., Orem, W. H., Simůnek, Z., and Bashforth, A. R. (2000). Functional groups and elemental analyses of cuticular morphotypes of Cordaites principalis (germar) geinitz, carboniferous maritimes basin, Canada. *Int. J. Coal Geol.* 45 (1), 1–19. doi:10.1016/S0166-5162(00)00018-5

Zumberge, J. E. (1987). Prediction of source rock characteristics based on terpane biomarkers in crude oils: A multivariate statistical approach. *Geochim. Cosmochim. Ac.* 51 (6), 1625–1637. doi:10.1016/0016-7037(87)90343-7

frontiers | Frontiers in Earth Science

TYPE Original Research
PUBLISHED 19 January 2023
DOI 10.3389/feart.2023.1105992

OPEN ACCESS

EDITED BY
Meng Wang,
Chang'an University, China

REVIEWED BY
Guangyan Zhou,
China University of Geosciences Wuhan, China
Chao Wang,
Northwest University, China

*CORRESPONDENCE
Jianxin Zhang,
zjx66@yeah.net

SPECIALTY SECTION
This article was submitted to Petrology, a section of the journal Frontiers in Earth Science

RECEIVED 23 November 2022
ACCEPTED 03 January 2023
PUBLISHED 19 January 2023

CITATION
Teng X, Zhang J, Mao X, Wu Y and Guo Q (2023), Geochemistry, zircon U-Pb age and Hf isotope for the Huatugou granitoid in western Qaidam: Petrogenesis and tectonic implications.
Front. Earth Sci. 11:1105992.
doi: 10.3389/feart.2023.1105992

Geochemistry, zircon U-Pb age and Hf isotope for the Huatugou granitoid in western Qaidam: Petrogenesis and tectonic implications

Xia Teng[1,2], Jianxin Zhang[1]*, Xiaohong Mao[1], Yawei Wu[1,2] and Qi Guo[1,2]

[1]Institute of Geology, Chinese Academy of Geological Sciences, Beijing, China, [2]School of Earth and Space Sciences, Peking University, Beijing, China

The Qaidam Precambrian block is located in the northeastern Tibetan Plateau and was intruded by numerous Ordovician-Devonian granitoids during and after the closure of the Proto-Tethys Ocean. In the past 20 years, the granitoids within early Paleozoic subduction-collision belts have been investigated in detail. However, the granitoids intruding the inner part of the Qaidam block, bearing the tectonic significance for the whole block, still need to be understood. This study presents new whole-rock geochemical and zircon U-Pb-Hf isotopic data for the Huatugou granitoids in the Qaidam Precambrian block. The investigated granitoids include granodiorite, monzogranite, biotite granite, and muscovite granite, which intruded the Precambrian basements during 451–400 Ma. The granodiorites (451 ± 6 Ma) display adakitic geochemical features and syn-tectonic textures, and their magmas were generated by the partial melting of the lower mafic crust within a thickened continent. The muscovite granites (410 ± 6 Ma), with negative zircon εHf(t) values of −14.5 to −10.4, were crystallized from fractionated S-type magmas, which were derived from the partial melting of ancient crustal materials. The biotite granite (410 ± 3 Ma) and monzogranites (400 ± 4 Ma) are high-temperature A_2-type granites. The biotite granite displays positive zircon εHf(t) values of +1.7 to +5.6. Its magma was generated by the high-temperature partial melting of juvenile crustal rocks in a thinned lower crust. The monzogranites exhibit higher SiO_2 contents and lower εHf(t) values, and their magmas were derived from the same source but underwent assimilation and fractional crystallization during emplacement. From the thickened to the thinned continent during 451–410 Ma, the western Qaidam block experienced a tectonic transition from compression to extension. Combined with regional geological data, this study suggests that the Qaidam block consisted of the thickened continental crust during subduction processes until the detachment of the subducted slab during the continental collision. The regional extension of the Qaidam block commenced at ~420 Ma, soon after the exhumation of ultrahigh-pressure metamorphic rocks within the northern Qaidam subduction-collision complex belt.

KEYWORDS

Qaidam block, Huatugou granitoids, early paleozoic, zircon U-Pb ages, Hf isotope

1 Introduction

Granitic plutons account for a significant volume of many ancient orogenic belts and have been a primary investigated object concerning orogenic evolution. On the one hand, observations from partial melting experiments indicate that the chemical features of granite products are directly related to melting conditions and source compositions (e.g., Clemens et al., 1986; Patiño Douce, 1995; Winther, 1996; Patiño Douce and Harris, 1998; Castro et al., 1999; Acosta-Vigil et al., 2006), most of which are not exclusively encountered in one specific tectonic setting (Whalen et al., 1987; Eby., 1992; Chappell and White, 2001; Frost et al., 2001; Castillo, 2012). On the other hand, most ancient orogenic belts contain various granitic plutons, each of which was derived from a specific source at different periods of tectonic evolution. In turn, the petrogenesis and formation ages of such a set of various granitoids provide critical constraints on changes in *P-T* conditions and source regions with time, which can be related to a sequential transition of tectonic settings in a relatively well-constrained geological framework (e.g., Zhang et al., 2013; Zhu et al., 2018; Hopkinson et al., 2019).

The Qaidam block, located in the northeastern Tibetan Plateau, is a Precambrian block surrounded by Paleozoic orogenic belts (Zhang et al., 2021). Previous studies indicate that granitic magmas intruding the Qaidam block were mainly crystallized at 470–370 Ma and 270–215 Ma (Wu C. L. et al., 2014b; Cheng et al., 2017; Chen et al., 2020). The early Paleozoic granitic magmatism (470–370 Ma) has been linked to the subduction of the Proto-Tethys Ocean and following collisional to post-collisional processes experienced by the Qaidam block (Wu et al., 2014a; Yu et al., 2019; Yang et al., 2020). This series of tectonic processes also resulted in arc-related magmatism, exhumated high-to ultrahigh-pressure metamorphic associations, and preservation of possible ophiolites (relict of oceanic crust) within the

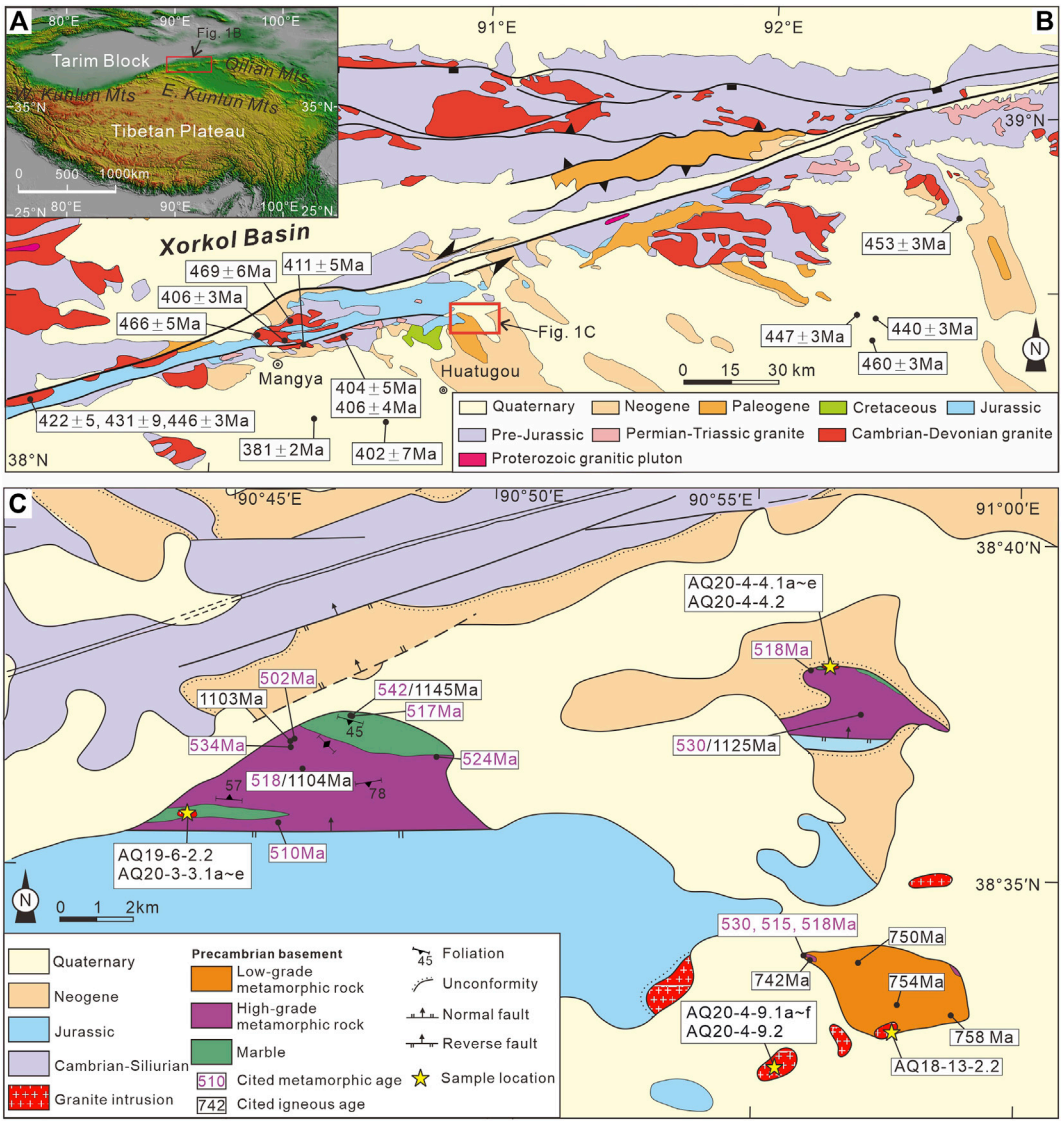

FIGURE 1
(A) Location of the Qaidam basin. **(B)** Simplified western Qaidam geological map (after Cheng et al., 2017). Zircon U-Pb data of early Paleozoic granitoids are cited from Cheng et al. (2017), Wang C. et al., (2014a), and Wu C. L. et al. (2014b). **(C)** Simplified geological map of the study region showing primary lithologies and sample locations. Magmatic and metamorphic zircon U-Pb data are cited from Teng et al. (2020, 2022).

TABLE 1 Sampling location, ICPW norm calculation, and analytic items for granitoids from the western Qaidam block.

No.	Sample no.	Location		Lithology	ICPW norm/wt%				
		Latitude	Longitude		Qtz	Pl	Or	Co	Hy
1	AQ18-13-2.2	38°32′53.44″N	90°57′42.07″E	Biotite granite	22.04	41.52	25.07	0.81	7.76
2	AQ20-4-9.1a	38°32′25.27″N	90°55′35.44″E	Monzogranite	27.40	43.23	22.98	0.34	4.63
3	AQ20-4-9.1b	38°32′25.27″N	90°55′35.44″E		28.34	41.04	23.93	0.62	4.60
4	AQ20-4-9.1c	38°32′25.27″N	90°55′35.44″E		28.57	39.36	25.18	0.86	4.60
5	AQ20-4-9.1d	38°32′25.27″N	90°55′35.44″E		28.57	41.07	23.58	0.69	4.62
6	AQ20-4-9.1e	38°32′25.27″N	90°55′35.44″E		29.36	38.64	24.96	0.94	4.63
7	AQ20-4-9.1f	38°32′25.27″N	90°55′35.44″E		29.70	41.11	22.33	0.78	4.62
8	AQ20-4-9.2	38°32′25.27″N	90°55′35.44″E		26.82	35.29	31.61	0.07	4.57
9	AQ19-6-2.2	38°36′2.17″N	90°44′21.65″E	Muscovite granite	30.96	29.33	35.11	2.03	1.77
10	AQ20-3-3.1a	38°36′2.31″N	90°44′27.04″E		32.56	31.73	29.91	2.77	2.19
11	AQ20-3-3.1b	38°36′2.31″N	90°44′27.04″E		34.74	33.23	28.22	1.60	1.51
12	AQ20-3-3.1c	38°36′2.31″N	90°44′27.04″E		30.52	31.47	33.77	1.60	1.80
13	AQ20-3-3.1d	38°36′2.31″N	90°44′27.04″E		28.35	29.09	38.47	1.43	1.84
14	AQ20-3-3.1e	38°36′2.31″N	90°44′27.04″E		34.29	32.79	28.90	1.83	1.55
15	AQ20-4-4.1a	38°38′11.93″N	90°56′41.88″E	Granodiorite	33.65	50.89	10.36	1.41	2.95
16	AQ20-4-4.1b	38°38′11.93″N	90°56′41.88″E		33.25	51.07	10.46	1.41	3.03
17	AQ20-4-4.1c	38°38′11.93″N	90°56′41.88″E		33.13	51.13	10.93	1.20	2.90
18	AQ20-4-4.1d	38°38′11.93″N	90°56′41.88″E		33.01	50.51	11.41	1.24	3.06
19	AQ20-4-4.1e	38°38′11.93″N	90°56′41.88″E		32.49	52.36	10.08	1.25	3.10
20	AQ20-4-4.2	38°38′13.55″N	90°56′30.93″E		33.32	50.83	10.61	1.27	3.20

Qtz, Quartz; Pl, Plagioclase; Or, Orthoclase; Co, Corundum; Hy, Hypersthene.

northern Qaidam and northern East Kunlun (southern Qaidam) subduction-collision belts (Zhang et al., 2017; Dong et al., 2018; Song et al., 2018 and references therein). In the past 20 years, most investigated granitoids, especially syn-collisional granitoids, came from subduction-collision belts, which are complex belts resulting from processes including continental subduction, collision, exhumation of subducted crust, and post-collisional extension. In addition to the complexity of interpreting the petrogenesis, the tectonic processes, inferred from granitoids within subduction-collision belts, hardly reflect the response of the whole Qaidam block, which used to be a Precambrian micro-continent located on the margin of East Gondwana (Teng et al., 2020; Zhang et al., 2021; Teng et al., 2022). Recognizing the early Cambrian ultrahigh-temperature (UHT, >900°C) metamorphism within western Qaidam provides new constraints on the paleo-geographic position of the Qaidam block (Teng et al., 2020), a continent arc of the Gondwana facing the Proto-Tethys Ocean, before early Paleozoic subduction-collision. Meanwhile, it also evokes a tectonic interest in granitic intrusions in the same region in the Precambrian Qaidam block. It is recognized that the western Qaidam was affected by Ordovician-Devonian felsic magmatism, inferred from 469 to 381 Ma granitoids along the Altyn Tagh Fault and in drills (Figure 1B; Cheng et al., 2017; Wang C. et al., 2014a; Wu C. L. et al., 2014b). However, the tectonic transitions during the prolonged felsic magmatism in western Qaidam, a part of the Precambrian micro-continent, have not been well constrained.

This study presents whole-rock geochemical and zircon U-Pb-Hf isotopic data for Huatugou granitoids, which were emplaced into the UHT metamorphic rocks-bearing Precambrian basements (Figure 1C). Our new data not only put new constraints on the ages, sources, and petrogenesis of these granitoids but also provide essential insights into the tectonic processes of the whole Qaidam block.

2 Geological setting and sampling

2.1 Geological setting

The Qaidam Basin, located in the northeastern Tibetan Plateau, is bounded by the Qilian Mountains to the northeast, the Altyn Tagh Mountains to the northwest, and the East Kunlun Mountains to the south (Figure 1A). The main body of the Qaidam basement is covered by thick Mesozoic-Cenozoic sediments. Hence, the nature of the basement is mainly studied with outcrops and drills on the basin's margins.

The Paleoproterozoic basement of the Qaidam block, Jinshuikou Group, comprises migmatite, gneiss, amphibolite, schist, quartzite,

and marble and is mainly exposed in the south of the Qaidam Basin (Wang et al., 1983). During early Neoproterozoic, the Jinshuikou Group, as well as some Mesoproterozoic protoliths in the northern Qaidam (the northeast of the Qaidam Basin), underwent a series of high-grade metamorphism, which is characterized by transitions from Buchan-type (low-pressure) metamorphism at ~1.0 Ga to Barrovian-type up to high-pressure granulite-facies metamorphism at 0.94–0.92 Ga (Ren et al., 2019; He et al., 2020; Ren et al., 2021; He et al., 2022). Coeval magmatism produced abundant S-type granites, whose emplacements started as early as ~1.1 Ga and widely occurred during 1.0–0.9 Ga (He et al., 2016; He et al., 2018; Teng et al., 2022 and references therein). The 1.1–0.9 Ga metamorphism and magmatism resulted from prolonged subduction-collision and were followed by 0.85–0.75 Ga felsic and mafic magmatism in a continental rifting setting, linked to the assembly and breakup of the Rodinia supercontinent, respectively (Song et al., 2010; Yu et al., 2013; Ren et al., 2021; He et al., 2022; Teng et al., 2022).

During the early Paleozoic, the Qaidam block underwent continental subduction-collision following the closure of the Proto-Tethys Ocean, as implied by arc-related Tanjianshan Group metavolcanic rocks and gabbro dikes (514–465 Ma, Wu et al., 1987; Li et al., 1999; Yuan et al., 2002; Shi et al., 2004) and subduction-related (U)HP metamorphic rocks (457–422 Ma, Song et al., 2005; Yang et al., 2005; Mattinson et al., 2006; Chen et al., 2009; Zhang et al., 2010; Meng et al., 2013; Song et al., 2018) within the northern and southern Qaidam. In northern Qaidam (the northeast of the Qaidam Basin), granitic magma emplacement started as early as ~470 Ma in a continental arc setting, prevailed at 446–397 Ma during the exhumation of subducted crust, and continued to 382–372 Ma in a post-collisional environment (Wu et al., 2014a; Sun et al., 2020; Yang et al., 2020). In the southern Qaidam (including the northern East Kunlun), Paleozoic magmatism primarily occurred during 424–394 Ma in a post-collisional extension, forming granitic plutons (Zhang et al., 2003; Chen et al., 2006; Cheng et al., 2017; Chen et al., 2020), mafic-ultramafic intrusions (Wang G. et al., 2014b; Peng et al., 2016; Song et al., 2016), and rhyolitic rocks of the Maoniushan Formation (Lu et al., 2010). In addition, the western Qaidam, to the south of the active left-slip Altyn Tagh Fault, was also affected by Ordovician-Devonian felsic magmatism, inferred from 469 to 381 Ma granitoids along the Altyn Tagh Fault and in drills (Figure 1B; Cheng et al., 2017; Wang C. et al., 2014a; Wu C. L. et al., 2014b).

The rock records regarding geological activities of the Qaidam block between 750 and 520 Ma are mainly found in the western Qaidam. Exposed in the north of Huatugou City, the Precambrian basements of western Qaidam consist of granulite-facies metamorphic rocks and low-grade metamorphic supracrustal rocks (Figure 1C). The Huatugou granulite-facies rocks include felsic gneisses with protolith ages of ~1.1 Ga (Teng et al., 2022), pelitic gneisses, and olivine-bearing marbles, with minor Mg-Al granulite and mafic granulite lenses. They experienced early Cambrian (540–500 Ma) UHT metamorphism, which is characterized by a clockwise *P-T* path with a prograde *P* peak >1.4 GPa (Teng et al., 2020). The UHT metamorphism was thought to occur within the Kuunga Orogen; hence, the Qaidam block was located on the margin of East Gondwana (Teng et al., 2020; Teng and Zhang, 2020). The low-grade metamorphic supracrustal association comprises metavolcanic rocks, quartzofeldspathic leptynite, mica schist, and quartzite. The protoliths of felsic metavolcanic rocks were crystallized from high-temperature A-type magmas with positive zircon εHf(t) values (+0.9 to +6.1), which were emplaced in a continental rifting environment at ~0.75 Ga (Teng et al., 2022). Both high-grade and low-grade metamorphic basements exposed in the Huatugou area were intruded by granitic plutons and dikes (Figure 1C), whose petrogenesis and tectonic significance are the focus of this study.

2.2 Sampling

In the Huatugou area, the granitoids mainly occurred as small plutons and dikes intruding Precambrian basements (Figure 1C). In this study, investigated granitoids include biotite granite, monzogranite, muscovite monzogranite, and granodiorite. A total of 20 samples were used for whole-rock geochemical analyses, and four representative samples were selected for zircon U-Pb age and Hf isotope analyses (Table 1).

The biotite granite, sample AQ18-13-2.2, was collected from a dike, which is 1–5 m wide and intruded mylonitic quartzite (Figure 2A). The sample consists of plagioclase (40%–45%), K-feldspar (20%–25%), quartz (20%–25%), biotite (7%–10%), and amphibole (1%–3%) (Figure 2B). The monzogranite samples AQ20-4-9.1a~f and AQ20-4-9.2 were collected from a granitic pluton that was broken into fragments widespread the hills and buried by the sediments (Figure 2C). Monzogranites are fine-to coarse-grained and composed of K-feldspar (20%–30%), plagioclase (35%–45%), quartz (25%–30%), biotite (1%–3%), and muscovite (<1%) (Figure 2D). The muscovite granites, including samples AQ19-6-2.2 and AQ20-3-3.1a~e, were collected from a granitic dike, which is ~20 m wide and intruded marble (Figures 1C, 2E). Muscovite granites consist of K-feldspar (28%–33%), plagioclase (30%–35%), quartz (30%–35%), muscovite (5%–7%), and biotite (~1%). Muscovite and plagioclase are deformed and aligned under the microscope (Figure 2F). The granodiorite samples (AQ20-4-4.1a~e and AQ20-4-4.2) were collected from a granitic pluton intruding marble near a talc deposit (Figure 1C). Granodiorites exhibit porphyritic textures and are locally mylonitized in the contacting zone with marble (Figure 2G). Granodiorites mainly consist of plagioclase (50%–55%), quartz (30%–35%), K-feldspar (9%–12%), and biotite (~3%). The phenocrysts consist of K-feldspar and plagioclase, while quartz mainly occurs in the matrix (Figure 2H).

3 Analytical methods

3.1 Whole-rock major and trace elemental analysis

The whole-rock composition analysis was conducted at the Wuhan Samplesolution Analytical Technology Co., Ltd., China. The major elements were measured by a Primus II X-ray fluorescence spectrometer (XRF). The trace elements were measured by an Agilent 7700e inductively coupled plasma mass spectrometry (ICP-MS). The analytical uncertainties are ~5%.

3.2 Zircon U-Pb isotopic and trace elemental analysis

Zircon grains were extracted from pulverized rock samples using combined heavy liquid and magnetic techniques and handpicked

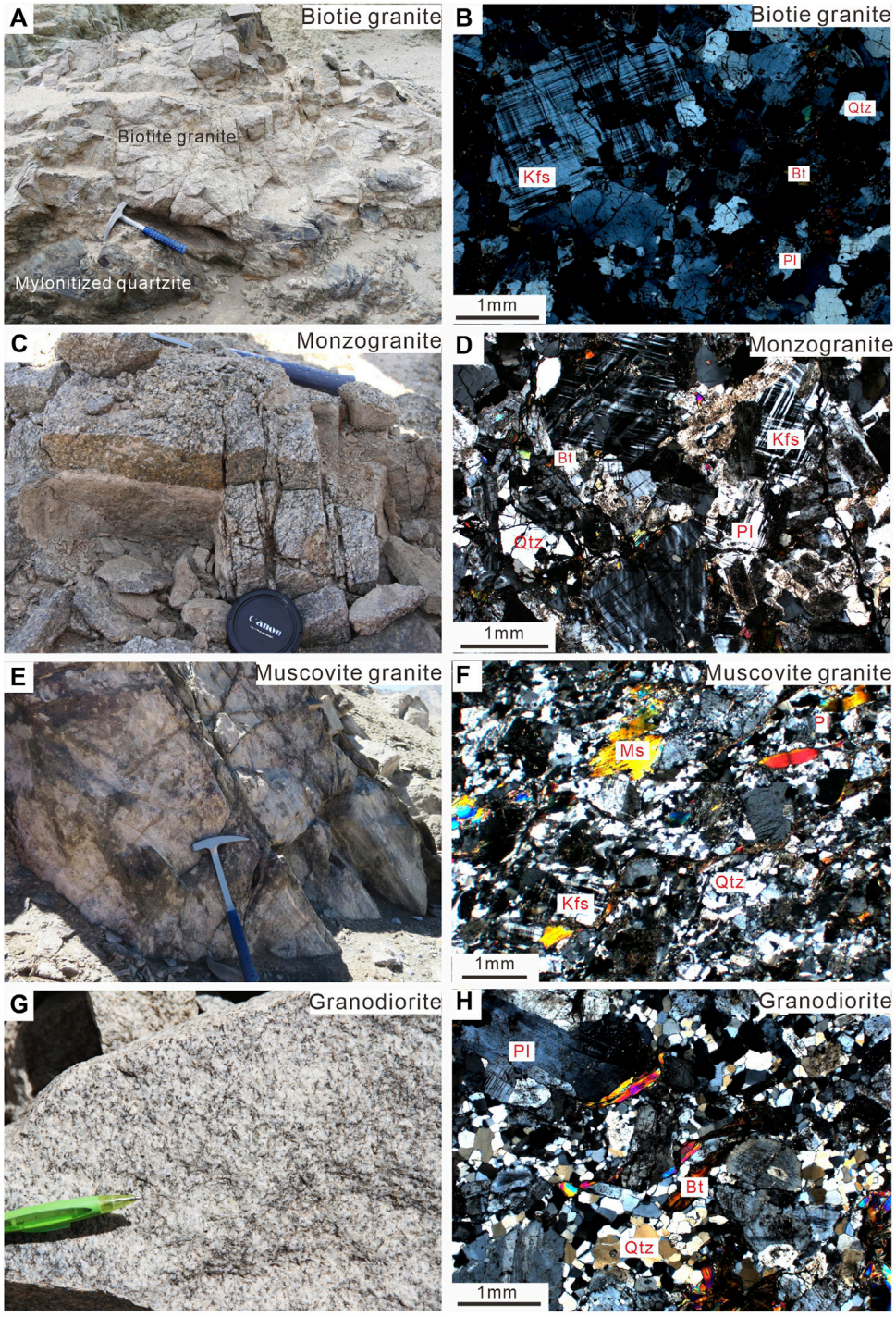

FIGURE 2
Field photographs and photomicrographs of **(A,B)** biotite granite, **(C,D)** monzogranite, **(E,F)** muscovite granite, and **(G,H)** granodiorite in the Huatugou area. Bt, biotite; Kfs, K-feldspar; Ms, muscovite; Pl, plagioclase; Qtz, quartz.

under a binocular microscope. Separated zircon grains were mounted in an epoxy resin and polished to expose about half the grains. Cathodoluminescence (CL) images were taken using an FEI PHILIPS XL30 SFEG scanning electron microscope (SEM) at the Institute of Geology, Chinese Academy of Geological Sciences (CAGS). Zircon U-Pb isotope and trace element concentrations were measured by an Analytikjena PQMS Elite ICP-MS equipped with a RESOlution 193 nm laser ablation system at Beijing Createch Testing Technology Co., Ltd. The laser spot was set to 24 μm with a repetition rate of 6 Hz and an energy density of 6 J/cm^2. Zircon standards GJ-1 (602 Ma, Jackson et al., 2004), 91500 (1065 Ma, Wiedenbeck et al., 1995), and Plesovice (337 Ma, Sláma et al., 2008) were analyzed together with samples for quality control of zircon U-Pb isotope data. Each measurement consisted of a 15 s background signal acquisition followed by a 45 s data acquisition from the samples. Off-line raw data selection, background and

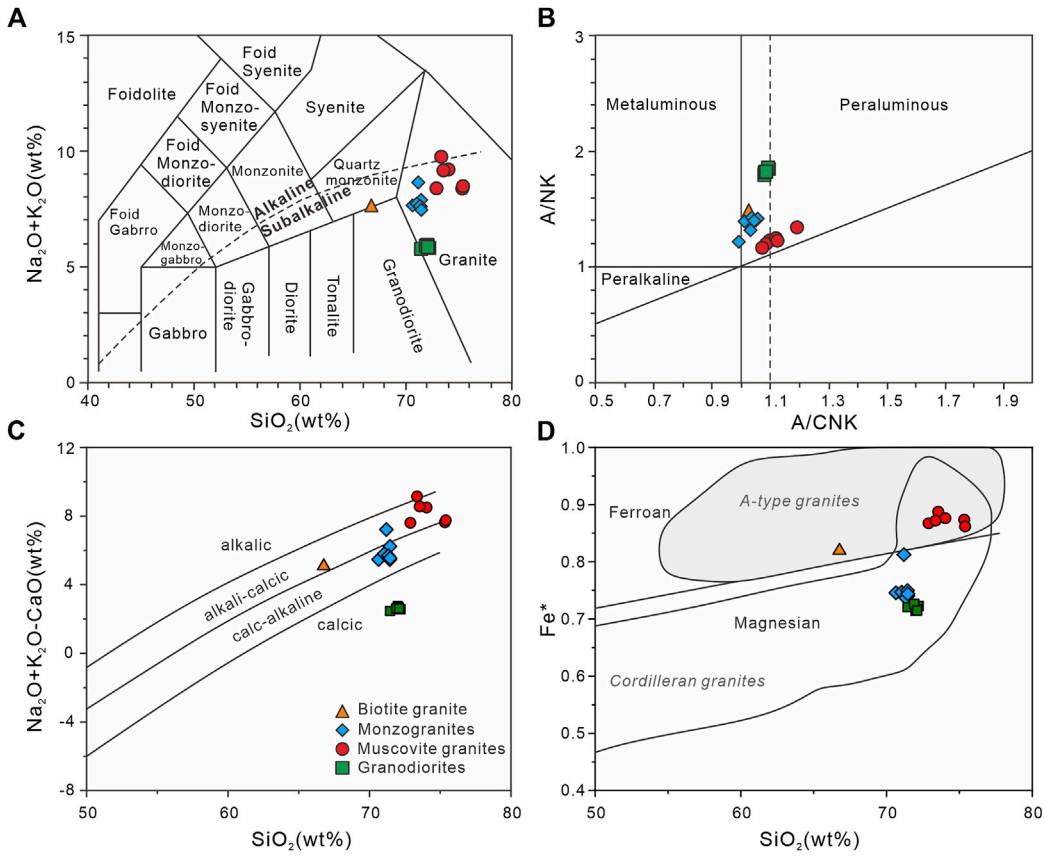

FIGURE 3
Geochemical classification diagrams using major element oxides. **(A)** (Na_2O+K_2O) *vs.* SiO_2 (Irvine and Baragar, 1971; Middlemost, 1994). **(B)** A/NK *vs.* A/CNK (Maniar and Piccoli, 1989). A/CNK = molar $Al_2O_3/(CaO+Na_2O+K_2O)$; A/NK = molar $Al_2O_3/(Na_2O+K_2O)$. **(C)** (Na_2O+K_2O-CaO) *vs.* SiO_2 and **(D)** FeO* *vs.* SiO_2 (Frost et al., 2001). Fe*=$FeO^T/(FeO^T+MgO)$.

analyzed signals integration, time-drift correction, and quantitative calibration for U-Pb dating were performed using ICPMSDataCal (Liu et al., 2010). U-Pb concordia plots and weighted mean $^{206}Pb/^{238}U$ age calculations were conducted using Isoplot 4.15 (Ludwig, 2012). Uncertainty of individual analysis was reported with a 1σ error, and weighted mean ages were calculated at a 95% confidence level. Trace element concentrations were corrected using NIST610 as an external and Si as an internal standard.

3.3 Zircon Hf isotopic analysis

Hf isotope compositions of the dated zircons were measured using a Neptune Plus ICP-MS (Thermo Fisher Scientific, Germany) in combination with a Geolas HD excimer ArF laser ablation system (Coherent, Germany) at the Wuhan Samplesolution Analytical Technology Co., Ltd., China. All data were acquired with a beam size of 44 μm, a laser repetition rate of 8 Hz, and an energy density of 10 J/cm^2. The zircon 91500, GJ-1, and Plesovice were used as external standards and have weighted mean $^{176}Hf/^{177}Hf$ values of 0.2822939 ± 0.0000093, 0.282008 ± 0.000022, and 0.2824780 ± 0.0000049, respectively. Offline selection, background and analyzed signals integration, and mass calibration were performed using ICPMSDataCal (Liu et al., 2010). All calculated data were considered for isobaric interferences and normalized to $^{179}Hf/^{177}Hf$ of 0.7325 using an exponential correction for mass bias.

4 Results

4.1 Whole-rock geochemistry

Whole-rock compositions are presented in Supplementary Table S1 and illustrated in Figures 3, 4. The biotite granite has 66.77 wt% SiO_2, 7.62 wt% total alkali (Na_2O+K_2O), 2.53 wt% CaO, 15.19 wt% Al_2O_3, 4.68 wt% $Fe_2O_3^T$, and 0.93 wt% MgO, with high FeO^T/MgO (4.21) and Fe* [=$FeO^T/(FeO^T+MgO)$=0.82]. In the classification diagram, the biotite granite falls on the boundary between quartz monzonite and granodiorite (Figure 3A). In discrimination diagrams of A/NK *vs.* A/CNK, (Na_2O+K_2O-CaO) *vs.* SiO_2, and Fe* *vs.* SiO_2 (Figures 3B–D), the biotite granite falls in weakly peraluminous, alkali-calcic, and ferroan fields. The biotite granite contains 367 ppm REE. In the chondrite-normalized REE diagram, it displays LREE enrichment relative to HREE [$(La/Yb)_N$=12.64] and a negative Eu anomaly ($Eu/Eu^*=Eu_N/(Sm_N\times Gd_N)^{1/2}$ =0.49) (Figure 4A). In the primitive mantle-normalized diagram, the biotite granite exhibits enrichments of Th, La, Nd, and Zr and depletions of Ba, Nb, Ta, and Sr (Figure 4B).

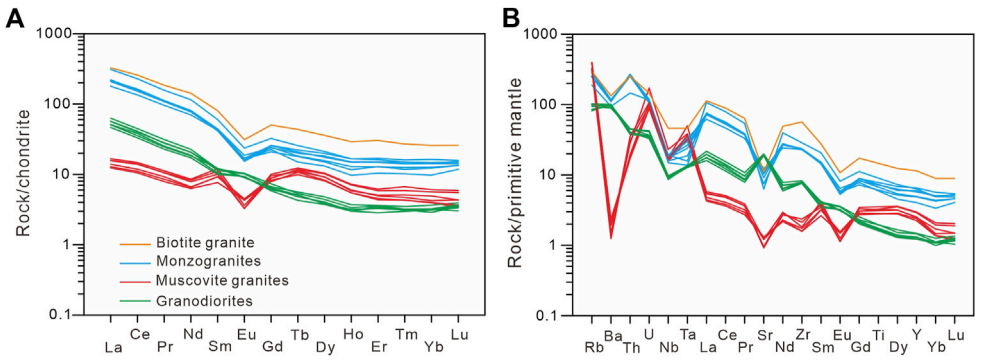

FIGURE 4
(A) Chondrite-normalized rare Earth elements (REE) diagram and **(B)** Primitive-mantle normalized trace element diagram for investigated Huatugou granitoids. Chondrite and Primitive-mantle reference values are from Sun and McDonough (1989).

The monzogranites have 70.64–71.46 wt% SiO_2, 7.43–8.60 wt% total alkali, 1.39–2.15 wt% CaO, 13.59–14.58 wt% Al_2O_3, 2.37–2.74 wt % $Fe_2O_3^T$, and 0.57–0.76 wt% MgO, with 0.74–0.81 for Fe*. In the geochemical classification diagrams (Figure 3), all monzogranite samples are plotted in the magnesian granite field, and most of them exhibit weekly peraluminous and calc-alkaline characteristics. Total REE contents of monzogranites vary from 192 to 312 ppm. In the chondrite-normalized REE diagram, monzogranites show LREE enrichments relative to HREE [$(La/Yb)_N$=11–23], with notably negative Eu anomalies (Eu/Eu*=0.48–0.57) (Figure 4A). In the primitive mantle-normalized diagram, they show enrichments of Th, La, and Nd and depletions of Ba, Nb, Ta, and Sr (Figure 4B).

The muscovite granites contain 72.89–75.40 wt% SiO_2, 8.34–9.71 wt% total alkali, 0.57–0.75 wt% CaO, 13.54–14.63 wt% Al_2O_3, 0.94–1.35 wt% $Fe_2O_3^T$, and 0.12–0.15 wt% MgO, with high Fe* (0.86–0.89). In the classification diagrams (Figure 3), the muscovite granites fall in the granite area and display peraluminous, ferroan, and alkali-calcic to alkalic characteristics. In the chondrite-normalized diagram (Figure 4A), the muscovite granites exhibit low REE contents (21–27 ppm) and flat REE patterns [$(La/Yb)_N$=3–4], with notably negative Eu anomalies (Eu/Eu*=0.32–0.56). In the Primitive mantle-normalized diagram (Figure 4B), the muscovite granites show depletions of Ba, Nb, Sr, Zr, and Eu and enrichments of Rb, U, Ta, and Sm.

The granodiorites have 71.46–72.20 wt% SiO_2, 5.75–5.93 wt% total alkali, 3.18–3.29 wt% CaO, 15.66–15.94 wt% Al_2O_3, 1.35–1.50 wt% $Fe_2O_3^T$, and 0.49–0.54 wt% MgO, with the Fe* of 0.71–0.73. According to classification diagrams (Figure 3), all granodiorite samples belong to granites of peraluminous, calc, and ferroan series. The granodiorites contain 47–62 ppm REE. In the chondrite-normalized REE diagram (Figure 4A), they exhibit LREE enrichments relative to HREE [$(La/Yb)_N$=15–20] with weekly positive Eu anomalies (Eu/Eu*=1.02–1.21). The Primitive mantle-normalized diagram shows that they are enriched in Ba, La, Sr, and Zr and depleted in Nb (Figure 4B).

4.2 Zircon U-Pb geochronology

Representative zircon CL images are presented in Figure 5. Zircon geochronological data are presented in Supplementary Table S2 and illustrated in Figure 6. Zircons in biotite granite (AQ18-13-2.2) and monzogranite (AQ20-4-9.2) are euhedral, 100–220 μm in length with length/width ratios of 2:1 to 3:1 (Figures 5A, B). In CL images, most zircons exhibit clear oscillatory zoning, which is interrupted by irregularly patchy zones in some monzogranite zircons (Figure 5B). Zircons from the biotite granite contain 36–492 ppm Th and 66–559 ppm U, with Th/U ratios of 0.43–0.96 (Supplementary Table S2). Twenty-nine of 30 analyses yield $^{206}Pb/^{238}U$ ages of 432–393 Ma, with a weighted mean $^{206}Pb/^{238}U$ age of 410 ± 3 Ma (MSWD=2.9) (Figure 6A). Twenty-two zircons were analyzed for the monzogranite and had 59–531 ppm Th and 102–1029 ppm U, with Th/U ratios varying from 0.32 to 1.47 (Supplementary Table S2). Except for one inherited zircon, the remaining 21 zircons yield $^{206}Pb/^{238}U$ ages of 414–382 Ma, with a weighted mean $^{206}Pb/^{238}U$ age of 400 ± 4 Ma (MSWD=3.9) (Figure 6C). In the chondrite-normalized REE diagram (Figures 6B, D), biotite granite and monzogranite zircons exhibit HREE enrichments relative to LREE, with positive Ce anomalies and negative Eu anomalies.

The muscovite granite (AQ19-6-2.2) contains zircons with 30–80 μm in length and length/width ratios of 1:1 to 2:1. In CL images, zircons exhibit oscillatory or sector zoning; some zircons contain inherited cores with relatively dark-CL luminance (Figure 5C). Twenty analyzed zircons have 25–444 ppm Th and 70–418 ppm U with Th/U ratios of 0.27–1.06, and their $^{206}Pb/^{238}U$ ages vary from 393 to 455 Ma. Except for two inherited zircons (Figure 5C), the rest 18 analyzed zircons yield a weighted mean $^{206}Pb/^{238}U$ age of 410 ± 6 Ma (MSWD=5.7) (Figure 6E). The chondrite-normalized REE diagram displays that the muscovite granite zircons are enriched in HREE relative to LREE with notably positive Ce anomalies (Figure 6F).

Zircons from the granodiorite (AQ20-4-4.2) are 60–160 μm in length with length/width ratios of 3:2 to 3:1. CL images show that most zircons are oscillatory-zoned, and many of them are either mantled by dark rims or contain fragmental cores (Figure 5D). Among 28 analyzed spots, twelve spots were ignored owing to high discordance. Four analyses on inherited cores yield $^{206}Pb/^{238}U$ ages of 1632–509 Ma (Supplementary Table S2). The remaining 12 analyses on oscillatory-zoned zircons yield $^{206}Pb/^{238}U$ ages of 470–441 Ma, with a weighted mean $^{206}Pb/^{238}U$ age of 451 ± 6 Ma (MSWD=4.0) (Figure 6G). These zircons contain 70–394 ppm Th and 229–1344 ppm U with variable Th/U ratios (0.07–0.40) and highly scattered chondrite-normalized REE patterns (Figure 6H).

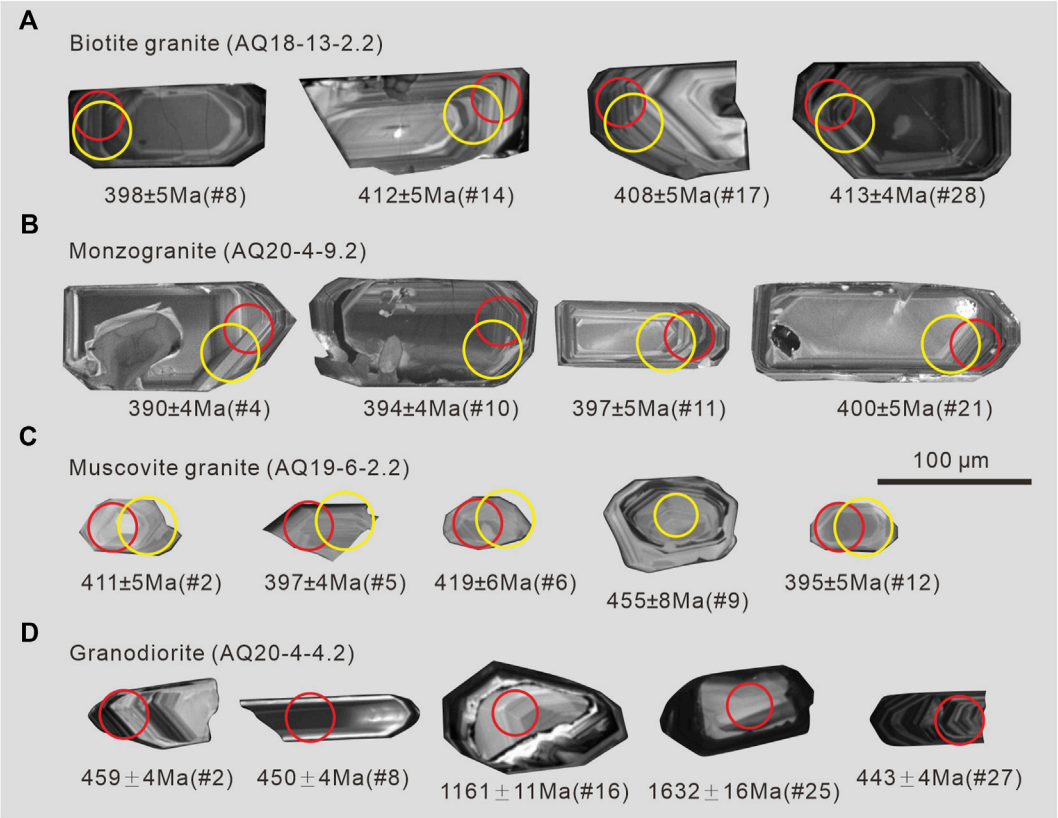

FIGURE 5
(A–D) Cathodoluminescence (CL) images of investigated granitic zircons. The red and yellow circles indicate the locations of U-Pb dating and Hf isotopic analyses.

4.3 Zircon Hf isotopes

The zircon Hf isotopic data are presented in Supplementary Table S3 and illustrated in Figure 7. For the biotite granite (AQ18-13-2.2), zircon $^{176}Hf/^{177}Hf$ ratios are 0.282574–0.282688. Zircons exhibit the initial εHf(t) values of +1.7 to +5.6 (at 410 Ma) and Hf two-stage model ages (T_{DM2}) of 1293–1042 Ma (Figure 7). The monzogranite (AQ20-4-9.2) zircons have $^{176}Hf/^{177}Hf$ ratios of 0.282497–0.282581 and εHf(t) values of −2.0 to +1.8 at 400 Ma. Their T_{DM2} ages vary from 1520 to 1280 Ma. Zircons from the muscovite granite (AQ19-6-2.2) display $^{176}Hf/^{177}Hf$ ratios of 0.282119–282230 and εHf(t) values of −14.5 to −10.4 (at 410 Ma), with T_{DM2} ages of 2317–2058 Ma.

5 Discussion

5.1 Petrogenesis

5.1.1 Biotite granite and monzogranites

The biotite granite displays similar chemical features to A-type granites (Figure 8A, B; Whalen et al., 1987), including high contents of total alkali (7.62 wt%), $Fe_2O_3^T$ (4.68 wt%), highly charged cations (Nb, Y, Zr, REE), and high ratios of FeO^T/MgO (4.54) and 10000Ga/Al (3.06), but low CaO (2.53 wt%). In addition, the high Fe* (0.82) of biotite granite also indicates an A-type affinity (Figure 3D; Frost et al., 2001). Although there is no alkaline mineral, such as arfvedsonite and riebeckite, the high zircon saturation temperature (908°C) was obtained for the biotite granite using the zircon solubility model of Watson and Harrison (1983). In the absence of inherited zircons, the calculated temperature reflects the magma temperature. Therefore, the biotite granite was formed by a high-temperature melting process, similar to A-type granites (Collins et al., 1982; Clemens et al., 1986; Whalen et al., 1987; Chappell and White, 2001).

Similar to the biotite granite, the monzogranites sampled nearby exhibit high total alkali (7.43–8.6 wt%), $Fe_2O_3^T$ (2.37–2.74 wt%), and Fe*(0.74–0.81), and low CaO (1.39–2.15 wt%). In addition, the monzogranites and biotite granite share similar distribution patterns for trace elements and Hf isotopic compositions (Figures 4, 7), implying that they were derived from the same source. The Ga/Al ratios in the biotite granite and monzogranites decrease with decreasing Zr, consistent with the chemical trend of A-type granite fractionation (Wu et al., 2017). In comparison with the biotite granite, the monzogranites have higher SiO_2 and lower CaO, $Fe_2O_3^T$, MgO, Al_2O_3, Zr, and total REE contents with lower εHf(t) values (Figures 7, 9), which likely resulted from an assimilation and fractional crystallization (AFC) process. For instance, the assimilation of upper-crustal materials would decrease the εHf(t) values of ascending magma. The decreases in CaO and Al_2O_3 with increasing SO_2 could result from the fractionation of feldspar and decreases in $Fe_2O_3^T$ and MgO from the fractionation of biotite (Figure 10A). The fractionation of zircon, as well as monazite and apatite (Figure 10B), would decrease Zr and total REE contents.

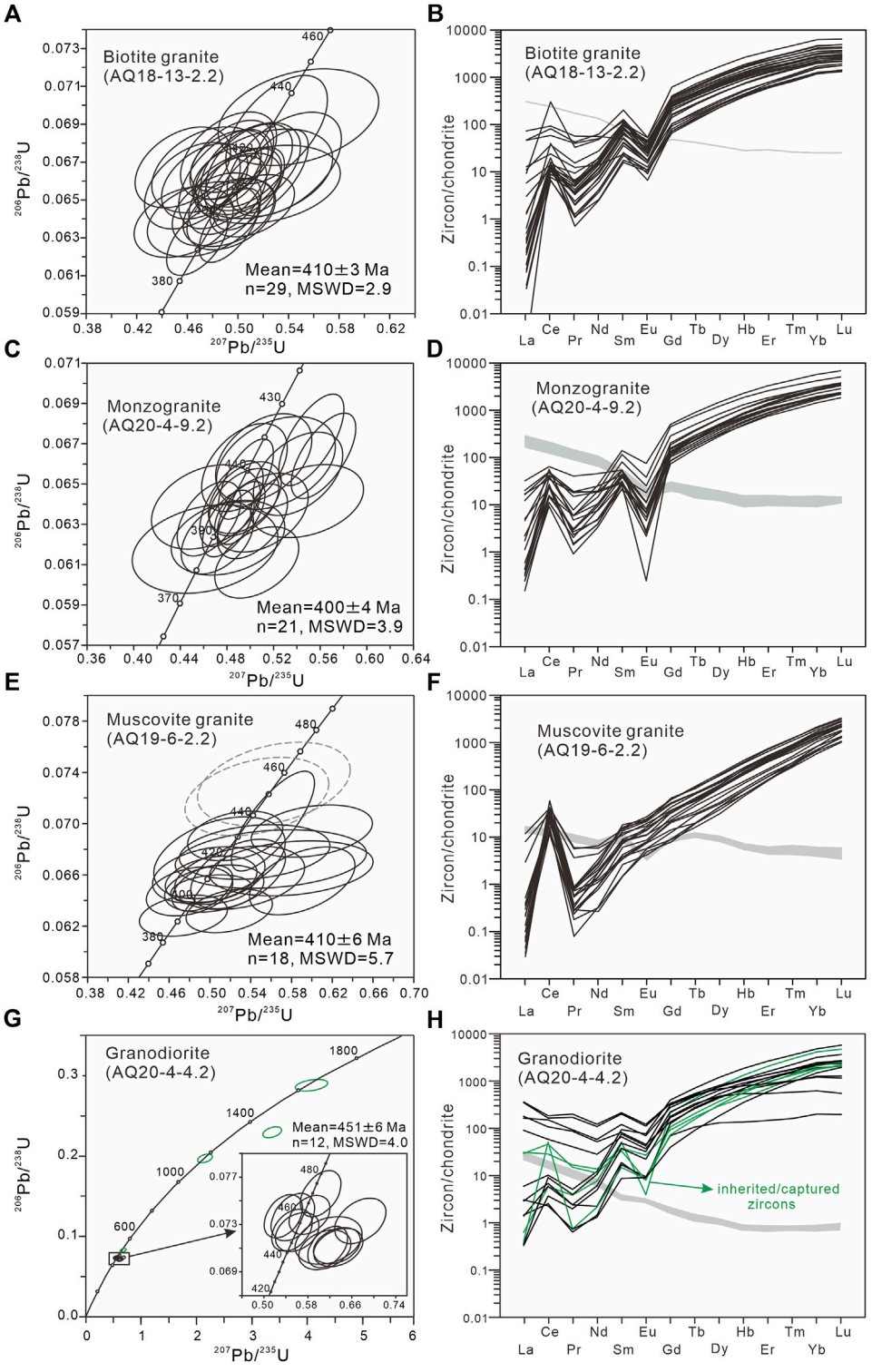

FIGURE 6
Zircon U-Pb concordia diagrams and chondrite-normalized REE diagrams for **(A,B)** biotite granite, **(C,D)** monzogranite, **(E,F)** muscovite granite, and **(G,H)** granodiorite in the Huatugou area. The whole-rock REE patterns in Figure 3A are gray-shaded here.

The least fractionated sample (biotite granite) shows depletions of Eu and Sr and the enrichment of Y (Figure 4), suggesting that plagioclase (instead of garnet) is stable in the source region, consistent with a low-pressure melting condition. The biotite granite has Yb/Ta and Y/Nb ratios of 2.3 and 1.6, similar to continental crust (Taylor and McLennan, 1995). Biotite granite and monzogranites are chemically classified into the A_2 group (Figures 8C, D), which represents magmas generated by the remelting of the continental crust or underplated crust that was initially formed during subduction or continent-continent collision (Eby, 1992).

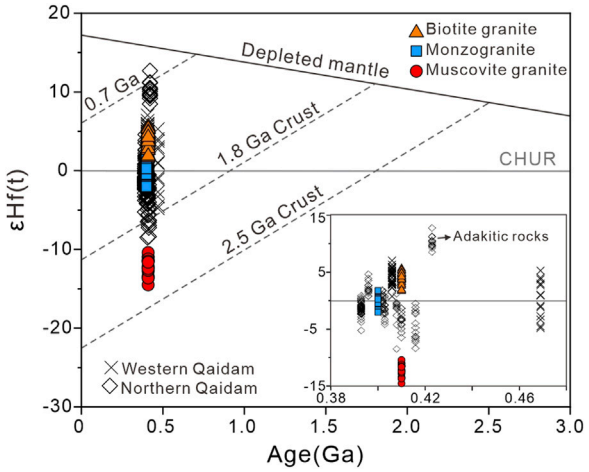

FIGURE 7
The plot of zircon εHf(t) values *vs.* U-Pb ages for investigated Huatugou granitoids, compared with published data of early Paleozoic granitoids in western and northern Qaidam (Song et al., 2014; Wu et al., 2014b; and Sun et al., 2020).

The biotite granite has positive zircon εHf(t) values of +1.7 to +5.6 (Figure 7), indicating that melted crustal igneous rocks were derived from juvenile materials. In addition, the high-temperature melting condition for producing A-type magma implies residual sources with an additional heat input from the mantle, which was encountered within the lower continental crust (Clemens et al., 1986). Therefore, the magmas of the biotite and monzogranites in the Huatugou area were generated by the partial melting of the lower continental crust under high-temperature and low-pressure conditions and underwent an AFC process during emplacement.

5.1.2 Muscovite granites

The muscovite granites are peraluminous granites (A/CNK=1.07–1.19) with 5%–7% muscovite and >1% CIPW normative corundum. Similar to typical S-type granite (Chappell and White, 2001), the muscovite granites exhibit high contents of SiO_2 (>72 wt%), K_2O (4.7–6.5 wt%), Rb (≥200 ppm), and Pb (36–51 ppm), and low contents of CaO (<1 wt%) and Sr (<30 ppm). With increasing SiO_2, P_2O_5 increases and Pb decreases (Figures 9G, H), typical S-type granite trends (Chappell and White, 2001). The muscovite granites are fractionated granites, indicated by their high Rb/Sr ratios (8.2–10.4) and REE tetrad effect (Figure 4). Additionally, Th, La, and Y contents decrease with increasing Rb (Figure 9I). According to Chappell (1999), these chemical trends are typical in fractionated S-type granites, indicating the fractionation of biotite, plagioclase, and monazite (Figure 10). S-type granites are generally derived from sedimentary or supracrustal rocks (Chappell and White, 2001). The muscovite granites yielded low zircon saturation temperatures of 638–656°C (Watson and Harrison, 1983), consistent with low-temperature magmas. Combined with

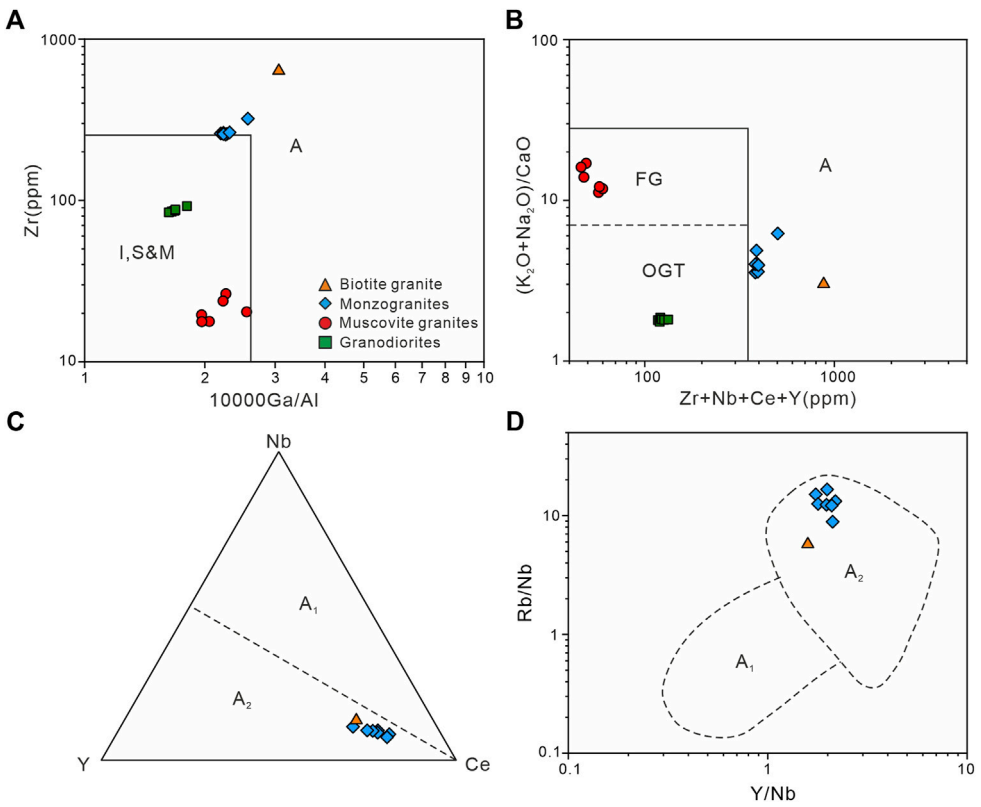

FIGURE 8
(A) Zr *vs.* 10000Ga/Al and **(B)** (Na_2O+K_2O)/CaO *vs.* Zr+Nb+Ce+Y discrimination diagrams (Whalen et al., 1987), indicating that the biotite granite and monzogranites in the Huatugou area are A-type granites. FG: Fractionated granites; OGT: unfractionated M-, I-, and S-type granites. **(C)** Nb-Y-Ce and **(D)** Rb/Nb *vs.* Y/Nb classification diagrams (Eby, 1992), where Huatugou biotite granite and monzogranites are plotted in the A_2 field.

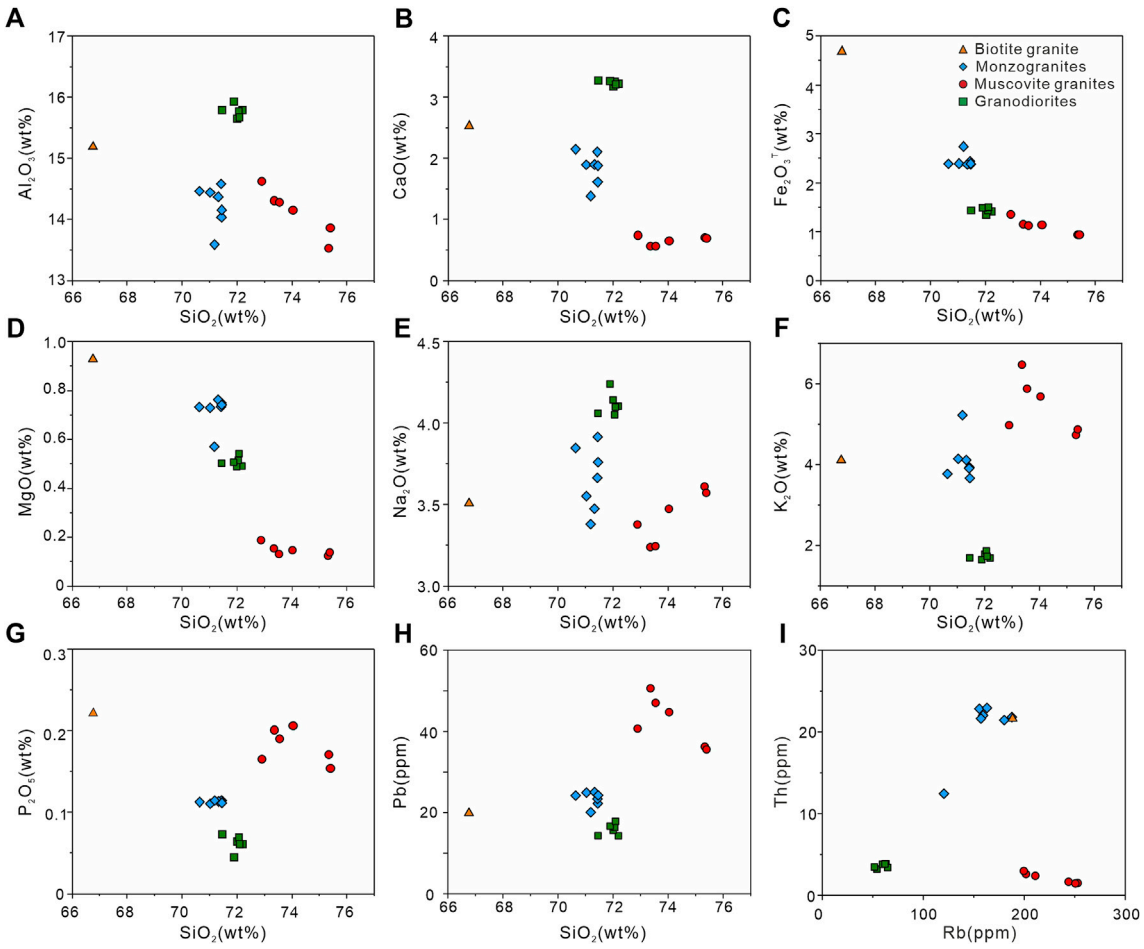

FIGURE 9
(A) Al_2O_3 *vs.* SiO_2, **(B)** CaO *vs.* SiO_2, **(C)** $Fe_2O_3^T$ *vs.* SiO_2, **(D)** MgO *vs.* SiO_2, **(E)** Na_2O *vs.* SiO_2, **(F)** K_2O *vs.* SiO_2, **(G)** P_2O_5 *vs.* SiO_2, **(H)** Pb *vs.* SiO_2, and **(I)** Rb *vs.* Th variation diagrams, showing that muscovite granites in the Huatugou area follow chemical trends of S-type proposed by Chappell (1999).

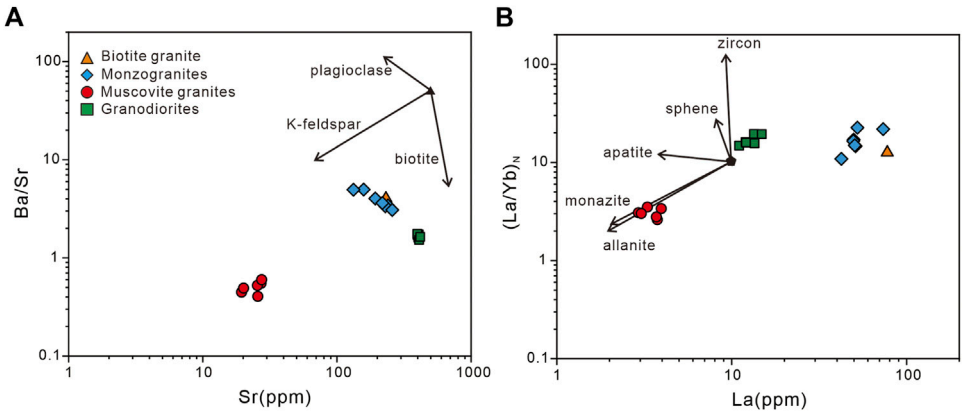

FIGURE 10
(A) Ba/Sr *vs.* Sr and **(B)** $(La/Yb)_N$ *vs.* La diagrams (Wu et al., 2003).

negative zircon εHf(t) values (−14.5 to −10.4, Figure 7), it is suggested that the magma of the muscovite granites resulted from the low-temperature partial melting of ancient crustal materials.

5.1.3 Granodiorites

The granodiorites are magnesian calcic granitoids characterized by high contents of Al_2O_3 (>15wt%) and Na_2O (>4 wt%) with low K_2O/

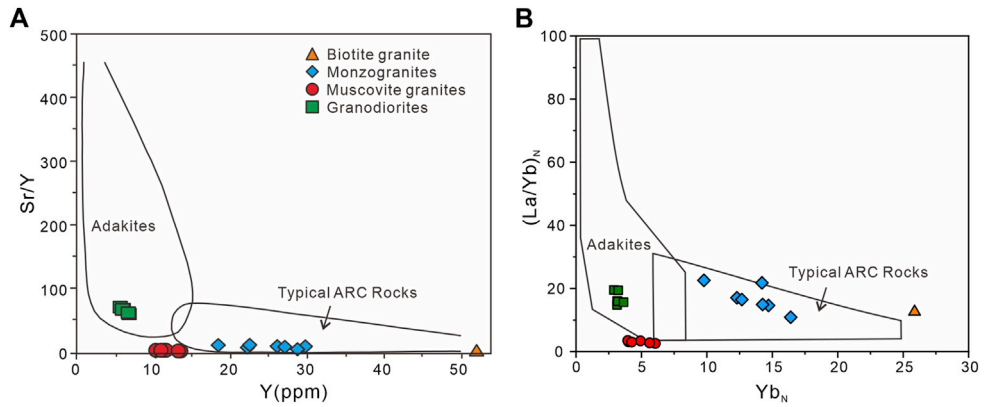

FIGURE 11
(A) Sr/Y *vs.* Y and **(B)** $(La/Yb)_N$ *vs.* Yb_N discrimination diagrams (Defant and Drummond, 1990; Martin, 1999), indicating that granodiorites in the Huatugou area are adakitic rocks.

Na_2O ratios (0.39–0.46). As to trace elements, the granodiorites exhibit strongly fractionated REE patterns ($(La/Yb)_N$=(15–20), low Y (6–7 ppm), and high Sr (398–418 ppm) and Sr/Y ratios (61–72), which are distinctive chemical features of adakitic rocks (Figure 11; Defant and Drummond, 1990; Martin, 1999). These adakitic affinities, combined with high CaO (3.18–3.29 wt%) and insignificant Eu anomalies (Figure 4A), imply that the garnet was stable and plagioclase was unstable in the source, indicative of a high-pressure condition.

The generation of adakitic rocks may have different mechanisms, including partial melting of the subducted oceanic slab with or without the involvement of mantle peridotite, partial melting of mafic lower crust with or without the participation of mantle peridotite, and fractional crystallization of arc basaltic magma (Castillo, 2012 and references therein). The high Ba contents (623–705 ppm), low Rb/Sr ratios (<0.2), and the absence of correlations between SiO_2 and other major oxides (Figure 9) of these granodiorites, indicate no or insignificant fractionation. Hence, the fractional crystallization model is largely ruled out. The granodiorites display consistently high SiO_2 (71.46–72.2 wt%) and low MgO (0.49–0.54 wt%) contents with high Fe* (0.71–0.73), inconsistent with the chemical signatures of mantle peridotite or mantle-derived magma. The granodiorites have zircons that contain Proterozoic cores and display complex growth patterns (Figure 5D). These zircon cores show chondrite-normalized REE patterns similar to (re) crystallized zircons (Figure 6H), indicating that they were captured in the source. Since there were ancient continental materials in the source, we favor the partial melting of the lower mafic crust over the oceanic slab to generate the granodiorites.

5.2 Granitic magmatism in the western Qaidam

The investigated Huatugou granitoids in this study, including granodiorites, muscovite granites, biotite granite, and monzogranites, yield weighted mean $^{206}Pb/^{238}U$ ages of 451 ± 6, 410 ± 6, 410 ± 3, and 400 ± 4 Ma (Figure 6). Dated zircons are euhedral and oscillatory-zoned with most Th/U ratios of > 0.5 (except the granodiorites), indicating a magmatic origin (Corfu 2003; Hoskin, 2003). For granodiorite zircons, the variations in Th/U ratios (0.07–0.40) might be due to disequilibrium crystallization (Wang et al., 2011). Hence, the weighted mean $^{206}Pb/^{238}U$ ages are interpreted as the timing of granitic magma crystallization, suggesting that the Huatugou granitoids were mainly emplaced during the late Ordovician-early Devonian. This study, combined with published U-Pb data (Figure 1B; Cheng et al., 2017; Wang C. et al., 2014a; Wu C. L. et al., 2014b), indicates that the western Qaidam block experienced multiple felsic magmatic events during 469–381 Ma (Figure 1B), mainly at 469–460 Ma, 453–440 Ma, and 411–400 Ma. The first granitic magmatism (469 to 460 Ma) is characterized by quartz diorite, diorite, and granite with zircon εHf(t) values varying from −4.8 to +5.3 (Figure 7; Wu C. L. et al., 2014b; Cheng et al., 2017), indicative of variations in melted sources.

The second granitic magmatism (453–440 Ma) formed granodiorite and granite with mylonitic textures (Cheng et al., 2017, this study), reflecting a syn-tectonic origin. In this study, the granodiorites exhibit adakitic features (Figure 11), and their magmas were generated by the partial melting of the lower mafic crust under high-pressure conditions. Similar granodiorite was also reported in the Yusupuleke area, west of western Qaidam, which was thought to result from the partial melting of garnet amphibolite within the thickened lower crust (Wang C. et al., 2014a).

The third granitic magmatism (411–400 Ma) is characterized by A-type granitoids with minor S-type granites, including monzogranite, syenogranite, granodiorite, biotite granite, muscovite granite (Cheng et al., 2017; Wu et al., 2014b; this study). A-type granitoids mainly exhibit positive zircon εHf(t) values (Figure 7), suggesting that their high-temperature magmas were derived from juvenile crustal sources. In Huatugou, monzogranites show lower zircon εHf(t) values with more fractionated features than the biotite granite, resulting from an AFC process during the emplacement of A-type magmas. S-type granites, such as the Huatugou muscovite granites, have negative zircon εHf(t) values (Figure 7), and their magmas were produced by low-temperature (650°C) partial melting of ancient crustal materials and experienced fractionation process (Figure 9).

5.3 Tectonic implications

According to this study, the Huatugou granitoid comprises three types: adakitic rocks (451 Ma), S-type granites (410 Ma), and A_2-type granites (410–400 Ma). Both magmas of adakitic rocks and A-type granitoids were generated by the partial melting of the lower crust. Differently, adakitic rocks were crystallized from magma produced by the high-pressure remelting without significant fractionation, which implies a relatively fast emplacement within a thickened continental crust. The A-type granitic magma was generated under high-temperature and low-pressure partial melting conditions and experienced an AFC process during emplacement, indicating a relatively slow emplacement/cooling within a thinned continental crust. The thickness change from the thickened to the thinned continent suggests that the western Qaidam experienced a tectonic transition from compression to extension. Considering three magmatism pulses, as summarized in section 5.2, this transition likely occurred between 440 and 411 Ma.

During 445–423 Ma, parts of northern Qaidam experienced ultrahigh-pressure metamorphism related to continental subduction (Song et al., 2005; Yang et al., 2005; Zhang et al., 2010). As ultrahigh-pressure metamorphic rocks are now exposed to the surface, the exhumation of the subducted continental crust should start around the same time. Otherwise, with ongoing subduction, the exhumed rocks would record younger peak metamorphic ages. The exhumation of deeply subducted continental crust was thought to result from the detachment of the dense oceanic slab (Zhang et al., 2016). The slab breakoff also induced mantle upwelling, which heated the thickened lower crust to produce adakitic magmas under high-pressure granulite-facies conditions in the Dulan area, south of northern Qaidam (Yu et al., 2019). The emplacement of high-temperature A-type granitoids as early as 418 Ma (Chen et al., 2020), as well as mantled-derived mafic-ultramafic plutons during 424–406 Ma in the southern Qaidam (Peng et al., 2016; Song et al., 2016; Wang et al., 2016), indicates that the exhumation of the subducted continental slab was followed by post-collisional extension of the whole Qaidam block. The third granitic magmatism (411–400 Ma) in western Qaidam also occurred in this extensional regime.

Moreover, the Dulan adakitic rocks (433–423 Ma) exhibit positive zircon εHf(t) values of 8.5–12.7 (Figure 7; Song et al., 2014; Yu et al., 2019). The protoliths of melted high-pressure granulite-facies sources are ~470 Ma gabbroic rocks with an arc affinity, similar to gabbro dikes intruding the Tanjianshan Group metavolcanic rocks (514–465 Ma, Wu et al., 1987; Li et al., 1999; Yuan et al., 2002; Shi et al., 2004). On the one hand, the Tanjianshan Group was exposed to the east and north margins of the Qaidam Basin. Their existence implies that the Proto-Tethys Ocean commenced subducting under the Qaidam block before 514 Ma. On the other hand, in Huatugou, the northwest margin of Qaidam, the UHT metamorphic rocks were formed at 540–500 Ma (Teng et al., 2020). If the Huatugou UHT metamorphism was linked to a collisional event alone, as inferred from clockwise P-T paths with prograde high-pressure (>1.4 GPa) history, the scenario would contradict the oceanic subduction. Nevertheless, the Huatugou ultrahigh-temperature metamorphic rocks were suggested as the result of the late Pan-African UHT metamorphism during the final assembly of the Gondwana (Teng et al., 2020; Teng and Zhang, 2020). The Qaidam block on the margin of East Gondwana, as a continental arc, is in line with the subduction of the Proto-Tethys Ocean around the Gondwana. In this position, the tectonic processes controlling the UHT metamorphism of the western Qaidam block are more intriguing than proposed and deserve further investigation. Nevertheless, our study suggests that the thickened continental crust of the Qaidam block was likely sustained until the detachment of the subducted crust during the continental collision. The extension of the Qaidam block commenced at ~420 Ma, likely after the exhumation of ultrahigh-pressure metamorphic rocks in subduction-collision complex belts.

6 Conclusion

1) The Huatugou granitoids, including granodiorites, monzogranites, biotite granites, and muscovite granites, intruded the Qaidam Precambrian basements during 451–400 Ma.
2) The granodiorites (451 ± 6 Ma) have adakitic affinities, and their magmas were generated by high-pressure remelting of the lower mafic crust. The muscovite granites (410 ± 6 Ma) with negative zircon εHf(t) values of −14.5 to −10.4 resulted from the partial melting of ancient crustal materials and S-type granite fractionation. The biotite granite (410 ± 3 Ma) was crystalized from a high-temperature A-type magma with positive zircon εHf(t) of +1.7 to +5.6, which was generated by the partial melting of juvenile crustal rocks in an extensional setting. The magmas of monzogranites (400 ± 4 Ma) derived from the same source as that of the biotite granite but experienced an AFC process during emplacement.
3) Combined with former studies, it is inferred that the Qaidam block consisted of the thickened continental crust during subduction processes until the detachment of subducted crust during the continental collision. The regional extension of the Qaidam block commenced at ~420 Ma, likely after the exhumation of ultrahigh-pressure metamorphic rocks in subduction-collision complex belts.

Data availability statement

The original contributions presented in the study are included in the article/Supplementary Material, further inquiries can be directed to the corresponding author.

Author contributions

XT and JZ contributed to the conception and design of the study. XT, XM, YW, and QG contributed to the acquisition and analysis of data. XT wrote the first draft of the manuscript. All authors contributed to the manuscript revision, and read, and approved the submitted version.

Funding

This work was financially supported by the National Natural Science Foundation of China (Grant nos. 41630207 and 42072237)

and the Geological Survey Project of China (Grant no. DD20221649).

Acknowledgments

We thank handling editor Meng Wang and two reviewers for constructive comments and suggestions to improve the manuscript.

Conflict of interest

The authors declare that the research was conducted in the absence of any commercial or financial relationships that could be construed as a potential conflict of interest.

Publisher's note

Supplementary material

The Supplementary Material for this article can be found online at: https://www.frontiersin.org/articles/10.3389/feart.2023.1105992/full#supplementary-material

References

Acosta-Vigil, A., London, D., and Morgan, G. B. (2006). Experiments on the kinetics of partial melting of a leucogranite at 200 MPa H_2O and 690–800°C: compositional variability of melts during the onset of H_2O-saturated crustal anatexis. *Contrib. to Mineral. Petrol.* 151 (5), 539–557. doi:10.1007/s00410-006-0081-8

Castillo, P. R. (2012). Adakite petrogenesis. *Lithos* 134-135, 304–316. doi:10.1016/j.lithos.2011.09.013

Castro, A., Douce, A. E. P., Corretge, L. G., de la Rosa, J. D., El-Biad, M., and El-Hmidi, H. (1999). Origin of peraluminous granites and granodiorites, iberian massif, Spain: an experimental test of granite petrogenesis. *Contrib. Mineral. Petrol.* 135 (2-3), 255–276. doi:10.1007/s004100050511

Chappell, B. W., and White, A. J. R. (2001). Two contrasting granite types: 25 years later. *Aust. J. Earth Sci.* 48 (4), 489–499. doi:10.1046/j.1440-0952.2001.00882.x

Chappell, B. W. (1999). Aluminium saturation in I- and S-type granites and the characterization of fractionated haplogranites. *Lithos* 46 (3), 535–551. doi:10.1016/s0024-4937(98)00086-3

Chen, H. W., Luo, Z. H., Mo, X. X., Zhang, X. T., Wang, J., and Wang, B. Z. (2006). SHRIMP ages of Kayakedengtage complex in the East Kunlun Mountains and their geological implications. *Acta Petrol. Mineral.* 25, 25–32. [in Chinese with English abstract].

Chen, D. L., Liu, L., Sun, Y., and Liou, J. G. (2009). Geochemistry and zircon U–Pb dating and its implications of the Yukahe HP/UHP terrane, the North Qaidam, NW China. *J. Asian Earth Sci.* 35 (3-4), 259–272. doi:10.1016/j.jseaes.2008.12.001

Chen, J., Fu, L., Wei, J., Selby, D., Zhang, D., Zhou, H., et al. (2020). Proto-tethys magmatic evolution along northern Gondwana: Insights from late silurian–middle devonian A-type magmatism, East Kunlun orogen, northern Tibetan plateau, China. *Lithos* 356-357, 105304. doi:10.1016/j.lithos.2019.105304

Cheng, F., Jolivet, M., Hallot, E., Zhang, D. W., Zhang, C. H., and Guo, Z. J. (2017). Tectono-magmatic rejuvenation of the Qaidam craton, northern Tibet. *Gondwana Res.* 49, 248–263. doi:10.1016/j.gr.2017.06.004

Collins, W. J., Beams, S. D., White, A. J. R., and Chappell, B. W. (1982). Nature and origin of A-type granites with particular reference to southeastern Australia. *Contrib. to Mineral. Petrol.* 80 (2), 189–200. doi:10.1007/BF00374895

Clemens, J. D., Holloway, J. R., and White, A. J. R. (1986). Origin of an A-type granite; experimental constraints. *Am. Mineral.* 71 (3-4), 317–324.

Corfu, F. (2003). Atlas of zircon textures. *Rev. Mineral. Geochem.* 53 (1), 469–500. doi:10.2113/0530469

Defant, M. J., and Drummond, M. S. (1990). Derivation of some modern arc magmas by melting of young subducted lithosphere. *Nature* 347 (6294), 662–665. doi:10.1038/347662a0

Dong, Y. P., He, D. F., Sun, S. S., Liu, X. M., Zhou, X. H., Zhang, F. F., et al. (2018). Subduction and accretionary tectonics of the East Kunlun orogen, Western segment of the central China orogenic system. *Earth-Sci. Rev.* 186, 231–261. doi:10.1016/j.earscirev.2017.12.006

Eby, G. N. (1992). Chemical subdivision of the A-type granitoids: Petrogenetic and tectonic implications. *Geology* 20 (7), 641–644. doi:10.1130/0091-7613(1992)020<0641:csotat>2.3.co;2

Frost, B. R., Barnes, C. G., Collins, W. J., Arculus, R. J., Ellis, D. J., and Frost, C. D. (2001). A geochemical classification for granitic rocks. *J. Petrol.* 42 (11), 2033–2048. doi:10.1093/petrology/42.11.2033

He, D., Dong, Y., Zhang, F., Yang, Z., Sun, S., Cheng, B., et al. (2016). The 1.0Ga S–type granite in the East Kunlun orogen, northern Tibetan plateau: Implications for the meso– to neoproterozoic tectonic evolution. *J. Asian Earth Sci.* 130, 46–59. doi:10.1016/j.jseaes.2016.07.019

He, D., Dong, Y., Liu, X., Zhou, X., Zhang, F., and Sun, S. (2018). Zircon U–Pb geochronology and Hf isotope of granitoids in East Kunlun: Implications for the neoproterozoic magmatism of Qaidam block, northern Tibetan plateau. *Precambrian Res.* 314, 377–393. doi:10.1016/j.precamres.2018.06.017

He, F., Song, S. G., and ShuGuang, S. (2020). The grenvillian-aged UHT granulite in Jinshuikou region, East Kunlun orogenic belt. *Acta Petrol. Sin.* 36, 1030–1040. [in Chinese with English abstract]. doi:10.18654/1000-0569/2020.04.04

He, D., Dong, Y., Hauzenberger, C. A., Sun, S., Neubauer, F., Zhou, B., et al. (2022). Neoproterozoic HP granulite and its tectonic implication for the East Kunlun orogen, northern Tibetan plateau. *Precambrian Res.* 378, 106778. doi:10.1016/j.precamres.2022.106778

Hopkinson, T., Harris, N., Roberts, N. M. W., Warren, C. J., Hammond, S., Spencer, C. J., et al. (2019). Evolution of the melt source during protracted crustal anatexis: An example from the Bhutan Himalaya. *Geology* 48 (1), 87–91. doi:10.1130/g47078.1

Hoskin, P. W. O. (2003). The composition of zircon and igneous and metamorphic petrogenesis. *Rev. Mineral. Geochem.* 53 (1), 27–62. doi:10.2113/0530027

Irvine, T. N., and Baragar, W. R. A. (1971). A guide to the chemical classification of the common volcanic rocks. *Can. J. Earth Sci.* 8 (5), 523–548. doi:10.1139/e71-055

Jackson, S. E., Pearson, N. J., Griffin, W. L., and Belousova, E. A. (2004). The application of laser ablation-inductively coupled plasma-mass spectrometry to *in situ* U–Pb zircon geochronology. *Chem. Geol.* 211 (1-2), 47–69. doi:10.1016/j.chemgeo.2004.06.017

Li, H. K., Lu, S. N., Zhao, F. Q., Li, H. M., Yu, H. F., and Zheng, J. K. (1999). Geochronological framework of the Neoproterozoic major geological events in the northern margin of the Qaidam basin. *Geoscience* (2), 224–225. [in Chinese].

Liu, Y. S., Gao, S., Hu, Z. C., Gao, C. G., Zong, K. Q., and Wang, D. B. (2010). Continental and oceanic crust recycling-induced melt-peridotite interactions in the trans-north China orogen: U-Pb dating, Hf isotopes and trace elements in zircons from mantle xenoliths. *J. Petrol.* 51 (1-2), 537–571. doi:10.1093/petrology/egp082

Lu, L., Wu, Z. H., Hu, D. G., Barosh, P. J., Hao, S., and Zhou, C. J. (2010). Zircon U-Pb age for rhyolite of the Maoniushan Formation and its tectonic significance in the East Kunlun Mountains. *Acta Petrol. Sin.* 26, 1150–1158. [in Chinese with English abstract].

Ludwig, K. (2012). *User's manual for Isoplot 3.75: A geochronological toolkit for microsoft excel*. Berkley: Berkley Geochronological Centre, Special Publication 5.

Maniar, P. D., and Piccoli, P. M. (1989). Tectonic discrimination of granitoids. *GSA Bull.* 101 (5), 635–643. doi:10.1130/0016-7606(1989)101<0635:tdog>2.3.co;2

Martin, H. (1999). Adakitic magmas: Modern analogues of archaean granitoids. *Lithos* 46 (3), 411–429. doi:10.1016/s0024-4937(98)00076-0

Mattinson, C. G., Wooden, J. L., Liou, J. G., Bird, D. K., and Wu, C. L. (2006). Age and duration of eclogite-facies metamorphism, North Qaidam HP/UHP terrane, Western China. *Am. J. Sci.* 306 (9), 683–711. doi:10.2475/09.2006.01

Meng, F. C., Zhang, J. X., and Cui, M. H. (2013). Discovery of early paleozoic eclogite from the East Kunlun, western China and its tectonic significance. *Gondwana Res.* 23 (2), 825–836. doi:10.1016/j.gr.2012.06.007

Middlemost, E. A. K. (1994). Naming materials in the magma/igneous rock system. *Earth-Sci. Rev.* 37 (3), 215–224. doi:10.1016/0012-8252(94)90029-9

Patiño Douce, A. E., and Harris, N. (1998). Experimental constraints on himalayan anatexis. *J. Petrol.* 39 (4), 689–710. doi:10.1093/petroj/39.4.689

Patiño Douce, A. E. (1995). Experimental generation of hybrid silicic melts by reaction of high-Al basalt with metamorphic rocks. *J. Geophys. Res. Solid Earth* 100 (B8), 15623–15639. doi:10.1029/94jb03376

Peng, B., Sun, F., Li, B., Wang, G., Li, S., Zhao, T., et al. (2016). The geochemistry and geochronology of the Xiarihamu II mafic–ultramafic complex, Eastern Kunlun, Qinghai Province, China: Implications for the Genesis of magmatic Ni–Cu sulfide deposits. *Ore Geol. Rev.* 73, 13–28. doi:10.1016/j.oregeorev.2015.10.014

Ren, Y., Chen, D., Zhu, X., Ren, Z., Gong, X., and Luo, F. (2019). Two orogenic cycles recorded by eclogites in the Yuka–Luofengpo terrane: Implications for the Mesoproterozoic to early Paleozoic tectonic evolution of the North Qaidam orogenic belt, NW China. *Precambrian Res.* 333, 105449. doi:10.1016/j.precamres.2019.105449

Ren, Y., Chen, D., Wang, H., Zhu, X., and Bai, B. (2021). Grenvillian and early Paleozoic polyphase metamorphism recorded by eclogite and host garnet mica schist in the North Qaidam orogenic belt. *Geosci. Front.* 12 (4), 101170. doi:10.1016/j.gsf.2021.101170

Shi, R. D., Yang, J. S., Wu, C. L., Iizuka, T., and Hirata, T. (2004). Island arc volcanic rocks in the North Qaidam UHP metamorphic Belt. *Acta Geol. Sin.* 78, 52–64. [in Chinese with English abstract].

Sláma, J., Košler, J., Condon, D. J., Crowley, J. L., Gerdes, A., Hanchar, J. M., et al. (2008). Plešovice zircon — a new natural reference material for U–Pb and Hf isotopic microanalysis. *Chem. Geol.* 249 (1-2), 1–35. doi:10.1016/j.chemgeo.2007.11.005

Song, S. G., Zhang, L. F., Niu, Y. L., Su, L., Jian, P., and Liu, D. Y. (2005). Geochronology of diamond-bearing zircons from garnet peridotite in the north Qaidam UHPM belt, northern Tibetan plateau: A record of complex histories from oceanic lithosphere subduction to continental collision. *Earth Planet. Sci. Lett.* 234 (1-2), 99–118. doi:10.1016/j.epsl.2005.02.036

Song, S. G., Su, L., Li, X. H., Zhang, G. B., Niu, Y. L., and Zhang, L. F. (2010). Tracing the 850-Ma continental flood basalts from a piece of subducted continental crust in the North Qaidam UHPM belt, NW China. *Precambrian Res.* 183 (4), 805–816. doi:10.1016/j.precamres.2010.09.008

Song, S. G., Niu, Y. L., Su, L., Wei, C. J., and Zhang, L. F. (2014). Adakitic (tonalitic-trondhjemitic) magmas resulting from eclogite decompression and dehydration melting during exhumation in response to continental collision. *Geochim. Cosmochim. Acta* 130, 42–62. doi:10.1016/j.gca.2014.01.008

Song, X. Y., Yi, J. N., Chen, L. M., She, Y. W., Liu, C. Z., Dang, X. Y., et al. (2016). The giant xiarihamu Ni-Co sulfide deposit in the East Kunlun orogenic belt, northern tibet plateau, China. *Econ. Geol.* 111 (1), 29–55. doi:10.2113/econgeo.111.1.29

Song, S., Bi, H., Qi, S., Yang, L., Allen, M. B., Niu, Y., et al. (2018). HP–UHP metamorphic belt in the East Kunlun orogen: Final closure of the Proto-Tethys Ocean and formation of the pan-north-China continent. *J. Petrol.* 59 (11), 2043–2060. doi:10.1093/petrology/egy089

Sun, S. S., and McDonough, W. F. (1989). Chemical and isotopic systematics of oceanic basalts: Implications for mantle composition and processes. *Geol. Soc. Lond. Spec. Publ.* 42 (1), 313–345. doi:10.1144/gsl.sp.1989.042.01.19

Sun, G. C., Gao, P., Zhao, Z. F., and Zheng, Y. F. (2020). Syn-exhumation melting of the subducted continental crust: Geochemical evidence from early Paleozoic granitoids in North Qaidam, northern Tibet. *Lithos* 374-375, 105707–106375. doi:10.1016/j.lithos.2020.105707

Taylor, S. R., and McLennan, S. M. (1995). The geochemical evolution of the continental crust. *Rev. Geophys.* 33 (2), 241–265. doi:10.1029/95rg00262

Teng, X., Zhang, J. X., and JianXin, Z. (2020). Ultrahigh temperature metamorphism in collisional orogen and its tectonic significance: An example from the Pan-African orogens. *Acta Petrol. Sin.* 36 (10), 2963–2982. [in Chinese with English abstract]. doi:10.18654/1000-0569/2020.10.03

Teng, X., Zhang, J., Mao, X., Lu, Z., and Zhou, G. (2020). The earliest cambrian UHT metamorphism in the Qaidam block, Western China: A record of the final assembly of greater Gondwana? *Gondwana Res.* 87, 118–137. doi:10.1016/j.gr.2020.06.009

Teng, X., Zhang, J., Mao, X., Lu, Z., Zhou, G., Wu, Y., et al. (2022). Qaidam block situated in the interior of Rodinia and Gondwana: New magmatic and metamorphic constraints. *Precambrian Res.* 381, 106866. doi:10.1016/j.precamres.2022.106866

Wang, Y. S., Zhuang, Q. X., and Shi, C. Y. (1983). *The precambrian feature of qinghai" in contribution to the geology of the qinghai-xizang (tibet) plateau (2).* Beijing: Geological Publishing House, 56–69. [in Chinese with English abstract].

Wang, X., Griffin, W. L., Chen, J., Huang, P., and Li, X. (2011). U and Th contents and Th U ratios of zircon in felsic and mafic magmatic rocks: Improved zircon-melt distribution coefficients. *Acta Geol. Sin.* 85 (1), 164–174. doi:10.1111/j.1755-6724.2011.00387.x

Wang, C., Liu, L., Xiao, P. X., Cao, Y. T., Yu, H. Y., Meert, J. G., et al. (2014a). Geochemical and geochronologic constraints for Paleozoic magmatism related to the orogenic collapse in the Qimantagh–South Altyn region, northwestern China. *Lithos* 202-203, 1–20. doi:10.1016/j.lithos.2014.05.016

Wang, G., Sun, F. Y., Li, B. L., Li, S. J., Zhao, J. W., Ao, Z., et al. (2014b). Petrography, zircon U-Pb geochronology and geochemistry of the mafic-ultramafic intrusion in Xiarihamu Cu-Ni deposit from East Kunlun, with implications for geodynamic setting. *Earth Sci. Front.* 21, 381–401. [in Chinese with English abstract].

Wang, G., Sun, F., Li, B., Ao, C., Li, S., Zhao, J., et al. (2016). Geochronology, geochemistry and tectonic implication of Early Neoproterozoic monzogranite in Xiarihamu ore district from East Kunlun. *Geotect. Metallog.* 40, 1247–1260. [in Chinese with English abstract].

Watson, E. B., and Harrison, T. M. (1983). Zircon saturation revisited - temperature and composition effects in a variety of crustal magma types. *Earth Planet. Sci. Lett.* 64 (2), 295–304. doi:10.1016/0012-821x(83)90211-x

Whalen, J. B., Currie, K. L., and Chappell, B. W. (1987). A-type granites: geochemical characteristics, discrimination and petrogenesis. *Contrib. Mineral. Petrol.* 95 (4), 407–419. doi:10.1007/bf00402202

Wiedenbeck, M., AllÉ, P., Corfu, F., Griffin, W. L., Meier, M., Oberli, F., et al. (1995). Three natural zircon standards for U-Th-Pb, Lu-Hf, trace element and REE analyses. *Geostand. Geoanal. Res.* 19 (1), 1–23. doi:10.1111/j.1751-908x.1995.tb00147.x

Winther, K. T. (1996). An experimentally based model for the origin of tonalitic and trondhjemitic melts. *Chem. Geol.* 127 (1-3), 43–59. doi:10.1016/0009-2541(95)00087-9

Wu, J. R., Ren, B. S., Zhang, M., Gao, D. C., Zhao, T., Zhang, H. W., et al. (1987). The genetic type and geological characteristics of the Xitieshan massive sulphide deposit, Qinghai. *Bull. Xi'an Inst. Geol. Mineral Resour. Chin. Acad. Geol. Sci.* (20), 1–81. [in Chinese with English abstract].

Wu, F. Y., Jahn, B. M., Wilde, S. A., Lo, C. H., Yui, T. F., Lin, Q., et al. (2003). Highly fractionated I-type granites in NE China (I): geochronology and petrogenesis. *Lithos* 66 (3), 241–273. doi:10.1016/s0024-4937(02)00222-0

Wu, C., Gao, Y., Li, Z., Lei, M., Qin, H., Li, M., et al. (2014a). Zircon SHRIMP U-Pb dating of granites from Dulan and the chronological framework of the North Qaidam UHP belt, NW China. *Sci. China Earth Sci.* 57 (12), 2945–2965. doi:10.1007/s11430-014-4958-5

Wu, C. L., Gao, Y. H., Lei, M., Qin, H. P., Liu, C. H., Li, M. Z., et al. (2014b). Zircon SHRIMP U-Pb dating, Lu-Hf isotopic characteristics and petrogenesis of the Palaeozoic granites in Mangya area, southern Altun, NW China. *Acta Petrol. Sin.* 30 (8), 2297–2323. [in Chinese with English abstract].

Wu, F. Y., Liu, X. C., Ji, W. Q., Wang, J. M., and Yang, L. (2017). Highly fractionated granites: Recognition and research. *Sci. China Earth Sci.* 60, 1201–1219. doi:10.1007/s11430-016-5139-1

Yang, J. S., Liu, F. L., Wu, C. L., Xu, Z. Q., Shi, R. D., Chen, S. Y., et al. (2005). Two ultrahigh-pressure metamorphic events recognized in the Central Orogenic Belt of China: Evidence from the U-Pb dating of coesite-bearing zircons. *Int. Geol. Rev.* 47 (4), 327–343. doi:10.2747/0020-6814.47.4.327

Yang, S., Su, L., Song, S., Allen, M. B., Feng, D., Wang, M., et al. (2020). Melting of subducted continental crust during collision and exhumation: Insights from granitic rocks from the North Qaidam UHP metamorphic belt, NW China. *Lithos* 378-379, 105794–106379. doi:10.1016/j.lithos.2020.105794

Yu, S., Zhang, J., del Real, P. G., Zhao, X., Hou, K., Gong, J., et al. (2013). The Grenvillian orogeny in the Altun–Qilian–North Qaidam mountain belts of northern Tibet Plateau: Constraints from geochemical and zircon U–Pb age and Hf isotopic study of magmatic rocks. *J. Asian Earth Sci.* 73, 372–395. doi:10.1016/j.jseaes.2013.04.042

Yu, S., Zhang, J., Li, S., Santosh, M., Li, Y., Liu, Y., et al. (2019). TTG-Adakitic-Like (Tonalitic-Trondhjemitic) magmas resulting from partial melting of metagabbro under high-pressure condition during continental collision in the north Qaidam UHP terrane, western China. *Tectonics* 38 (3), 791–822. doi:10.1029/2018tc005259

Yuan, G. B., Wang, H. C., Li, H. M., Hao, G. J., Xin, H. T., Zhang, B. H., et al. (2002). Zircon U-Pb age of the gabbros in Luliangshan area on the Northern margin of Qaidam basin and its geological implication. *Prog. Precambrian Res.* 25, 36–40. [in Chinese with English abstract].

Zhang, J. X., Meng, F. C., and Wan, Y. S. (2003). Early Paleozoic tectono-thermal event of the Jinshuikou Grop on the southern margin of Qaidam: Zircon U-Pb SHRIMP age evidence. *Geol. Bull. China* 22 (6), 397–404. [in Chinese with English abstract].

Zhang, J. X., Mattinson, C. G., Yu, S. Y., Li, J. P., and Meng, F. C. (2010). U-Pb zircon geochronology of coesite-bearing eclogites from the southern dulan area of the north Qaidam UHP terrane, northwestern China: Spatially and temporally extensive UHP metamorphism during continental subduction. *J. Metamorph. Geol.* 28 (9), 955–978. doi:10.1111/j.1525-1314.2010.00901.x

Zhang, Z., Dong, X., Xiang, H., Liou, J. G., and Santosh, M. (2013). Building of the deep gangdese arc, south tibet: Paleocene plutonism and granulite-facies metamorphism. *J. Petrol.* 54 (12), 2547–2580. doi:10.1093/petrology/egt056

Zhang, L., Chen, R. X., Zheng, Y. F., Li, W. C., Hu, Z., Yang, Y., et al. (2016). The tectonic transition from oceanic subduction to continental subduction: Zirconological constraints from two types of eclogites in the North Qaidam orogen, northern Tibet. *Lithos* 244, 122–139. doi:10.1016/j.lithos.2015.12.003

Zhang, J. X., Yu, S. Y., and Mattinson, C. G. (2017). Early Paleozoic polyphase metamorphism in northern Tibet, China. *Gondwana Res.* 41, 267–289. doi:10.1016/j.gr.2015.11.009

Zhang, J. X., Lu, Z. L., Mao, X. H., Teng, X., Zhou, G. S., Wu, Y. W., et al. (2021). Revisiting the precambrian micro-continental blocks within the early paleozoic orogenic system of the northeastern qinghai-tibet plateau: Insight into the origin of Proto tethyan ocean. *Acta Petrol. Sin.* 37 (1), 74–94. [in Chinese with English abstract]. doi:10.18654/1000-0569/2021.01.06

Zhu, D. C., Wang, Q., Chung, S. L., Cawood, P. A., and Zhao, Z. D. (2018). Gangdese magmatism in southern tibet and India–asia convergence since 120 Ma. *Geol. Soc. Lond. Spec. Publ.* 483, 583–604. doi:10.1144/sp483.14

frontiers | Frontiers in Earth Science

TYPE Original Research
PUBLISHED 20 January 2023
DOI 10.3389/feart.2023.1133539

OPEN ACCESS

EDITED BY
Jiyuan Yin,
Chinese Academy of Geologi-cal Sciences (CAGS), China

REVIEWED BY
Xiaochen Zhao,
Xi'an University of Science and Technology, China
Zhongnan Wang,
Research Institute of Petroleum Exploration and Development (RIPED), China

*CORRESPONDENCE
Aiguo Wang,
wag@nwu.edu.cn

SPECIALTY SECTION
This article was submitted to Petrology, a section of the journal Frontiers in Earth Science

RECEIVED 29 December 2022
ACCEPTED 12 January 2023
PUBLISHED 20 January 2023

CITATION
Yang Z, Wang A, Meng P, Chen M, Guo K and Zhu N (2023), Combined use of in-reservoir geological records for oil-reservoir destruction identification: A case study in the Jingbian area (Ordos Basin, China).
Front. Earth Sci. 11:1133539.
doi: 10.3389/feart.2023.1133539

Combined use of in-reservoir geological records for oil-reservoir destruction identification: A case study in the Jingbian area (Ordos Basin, China)

Zeguang Yang[1], Aiguo Wang[1]*, Pengyun Meng[2], Min Chen[2], Kai Guo[1] and Nan Zhu[1]

[1]State Key Laboratory of Continental Dynamics, Department of Geology, Northwest University, Xi'an, China, [2]No.1 Oil Production Plant of Changqing Oilfield Company, Yan'an, China

Rapid identification of reservoir destruction is critical to avoid exploration failure. More indicators of reservoir destruction are urgently needed to be developed besides the evaluation methods of trap effectiveness based on structural analysis. Here, we provide a case study in the Ordos Basin to show that the combined use of in-reservoir geological records is a robust tool to rapidly identify oil-reservoir destruction. The sandstones within the Yanchang Formation in the oil-depleted Jingbian area were investigated by petrological and geochemical analysis. The results show that 1) the oils with increased density and viscosity occur in the low permeability sandstones, whereas the high permeability sandstones were occupied by water, 2) abundant solid bitumen occur in the intergranular pores, 3) the n-alkanes with carbon numbers less than 19 are significantly lost from the original oils, and 4) the majority of paleo oil layers have evolved into present water layers. All these in-reservoir physicochemical signatures unravel the same geological event (i.e., oil-reservoir destruction) in the Jingbian area. This oil-reservoir destruction was likely caused by the uplift-induced erosion and the fault activities after oil accumulation during the Late Early Cretaceous.

KEYWORDS

Ordos Basin, jingbian area, Yanchang Formation, oil-reservoir destruction, geological record

1 Introduction

Reservoir destruction is a common geological event (Beydoun, 1997; Fu et al., 2000; Gartrell et al., 2004; Pang et al., 2012; Isiaka et al., 2017; Wang W. Y. et al., 2019), and is extremely unfavorable to oil and gas exploration. In order to reduce exploration risks, it is necessary to carry out the reservoir destruction identification and assessment in the exploration area. Uplift-induced erosion and fault activity are considered to be the two main causes of reservoir destruction (e.g., Fu et al., 2000; Pang et al., 2018). Faulting activity (e.g., Gartrell et al., 2004; Isiaka et al., 2017; Palladino et al., 2020) and tectonic evolution (e.g., Pang et al., 2012; Wang W. Y. et al., 2019) were always studied through geological and geophysical methods to evaluate trap effectiveness in the previous studies. However, these structural analyses for reservoir destruction still need the supports from in-reservior evidences. In fact, tectonic uplift and fault activity can cause a series of secondary physicochemical and microbial alteration which occur within the reservoirs or the overlying strata, such as phase fractionation (e.g., Thompson, 1987; Meulbroek et al., 1998), water washing (e.g., Lafargue and Barker, 1988), biodegradation

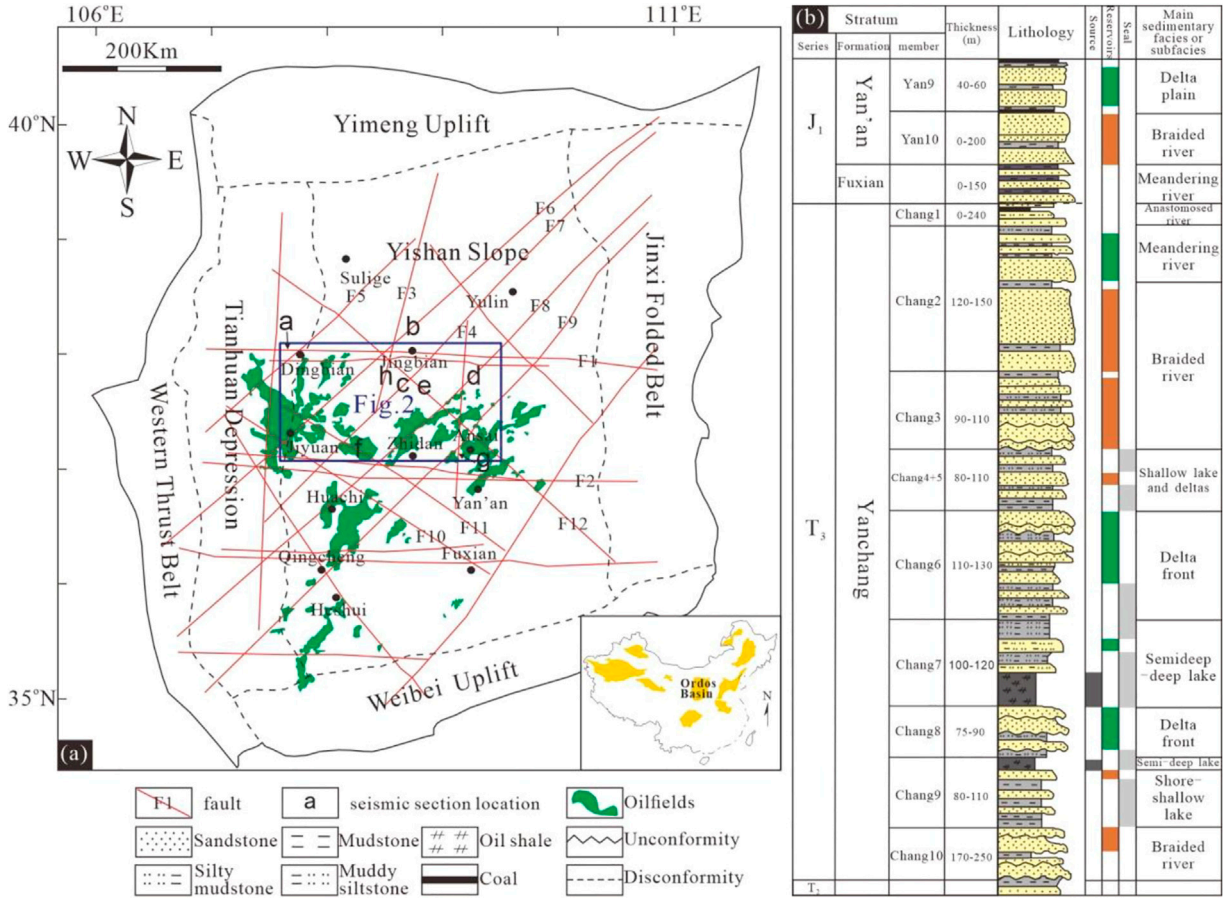

FIGURE 1
Tectonic units and oil-reservoir distribution **(A)** and Lithology, source rocks, reservoirs, seals and sedimentary facies of the Yanchang-Yan'an Formations **(B)** in the Ordos Basin (Modified from Hui et al., 2019; Qu et al., 2020; Wu, 2020; Yang et al., 2021).

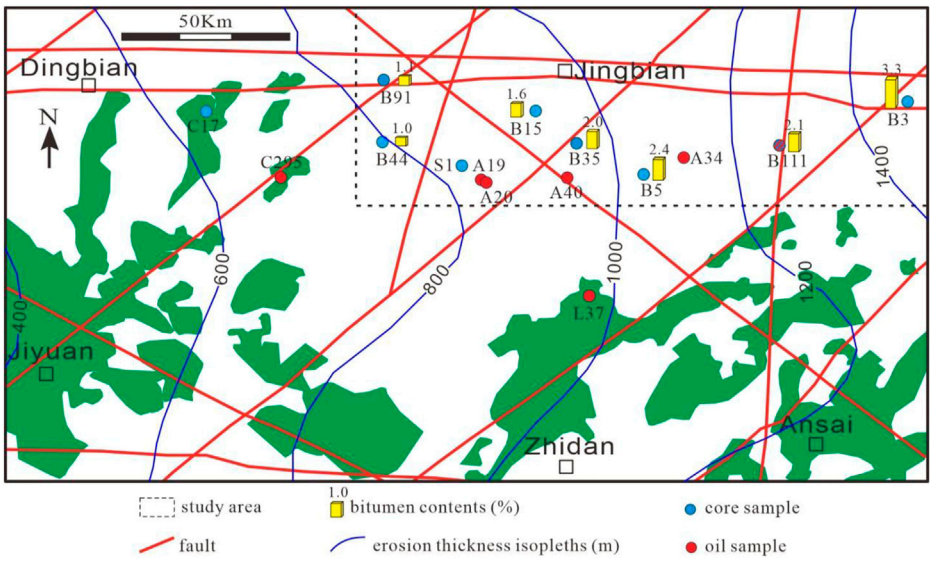

FIGURE 2
Distribution of oil-reservoirs and sampling wells in the Jingbian and adjacent areas (erosion thickness during the Late Cretaceous according to Chen et al., 2006; fault distribution according to Wu, 2020).

(e.g.,Curiale and Bromley, 1996; Oldenburg et al., 2017), diagenetic alteration (Xie et al., 2021; Zhang et al., 2022) and surface oil/gas seepages. Such geological records are all potential indicators of reservoir destruction, and the combined use of them are expected to be powerful to rapidly identify reservoir destruction. Here, we provide a case study in the Ordos Basin to show the important role of in-reservoir geological records play in the identification of oil-reservoir destruction.

During the 40 years of petroleum exploration, 4 oil-enriched areas (OEA) have been founded in the central Ordos Basin (Figure 1A). Each of them contains oil reserves over 10×10^8t (Hui et al., 2019). The Jingbian area is adjacent to the Dingbian-Jiyuan OEA to the west and Zhidan-Ansai OEA to the south (Figure 1; Figure 2) but contains few oil resources. The cause of oil depletion in this area is still unclear, which has resulted in frequent exploration failure. In this study, the sandstone reservoirs in the Jingbian area were investigated through an integrated analysis including microscopic observation, laser Raman, whole-hydrocarbon gas chromatography, quantitative grain fluorescence (QGF) and QGF on extract (QGF-E). The aim of this study is to 1) identify the oil-reservoir destruction in the studied area, and 2) show the important role of in-reservoir geological records play in the identification of oil-reservoir destruction.

2 Geological setting

The Ordos Basin, which covers an area of about 36×10^4 km^2, is the second largest petroliferous basin in China, and produces more than 400 million barrels of oil equivalent per year (Hui et al., 2019). According to the diversity of basement structure, the basin is divided into six tectonic units, including Yimeng Uplift, Yishan Slope, Weibei Uplift, Western Thrust Belt, Tianhuan Depression, and Jinxi Folded Belt (Cui et al., 2019; Cui et al., 2022) (Figure 1A). The Yishan Slope, which contains the 4 OEAs, is now a west dipping monocline with an angle less than 1° (Xu et al., 2017). Within the slope, there exists six NE-SW trending, five NW-SE trending, four nearly E-W trending and two N-S trending faults (Figure 1A) (Wu, 2020).

The oil resources in the Ordos Basin are mainly stored in the Mesozoic petroleum system, including the Triassic Yanchang Formation and Jurassic Fuxian- Yan'an formations (Qu et al., 2020) (Figure 1B), which were deposited in fluvial-delta-lake sedimentary systems (Zhou et al., 2008; Qiu et al., 2015). Both of them are subdivided into 10 members, numbered from top to bottom as Chang 1 to Chang 10, and Yan 1 to Yan 10, respectively. The Chang 7 Member containing black organic-rich shale is the chief oil source (Cui et al., 2019), while the sandstones in the Yan 9, Chang 2, Chang 6, Chang 7 and Chang 8 members are the major reservoirs. Thick mudstone and shale layers in the two formations are the seals of underlying oil reservoirs (Figure 1B) (Qu et al., 2020).

The Ordos basin has experienced multiple tectonic movements since the Yanchang Formation was deposited. With the continent-continent collision of the Yangtze plate and North China plate during the late Triassic (Bao et al., 2020; Wu et al., 2020), the Ordos Basin was uplifted and underwent the erosion of the Chang 1 ~ Chang 3 members. Subsequently, the Fuxian and Yan'an formations unconformably covered the Yanchang Formation. During the middle to late Jurassic, the thrust-nappe belt in the western margin of the basin developed, leading to erosion in the middle and eastern basin with a maximum erosion thickness of 300 m (Chen et al., 2006). During the Early Cretaceous, the Ordos Basin subsided to maximum buried depth due to the movement of paleo-Pacific plate (Wu et al., 2020). During the Late Cretaceous to early-middle Eocene, the Ordos Basin experienced the strongest tectonic uplift, resulting in the erosion of the pre-Late Cretaceous. The erosion thicknesses in the Jingbian area vary from the 800 m–1400 m (Figure 2), and the maximum erosion thicknesses can be up to 1800–2000 m in the eastern basin (Liu et al., 2006). Since the Late Miocene, the Tibet Plateau uplift has caused the uplift in the west and subsidence in the east of the basin, forming the present tectonic framework (Ma et al., 2019).

The present exploration target in the Jingbian area and adjacent OEAs is the Chang 6 Member. Its burial depths vary from ~2500 m in the western Dingbian area to ~700 m in the eastern Jingbian area. The petrological characteristic and physical property of the Chang 6 reservoir are almost the same between the studied Jingbian area and adjacent OEAs, which is characterized by fine-medium grain (0.125–0.5 mm) arkose, dominated calcite/laumontite cements and low/ultra-low permeability (Wei et al., 2003; Hui et al., 2019; Ao et al., 2022).

3 Samples and methods

Twenty-five sandstone-reservoir samples and six crude oil samples were collected from the wells in the Jingbian area and adjacentDingbian-JiyuanOEAs (Figure 2). Gas chromatography was conducted on the crude oils using Trace 1300 system equipped with an HP-1 capillary column (30 m × 0.25 mm × 0.25 m). The temperatures of the sample inlet and FID detector are all 300°C. The temperature program was 40°C for 10 min, 40°C–70°C at 4°C/min, 70°C–300°C at 8°C/min, and finally held at 310°C for 40 min. Nitrogen was used as carrier gas at a flow rate of 1 mL/min.

Casting thin sections without cover glass and doubly polished thin sections for fluid inclusion were prepared for the observation of petrography and fluid inclusion under a ZEISS Axio Scope A1 microscope (with 100 W high-pressure mercury lamp). Coeval oil and aqueous inclusions in the doubly polished thin sections were examined on a THMS600 Linkam Heating and Freezing stage for homogenization temperatures (T_h). The analytical uncertainties are better than 0.1°C.

The burial and thermal history for single well was recovered through basin model 1D and constrained by the measured vitrinite reflectance at various depths. Lithology was determined by the cuttings logging and log data. The main parameters erosion thickness and geothermal gradient were cited from Chen et al. (2006) and Ren et al. (2017).

A HORIBA LabRAM Odyssey spectrometer was applied to identify the unrecognizable minerals in the casting thin sections through Raman spectral analysis. The measuring conditions are: laser wavelength 785 nm, exposure time 20 s, scanning wave number range 1000–2000 cm^{-1}, and superposition twice.

QGF is measured by fluorescence emission spectra from reservoir grains, after a cleaning procedure involving solvent, hydrogen peroxide and hydrochloric acid. QGF-E is measured by fluorescence emission spectra from the solvent extract from reservoir grains after the QGF cleaning procedure following Liu and Eadington (2005).

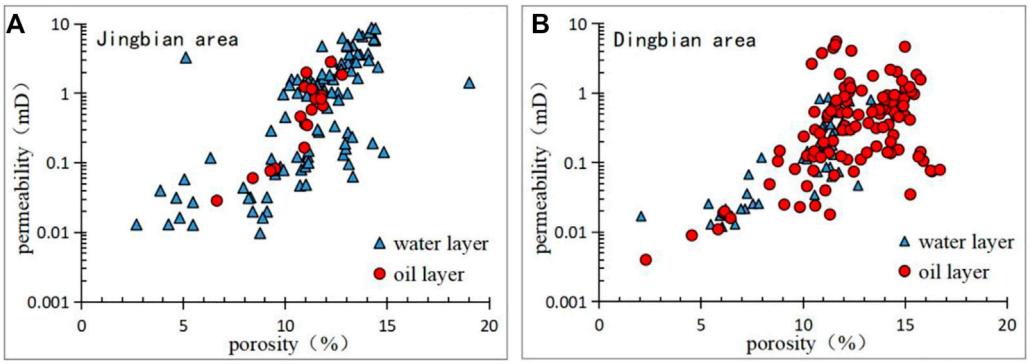

FIGURE 3
Porosity and permeability of oil/water layers in the Chang 6 Member in the Jingbian **(A)** and Dingbian **(B)** areas.

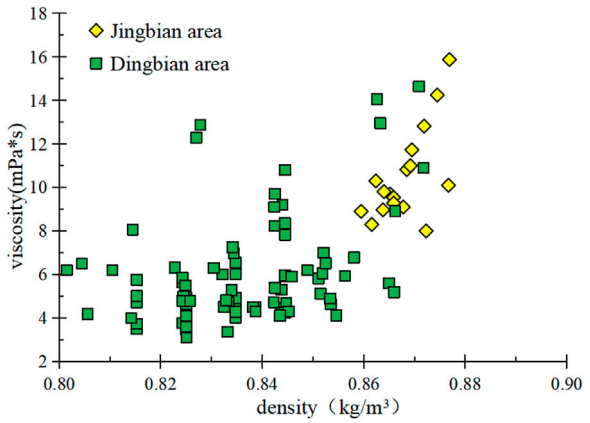

FIGURE 4
Density and viscosity of the Chang 6 oils in the Jingbian and Dingbian areas.

In addition, the physical properties of core and crude oils, as well as the formation testing data in the study area and adjacent areas were collected from the PetroChina Changqing Oilfield Company.

4 Results

4.1 Porosity-permeability of oil and water layers

The sandstone reservoirs were divided into oil layers and water layers based on the collected formation testing data. Subsequently, the measured core porosity-permeability corresponding to oil layers and water layers were respectively counted. The sandstone reservoirs in the study area and adjacent OEAs are both typical tight sandstone reservoir with significant heterogeneity (Wei et al., 2003; Hui et al., 2019; Ao et al., 2022), but the oil-bearing property is obviously different between them. As shown in Figure 3, the porosity and permeability ranges of oil layers in the Jingbian area are limited, mainly varying from 10% to 12%, and from 0.1 mD to 2 mD, respectively (Figure 3A). On the contrary, the water layers are characterized by much larger porosity-permeability ranges, including the high-quality sandstones with porosity greater than 12% (Figure 3A). However, in the adjacent Dingbian OEA, the oils mainly occur in the high-quality reservoirs with porosity greater than 10% and permeability greater than 0.1 mD, while the water occupies the sandstones with porosity and permeability respectively less than 12% and 1 mD (Figure 3B).

In summary, the present high-quality sandstones were occupied by water in the Jingbian area, but were occupied by oils in the adjacent OEA.

4.2 Density and viscosity of oils

As shown in Figure 4, the density of crude oils in the Jingbian area varies from 0.86 kg/m^3 to 0.88 kg/m^3, which are obviously heavier than the oils in the Dingbian area. The viscosity of crude oils in the Jingbian area varies from 8 mPa*s to 16 mPa*s, which are more viscous than the oils in the Dingbian area.

4.3 Solid bitumen

Microscopic observation shows that the majority of intergranular pores within the Chang 6 Member in the Jingbian area are filled by the black solid matters (Figures 5A, C). They are identified to be solid bitumen by the Raman spectra with the two first-order characteristic bands, i.e., the D band near 1380 cm^{-1} and G band near 1590cm^{-1} (Figures 5B, D) (Zerda et al., 1981).

According to the estimated solid bitumen content in each casting thin section, the solid bitumen abundance in the study area is shown (Figure 2). The solid bitumen content gradually increases from 1.0% in the west to 3.3% in the east. The average content of the whole study area is 2.1%.

4.4 N-alkane abundance distribution of oils

The abundance of n-alkane in primary maturated oils exponentially decreases as the carbon number increases (Kissin, 1987; Meulbroek et al., 1998). This pattern, however, can be broken by several geological processes (e.g., biodegradation and phase fractionation).

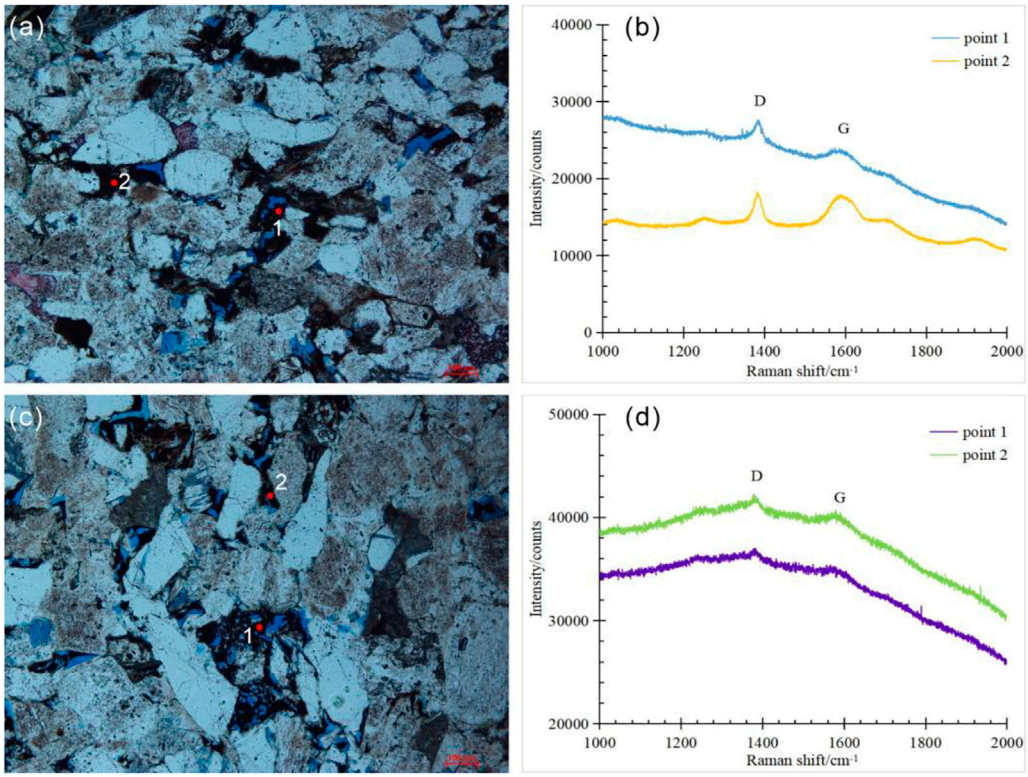

FIGURE 5
Solid bitumen occurrence in the reservoir and its Raman spectra (red points indicate Laser Raman testing location; **(A,B)** B111 well, 969.56 m, Chang 6 Member; **(C,D)** Q3 well, 719.15 m, Chang 6 Member).

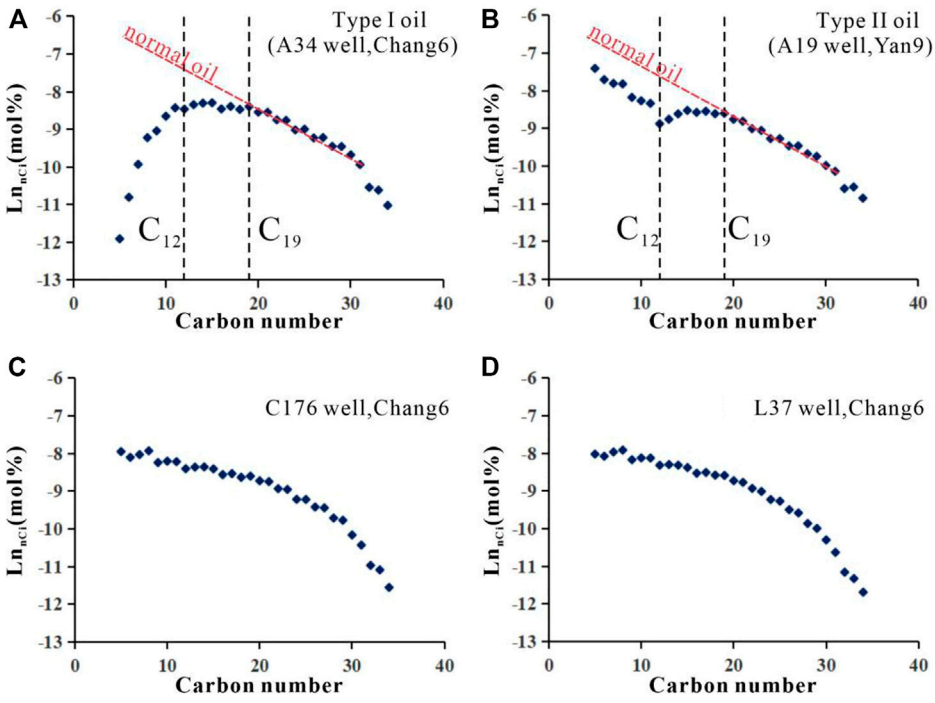

FIGURE 6
N-alkane abundance distributions of crude oils in the Jingbian and adjacent areas. **(A)**: oil with the n-alkane abundance negative deviation from the exponential pattern at C19, and the deviation degree obviously increases for the carbon numbers less than C12. **(B)**: oil with the n-alkane abundance negative deviation from the exponential pattern at C19, but the deviation degree decreases for the carbon numbers less than C12. **(C,D)**: oil with the n-alkane abundance approximate to exponential distribution.

TABLE 1 Geochemical parameters of crude oils in the Jingbian area and the adjacent OEAs.

Sample ID	Well	Formation	Pr/nC_{17}	Ph/nC_{18}	Tol/nC_7	nC_7/MCC_6	Q (%)
O1	B111	Chang 6	0.43	0.50	0.20	0.50	63.7
O2	A34	Chang 6	0.46	0.54	0.19	0.51	61.9
O3	A19	Yan 9	0.41	0.43	0.10	0.71	—
O4	A40	Yan 9	0.40	0.42	0.11	0.71	—
O5	C176	Chang 6	0.40	0.38	0.25	0.50	—
O6	L37	Chang 6	0.32	0.34	0.33	0.73	—

Abbreviations: Pr = pristine; nC_{17} = n-heptadecane; Ph = phytane; nC_{18} = n-octadecane; Tol =Toluene; nC_7 = heptane; MCC_6 = Methyl-cyclohexane; Q = light-end loss percentage.

TABLE 2 QGF & QGF-E data and identified results in the study area and adjacent areas.

Well	Depth m)	QGF index	QGF-E intensity (pc)	Paleo		Present	
				Oil layer	water layer	Oil layer	water layer
B5	1535.5	7.34	34.31		√		
	1539.83	12.17	59.82	√		√	
	1541.5	9.83	18.3		√		√
	1542.47	15.02	6.23	√			√
	1543.2	18.47	21.6	√			
B3	701	6.24	29.94		√		
	704.35	10.13	3.22				√
	708.6	18.92	31.02	√			
	715.4	12.4	40.21	√		√	
	718.6	18.7	41.23	√		√	
	722.8	29.37	5.22	√			√
	727	18.06	11.23	√			√
C17	1912.03	5.68	2.92		√		√
	1915.2	33.42	289.53	√		√	
	1916.95	19.8	51.62	√		√	
	1920.1	7.61	10.63		√		√
	1922.54	8.94	9.42		√		√
	1924.9	19.97	83.2	√		√	

The studied oils from the Chang 6 Member in the Jingbian area are characterized by a negative deviation from the exponential pattern at C_{19} (Figure 6A). The deviation degree obviously increases for the n-alkanes with carbon numbers less than C_{12} (nC_{12-}), indicating a significant nC_{12-} depletion. The n-alkanes of the oils from the overlying Yan'an Formation also deviate negatively at C_{19}, but the deviation degree decreases for the nC_{12-} (Figure 6B), indicating an nC_{12-} invasion into the nC_{19-} depleted oils. Notably, the oils from the adjacent OEAs display a pattern approximate to exponential distribution (Figures 6C, D), suggesting that they are mature and unaltered oils.

Based on the whole-hydrocarbon gas chromatography, the geochemical parameters for biodegradation: pristine/n-heptadecane (Pr/nC_{17}), phytane/n-octadecane (Ph/nC_{18}), and the parameters for phase fractionation: toluene/heptane (Tol/nC_7) and heptane/methylcyclohexane (nC_7/MCC_6) were calculated for further analysis (Table 1).

4.5 QGF & QGF-E

QGF & QGF-E is a set of fluorescence detection technology developed by Liu and Eadington (2005) and Liu et al. (2007) to detect the fluorescence of oil inclusions in clastic grains and adsorbed hydrocarbons on the surface of clastic grains. Two parameters, QGF

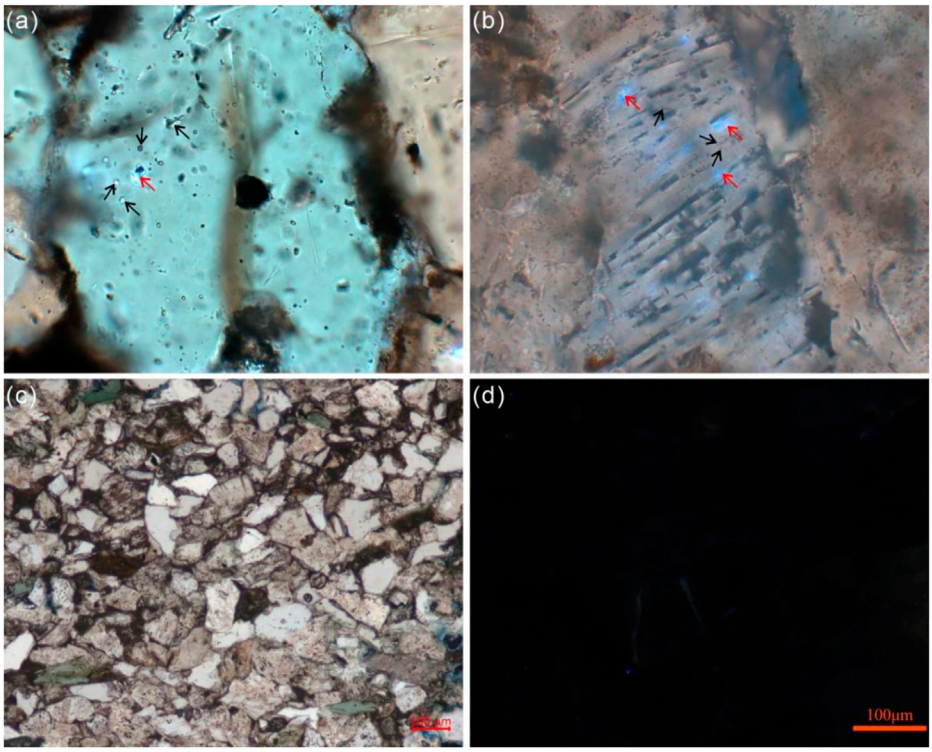

FIGURE 7
Micrographs of sandstones in the Jingbian area **(A)**. S1 well, 1890.48 m, Chang 7; **(B)**. B3 well, 709.9 m, Chang 6; **(C,D)**. B3 well, 704.35 m, Chang 6; the red and black arrows indicate oil and queous inclusions, respectively.

TABLE 3 T_h values of aqueous inclusions coeval with oil inclusions in the study area.

Well	Depth(m)	Formation	Hosting mineral	Occurrence	T_h (°C)
S1	1887.9	Chang 7	feldspar	healed intragranular pore	112.8
					110.3
	1889.06				113.3
	1890.48				112.3
					113.0
					109.9
B3	709.9	Chang 6	feldspar	healed intragranular pore	91.0
					89.4
					94.0
	706.9		quartz	healed fractures	93.2
					92.5
					87.4
					91.5

index and QGF-E intensity, were created to identify paleo- and present oil layers, respectively (Liu et al., 2007). The QGF index of core samples from the Chang 6 Member in the Jingbian area varies from 6.24 to 29.37 with an average of 14.72, while the QGF-E intensity ranges from 3.22 pc to 59.82pc, with an average of 25.19pc (Table 2).

4.6 Fluid inclusion

The coeval oil and aqueous inclusions in the sandstones in the Yanchang Formation in the Jingbian area have been observed (Figures 7A, B). The oil inclusions were trapped within healed secondary

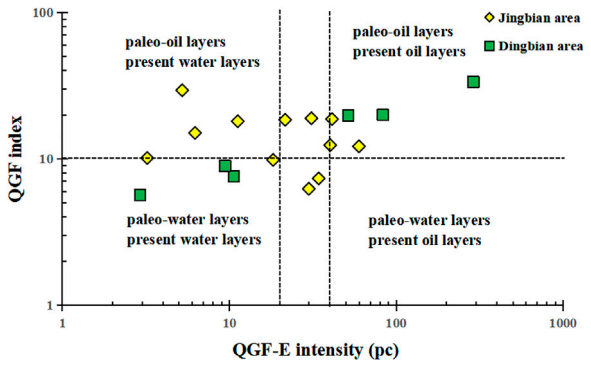

FIGURE 8
Cross plot of QGF index and QGF-E intensity in the Jingbian and Dingbian areas.

fractures in quartz and intragranular pore in feldspar grains, and exhibit bluish-white fluorescence. The T_h values of aqueous inclusions coeval with oil inclusions in the western and eastern parts of Jingbian area are 109.9–113.3°C and 87.4–94.0°C respectively (Table 3).

5 Discussion

5.1 Oil accumulation in the Jingbian area

Undoubtedly, solid bitumen is an indicator of oil charging (Littke et al., 1996; Huc et al., 2000; Liu et al., 2009). Wang et al. (2006) suggested that the reservoir with solid bitumen content greater than 2.0% can be defined as a paleo-oil reservoir. Solid bitumen is widely distributed in the study area (Figure 2), and 57% core samples contain the solid bitumen content greater than 2.0%, indicating that the Jingbian area, like the adjacent OEAs, is also a favorable area for oil accumulation.

QGF & QGF-E is widely used in the reconstruction of reservoir evolution (Wang et al., 2017; Liu et al., 2019; Song et al., 2022). According to the previous experience (Liu and Eadington, 2005; Liu et al., 2007), the QGF index of paleo-oil layers are generally greater than 4, and those of paleo-water layers are generally less than 4; The QGF-E intensity of present oil layers are generally greater than 40pc, while those of present water layers are generally less than 20pc. If the experiential QGF index is applied to the Jingbian area, all the studied core samples will be identified as paleo-oil layers.

The developer of QGF & QGF-E emphasized that the identification standards for paleo (present) oil (water) layers should be in line with local conditions (Liu and Eadington, 2005; Liu et al., 2007). According to the comparison between the QGF&QGF-E values and core observation, microscopic observation and formation testing results, the experiential QGF-E intensity ranges for identifying present oil/water layer are still applicable in the Jingbian area. However, the experiential QGF index value for distinguishing paleo oil/water layer is not effective anymore. Take the sandstone at 704.35 m of B3 well for example, its QGF index is 10.13, and will be classified into paleo oil layer according to the experiential standard. In fact, this sandstone is characterized by water wetting, 5.3% matrix content, strong compaction (linear contact among clastic grains), little bitumen (Figure 7C), few cements and no fluorescence (Figure 7D), which suggests that the subsurface fluids including oil have not charged this sandstone at all. Eventually, the QGF index boundary between paleo-oil and water layers in the study area is suggested as 10.13.

According to the QGF index and QGF-E intensity, the paleo- and present oil/water layers were identified (Figure 8; Table 2). Of 12 reservoir samples in the Jingbian area, 8 samples (accounting for 67%) belong to paleo-oil layers, showing that the large scale of oil accumulation have ever occurred in the study area.

The time of oil accumulation is determined using the T_h values of fluid inclusion and burial-thermal history (Figure 9). The T_h values of aqueous inclusions coeval with oil inclusions in the Chang 7 reservoir of S1 well range from 109.9°C to 113.3°C, while those in the Chang 6 reservoir of B3 well range from 87.4°C to 94.0°C (Table 3). These two T_h ranges plotting within the burial-thermal histories in the S1 and B3 wells both indicate that the oil accumulation occurred during the Late Early Cretaceous, prior to the tectonic uplift of the Ordos Basin during the Late Cretaceous (Figure 9).

5.2 Oil-reservoir destruction

As mentioned above, oils have accumulated during the Late Early Cretaceous in the Jingbian area. However, no commercial oil pools have been found now, which is likely attributed to paleo-oil reservoir destruction based on the following in-reservoir geological evidences.

5.2.1 Evolution from paleo-oil layers into present water layers

QGF & QGF-E provides direct evidence for the paleo-oil reservoir destruction occurred in the Jingbian area. Take B5 well with thick-bedded sandstones in the Chang 6 Member for example, the sandstones are dominated by water layers and oil-water layers, consistent with the results indicated by QGF-E intensity (Figure 10A). The QGF index, however, indicate that the oil-water layer in the lower part was an oil layer before (Figure 10A). This evolution from paleo oil layers into present water layers is more obvious in B3 well. The most majority of sandstones in Figure 10B were paleo oil layers, but now are dominated by water layers and oil-water layers. Overall, of the 8 samples identified as paleo oil layer, 3 samples are identified as present oil layer (Figure 8; Table 2), indicating that 62.5% of paleo oil layers have been destructed and evolved into present water layers.

In comparison, the QGF & QGF-E values in the Dingbian OEA show that the samples that were identified as paleo oil layer were also identified as present oil layer (Figure 8 and Figure 10C), indicating that the paleo oil reservoirs in the Dingbian area have not been destructed yet. That is why the oils are enriched there now.

5.2.2 Light fraction loss of oils

The n-alkane abundance distribution pattern of oils also provides the evidence for paleo oil-reservoir destruction. As shown in Figures 6A, B, the oils in the study area are characterized by the loss and invasion of light fraction. To explain this, we have carefully considered several geological processes and sampling process that may affect the oil compositions. Organic molecules tend to be degraded at different rates due to different resistance to biodegradation (Bennett et al., 2013;

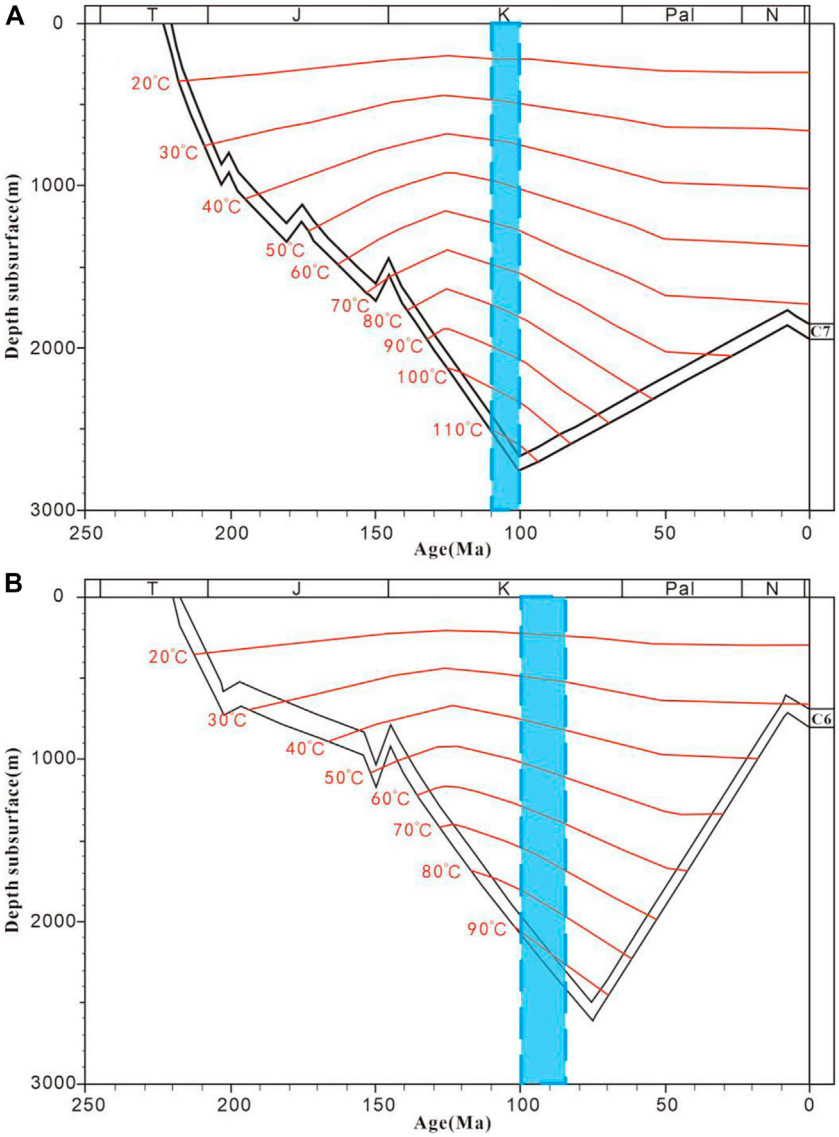

FIGURE 9
Oil accumulation time determined by T_h vales and burial-thermal history in S1 **(A)** and B3 **(B)** wells in the Jingbian area (C6= Chang 6 Member; C7=Chang 7 Member).

Wang et al., 2013). The first indications of oil biodegradation typically occurred with the selective removal of normal alkanes. As biodegradation proceeded, normal alkanes are degraded faster than mono- and multi-methylated alkanes (Peters et al., 2005). Thus, biodegradation can be ruled out due to a full range of n-alkanes observed in the oils and normal Pr/nC_{17} and Ph/nC_{18} values (Table 1). Water washing was also ruled out because the oils contain significant amounts of toluene (Table 1) (Napitupulu et al., 2000). Paraffin precipitation only affects n-alkanes at high carbon number end (e.g., >30, Losh et al., 2002). Fractionation in the separator and short term evaporation of samples after collection have been shown by Meulbroek et al. (1998) to affect the compounds as heavy as decane. Instead, evaporative fractionation is the most likely cause for the n-alkane distribution patterns of the studied oils based on the two facts: 1) the Chang 6 oils have lost the nC_{12-} which are exact the compositions invading into the overlying Yan 9 oils in the Jingbian area, and 2) the Tol/nC_7 values of Chang 6 oils are greater than those of Yan 9 oils, while the nC_7/MCC_6 values of Chang 6 oils are less than those of Yan 9 oils.

The evaporative fractionation resulted in the upward migration of light-end compositions originating from the Chang 6 Member, which is expected to have caused oil-reservoir destruction in the study area. According to the calculation method proposed by Losh et al. (2002), the light-end loss percentage are 63.66% and 61.91% for the two residual oils (Table 1; Figure 11), indicating that the original oil-reservoirs have lost more than half of oil compositions. In the adjacent OEAs, however, the Chang 6 oils show little compositional loss (Figures 6C, D), suggesting that the oil-reservoirs there have not been destructed yet.

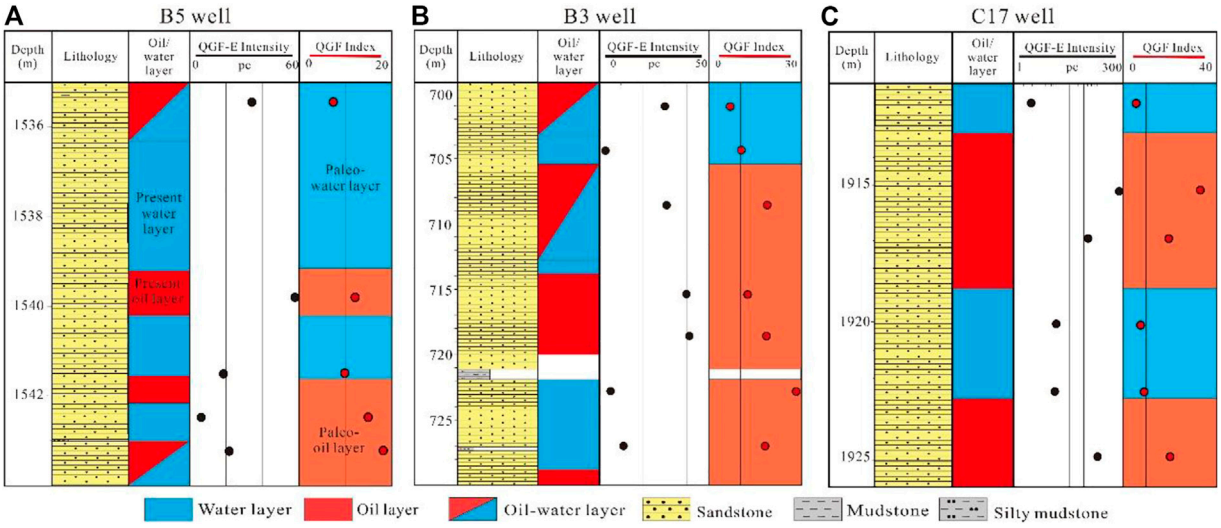

FIGURE 10
Paleo oil/water layers and present oil/water layers in the Chang 6 members of B5 well **(A)**, B3 well **(B)** in the Jingbian area and C17 well **(C)** in the adjacent Dingbian area.

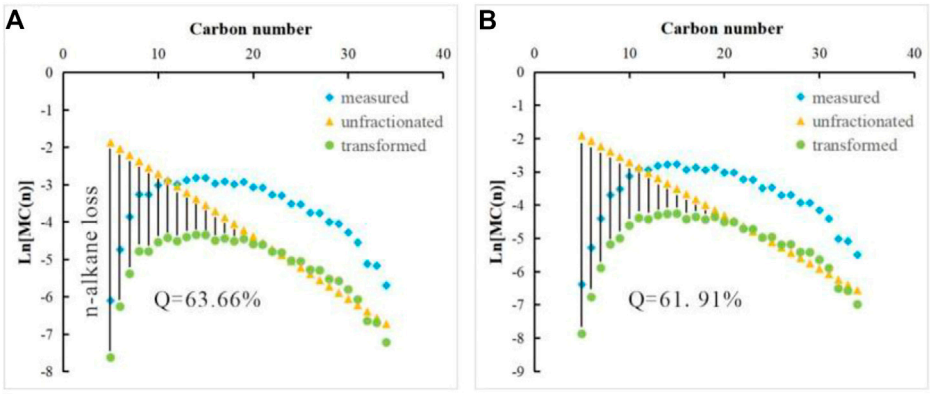

FIGURE 11
N-alkanes loss percentage of the studied oils **(A)** B111 well, Chang 6 Member; **(B)** A34 well, Chang 6 Member).

5.2.3 Elevated density-viscosity of oils and enrichment of solid bitumen

The density and viscosity of oils are controlled by the temperature, pressure and its chemical composition (Morales-Medina and Guzman, 2012; Said et al., 2016). The oils in the Yishan Slope mainly originated from the black shales in the Chang 7 Member in the central basin and accumulated during the Late Early Cretaceous (Hui, et al., 2019). Thus, the initial chemical compositions of these oils are expected to be similar. Under the same experimental conditions (20°C, 1atm), the elevated density-viscosity of oils suggests the occurrence of oil-reservoir destruction in the Jingbian area. Continuous compositional loss of light-end fraction during the oil-reservoir destruction will inevitably lead to the relative increase of heavy-end fraction in residual oils and finally form solid bitumen (Wang A. G. et al., 2019). It is should be noted that the density and viscosity of oils in the Jingbian area are obviously greater than those in the Dingbian OEA (Figure 5) and the solid bitumen are indeed more abundant in the Jingbian area (Figure 2; Figures 5A, C).

5.2.4 Oil occurrence in low-quality rather than high-quality reservoirs

Migrating oils tend to preferentially occupy the porosity with the lower capillary resistance (i.e., high porosity and permeability portions) after charging into the reservoirs. With the increase of oil saturation in trap, oils have to charge into the low porosity and permeability portions (England et al., 1987). Take the adjacent Dingbian OEA for example, oils are indeed occupying the high porosity and permeability reservoirs (Figure 3B).

On the other hand, when the oil-reservoirs were destructed, the oils in high porosity and permeability portions preferentially migrate out the trap, whereas the oils in low porosity and permeability portions were most likely left due to poor liquidity. In the Jingbian area, the sandstone reservoirs with high porosity and permeability are occupied by water, whereas the oils occur in the sandstone reservoirs with relative low porosity and permeability (Figure 3A). These oil-bearing characteristics in the Jingbian area are exactly consistent with the above oil/water behaviors caused by oil-reservoir destruction.

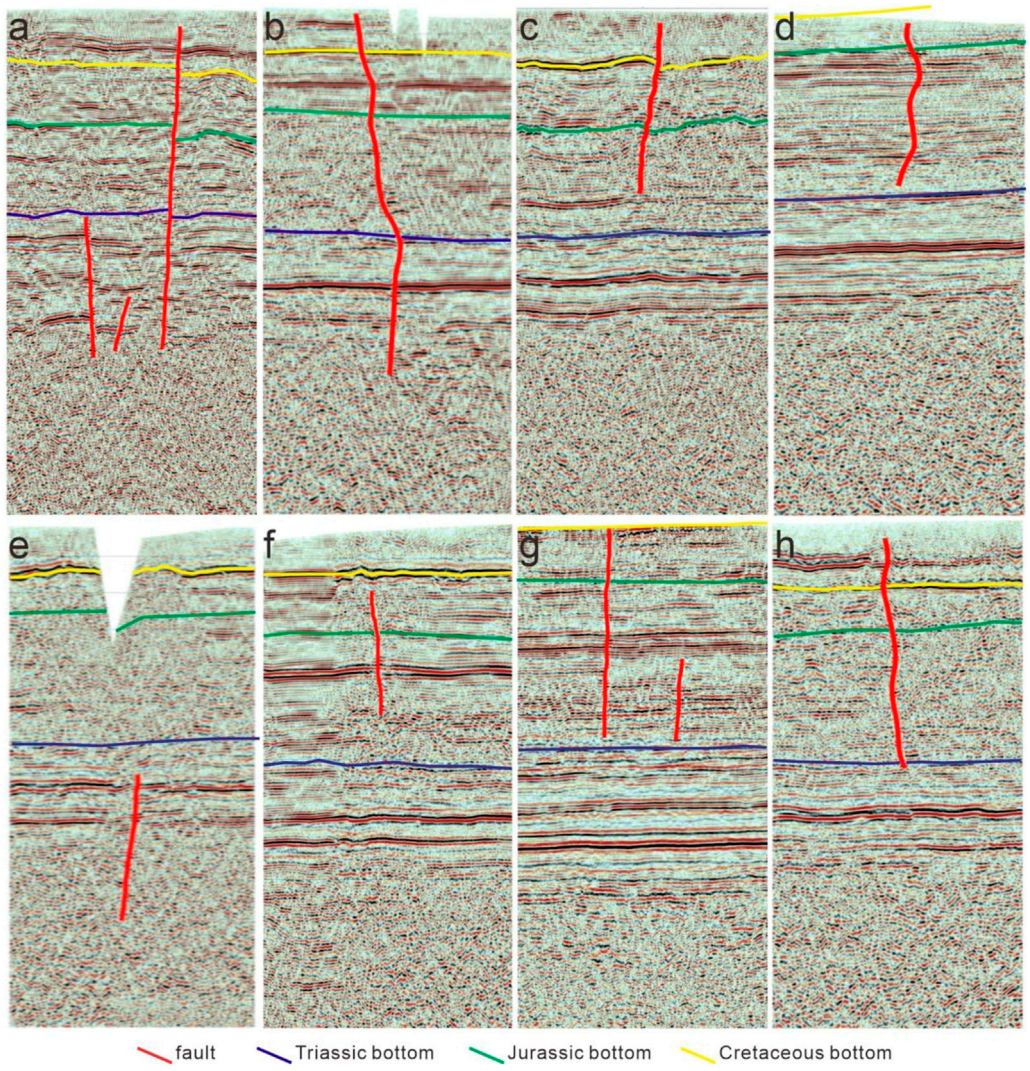

FIGURE 12
Seimic interpretation sections in the Jingbian and adjacent areas (modified from Wu, 2020). **(A)**: F1 fault. **(B)**: F6 fault. **(C)**: F7 fault. **(D)**: F8 fault. **(E)**: F12 fault. **(F)**: F11 fault. **(G)**: F4 fault. **(H)**: F3 fault.

5.3 Cause of oil-reservoir destruction

As mentioned above, uplift-induced erosion and fault activity were considered to be the two main causes of reservoir destruction (Fu et al., 2000; Pang et al., 2018), which should be responsible for the oil-reservoir destruction in the Jinbian area.

Since the oil accumulation during the Late Early Cretaceous, the Ordos Basin has experienced a long-period tectonic uplift from the Late Creataceous to Early-Middle Eocene. This tectonic uplift caused intense erosion with the erosion thickness increasing from west to east (Liu et al., 2006). In the study area, the erosion thicknesses vary from 800m to 1400 m (Figure 2) (Chen et al., 2006), generating a unconformity between the Middle Jurassic and Quaternary. Compared with the Dingbian OEA to the west, the uplift-induced erosion in the Jingbian area is more intense, which maybe has degraded the sealing of oil-reservoir and caused the oil-reservoir destruction in the area.

The Ordos Basin used to be considered as a stable cratonic basin with undeveloped faults. In recent years, however, multiple basement faults and concealed faults have been reported in the basin (Liu et al., 2013; Wu, 2020). There exist two E-W trending (F1, F2), two N-S trending (F3, F4), five NE-SW trending (F5-F9) and three NW-SW trending (F10-F12) faults in the Jingbian and adjacent areas (Figure 1A and Figure 2) (Wu, 2020). According to the seismic sections (Figure 12; Wu, 2020), the faults that cut across the Cretaceous (e.g., Figure Figures 12A–H) were likely active during the uplift and maybe have caused the oil-reservoir destruction. The faults that do not cut across the Cretaceous (e.g., Figures Figures 12E, F) were not active during the Cretaceous, and are thus not responsible for the oil-reservoir destruction. Overall, all the faults in the Jingbian and adjacent areas are likely active during the uplift, except the NW-SE trending faults. As shown in Figure 1A, there exist six potential faults (i.e., F1, F3, F4, F6, F7, and F8) for oil-reservoir destruction across the Jingbian area, whereas there exist two potential faults (i.e., F5 and F6) and three potential faults (i.e., F4, F8 and F9) in the Dingbian-Jiyuan OEA and Zhidan-Ansai OEA, respectively. Thus, the faults in the Jingbian area are more developed than those in the OEAs.

In summary, the tectonic uplift during the Late Cretaceous has caused uplift-induced erosion and fault activities, which likely further

caused the oil-reservoir destruction in the Jingbian area. In comparison, uplift-induced erosion and fault activities in the Dingbian and Ansai OEAs are relatively undeveloped, which is thus favorable for oil-reservoir preservation.

6 Conclusion

The Jingbian area in the Ordos Basin was used as a case to demonstrate that combined use of in-reservoir geological records is a robust tool to rapidly identify oil-reservoir destruction. The following conclusions were obtained from this study:

The Jingbian area is also a favorable area for oil accumulation, which occurred during the Late Early Cretaceous. The uplift-induced erosion and fault activities during the Late Cretaceous degraded the sealing of the oil-reservoir, and led to the oil-reservoir destruction. This process has been recorded by a series of geological signals in reservoirs, including 1) the loss of light fraction, 2) the increases of oil density and viscosity, 3) the enrichment of solid bitumen, 4) the evolution from paleo oil layers into current water layers, and 5) the oil occurrence in low-quality rather than high-quality reservoirs. These in-reservoir geological records provide a new technical approach for the oil-reservoir destruction identification.

Data availability statement

The original contributions presented in the study are included in the article/supplementary material, further inquiries can be directed to the corresponding author.

Author contributions

ZY, writing, mapping, experiment; AW, supervision, writing; PM, data collection, sampling, writing; MC, data collection, sampling, writing; KG, Sample preparation and editing; NZ, sample Sample preparation and polishing.

Funding

This work was supported by the National Natural Science Foundation of China (No.41402115); the Natural Science Basic Research Program of Shaanxi (2020JQ-591).

Conflict of interest

PM and MC were employed by No.1 Oil Production Plant of Changqing Oilfield Company

The remaining author declares that the research was conducted in the absence of any commercial or financial relationships that could be construed as a potential conflict of interest.

Publisher's note

References

Ao, C., Cheng, Y. H., Tang, Y. H., Wang, S. Y., Teng, X. M., Jin, R. S., et al. (2022). Detrital zircon analysis of the mesozoic strata in the northern Ordos Basin: Revealing the source-to-sink relationships and tectonic settings. *Geol. J.* 57, 3251–3266. doi:10.1002/gj.4472

Bao, H. P., Guo, W., Liu, G., Li, L., Wu, C. Y., and Bai, H. F. (2020). Tectonic evolution in the southern Ordos block and its significance in the tectono-depositional differentiation in the interior of the Ordos Basin. *Chin. J. Geol.* 55, 703–725. (in Chinese with English abstract). doi:10.12017/dzkx.2020.043

Bennett, B., Adams, J., Gray, N., Sherry, A., Oldenburg, T., Huang, H., P., et al. (2013). The controls on the composition of biodegraded oils in the deep subsurface - Part 3. The impact of microorganism distribution on petroleum geochemical gradients in biodegraded petroleum reservoirs. *Org. Geochem.* 56, 94–105. doi:10.1016/j.orggeochem.2012.12.011

Beydoun, Z. (1997). Prehistoric, ancient and mediaeval occurrences and uses of hydrocarbons in the greater Middle East region. *J. Pet. Geol.* 20, 91–95. doi:10.1111/j.1747-5457.1997.tb00757.x

Chen, R. Y., Luo, X. R., Chen, Z. K., Wang, Z. M., and Zhou, B. (2006). Estimation of denudation thickness of mesozoic stata in the Ordos Basin and its geological significance. *Acta Geol. Sin.* 05, 685–693. (in Chinese with English abstract).

Cui, J. W., Zhu, R. K., Li, S., Qi, Y. L., Shi, X. Z., and Mao, Z. G. (2019). Development patterns of source rocks in the depression lake basin and its influence on oil accumulation: Case study of the Chang 7 member of the triassic Yanchang Formation, Ordos Basin, China. *Nat. Gas. Geosci.* 4, 191–204. doi:10.1016/j.jnggs.2019.08.002

Cui, J. W., Zhang, Z. Y., Zhang, Y., Liu, G. L., and Qi, Y. L. (2022). Oil and gas accumulation periods and charging path of continental lake basin: A case study of the Chang 9-chang 10 oil reservoir in the Yanchang Formation in the Ordos Basin. *J. Pet. Sci. Eng.* 219, 111136–136. doi:10.1016/j.petrol.2022.111136

Curiale, J., and Bromley, B. (1996). Migration induced compositional changes in oils and condensates of A single field. *Org. Geochem.* 24, 1097–1113. doi:10.1016/S0146-6380(96)00099-X

England, W., Mackemzie, A., Mann, D., and Quigley, T. (1987). The movement and entrapment of petroleum fluids in the subsurface. *J. Geol. Soc.* 144, 327–347. doi:10.1144/gsjgs.144.2.0327

Fu, G., Fu, X. F., Xue, Y. C., and Yang, M. (2000). Analysis on geological factors causing the destroy and redistribution of oil and gas reservoirs. *Nat. Gas. Geosci.* 11, 1–7. (in Chinese with English abstract).

Gartrell, A., Zhang, Y., Lisk, M., and Dewhurst, D. (2004). Fault intersections as critical hydrocarbon leakage zones: Integrated field study and numerical modelling of an example from the timor sea, Australia. *Mar. Pet. Geol.* 21, 1165–1179. doi:10.1016/j.marpetgeo.2004.08.001

Huc, A. Y ., Nederlof, P., Debarre, R., Carpentier, B., Boussafir, M., Laggoun, F., et al. (2000). Pyrobitumen occurrence and formation in a cambro–ordovician sandstone reservoir, fahud salt basin, North Oman. *Chem. Geol.* 168, 99–112. doi:10.1016/S0009-2541(00)00190-X

Hui, X., Zhao, Y. D., Shao, X. Z., Zhang, W. X., Cheng, D. X., and Luo, A. X. (2019). The geological conditions, resource potential, and exploration direction of oil in Ordos Basin. *Mar. Orig. Pet. Geol.* 24, 14–22. (in Chinese with English abstract). doi:10.3969/j.issn.1672-9854.2019.02.002

Isiaka, A., Durrheim, R., Manzi, M., and Andreoli, M. (2017). 3D seismic analysis of the ak fault, orange basin, south Africa: Implications for hydrocarbon leakage and offshore neotectonics. *Tectonophysics* 721, 477–490. doi:10.1016/j.tecto.2017.10.011

Kissin, Y. (1987). Catagenesis and composition of petroleum: Origin of N-alkanes and isoalkanes inpetroleum crudes. *Geochim. Cosmochim. Ac.* 51, 2445–2457. doi:10.1016/0016-7037(87)90296-1

Lafargue, E., and Barker, C. (1988). Effect of water washing on crude oil composition. *AAPG Bull.* 73, 263–276. doi:10.1306/703C8C13-1707-11D7-8645000102C1865D

Littke, R., Brauckmann, F. J., Radke, M., and Schaefer, R. G. (1996). Solid bitumen in rotliegend gas reservoirs in northern Germany: Implications for their thermal and filling history. *Geol. Palaont. Teil.* 11, 1275–1292.

Liu, C. Y., Zhao, H. G., Gui, X. J., Yue, L. P., Zhao, J. F., and Wang, J. Q. (2006). Space—Time coordinate of the evolution and reformation and mineralization response in Ordos Basin. *Acta Geol. Sin.* 80, 617–638. (in Chinese with English abstract).

Liu, K., Eadington, P., Middleton, H., Fenton, S., and Cable, T. (2007). Applying quantitative fluorescence techniques to investigate petroleum charge history of sedimentary basins in Australia and Papuan New Guinea. *J. Pet. Sci. Eng.* 57, 139–151. doi:10.1016/j.petrol.2005.11.019

Liu, D., Xiao, X., Tian, H., Yang, C., Hu, A., and Song, Z. G. (2009). Identification of natural gas origin using the characteristics of bitumen and fluid inclusions. *Pet. explor. Dev.* 36, 375–382.

Liu, Z., Yao, X., Hu, X., D., and Wang, Q. (2013). Discovery of the mesozoic fault and its implication on the hydrocarbon accumulation in Ordos Basin. *J. Earth Sci. Environ.* 35, 56–66. (in Chinese with English abstract).

Liu, B., Bai, L., H., Chi, Y., A., Jia, R., Fu, X., F., and Yang, L. (2019). Geochemical characterization and quantitative evaluation of shale oil reservoir by two-dimensional nuclear magnetic resonance and quantitative grain fluorescence on extract: A case study from the qingshankou Formation in southern songliao basin, northeast China. *Mar. Pet. Geol.* 109, 561–573. doi:10.1016/j.marpetgeo.2019.06.046

Liu, K., and Eadington, P. (2005). Quantitative fluorescence techniques for detecting residual oils and reconstructing hydrocarbon charge history. *Org. Geochem.* 36, 1023–1036. doi:10.1016/j.orggeochem.2005.02.008

Losh, S., Cathles, L., and Meulbroek, P. (2002). Gas washing of oil along a regional transect, offshore Louisiana. *Org. Geochem.* 33, 655–663. doi:10.1016/S0146-6380(02)00025-6

Ma, X. J., Liang, J. W., Li, J. X., Jia, W. H., Tao, W. X., Liu, Y. L., et al. (2019). Meso-cenozoic tectonic uplift and evolution of central and western Ordos basin. *Northwest. Geol.* 52, 127–136. (in Chinese with English abstract). doi:10.19751/j.cnki.61-1149/p.2019.04.011

Meulbroek, P., Cathles, L., and Whelan, J. (1998). Phase fractionation at south eugene island block 330. *Org. Geochem.* 29, 223–239. doi:10.1016/S0146-6380(98)00180-6

Morales-Medina, G., and Guzman, A. (2012). Prediction of density and viscosity of Colombian crude oils from chromatographic data. *Ct&F - Cienc. Tecnol. Y Futuro* 4, 57–73.

Napitupulu, H., Ellis, L., and Mitterer, R. (2000). Post-generative alteration effects on petroleum in the onshore northwest java basin, Indonesia. *Org. Geochem.* 31, 295–315. doi:10.1016/S0146-6380(99)00154-0

Oldenburg, T., Jones, M., Huang, H., Bennett, B., Shafiee, N. S., Head, I. M., et al. (2017). The controls on the composition of biodegraded oils in the deep subsurface- Part 4. Destruction and production of high molecular weight non-hydrocarbon species and destruction of aromatic hydrocarbons during progressive in-reservoir biodegradation. *Org. Geochem.* 114, 57–80. doi:10.1016/j.orggeochem.2017.09.003

Palladino, G., Rizzo, R. E ., Zvirtes, G., Grippa, A., Philipp, R. P., Healy, D., et al. (2020). Multiple episodes of sand injection leading to accumulation and leakage of hydrocarbons along the san andreas/san gregorio fault system, California. *Mar. Pet. Geol.* 118, 104431. doi:10.1016/j.marpetgeo.2020.104431

Pang, H., Chen, J., Pang, X., Liu, K., and Xiang, C. (2012). Estimation of the hydrocarbon loss through major tectonic events in the tazhong area, tarim basin, west China. *Mar. Pet. Geol.* 38, 195–210. doi:10.1016/j.marpetgeo.2011.11.006

Pang, X., Jia, C., Pang, H., and Yang, H. (2018). Destruction of hydrocarbon reservoirs due to tectonic modifications: Conceptual models and quantitative evaluation on the tarim basin, China. *Mar. Pet. Geol.* 91, 401–421. doi:10.1016/j.marpetgeo.2018.01.028

Peters, K., Walters, C., and Moldowan, J. (2005). *The biomarker guide*. Editors K. E. Peters, C. C. Walters, and J. M. Moldowan (Cambridge, Uk: Cambridge University Press), 2, 490. Isbn 0521781582. The Biomarker Guide. doi:10.1017/CBO9780511524868

Qiu, X. W., Liu, C. Y., Mao, G. Z., Deng, Y., Wang, F. F., and Wang, J. Q. (2015). Major, Trace and platinum-group element geochemistry of the upper triassic nonmarine hot shales in the Ordos Basin, central China. *Appl. Geochem.* 53, 42–52. doi:10.1016/j.apgeochem.2014.11.028

Qu, H. J., Yang, B., Gao, S. L., Zhao, J. F., Han, X., Chen, S., et al. (2020). Controls on hydrocarbon accumulation by facies and fluid potential in large-scale lacustrine petroliferous basins in compressional settings: A case study of the mesozoic Ordos Basin, China. *Mar. Pet. Geol.* 122, 104668. doi:10.1016/j.marpetgeo.2020.104668

Ren, Z., Yu, Q., Cui, J. P., Qi, K., Chen, Z. J., Cao, Z. P., et al. (2017). Thermal history and its controls on oil and gas of the Ordos Basin. *Earth Sci. Front.* 24, 137–148. doi:10.13745/j.esf.2017.03.012

Said, S., Aboul-Fotouh, T., and Ashour, I. (2016). A current viscosity of different Egyptian crude oils: Measurements and modeling over A certain range of temperature and pressure. *J. Petroleum Environ. Biotechnol.* 7. doi:10.4172/2157-7463.1000305

Song, J., Chen, T., and Zhang, J. (2022). Permian and triassic hydrocarbon migration and accumulation in the cainan area, junggar basin, China. *J. Pet. Sci. Eng.* 210, 109965. doi:10.1016/j.petrol.2021.109965

Thompson, K. F. M. (1987). Fractionated aromatic petroleums and the generation of gas-condensates. *Org. Geochem.* 11, 573–590. doi:10.1016/0146-6380(87)90011-8

Wang, F. Y., Shi, Y. L., Zeng, H. S., and Liu, K. Y. (2006). To identify paleo-oil reservoir and to constrain petroleum charging model using the abundance of oil inclusions. *Bull. China Soc. Mineral. Pet. Geochem.* 25, 12–18.

Wang, G., Wang, T. G., Simoneit, B. R. T., and Zhang, L. (2013). Investigation of hydrocarbon biodegradation from A downhole profile in bohai bay basin: Implications for the origin of 25-norhopanes. *Org. Geochem.* 55, 72–84. doi:10.1016/j.orggeochem.2012.11.009

Wang, C., Zeng, J., Wang, F., Lin, X., Y., Liu, X., F., Wang, F., F., et al. (2017). Utility of GOI, QGF, and QGF-E for interpreting reservoir geohistory and oil remigration in the hudson Oilfield, tarim basin, northwest China. *Mar. Pet. Geol.* 86, 486–498. doi:10.1016/j.marpetgeo.2017.06.009

Wang, W. Y., Pang, X. Q., Chen, Z. X., Dongxia, C., Tianyu, Z., Luo, B., et al. (2019a). Quantitative prediction of oil and gas prospects of the sinian-lower paleozoic in the sichuan basin in central China. *Energy* 174, 861–872. doi:10.1016/j.energy.2019.03.018

Wang, A. G., Wang, Z. L., Li, L., Fan, C. Y., Zhang, K., Xiang, B. L., et al. (2019b). Hydrocarbon migration in the multiple-sourced petroleum system in the northwestern junggar basin (northwestern China): Constraint from geochemical and phase fractionation analysis. *AAPG Bull.* 103, 2247–2284. doi:10.1306/01211916512

Wei, B., Wei, H. H., Chen, Q. H., and Zhao, H. (2003). "Sediment provence analysis of Yanchang Formation in Ordos Basin," in *Journal of northwest university(natural science edition)*, 447–450. (in Chinese with English abstract).

Wu, Z. J., Han, X. Z., Lin, Z. X., Li, Z. N., Ji, H., Yin, D. F., et al. (2020). Tectonic, sedimentary, and climate evolution of meso-cenozoic basins in North China and its significance of coal accumulation and uranium mineralization. *Geotect. Metallogenia* 44, 710–724. (in Chinese with English abstract). doi:10.16539/j.ddgzyckx.2020.04.012

Wu, Z. Q. (2020). *Analysis on the relationship between faults and mesozoic and paleozoic oil and gas reservoirs in Ordos Basin*. M.S. thesis. Xi'an: Northwest University in Xi'an. (in Chinese with English abstract).

Xie, D. L., Yao, S. P., Cao, J., Hu, W. X., Wang, X. L., and Zhu, N. (2021). Diagenetic alteration and geochemical evolution during sandstones bleaching of deep red-bed induced by methane migration in petroliferous basins. *Mar. Pet. Geol.* 127, 104940. doi:10.1016/j.marpetgeo.2021.104940

Xu, Z. J., Liu, L. F., Wang, T. G., Wu, K. J., Dou, W. C., Song, X. P., et al. (2017). Characteristics and controlling factors of lacustrine tight oil reservoirs of the triassic Yanchang Formation Chang 7 in the Ordos Basin, China. *Mar. Pet. Geol.* 82, 265–296. doi:10.1016/j.marpetgeo.2017.02.012

Yang, P., Ren, Z., Zhou, R. J., Cui, J. P., Qi, K., Fu, J. H., et al. (2021). Tectonic evolution and controls on natural gas generation and accumulation in the ordovician system of the Ordos Basin, North China. *Energy Rep.* 7, 6887–6898. doi:10.1016/j.egyr.2021.10.066

Zerda, T., John, A., and Chmura, K. (1981). Raman studies of coals. *Fuel* 60, 375–378. doi:10.1016/0016-2361(81)90272-6

Zhang, L., Liu, C. Y., Zhang, S. H., Fayek, M., Lei, K. Y., and Quan, X. Y. (2022). Unconformity-controlled bleaching of jurassic-triassic sandstones in the Ordos Basin, China. *J. Pet. Sci. Eng.* 211, 110154. doi:10.1016/j.petrol.2022.110154

Zhou, J. G., Yao, G. S., Deng, H. Y., Xin, Y. G., Hu, H., Zheng, X. P., et al. (2008). Exploration potential of Chang 9 member, Yanchang Formation, Ordos Basin. *Pet. explor. Dev.* 35, 289–293. doi:10.1016/S1876-3804(08)60074-9

frontiers | Frontiers in Earth Science

TYPE Original Research
PUBLISHED 23 March 2023
DOI 10.3389/feart.2023.1028445

OPEN ACCESS

EDITED BY
Marco Meschis,
Instituto Nazionale di Geofisica e Vulcanologia (Sezione Palermo) - INGV, Italy

REVIEWED BY
Julius Jara-Muñoz,
University of Potsdam, Germany
Vasiliki Mouslopoulou,
National Observatory of Athens, Greece

*CORRESPONDENCE
Dee Ninis,
dee.ninis@src.com.au

SPECIALTY SECTION
This article was submitted to Structural Geology and Tectonics, a section of the journal Frontiers in Earth Science

RECEIVED 26 August 2022
ACCEPTED 24 February 2023
PUBLISHED 23 March 2023

CITATION
Ninis D, Howell A, Little T and Litchfield N (2023), Causes of permanent vertical deformation at subduction margins: Evidence from late Pleistocene marine terraces of the southern Hikurangi margin, Aotearoa New Zealand. *Front. Earth Sci.* 11:1028445. doi: 10.3389/feart.2023.1028445

Causes of permanent vertical deformation at subduction margins: Evidence from late Pleistocene marine terraces of the southern Hikurangi margin, Aotearoa New Zealand

Dee Ninis[1,2]*, Andy Howell[3,4], Timothy Little[1] and Nicola Litchfield[4]

[1]School of Geography, Environment and Earth Sciences, Victoria University of Wellington, Wellington, Aotearoa, New Zealand, [2]Seismology Research Centre, Richmond, VIC, Australia, [3]School of Earth and Environment, University of Canterbury, Christchurch, Aotearoa, New Zealand, [4]GNS Science, Lower Hutt, Aotearoa, New Zealand

Theoretical studies of the seismic cycle at convergent plate boundaries anticipate that most coseismic deformation is recovered, yet significant permanent vertical displacement of the overriding plate is observed at many subduction margins. To understand the mechanisms driving permanent vertical displacement, we investigate tectonic uplift across the southern Hikurangi subduction margin, Aotearoa New Zealand, in the last ~200 ka. Marine terraces preserved along the Wellington south coast have recently been dated as Marine Isotope Stage (MIS) 5a (~82 ka), 5c (~96 ka), 5e (~123 ka) and 7a (~196 ka) in age. We use these ages, together with new reconstructions of shoreline angle elevations, to calculate uplift rates across the margin and to examine the processes responsible for their elevation. The highest uplift rate—1.7 ± 0.1 mm/yr–and maximum tilting—2.9° to the west–are observed near Cape Palliser, the closest site to (~50 km from) the Hikurangi Trough. Uplift rates decrease monotonically westward along the Palliser Bay coast, to 0.2 ± 0.1 mm/yr at Wharekauhau (~70 km from the trough), defining a gently west-tilted subaerial forearc domain. Locally, active oblique-slip upper-plate faults cause obvious vertical offsets of the marine terraces in the axial ranges (>70 km from the trough). Uplift rates at Baring Head, on the upthrown side of the Wairarapa-Wharekauhau fault system, are ~0.7–1.6 mm/yr. At Tongue Point, uplift on the upthrown side of the Ōhāriu Fault is 0.6 ± 0.1 mm/yr. Dislocation and flexural-isostatic modelling shows that slip on faults within the overriding plate—specifically the Palliser-Kaiwhata Fault and the Wairarapa-Wharekauhau fault system—may dominate uplift in their immediate hanging walls. Depending on their slip rate and geometry, slip on these two upper-plate fault systems could plausibly cause >80% of late Pleistocene uplift everywhere along the south coast of North Island. Our modelling suggests that subduction of the buoyant Hikurangi Plateau contributes uplift of 0.1–0.2 mm/yr and uplift due to sediment underplating at Tongue Point and Wharekauhau is likely ≤0.6 mm/yr but could be significantly lower. Earthquakes on the subduction interface probably contribute ≤0.4 mm/yr of late Pleistocene uplift, with ≤10% of uplift due to each earthquake being stored permanently, similar to other subduction zones. These results indicate a significant contribution of slip on upper-plate faults to

permanent uplift and tilting across the subduction margin and suggest that in regions where upper-plate faults are prevalent, strong constraints on fault geometry and slip rate are necessary to disentangle contributions of deeper-seated processes to uplift.

KEYWORDS

subduction, active crustal fault, marine terrace, coastal uplift, Hikurangi margin, Wellington, Aotearoa New Zealand

1 Introduction

Marine terraces preserved along coastal regions can be used to infer rates and patterns of tectonic uplift across active margins. By combining shore platform (specifically shoreline angle) elevation data with the age of the corresponding terrace, uplift rates can be quantified (e.g., Bradley and Griggs, 1976; Ota et al., 1981; Muhs et al., 1990; Muhs et al., 1992; Zazo et al., 2003; Yildirim et al., 2013; Karymbalis et al., 2022). Accruing over tens to hundreds of thousands of years, patterns of uplift of the overriding plate have the potential to provide insight into local subduction margin processes (e.g., Merritts and Bull, 1989; Berryman, 1993a; 1993b; Wilson et al., 2007a; Wilson et al., 2007b; Matsu'ura, 2015; Meschis et al., 2022).

Beneath the east coast of the northern and central North Island of New Zealand, the Hikurangi subduction interface is weakly to moderately elastically coupled (e.g., Walcott, 1984; Reyners, 1998; Wallace et al., 2004; Wallace et al., 2012) (Figure 1). Previous marine terrace studies in this region have attributed the observed coastal uplift to some combination of rupture on upper-plate faults, subduction of an overthickened and buoyant Hikurangi Plateau with occasional seamounts, and sediment underplating (e.g., Berryman et al., 1989; Ota et al., 1991; Wilson et al., 2007a; Wilson et al., 2007b; Litchfield et al., 2007; Berryman et al., 2011; Mouslopoulou et al., 2016; Litchfield et al., 2022). In contrast to the northern and central North Island, the subduction interface beneath the southern North Island has been shown to be elastically almost fully coupled or "locked" (φ_{ic} = 0.8–1.0—e.g., Walcott, 1984; Reyners, 1998; Darby and Beavan, 2001; Wallace et al., 2004; Wallace et al. 2007; Wallace et al. 2012) (Figure 1). Investigations along the southeast coast of the North Island concluded that elevated Holocene marine terraces preserved there are the result of coseismic uplift from rupture on nearby offshore faults, such as the reverse Palliser-Kaiwhata Fault (Berryman et al., 2011; Litchfield and Clark, 2015) (Figure 2). Rupture of the subduction interface at the southern Hikurangi Margin, which dislocation models suggest could be M_w 8.0–8.5 or larger (Wallace et al., 2009; Stirling et al., 2012; Clark et al., 2019), has also contributed to uplift since the Holocene, with recent analyses of marine terraces indicating uplift from at least one subduction earthquake within the locked area (Litchfield et al., 2021). Whether or not other processes influence permanent vertical displacement across the southern Hikurangi Margin over longer periods, and their relative contributions, remains largely unknown.

This investigation is the first to present late Pleistocene coastal uplift rates along the Wellington south coast of the North Island of New Zealand using emergent shoreline angle elevations (rather than terrace tread elevations, which include the thickness of coverbed deposits) in a margin-wide and systematic way, and to evaluate the causes of vertical displacement along this southernmost part of the Hikurangi subduction margin. Our study area spans ~100 km of coastline between Tongue Point west of Wellington, and Ngawi near Cape Palliser to the east (Figure 2), where a series of late Pleistocene marine terrace remnants are today elevated to up to ~400 m above current day sea level (e.g., Ghani, 1974; Ghani, 1978; Ota et al., 1981; Begg and Johnston, 2000; Ninis et al., 2022). Seven marine terraces have previously been identified and recently dated; the youngest four of which have been shown to correspond to formation during Marine Isotope Stage (MIS) 5a (peak age 82 ka), 5c (96 ka), 5e (123 ka) and MIS 7a (196 ka) (Ninis et al., 2022) (Figure 2). In this paper, we apply recently published shore platform elevation data (Ninis et al., 2022) to reconstruct shoreline angle elevations for these terraces. Using available paleo-sea level data, we then correct these elevations for sea level at the time of their formation. We are thus able to provide robust uplift estimates for a margin-normal transect across the southern Hikurangi Margin since the late Pleistocene. Finally, we consider the distribution of uplift across this transect and compare this with results of coupled elastic dislocation and flexural-isostatic models. These models allow us to quantify the likely contribution to late Pleistocene uplift from slip on known upper-plate fault systems, and to constrain likely contributions to uplift from other processes such as the subduction of a buoyant Hikurangi Plateau, the earthquake cycle on the Hikurangu subduction interface, and sediment underplating.

2 Background

2.1 Tectonic uplift processes at subduction margins

Vertical displacement due to megathrust earthquakes such as the 2011 M_w 9.1 Tohoku-Oki earthquake, the 2004 M_w 9.3 Sumatra-Andaman earthquake, the 1964 M_w 9.4 in Alaska, and the 1960 M_w 9.5 Chile earthquake, generally results in coseismic uplift of the coast closest to the subduction trench (within ~150 km), and a similarly-oriented region of subsidence further from the trench (between ~150 and 250 km) (Figure 3A) (e.g., Grantz et al., 1964; Plafker, 1965; Plafker, 1972; Briggs et al., 2006; Subarya et al., 2006; Vigny et al., 2011), the precise distances being controlled by the geometry of the underlying subduction interface and the distribution of coseismic fault slip. Earthquake ruptures of upper-plate faults can also result in coastal uplift; as a result of the M_w 7.8 Hawke's Bay earthquake of 1931, the coast near Napier was uplifted by up to

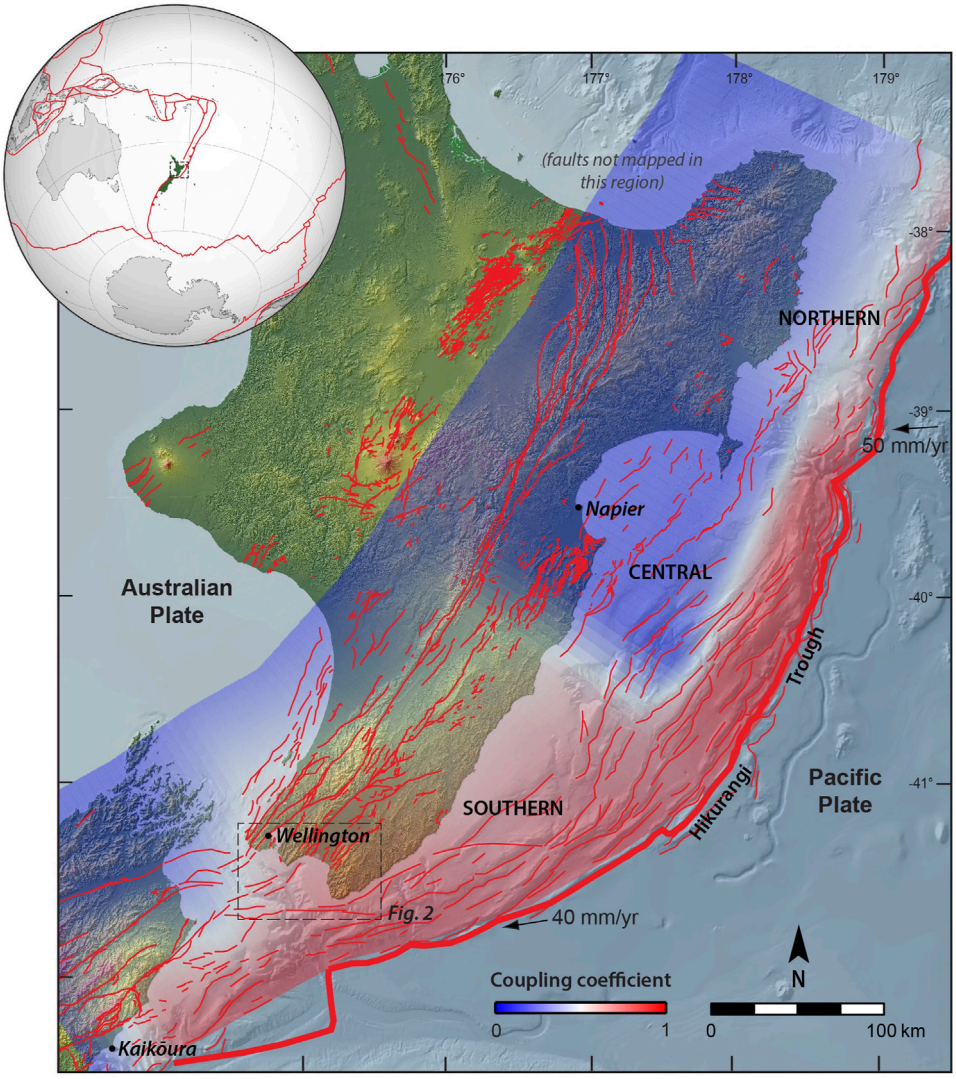

FIGURE 1
Tectonic setting of New Zealand showing plate boundary components and motion rates (DeMets et al., 1990; DeMets et al., 1994; DeMets et al., 2010), and Hikurangi subduction interface coupling of the North Island - regions in blue are weakly coupled (undergoing aseismic slow slip), regions in red are fully elastically coupled (locked) (from Wallace et al., 2012). Also shown are active crustal faults (red lines) (onshore faults from the New Zealand Community Fault Model (NZ CFM) - Seebeck et al., 2022; offshore active faults from Barnes and Audru, 1999; Barnes et al., 2002; Nodder et al., 2007; Mountjoy et al., 2009; Barnes et al., 2010; Pondard and Barnes, 2010; Mountjoy and Barnes, 2011; Barnes et al., 2019; Litchfield et al., 2022).

~2.7 m to a distance of ~20 km from a mostly blind source fault (Hull, 1990) (Figure 3C). The above coseismic displacements are indicative of global observations which propose that the wavelength of deformation can be used to infer whether uplift is the result of slip on the subduction interface or rupture of upper-plate faults; typically, broad-wavelength (100s of km wide) zones of uplift result from megathrust earthquakes, whereas short wavelength (up to ~20 km) are more likely sourced by a more steeply-dipping upper-plate fault. More complex earthquakes at convergent margins may involve rupture on both an upper-plate fault as well as along the subduction interface. A currently documented example is the 1855 M_w 8.2 Wairarapa earthquake, which resulted in uplift of the Wellington coast to the west of the Wairarapa Fault (e.g., Turakirae Head, Wellington Harbour and Porirua Harbour) across a distance of >30 km (Darby and Beanland, 1992; Beavan and Darby, 2005; Begg and McSaveney, 2005; Downes, 2005; McSaveney et al., 2006). Another example of simultaneous rupture of upper-plate faults and the subduction interface is the 2016 M_w7.8 Kaikōura earthquake (e.g., Hamling et al., 2017; Furlong and Herman, 2017; Wang et al., 2018; Mouslopoulou et al., 2019).

Vertical displacement can also be the result of ongoing aseismic movement. Following a megathrust earthquake, post-seismic relaxation followed by longer-term interseismic elastic strain accumulation generally results in vertical motion in the opposite sense to the coseismic displacement. For example, after the 1950 M_w 7.7 Nicoya Peninsula, Costa Rica earthquake, post-seismic relaxation removed the uplift which accompanied the earthquake; locals reported the shoreline dropping in elevation at the time of the earthquake, only to return to its former elevation 40 years later (Marshall and Anderson, 1995). Slow slip events

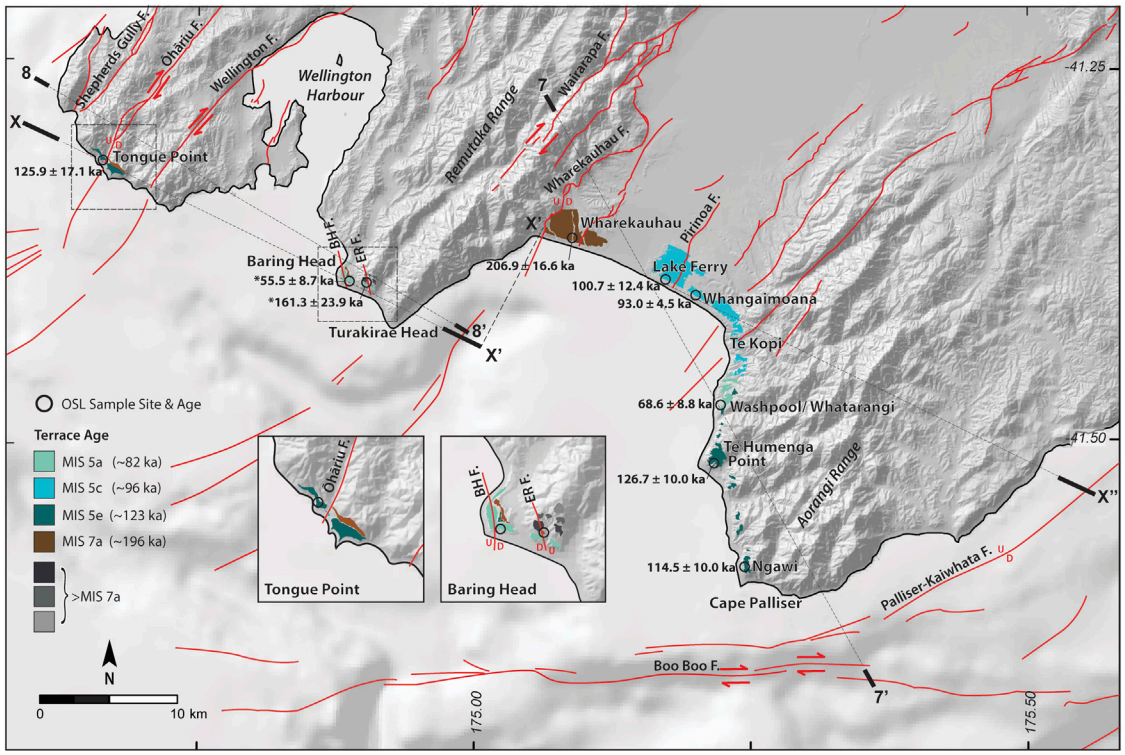

FIGURE 2
Late Pleistocene marine terrace MIS ages and distribution along the Wellington south coast, including OSL sample collection sites (black open circles) and corresponding ages (asterisks denotes minimum age)—only ages relevant to dating the shore platform are shown; MIS and OSL ages from Ninis et al. (2022). Also shown are active crustal faults (red lines) (onshore faults from the New Zealand Community Fault Model (NZ CFM) - Seebeck et al., 2022; offshore faults from Barnes et al., 2008) (BHF, Baring Head Fault; ERF, East River Fault). Location of profiles for Figure 7, Figure 8 and Profile X of Figure 6, Figure 9 are shown. Figure modified from Ninis et al., 2022.

(SSEs) can also contribute to vertical displacement, with uplift and subsidence expressed in a similar sense to subduction zone earthquakes. For example, offshore of the southwestern North Island, New Zealand, SSEs have resulted in uplift of up to ~2 cm onland (Wallace, 2020). Similarly, the SSE offshore of the northeastern South Island triggered by the 2016 M_w 7.8 Kaikōura earthquake produced coastal uplift at the southern end of North Island of up to ~2 cm (Wallace et al., 2018).

When vertical coseismic displacement is not completely removed by post-seismic relaxation and interseismic strain accumulation, megathrust earthquakes can leave a permanent signal of uplift in the landscape. In these instances, over many seismic cycles (1,000s of years) evidence of coseismic uplift as a result of multiple earthquakes can be preserved as a stepped pattern in the coastal topography. For example, each of the Holocene marine terraces preserved at Cape Mendocino, California, are thought to be a result of separate ruptures on the Cascadia megathrust (e.g., Merritts and Bull, 1989; Carver et al., 1994; Merritts, 1996; Murray et al., 1996), as are some of the emergent terraces along the coast of south-central Chile (e.g., Nelson and Manley, 1992; Bookhagen et al., 2006). Multiple ruptures on upper-plate faults could also be expressed as a stepped pattern in the coastal topography. For example, at Kaikōura Peninsula, on the east coast of the South Island, New Zealand, a suite of uplifted and tilted Pleistocene to Holocene-aged marine terraces have been inferred to be the result of repeated rupture on nearby faults (Ota et al., 1996; Gardner, 2011; Duffy, 2020; Howell and Clark, 2022; Nicol et al., 2022). This coastline was again uplifted by up to 6.5 m during the 2016 M_w 7.8 Kaikōura multi-fault rupture earthquake (Clark et al., 2017; Hamling et al., 2017).

Over 100,000s of years, characteristics of the subducting plate such as variations in crustal thickness, density and topography, or deep-seated processes such as sediment underplating, can also drive long-term uplift of the upper-plate (e.g., Merritts and Bull, 1989; Saillard et al., 2011) (Figure 3B). In summary, long-term net vertical displacement can be the result of a number of both seismic and aseismic processes combined; the challenge is to disentangle the different causes as expressed in the topography.

2.2 Tectonic setting

New Zealand straddles the Pacific-Australian plate boundary (Figure 1). Offshore of the northeast of the North Island, and to its southernmost extent at the northernmost South Island, the oceanic Pacific Plate subducts westward beneath the continental crust of the Australian Plate at the Hikurangi Trough; a process which began

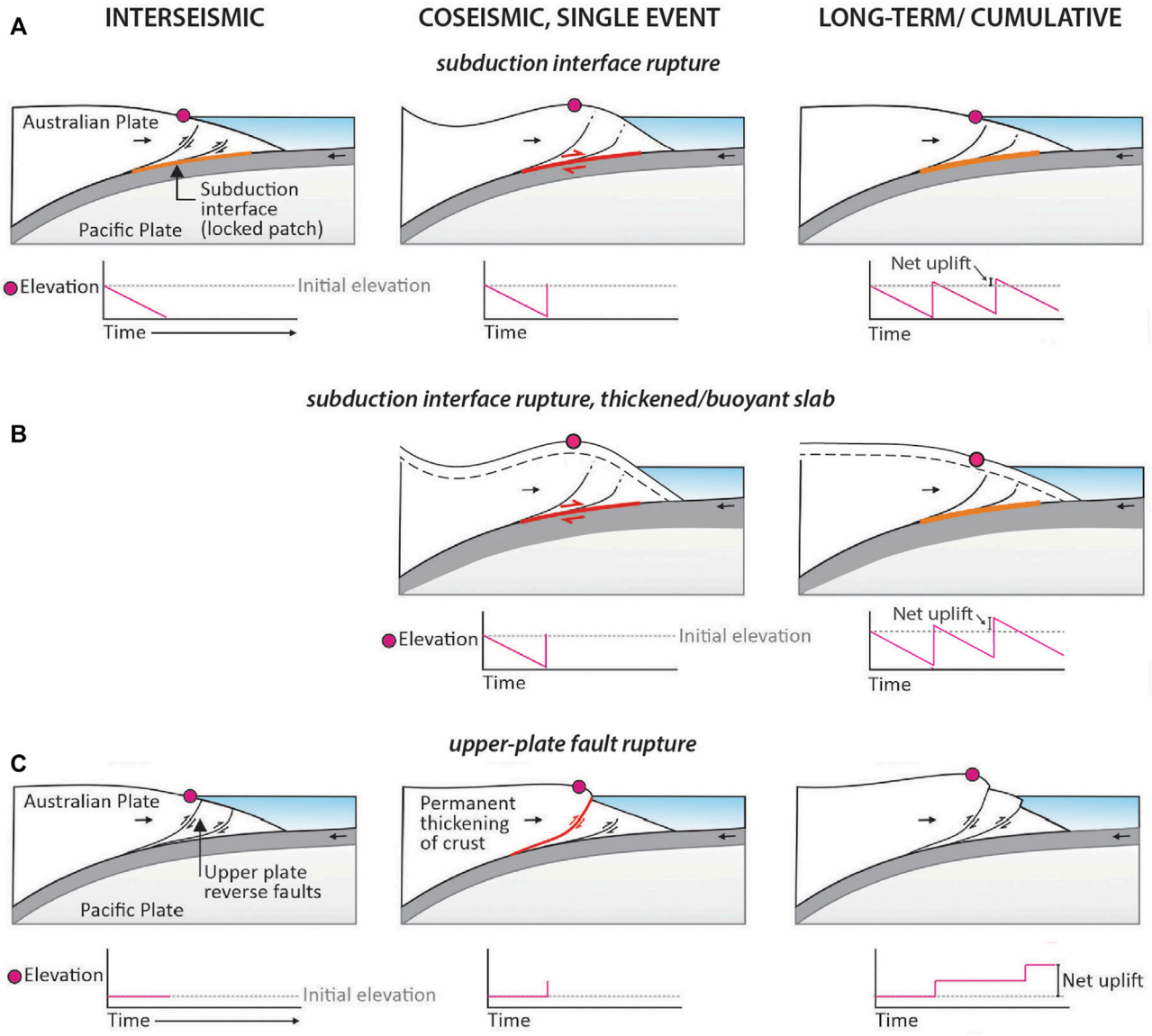

FIGURE 3
Possible causes of long-term vertical deformation at the Hikurangi Margin, and their likely expression: **(A)** subduction interface rupture; **(B)** subduction interface rupture involving a thickened buoyant Hikurangi Plateau (dashed line depicts vertical deformation without the down-going buoyant slab); **(C)** upper-plate fault rupture. Figure modified after Howell and Clark (2022).

~23 Ma ago (e.g., Kamp, 1999). During the past ~1–2 Ma, the subducting Pacific Plate has consisted of the Hikurangi Plateau, a thick and buoyant igneous province (e.g., Davy and Wood, 1994; Nicol et al., 2002; Reyners et al., 2006; Wallace et al., 2009). Convergence rates vary along the plate boundary (DeMets et al., 1990; Plafker, 1994; Wallace et al., 2007; Plafker, 2010) (Figure 1) and a subtle change in plate convergence direction and orientation of the plate boundary results in greater obliquity in plate convergence towards the south, such that in the South Island of New Zealand the two plates collide through oblique continental transpression (e.g., Van Dissen and Yeats, 1991).

The Hikurangi Trough is located ~50 km offshore of the east coast of the southern North Island (Figure 1). Onshore, long term contractional upper-plate deformation is expressed by folding and reverse faulting, with associated features including the uplifted Remutaka, Aorangi, and Tararua ranges trending northeast (Begg and Mazengarb, 1996; Begg and Johnston, 2000). The majority of margin-parallel motion (>50->70%) is taken up by slip on several predominately dextral strike-slip upper-plate faults in the exposed forearc; these include the Wairarapa, Wellington, Ōhāriu, and Shepherds Gully/Pukerua faults (Figure 2). The Wellington Fault (slip rate 5.5 ± 2.3 mm/yr–New Zealand Community Fault Model (NZ CFM), Seebeck et al. (2022)) has a near-vertical dip and exhibits minimal dip-slip motion where it crosses the coast, while the Wairarapa [slip rate 11 ± 3 mm/yr–Seebeck et al. (2022)] and Ōhāriu faults [slip rate 1.5 ± 0.5 mm/yr–Seebeck et al. (2022)] dip

steeply northwest and host a larger component of dip-slip motion. Many of these faults may be listric at depth (Henrys et al., 2013), and the Wairarapa Fault may connect at a relatively shallow depth (~5–10 km) with the nearby Wharekauhau Thrust Fault [slip rate 2.5 ± 1 mm/yr—Seebeck et al. (2022)] depending on their respective geometries. Most (~80%) of the margin-perpendicular motion is believed to be accommodated by slip on the subduction interface and connected imbricate thrusts in the offshore accretionary wedge (Darby and Beavan, 2001; Nicol and Beavan, 2003; Wallace et al., 2004; Nicol et al., 2007), the closest of which, at ~5 km from the coast, is the west-dipping, dextral reverse Palliser-Kaiwhata Fault (e.g., Barnes and Mercier de Lepinay, 1997; Barnes et al., 1998; Barnes and Audru, 1999; Mountjoy et al., 2009) (vertical slip rate 5.0 ± 2.0 mm/yr (Seebeck et al., 2022) (Figure 2).

Results from the 2009–2011 Seismic Array Hikurangi Experiment (SAHKE) (e.g., Henrys et al., 2013; Williams et al., 2013) show that across the southern Hikurangi Margin (41°S latitude), the subduction interface has a dip of <5° at shallow depths (within ~15 km of the surface) west of which there is a sudden increase in dip to >15° at greater depths. This kink in the interface occurs beneath the Tararua Ranges where a zone of sediment underplating may exist near the juncture between the Wairarapa Fault and the plate interface. Here, the seismogenic behaviour of the subduction interface changes, from weakly elastically coupled to strongly coupled (Walcott, 1984; Henrys et al., 2013). Historically (post-1840 AD), no significant ($>M_w$ 7.2) earthquakes have occurred on the southern Hikurangi subduction interface, however previous studies have revealed evidence of several pre-historic subduction earthquakes (e.g., Cochran et al., 2007; Clark et al., 2011; Clark et al., 2015; Clark et al. 2019; Litchfield et al., 2021; Pizer et al., 2021). Rupture of the currently strongly coupled subduction interface, in the form of a megathrust earthquake, was modelled by Clark et al. (2015) to determine the areas that are likely to experience coseismic uplift or subsidence. According to their elastic dislocation model, which assumes a megathrust recurrence interval of 500 years, the expected maximum coseismic uplift of the southern North Island would be ~1.0–1.5 m along the east coast ~50 km from the Hikurangi Trough, ~1 m between Cape Palliser and Te Kopi, <0.5 m at Wharekauhau, and negligible at Turakirae Head ~90 km from the trough; sites further to the west were estimated to experience subsidence.

Continuous Global Navigation Satellite System (GNSS) and Interferometric Synthetic Aperture Radar (InSAR) data from the last few decades from the lower North Island show that interseismic strain in this region, presumed to be the result of interseismic coupling on the subduction interface, is currently causing the area to subside (Beavan and Litchfield, 2012; Houlié and Stern, 2017; Hamling et al., 2022). The rates increase towards the Hikurangi Trough, from 0 mm/yr at Tongue Point, to 3 mm/yr at Turakirae Head, and 7 mm/yr in the area between Te Humenga Point and Cape Palliser (Hamling et al., 2022).

2.3 Previous work

The elevated late Pleistocene shore platforms of the Wellington south coast are discontinuously preserved between near Tongue Point, west of Wellington, and Ngawi near Cape Palliser to the east (Figure 2). These terraces are variably cut into Triassic-Cretaceous Torlesse Supergroup bedrock or Neogene to Pleistocene-aged sedimentary rocks that mantle the Torlesse bedrock (Begg and Johnston, 2000). The original shore platforms, including the former shorelines, are typically overlain by marine/beach deposits, and are now mostly obscured by younger terrestrial coverbeds (alluvium, loess, colluvium) ranging from a few metres to up to ~30 m in thickness (Ninis et al., 2022). The terraces are best preserved and most continuous within the Hikurangi Margin forearc, along the coast of Palliser Bay, where they decrease in altitude towards the west, indicating long wavelength, westward tectonic tilting across this region. Further from the Hikurangi Trough, the terraces are locally offset by a number of active crustal faults, most notably the Wairarapa and Ōhāriu faults (Ninis et al., 2022).

Previous investigations of the late Pleistocene marine terraces along the south coast of the North Island by Ghani (1974); Ghani (1978) and Ota et al. (1981) calculated local uplift using the terrace tread as the elevation datum (i.e., including the thickness of coverbed deposits). To calculate uplift for the terraces preserved along the Palliser Bay and southern Wairarapa coasts only (Figure 2), Ghani (1974); Ghani (1978) estimated that sea level during MIS 5e at 125 ka was exactly equal to that of the current day and, assuming a constant uplift rate, yielded rates of 1.5–2.0 mm/yr at Cape Palliser, decreasing to 0.5 mm/yr at Lake Ferry, and slightly increasing again to 1.0 mm/year at the westernmost site of his study, at Wharekauhau. For their study along the Wellington south coast west of the Wairarapa Fault only (Figure 2), Ota et al. (1981) had assumed that all of the "main" preserved terraces were created during the "main high sea level event of the last interglacial", which at the time was estimated to be 120 ka. In their uplift rate calculations, Ota et al. (1981) inferred that sea level during this time was the same as that of the current day, based on work by Chappell (1974); their uplift rate estimates ranged from ~0.6 mm/yr at Tongue Point to 0.9–1.0 mm/yr at Baring Head.

Subsidence of inferred Last Interglacial beach deposits has been documented on the north side of Wellington Harbour (Figure 2). Using drillhole core logs, Mildenhall (1995) and Begg and Mazengarb (1996) identified a marginal marine facies sequence on the downthrown side of the Wellington Fault, ~48–105 m below sea level. These deposits were not dated, but were correlated to MIS 5 (71–128 ka) in age. This subsidence has resulted from localised extension at a releasing bend (e.g., Begg and Johnston, 2000) on the otherwise predominately strike-slip Wellington Fault (e.g., Van Dissen et al., 1992; Little et al., 2010; Langridge et al., 2011; Ninis et al., 2013).

More recently, Ninis et al. (2022) undertook an investigation of the emergent marine terraces along the entire length of the Wellington south coast. Their study employed Optically Stimulated Luminescence (OSL) dating of shore platform coverbeds which provided the first numerical ages for the majority of these terraces, most of which were shown to be between MIS 5a (peak age 82 ka) and MIS 7a (196 ka) in age (Figure 2). They also employed differential Global Navigation Satellite System (GNSS) elevation measurements of exposures of

the wave-cut bedrock shore platform straths (i.e., excluding the variable thickness of coverbeds) allowing for their attitudes to be determined and for the terraces to be temporally correlated across the margin.

3 Methods

3.1 Terrace chronology

For each of the late Pleistocene marine terraces preserved along the Wellington south coast, we apply the formative ages provided by Ninis et al. (2022) (Figure 2) who made the assumption that shore platforms were cut during sea level highstands. They used OSL ages of marine (beach) deposits directly overlying the ancient shore platforms to determine the corresponding marine isotope stage (MIS), and then assigned them peak sea level ages as defined by Lisiecki and Raymo (2005). They also dated younger coverbed deposits, higher in the stratigraphic sequence (loess, colluvium), in order to provide assurance that the OSL ages defined a coherent "younging upwards" stratigraphic sequence. The terraces preserved at each site are listed by their corresponding MIS age in Table 1.

3.2 Shoreline angle elevation reconstructions

The elevation measurement required to calculate uplift of a shore platform is that of the ancient shoreline, which we refer to as the shoreline angle (Lajoie, 1986) (Figure 4). This feature coincides with the most landward extent of the shore platform–the back edge, at the base of the ancient sea cliff–and is assumed to have been cut at the maximum reach of sea-level at the time of formation (Jara-Muñoz et al., 2016). During our study, exposures of the shoreline angle in bedrock were not found, due to shore platform cover bed deposits at the back edge of the terrace (predominately loess and colluvium) obscuring them. For this reason, the position and corresponding elevation of the shoreline angle beneath the younger coverbeds had to be reconstructed.

We use the mean planar attitude (strike/dip/dip direction) of the shore platform at each site, as calculated by Ninis et al. (2022). These

TABLE 1 Wellington south coast late Pleistocene marine terraces ages, shoreline angle elevations, absolute tectonic uplift and corresponding uplift rates. Marine terrace MIS ages are from Ninis et al. (2022) and peak ages are from Lisiecki and Raymo (2005).

Location	Marine terrace age (MIS)	Marine terrace age (MIS peak) (ka)	Elevation (m)		Absolute tectonic uplift (m)	Uplift rate (mm/yr)
			Shoreline angle	Shore platform		
Tongue Point	**5a**	82 ± 4		16.0 ± 3.0 (U)	26.0 ± 9.0	***0.3 ± 0.1 (U)***
				7.0 ± 3.0 (D)	17.0 ± 9.0	***0.2 ± 0.1 (D)***
	5c	96 ± 4		16.0 ± 3.0 (U)	27.0 ± 10.0	***0.3 ± 0.1 (U)***
				7.0 ± 3.0 (D)	18.0 ± 10.0	***0.2 ± 0.1 (D)***
	5e	123 ± 4		75.0 ± 3.0 (U)	67.8 ± 4.8	***0.6 ± 0.1 (U)***
				27.0 ± 3.0 (D)	19.8 ± 4.8	***0.2 ± 0.1 (D)***
	7a	196 ± 4		82.7 ± 3.0 (D)	94.7 ± 6.0	***0.5 ± 0.1 (D)***
Baring Head	**5a**	82 ± 4		120.5 ± 3.0	130.5 ± 9.0	***1.6 ± 0.2***
	5a	82 ± 4	89.8 ± 4.7		99.8 ± 10.7	**1.2 ± 0.2**
"	**5e**	123 ± 4		95.8 ± 3.0	88.6 ± 4.8	***0.7 ± 0.1***
"	**7a**	196 ± 4		173.6 ± 3.0	185.6 ± 6.0	***1.0 ± 0.1***
Wharekauhau	**7a**	196 ± 4	17.9 ± 3.0		29.9 ± 6.0	**0.2 ± 0.1**
Lake Ferry	**5c**	96 ± 4	61.1 ± 0.1		72.1 ± 7.1	**0.8 ± 0.1**
Te Kopi	**5c**	96 ± 4	94.9 ± 0.4		105.9 ± 7.4	**1.1 ± 0.1**
Washpool	**5a**	82 ± 4	92.1 ± 0.7		102.1 ± 6.7	**1.3 ± 0.2**
	5e (5c)	123 ± 4 (96 ± 4)		114.0 ± 3.0	106.8 ± 4.8	***0.9 ± 0.1***
					125.0 ± 10.0	***1.3 ± 0.2***
Te Humenga	**5e**	123 ± 4	195.9 ± 2.0		188.7 ± 3.8	**1.5 ± 0.1**
Ngawi	**5e**	123 ± 4	213.6 ± 8.3		206.4 ± 10.1	**1.7 ± 0.1**

Where shown in *Italics*, uplift rate has been calculated from a shore platform exposure, and so is a minimum value for that location. MIS 5a: Sea level −4 to −16 m (Creveling et al., 2017); MIS 5c: Sea level −4 to −18 m (Creveling et al., 2017); MIS 5e: Sea level +5.5 to +9 m (Dutton and Lambeck, 2012); MIS 7a: Sea level −9 to −15 m (Bard et al., 2002; Siddall et al., 2007; Grant et al., 2012; 2014).(U) and (D) denote the upthrown and downthrown sides of the Ōhāriu Fault, respectively.

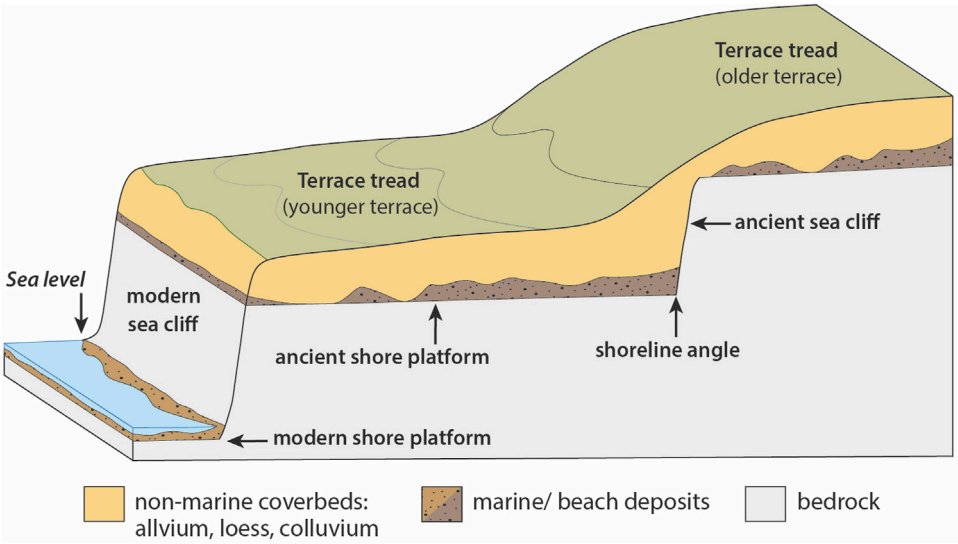

FIGURE 4
Schematic diagram showing typical geomorphic and geological features of marine terraces. Figure modified after Pillans (1990). Thickness of marine deposits and non-marine coverbeds (e.g., loess, colluvium) are illustrative only - they do not represent true thickness.

were determined from GNSS Real-Time Kinematic (RTK) surveyed elevations of the shore platform wherever it was exposed, mainly in the coastal cliffs at the current-day front edge of the terrace, but also in drainage channels which cut through the terraces, as well as in man-made track cuttings. Ninis et al. (2022) describe the precision of the instrumentation and surveying technique used to collect these elevation points as within the natural variation of relief of the shore platform, which they estimated to be ±3 m. The shore platform data points (latitude, longitude, elevation), were then used to calculate a plane of best fit. The accuracy of their fitted plane was governed by the number of elevation points used, the effects of any outliers within the elevation dataset (for instance, measuring local lows due to channels, or highs due to stacks on the shore platform) and the spatial distribution of the data points. Each plane was associated with a corresponding residual of the fit - the smaller the residual, the better the fit.

In this study, we reconstruct the position and elevation of the shoreline angle using a series of profiles (e.g., Figure 5) parallel to the calculated dip of the shore platform. Because the paleo-shoreline is located at the intersection of the shore platform and the ancient sea cliff behind it, for each profile the shore platform surface was projected (with the appropriate dip angle) from a surveyed exposure site towards the sea cliff at the rear of the terrace. Since the ancient sea cliff has been modified by subsequent erosion and deposition, its original slope was estimated for each profile using the mid-point of the local modern-day sea cliff as an analogue for that site, with the assumption that the mid-point is least modified by erosion (which is most likely to be experienced at the top of the sea cliff) and least obscured by colluvial deposition (likely to occur at the bottom of the sea cliff). On each profile, the intersection of these two lines–representing the shore platform and ancient sea cliff–provided the elevation of the shoreline angle for that site. The uncertainty value of each calculated shoreline angle elevation is dependent on how well the calculated shore platform "fit" the surveyed elevation data at that site; we have used the residual of the plane fit (the average distance of each surveyed elevation point to the corresponding calculated shore platform) to define this uncertainty. Strandline elevations and associated uncertainties are listed in Table 1, and the full set of shoreline angle reconstruction profiles are provided in the Supplementary Material accompanying this manuscript.

3.3 Determining absolute tectonic uplift

The formation of the sequence of preserved late Pleistocene shore platforms on the Wellington south coast spans several highstands, between which sea level has varied. As a result, shoreline angle elevations measured above current-day mean sea level may be more or less than the absolute value of tectonic uplift, depending on whether sea level was lower or higher, respectively, at the time of their formation. Absolute tectonic uplift of a shore platform is calculated by the difference between the present-day shoreline angle elevation and paleo-sea level at the time that it was formed.

Some eustatic sea level reconstructions are based on radiometric dating and elevation measurements of paleo-sea level indicators–sediments or landforms whose position relative to sea level at the time of their formation is known (e.g., Huon Peninsula in Papua New Guinea - Chappell et al., 1996; Stirling et al., 1998; Chappell, 2002; Potter et al., 2004; Thompson and Goldstein, 2005; O'Leary et al., 2008; Thompson et al., 2011). Others are based on the ratio of oxygen-18 (^{18}O) and oxygen-16 (^{16}O) in fossil calcite contained within benthic and planktonic foraminifera of marine sediments, which is a function of the total global ice volume and deep ocean temperature (e.g., Red Sea - Rohling et al., 2008; Grant et al., 2012; Grant et al., 2014). Results of method-specific and site-specific sea level studies can depart significantly from the global

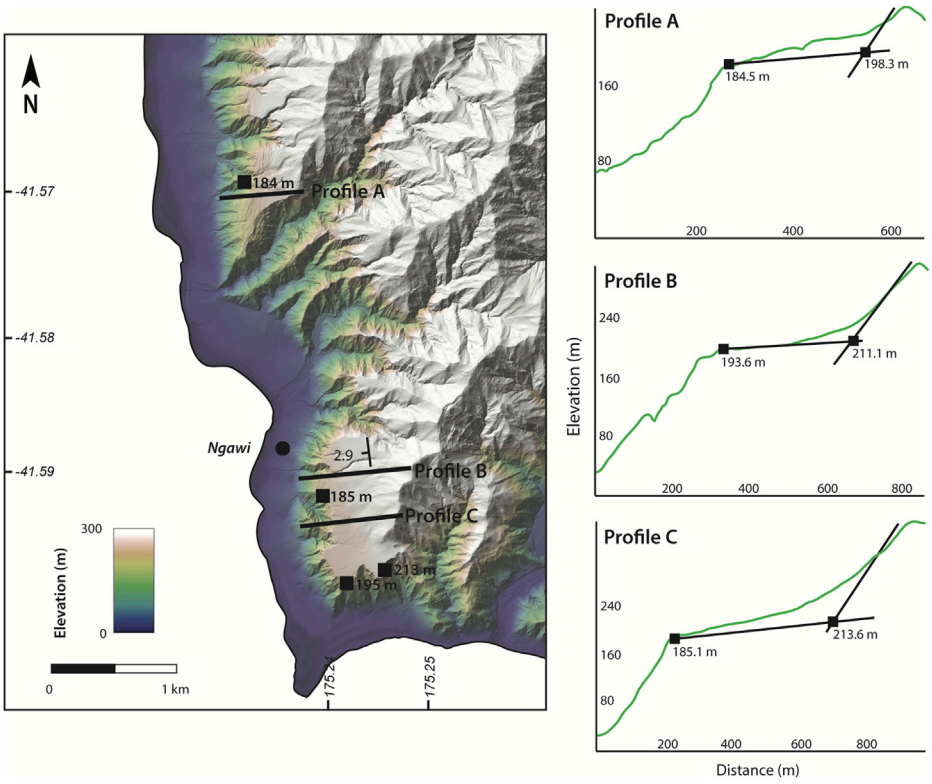

FIGURE 5
Late Pleistocene marine terraces at Ngawi, near Cape Palliser, showing shoreline angle elevation profiles reconstructions - Profiles **(A–C)** - on a 1 m lidar shaded hillslope model (courtesy GWRC/https://data.linz.govt.nz/layer/53621-wellington-lidar-1m-dem-2013-2014/).

mean; the latter is particularly true for sites where sea level is strongly influenced by glacio-hydro-isostatic effects (e.g., Lambeck and Nakada, 1992). As a result, studies using different methods and/or from different sites often result in varying paleo-sea level estimates. Although eustatic sea level reconstructions are available for New Zealand for the Holocene (e.g., Gibb, 1986; Clement et al., 2016), reliable estimates are not available for the MIS highstands relevant to this investigation - MIS 5a (peak age 82 ka), 5c (96 ka), 5e (123 ka) and 7a (196 ka). As such, for this study, we use eustatic sea level estimates determined from the "pooling" of high-quality data derived from a number of global sites, which have been corrected for isostatic contributions and probabilistically analysed.

A study of sea level that encompasses the penultimate interglacial, MIS 7, by Bard et al. (2002), measured the depth of, and radiometrically dated the calcite within, drowned speleothems in Italy. They compared their results to the depth and age of speleothems in the Bahamas (Li et al., 1989) to constrain sea level during MIS 7a to between −18 m and −9 m. This data was included in a review of all previously published data by Siddall et al. (2007) who constrained sea level for MIS 7a to between −5 and −15 m. In this study, we apply the overlapping values of the estimates of Bard et al. (2002) and Siddall et al. (2007) to obtain 9–15 m below present.

All recent studies for MIS 5e agree that sea level was higher than at present, with some studies suggesting that it was higher even than the previous long-standing estimates of +2–6 m (e.g., Neumann and Hearty, 1996; Stirling et al., 1998; McCulloch and Esat, 2000). Using a compilation of previously published sea level data from >40 different sites around the world, Kopp et al. (2009) undertook a probabilistic assessment of sea level during MIS 5e; their results showed a 95% probability that it had exceeded +6.6 m. In a review of global data which also takes into consideration glacio-hydro-isostatic effects, Dutton and Lambeck (2012) estimate sea level during MIS 5e at +5.5–9 m, which we apply in this study.

Estimates of peak sea level for MIS 5a and 5c vary widely depending on the study site, due to stronger glacio-hydro-isostatic effects resulting from the load of the Northern Hemisphere ice sheets (Lambeck, 2004; Potter and Lambeck, 2004; Thompson and Goldstein, 2005; Dumas et al., 2006). To reduce uncertainty in the variable sea level estimates for MIS 5a and 5c, Creveling et al. (2017) considered regional sea level estimates determined from geomorphic paleo-sea level indicators from 38 sites across the world. The data were included in a sensitivity analysis incorporating glacial isostatic adjustment simulations to constrain peak global sea level bounds for MIS 5a to ~4–16 m below present, and for MIS 5c to ~4–18 m below present, which we assume in our calculations.

Although applying these eustatic sea level estimates to the lower North Island means that any local glacio-hydro-isostatic effects are not taken into consideration, it is likely that such effects to

New Zealand were small due to the relative isolation of New Zealand from the ice sheets; <1 m during the Holocene (Clement et al., 2016) and as far back as MIS 5c (Creveling et al., 2017).

3.4 Uplift rate calculations

To calculate the tectonic uplift rate, we apply the equation:

Uplift Rate (mm/yr) = Absolute Tectonic Uplift (m)/MIS Peak Age (ka)

The uncertainties in the uplift rate calculations incorporate those described in Ninis et al. (2022), namely: 1) the geologically-observed variability of each surveyed elevation point of ±3 m (1σ) which was included in the shore platform best-fit plane calculations; 2) the residual value of each calculated shore platform plane, representing the average distance (m) each surveyed shore platform elevation point deviated from the calculated best-fit plane, which was assigned as the uncertainty to the calculated shoreline angle elevation of that shore platform; these ranged from 0.1 to 8.3 m (Table 1). In addition, we consider 3) the full range of sea level estimated for each MIS under consideration and 4) ± 4 ka to each corresponding peak sea level age, as defined by Lisiecki and Raymo (2005).

Although uplift is most accurately determined from shoreline angle elevations, in some instances, where a shoreline angle elevation could not be reconstructed, we have used surveyed elevation measurements from shore platform exposures as close to the rear of the terrace as possible (i.e., nearest to the shoreline angle) to estimate a minimum uplift rate for that site.

3.5 Modelling of geodynamic contributions to uplift

We combine elastic dislocation models with simple isostatic calculations to assess contributions to uplift across the southern Hikurangi Margin since the late Pleistocene from four subduction-related processes: 1) slip on upper-plate faults; 2) subduction of the buoyant Hikurangi Plateau beneath the North Island; 3) permanent strain in the upper-plate associated with the earthquake cycle on the Hikurangi subduction interface; and 4) crustal thickening due to underplating of subducted sediment. The possible combined contributions of these processes to uplift rates were explored by Litchfield et al. (2007) using thermomechanical finite element models. We here build on that work by considering each process separately, with the aim of establishing upper bounds on the contribution to observed uplift from each process, rather than estimating combined uplift rates due to multiple processes together. We introduce our modelling of faulting within the upper-plate here, and include the simple calculations underpinning our estimates of uplift rates associated with the other processes in the Discussion (Section 5.2).

3.5.1 Elastic dislocation models

Slip on reverse faults within the overriding Australian Plate thickens the crust and would therefore be expected to contribute to permanent uplift (Figure 3C). The aim of this analysis is to identify approximate end member models, representing the likely minimum and maximum contributions of slip on upper-plate faults to uplift since the late Pleistocene. We model deformation using the elastic dislocation method of Okada (1985). Strictly, our use of this method models terrace uplift as the elastic response of a homogeneous solid to hundreds of metres of slip on a fault, as many previous studies have done (e.g., Anderson and Menking, 1994; Jara-Muñoz et al., 2019; Jara-Muñoz et al., 2022; Nicol et al., 2022). Since surface displacement scales linearly with fault slip in this formulation, the calculated uplift response is equivalent to the cumulative sum of the metre-scale individual elastic response to each earthquake. Although this form of elastic support is not a plausible mechanism to explain permanent uplift, the distribution of modelled uplift is closely related to the distribution of rates of crustal thickening through fault slip, which does lead to permanent uplift.

The overall pattern of westward tilting and corresponding decreasing uplift of the marine terraces closest to the Hikurangi Trough, between Cape Palliser and Wharekauhau, suggests that the structures responsible for this uplift are likely to be offshore of the east coast. This uplift pattern is abruptly interrupted across the Wairarapa Fault, west of which the marine terraces are preserved less continuously and are obviously vertically displaced by upper-plate faults (Ninis et al., 2022) (Figure 2). Based on these observations, we consider two separate sets of elastic dislocation models to represent permanent uplift that might be contributed to by repeated slip on 1) the Palliser-Kaiwhata Fault–the main active fault offshore of the east coast, which has previously been shown to be responsible for uplifted Holocene marine terraces on the southeast coast of the North Island (Berryman et al., 2011; Litchfield and Clark, 2015), and 2) the Wairarapa-Wharekauhau fault system, respectively. At Wharekauhau we also consider the possible opposing contributions associated with the site being located on the downthrown site of the Wairarapa Fault. Although there are several other faults in the hanging walls of both these fault systems, their dip-slip rates are an order of magnitude smaller; they can therefore be neglected in our modelling, which seeks to explain the large-scale features of Late Pleistocene marine terrace uplift. We choose not to model slip on the Wellington Fault, because there are no late Pleistocene marine terraces preserved nearby to where the fault crosses the coast, from which to quantify vertical displacement. Moreover Van Dissen et al. (1992) have shown little dip-slip motion across the fault near where it crosses the Wellington south coast, even though some vertical displacement has been observed across the fault further north, away from our modelled profile.

Although the upper-plate faults we consider are dextral-reverse, the strike-slip component causes negligible crustal thickening and would not lead to uplift on the timescale of multiple seismic cycles. Consequently, we only model deformation associated with the dip-slip component of these faults (i.e., we assume pure reverse slip). We experiment with a variety of fault geometries–both planar and listric–and slip rates, using a trial-and-error approach to match absolute uplift, within the constraints of the available data and informed by previous interpretations (e.g., Berryman et al., 2011; Henrys et al., 2013; Litchfield and Clark, 2015; Seebeck et al., 2022). The fault geometry is represented by one or more rectangular patches, and we assume uniform slip and Lamé parameters μ and ν of 3×10^{10} Pa and 0.25 respectively. We extend our modelled fault 100 km along strike from the marine terrace

transect, in effect producing a 1D profile transect rather than a 2D map of modelled displacements. This approach is reasonable because the sites where we calculate uplift rates lie close to a line sub-perpendicular to the strike of faults of interest; it also allows us to model the possible influences of flexure and isostasy on terrace elevations, which we describe next.

3.5.2 Flexural modelling

One limitation of our dislocation modelling is that it does not consider a key prerequisite of permanent uplift: support of the uplifted topographic load through some combination of flexure and isostatic compensation. Both these mechanisms require that not all crustal thickening is translated to an equivalent amount of permanent uplift; they are often neglected in slip rate studies involving marine terraces (e.g., Jara-Munoz et al., 2022; Nicol et al., 2022), but we model them to avoid underestimating slip rates for our end-member models.

We model flexural isostatic responses to topographic loading by fault slip using gFlex (Wickert, 2016). We assume that the crust of the overriding Australian Plate is much weaker than that of the Pacific Plate (Watts et al., 2013), so that any flexural support is dominated by the subducting plate. We use 500 km-wide 1D flexural profiles, and assume a Young's modulus (E) of 2×10^{11} Nm^{-2}, a Poisson's ratio of 0.25 and a mantle density ρ_m of 3,300 kg m^{-3} (Cohen and Darby, 2003; Evanzia et al., 2019). We impose a "no slope, no shear" boundary condition (Wickert, 2016) at each end of our modelled profile, where the modelled plate is clamped but free to translate up and down. However, for this scenario, the choice of boundary condition makes a negligible (<1%) difference to the model results. The main controls on the magnitude of the flexural-isostatic response to our imposed topographic load are elastic thickness, T_e, and crustal density ρ_c. Since one purpose of this study is to determine how much of the observed uplift can reasonably be attributed to slip on upper-plate faults, we run three suites of models to demonstrate the effect on our results of a conservative value for T_e. For our preferred suite of models, we assume a T_e of 40 km. This value is close to the lower bound of previous estimates of elastic thickness for the Pacific Plate under southern North Island (Cohen and Darby, 2003); although this value is higher than some others, it is consistent with suggestions that oceanic lithosphere is stronger over 100-kyr timescales than the million-year timescales over which T_e is usually estimated (Watts et al., 2013). To account for uncertainty in this T_e estimate, we also run alternative, more conservative models using a T_e of 15 km, which is at the lower end of the range of observed estimates for oceanic lithosphere worldwide (Watts et al., 2013). Finally, to demonstrate the effect of assuming a very thick T_e, we run some models assuming T_e is 100 km, minimising flexural-isostatic effects in the model. For ρ_c, we assume a density of 2,600 kg m^{-3} when calculating the weight of our modelled topographic load. This density is slightly lower than the average density of the wet greywacke that likely comprises much of the uplifted material (2,650 kg m^{-3}—Brideau et al., 2022), but remains an appropriate conservative value to use because: 1) much of the uplifted material probably has a lower density than greywacke (e.g., unconsolidated fan material); 2) we do not account for erosion and removal of some of the uplifted rock; and 3) some of the uplifted terrace material was previously underwater and therefore subject to an extra load which was removed through uplift above sea level. These conservative assumptions maximise the deflection associated with a given uplift distribution, thereby maximizing the amount of fault slip required to match observed terrace uplift.

3.5.3 Fit to observed uplift

The models presented are intended to be indicative and are based on several simplifying assumptions described above, so a perfect fit to the observed uplift rates should not be expected. Despite their simplicity, we assess the root mean square misfit of our models to available data.

For our models of slip on the Palliser-Kaiwhata Fault, we assess their fit to observations by calculating the RMS misfit between modelled and observed uplift at five sites: east of Lake Ferry, at Te Kopi, Washpool/Whatarangi, Te Humenga Point and Ngawi (Figure 2). We also model uplift at Wharekauhau, but exclude the site from our RMS misfit calculation because it lies in the immediate footwall of the Wharekauhau Thrust Fault. Footwall subsidence due to slip on that fault may influence the elevation of the terraces at Wharekauhau. Moreover, Ninis et al. (2022) highlight a likely complex history of both subsidence and uplift at this site, which is contributed to by movement on other nearby faults in addition to the Wairarapa-Wharekauhau fault system. We therefore do not use observed uplift at this site to constrain slip on the Palliser-Kaiwhata Fault.

For the Wairarapa-Wharekauhau fault system, it is harder to use terrace elevations to constrain fault slip rates as there are far fewer sites with preserved late Pleistocene marine terraces (Ninis et al., 2022); they are restricted to two broad areas: at Tongue Point, and the area around Baring Head. Marine terrace elevations at these sites are influenced by slip on the Ōhāriu Fault, and the Baring Head and East River faults, respectively, so it would be challenging to use terrace uplift to constrain the slip rate on the deeper Wairarapa-Wharekauhau fault system. Instead, our models test whether slip on the Wairarapa-Wharekauhau fault system could plausibly be responsible for uplift at Tongue Point, where in addition to the terraces being offset by the Ōhāriu Fault, the site is overall uplifted. For this test, we attempt to match the uplift rate of the MIS 5e marine terrace averaged across the fault (Ninis et al., 2022).

In order to observe temporal variations in uplift rates, it would be required that shore platforms from each of MIS 5a, 5c, 5e and 7a be preserved at every site across the Wellington south coast–this is not the case. As we are constrained by the available preservation of marine terraces, and that, the terraces at the sites used to constrain our models are of different ages (MIS 5a, 5c and 5e), in this investigation it is necessary to assume that uplift rates have been constant across the southern Hikurangi Margin since the late Pleistocene. This assumption is widespread in studies that aim to constrain uplift rates by matching terrace elevations to sea-level curves (e.g., Pedoja et al., 2006; Authemayou et al., 2017; Jara-Munoz et al., 2017; De Gelder et al., 2020), but has been challenged by Mouslopoulou et al. (2016) and McKenzie et al. (2022). We prefer the assumption of constant uplift rates to alternative approaches—such as attempting to fit uplift of an inferred MIS 5e terrace in places where there are no direct dating constraints—for two reasons. First, Mouslopoulou et al. (2016) suggest that fluctuations in uplift rate over the time period of interest (~80–120 ka) are relatively small (a factor of 1–2 compared with

TABLE 2 Elastic dislocation model scenarios for our model of the Palliser-Kaiwhata Fault.

Model ID	Model geometry	Dip slip rate (mm/yr)	Oblique slip rate (mm/yr)	T_e (km)	Regional uplift rate (mm/yr)	Wharekauhau TF slip rate (mm/yr)	RMS misfit (m)	Deflection						Figure
								Mean (m)	Mean (%)	Min (m)	Min (%)	Max (m)	Max (%)	
1	PK listric	5.3	7.5	40	0	0	21.93	38.4	57.4	26.7	19.5	61.5	205.6	Figure 7
2	PK listric	5.7	8.1	40	0	2.5	24.54	40.6	60.7	28.2	20.6	65	217.3	Supplementary Figure SC1
3	PK listric	6.9	9.8	15	0	0	30.79	101.7	148.2	72.8	53	154.3	515.9	Supplementary Figure SC2
4	PK listric	7.3	10.3	15	0	2.5	36.19	105.8	154.3	75.6	55	160.9	538	Supplementary Figure SC3
5	PK listric	4.6	6.5	40	0.2	0	20.56	33.3	49.8	23.2	16.9	53.4	178.4	Supplementary Figure SC4
6	PK listric	5	7.1	40	0.1	0	21.03	36.2	54.2	25.2	18.4	58	193.9	Supplementary Figure SC5
7	PK listric	3.8	5.4	40	0.4	0	21.31	27.5	41.2	19.2	14	44.1	147.4	Supplementary Figure SC6
8	PK listric	4.2	5.9	40	0.4	2.5	19.28	29.7	44.4	20.7	15	47.6	159.1	Supplementary Figure SC7
9	PK listric	5.3	7.5	40	0.1	2.5	22.59	37.7	56.3	26.2	19.1	60.3	201.8	Supplementary Figure SC8
10	PK listric	4.9	6.9	40	0.2	2.5	21.02	34.8	52	24.2	17.6	55.7	186.2	Supplementary Figure SC9
11	PK listric	4.8	6.8	100	0	2.5	20.61	7.1	10.6	4.9	3.6	11.4	38.1	Supplementary Figure SC10
12	PK listric	4.5	6.4	100	0	0	20.44	6.8	10.2	4.7	3.5	10.9	36.5	Supplementary Figure SC11
13	PK listric	4.2	5.9	100	0.2	2.5	19.21	6.2	9.3	4.3	3.1	9.9	33.2	Supplementary Figure SC12
14	PK listric	3.9	5.5	100	0.2	0	21.09	5.9	8.8	4.1	3	9.5	31.6	Supplementary Figure SC13
15	PK listric	6	8.5	15	0.2	0	25.24	88.5	128.9	63.3	46.1	134.1	448.6	Supplementary Figure SC14
16	PK listric	6.4	9.1	15	0.2	2.5	29.35	92.5	135	66.1	48.1	140.7	470.7	Supplementary Figure SC15
17	PK listric	5	7.1	40	0.1	0	21.03	36.2	54.2	25.2	18.4	58	193.9	

(Continued on following page)

10.3389/feart.2023.1028445

TABLE 2 (*Continued*) Elastic dislocation model scenarios for our model of the Palliser-Kaiwhata Fault.

Model ID	Model geometry	Dip slip rate (mm/yr)	Oblique slip rate (mm/yr)	T_e (km)	Regional uplift rate (mm/yr)	Wharekauhau TF slip rate (mm/yr)	RMS misfit (m)	Deflection						Figure
								Mean (m)	Mean (%)	Min (m)	Min (%)	Max (m)	Max (%)	
														Supplementary Figure SC16
18	PK listric	5.3	7.5	40	0.1	2.5	22.59	37.7	56.3	26.2	19.1	60.3	201.8	Supplementary Figure SC17
19	PK listric	6.5	9.2	15	0.1	0	27.82	95.8	139.6	68.6	49.9	145.3	486	Supplementary Figure SC18
20	PK planar	5.4	7.6	40	0	0	66.74	23.6	35	16.5	12.1	37.3	124.7	Supplementary Figure SC19
21	PK planar	5.7	8.1	40	0	2.5	76.96	24.1	35.9	16.9	12.4	38.2	127.8	Supplementary Figure SC20
22	PK planar	4.8	6.8	40	0.2	0	52.86	21	31.1	14.6	10.8	33.1	110.8	Supplementary Figure SC21
23	PK planar	5	7.1	40	0.2	2.5	62.9	21.1	31.3	14.7	10.8	33.4	111.6	Supplementary Figure SC22
24	PK planar	4.1	5.8	40	0.4	0	39.36	17.9	26.6	12.5	9.2	28.3	94.7	Supplementary Figure SC23
25	PK planar	4.4	6.2	40	0.4	2.5	49.04	18.5	27.4	12.9	9.5	29.2	97.8	Supplementary Figure SC24
26	PK planar	3.5	4.9	40	0.6	0	26.72	15.3	22.7	10.7	7.9	24.2	80.8	Supplementary Figure SC25
27	PK planar	3.7	5.2	40	0.6	2.5	35.55	15.4	22.9	10.8	7.9	24.4	81.6	Supplementary Figure SC26
28	PK planar	5.5	7.8	15	0.1	0	74.71	48.3	68.4	35	26.5	69.4	232.3	Supplementary Figure SC27
29	PK planar	5.6	7.9	15	0.1	2.5	84.74	47.3	67.2	34.3	25.9	68.4	228.7	Supplementary Figure SC28
30	PK planar	4.5	6.4	15	0.4	0	51.14	39.5	56	28.6	21.7	56.8	190	Supplementary Figure SC29

Fault model geometries are found in Table 3. Dip slip rate is the slip rate that fits the observed uplift best, with the listed RMS (root mean square) misfit. Oblique slip rate is the full fault slip rate calculated from the dip slip rate by assuming a rake of 45°. T_e is the elastic thickness assumed for the downgoing Pacific Plate for each model scenario. Regional uplift rate is a uniform rate applied to all modelled points to simulate long-wavelength contributions to uplift from processes other than Palliser-Kaiwhata Fault slip. Wharekauhau Fault slip rate refers to slip rate of a modelled Wharekauhau Thrust to investigate its effect on model results. Deflections are the maximum, minimum and mean subsidence caused by the flexural isostatic response to fault slip and consequent crustal thickening at each site where uplift rates have been calculated. These are expressed as absolute deflections (in metres) and percentages of the magnitude of total uplift at that site.

10.3389/feart.2023.1028445

TABLE 3 Fault model geometries for the model scenarios in Table 2. Depths shown are vertically downwards from the surface.

Fault model geometry	From (depth, km)	To (depth, km)	Dip (°)
Palliser-Kaiwhata F. - Listric	0	2	40
	2	6	30
	6	23	20
Palliser-Kaiwhata F. - Planar	0	18	40
Wairarapa-Wharekauhau F. - Listric	0	5	45
	5	10	40
	10	15	30
	15	20	20
	20	30	35

an order of magnitude for shorter timescales). Second, and more importantly, if variability in uplift rates is significant, we should not be able to achieve an adequate fit between our model and observed uplift.

3.5.4 Palliser-Kaiwhata Fault model scenarios

We run 30 different model scenarios (Table 2) to determine the possible contribution to observed uplift from slip on the Palliser-Kaiwhata Fault, and to demonstrate the effects of different parameters on the spatial distribution of modelled uplift. The parameters considered are: fault geometry (listric or planar); T_e, (Section 3.5.2); Wharekauhau Thrust Fault slip rate; and regional uplift rate. Our modelled listric and planar fault geometries are provided in Table 3. The planar modelled geometry has a constant dip of 40°—based primarily on shallow seismic reflection data (Barnes et al., 1998; Seebeck et al., 2022)—from the surface to its junction with the subduction interface of Williams et al. (2013). The modelled listric geometry reflects the possibility that the dip of the Palliser-Kaiwhata Fault may become shallower at depth, and is loosely based on faults in the profiles presented by Henrys et al. (2013). We consider three different values for T_e—our preferred value of 40 km and maximum and minimum likely values of 100 km and 15 km, respectively. The regional uplift rate parameter is designed to represent long-wavelength uplift due to processes such as subduction of the buoyant Hikurangi Plateau and the subduction interface earthquake cycle, and is applied as a spatially-uniform uplift across our whole modelled profile. Finally, the Wharekauhau Thrust Fault slip rate parameter is included to demonstrate the possible effect of slip on this structure on uplift further east; for some models we impose a slip rate of 0 mm/yr, and for others we use a slip rate of 2.5 mm/yr and assume a dip of 45° from the surface to 10 km depth (Seebeck et al., 2022).

3.5.5 Wairarapa-Wharekauhau fault system model scenarios

Since the purpose of our Wairarapa-Wharekauhau fault system models is to test whether slip on that fault could contribute to uplift at Tongue Point, we run a much narrower range of models than for the Palliser-Kaiwhata Fault. We use a single listric fault model geometry (Table 3), based on that inferred for the Wairarapa Fault further north by Henrys et al. (2013). We experiment with different values for T_e and slip rate, taking our preferred values of 40 km and 2.5 mm/yr (Seebeck et al., 2022) as starting points.

4 Results

4.1 Shoreline angle elevations and uplift rates

In this section we apply the marine terrace shore platform mean planar attitudes from Ninis et al. (2022) and create profiles across each shore platform and corresponding sea cliff, in order to determine the shoreline angle elevations of the late Pleistocene terraces preserved along the Wellington south coast. We then use the reconstructed shoreline angle elevations, corrected for sea level during the relevant, formative highstand, to determine absolute tectonic uplift and calculate uplift rates. Calculations have been made for shore platforms corresponding to MIS 5a (peak age 82 ka), 5c (96 ka), 5e (123 ka) and 7a (196 ka) (Ninis et al., 2022), and are described by field site, presented west to east. Results are summarised in Figure 6 and Table 1.

4.2 Tongue Point

There are three late Pleistocene marine terraces preserved at Tongue Point. The youngest has been inferred as MIS 5c (or possibly MIS 5a), based on its position in the terrace sequence; it is lower than the main terrace at this site, which OSL dating indicates formed during MIS 5e. One older, higher terrace is inferred to have formed during MIS 7a. The terraces are offset–uplifted on the western side–by the Ōhāriu Fault (Figure 2).

With only a few remnant stacks of the youngest late Pleistocene terrace remaining at Tongue Point, this shore platform was not expansive enough to meaningfully determine a shore platform attitude. Instead, to estimate uplift rates, we use surveyed shore platform spot elevations of 16 ± 3 m on the west of the fault, and 7 ±

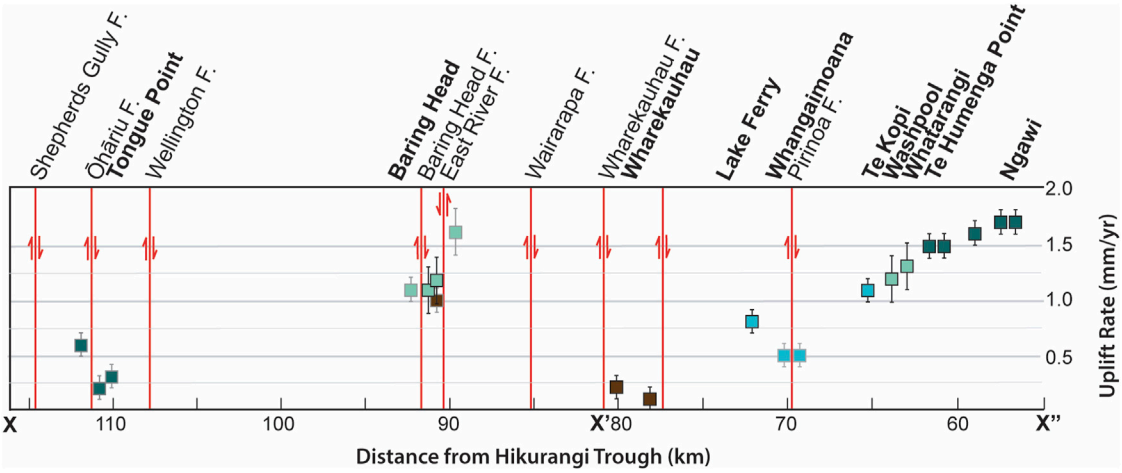

FIGURE 6
Uplift rates and associated uncertainties calculated from the shore platforms preserved along the Wellington south coast; black outline–rates determined from shoreline angle reconstructions; grey outline–minimum uplift rates calculated from shore platfrom spot elevations, where shoreline angle elevations could not be determined. The different colours denote the different aged marine terraces (coloured as in Figure 2).

3 m on the east; these yield values of 0.3 ± 0.1 mm/yr and 0.2 ± 0.1 mm/yr respectively, whether the shore platform was cut during MIS 5a or MIS 5c. These values provide a vertical slip rate across the fault of ~0.1 mm/yr at this site since the formation of this shore platform.

The MIS 5e shore platform attitudes show that they are strongly tilted on both sides of the Ōhāriu Fault. On the western side, the shore platform is oriented 111/8.8° NE; it dips in an inland direction, in contrast to the modern-day shore platform which is near-horizontal. Ninis et al. (2022) inferred that this dip reflects localised deformation by the Ōhāriu Fault. Alternatively, this dip could be the result of an erroneously high elevation point (e.g., a preserved stack) at the coastal extent of the terrace. For this reason, a shoreline angle elevation was not reconstructed here; instead, we use a surveyed elevation at a shore platform exposure of 75 ± 3 m to calculate a minimum uplift rate of 0.6 ± 0.1 mm/yr since 123 ka. On the eastern side of the fault, the shore platform attitude was determined as 118/16.8° SW. Ninis et al. (2022) observed that elevation data here showed a bimodal distribution, with several lower elevation points occurring where the shore platform abuts the Waiariki Stream; they attributed this unusually steep apparent dip of the MIS5e shore platform here to localised tectonic tilting adjacent to the Ōhāriu Fault, possibly in combination with erosion of the bedrock by the Waiariki Stream producing a local topographic low; this latter scenario is consistent with the shore platform here being repeatedly downthrown and exposed to river and marine erosion. To constrain uplift for this east side of the fault, we use a shore platform elevation surveyed near to the fault, of 27.0 ± 3 m, to yield a minimum uplift rate of 0.2 ± 0.1 mm/yr; further from the eastern side of the fault, where a shore platform elevation is 48.0 ± 3 m, uplift is calculated at 0.3 ± 0.1 mm/yr. The difference in uplift observed between the two MIS 5e shore platforms on either side of the Ōhāriu Fault, provides a vertical slip rate of ~0.3–0.4 mm/yr across this fault at this site. Using absolute tectonic uplift from the MIS 5e shoreline platform on the upthrown (67.3 ± 3.0 m) and downthrown (19.3 ± 3.0 m) side of the Ōhāriu Fault gives a mean uplift rate of ~0.35 mm/yr since 123 ka.

The oldest marine terrace preserved at Tongue Point, corresponding to MIS7a, is only exposed to the east of the Ōhāriu Fault; it is buried by colluvium deposits on the western side of the fault. The corresponding shore platform is not expansive enough to determine a shoreline angle elevation. Instead, a spot elevation of 82.7 ± 3 m provides a minimum uplift rate of 0.5 ± 0.1 mm/yr on this eastern side of the Ōhāriu Fault since 196 ka.

4.3 Baring Head

There are six late Pleistocene terraces preserved at Baring Head; the youngest three correlate to MIS 5a, MIS 5e and MIS 7a (Figure 2) with OSL dating constraining the ages of the youngest and oldest of these. The terraces are dissected by the Baring Head Fault, the Wainuiomata River, and the East River Fault. Due to the potential tectonic deformation of the shore platforms by the two faults, shore platform orientation calculations were considered separately west of the Baring Head Fault, between the Baring Head and East River fault, and east of East River Fault.

There were too few elevation measurements to calculate a shore platform attitude and shoreline angle elevation for the inferred MIS 5e terrace preserved to the west of Baring Head Fault; we have instead used a surveyed shore platform spot elevation of 79.1 ± 3 m to calculate a minimum uplift rate of 1.1 ± 0.1 mm/yr for the last 82 ka yr. In order to quantify uplift across the Baring Head Fault, we use a shore platform elevation surveyed directly on the other side of the fault, of 66.2 ± 3 m; this yields a minimum uplift rate of 0.9 ± 0.1 mm/yr for this downthrown side of the fault. The difference between the uplift rates calculated for either side of the Baring Head Fault suggest that this structure has a vertical slip rate of ~0.2 mm/yr at this location since 82 ka.

Between the Baring Head Fault and the East River Fault, a shore platform attitude of 136/3.0 SW was calculated for the MIS 5a terrace. Here, two profiles were constructed to determine shoreline angle elevations. Results from both profiles were consistent, providing values of 82.8 ± 4.7 m and 89.8 ± 4.7 m. From these elevations we calculate uplift rates of 1.1 ± 0.2 mm/yr and 1.2 ± 0.2 mm/yr, respectively, for the MIS 5a terrace between the Baring Head Fault and the East River Fault since 82 ka. To quantify vertical displacement across the East River Fault that offsets the MIS 5a terrace, we used a surveyed elevation measurement from either side of the fault. To the west and on the downthrown side of the fault, from a shore platform exposure at 108.5 ± 3 m, we have calculated a minimum uplift rate of 1.5 ± 0.2 mm/yr. To the east of the fault, a minimum uplift rate of 1.6 ± 0.2 mm/yr was calculated from a shore platform elevation measurement of 120.5 m ± 3; this gives a vertical slip rate on the East River Fault of ~0.1 mm/yr for the last 82 ka. Because these uplift rates were calculated from points ~300–350 m on either side of the fault, and in combination with the shore platform tilting to the west and the fault uplifting the eastern side, we consider this slip rate to be a maximum.

A narrow strip (~100 m at its widest point) of the inferred MIS 5e terrace is preserved at Baring Head, between the Baring Head Fault and the East River Fault. Because this shore platform was not expansive enough to collect many elevation data points from which to calculate its attitude, we have not reconstructed a corresponding shoreline elevation. We have instead used a spot elevation surveyed directly from a shore platform exposure at the rear of the terrace, near to (<20 m from) where we anticipate the shoreline angle to be located. The elevation here is 95.8 ± 3 m, which yields a minimum uplift rate of 0.7 ± 0.1 mm/yr since 123 ka.

Similarly, the limited size of what remains of the inferred MIS 7a terrace at Baring Head, coupled with the limited elevation data available from exposures of this shore platform, did not warrant a calculation of its attitude. Instead, we use a shore platform spot elevation to the west of East River Fault of 173.6 m ± 3 m to calculate a minimum uplift rate of 1.0 ± 0.1 mm/yr at this location since 196 ka.

4.4 Wharekauhau

One terrace is preserved along the coast between Wharekauhau and Lake Onoke (Figure 2). The available OSL data, obtained from marine deposits overlying this shore platform, range in ages which correspond to all the main highstands of MIS 5 (Schermer et al., 2009), through to MIS 7a (Ninis et al., 2022); this has been interpreted by Ninis et al. (2022) to indicate that this shore platform was occupied by the sea during all of these highstands. The orientation of the shore platform along this stretch of coast has been calculated as 132/0.2° SW. Two profiles were constructed across this terrace, providing two shoreline angle elevations of 17.9 ± 3.0 m and 15.5 ± 3.0 m. These yield uplift rates of 0.2 ± 0.1 mm/yr and 0.1 ± 0.1 mm/yr, respectively, for this site since 196 ka.

4.5 Lake Ferry–Te Kopi

The main coastal terrace preserved between Lake Ferry and Te Kopi has been identified as MIS 5c in age. The terrace is offset by ~3 m west-side-up near Whangaimoana Beach, most likely by the coastal extension of the Pirinoa Fault, which has been mapped further inland (e.g., Begg and Johnston, 2000; Ninis et al., 2022). As such, the orientation of the shore platform and elevation of the shoreline angle were calculated separately for either side of this fault.

West of the Pirinoa Fault, the shore platform has a calculated orientation of 156/0.7° W. One profile was constructed at the western extent of this shore platform, near Lake Ferry, and the shoreline angle on this profile was located at an elevation of 61.1 ± 0.1 m. This yields an uplift rate of 0.8 ± 0.1 mm/yr since 96 ka. Close to the Pirinoa Fault, uplift rates determined from surveyed shore platform elevations of 41.1 ± 3 m on the western, upthrown side yields a minimum uplift rate of 0.5 ± 0.1 mm/yr; to the immediate east of the fault, a shore platform elevation of 39.1 ± 3 also yields a minimum uplift rate of 0.5 ± 0.1 mm/yr. Although not significantly contributing to a difference in uplift on either side of it, the Pirinoa Fault is likely responsible for the slight change in dip and dip direction of the shore platform, which to the east of the fault is 028/0.6° W. A profile constructed near Te Kopi, at the eastern end of this area, gives a shoreline angle elevation of 94.9 ± 0.4 m. This elevation yields an uplift rate of 1.1 ± 0.1 mm/yr for the last 96 ka.

4.6 Washpool/Whatarangi

The age of the main marine terrace at Washpool/Whatarangi has been constrained as MIS 5a. At the southern end of the site, a higher terrace is preserved locally along the coast; this terrace then curves inland and is preserved behind the expansive MIS 5a terrace.

The orientation of the MIS 5a shore platform at Washpool/Whatarangi has been calculated as 024/1.5 W. Two profiles were constructed at this site, with the shoreline angle elevations determined from these yielding values of 92.1 ± 0.7 m and 89.9 ± 0.7 m. These produce uplift rates of 1.3 ± 0.2 mm/yr and 1.2 ± 0.2 mm/yr, respectively, for the last 82 ka.

The higher terrace preserved along the coast at Washpool/Whatarangi has been inferred to be MIS 5e in age, based on the shore platform and terrace tread elevations, which in the field appear to be approximately consistent with those of the dated MIS 5e terrace preserved further southeast, between Te Humenga Point and Cape Palliser (Ninis et al., 2022). There were too few shore platform exposures for the MIS 5e terrace preserved locally at Washpool/Whatarangi from which to calculate a shore platform orientation and shoreline angle elevation for the inferred MIS 5e terrace preserved here. Instead, we use a surveyed shore platform elevation of 114.0 ± 3.0 m to calculate a minimum uplift rate from this terrace of 0.9 ± 0.1 mm/yr. If the inferred age for this terrace of MIS 5e is incorrect, and this terrace is instead MIS 5c in age, then the calculated uplift rate would be 1.3 ± 0.1 mm/yr, which is within error of the rates calculated from the dated MIS 5a terrace at this site.

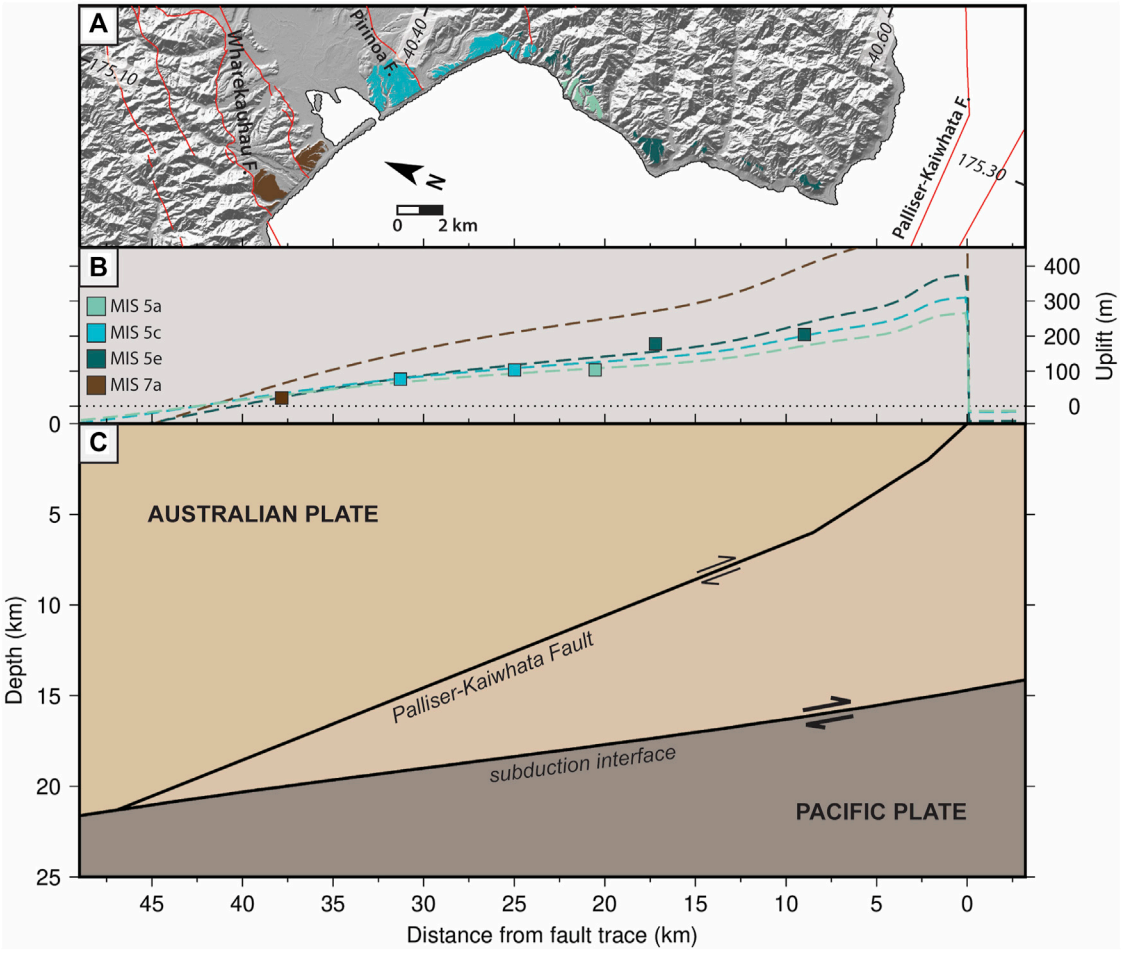

FIGURE 7
Dislocation modelling results of uplift from 5.3 mm/yr of dip-slip motion on the Palliser-Kaiwhata Fault with a listric geometry and assuming a T_e of 40 km (Model 1 in Table 3). This modelled fault dips 40° NW between the surface and 2 km vertical depth, 30° NW between 2 km and 6 km depth, and 20° NW between 6 km depth and 23 km. **(A)** Hillshaded topography, major onshore and offshore fault zones and mapped marine terrace treads (coloured by terrace age) in the area of our modelled profile. **(B)** Modelled and observed uplift along the profile. Dashed lines show modelled uplift and coloured squares show observed uplift; both modelled and observed uplift are colour-coded by age. **(C)** Modelled fault geometry and depth to the Hikurangi Subduction interface along our profile.

4.7 Te Humenga Point–Cape Palliser

There is one main terrace preserved between Te Humenga Point and Cape Palliser (Figure 2), which has been shown to be MIS 5e. Due to the distance over which this terrace is discontinuously preserved (~10 km along the coast), we analysed the elevation data at Te Humenga Point and Ngawi separately, to assess whether the shore platform attitude is consistent between these locations. Where it is preserved at Te Humenga Point, the shore platform has a calculated orientation of 167/2.5 W. The calculation of the orientation of the shore platform at Ngawi yielded a similar result of 173/2.9 W.

Five shoreline angle elevations were calculated for the Te Humenga Point–Cape Palliser terrace, two from Te Humenga Point, two from Ngawi, and one profile in between (Figure 5). The two profiles constructed at Te Humenga Point give consistent shoreline angle elevations of 193.4 ± 2.0 m and 195.9 ± 2.0 m. These shoreline angle elevations yield an uplift rate of 1.5 ± 0.1 mm/yr for the last 123 ka yr at this location. At Ngawi, the two calculated shoreline angle elevations were again consistent, yielding values of 213.6 ± 8.3 m and 211.1 ± 8.3 m, providing an uplift rate of 1.7 ± 0.1 mm/yr. The profile constructed in between the Te Humenga Point and Ngawi sites provides a shoreline angle elevation of 198.3 ± 8.3 m and a corresponding uplift rate of 1.6 ± 0.1 mm/yr.

4.8 Dislocation and flexural-isostatic modelling

Although we estimate uplift rates due to four separate processes (slip on upper-plate faults, subduction of the buoyant Hikurangi Plateau, the subduction earthquake cycle and sediment underplating), most of the estimates are in the form of simple calculations rather than formal modelling. We therefore present only the results of our dislocation and flexural-isostatic upper-plate fault models here, leaving the estimates of uplift due to other

processes until the Discussion (Section 5.2). Hereafter, discussion of uplift due to slip on upper-plate faults refers to the coupled results of our elastic dislocation and flexural-isostatic models.

Modelling of uplift from slip on upper-plate faults shows that it is possible to achieve a good fit with observed terrace uplift and uplift rates, but results exhibit a strong dependence on fault geometry. Uplift from 5.3 mm/yr of dip-slip motion on a modelled Palliser-Kaiwhata Fault with a listric geometry and assuming a T_e of 40 km is shown (Figure 7). This modelled fault dips 40° NW between the surface and 2 km vertical depth, 30° NW between 2 km and 6 km depth, and 20° NW between 6 km depth and 23 km (Table 3), where it reaches the subduction interface of Williams et al. (2013). If a T_e of either 40 or 100 km and a listric geometry are assumed, it is possible to fit observed uplift with acceptable RMS misfits of 19–24 m for a wide range of models (Table 2). This RMS misfit is dominated by the differences between modelled and observed uplift for the MIS 5e terrace at Te Humenga Point and Ngawi. The uplift at these two sites is very similar (188.7 ± 3.8 m at Te Humenga Point compared with 206.4 ± 10.1 m at Ngawi) despite the ~9 km distance between these sites. We were unable to fit the uplift at both these sites using a wide range of models (including many that are not reported here); it is possible that local minor faulting and folding or some other process influences observed uplift at Ngawi or Te Humenga Point. Based on visual inspection of Figure 7 and Supplementary Figures SC1–29, we consider an RMS value <30 m to represent an adequate fit to uplift observations.

Models that assume a listric geometry but a T_e of 15 km generally have a poorer fit to the observed uplift. However, it is possible to obtain better (<30 m) RMS misfits for these models if a regional uplift rate of 0.4 mm/yr is assumed. Similarly, for our models that assume a planar geometry for the Palliser-Kaiwhata Fault, the fit is generally much worse than for the modelled listric geometry, but an adequate fit can be achieved (Model 26; Supplementary Figure SC25) if a regional uplift rate of 0.6 mm/yr is assumed. These results show that a higher modelled regional uplift rate can improve the fit of the model to observations. However, the fit is still poorer than models that assume a listric fault geometry and a T_e of 40 or 100 km. These regional uplift rate values are determined by trial and error, but are consistent with estimates from Litchfield et al. (2007).

A "minimum upper-plate fault" model, with a planar Palliser-Kaiwhata Fault that dips 40° NW between the surface and 18 km matches uplift at Ngawi with 5.3 mm/yr of dip-slip motion if T_e is 15 km (3.7 mm/yr dip-slip if T_e is 40 km). However, this model predicts significantly lower terrace uplift farther northwest; for a planar, 40°-dipping fault, processes other than upper-plate faulting would be required to explain terrace elevations between Te Humenga Point and Wharekauhau.

Our preferred Wairarapa-Wharekauhau fault system model (Supplementary Table SD1; Figure 8) shows that it is possible for slip on that fault to drive uplift of 0.35 mm/yr at Tongue Point, across both sides of the Ōhāriu Fault. Assuming the geometry taken from Henrys et al. (2013) and a T_e of 40 km, this uplift rate can be matched through a modelled dip-slip rate of 2–3 mm/yr on the Wairarapa-Wharekauhau fault system. These slip rates predict uplift rates of ~1–1.5 mm/yr at Baring Head, which is similar to our observed uplift rate estimates for Baring Head (Table 1).

In many of the figures showing our model results, the modelled uplift (or subsidence) is not zero at the edge of the figure. This is a consequence of our use of flexural-isostatic models, for which the subsidence in response to an imposed topographic load can be in the order of 10s or 100s of km. We include a profile showing modelled vertical motions over a much longer wavelength in the Supplementary Figure SB1 to show that modelled vertical motions do tend to zero in the far field.

5 Discussion

5.1 Uplift rates and tilting of the Wellington south coast terraces

Uplift rates along the Wellington south coast, between Cape Palliser and Wharekauhau, gradually decrease from east to west (Figures 6, 7, 9), despite the fact that rates have been determined from different-aged terraces. The uplift rate calculated from the MIS 5e terrace near Cape Palliser, the eastern-most preserved terrace on the Wellington south coast and the closest to the Hikurangi Trough, is 1.7 ± 0.1 mm/yr, decreasing slightly to 1.5 ± 0.1 mm/yr at Te Humenga Point. This terrace is tilted by 2.5°–2.9° towards the west. At Washpool, the uplift rate determined from the younger MIS 5a terrace preserved locally is 1.3 ± 0.2 mm/yr; this terrace is tilted less than the nearby older terraces, with a dip of 1.5° towards the west. This is consistent with what we would expect–that the older terraces, being exposed to tectonic deformation over a longer period of time, are more tilted than the younger terraces. A comparison of the degree of tilting of these two different-aged shore platforms over time provides us with a tilt rate of ~0.02°/ka. Uplift determined from the MIS 5c terrace preserved along the coast at Te Kopi yields a rate of 1.0 ± 0.1 mm/yr; to the west near Lake Ferry, this terrace has been uplifted by 0.8 ± 0.1 mm/yr (Figure 6). Despite being older than the MIS 5a terrace preserved at Washpool, the MIS5c terrace between Te Kopi and Lake Ferry is only tilted by 0.6°–0.7° to the west. At Wharekauhau, uplift determined from the MIS 7a terrace yields a rate of 0.2 ± 0.1 mm/yr. Despite this terrace being the oldest along this length of coast, it is tilted the least, with a calculated dip of only 0.2° towards the southwest. With such a shallow dip in a direction towards the coast, it may be that this shore platform still maintains much of its original, formative gradient, despite being located near to the Wairarapa and Wharekauhau Thrust faults.

Although our uplift calculations yield results similar to earlier estimates by Ghani (1974; 1978) for Cape Palliser, and are within error of his estimates at Lake Ferry, our uplift evaluation for Wharekauhau is much less than the 1.0 mm/yr reported by Ghani (1974; 1978). This is likely due to the additional three terraces Ghani (1974; 1978) allocated to this site, which Ninis et al. (2022) interpreted as a series of fan deposits that give the appearance of additional older terrace treads.

West of Palliser Bay, at a distance of ~70–100 km from the Hikurangi Trough, marine terrace elevations are visibly influenced by upper-plate faults (Figures 6, 8, 9). Uplift rates calculated from the marine terraces preserved on either side of the Wairarapa-Wharekauhau fault system, at Wharekauhau and Baring Head

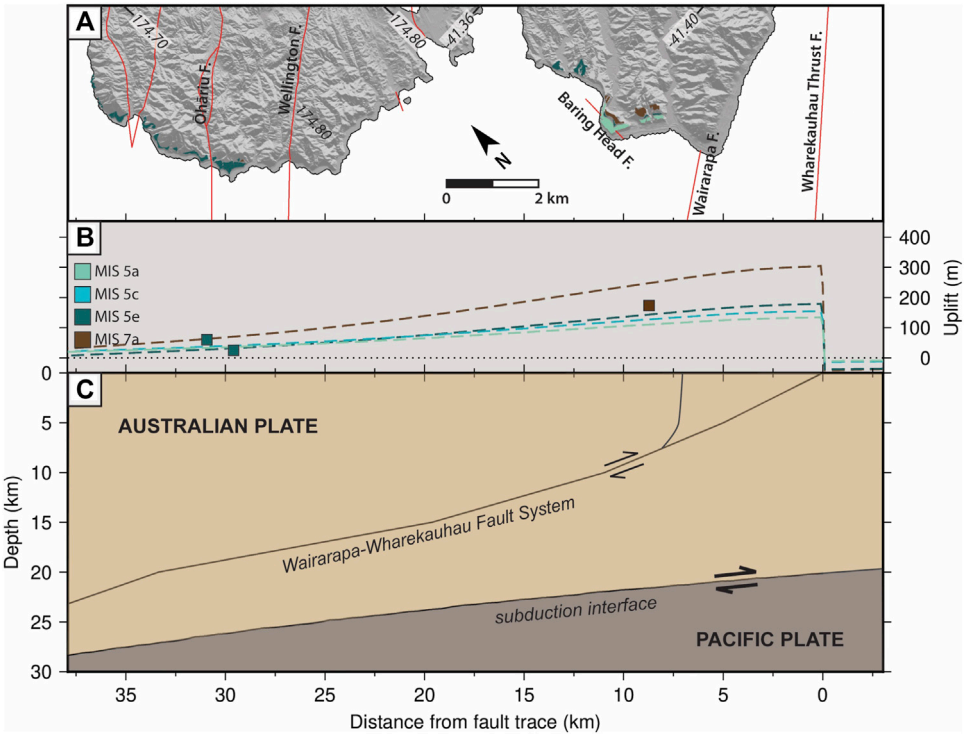

FIGURE 8
Dislocation modelling results of uplift from 2 mm/yr slip on a listric Wairarapa-Wharekauhau fault system—selected to mimic the geometry inferred by Henrys et al. (2013) further north—and assuming a T_e of 40 km. The modelled fault system dips 45° W between the surface and 5 km vertical depth; 40° between 5 and 10 km depth; 30° from 10 to 15 km depth; and 20° to 20 km depth. The fault then steepens, dipping at 35° W to 30 km depth. **(A)** Hillshaded topography, major onshore and offshore fault zones and mapped marine terrace treads (coloured by terrace age) in the area of our modelled profile. **(B)** Modelled and observed uplift along the profile. Dashed lines show modelled uplift and coloured squares show observed uplift; both modelled and observed uplift are colour-coded by age. **(C)** Modelled fault geometry and depth to the Hikurangi Subduction interface along our profile. Note 2x vertical exaggeration.

(Figure 6), provide an estimate of vertical slip on this structure of ~1.4 mm/yr. This is a minimum value; uplift quantified from sites closer to the fault system would yield an even higher uplift rate. At Baring Head, vertical offsets are also observed, albeit to a lesser extent, across the Baring Head and East River faults which cut the marine terraces. The closest late Pleistocene shore platform exposure to the west of the Wairarapa-Wharekauhau fault system, which is MIS 5a in age, yields a minimum uplift rate of 1.6 ± 0.2 mm/yr. This is higher than that estimated by Ota et al. (1981) who inferred an age of MIS 5e for this terrace, and also slightly higher than the Holocene uplift rate of ~1.3 mm/yr estimated for this location by Begg and McSaveney (2005). The uplift rates calculated from the MIS 5a, MIS 5e and MIS 7a shore platforms where they are preserved between the Baring Head and East River faults are inconsistent across the different time periods, yielding values of 1.2 ± 0.2 mm/yr since 82 ka, 0.7 ± 0.1 mm/yr since 123 ka, and 1.0 ± 0.1 mm/yr since 196 ka. Some factors which could explain this variability include 1) alternating periods of activity and quiescence on the nearby Wairarapa Fault, much like that reported on the Wellington Fault (Robinson et al., 2011; Ninis et al., 2013), 2) a complex interaction between overall uplift at the Baring Head site due to slip on the Wairarapa Fault, and localised down-throwing as a result of slip on the Baring Head and East River faults, and 3) the competing vertical displacement processes resulting from coseismic subsidence from megathrust earthquakes (Clark et al., 2015) and possible localised uplift from sediment underplating at the subduction interface beneath this region (Henrys et al., 2013).

When comparing uplift rates calculated from either side of the Ōhāriu Fault at our westernmost field site at Tongue Point (Figure 6), it is evident that movement on this structure has vertically displaced the locally preserved marine terraces. The calculated uplift rates for the MIS 5e terrace preserved on the western, upthrown side of the Ōhāriu Fault is 0.6 ± 0.1 mm/yr, equivalent to that estimated by Ota et al. (1981). This rate is higher than that calculated from the younger terrace preserved beneath it, irrespective of whether the younger terrace formed during MIS 5a or 5c, both of which yield an uplift rate of 0.3 ± 0.1 mm/yr. On the eastern and downthrown side of the Ōhāriu Fault, the uplift rate calculated from the youngest Pleistocene terrace - 0.2 ± 0.1 mm/yr - is within error of that calculated from MIS 5e, irrespective of whether the younger terrace is MIS 5a or 5c in age. The minimum uplift rate calculated from the MIS 7a terrace on this same side of the fault is slightly higher, at 0.5 ± 0.1 mm/yr. Though the Ōhāriu Fault has vertically offset the marine terraces at Tongue Point, both sides of the fault are uplifted by a mean rate of ~0.35 mm/yr since 123 ka. The manifestation of uplift at this site during the last ~123 ka likely reflects a complex interaction of factors in addition to deformation by the Ōhāriu Fault, which potentially

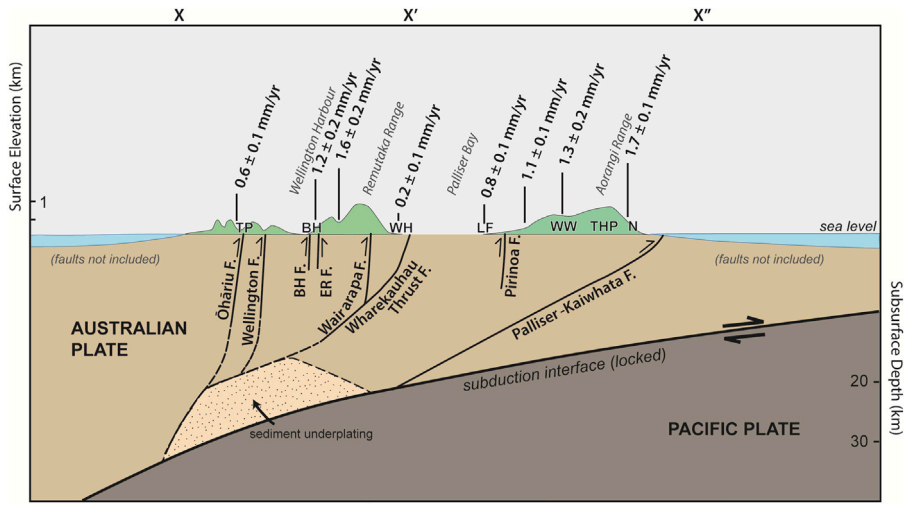

FIGURE 9
Schematic cross Section X-X′-X″ (see Figure 2 for location of profile) across the Wellington south coast, showing representative topography (vertically exaggerated), calculated uplift rates and locations of major faults and those observed to offset the late Pleistocene marine terraces; "BH F" is Baring Head Fault, "ER F" is East River Fault. Locations from west to east: TP, Tongue Point; BH, Baring Head; WH, Wharekauhau; LF, Lake Ferry; WW, Washpool/Whatarangi; THP, Te Humenga Point; N, Ngawi. Figure modified after Little et al. (2009) and updated using subsurface data from Begg and Johnston (2000), Henrys et al. (2013), Williams et al. (2013) and this study.

also shows alternating periods of activity and then relative quiescence. As the late Pleistocene marine terraces preserved on the downthrown sides of the faults at both Baring Head and Tongue Point have been elevated relative to sea level, some other process, or processes, must be contributing to the broader uplift across this region.

5.2 Upper-bound contributions to late Pleistocene uplift

Several processes may contribute to late Pleistocene uplift of the Wellington south coast. It is likely that slip on upper-plate faults is a major contributor to uplift, and possible that Hikurangi Plateau buoyancy, the subduction earthquake cycle and sediment underplating also contribute in some areas. We here discuss the likely upper bounds on the contribution to uplift from each process, and whether the contribution of each is on the order of mm/yr, or less.

5.2.1 Slip on upper-plate faults

The dislocation modelling results (Figure 7; Figure 8) indicate that slip on upper-plate faults is likely a major contributor to the late Pleistocene uplift observed along the Wellington south coast. Even when making very conservative assumptions about fault geometry, slip rate and T_e, our models of slip on the Palliser-Kaiwhata Fault and the Wairarapa-Wharekauhau fault system predict ≥1 mm/yr of uplift at both Ngawi and Baring Head, respectively, contributing ≥50% of uplift at both of these sites. Models relying on less conservative assumptions that are nevertheless consistent with available data (Figure 7; Figure 8) suggest that slip on upper-plate faults may also be the dominant contributor ->80% of long-wavelength uplift- to late Pleistocene uplift everywhere in our study area.

The model of slip on the Palliser-Kaiwhata Fault (Figure 7) requires a relatively high slip rate to match observed terrace elevations. If we convert the dip-slip rate of 5.3 mm/yr required by this model to a full slip rate by assuming the best estimate of rake (135°—NZ CFM, Seebeck et al., 2022), the slip rate required by this model is 7.5 mm/yr. This is slightly higher than the 5 ± 2 mm/yr slip rate specified for the Palliser-Kaiwhata Fault in the NZ CFM (Seebeck et al., 2022). However, the reported slip rate is derived from Pleistocene marine terrace uplift (Litchfield et al., 2014) and does not account for flexural or isostatic effects, which may explain why it is slightly lower than our modelled rate. A better comparison is with the slip rate of the dextral strike-slip Boo Boo Fault to the immediate west of the Palliser-Kaiwhata Fault (Figure 2), which is well constrained at 8.3 ± 1.2 mm/yr and is not derived from terrace elevations, but rather on the measured offset of seafloor geomorphic features (Wallace et al., 2012; Seebeck et al., 2022). Despite their different orientations, both the Boo Boo and Palliser-Kaiwhata faults accommodate east-west shortening and probably have a similar horizontal azimuth of slip vector. Due to an absence of other fast-slipping faults nearby, it is likely that most of the slip rate of the Boo Boo Fault is transferred onto the Palliser-Kaiwhata Fault, in which case 7.5 mm/yr is a plausible slip rate for the Palliser-Kaiwhata Fault. If a T_e of 15 km is assumed, the required full slip rate is 9.9 mm/yr; this is probably unrealistically high and would require processes other than slip on the Palliser-Kaiwhata Fault to explain observed terrace uplift.

The slip rates above are calculated based on an assumption that processes other than slip on the Palliser-Kaiwhata Fault do not

contribute to uplift along the transect of interest. If the aggregated effect of other processes—such as subduction of a buoyant Hikurangi Plateau, the subduction earthquake cycle and sediment underplating—is included in the form of a regional uplift rate, the dip-slip rate required to match terrace uplift is significantly reduced. For example, Model 7 (Table 2; Supplementary Figure SC6) includes a regional uplift rate of 0.4 mm/yr and achieves an adequate fit to observed uplift with a dip-slip of 3.8 mm/yr (oblique slip of 5.4 mm/yr). We discuss the processes that could contribute to regional uplift below, but the magnitude of their contribution to uplift remains poorly constrained, in turn making it difficult to constrain the slip rate of the Palliser-Kaiwhata Fault. In the absence of better data, we suggest that the NZ CFM slip rate could be adjusted to 6 +3/−2 mm/yr to reflect these uncertainties and the results of our modelling.

For our modelled Wairarapa-Wharekauhau fault system, independent of the value we assume for T_e, a dip-slip rate of 2 mm/yr is required to match the observed uplift rate at Tongue Point of 0.35 mm/yr since ~123 ka; this is consistent with the 2.5 ± 1 mm/yr dip-slip quoted for this fault in the NZ CFM. We note that although our modelled listric geometry is based on the interpretation of Henrys et al. (2013), theirs is not the only geometry consistent with available data. Based on our modelling, it is plausible that slip on this fault system could uplift both sides of the Ōhāriu Fault. This accords with observations from the 1855 M_w 8.2 Wairarapa earthquake (Darby and Beanland, 1992), where uplift at Tongue Point was documented at between 0.3 m and <2 m, and suggests that the previous inference of rupture on the subduction interface at depth during this earthquake is not required to explain the co-seismic uplift at Tongue Point.

5.2.2 Hikurangi Plateau buoyancy

Subduction of the buoyant crust of the Hikurangi Plateau has previously been suggested as a significant contributor to uplift across the southern North Island (Litchfield et al., 2007). We here estimate a maximum value for the isostatic component of this contribution. The subducted crust of the plateau appears to thicken from 9.5–10 km beneath the Wanganui Basin (Tozer et al., 2017) to ~12 km at the Hikurangi Trough (Herath et al., 2020). To account for the uncertainties in these estimates, we assume a maximum of 4 km (linear) increase in thickness over the ~150 km between the Wanganui Basin and the trough, so that the thickness of the plateau increases by ~27 m every kilometre towards the trough. If we assume a dip-slip rate for the subduction interface of 30 mm/yr (a likely maximum based on results from Wallace et al., 2012) and ignore the dip of the subduction interface (assuming a dip of 0° instead of 20° affects results by <5%), it follows that beneath the southern North Island, the rate of thickening of the subducting Hikurangi Plateau is ~0.8 mm/yr at any given locality. We assume that the thicker crust is supported isostatically, because the ~500–1,000 km width of the Hikurangi Plateau is too long for flexural support by the upper mantle to be significant. Assuming Airy isostasy, a density of plateau crust ρ_c of 2,750 kg m^{-3} and a mantle density ρ_m of 3,300 kg m^{-3}, we calculate a maximum uplift rate of 0.16 mm/yr associated with this buoyancy, at least in terms of direct isostatic support. This rate is similar to the ~0.15 mm/yr uplift rate at our Wharekauhau site, suggesting that the buoyancy of the down-going plate may have a significant influence on uplift rates in places where the contribution from upper-plate faults is relatively small. However, Wharekauhau is in the immediate footwall of the Wharekauhau Thrust Fault, so that further contributions to uplift—from sources other than plateau buoyancy—may be required to overcome footwall subsidence at that site.

The maximum uplift rate above is lower than the uplift rates associated with subduction of the Hikurangi Plateau modelled by Litchfield et al. (2007), who estimated rates lower than 1 mm/yr but often ≳0.4 mm/yr. There are at least two reasons for this difference. First, their study (which covered the whole Hikurangi Margin) used a convergence rate of 45 mm/yr to calculate uplift rates, while we used a value of 30 mm/yr that is more appropriate for our study area. Second, the two models implicitly include different processes; the Litchfield et al. (2007) estimate includes secondary processes, such as upper-plate faulting and sedimentary underplating, which we explicitly treat as separate contributors to uplift in this study.

5.2.3 The earthquake cycle on the Hikurangi subduction interface

It is widely suggested that some part of the subduction interface earthquake cycle may cause permanent vertical deformation of the overriding plate and thereby contribute to marine terrace uplift (e.g., Briggs et al., 2008; Wesson et al., 2015; Melnick, 2016; Jolivet et al., 2020). However, a significant proportion of any coseismic uplift is typically recovered by subsidence during the interseismic period (Figure 3), like that currently observed in our study area (Hamling et al., 2022). The net uplift associated with each earthquake cycle is therefore expected to be significantly less than coseismic and/or postseismic uplift during that cycle. In Sumatra, Briggs et al. (2008) estimated that <4% of coseismic uplift was preserved permanently. In Chile, Wesson et al. (2015) suggested that 10%–20% of uplift over a seismic cycle is preserved in the long term. Here, we estimate maximum long-term uplift rates due to subduction earthquakes at two sites, to determine whether the behaviour of the Hikurangi Margin is similar to those other subduction zones.

Tongue Point is the most suitable site from which to estimate uplift due to the subduction interface earthquake cycle, because although the terraces preserved there are offset by slip on the Ōhāriu Fault, both sides of the fault have been uplifted, presumably from some combination of slip on other upper-plate faults, subduction of the buoyant Hikurangi Plateau, permanent deformation due to subduction earthquakes, and sediment underplating. There is no clear evidence for any processes that promote long-term subsidence in this region; consequently, we can estimate a maximum subduction earthquake contribution to the observed ~0.35 mm/yr uplift at Tongue Point by neglecting all drivers other than subduction earthquakes. Note that this value is clearly a maximum because it neglects the possible contribution of slip on the Wairarapa-Wharekauhau fault system, which could plausibly explain all of this uplift.

To estimate the vertical component of slip on the subduction interface, we assume a margin-normal rate of ~25 mm/yr (Wallace et al., 2012) and a change in dip immediately beneath Tongue Point to 15° (Williams et al., 2013); using these values gives a vertical slip rate of 6.5 mm/yr. More details of our modelling strategy (which involves simple geometric calculations rather than elastic dislocation models) are found in the Supplementary Section SB. Our calculated

maximum uplift rate contribution from subduction earthquakes of ~0.35 mm/yr is 5.4% of this, indicating that the vast majority of coseismic uplift is recovered interseismically. We note that our value of 6.5 mm/yr for the vertical component of slip on the subduction interface is probably an overestimate, since it comprises the total of footwall subsidence and hanging-wall uplift during subduction earthquakes. However, hanging-wall uplift will be at least twice as great as footwall subsidence. Conservatively, we conclude that at Tongue Point, <10% of coseismic and postseismic uplift associated with subduction earthquakes is preserved as permanent uplift. This percentage is similar to those calculated from Sumatra and Chile (Briggs et al., 2008; Wesson et al., 2015), suggesting that buoyancy of the Hikurangi Plateau does not necessarily enhance uplift due to subduction earthquakes.

It is possible to perform a similar calculation at Wharekauhau, where we infer an uplift rate of 0.16 mm/yr over the past 196 ka. If this uplift rate is assumed to be entirely due to subduction earthquakes, it would equate to 4.6% of the vertical component of slip on the subduction interface (again assuming a dip-slip rate of 25 mm/yr, but a dip of 8° for the subduction interface beneath Wharekauhau). However, this percentage is a less reliable maximum than at Tongue Point; Wharekauhau lies in the immediate footwall of the Wharekauhau Thrust Fault, so that footwall subsidence may counteract long-term uplift due to subduction earthquakes and other processes. Nevertheless, based on our dislocation modelling, we suggest that any footwall subsidence is almost certainly less than 0.4 mm/yr. An uplift rate due to subduction earthquakes at Wharekauhau of 0.56 mm/yr—0.4 mm/yr to counteract footwall subsidence and 0.16 mm/yr of long-term uplift—would equate to permanent preservation of ~16% of vertical displacement due to subduction earthquakes.

The calculations presented above do not discount subduction earthquakes as a significant contributor to late Pleistocene uplift (up to ~0.35 mm/yr maximum at Tongue Point), although equally subduction earthquakes are not required to explain observed terrace uplift. However, if <10% of uplift due to subduction earthquakes is permanent, there are important implications for Holocene marine terrace formation as a recorder of past subduction earthquakes. For example, for a subduction earthquake that caused 2 m of combined coseismic and postseismic uplift, less than 0.2 m of that uplift would be preserved permanently. In some settings, this small amount of permanent uplift might be insufficient to form a distinct Holocene marine terrace, reducing the likelihood of a complete subduction earthquake record.

5.2.4 Sediment underplating

If sediment underplating is treated as a wholly separate process from upper-plate faulting, the same arguments apply to its contribution to uplift as for permanent deformation associated with subduction earthquakes. The maximum uplift rate due to sediment underplating at Tongue Point—estimated by neglecting uplift due to other processes—would be ~0.4 mm/yr and potentially much lower. Since slip on the Wharekauhau Thrust Fault can explain uplift at Baring Head, significant uplift due to underplating would not be required there either. However, the inferred Wairarapa Fault geometry of Henrys et al. (2013) intersects with their region of inferred underplating at depth. If some (presently unknown) processes links underplating at depth with slip on the Wairarapa Fault, then it may not be appropriate to consider underplating and slip on upper-plate faults as separate processes. Better constraints on fault geometry and more detailed modelling than we present here are required to explore the relative roles of sediment underplating and upper-plate fault slip. We note that episodes of sediment underplating may occur over longer timescales than the ~200 kyr considered here (e.g., Mouslopoulou et al., 2016), but underplating may nevertheless contribute to uplift over our timescale of interest.

5.3 Influence of flexural-isostasy compensation on fault slip rates constrained by modelling of terrace uplift

During our modelling of slip on the Palliser-Kaiwhata Fault (Figure 7; Table 2 and Supplementary Sections SC, SD), we attempted to fit observed uplift by varying fault slip rate, making different assumptions about elastic thickness T_e. An acceptable fit to the data was achieved for T_e values of 100, 40 and 15 km, but the slip rate required to match uplift was much higher for lower (but plausible) T_e values. This result is unsurprising, since a lower T_e means less flexural support of topography, with more fault slip required to uplift a terrace to the observed elevations. For the example of an otherwise identical pair of models, the dip-slip rate required to match observed uplift assuming our preferred T_e of 40 km (5.3 mm/yr; Model 1, Figure 7) is 18% greater than when a very high T_e of 100 km is assumed (4.5 mm/yr for Model 12, Supplementary Figure SC11). The magnitude of the difference varies depending on model parameters such as regional uplift rate, but the required slip rate is typically ~15–25% higher if T_e is 40 km than if T_e is 100 km. This effect is important because flexural-isostatic effects are sometimes neglected in studies that use terrace uplift to constrain fault slip rates (e.g., Jara-Muñoz et al., 2022; Nicol et al., 2022). We acknowledge that it is often difficult to constrain T_e, but recommend that future studies consider the possible impact of flexural-isostatic compensation on their estimated slip rates and adjust their uncertainties where appropriate.

6 Conclusion

We have used shore platform elevation data and corresponding attitudes to reconstruct the otherwise buried shoreline angle elevations for the late Pleistocene marine terraces along the Wellington south coast, North Island New Zealand. Together with the age of formation of these shore platforms, uplift rates have been calculated across this region–at the southern Hikurangi subduction margin–since the late Pleistocene. In general, uplift rates are highest closest to the Hikurangi Trough, with 1.7 ± 0.1 mm/yr observed at the easternmost preserved terraces, near Cape Palliser, ~50 km from the trough. Uplift rates decreases steadily along the Palliser Bay coast to 0.2 ± 0.1 mm/yr at Wharekauhau, ~70 km from the trough. Further from the Hikurangi Trough, at distances >70 km, uplift rates increase again at Baring Head, on

the upfaulted side of the Wairarapa-Wharekauhau fault system, to between 0.7 ± 0.1 and 1.6 ± 0.2 mm/yr. At Tongue Point, west of Wellington, uplift rates across the Ōhāriu Fault are 0.2 ± 0.1 mm/yr (downthown side) and 0.6 ± 0.1 mm/yr (upthrown side) for the MIS 5e shore platform preserved there. The abrupt increases in uplift rates across the major upper-plate faults suggest that movement on these structures is a major contributor to tectonic uplift across this region. Dislocation and flexural-isostatic modelling shows that slip on faults within the overriding plate—specifically the Palliser-Kaiwhata Fault and the Wairarapa-Wharekauhau fault system—may dominate uplift in their immediate hanging walls. Depending on their slip rate and geometry, slip on these two upper-plate fault systems could plausibly cause >80% of late Pleistocene uplift along the entire length of the south coast of North Island; for example, at Tongue Point, uplift of both sides of the Ōhāriu Fault by ~0.35 mm/yr may be due to slip on the Wairarapa-Wharekauhau Fault System. Our modelling shows that subduction of the buoyant Hikurangi Plateau contributes uplift of 0.16 mm/yr which is broadly consistent with previous estimates. Earthquakes on the subduction interface probably contribute ≤0.4 mm/yr of late Pleistocene uplift, with ≤10% of uplift due to each earthquake being stored permanently, similar to other subduction zones. Uplift rates due to sediment underplating at Tongue Point and Wharekauhau are likely ≤0.4 mm/yr but could be significantly lower. These results highlight the complex processes driving uplift in subduction settings, and demonstrate the important contribution upper-plate faults can make to such uplift.

Data availability statement

The original contributions presented in the study are included in the article/Supplementary Material, further inquiries can be directed to the corresponding author.

Author contributions

DN, TL, and NL conceptualised the investigation and successfully applied for funding. DN undertook the strandline elevation reconstructions and uplift rate analysis, drafted the manuscript and produced figures. AH undertook the elastic dislocation modelling, produced associated text and figures and reviewed the manuscript. TL and NL supervised this investigation (DN's PhD), and contributed to, and edited the manuscript.

Funding

Earthquake Commission (EQC) Grant No. 09/U576.

Acknowledgments

The authors would like to thank Brad Pillans, John Begg and Tim Stern for helpful comments on an earlier version of this manuscript. We are grateful to our reviewers - Julius Jara-Muñoz for his constructive suggestions and Vasiliki Mouslopoulou for her feedback. Sincere thanks to our Handling Editor–Marco Meschis–for his guidance during the submission process. We appreciate the feedback of Camilla Penney on the modelling in this study. DN, TL, and NL would like to thank the Earthquake Commission for funding (Grant No. 09/U576) to undertake this investigation. NL and AH were supported by the New Zealand Ministry of Business, Innovation and Employment (MBIE) through the Te Riu a Maui Understanding Zealandia programme (Strategic Science Investment Fund, contract C05X1702), as well as the It's Our Fault Programme, funded by Toka Tū Ake EQC, Wellington City Council and the Wellington Regional Emergency Management Organisation.

Conflict of interest

The authors declare that the research was conducted in the absence of any commercial or financial relationships that could be construed as a potential conflict of interest.

Publisher's note

Supplementary material

The Supplementary Material for this article can be found online at: https://www.frontiersin.org/articles/10.3389/feart.2023.1028445/full#supplementary-material

References

Anderson, R. S., and Menking, K. M. (1994). The quaternary marine terraces of santa cruz, California: Evidence for coseismic uplift on two faults. *Geol. Soc. Am. Bull.* 106, 649–664. doi:10.1130/0016-7606(1994)106<0649:tqmtos>2.3.co;2

Authemayou, C., Pedoja, K., Heddar, A., Molliex, S., Boudiaf, A., Ghaleb, B., et al. (2017). Coastal uplift west of algiers (Algeria): Pre-and post-messinian sequences of marine terraces and rasas and their associated drainage pattern. *Int. J. Earth Sci.* 106 (1), 19–41. doi:10.1007/s00531-016-1292-5

Bard, E., Antonioli, F., and Silenzi, S. (2002). Sea-level during the penultimate interglacial period based on a submerged stalagmite from Argentarola Cave (Italy). *Earth Planet. Sci. Lett.* 196 (3), 135–146. doi:10.1016/s0012-821x(01)00600-8

Barnes, P. M. (2009). Postglacial (after 20 ka) dextral slip rate of the offshore Alpine fault, New Zealand. *Geology* 37 (1), 3–6.

Barnes, P. M., and Audru, J. C. (1999). Quaternary faulting in the offshore flaxbourne and Wairarapa basins, southern cook strait, New Zealand. *New zeal. J. Geol. geophys.* 42 (3), 349–367. doi:10.1080/00288306.1999.9514851

Barnes, P. M., Lamarche, G., Bialas, J., Henrys, S., Pecher, I., Netzeband, G. L., et al. (2010). Tectonic and geological framework for gas hydrates and cold seeps on the Hikurangi subduction margin, New Zealand. *Mar. Geol.* 272 (1–4), 26–48.

Barnes, P. M., Mercier de Lepinay, B., Collot, J-Y., Delteil, J., and Audru, J-C. (1998). Strain partitioning in the transition area between oblique subduction and continental

collision, Hikurangi margin, New Zealand. *Tectonics* 17, 534–557. doi:10.1029/98tc00974

Barnes, P. M., and Mercier de Lepinay, B. (1997). Rates and mechanics of rapid frontal accretion along the very obliquely convergent southern Hikurangi margin, New Zealand. *J. Geophys. Res.* 102 (B11), 24931–24952. doi:10.1029/97jb01384

Barnes, P. M., Nodder, S. D., Woelz, S., and Orpin, A. R. (2019). The structure and seismic potential of the Aotea and Evans Bay faults, Wellington, New Zealand. *J. Geol.* 62 (1), 46–71.

Beavan, J., and Darby, D. (2005). "Fault slip in the 1855 Wairarapa earthquake, based on new and reassessed vertical motion observations: Did slip occur on the subduction interface?," in *The 1855 Wairarapa earthquake symposium — proceedings volume* (Wellington: Greater Wellington Regional Council Publication Number: GW/RINV-T-05/205). ISBN: 0-909016-87-9.

Beavan, R. J., and Litchfield, N. J. (2012). *Vertical land movement around the New Zealand coastline: Implications for seasea-level rise*, 41. GNS Science Report 2012/29 https://shop.gns.cri.nz/sr_2012-029-pdf/.

Begg, J., and McSaveney, M. J. (2005). "Wairarapa Fault rupture – vertical deformation in 1855 and a history of similar events from Turakirae Head," in *The 1855 Wairarapa earthquake symposium — proceedings volume. Greater Wellington regional Council publication number: GW/RINV-T-05/205*. ISBN: 0-909016-87-9.

Begg, J. G., and Johnston, M. R. (2000). *Geology of the Wellington area. 1: 250 000 geological map 10*. Lower Hutt, New Zealand: Institute of Geological and Nuclear Sciences.

Begg, J. G., and Mazengarb, C. (1996). *Geology of the Wellington area. 1: 50,000 geological map 22*. Lower Hutt: Institute of Geological and Nuclear Sciences.

Berryman, K. (1993a). Age, height, and deformation of Holocene marine terraces at Mahia Peninsula, Hikurangi subduction margin, New Zealand. *Tectonics* 12 (6), 1347–1364. doi:10.1029/93tc01542

Berryman, K. R. (1993b). Distribution, age, and deformation of late Pleistocene marine terraces at Mahia Peninsula, Hikurangi subduction margin, New Zealand. *Tectonics* 12 (6), 1365–1379. doi:10.1029/93tc01543

Berryman, K., Ota, Y., Miyauchi, T., Hull, A., Clark, K., Ishibashi, K., et al. (2011). Holocene paleoseismic history of upper-plate faults in the southern Hikurangi subduction margin, New Zealand, deduced from marine terrace records. *Bull. Seismol. Soc. Am.* 101 (5), 2064–2087. doi:10.1785/0120100282

Berryman, K. R., Ota, Y., and Hull, A. G. (1989). Holocene paleoseismicity in the fold and thrust belt of the Hikurangi subduction zone, eastern North Island, New Zealand. *Tectonophysics* 163, 185–195. doi:10.1016/0040-1951(89)90256-4

Bookhagen, B., Echtler, H. P., Melnick, D., Strecker, M. R., and Spencer, J. Q. G. (2006). Using uplifted Holocene beach berms for paleoseismic analysis on the Santa María Island, south-central Chile. *Geophys. Res. Lett.* 33 (15), L15302. doi:10.1029/2006GL026734

Bradley, W. C., and Griggs, G. B. (1976). Form, Genesis, and deformation of central California wave-cut platforms. *Geol. Soc. Am. Bull.* 87 (3), 433–449. doi:10.1130/0016-7606(1976)87<433:fgadoc>2.0.co;2

Brideau, M-A., Massey, C. I., Carey, J. M., and Lyndsell, B. (2022). Geomechanical characterisation of discontinuous greywacke from the Wellington region based on laboratory testing. *New zeal. J. Geol. geophys.* 65 (2), 265–282. doi:10.1080/00288306.2020.1853181

Briggs, R. W., Sieh, K., Amidon, W. H., Galetzka, J., Prayudi, D., Suprihanto, I., et al. (2008). Persistent elastic behavior above a megathrust rupture patch: Nias island, West Sumatra. *J. Geophys. Res.* 113 (B12), B12406. doi:10.1029/2008JB005684

Briggs, R. W., Sieh, K., Meltzner, A. J., Natawidjaja, D., Galetzka, J., Suwargadi, B., et al. (2006). Deformation and slip along the Sunda megathrust in the great 2005 Nias-Simeulue earthquake. *Science* 311 (5769), 1897–1901. doi:10.1126/science.1122602

Carver, G. A., Jayko, A. S., Valentine, D. W., and Li, W. H. (1994). Coastal uplift associated with the 1992 Cape Mendocino earthquake, northern California. *Geology* 22 (3), 195–198. doi:10.1130/0091-7613(1994)022<0195:cuawtc>2.3.co;2

Chappell, J. (1974). Geology of coral terraces, Huon Peninsula, new Guinea: A study of quaternary tectonic movements and sea-level changes. *Geol. Soc. Am. Bull.* 85 (4), 553–570. doi:10.1130/0016-7606(1974)85<553:gocthp>2.0.co;2

Chappell, J., Omura, A., Esat, T., McCulloch, M., Pandolfi, J., Ota, Y., et al. (1996). Reconciliaion of late Quaternary sea levels derived from coral terraces at Huon Peninsula with deep sea oxygen isotope records. *Earth Planet. Sci. Lett.* 141 (1-4), 227–236. doi:10.1016/0012-821x(96)00062-3

Chappell, J. (2002). Sea level changes forced ice breakouts in the last glacial cycle: New results from coral terraces. *Quat. Sci. Rev.* 21 (10), 1229–1240. doi:10.1016/s0277-3791(01)00141-x

Clark, K., Howarth, J., Litchfield, N., Cochran, U., Turnbull, J., Dowling, L., et al. (2019). Geological evidence for past large earthquakes and tsunamis along the Hikurangi subduction margin, New Zealand. *Mar. Geol.* 412, 139–172. doi:10.1016/j.margeo.2019.03.004

Clark, K. J., Hayward, B. W., Cochran, U. A., Grenfell, H. R., Hemphill–Haley, E., Mildenhall, D. C., et al. (2011). Investigating subduction earthquake geology along the southern Hikurangi margin using palaeoenvironmental histories of intertidal inlets. *New zeal. J. Geol. geophys.* 54 (3), 255–271. doi:10.1080/00288306.2011.562903

Clark, K. J., Hayward, B. W., Cochran, U. A., Wallace, L. M., Power, W. L., and Sabaa, A. T. (2015). Evidence for past subduction earthquakes at a plate boundary with widespread upper plate faulting: Southern Hikurangi margin, New Zealand. *Bull. Seismol. Soc. Am.* 105, 1661–1690. doi:10.1785/0120140291

Clark, K. J., Nissen, E. K., Howarth, J. D., Hamling, I. J., Mountjoy, J. J., Ries, W. F., et al. (2017). Highly variable coastal deformation in the 2016 MW7.8 Kaikōura earthquake reflects rupture complexity along a transpressional plate boundary. *Earth Planet. Sci. Lett.* 474, 334–344. doi:10.1016/j.epsl.2017.06.048

Clement, A. J., Whitehouse, P. L., and Sloss, C. R. (2016). An examination of spatial variability in the timing and magnitude of Holocene relative sea-level changes in the New Zealand archipelago. *Quat. Sci. Rev.* 131, 73–101. doi:10.1016/j.quascirev.2015.09.025

Cochran, U., Hannah, M., Harper, M., Van Dissen, R., Berryman, K., and Begg, J. (2007). Detection of large, Holocene earthquakes using diatom analysis of coastal sedimentary sequences, Wellington, New Zealand. *Quat. Sci. Rev.* 26 (7), 1129–1147. doi:10.1016/j.quascirev.2007.01.008

Cohen, S. C., and Darby, D. J. (2003). Tectonic plate coupling and elastic thickness derived from the inversion of a steady state viscoelastic model using geodetic data: Application to southern North Island, New Zealand. *J. Geophys. Res.* 108 (B3), 2164. doi:10.1029/2001JB001687

Creveling, J. R., Mitrovica, J. X., Clark, P. U., Waelbroeck, C., and Pico, T. (2017). Predicted bounds on peak global mean sea level during marine isotope stages 5a and 5c. *Quat. Sci. Rev.* 163, 193–208. doi:10.1016/j.quascirev.2017.03.003

Darby, D., and Beavan, J. (2001). Evidence from GPS measurements for contemporary interplate coupling on the southern Hikurangi subduction thrust and for partitioning of strain in the upper plate. *J. Geophys. Res.* 106 (12), 30881–30891. doi:10.1029/2000jb000023

Darby, D. J., and Beanland, S. (1992). Possible source models for the 1855 Wairarapa earthquake, New Zealand. *J. Geophys. Res.* 97 (B9), 12375–12389. doi:10.1029/92jb00567

Davy, B., and Wood, R. (1994). Gravity and magnetic modelling of the Hikurangi Plateau. *Mar. Geol.* 118 (1-2), 139–151. doi:10.1016/0025-3227(94)90117-1

De Gelder, G., Jara-Muñoz, J., Melnick, D., Fernández-Blanco, D., Rouby, H., Pedoja, K., et al. (2020). How do sea-level curves influence modeled marine terrace sequences? *Quat. Sci. Rev.* 229, 106132. doi:10.1016/j.quascirev.2019.106132

DeMets, C., Gordon, R. G., and Argus, D. F. (2010). Geologically current plate motions. *Geophys. J. Int.* 181 (1), 1–80. doi:10.1111/j.1365-246x.2009.04491.x

DeMets, C., Gordon, R. G., Argus, D. F., and Stein, S. (1990). Current plate motions. *Geophys. J. Int.* 101, 425–478. doi:10.1111/j.1365-246x.1990.tb06579.x

DeMets, C., Gordon, R. G., Argus, D. F., and Stein, S. (1994). Effect of recent revisions to the geomagnetic reversal time scale on estimates of current plate motions. *Geophys. Res. Lett.* 21, 2191–2194. doi:10.1029/94gl02118

Downes, G. L. (2005). "The 1855 January 23 M8+ Wairarapa Earthquake – what contemporary accounts tell us about it," in *The 1855 Wairarapa earthquake symposium — proceedings volume* (Wellington: Greater Wellington Regional Council Publication Number: GW/RINV-T-05/205). ISBN: 0-909016-87-9.

Duffy, B. (2020). A geometric model to estimate slip rates from terrace rotation above an offshore, listric thrust fault, Kaikōura, New Zealand. *Tectonophysics* 786, 228460. doi:10.1016/j.tecto.2020.228460

Dumas, J. A., Flato, G. M., and Brown, R. D. (2006). Future projections of landfast ice thickness and duration in the Canadian Arctic. *J. Clim.* 19 (20), 5175–5189. doi:10.1175/jcli3889.1

Dutton, A., and Lambeck, K. (2012). Ice volume and sea level during the last interglacial. *Science* 337 (6091), 216–219. doi:10.1126/science.1205749

Evanzia, D., Lamb, S., Savage, M. K., and Stern, T. (2019). Illumination of deformation by bending stresses and slab pull within the southern Hikurangi double benioff zone. *New zeal. J. Geol. geophys.* 62 (1), 111–120. doi:10.1080/00288306.2018.1532439

Furlong, K. P., and Herman, M. (2017). Reconciling the deformational dichotomy of the 2016 Mw 7.8 Kaikoura New Zealand earthquake. *Geophys. Res. Lett.* 44 (13), 6788–6791. doi:10.1080/00288306.2018.1532439

Gardner, T. (2011). "Late Holocene deformation, fold, growth and the seismic cycle, Kaikōura peninsular, South Island, New Zealand," in *GSA annual meeting in minneapolis*.

Ghani, M. A. (1978). Late Cenozoic vertical crustal movements in the southern North Island, New Zealand. *New zeal. J. Geol. geophys.* 21 (1), 117–125. doi:10.1080/00288306.1978.10420728

Ghani, M. A. (1974). *Late Cenozoic vertical crustal movements in the southern North Island, New Zealand. Dissertation thesis*. Wellington, New Zealand: Victoria University of Wellington.

Gibb, J. G. (1986). "A New Zealand regional Holocene eustatic sea-level curve and its application to determination of vertical tectonic movements," in *Recent Crustal Movements of the Pacific Region*. Editors W. I. Reilly and B. E. Harford 24, 377–395.

Grant, K. M., Rohling, E. J., Bar-Matthews, M., Ayalon, A., Medina-Elizalde, M., Ramsey, C. B., et al. (2012). Rapid coupling between ice volume and polar temperature over the past 150,000 years. *Nature* 491 (7426), 744–747. doi:10.1038/nature11593

Grant, K. M., Rohling, E. J., Ramsey, C. B., Cheng, H., Edwards, R. L., Florindo, F., et al. (2014). Sea-level variability over five glacial cycles. *Nat. Comm.* 5, 5076. doi:10.1038/ncomms6076

Grantz, A., Plafker, G., and Kachadoorian, R. (1964). *Alaska's good friday earthquake, march 27, 1964: A preliminary geologic evaluation*, 491. Washington, D.C., United States: US Department of the Interior, Geological Survey.

Hamling, I. J., Hreinsdóttir, S., Clark, K., Elliott, J., Liang, C., Fielding, E., et al. (2017). Complex multifault rupture during the 2016 M_w 7.8 Kaikōura earthquake, New Zealand. *Science* 356 (6334), eaam7194. doi:10.1126/science.aam7194

Hamling, I. J., Wright, T. J., Hreinsdóttir, S., and Wallace, L. M. (2022). A snapshot of New Zealand's dynamic deformation field from Envisat InSAR and GNSS observations between 2003 and 2011. *Geophys. Res. Lett.* 49 (2), e2021GL096465. doi:10.1029/2021gl096465

Henrys, S., Wech, A., Sutherland, R., Stern, T., Savage, M., Sato, H., et al. (2013). SAHKE geophysical transect reveals crustal and subduction zone structure at the southern Hikurangi margin, New Zealand. *Geochem. Geophys. Geosyst.* 14 (7), 2063–2083. doi:10.1002/ggge.20136

Herath, P., Stern, T. A., Savage, M. K., Bassett, D., Henrys, S., and Boulton, C. (2020). Hydration of the crust and upper mantle of the Hikurangi Plateau as it subducts at the southern Hikurangi margin. *Earth Planet. Sci. Lett.* 541, 116271. doi:10.1016/j.epsl.2020.116271

Houlié, N., and Stern, T. A. (2017). Vertical tectonics at an active continental margin. *Earth Planet. Sci. Lett.* 457, 292–301. doi:10.1016/j.epsl.2016.10.018

Howell, A., and Clark, K. J. (2022). Late Holocene coseismic uplift of the Kaikōura coast, New Zealand. *Geosphere* 18 (3), 1104–1137. doi:10.1130/ges02479.1

Hull, A. G. (1990). Tectonics of the 1931 Hawke's Bay earthquake. *New zeal. J. Geol. geophys.* 33, 309–320. doi:10.1080/00288306.1990.10425689

Jara-Muñoz, J., Melnick, D., Li, S., Socquet, A., Cortés-Aranda, J., Brill, D., et al. (2022). The cryptic seismic potential of the Pichilemu blind fault in Chile revealed by off-fault geomorphology. *Nat. Comm.* 13, 3371. doi:10.1038/s41467-022-30754-1

Jara-Muñoz, J., Melnick, D., Pedoja, K., and Strecker, M. R. (2019). TerraceM-2: A Matlab® interface for mapping and modeling marine and lacustrine terraces. *Front. Earth Sci.* 7, 1–18. doi:10.3389/feart.2019.00255

Jara-Muñoz, J., Melnick, D., and Strecker, M. R. (2016). TerraceM: A MATLAB® tool to analyze marine and lacustrine terraces using high-resolution topography. *Geosphere* 12, 176–195. doi:10.1130/ges01208.1

Jara-Muñoz, J., Melnick, D., Zambrano, P., Rietbrock, A., González, J., Argandoña, B., et al. (2017). Quantifying offshore fore-arc deformation and splay-fault slip using drowned Pleistocene shorelines, Arauco Bay, Chile. *J. Geophys. Res.* 122 (6), 4529–4558. doi:10.1002/2016jb013339

Jolivet, R., Simons, M., Duputel, Z., Olive, J. A., Bhat, H. S., and Bletery, Q. (2020). Interseismic loading of subduction megathrust drives long-term uplift in northern Chile. *Geophys. Res. Lett.* 47 (8), e2019GL085377. doi:10.1029/2019gl085377

Kamp, P. J. (1999). Tracking crustal processes by FT thermochronology in a forearc high (Hikurangi margin, New Zealand) involving Cretaceous subduction termination and mid-Cenozoic subduction initiation. *Tectonophysics* 307 (3), 313–343. doi:10.1016/s0040-1951(99)00102-x

Karymbalis, E., Tsanakas, K., Tsodoulos, I., Gaki-Papanastassiou, K., Papanastassiou, D., Batzakis, D. V., et al. (2022). Late quaternary marine terraces and tectonic uplift rates of the broader neapolis area (SE peloponnese, Greece). *J. Mar. Sci. Eng.* 10 (1), 99. doi:10.3390/jmse10010099

Kopp, R. E., Simons, F. J., Mitrovica, J. X., Maloof, A. C., and Oppenheimer, M. (2009). Probabilistic assessment of sea level during the last interglacial stage. *Nature* 462 (7275), 863–867. doi:10.1038/nature08686

Lajoie, K. R. (1986). *Coastal tectonics" in studies in geophysics, active tectonics*. Washington, D.C., United States: National Academy Press, 95–124.

Lambeck, K., and Nakada, M. (1992). Constraints on the age and duration of the last interglacial period and on sea-level variations. *Nature* 357 (6374), 125–128. doi:10.1038/357125a0

Lambeck, K. (2004). sea-level change through the last glacial cycle: Geophysical, glaciological and palaeogeographic consequences. *Comptes Rendus Geosci.* 336, 677–689. doi:10.1016/j.crte.2003.12.017

Langridge, R., Van Dissen, R., Rhoades, D., Villamor, P., Little, T., Litchfield, N., et al. (2011). Five thousand years of surface ruptures on the Wellington Fault, New Zealand: Implications for recurrence and fault segmentation. *Bull. Seismol. Soc. Am.* 101 (5), 2088–2107. doi:10.1785/0120100340

Li, W. X., Lundberg, J., Dickin, A. P., Ford, D. C., Schwarcz, H. P., McNutt, R., et al. (1989). High-precision mass-spectrometric uranium-series dating of cave deposits and implications for palaeoclimate studies. *Nature* 339, 534–536. doi:10.1038/339534a0

Lisiecki, L. E., and Raymo, M. E. (2005). A Pliocene-Pleistocene stack of 57 globally distributed benthic 18O records. *Paleoceanography* 20, PA1003. doi:10.1029/2004PA001071

Litchfield, N., Ellis, S., Berryman, K., and Nicol, A. (2007). Insights into subduction-related uplift along the Hikurangi Margin, New Zealand, using numerical modeling. *J. Geophys. Res.* 112, F02021. doi:10.1029/2006JF000535

Litchfield, N. J., Howell, A., Clark, K. J., and Coffey, G. (2021). *It's Our Fault Hikurangi subduction zone hazard: South Palliser Bay Holocene marine terraces*. Lower Hutt (NZ): GNS Science, 47. GNS Science report; 2021/28). doi:10.21420/8VDN-AE32

Litchfield, N. J., and Clark, K. J. (2015). Fluvial terrace formation in the lower awhea and pahaoa river valleys, New Zealand: Implications for tectonic and sea-level controls. *Geomorphology* 231, 212–228. doi:10.1016/j.geomorph.2014.12.009

Litchfield, N. J., Van Dissen, R., Sutherland, R., Barnes, P. M., Cox, S. C., Norris, R., et al. (2014). A model of active faulting in New Zealand. *New zeal. J. Geol. geophys.* 57 (1), 32–56. doi:10.1080/00288306.2013.854256

Litchfield, N., Morgenstern, R., Clark, K., Howell, A., Grant, G., and Turnbull, J. (2022). Holocene marine terraces as recorders of earthquake uplift: Insights from a rocky coast in southern Hawke's Bay, New Zealand. *Earth Surf. Process. Landforms* 48, 452–474. doi:10.1002/esp.5496

Little, T. A., Van Dissen, R., Rieser, U., Smith, E. G., and Langridge, R. M. (2010). Coseismic strike slip at a point during the last four earthquakes on the Wellington fault near Wellington, New Zealand. *J. Geophys. Res. Solid Earth* 115 (B5), B05403. doi:10.1029/2009jb006589

Little, T. A., Van Dissen, R., Schermer, E., and Carne, R. (2009). Late Holocene surface ruptures on the southern Wairarapa fault, New Zealand: Link between earthquakes and the uplifting of beach ridges on a rocky coast. *Lithosphere* 1 (1), 4–28.

Marshall, J. S., and Anderson, R. S. (1995). Quaternary uplift and seismic cycle deformation, Peninsula de Nicoya, Costa Rica. *Geol. Soc. Am. Bull.* 107 (4), 463–473.

Matsu'ura, T. (2015). Late Quaternary uplift rate inferred from marine terraces, Muroto Peninsula, southwest Japan: Forearc deformation in an oblique subduction zone. *Geomorphology* 234, 133–150. doi:10.1016/j.geomorph.2015.01.012

McCulloch, M. T., and Esat, T. (2000). The coral record of last interglacial sea levels and sea surface temperatures. *Chem. Geol.* 169 (1), 107–129. doi:10.1016/s0009-2541(00)00260-6

McKenzie, K. A., Kelsey, H. M., Kirby, E., Rittenour, T. M., and Furlong, K. P. (2022). Differential coastal uplift quantified by luminescence dating of marine terraces, central Cascadia forearc, Oregon. *Quat. Sci. Rev.* 298, 107853. doi:10.1016/j.quascirev.2022.107853

McSaveney, M. J., Graham, I. J., Begg, J. G., Beu, A. G., Hull, A. G., Kim, K., et al. (2006). Late Holocene uplift of beach ridges at Turakirae Head, south Wellington coast, New Zealand. *New zeal. J. Geol. geophys.* 49 (3), 337–358. doi:10.1080/00288306.2006.9515172

Melnick, D. (2016). Rise of the central Andean coast by earthquakes straddling the Moho. *Nat. Geosci.* 9 (5), 401–407. doi:10.1038/ngeo2683

Merritts, D., and Bull, W. B. (1989). Interpreting Quaternary uplift rates at the Mendocino triple junction, northern California, from uplifted marine terraces. *Geology* 17 (11), 1020–1024. doi:10.1130/0091-7613(1989)017<1020:iqurat>2.3.co;2

Merritts, D. J. (1996). The Mendocino triple junction: Active faults, episodic coastal emergence, and rapid uplift. *J. Geophys. Res.* 101 (B3), 6051–6070. doi:10.1029/95jb01816

Meschis, M., Roberts, G. P., Robertson, J., Mildon, Z. K., Sahy, D., Goswami, R., et al. (2022). Out of phase Quaternary uplift-rate changes reveal normal fault interaction, implied by deformed marine palaeoshorelines. *Geomorphology* 416, 108432. doi:10.1016/j.geomorph.2022.108432

Mildenhall, D. C. (1995). Pleistocene palynology of the petone and seaview drillholes, petone, lower Hutt valley, North Island, New Zealand. *J. Roy. Soc. N. Z.* 25 (2), 207–262. doi:10.1080/03014223.1995.9517488

Mountjoy, J. J., and Barnes, P. M. (2011). Active upper plate thrust faulting in regions of low plate interface coupling, repeated slow slip events, and coastal uplift: Example from the Hikurangi Margin, New Zealand. *Geochem. Geophys. Geosyst.* 12 (1). doi:10.1029/2010gc003326

Mountjoy, J. J., Barnes, P. M., and Pettinga, J. R. (2009). Morphostructure and evolution of submarine canyons across an active margin: Cook Strait sector of the Hikurangi Margin, New Zealand. *Mar. Geol.* 260 (1-4), 45–68. doi:10.1016/j.margeo.2009.01.006

Mouslopoulou, V., Oncken, O., Hainzl, S., and Nicol, A. (2016). Uplift rate transients at subduction margins due to earthquake clustering. *Tectonics* 35, 2370–2384. doi:10.1002/2016TC004248

Mouslopoulou, V., Saltogianni, V., Nicol, A., Oncken, O., Begg, J., Babeyko, A., et al. (2019). Breaking a subduction-termination from top to bottom: The large 2016 Kaikōura earthquake, New Zealand. *Earth Planet Sci. Lett.* 506, 221–230. doi:10.1016/j.epsl.2018.10.020

Muhs, D. R., Kelsey, H. M., Miller, G. H., Kennedy, G. L., Whelan, J. F., and McInelly, G. W. (1990). Age estimates and uplift rates for late Pleistocene marine terraces' Southern Oregon portion of the Cascadia forearc. *J. Geophys. Res.* 95 (B5), 6685–6698. doi:10.1029/jb095ib05p06685

Muhs, D. R., Rockwell, T. K., and Kennedy, G. L. (1992). Late Quaternary uplift rates of marine terraces on the Pacific coast of North America, southern Oregon to Baja California Sur. *Quat. Int.* 15, 121–133. doi:10.1016/1040-6182(92)90041-y

Murray, M. H., Marshall, G. A., Lisowski, M., and Stein, R. S. (1996). The 1992 M= 7 Cape Mendocino, California, earthquake: Coseismic deformation at the south end of the Cascadia megathrust. *J. Geophys. Res.* 101 (B8), 17707–17725. doi:10.1029/95jb02623

Nelson, A. R., and Manley, W. F. (1992). Holocene coseismic and aseismic uplift of Isla Mocha, south-central Chile. *Quat. Int.* 15, 61–76. doi:10.1016/1040-6182(92)90036-2

Neumann, A. C., and Hearty, P. J. (1996). Rapid sea-level changes at the close of the last interglacial (substage 5e) recorded in Bahamian island geology. *Geology* 24 (9), 775–778. doi:10.1130/0091-7613(1996)024<0775:rslcat>2.3.co;2

Nicol, A., and Beavan, J. (2003). Shortening of an overriding plate and its implications for slip on a subduction thrust, central Hikurangi Margin, New Zealand. *Tectonics* 22 (6). doi:10.1029/2003tc001521

Nicol, A., Begg, J., Saltogianni, V., Mouslopoulou, V., Oncken, O., and Howell, A. (2022). Uplift and fault slip during the 2016 Kaikōura earthquake and late quaternary, Kaikōura Peninsula, New Zealand. *New zeal. J. Geol. geophys.*, 1–16. doi:10.1080/00288306.2021.2021955

Nicol, A., Mazengarb, C., Chanier, F., Rait, G., Uruski, C., and Wallace, L. (2007). Tectonic evolution of the active Hikurangi subduction margin, New Zealand, since the Oligocene. *Tectonics* 26 (4). doi:10.1029/2006tc002090

Nicol, A., Van Dissen, R., Vella, P., Alloway, B., and Melhuish, A. (2002). Growth of contractional structures during the last 10 m.y. at the southern end of the emergent Hikurangi forearc basin, New Zealand. *New Zeal. J. Geol. Geophys.* 45 (3), 365–385. doi:10.1080/00288306.2002.9514979

Ninis, D., Little, T. A., Van Dissen, R. J., Litchfield, N. J., Smith, E. G., Wang, N., et al. (2013). Slip rate on the Wellington Fault, New Zealand, during the late quaternary: Evidence for variable slip during the Holocene. *Bull. Seismol. Soc. Am.* 103 (1), 559–579. doi:10.1785/0120120162

Ninis, D., Little, T., Litchfield, N., Wang, N., Jacobs, K., and Henderson, C. M. (2022). Pleistocene marine terraces of the Wellington south coast–their distribution across multiple active faults at the southern Hikurangi subduction margin, Aotearoa New Zealand. *New zeal. J. Geol. geophys.* 65 (1), 242–263. doi:10.1080/00288306.2021.2011329

Nodder, S. D., Lamarche, G., Proust, J. N., and Stirling, M. (2007). Characterizing earthquake recurrence parameters for offshore faults in the low-strain, compressional Kapiti-Manawatu Fault System, New Zealand. *J. Geophys. Res. Solid Earth* 112 (B12).

O'Leary, M. J., Hearty, P. J., and McCulloch, M. T. (2008). Geomorphic evidence of major sea-level fluctuations during marine isotope substage-5e, Cape Cuvier, Western Australia. *Geomorphology* 102 (3), 595–602. doi:10.1016/j.geomorph.2008.06.004

Okada, Y. (1985). Surface deformation due to shear and tensile faults in a half-space. *Bull. Seismol. Soc. Am.* 75 (4), 1135–1154. doi:10.1785/BSSA0750041135

Ota, Y., Hull, A. G., and Berryman, K. R. (1991). Coseismic uplift of Holocene marine terraces in the pakarae river area, eastern North Island, New Zealand. *Quat. Res.* 35 (3), 331–346. doi:10.1016/0033-5894(91)90049-b

Ota, Y., Pillans, B., Berryman, K., Beu, A., Fujimori, T., Miyauchi, T., et al. (1996). Pleistocene coastal terraces of Kaikōura Peninsula and the marlborough coast, South Island, New Zealand. *New zeal. J. Geol. geophys.* 39 (1), 51–73. doi:10.1080/00288306.1996.9514694

Ota, Y., Williams, D. N., and Berryman, K. R. (1981). *Late quaternary tectonic map of New Zealand 1:50,000 parts sheets Q27, R27 and R28*. Lower Hutt: New Zealand Geological Survey.

Pedoja, K., Ortlieb, L., Dumont, J. F., Lamothe, M., Ghaleb, B., Auclair, M., et al. (2006). Quaternary coastal uplift along the Talara Arc (Ecuador, Northern Peru) from new marine terrace data. *Mar. Geol.* 228 (1-4), 73–91. doi:10.1016/j.margeo.2006.01.004

Pillans, B. (1990). Pleistocene marine terraces in New Zealand: A review. *New zeal. J. Geol. geophys.* 33 (2), 219–231. doi:10.1080/00288306.1990.10425680

Pizer, C., Clark, K., Howarth, J., Garrett, E., Wang, X., Rhoades, D., et al. (2021). Paleotsunamis on the southern Hikurangi subduction zone, New Zealand, show regular recurrence of large subduction earthquakes. *Seismic Rec.* 1 (2), 75–84. doi:10.1785/0320210012

Plafker, G. (1972). Alaskan earthquake of 1964 and Chilean earthquake of 1960: Implications for arc tectonics. *J. Geophys. Res.* 77 (5), 901–925. doi:10.1029/jb077i005p00901

Plafker, G. (1965). Tectonic deformation associated with the 1964 Alaska earthquake. *Science* 148 (3678), 1675–1687. doi:10.1126/science.148.3678.1675

Pondard, N., and Barnes, P. M. (2010). Structure and paleoearthquake records of active submarine faults, Cook Strait, New Zealand: Implications for fault interactions, stress loading, and seismic hazard. *J. Geophys. Res. Solid Earth* 115 (B12).

Potter, E. K., Esat, T. M., Schellmann, G., Radtke, U., Lambeck, K., and McCulloch, M. T. (2004). Suborbital-period sea-level oscillations during marine isotope substages 5a and 5c. *Earth Planet. Sci. Lett.* 225 (1), 191–204. doi:10.1016/j.epsl.2004.05.034

Potter, E. K., and Lambeck, K. (2004). Reconciliation of sea-level observations in the Western North Atlantic during the last glacial cycle. *Earth Planet Sci. Lett.* 217 (1), 171–181. doi:10.1016/s0012-821x(03)00587-9

Reyners, M., Eberhart-Phillips, D., Stuart, G., and Nishimura, Y. (2006). Imaging subduction from the trench to 300 km depth beneath the central North Island, New Zealand, with vp and vp/vs. *Geophys. J. Int.* 165 (2), 565–583. doi:10.1111/j.1365-246x.2006.02897.x

Reyners, M. (1998). Plate coupling and the hazard of large subduction thrust earthquakes at the Hikurangi subduction zone, New Zealand. *New zeal. J. Geol. geophys.* 41, 343–354. doi:10.1080/00288306.1998.9514815

Robinson, R., Van Dissen, R., and Litchfield, N. (2011). Using synthetic seismicity to evaluate seismic hazard in the Wellington region, New Zealand. *Geophys. J. Int.* 187 (1), 510–528. doi:10.1111/j.1365-246x.2011.05161.x

Rohling, E. J., Grant, K., Hemleben, C. H., Siddall, M., Hoogakker, B. A. A., Bolshaw, M., et al. (2008). High rates of sea-level rise during the last interglacial period. *Nat. Geosci.* 1 (1), 38–42. doi:10.1038/ngeo.2007.28

Saillard, M., Hall, S. R., Audin, L., Farber, D. L., Regard, V., and Hérail, G. (2011). Andean coastal uplift and active tectonics in southern Peru: ^{10}Be surface exposure dating of differentially uplifted marine terrace sequences (san juan de Marcona, ~15.4°S). *Geomorphology* 128 (3), 178–190. doi:10.1016/j.geomorph.2011.01.004

Schermer, E. R., Little, T. A., and Rieser, U. (2009). Quaternary deformation along the Wharekauhau fault system, North Island, New Zealand: Implications for an unstable linkage between active strike-slip and thrust faults. *Tectonics* 28 (6), TC6008. doi:10.1029/2008TC002426

Seebeck, H., Van Dissen, R., Litchfield, N., Barnes, P., Nicol, A., Langridge, R., et al. (2022). *New Zealand community Fault Model – version 1.0. Lower Hutt (NZ): GNS science*, 96. (GNS Science report; 2021/57). doi:10.21420/GA7S-BS61

Siddall, M., Chappell, J., and Potter, E-K. (2007). 7. Eustatic sea level during past interglacials. *Dev. Quat. Sci.* 7, 75–92.

Stirling, C. H., Esat, T. M., Lambeck, K., and McCulloch, M. T. (1998). Timing and duration of the last interglacial: Evidence for a restricted interval of widespread coral reef growth. *Earth Planet. Sci. Lett.* 160 (3), 745–762. doi:10.1016/s0012-821x(98)00125-3

Stirling, M., McVerry, G., Gerstenberger, M., Litchfield, N., Van Dissen, R., Berryman, K., et al. (2012). National seismic hazard model for New Zealand: 2010 update. *Bull. Seismol. Soc. Am.* 102 (4), 1514–1542. doi:10.1785/0120110170

Subarya, C., Chlieh, M., Prawirodirdjo, L., Avouac, J. P., Bock, Y., Sieh, K., et al. (2006). Plate-boundary deformation associated with the great Sumatra–Andaman earthquake. *Nature* 440 (7080), 46–51. doi:10.1038/nature04522

Thompson, W. G., Curran, H. A., Wilson, M. A., and White, B. (2011). Sea-level oscillations during the last interglacial highstand recorded by Bahamas corals. *Nat. Geosci.* 4 (10), 684–687. doi:10.1038/ngeo1253

Thompson, W. G., and Goldstein, S. L. (2005). Open-system coral ages reveal persistent suborbital sea-level cycles. *Science* 308 (5720), 401–404. doi:10.1126/science.1104035

Tozer, B., Stern, T. A., Lamb, S. L., and Henrys, S. A. (2017). Crust and upper-mantle structure of Wanganui Basin and southern Hikurangi margin, North Island, New Zealand as revealed by active source seismic data. *Geophys. J. Int.* 211 (2), 718–740. doi:10.1093/gji/ggx303

Van Dissen, R. J., Berryman, K. R., Pettinga, J. R., and Hill, N. L. (1992). Paleoseismicity of the wellington-hutt valley segment of the Wellington Fault, North Island, New Zealand. *N. Z. J. Geol. Geophys.* 35 (2), 165–176. doi:10.1080/00288306.1992.9514511

Van Dissen, R., and Yeats, R. S. (1991). Hope fault, Jordan thrust, and uplift of the seaward Kaikoura Range, New Zealand. *Geology* 19 (4), 393–396. doi:10.1130/0091-7613(1991)019<0393:hfjtau>2.3.co;2

Vigny, C., Socquet, A., Peyrat, S., Ruegg, J. C., Métois, M., Madariaga, R., et al. (2011). The 2010 M_w 8.8 Maule megathrust earthquake of Central Chile, monitored by GPS. *Science* 332 (6036), 1417–1421. doi:10.1126/science.1204132

Walcott, R. I. (1984). The kinematics of the plate boundary zone through New Zealand: A comparison of short-and long-term deformations. *Geophys. J. Int.* 79 (2), 613–633. doi:10.1111/j.1365-246x.1984.tb02244.x

Wallace, L. M., Barnes, P., Beavan, J., Van Dissen, R. J., Litchfield, N. J., Mountjoy, J., et al. (2012). The kinematics of a transition from subduction to strike-slip: An example from the central New Zealand plate boundary. *J. Geophys. Res.* 117, B11402. doi:10.1029/2011JB008640

Wallace, L. M., Beavan, J., McCaffrey, R., Berryman, K., and Denys, P. (2007). Balancing the plate motion budget in the South Island, New Zealand using GPS, geological and seismological data. *Geophys. J. Int.* 168 (1), 332–352. doi:10.1111/j.1365-246x.2006.03183.x

Wallace, L. M., Beavan, J., McCaffrey, R., and Darby, D. (2004). Subduction zone coupling and tectonic block rotations in the North Island, New Zealand. *J. Geophys. Res.* 109, B12406. doi:10.1029/2004JB003241

Wallace, L. M., Hreinsdóttir, S., Ellis, S., Hamling, I., D'Anastasio, E., and Denys, P. (2018). Triggered slow slip and afterslip on the southern Hikurangi subduction zone following the Kaikōura earthquake. *Geophys. Res. Lett.* 45 (10), 4710–4718. doi:10.1002/2018gl077385

Wallace, L. M., Reyners, M., Cochran, U., Bannister, S., Barnes, P. M., Berryman, K., et al. (2009). Characterizing the seismogenic zone of a major plate boundary subduction thrust: Hikurangi Margin, New Zealand. *Geochem. Geophys. Geosyst.* 10 (10). doi:10.1029/2009gc002610

Wallace, L. M. (2020). Slow slip events in New Zealand. *Ann. Rev. Earth Planet. Sci.* 48, 175–203. doi:10.1146/annurev-earth-071719-055104

Wang, T., Wei, S., Shi, X., Qiu, Q., Li, L., Peng, D., et al. (2018). The 2016 Kaikōura earthquake: Simultaneous rupture of the subduction interface and overlying faults. *Earth Planet. Sci. Lett.* 482, 44–51. doi:10.1016/j.epsl.2017.10.056

Watts, A. B., Zhong, S. J., and Hunter, J. (2013). The behavior of the lithosphere on seismic to geologic timescales. *Ann. Rev. Earth Planet. Sci.* 41 (1), 443–468. doi:10.1146/annurev-earth-042711-105457

Wesson, R. L., Melnick, D., Cisternas, M., Moreno, M., and Ely, L. L. (2015). Vertical deformation through a complete seismic cycle at Isla Santa María, Chile. *Nat. Geosci.* 8 (7), 547–551. doi:10.1038/ngeo2468

Wickert, A. D. (2016). Open-source modular solutions for flexural isostasy: gFlex v1.0. *Geosci. Model. Dev.* 9, 997–1017. doi:10.5194/gmd-9-997-2016

Williams, C. A., Eberhart-Phillips, D., Bannister, S., Barker, D. H., Henrys, S., Reyners, M., et al. (2013). Revised interface geometry for the Hikurangi subduction zone, New Zealand. *Seismol. Res. Lett.* 84 (6), 1066–1073. doi:10.1785/0220130035

Wilson, K., Berryman, K., Cochran, U., and Little, T. (2007b). Holocene coastal evolution and uplift mechanisms of the northeastern Raukumara Peninsula, North Island, New Zealand. *Quat. Sci. Rev.* 26 (7), 1106–1128. doi:10.1016/j.quascirev.2007.01.005

Wilson, K., Litchfield, N., Berryman, K., and Little, T. (2007a). Distribution, age, and uplift patterns of Pleistocene marine terraces of the northern Raukumara Peninsula, North Island, New Zealand. *New zeal. J. Geol. geophys.* 50 (3), 181–191. doi:10.1080/00288300709509830

Yildirim, C., Melnick, D., Ballato, P., Schildgen, T. F., Echtler, H., Erginal, A. E., et al. (2013). Differential uplift along the northern margin of the central anatolian plateau: Inferences from marine terraces. *Quat. Sci. Rev.* 81, 12–28. doi:10.1016/j.quascirev.2013.09.011

Zazo, C., Goy, J. L., Dabrio, C. J., Bardajı´, T., Hillaire-Marcel, C., Ghaleb, B., et al. (2003). Pleistocene raised marine terraces of the Spanish mediterranean and atlantic coasts: Records of coastal uplift, sea-level highstands and climate changes. *Mar. Geol.* 194 (1), 103–133. doi:10.1016/s0025-3227(02)00701-6

frontiers | Frontiers in Earth Science

TYPE Brief Research Report
PUBLISHED 17 April 2023
DOI 10.3389/feart.2023.1156034

OPEN ACCESS

EDITED BY
Taras Gerya,
ETH Zürich, Switzerland

REVIEWED BY
Gaoxue Yang,
Chang'an University, China
Zhong-Hai Li,
University of Chinese Academy of Sciences, China
Jie Liao,
School of Earth Sciences and Engineering, Sun Yat-Sen University, China

*CORRESPONDENCE
Yida Li,
yidali@caltech.edu

SPECIALTY SECTION
This article was submitted to Solid Earth Geophysics, a section of the journal Frontiers in Earth Science

RECEIVED 01 February 2023
ACCEPTED 30 March 2023
PUBLISHED 17 April 2023

CITATION
Li Y and Gurnis M (2023), Strike slip motion and the triggering of subduction initiation.
Front. Earth Sci. 11:1156034.
doi: 10.3389/feart.2023.1156034

Strike slip motion and the triggering of subduction initiation

Yida Li* and Michael Gurnis

Seismological Laboratory, California Institute of Technology, Pasadena, CA, United States

Plate tectonic reconstructions of three of the best-defined Cenozoic subduction initiation (SI) events in the western Pacific, Izu-Bonin-Mariana, Vanuatu, and Puysegur subduction zones, show substantial components of strike-slip motion before and during the subduction initiation. Using computational models, we show that strike-slip motion has a large influence on the effective strength of incipient margins and the ease of subduction initiation. The parameter space associated with visco-elasto-plastic rheologies, plate weakening, and plate forces and kinematics is explored and we show that subduction initiates more easily with a higher force, a faster weakening, or greater strike-slip motion. With the analytical solution, we demonstrate that the effect of strike-slip motion can be equivalently represented by a modified weakening rate. Along transpressive margins, we show that a block of oceanic crust can become trapped between a new thrust fault and the antecedent strike-slip fault and is consistent with structural reconstructions and gravity models of the Puysegur margin. Together, models and observations suggest that subduction initiation can be triggered when margins become progressively weakened to the point that the resisting forces become smaller than the driving forces, and as the negative buoyancy builds up, the intraplate stress eventually turns from compressional into extensional. The analytical formulation of the initiation time, t_{SI}, marking the moment when intraplate stress flips sign, is validated with a computational models. The analytical solution shows that t_{SI} is dominated by convergence velocity, while the plate age, strike-slip velocity, and weakening rate all have a smaller but still important effect on the time scale of subduction initiation.

KEYWORDS

geodynamics, subduction, subduction initiation, faults, plate kinematics

1 Introduction

Consensus on a unified description of subduction initiation has been slow to develop as initiation is a transient process whose record is generally obscured by subsequent subduction zone processes, notably burial, overprinting, uplift, and compression and overthrusting. Nevertheless, there is a substantial geological record with nearly all ocean-ocean subduction zones having initiated since the end of the Mesozoic and about half of all ocean-continent ones having re-initiated since the mid-Mesozoic (Hu and Gurnis, 2020). Subduction initiation, moreover, occurs nearby existing subduction zones (Crameri et al., 2020), is a fundamental component of plate tectonics, and is putatively associated with key changes in the force balance of tectonic plates. For example, the Pacific Plate changed its direction of motion from NNW to NW at around 50 Ma (Whittaker et al., 2007; Torsvik et al., 2017), synchronously with the initiation of two major subduction zones in the western Pacific, the Izu-Bonin-Mariana (IBM) (Ishizuka et al., 2018; Reagan et al., 2019) and Tonga-Kermadec (Sutherland et al., 2020). However, why new subduction zones form

remains poorly understood, as subduction initiation appears to be mechanically unfavorable with initial slab pull being insufficient to overcome resistance from the friction between plates and bending of the slab (McKenzie, 1977; Toth and Gurnis, 1998; Li and Gurnis, 2022). An external force, or low initial strength between plates, is required to start subduction, with scenarios for initiation described as either spontaneous (Stern and Bloomer, 1992; Nikolaeva et al., 2010) (with no external force but low strength) or induced (Toth and Gurnis, 1998; Gurnis et al., 2004) (with an external force).

With theoretical and computational approaches, the thermal age of plates, compositional variations, trench-normal convergence and in–plane stress (Gurnis et al., 2004; Nikolaeva et al., 2010; Leng and Gurnis, 2011) and fault strength, fault weakening and plate bending (McKenzie, 1977; Toth and Gurnis, 1998; Thielmann and Kaus, 2012; Qing et al., 2021) having been identified as key mechanical factors which respectively drive and limit subduction initiation. Independent of spontaneous and induced scenarios, driving forces must overcome frictional resistance between plates and bending of the high, effective viscosity plate. If the plate boundary does not weaken sufficiently fast, the oceanic plate will not slide into the mantle to allow the negative thermal buoyancy to grow quickly enough. Constitutive models with strength that weakens with deformation, due to grain size reduction, grain damage, or volatile ingestion, have been identified (Hirth and Kohlstedt, 1996; Thielmann and Kaus, 2012; Bercovici and Ricard, 2014) and can lead to rapid instability (Leng and Gurnis, 2015; Zhou et al., 2018). Models exhibiting spontaneous initiation start in a critical state that verges on instability (Leng and Gurnis, 2015; Zhou et al., 2018), an unsatisfactory condition to address causes for the onset of initiation. If a plate boundary is in a state close to instability, the question arises as to why the boundary initiated at that point in time and not earlier.

Strike-slip motion might be one reason plate boundaries are brought closer to a state favorable for subduction initiation. Plate tectonic reconstructions of the IBM, Vanuatu and Puysegur subduction zones, three of the best constrained subduction initiation events in the western Pacific during the Cenozoic, each show a substantial component of strike-slip motion before and during initiation (**Figure 1**). The Puysegur subduction zone extending south from the South Island of New Zealand has a well-documented component of strike-slip motion during subduction initiation which continues to the present (Lamarche and Lebrun, 2000; Sutherland et al., 2006). The initiation of IBM, among the best studied and often used as a point of comparison with other subduction zones, ophiolite–origin models, and mechanical models (Arculus et al., 2019). Although less discussed, IBM experienced a strong component of strike slip motion during the well-documented period of initiation (Gurnis, 2023). The Vanuatu subduction initiation also saw a strong component of strike-slip motion during the interval 15 to 12 Ma when the new subduction zone was forming through a polarity reversal with velocities of about 5–6 cm/yr (**Figures 1B, D**). In addition to the main Vanuatu subduction zone, a new segment of the plate boundary is initiating at its southern boundary, referred to as the Matthew and Hunter subduction zone, with a small 2 cm/yr convergence and a subtantially larger strike-slip motion along the Hunter Ridge since 2 Ma (Patriat et al., 2019). All of these subduction initiation events must have been shaped by strike-slip motion, but do large components of strike-slip motion influence the mechanics of initiation?

2 Model formulation

We solve for the Stokes equations using traditional formulations used in geodynamics (Moresi et al., 2000; Ismail-Zadeh and Tackley, 2010) and show that a component of strike-slip motion can substantially reduce the strength of a nascent plate boundary while providing a triggering mechanism to nucleate a new subduction zone. The idea that strike-slip motion produces a more favorable condition for the far-field compression to induce subduction is examined by Zhong and Li (2023) with 3D models. Here, we address this problem with a sliced 3D geometry extended from the trench-perpendicular cross-section (x-z dimension), with an additional trench-parallel dimension (y-dimension) that accounts for the strike-slip motion (**Supplementary Figure S1**). In the trench-perpendicular (x-z) dimension, we apply either a convergent velocity or a convergent force on the right side of the subducting plate to induce subduction initiation. In the trench-parallel dimension, a strike-slip velocity is applied on the right wall of the subducting plate to drive the strike-slip velocity. For the two boundaries normal to the strike direction, we apply a periodic boundary condition, which allows the material to flow through the two boundaries freely. As the width of the trench parallel dimension is small (≈6 km) with only two layers of elements and periodic boundary conditions enforcing the strike-slip velocity, the models virtually solve for a plane strain problem with no variation along strike.

A younger overriding plate is to the left of an old oceanic plate with either a compressional force or a convergent velocity added on the right edge of the older plate. A pre-existing weak zone with yielding stress being reduced by half is located at the plate boundary. As plate convergence and strike-slip motion accumulates, the strain will eventually localize at the plate boundary.

The deformation of a visco-elasto-plastic material is computed with the finite element code Underworld (Mansour et al., 2019). The constitutive relationship between strain rate, $\dot{\varepsilon}$, and deviatoric stress, τ, is defined through a visco-elastic Maxwell body (Moresi et al., 2003),

$$\dot{\varepsilon} = \frac{\dot{\tau}}{2\mu} + \frac{\tau}{2\eta} \tag{1}$$

Viscosity follows the non-Newtonian Arrhenius law,

$$\eta = \eta_0 \left(\frac{\dot{\varepsilon}_{II}}{\dot{\varepsilon}_0} \right)^{\frac{1}{n}-1} e^{\frac{E}{nR}\left(\frac{1}{T}-\frac{1}{T_0}\right)} \tag{2}$$

where μ is the shear modulus, η the viscosity, T the temperature, and $\dot{\varepsilon}_{II}$ the second invariant of strain rate tensor. E, n and R are activation energy, non-linear exponent, and ideal gas constant. $\dot{\varepsilon}_0$, η_0 and T_0 are reference strain rate, reference viscosity and reference temperature.

Plasticity, describing the strength of the rock, is an essential component of subduction initiation. We assume a yielding envelope given by the Drucker-Prager failure criteria bounded by a maximum stress.

$$\tau = \min\left(C\cos\phi + P\sin\phi, \tau_{max}\right) \tag{3}$$

where τ is the yielding envelop, C and ϕ are cohesion and friction angle and τ_{max} the maximum stress the rock can sustain. With the accumulation of plastic strain, the yielding envelope is reduced through rock damage or grain size reduction. The weakening is

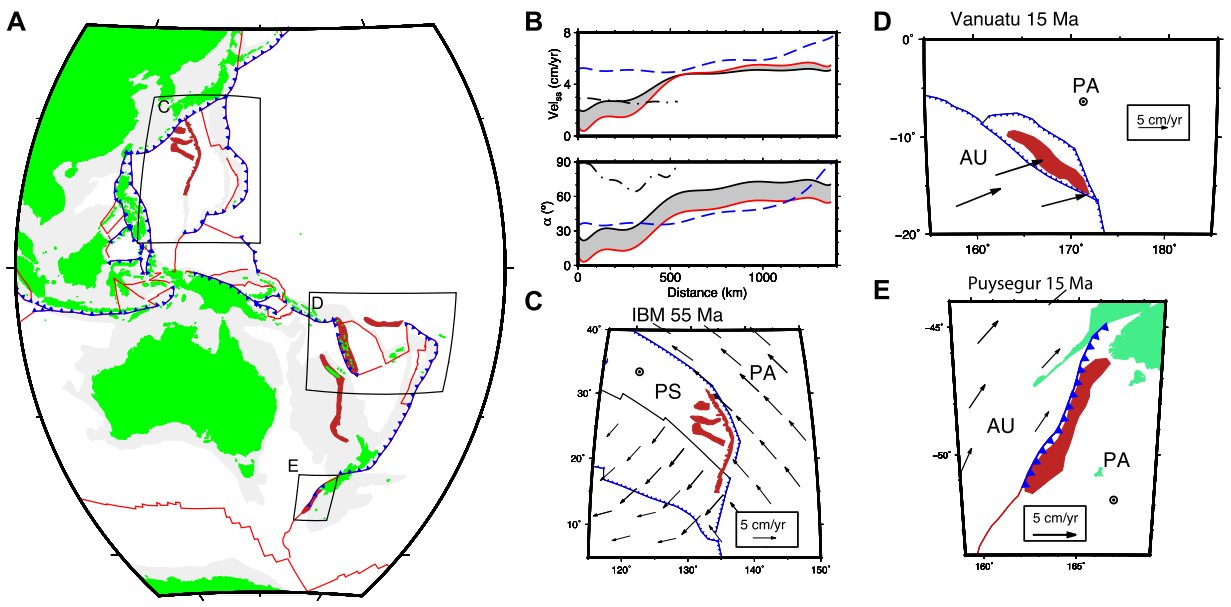

FIGURE 1
Three Cenozoic subduction initiation events that occurred in the western Pacific showing a substantial component of relative, strike-slip motions at the nascent trench just prior to initiation. **(A)**. Present-day western Pacific with the structures against which subduction initiated shown in brown. Regions of detail shown with boxes. **(B)**. Magnitude of strike slip motion (above) and convergence direction (below, with 0 being normal to the strike of the trench) before onset of initiation. Izu-Bonin-Mariana (IBM) shown at 55 Ma (red) and 50 Ma (black solid) with values for intermediate times shown with grey shading, Vanuatu at 15 Ma (blue dashed) and Puysegur (black, dot-dashed) using the plate model of Müller et al. (2019). **(C)**. Conditions at IBM at 55 Ma, 5 Myr before the onset of SI. **(D)**. Vanuatu at 15 Ma, 1–3 Myr before onset. **(E)**. Puysegur at 15 Ma, 1–3 Myr before onset. Abbreviations for plates: PA, Pacific Plate; AU, Australia Plate; PS, Philippine Sea Plate.

approximated as a two-stage process: The yielding envelope first reduces linearly with increasing plastic strain until saturation at which point the plastic parameters C and ϕ remain constant.

$$C = C_0 + \left(C_f - C_0\right)\min\left(1, \frac{\varepsilon_P}{\varepsilon_{P0}}\right) \quad (4)$$

$$\phi = \phi_0 + \left(\phi_f - \phi_0\right)\min\left(1, \frac{\varepsilon_P}{\varepsilon_{P0}}\right) \quad (5)$$

The reference plastic strain, ε_{P0}, controls the weakening rate with rocks weakening faster with smaller ε_{P0} and *vice versa*. With a lack of consensus on the underlying mechanisms responsible for weakening (Hirth and Kohlstedt, 1996; Thielmann and Kaus, 2012; Bercovici and Ricard, 2014), ε_{P0} is varied as an unknown along with other key parameters including the external compression, F_{xx}, and strike-slip velocity, V_{SS}. Details of model parameters are in **Supplementary Table S1**.

In addition to the numerical models, we formulate an analytical solution modified from Li and Gurnis (2022) considering the extra influence of the strike-slip motions. The formulation of the analytical solution is based on the horizontal force balance of the subducting plate between the forces that drive the plate motion and forces that resists plate motion. The strike-slip motion affects the force balance equation through accelerating the weakening process, thereby reducing the frictional resistance at the plate boundary. By varying modeling parameters of interest, like the strike-slip velocity and weakening rate, we measure quantities like the plate force, F_{xx}, initiation time, t_{SI}, and total work, W_{SI}, from numerical models, that are compared with the analytical predictions.

3 Results

3.1 Kinematic boundary condition

We use a kinematic boundary condition with a constant convergent velocity on the right end of the subducting plate to initiate subduction (**Supplementary Figure S1A**; **Figure 2A**). The different conditions controlling the evolution of subduction are evaluated by tracking the vertically–integrated horizontal compressional stress in the plate, i.e., $F_{xx} = \int_0^{d_{lith}} -\sigma_{xx} dz$, where d_{lith} is the thickness of lithosphere. Prior to initiation, plate motion is resisted by a large coupling stress at the plate boundary. Later, F_{xx} drops with plate convergence, ℓ, through plastic weakening and decoupling of the two plates and accumulation of negative buoyancy (Li and Gurnis, 2022). Eventually, F_{xx} becomes negative (extensional), indicating that subduction has become self-sustaining and driven by the negative buoyancy of the slab instead of external forces (**Figures 2B, C**), and we define the time when F_{xx} drops to 0 as the initiation time t_{SI}. Following Li and Gurnis (2022), we define the total work, W_{SI}, done by the boundary velocity to induce a subduction initiation until t_{SI} (i.e., $W_{SI} = \int_0^{t_{SI}} F_{xx} V_x dt$), characterizing the total resistance that the driving force overcomes. The tracking of plate force, initiation time, and total work quantitatively reflect the difficulty to induce subduction initiation. A larger F_{xx}, t_{SI} and W_{SI} indicate the subduction initiation encounters greater resistance. We develop an analytical solution of the strike-slip subduction initiation model, validate it with the numerical results, and expand the parametric space *via* the analytical solution.

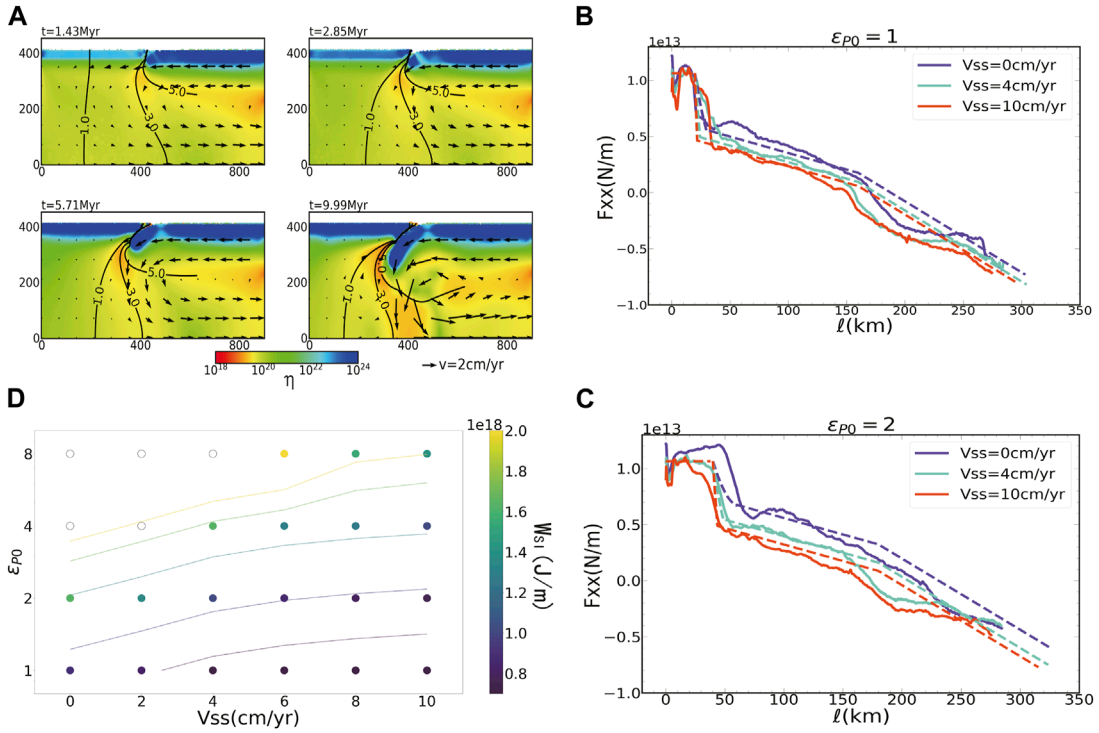

FIGURE 2
(A) An example of model with 1 cm/yr convergent velocity. Color shows the effective viscosity. Vectors show the in-plane component velocity and contours show strike slip velocity in cm/yr. **(B)** The integrated horizontal compressional force in the plate F_{xx} as a function of plate motion ℓ for models with different strike slip velocity V_{SS} under $\varepsilon_{P0} = 1$. Solid line for numerical model results and dashed line for analytical results. **(C)** Same as **(B)** but with slower weakening rate $\varepsilon_{P0} = 2$. **(D)** The work done to initiate a subduction W_{SI} of every numerical model (color-coded solid circle) in the parametric grid search varying the strike slip velocity V_{SS} and ε_{P0}. Contours show the prediction of W_{SI} from analytical model.

In 2D cross-sectional models (with no strike-slip motion), F_{xx} can be formulated analytically *via* a force balance analysis on the subducting plate, such that F_{xx}, together with slab pull as the driving force, is balanced by the resistance from plate bending, inter-plate friction, isostatic gradients at the boundary, and shear from mantle flow (Li and Gurnis, 2022). The addition of the third dimension (strike-slip) mainly changes the system by enhancing the weakening process. To analytically address the role of strike slip motion, we modify the formulation of inter-plate friction by enhancing the weakening as a result of the strike-slip velocity (see **Supplementary Material S1**). The contribution of strike-slip motion is analytically shown to be equivalent to reducing the effective weakening rate $\varepsilon_{P0\_eff} = \varepsilon_{P0} \frac{V_x}{\sqrt{{V_x}^2+{V_{SS}}^2}}$ and thereby reduce the inter-plate friction. This friction is balanced by the driving force, F_{xx}, and the analytical model (dashed line in **Figures 2B, C**) predicts a decrease of F_{xx} with increasing V_{SS}, in agreement with the numerical models (solid line in **Figures 2B, C**). Increasing strike-slip velocity and weakening rate consistently lowers F_{xx}, as both reduce the resistance inhibiting subduction initiation. A grid search of V_{SS} and ε_{P0} shows how these parameters influence W_{SI} (**Figure 2D**). In the limit of a small V_{SS} and a large ε_{P0}, convergence is insufficient to nucleate a weak zone and initiate a subduction (open circles, **Figure 2D**). Outside of that domain, subduction initiates and the resistance has a consistent trend: Increased V_{SS} and decreased ε_{P0} tend to lower W_{SI}.

Finally, we evaluate t_{SI} from the analytical model varying V_x, V_{SS}, ε_{P0} and subducting plate age (**Figure 3**). As discussed in Li and Gurnis (2022), the initiation time is dominantly controlled by the total plate convergence, so that convergence rate V_x has a first-order control on the predicted t_{SI}. Subducting plate age determines the plate thickness, which controls both the plate bending resistance and the slab pull. The plate age affects the force balance in two ways, the slab pull and plate bending because the plate thickness changes. As the dependence of slab pull on plate thickness is first order while plate rigidity (with plasticity) second order, the change of t_{SI} is dominated by slab pull when plate is young (<10 Ma), and for an old plate (>20 Ma) the t_{SI} is governed by plate bending. Therefore, below 10 Ma we see a decrease of t_{SI} as the plate gets older due to increased slab pull that drives plate motion, while above 20 Ma t_{SI} increases with plate age due to increased bending resistance. Both V_{SS} and ε_{P0} influence t_{SI} *via* the term of inter-plate friction. Both increase of V_{SS} and decrease of ε_{P0} lead to an acceleration of subduction initiation, thereby reducing the t_{SI}. However, compared to V_x, the impact of the plate age, V_{SS} and ε_{P0} is minor.

3.2 Force boundary conditions

Besides an applied convergent velocity, subduction initiation can be induced through applying a force on the edge of the plate (**Supplementary Figure S1B**). We use a geometry approximating

a mid-ocean ridge and a compressional force F_{xx} at the ridge edge of the subducting plate (**Supplementary Figure S1**). The total compression driving the plate motion is composed of the internal ridge push from the thermal contrast and the external force F_{xx}. When F_{xx} is sufficiently large, plate bending and resistance by shearing between plates at the nucleating boundary are overcome with subduction initiation (Leng and Gurnis, 2011; Zhong and Li, 2019); the minimum force needed for initiation is determined through systematic variation of parameters.

All prior models of subduction initiation in the literature have no strike-slip motion, and so we start with a case with no strike-slip velocity with (ε_{P0}, V_{SS}, f_{xx}) = (2, 0 cm/yr, 8.57×10^{12} N/m), as a reference (**Supplementary Figure S2B**) In this case, due to the insufficient compression to induce subduction initiation ($F_{xx} = 8.57\times10^{12}$ N/m) under a relatively low weakening rate ($\varepsilon_{P0} = 2$, larger ε_{P0} meaning slower weakening), the subduction initiation fails to occur and the plate boundary remains stable (**Supplementary Figure S2B**). Typical ridge push forces range from 2 to 4×10^{12} N/m (Bott, 1991; Toth and Gurnis, 1998) and so the F_{xx} used is not particularly small. Over time, the plate boundary remains stable with no subduction being induced. By taking this case as a reference, and then by either adding a V_{ss} of 2 cm/yr (**Supplementary Figure S2C**), or decreasing ε_{P0} from 2 to 1 (such that the fault weakens faster), the plate boundary initiates into a subduction zone (**Supplementary Figure S2D**). This shows that the presence of strike-slip motion and acceleration of the weakening process independently facilitate subduction initiation.

The key parameters, including strike-slip velocity, external compression, and the weakening rate, are systematically varied while computing the initiation time (**Supplementary Figure S3**). The grid search shows that regardless of the choice of weakening rate and resolution, increased strike-slip velocities lower the minimum required compressional force (**Supplementary Figure S3** thick lines) for subduction to initiate. A lower ε_{P0} (faster weakening) always reduces the required external force, therefore facilitating subduction initiation. Unlike the velocity boundary model where the strike-slip velocity has a minor influence on plate stress and initiation time, the addition of strike-slip motion significantly reduces the stress required to initiate a subduction zone (solid curves in **Supplementary Figures S3, S4**), indicating the strike-slip motion provide a more favorable condition for subduction initiation.

3.3 Fault evolution

The computations yield a fault system that evolves from a single strike-slip fault into a strain partitioned system composed of a vertical strike-slip fault and a dipping oblique thrust fault with partitioning of strike-slip velocity between the two (**Figure 4**). Initially, the plate boundary fault is vertical, and will remain so with only subsequent strike-slip motion; however, subduction requires a dipping thrust fault to decouple the two plates. In those cases where the system evolves into a subduction zone, we have found that the thrust fault emerges through the combined reuse of the strike-slip fault and new fault formation. The upper part of a trapped block is bound by a vertical strike-slip fault and an oblique thrust fault as the upper lithosphere has a high viscosity and brittle failure (faulting) is the dominant mechanism that accommodates the compression. The lower part of the vertical strike-slip fault rotates with compression of the somewhat lower viscosity, ductile lower lithosphere. Through this process, the lower part of the vertical strike-slip fault is transferred and becomes the lower part of the oblique thrust fault. The reuse of a vertical fault weakened by strike-slip motion is a primary reason why strike-slip motion can lower the required force to induce subduction and therefore facilitate subduction initiation.

In the case shown above, we choose a high yield stress (300 MPa) which makes the crust of the overriding plate strong. However, with a continental upper plate with a weaker crustal layer, the resultant morphology is different (**Supplementary Figure S5**). In this case, the rheology yields a typical continental strength envelope (Kohlstedt et al., 1995), with a weak layer present at the base of the continental crust, decoupling the lithosphere from the crust. Unlike the strong plate case where a new dipping fault emerges in the upper part of the subducting plate in response to the far–field compression, in the case of weak continental crust, the overriding plate severely deforms to accommodate the compression. In the overriding plate, the lower lithosphere delaminates at the base of the buoyant continental crust. The compression forces the subducting plate and the lower lithosphere of the upper plate to bend simultaneously, and a vertical strike-slip fault emerges in the upper plate crustal layer to reconcile the strike-slip motion. Consequently, a strain partitioning system emerges, but the wedge trapped between the strike-slip fault and the dipping thrust fault is composed of continental crust.

4 Discussion

With the numerical models that extend a traditional 2D trench perpendicular cross-sectional domain with orthogonal strike–slip motion, such motion influences subduction initiation. This builds on the concept that mature strike-slip faults like the San Andreas Fault (SAF) are weak [as revealed through stress indicators (Zoback et al., 1987) and heat flow (Brune et al., 1969)] and that the damage around faults grows with increasing fault displacement (Faulkner et al., 2011; Savage and Brodsky, 2011). A common conceptual idea is that a strike-slip fault will have local irregularities along the strike such there will be zones of convergence that could be sites for subduction initiation. A well-known example where local transpression leads to downwelling, although not subduction initiation, is the Miocene evolution of the San Andreas Fault (SAF) and Transverse Ranges of southern California in North America. Here, it is thought that the clear convergence across the Big Bend segment of the SAF north of Los Angeles has led to crustal and lithospheric thickening and convective instability (Humphreys and Clayton, 1990). However, we present a scenario that is distinctly different from this one, advancing the hypothesis that even with no irregularities in the orientation of faults along strike, subduction initiation is enhanced by strike-slip motion.

Can the models be applied to specific subduction initiation events? An obvious application is along the boundary between the Pacific and Australian Plates, south of New Zealand, the Puysegur subduction zone (**Figure 1E**). Here, a major strike-slip fault immediately to the east of the trench accommodates some of the relative plate motion (Collot et al., 1995; Lamarche and Lebrun,

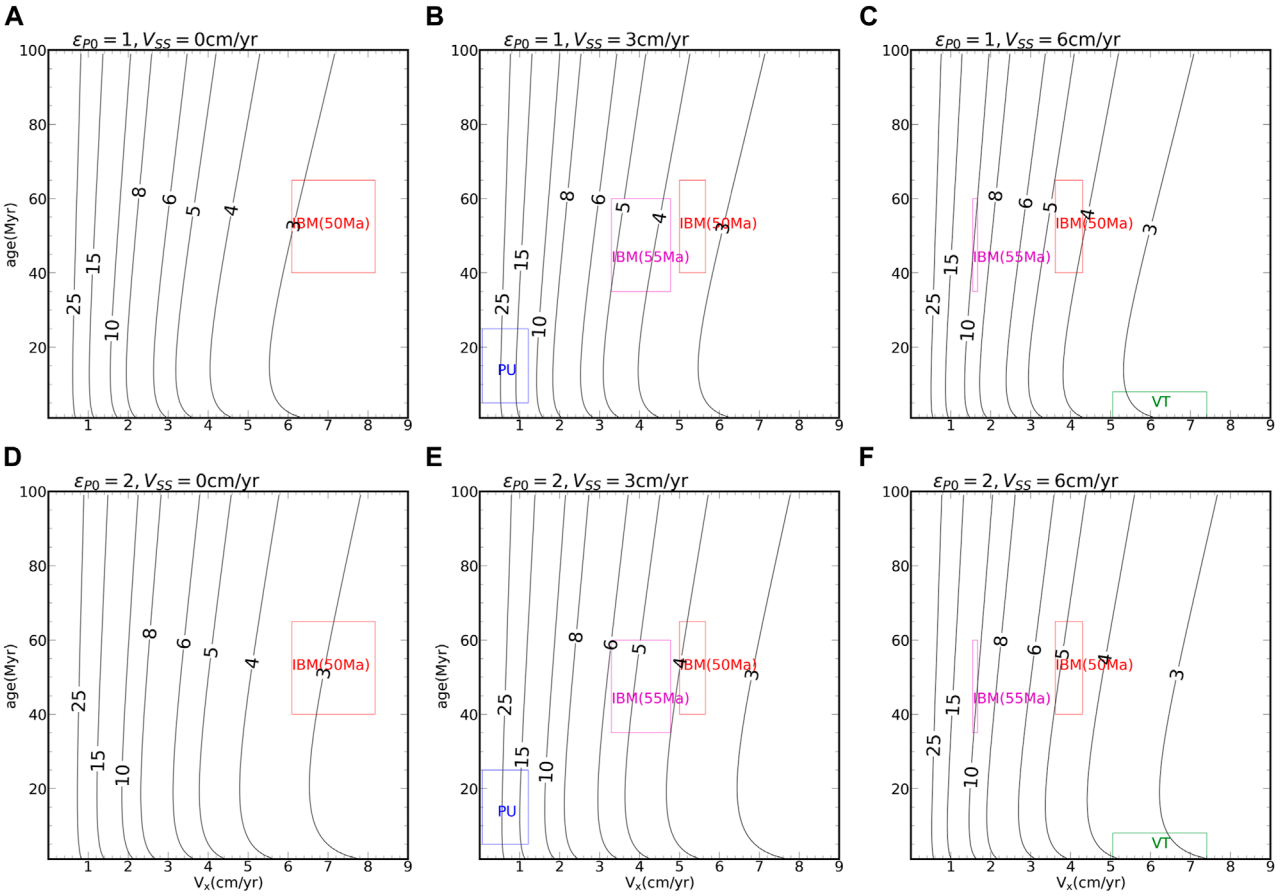

FIGURE 3
Analytical prediction of initiation time t_{SI} under different convergent velocity *Vx* and subducting plate age with **(A)**. $V_{SS} = 0$, $\varepsilon_{P0} = 1$, **(B)**. $V_{SS} = 3$ cm/yr, **(C)**. $V_{SS} = 6$ cm/yr, $\varepsilon_{P0} = 1$. **(D–F)** are the same as **(A–C)** except $\varepsilon_{P0} = 2$. Red, magenta, blue and green box show the parameter range of IBM (50 Ma), IBM (55 Ma), Puysegur (PU) and Vanuatu (VT) subduction initiation from the given V_{SS} with a ±1 cm/yr range.

2000). The age of the Puysegur subduction zone has been estimated in two ways. First is through a reconstruction using a combination of the depth extent of the seismic slab and plate kinematics, which date the onset of subduction to between 15 and 12 Ma (Sutherland et al., 2006). Second, the age has been estimated through detailed seismic imaging of the stratigraphy on the overriding Pacific Plate which shows basin inversion (Shuck et al., 2022). In the northern section of Puysegur, the compression starts at 15 Ma and transitions to mild extension by 8 Ma. During this interval, most of the relative motion between the Australian and Pacific Plates was strike-slip with velocities of about 3 cm/yr (**Figure 1B**). The subducting plate at Puysegur Trench formed along the Macquarie Ridge Complex (MRC) system, where sea–floor spreading was active since the Eocene (about 40 Ma) but terminating at about 15 Ma (Lebrun et al., 2003). The subducting plate age ranges from 25 Ma (north) to 5 Ma (south). With the given range of V_x, V_{SS}, and plate age for Puysegur, we predict a range of t_{SI} from the analytical model (**Figure 3**, blue box). The northern Puysegur trench corresponds to the top right corner of the blue box (V_x = 1 cm/yr, plate age = 25 Ma), yielding a model $t_{SI} \approx 12$ Myr which roughly agrees with the observed 8 Myr duration for the basin inversion (e.g., 16 to 8 Ma). For the southern Puysegur, the analytical model yields a larger t_{SI} (>30 Myr) given the small V_x (≈0.2 cm/yr) and young subducting plate (5 Myr old) at 15 Ma. This prediction may over-estimate t_{SI} as during the subduction initiation the convergent velocity V_x increases substantially from 0.2 cm/yr at 15 Ma to ~2 cm/yr today due to the change of plate motion direction (Choi et al., 2017), and the large predicted t_{SI} sheds light on why the southern Puysegur remains under compression today—in addition to the hypothesis of southward propagation of subduction initiation proposed in Shuck et al. (2022).

Puysegur has other features reflective of the initiation phase as it evolved from a strike-slip boundary to transpressional since 16 Ma, in particular a sliver of oceanic crust (Hightower et al., 2020) trapped at the Puysegur Trench, bounded by a vertical fault and an oblique thrust fault (Collot et al., 1995; Shuck et al., 2022). East of the Puysegur Trench, the morphology of the Puysegur Fault through the central part of the southern Puysegur Ridge is sharp and consistent with present-day activity (Shuck et al., 2021). The 2009 Mw 7.8 Dusky Sound earthquake below Fiordland, the strike-slip onshore extension of the nascent subduction zone, showed that nearly all of the relative motion, including the strike-slip motion, was accommodated on the thrust interface (Beavan et al., 2010). Consequently, the seismic imaging and 2009 event for Puysegur shows that it has a structure, morphology, and strain partitioning consistent with that shown in **Figure 4**, that is with substantial

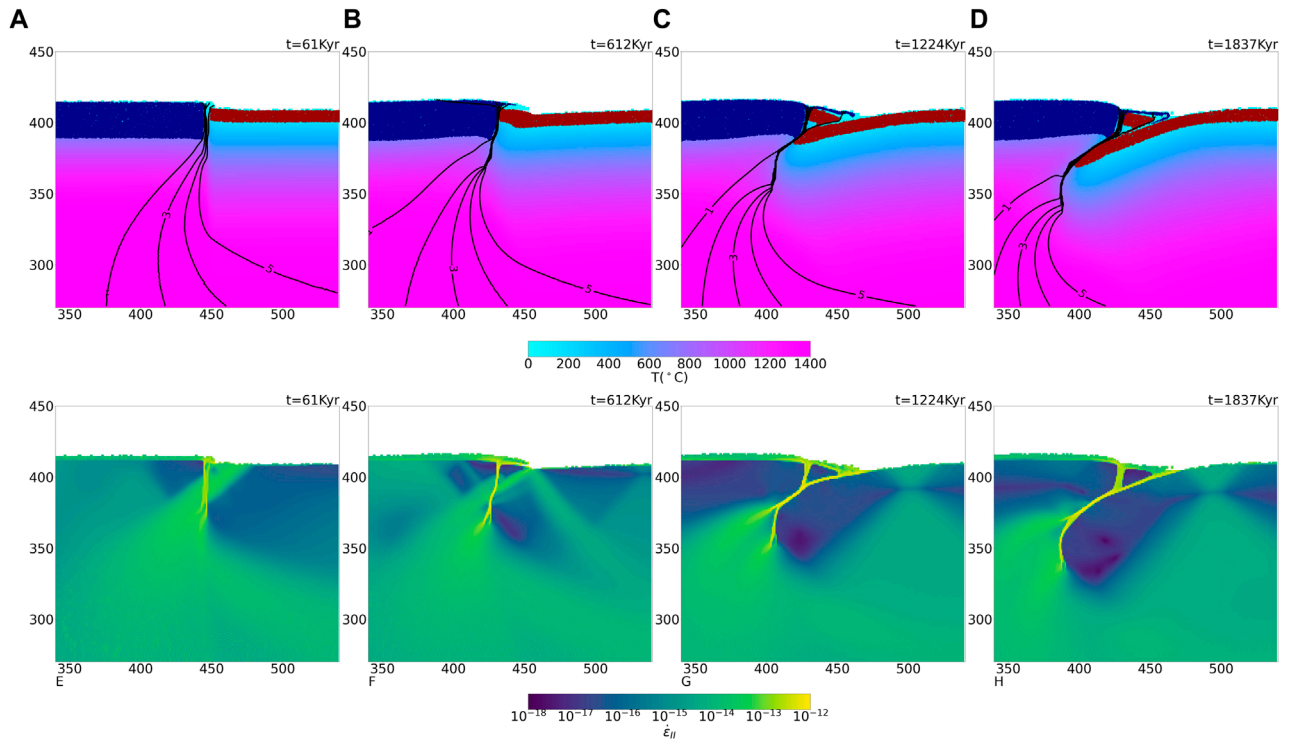

FIGURE 4
Fault evolution of a high resolution models with (ε_{P0}, V_{SS}, V_p) = (2, 6 cm/yr, 4 cm/yr). **(A–D)** Red and blue for oceanic and continental crust. Background color for temperature. **(E–H)** Second invariant of strain rate ($\dot{\epsilon}_{II}$).

strike-slip motion on the thrust interface, and the entrapment of an oceanic sliver between the newly formed thrust interface and the strike-slip fault.

Subduction along IBM initiated at the boundary between the Pacific Plate and the smaller West Philippine Sea Plate along the Kyushu Palau Ridge (**Figure 1C**). The new subduction zone is inferred to have formed between 52 and 50 Ma as indicated by ages within the forearc (Reagan et al., 2019) and basement of the West Philippine Sea Plate (Ishizuka et al., 2018). IBM is often viewed as a type locality for studying subduction initiation because of the rock record on the IBM fore–arc and an association with changes in Pacific Plate motion during the Cenozoic (Stern and Bloomer, 1992; Arculus et al., 2019). The IBM subduction zone may be an example of spontaneous subduction initiation (Stern and Bloomer, 1992), with a short, rapid burst of localized extension (Reagan et al., 2019). The overriding Philippine Sea Plate had a relic arc with thick buoyant crust adjacent to the old, cold Pacific plate at the location of apparent subduction initiation and this may have played a role in its initiation (Leng and Gurnis, 2015). Computational models suggest that compression of the incipient plate margin needs to overcome a large resisting force associated with bending the incipient slab (Gurnis et al., 2004; Li and Gurnis, 2022), but there is debate in the literature on the significance of the compression. On the one hand, Maunder et al. (2020) argued that early compression cannot lead to near–field extension and boninite formation and that a large vertical force is needed for such extension, a force which only can exsit if there is pre-existing subduction. Moreover, a recent interpretation of Baron isotope systematics on IBM forearc recovered samples apparently indicate an initial low–angle phase of thrusting prior to the formation of the distinctive basalt to boninite sequence (Li et al., 2022).

Although not widely discussed, several lines of evidence suggest that there was a strong component of strike-slip motion during IBM inception. Paleomagnetic observations show that since 50 Ma, the Philippine Sea Plate experienced nearly 90° of clockwise rotation (Hall et al., 1995); since the orientation of the Kyushu-Palau Ridge (the relic arc that formed at the new boundary) is currently N-S, it would have been more E-W during subduction initiation. The orientation of convergence between the West Philippine Sea and Pacific Plates depends on the absolute motion of the Pacific Plate, but the Pacific moved by the overriding plate in a mostly strike-slip orientation with velocities of about 5 cm/yr for at least five million years before initiation (**Figures 1B, C**), with V_{SS} and V_x varying substantially along strike due to the curved plate boundary. Independently, detailed bathymetry just to the west of the Kyushu Palau Ridge reveal a strike–slip fault subparallel and normal faults perpendicular to the ridge in which the basement dates to the time of subduction inception, 49 Ma (Gurnis, 2023). This is consistent with transverse motion along the KPR at the time of initiation. Nearly identical forearc volcanic stratigraphy near the Bonin Islands and near Gaum Islands, 500 km apart when plate tectonic motions are accounted for (Leng and Gurnis, 2015), could have been further seperated by strike slip motion.

The strike-slip model of induced subduction initiation can be applied to IBM. With subducting plate age varying between 40 and 60 Myr old at 50 Ma (Hall et al., 2003; Lallemand and

Arcay, 2021), the analytical model yields a range of initiation times (**Figure 3**). At 55 Ma, the predicted t_{SI} range from 5 to 10 Myr with V_{SS} =3–6 cm/yr. At 50 Ma, the reconstruction gives a larger range of V_{SS} (0–6 cm/yr), and the analytical model predicts a $t_{SI} \approx$ 3–5 Myr. Using the plate tectonic constraints at 55 and 50 Ma, we estimate the time for the IBM to experience conversion from compression to extension to be around 50 to 45 Ma, a 5 Myr duration slightly larger than the 2 Myr inferred from fore–arc opening determined from $^{40}Ar/^{39}Ar$ and U-Pb ages of the boninite-basalt sequence in the IBM fore–arc (52–50 Ma) (Reagan et al., 2019).

IBM subduction initiation may be associated with the shift in Pacific Plate motion from more northerly before 50 Ma to more westerly after 50 Ma, as evident from plate reconstructions and the bend in the Hawaiian–Emperor Seamount chain (e.g., Torsvik et al., 2017; Müller et al., 2019). Hu et al. (2022) showed that Pacific Plate motion could change by about 10° (from more northerly to northwesterly) with introduction of the IBM slab from 55 to 50 Ma. Most of the required change in absolute Pacific Plate motion must come from elsewhere, and Hu et al. (2022) show that this can be accomplished with termination of intra-oceanic subduction in the north Pacific between 55 and 50 Ma. Other west Pacific subduction zones forming during the Cenozoic, however, may have initially been induced, including the Tonga-Kermadec subduction zone that underwent vertical motions and folding within the future back-arc region prior to and contemporaneously with subduction initiation, indicating a strong compressive force during initiation (Sutherland et al., 2020). Strike–slip motion between Pacific and West Phillipine Sea Plates, along with compression along this boundary due to rearrangement of Pacific Plate driving forces can lead to IBM subduction initiation. The models favor an induced mode of subduction initiation, as the minimum stress (**Supplementary Figure S3** solid lines) never vanishes independent of the magnitude of V_{SS}.

The Vanuatu subduction zone initiated between 12 and 10 Ma, following the collision of the Ontong-Java Plateau with the Vitiaz subduction zone at 16 Ma (Mann and Taira, 2004) and may be an example of induced subduction polarity reversal (Auzende et al., 1988; Yang, 2022). Soon after Vanuatu subduction initiation, the Fiji basin opens at ~8 Ma, indicating a short initiation time (Auzende et al., 1988; Lallemand and Arcay, 2021). The plate reconstructions show a strong component of strike-slip motion (5–8 cm/yr), **Figure 1B** dashed blue curve) between the Australian and Pacific plates along the Vanuatu incipient boundary (**Figures 1B, D**) The strike-slip mechanical model yields a small value for t_{SI} (≈3 Myr, **Figure 3**), because of the large strike-slip velocity V_{SS}, large convergent velocity V_x and the young plate age (Lallemand and Arcay, 2021).

5 Conclusion

Three Cenozoic subduction zones—Puysegur, IBM and Vanuatu—all show substantial components of strike–slip motion prior to and during initiation. Application of the mechanical model developed here using plate reconstruction constraints all yield estimates of initiation times consistent with values estimated independently from geological observations. Together, the models and observations suggest that subduction initiation can be triggered when margins become progressively weakened to the point that the resisting forces become smaller than the driving forces. Despite the strike-slip velocity having a relatively minor influence on the evolution of plate stress and initiation time compared to the plate convergent velocity, it can still dramatically lower the force required to induce subduction initiation, thereby providing a favorable condition for subduction initiation.

Data availability statement

The datasets presented in this study can be found in online repositories. The names of the repository/repositories and accession number(s) can be found in the article/**Supplementary Material**. The datasets for this study can be found in the CaltechDATA at https://doi.org/110.22002/ae55y-m7q16.

Author contributions

YL contributes to study conception, model setup, manuscript preparation, interpretation MG contributes to study conception, manuscript preparation, interpretation. All authors reviewed the results and approved the final version of the manuscript.

Funding

Supported by the National Science Foundation through awards OCE–1654766, EAR–1645775, and OCE–2049086. This work used Stampede-2 at the Texas Advanced Computer Center from the Extreme Science and Engineering Discovery Environment (XSEDE), which was supported by National Science Foundation.

Conflict of interest

The authors declare that the research was conducted in the absence of any commercial or financial relationships that could be construed as a potential conflict of interest.

Publisher's note

Supplementary material

The Supplementary Material for this article can be found online at: https://www.frontiersin.org/articles/10.3389/feart.2023.1156034/full#supplementary-material

References

Arculus, R. J., Gurnis, M., Ishizuka, O., Reagan, M. K., Pearce, J. A., and Sutherland, R. (2019). How to create new subduction zones: A global perspective. *Oceanography* 32, 160–174. doi:10.5670/oceanog.2019.140

Auzende, J.-M., Lafoy, Y., and Marsset, B. (1988). Recent geodynamic evolution of the north Fiji basin (southwest Pacific). *Geology* 16, 925–929. doi:10.1130/0091-7613(1988)016<0925:rgeotn>2.3.co;2

Beavan, J., Samsonov, S., Denys, P., Sutherland, R., Palmer, N., and Denham, M. (2010). Oblique slip on the Puysegur subduction interface in the 2009 july Mw 7.8 Dusky Sound earthquake from GPS and InSAR observations: Implications for the tectonics of southwestern New Zealand. *Geophys. J. Int.* 183, 1265–1286. doi:10.1111/j.1365-246X.2010.04798.x

Bercovici, D., and Ricard, Y. (2014). Plate tectonics, damage and inheritance. *Nature* 508, 513–516. doi:10.1038/nature13072

Bott, M. H. P. (1991). Ridge push and associated plate interior stress in normal and hotspot regions. *Tectonophysics* 200, 17–32. doi:10.1016/0040-1951(91)90003-b

Brune, J. N., Henyey, T. L., and Roy, R. F. (1969). Heat flow, stress, and rate of slip along the San Andreas Fault, California. *J. Geophys. Res.* 74, 3821–3827. doi:10.1029/JB074i015p03821

Choi, H., Kim, S.-S., Dyment, J., Granot, R., Park, S.-H., and Hong, J. K. (2017). The kinematic evolution of the Macquarie plate: A case study for the fragmentation of oceanic lithosphere. *Earth Planet. Sci. Lett.* 478, 132–142. doi:10.1016/j.epsl.2017.08.035

Collot, J. Y., Lamarche, G., Wood, R. A., Delteil, J., Sosson, M., Lebrun, J. F., et al. (1995). Morphostructure of an incipient subduction zone along a transform plate boundary - Puysegur Ridge and Trench. *Geology* 23, 519–522. doi:10.1130/0091-7613(1995)023<0519:moaisz>2.3.co;2

Crameri, F., Magni, V., Domeier, M., Shephard, G. E., Chotalia, K., Cooper, G., et al. (2020). A transdisciplinary and community-driven database to unravel subduction zone initiation. *Nat. Commun.* 11, 3750–3814. doi:10.1038/s41467-020-17522-9

Faulkner, D. R., Mitchell, T. M., Jensen, E., and Cembrano, J. (2011). Scaling of fault damage zones with displacement and the implications for fault growth processes. *J. Geophys. Res. Solid Earth* 116, B05403. doi:10.1029/2010JB007788

Gurnis, M. (2023). "An evolutionary perspective on subduction initiation," in *Dynamics of plate tectonics and mantle convection*. Editor J. C. Duarte (Amsterdam: Elsevier), 357–383. doi:10.1016/B978-0-323-85733-8.00003-2

Gurnis, M., Hall, C., and Lavier, L. (2004). Evolving force balance during incipient subduction. *Geochem. Geophys. Geosystems* 5. doi:10.1029/2003gc000681

Hall, C., Gurnis, M., Sdrolias, M., Lavier, L. L., and Müller, R. D. (2003). Catastrophic initiation of subduction following forced convergence across fracture zones. *Earth Planet. Sci. Lett.* 212, 15–30. doi:10.1016/S0012-821X(03)00242-5

Hall, R., Ali, J. R., Anderson, C. D., and Baker, S. J. (1995). Origin and motion history of the Philippine Sea Plate. *Tectonophysics* 251, 229–250. doi:10.1016/0040-1951(95)00038-0

Hightower, E., Gurnis, M., and Van Avendonk, H. (2020). A bayesian 3-D linear gravity inversion for complex density distributions: Application to the Puysegur subduction system. *Geophys. J. Int.* 223, 1899–1918. doi:10.1093/gji/ggaa425

Hirth, G., and Kohlstedt, D. L. (1996). Water in the oceanic upper mantle: Implications for rheology, melt extraction and the evolution of the lithosphere. *Earth Planet. Sci. Lett.* 144, 93–108. doi:10.1016/0012-821x(96)00154-9

Hu, J., Gurnis, M., Rudi, J., Stadler, G., and Müller, D. (2022). Dynamics of the abrupt change in Pacific Plate motion around 50 million years ago. *Nat. Geosci.* 15, 74–78. doi:10.1038/s41561-021-00862-6

Hu, J., and Gurnis, M. (2020). Subduction duration and slab dip. *Geochem. Geophys. Geosystems* 21. doi:10.1029/2019GC008862

Humphreys, E. D., and Clayton, R. W. (1990). Tomographic image of the southern California mantle. *J. Geophys. Res.* 95, 19725. doi:10.1029/jb095ib12p19725

Ishizuka, O., Hickey-Vargas, R., Arculus, R. J., Yogodzinski, G., Savov, I. P., Kusano, A., et al. (2018). Age of Izu Bonin mariana arc basement. *Earth Planet. Sci. Lett.* 481, 80–90. doi:10.1016/j.epsl.2017.10.023

Ismail-Zadeh, A., and Tackley, P. J. (2010). *Computational methods for geodynamics*. Cambridge, U.K.: Cambridge University Press.

Kohlstedt, D. L., Evans, B., and Mackwell, S. J. (1995). Strength of the lithosphere: Constraints imposed by laboratory experiments. *J. Geophys. Res.* 100 (17), 17587–17602. doi:10.1029/95jb01460

Lallemand, S., and Arcay, D. (2021). Subduction initiation from the earliest stages to self-sustained subduction: Insights from the analysis of 70 Cenozoic sites. *Earth-Science Rev.* 221, 103779. doi:10.1016/j.earscirev.2021.103779

Lamarche, G., and Lebrun, J.-F. (2000). Transition from strike-slip faulting to oblique subduction: Active tectonics at the Puysegur margin, south New Zealand. *Tectonophysics* 316, 67–89. doi:10.1016/s0040-1951(99)00232-2

Lebrun, J.-F., Lamarche, G., and Collot, J.-Y. (2003). Subduction initiation at a strike-slip plate boundary: The Cenozoic Pacific-Australian plate boundary, south of New Zealand. *J. Geophys. Res. Solid Earth* 108. doi:10.1029/2002jb002041

Leng, W., and Gurnis, M. (2011). Dynamics of subduction initiation with different evolutionary pathways. *Geochem. Geophys. Geosys.* 12. doi:10.1029/2011gc003877

Leng, W., and Gurnis, M. (2015). Subduction initiation at relic arcs. *Geophys. Res. Lett.* 42, 7014–7021. doi:10.1002/2015gl064985

Li, H.-Y., Li, X., Ryan, J. G., Zhang, C., and Xu, Y.-G. (2022). Boron isotopes in boninites document rapid changes in slab inputs during subduction initiation. *Nat. Commun.* 13, 993–1010. doi:10.1038/s41467-022-28637-6

Li, Y., and Gurnis, M. (2022). A simple force balance model of subduction initiation. *Geophys. J. Int.* 232, 128–146. doi:10.1093/gji/ggac332

Mann, P., and Taira, A. (2004). Global tectonic significance of the Solomon islands and ontong java plateau convergent zone. *Tectonophysics* 389, 137–190. doi:10.1016/j.tecto.2003.10.024

Mansour, J., Kaluza, O., Giordani, J., Beucher, R., Farringtona, R., Kennedy, G., et al. (2019). *underworldcode/underworld2: v2.8.1b*. doi:10.5281/zenodo.3384283

Maunder, B., Prytulak, J., Goes, S., and Reagan, M. (2020). Rapid subduction initiation and magmatism in the Western Pacific driven by internal vertical forces. *Nat. Commun.* 11, 1874. doi:10.1038/s41467-020-15737-4

McKenzie, D. (1977). "The initiation of trenches: A finite amplitude instability," in *Island arcs, deep sea trenches and back-arc basins, Maurice Ewing Series*. Editors M. Talwani, and W. Pitman (Washington, DC: American Geophysical Union), 1, 57–61.

Moresi, L., Dufour, F., and Muhlhaus, H. B. (2003). A Lagrangian integration point finite element method for large deformation modeling of viscoelastic geomaterials. *J. Comput. Phys.* 184, 476–497. doi:10.1016/s0021-9991(02)00031-1

Moresi, L., Gurnis, M., and Zhong, S. (2000). Plate tectonics and convection in the Earth's mantle: Toward a numerical simulation. *Comp. Sci. Engin.* 2, 22–33. doi:10.1109/5992.841793

Müller, R. D., Zahirovic, S., Williams, S. E., Cannon, J., Seton, M., Bower, D. J., et al. (2019). A global plate model including lithospheric deformation along major rifts and orogens since the Triassic. *Tectonics* 38, 1884–1907. doi:10.1029/2018tc005462

Nikolaeva, K., Gerya, T., and Marques, F. (2010). Subduction initiation at passive margins: Numerical modeling. *J. Geophys. Res.* 115, B03406. doi:10.1029/2009JB006549

Patriat, M., Falloon, T., Danyushevsky, L., Collot, J., Jean, M. M., Hoernle, K., et al. (2019). Subduction initiation terranes exposed at the front of a 2 Ma volcanically–active subduction zone. *Earth Planet. Sci. Lett.* 508, 30–40. doi:10.1016/j.epsl.2018.12.011

Qing, J., Liao, J., Li, L., and Gao, R. (2021). Dynamic evolution of induced subduction through the inversion of spreading ridges. *J. Geophys. Res. Solid Earth* 126, e2020JB020965. doi:10.1029/2020jb020965

Reagan, M. K., Heaton, D. E., Schmitz, M. S., Pearce, J. A., Shervais, J. W., and Koppers, A. P. (2019). Forearc ages reveal extensive short–lived and rapid seafloor spreading following subduction initiation. *Earth Planet. Sci. Lett.* 506, 520–529. doi:10.1016/j.epsl.2018.11.020

Savage, H. M., and Brodsky, E. E. (2011). Collateral damage: Evolution with displacement of fracture distribution and secondary fault strands in fault damage zones. *J. Geophys. Res. Solid Earth* 116, B03405. doi:10.1029/2010JB007665

Shuck, B., Gulick, S. P. S., Van Avendonk, H. J. A., Gurnis, M., Sutherland, R., Stock, J., et al. (2022). Stress transition from horizontal to vertical forces during subduction initiation. *Nat. Geosci.* 15, 149–155. doi:10.1038/s41561-021-00880-4

Shuck, B., Van Avendonk, H., Gulick, S. P. S., Gurnis, M., Sutherland, R., Stock, J., et al. (2021). Strike-slip enables subduction initiation beneath a failed rift: New seismic constraints from Puysegur margin, New Zealand. *Tectonics* 40, e2020TC006436. doi:10.1029/2020tc006436

Stern, R. J., and Bloomer, S. H. (1992). Subduction zone infancy - examples from the Eocene izu–bonin–mariana and jurassic California arcs. *Geol. Soc. Am. Bull.* 104, 1621–1636. doi:10.1130/0016-7606(1992)104<1621:szieft>2.3.co;2

Sutherland, R., Barnes, P., and Uruski, C. (2006). Miocene-Recent deformation, surface elevation, and volcanic intrusion of the overriding plate during subduction initiation, offshore southern Fiordland, Puysegur margin, southwest New Zealand. *N.Z. J. Geol. geophys.* 49, 131–149. doi:10.1080/00288306.2006.9515154

Sutherland, R., Dickens, G. R., Blum, P., Agnini, C., Alegret, L., Asatryan, G., et al. (2020). Continental-scale geographic change across Zealandia during Paleogene subduction initiation. *Geology* 48, 419–424. doi:10.1130/G47008.1

Thielmann, M., and Kaus, B. J. P. (2012). Shear heating induced lithospheric-scale localization: Does it result in subduction? *Earth Planet. Sci. Lett.* 359, 1–13. doi:10.1016/j.epsl.2012.10.002

Torsvik, T. H., Doubrovine, P. V., Steinberger, B., Gaina, C., and Spakman, W. (2017). Pacific plate motion change caused the Hawaiian-Emperor bend. *Nat. Commun.* 8, 15660. doi:10.1038/ncomms15660

Toth, J., and Gurnis, M. (1998). Dynamics of subduction initiation at preexisting fault zones. *J. Geophys. Research-Solid Earth* 103, 18053–18067. doi:10.1029/98jb01076

Whittaker, J. M., Muller, R. D., Leitchenkov, G., Stagg, H., Sdrolias, M., Gaina, C., et al. (2007). Major Australian–Antarctic plate reorganization at Hawaiian–Emperor bend time. *Science* 318, 83–86. doi:10.1126/science.1143769

Yang, G. (2022). Subduction initiation triggered by collision: A review based on examples and models. *Earth-Science Rev.* 232, 104129. doi:10.1016/j.earscirev.2022.104129

Zhong, X., and Li, Z.-H. (2023). Compression at strike-slip fault is a favorable condition for subduction initiation. *Geophys. Res. Lett.* 50, e2022GL102171. doi:10.1029/2022gl102171

Zhong, X., and Li, Z.-H. (2019). Forced subduction initiation at passive continental margins: Velocity-driven versus stress-driven. *Geophys. Res. Lett.* 46, 11054–11064. doi:10.1029/2019gl084022

Zhou, X., Li, Z.-H., Gerya, T. V., Xu, Z., and Zhang, J. (2018). Subduction initiation dynamics along a transform fault control trench curvature and ophiolite ages. *Geology* 46, 607–610. doi:10.1130/G40154.1

Zoback, M. D., Zoback, M. L., Mount, V. S., Suppe, J., Eaton, J. P., Healy, J. H., et al. (1987). New evidence on the state of stress of the San Andreas Fault system. *Science* 238, 1105–1111. doi:10.1126/science.238.4830.1105

frontiers | Frontiers in Earth Science

TYPE Original Research
PUBLISHED 21 April 2023
DOI 10.3389/feart.2023.1192997

OPEN ACCESS

EDITED BY
Jiyuan Yin,
Chinese Academy of Geologi-cal Sciences (CAGS), China

REVIEWED BY
Gaoxue Yang,
Chang'an University, China
Xiaoping Long,
Northwest University, China

*CORRESPONDENCE
Xijun Liu,
xijunliu@glut.edu.cn
Hao Wu,
wuhaojlu@126.com

RECEIVED 24 March 2023
ACCEPTED 13 April 2023
PUBLISHED 21 April 2023

CITATION
Tian H, Liu X, Wu H, Li D, Liu X, Song Q, Li Z, Liu P, Hu R and Yang Q (2023), Development of a cambrian back-arc basin in the North Qilian orogenic belt: New constraints from gabbros in Yushigou ophiolite.
Front. Earth Sci. 11:1192997.
doi: 10.3389/feart.2023.1192997

Development of a cambrian back-arc basin in the North Qilian orogenic belt: New constraints from gabbros in Yushigou ophiolite

Hao Tian[1], Xijun Liu[1,2]*, Hao Wu[1,2]*, Dechao Li[1], Xiao Liu[1], Qi Song[1], Zhenglin Li[1], Pengde Liu[1], Rongguo Hu[1,2] and Qijun Yang[1]

[1]Guangxi Key Laboratory of Hidden Metallic Ore Deposits Exploration, College of Earth Sciences, Guilin University of Technology, Guilin, China, [2]Collaborative Innovation Center for Exploration of Nonferrous Metal Deposits and Efficient Utilization of Resource Guilin University of Technology, Guilin, China

Introduction: The North Qilian orogenic belt, as the Northern branch of the original Tethys tectonic domain, is important for reconstructing the tectonic evolution of the ancient Tethys. However, the tectonic history of the North Qilian orogenic belt remains controversial. This study addresses this issue from a geochemical perspective.

Methods: In this study, a comprehensive analysis of the geochronology, whole-rock geochemistry, clinopyroxene mineral geochemistry, zircon Ti crystallization temperature, and gabbromagma temperature and pressure in the Yushigou ophiolite of the North Qilian orogenic belt was conducted to provide constraints on its tectonic evolution.

Results and Discussion: Laser ablation inductively coupled plasma mass spectrometry zircon U-Pb dating results reveal that the gabbros have ages of 519 ± 3 Ma and 495 ± 4 Ma, belonging to the Cambrian period. Most of the studied gabbros exhibited geochemical characteristics of tholeiitic basaltic rocks with normal mid-ocean ridge basalt and island arc tholeiite dual geochemical affinities. The gabbros are interpreted to have formed by a high degree of partial melting of the depleted mantle spinel lherzolite. These results suggest that the back-arc basin of the North Qilian tectonic belt may have evolved to a relatively mature stage from 519 to 495 Ma. Overall, this study contributes to our understanding of the tectonic evolution of the North Qilian orogenic belt through geochemical analyses.

KEYWORDS

mid-ocean ridge basalt, geochemistry, gabbros, back-arc basin, North Qilian

Introduction

Ophiolite fragments of ancient oceanic crust play an irreplaceable role in the identification and reconstruction of ancient oceans, such as their formation and closure, the development of subduction, and the formation of large orogenic belts, and are the most important symbols for identifying converging plate boundaries in collisional and

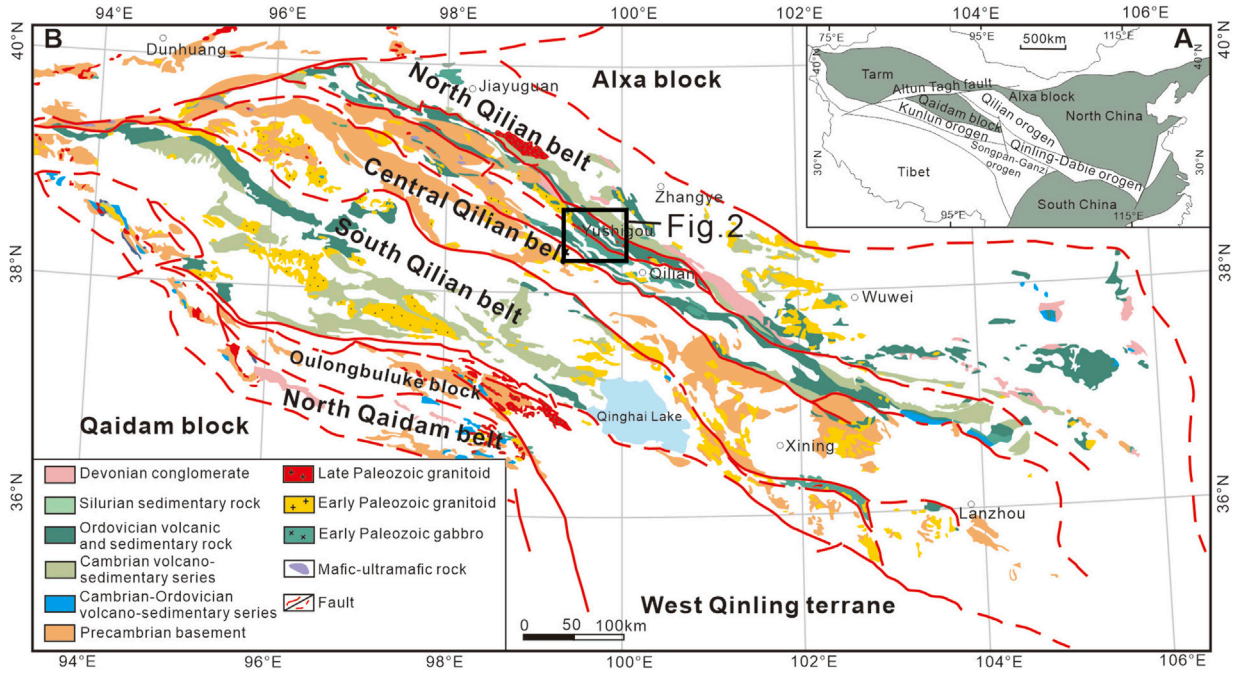

FIGURE 1
(A,B) Geological map of the Qilian orogenic belt (after Fu et al., 2018).

accretionary orogenies (Dilek, 2003; Dilek et al., 2007; Lister and Forster, 2009; Dilek and Furnes, 2011; Song et al., 2015; Wu et al., 2018; Yang et al., 2022).

The North Qilian orogenic belt is a typical Early Paleozoic accretionary orogenic belt. The study of the ophiolite suite in the North Qilian orogenic belt, one of the earliest orogenic belts in China, began in the mid-1970s (Xiao et al., 1978). It is located in central and western China, transecting the boundary of the southern margin of the North China and Qaidam plates between the Alashan Block and the Qilian-Qaidam Micro-Block. The belt stretches E-W for over 1,000 km (Yang et al., 2001). Among the ophiolite suite fragments in the North Qilian orogenic belt, the Yushigou ophiolite has been favored by scholars because of its relatively complete rock assemblage. Scholars began to study ophiolites early; however, ophiolites are complex rock assemblages that involve the interaction between mantle materials and oceanic crust materials, which has always been a difficult point in scientific research (Feng and He, 1995; Zhang et al., 1998; Shi et al., 2004; Tseng et al., 2007; Song et al., 2010).

The most important aspect is the delineation of the ophiolite formation age, which remains controversial (Shi et al., 2004). Previous studies have suggested that the Yushigou ophiolites formed during the Cambrian, Late Cambrian-Early Ordovician, and Precambrian (Xiao et al., 1978; xia et al., 1996; Shi et al., 2004). The tectonic environment of the North Qilian orogenic belt also remains controversial. It is believed to be a mid-ocean ridge, back-arc basin, or subduction environment (Hou et al., 2006; Tseng et al., 2007; Xia et al., 2012; Song et al., 2014). Previous studies on the siliceous rocks in the area suggest that they formed in a continental margin basin or tectonic environment (Du et al., 2006a; b; Zhu and Du, 2007). Previous researchers have also studied the geochemistry of siliceous rocks in the North Qilian orogenic belt and concluded that the tectonic environment of these siliceous rocks, which are associated with volcanic rocks in the rift valley, oceanic crust, island arc, and back-arc basin, was not an oceanic basin or mid-ocean ridge environment, but rather a poly oceanic island or continental margin environment (Du et al., 2007; Yan et al., 2008). In this study, a field geological survey, petrography, zircon U-Pb chronology, and whole-rock geochemistry of the Yushigou ophiolite were conducted in detail. Combined with previously published geological data, the formation age, petrogenesis, and tectonic evolution of the North Qilian orogenic belt were discussed.

Geological background and Petrology

The Qilian orogenic belt (Figure 1A) is part of the Qinling-Qilian-Kunlun fold system (Li et al., 1978), also known as the Central China orogenic belt. It is located in a joint region among the three major blocks in China, namely, the North China Craton in the Northeast, the Yangtze Craton in the southeast, and the Tarim Craton in the northwest (Song et al., 2013a). This study focused on the North Qilian belt and its surrounding areas. At the northeastern margin of the Tibetan Plateau, the North Qilian orogenic belt is an Early Paleozoic suture zone composed of three subunits: the North, Central, and South Qilian belts (Figure 1B; Chen et al., 2014). Furthermore, it is divided into two E-W segments and most ophiolites are distributed in the eastern segment. The ophiolite in the Eastern section of the North Qilian orogenic belt is divided from north to south into the Jiugequan, Dachadaban, Bianmagou, and Yushigou ophiolites.

10.3389/feart.2023.1192997

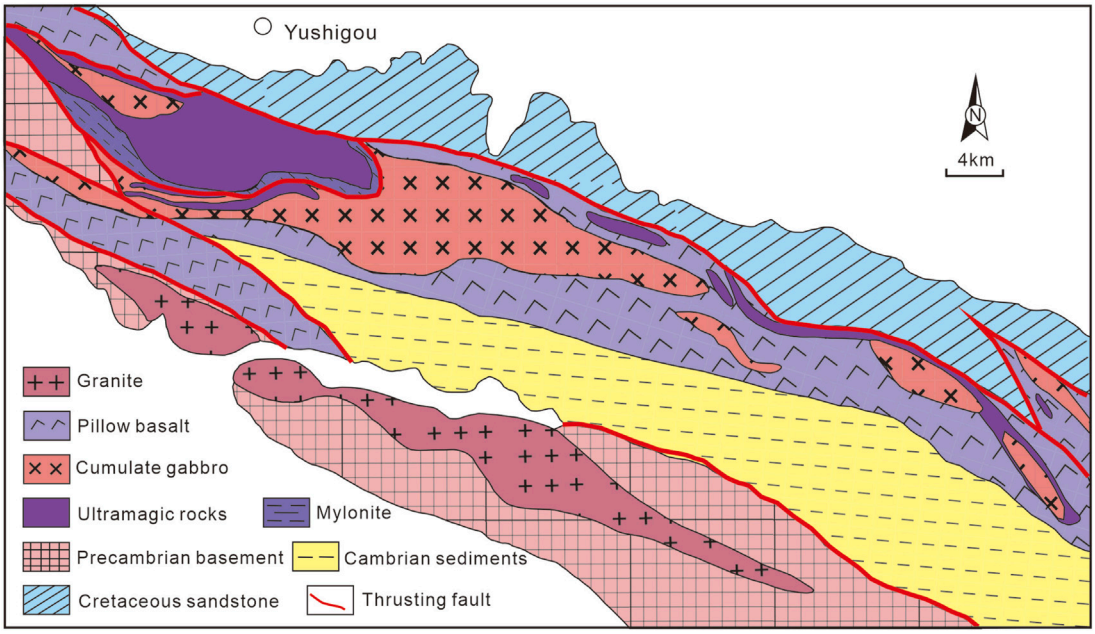

FIGURE 2
Geological map of the Yushigou ophiolite (after Song et al., 2013a).

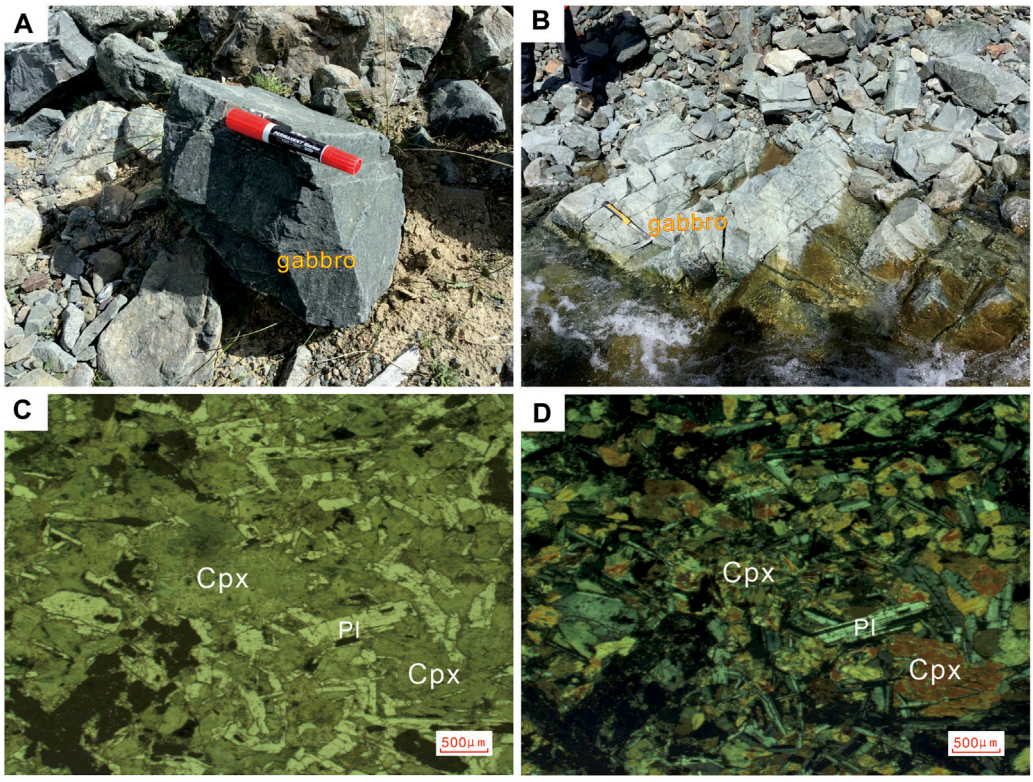

FIGURE 3
(A,B) Field survey photos and **(C,D)** gabbro microscopic photos; Cpx: Clinopyroxene; Pl: Plagioclase.

The Yushigou ophiolite (Figure 2) is found in the middle of the North Qilian belt and represents the boundary between the Alashan Block and the Qilian-Qaidam Micro-Block (Shi et al., 2004; Hou et al., 2006; Song et al., 2013a). The Yushigou ophiolite is 5.0–5.5 km wide from North to South and approximately 14.5 km long from east to west, occurring as a nappe thrust over the Precambrian crystalline basement of the Central Qilian block, in which an ophiolitic mélange appears on both sides (Song et al., 2013a). Carbonatite dykes and carbonated serpentinite blocks are widely observed in the Yushigou mantle complex and have been interpreted as syn-exhumation products formed after serpentinization (Rao, 2015). From North to South, the Yushigou ophiolite consists of peridotites, ultra-mafic to mafic (gabbroic) cumulates, pillow basalts, and sedimentary rocks, including marl and reddish radiolarian chert, in fault contact with each other (Shi et al., 2004; Hou et al., 2006). This set of rock assemblages is an important indicator of the horizontal motion of the plate and represents the remnants of the ancient oceanic crust. In this study, samples from the gabbro in the Yushigou ophiolite were analyzed.

The dominant mineral phase in the Yushigou gabbro is clinopyroxene (40–50 vol%), plagioclase (30–45 vol%), and minor amounts of hornblende (~5 vol%) and olivine (~1 vol%) (Figure 3). The studied gabbro displayed a texture of clinopyroxene and plagioclase reaching 0.5–1 mm in size. A small amount of clinopyroxene exhibited a good euhedral degree. Part of the plagioclase was altered, and another part was gray and translucent under plane-polarized light; the other parts were short, columnar, or plate-shaped.

Analytical methods

Zircon U–Pb geochronology, whole-rock and mineral major and trace element geochemistry, and zircon Hf isotope analyses were conducted at the Guangxi Key Laboratory of Hidden Metallic Ore Deposit Exploration, Guilin University of Technology, China (Zhang et al., 2019; Liu et al., 2020).

Zircon U-Pb dating and Hf isotope

Zircon crystals were extracted from rock samples using conventional crushing, heavy liquid, and magnetic separation techniques and then handpicked. Cathodoluminescence (CL) images of the crystals were used to assess the internal zircon structures and select sites for U–Pb dating. The U–Pb isotopic compositions of the zircons were analyzed using an Agilent 7,500 laser ablation inductively coupled plasma mass spectrometer (LA–ICP–MS). Laser ablation was performed at a constant energy of 80 mJ, with a repetition rate of 6 Hz and spot size of 32 μm. Helium was used to carry the ablated material to the ICP–MS. Elemental corrections were determined relative to the standard glass National Institute of Standards and Technology 610 (Pearce et al., 1997). During our analysis, the Plešovice zircon standard yielded a weighted mean $^{206}Pb/^{238}U$ age of 337.1 ± 0.6 Ma (2σ; mean square weighted deviation (MSWD) = 0.10; n = 52), which is within the error of the suggested value of 337.1 ± 0.4 Ma (Sláma et al., 2008). Age calculations were completed using ICP-MS DataCal (version 8.4; (Liu et al., 2008), and Concordia plots were constructed using Isoplot 3.75 (Ludwig, 2012).

The analyses were performed at a laser beam diameter of 40 μm, repetition rate of 10 Hz, laser power of 100 mJ/pulse, and ablation time of 30 s. GJ-l zircon was analyzed to check the reliability and stability of the instrument. Detailed analytical conditions and procedures were described by Griffin et al. (2000, 2002). Two to four samples were analyzed using the JG-1 standard analyses, and $^{206}Pb/^{207}Pb$ and $^{206}Pb/^{238}U$ values were time-corrected. The raw data were processed offline and reduced using an Excel worksheet (Bühn et al., 2009).

Mineral chemistry

The major elemental compositions of the minerals were measured using a JEOL JXA-8230 electron probe microanalyzer at an accelerating voltage of 15 kV, beam current of 20 nA, and 1–2 μm spot diameter. The dwell time was 10 s for the element peaks and 5 s for the backgrounds adjacent to the peaks. Data were reduced using the atomic number absorption fluorescence correction procedure. The trace elements in the Yushigou clinopyroxene were determined using LA-ICP-MS. The analysis was performed using an Agilent 7500cx ICP-MS and an NWR-193 excimer LA system from Elementary Scientific Company. To determine the clinopyroxene content, we used helium as the carrier gas, and each analysis was performed at 8 Hz, 4 J/cm^2 energy, 30 μm spot diameter, over 40 s. Standard reference glasses SRM 610, SRM 612, and BCR-2G were used as external standards to correct the mass discrimination and time-dependent drift. The analytical accuracy and precision of major and trace elements were better than 10%.

Major and trace element analyses

Fresh samples were collected and crushed, and the chips were soaked in 4 N hydrochloric acid for 30 min to remove any altered material. Rock chips were powdered using an alumina ceramic shatterbox. Prior to major element analyses, loss-on-ignition values were measured using a muffle furnace at a constant temperature of 1,000°C. The baked samples were then formed into glass disks with $Na_2B_4O_7$ $10H_2O$ at 1,150°C. ZSX Primus II X-ray fluorescence was used to determine the composition of major elements. The trace element compositions were measured using an Agilent 7500cx ICP-MS. The precision of the major and trace element measurements was 2%–5%. Standardization was performed using United States Geological Survey (USGS) standards BHVO, AGV, W-2, and G-2 and national rock standards GSR-1, GSR-2, and GSR-3 (Zhang et al., 2019).

Analytical results

Zircon U-Pb geochronology and Lu-Hf isotope

The Zircon U-Pb dating results are listed in Supplementary Table S1. The zircons are mostly euhedral and reveal long to short prismatic forms, with average crystal lengths of 150–300 μm and length-to-width ratios from 2:1 to 3:1. Most zircons were

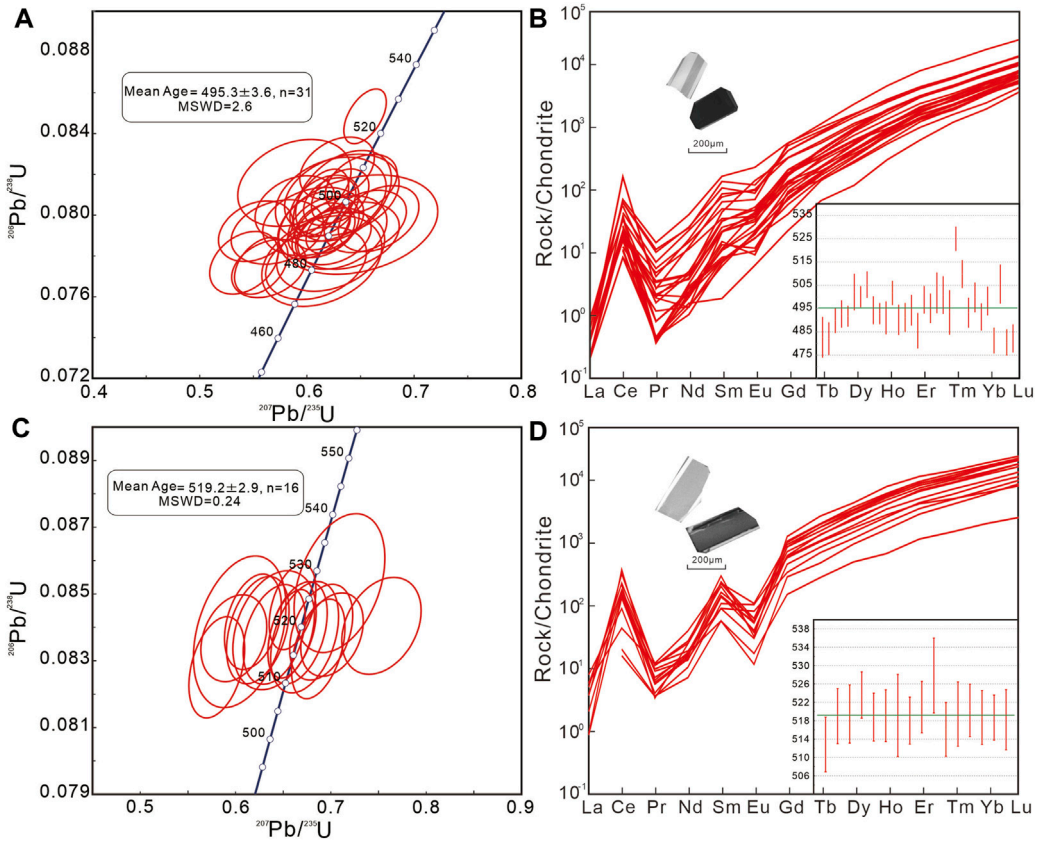

FIGURE 4
(A,C) U-Pb Concordia diagram, weighted mean ages, and mean square weighted deviation (MSWD); **(B,D)** chondrite-normalized rare Earth element (REE) patterns and cathodoluminescence (CL) images for zircons from the Yushigou gabbro. Normalizing values are from Sun and McDonough (1989).

transparent and colorless or pale brown. In the CL images, the zircon crystals are internally homogeneous with weak, broad zoning and without complex internal structures, as is typical of zircons formed in gabbroic magmas (Corfu et al., 2003). All zircon rare Earth element (REE) partition curves show depletion of light rare Earth elements (LREE) and enrichment of heavy rare Earth elements (HREE), with positive Ce anomalies and negative Pr and Eu anomalies. In addition, no overgrowths, mineral or fluid inclusions, or metamictization were observed in the analyzed zircons, suggesting that the zircons were not affected by post-magmatic processes. Thus, the interpretation of the zircon U-Pb isotopic results is simple (Figure 4), and the obtained ages represent the formation time of the gabbro. The Th/U value of the analyzed spots varies from 0.31 to 2.72, suggesting the zircons are of magmatic origin (Williams, 2001; Rubatto, 2002). U-Pb isotopic analyses yielded disparate zircon $^{206}Pb/^{238}U$ ages of 495.3 ± 3.6 Ma (mean square weighted deviation (MSWD) = 2.6) and 519.2 ± 2.9 Ma (MSWD = 0.24), respectively.

The Lu-Hf isotopes were analyzed on selected zircon grains from two different samples that were previously systematically analyzed with U-Pb. Lu-Hf analysis was performed on 41 representative zircon grains dated using the LA-ICP-MS U-Pb method. The results are shown in Supplementary Table S2. The initial Hf composition of zircon represents the $^{176}Hf/^{177}Hf$ value calculated at the time of zircon crystallization, namely, the U-Pb age, likely concordant with that previously obtained for the same crystal. The two-stage depleted mantle Hf model ages (T_{DM} Hf) were calculated using $^{176}Lu/^{177}Hf = 0.0384$ and $^{176}Hf/^{177}Hf = 0.28325$ for the depleted mantle (Chauvel and Blichert-Toft, 2001). The resulting $^{176}Lu/^{177}Hf$ values ranged from 0.282,809 to 0.282,973 with a mean of 0.282,877, indicating that the zircons were weak in radiogenic Hf. The initial zircon $^{176}Hf/^{177}Hf$ value varies with age. Zircons from sample 21-YSG335 had a high $\varepsilon_{Hf}(t)$ between +6.54 and +17.34, with an average of 14.28. The T_{DM} values were restricted to the narrow range from 0.41 to 0.86 Ga. Zircons from sample 21-YSG341 were characterized by positive $\varepsilon_{Hf}(t)$, ranging between +12.13 and +15.8, and T_{DM} values ranging between 0.44 and 0.67 Ga. Their $\varepsilon_{Hf}(t)$ values were close to that of the depleted mantle evolution curve, suggesting that these zircons crystallized from magma with a juvenile signature.

Geochemistry of the major elements

Supplementary Table S3 shows that the SiO_2 contents of the 12 samples range from 45.40 wt% to 57.20 wt%, and the rocks are characterized by low TiO_2 (0.24–1.78 wt%), K_2O (0.01–0.57 wt%) and high Na_2O (0.45–5.15 wt%) contents. The high loss of ignition of rocks (1.62–6.03 wt%) indicates that the samples are slightly altered. The K_2O and Na_2O contents of the rocks may be related to alteration by K- and Na-rich fluids (such as seawater) after

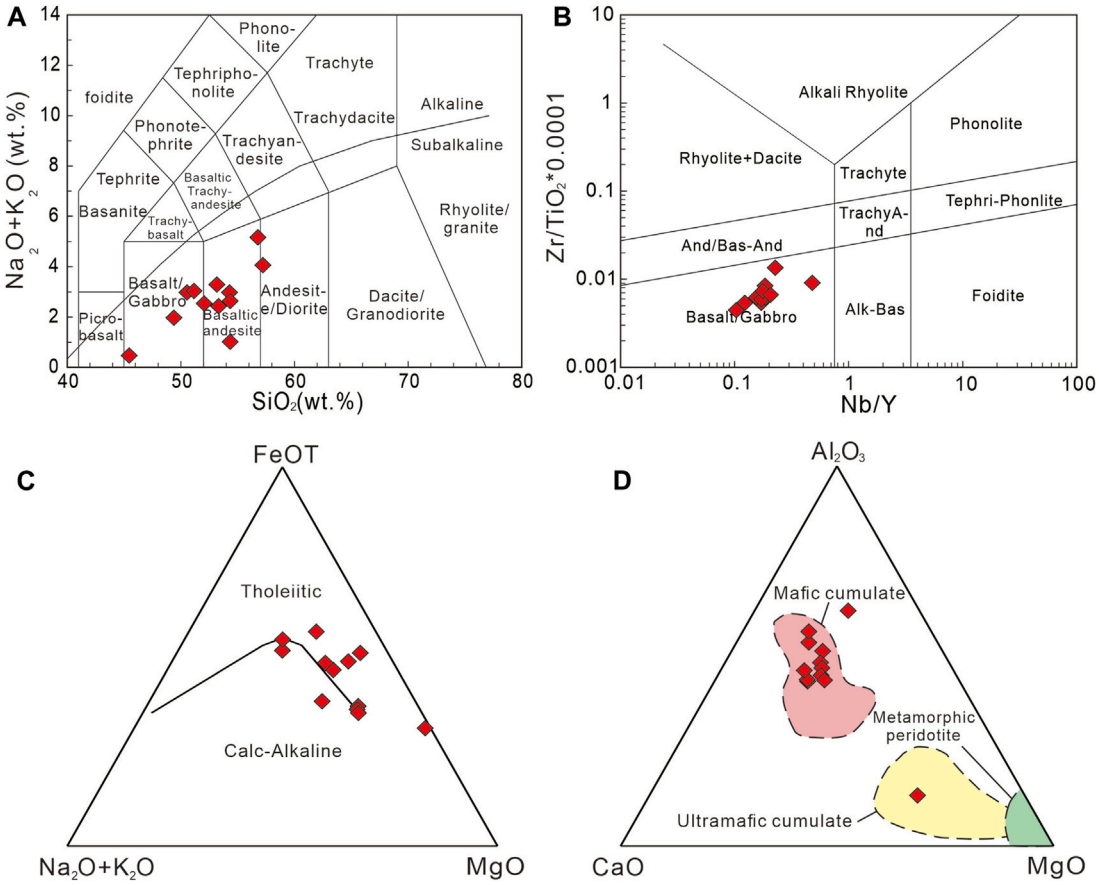

FIGURE 5
(A) Total alkali silica diagram (Le Bas et al., 1986); **(B)** Zr/TiO_2*0.0001-Nb/Y diagram (after Pearce, 1996); **(C)** Al_2O_3-FeOT-MgO composition diagram; and **(D)** Al_2O_3-CaO-MgO composition diagram (Coleman R G, 1977).

formation. The gabbros are enriched in MgO (4.09–25.22 wt%), $Mg^{\#}$ (46.9–82.0), and CaO (3.95–12.92 wt%). This reflects the combined plagioclase and clinopyroxene compositions of the initially formed basic rocks.

The samples collected in this study were greyish-black with medium-to coarse-grained structures. They were mainly composed of clinopyroxene and plagioclase in nearly equal amounts. The secondary mineral is amphibole, which contains small amounts of quartz. Under a single polarized electron microscope, the entire thin section of the sample was dark green, showing a gabbro structure, and the contents of clinopyroxene and feldspar were almost equal. Field and electron microscope observations indicated that the samples collected were gabbro. The results shown in the total alkali-silica diagram are consistent with field observations and electron microscopy (Figure 5A). As the samples were likely altered by K- and Na-rich fluids, the increase in the total alkali content and loss of ignition caused a shift in the rock composition. To further determine the rock type, immobile high-field-strength elements were used for discrimination (Figure 5B), showing that all samples fell into the basalt field. Regarding the relationship between FeO^T, MgO, and Na_2O+K_2O (Figure 5C), most of the rocks were of the tholeiitic series, and the rest were of the calc-alkaline series. In the Al_2O_3-CaO-MgO diagram (Figure 5D), almost all samples were distributed within the mafic cumulative rock fields, and one of the samples fell within the ultramafic cumulative rock fields.

Rare earth elements and trace element geochemistry

Yushigou gabbros have low ΣREE content ranging from 8.36 to 75.60 ppm, with low to slight enrichment in LREE in the chondrite-normalized REE distribution patterns (Figure 6A). The $(La/Yb)_N$ values range from 0.80 to 1.66, while the $(La/Sm)_N$ values vary from 0.54 to 1.61. The parallel REE distribution lines indicate that all samples were derived from the same magma source. In addition, the gabbro samples displayed mid-ocean ridge basalt (MORB)-like trace-element characteristics. Notably, two samples exhibited Nb and Ta depletion (Figure 6B).

Clinopyroxene characteristics

The major and trace element data for clinopyroxenes in the Yushigou gabbro are presented in Supplementary Tables S4, S5. The analyzed clinopyroxene grains from the Yushigou gabbro were augmented (Figure 7A). Clinopyroxene analysis of the Yushigou gabbro showed relatively high MgO (14.28–16.09 wt%) contents, with Mg# (100 × Mg/[Mg + Fe^{2+}]) values ranging from 61 to 65. The grains are characterized by relatively low Al_2O_3 (3.46–8.61 wt

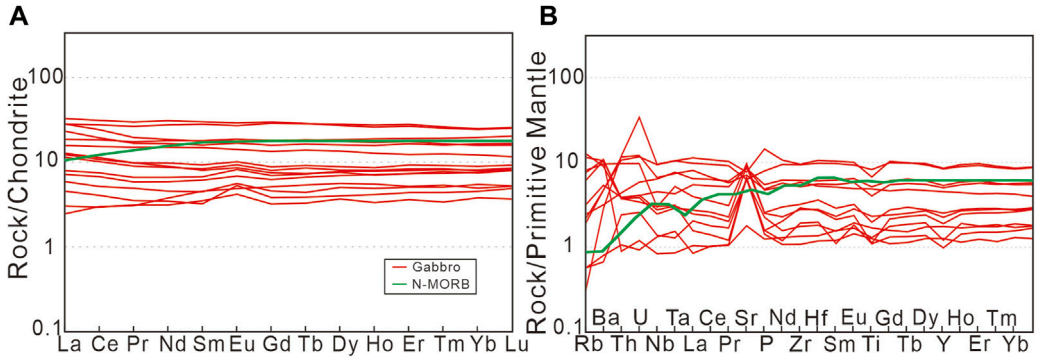

FIGURE 6
(A) Chondrite-normalized REEs; **(B)** Primitive-mantle-normalized trace elements. Normalization values are from Sun and McDonough (1989); N-MORB, normal mid-ocean ridge basalt.

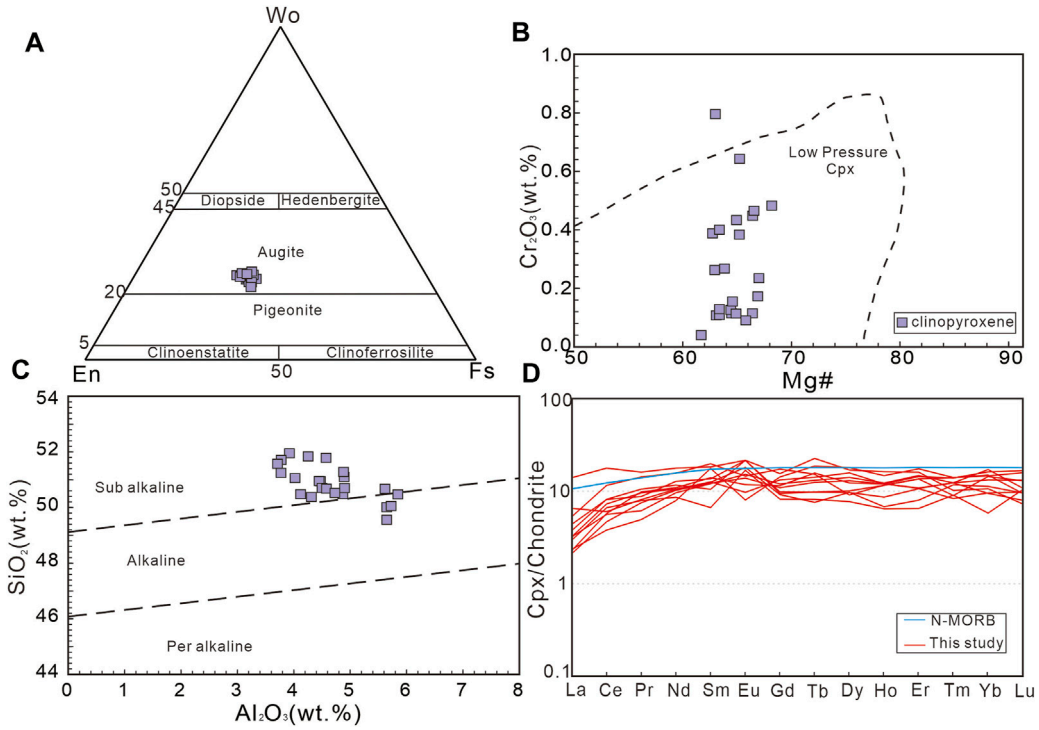

FIGURE 7
Clinopyroxene compositions diagrams; **(A)** Wo-En-Fs diagram modified after Mahoney et al. (1998); **(B)** Cr_2O_3 vs. Mg# in clinopyroxenes (Elthon, 1987), **(C)** SiO_2 vs. Al_2O_3 diagram (after Le Bas, 1962), and **(D)** Chondrite-normalized REEs. Normalization values are from Sun and McDonough. (1989).

%) and Na_2O (0.40–1.18 wt%) contents and high Cr_2O_3 (0.27–2.37 wt%) content. These results suggest that the clinopyroxenes of the Yushigou gabbro were subalkaline and crystallized under medium- and low-pressure conditions (Figures 7B, C). The clinopyroxenes exhibit low total REE contents (9.49–38.36 ppm). The REEs in the Yushigou clinopyroxene samples had characteristics of normal (N-)MORB with a relatively flat trend (Figure 7D). Compared to HREEs, LREEs were slightly depleted.

Discussion

Formation age

Based on previous studies of the North Qilian orogenic belt, we collected the ages of the ophiolites in Yushigou and adjacent areas, which can be divided into three major stages according to their formation time. The first stage occurred at ~550 Ma, and its lithology was mainly composed of gabbro (566–516 Ma),

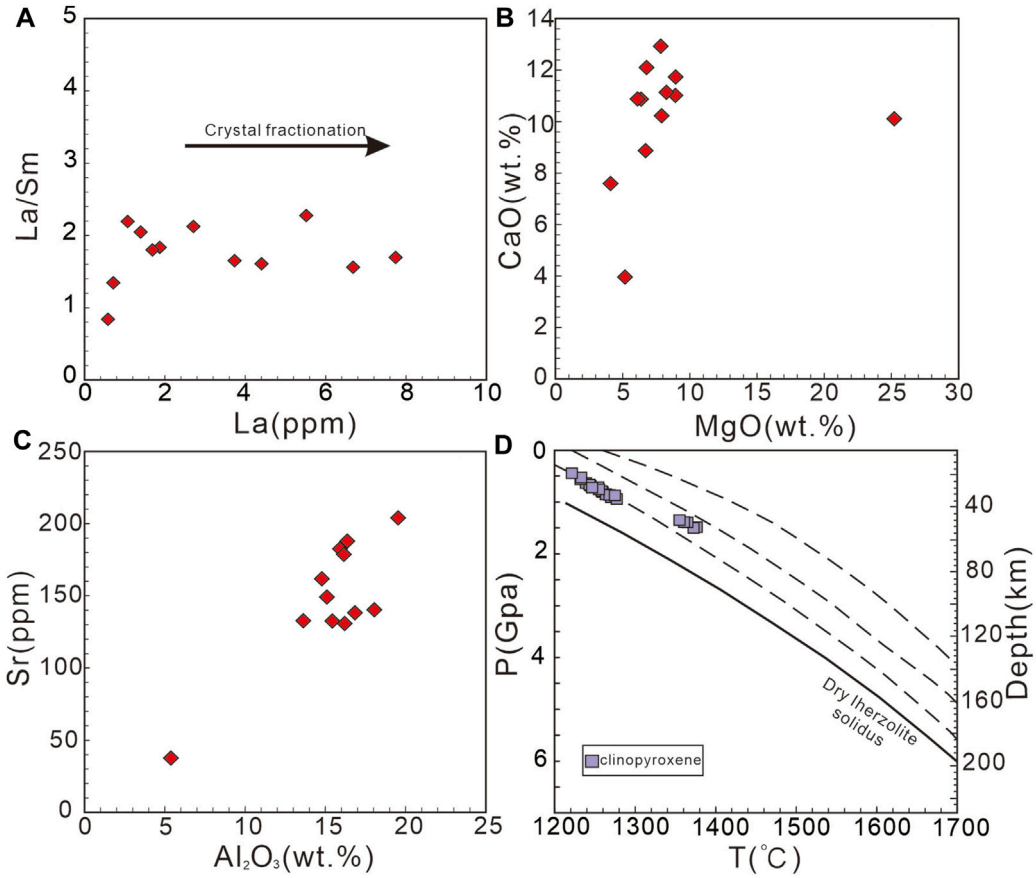

FIGURE 8
(A) La/Sm vs. La diagram; **(B)** CaO (wt%) vs. MgO (wt%) diagram; **(C)** Sr (ppm) vs. Al_2O_3 (wt%) diagram; **(D)** Relationship between temperature, pressure, and depth (Lee et al., 2009).

volcanic rock (593 Ma), amphibolite (534 Ma), and a subduction complex (545 Ma) (Xia et al., 1995; Shi et al., 2004; Song et al., 2019; Yan et al., 2019). The second stage was from 520 to 490 Ma; the lithology of this stage was mainly volcanic rock (495 Ma), gabbro (513–490 Ma), and ophiolites (504–495 Ma) (Xia et al., 1995; Xiang et al., 2007; Zeng et al., 2007; Xia and Song, 2010; Song et al., 2019). The third stage occurred at ~450 Ma, and its main lithology was gabbro (479–448 Ma) (Song et al., 2007; 2013a).

Shi et al. (2004) found that the complementarity between cumulative gabbro and lharzolite in the Yushigou ophiolite was stronger than that between the upper pillow lava and lharzolite, indicating that gabbro represents the melting products of the primitive mantle during the formation of the Yushigou ophiolite. Based on this, zircon U-Pb dating of two gabbro samples from the Yushigou ophiolite was conducted, showing weighted mean ages of 495.3 ± 3.6 Ma and 519.2 ± 2.9 Ma, respectively. This indicates that they formed during the second stage (520–490 Ma). Combined with the results of previous studies and our age determination, we suggest that the ophiolite in the North Qilian belt first formed in the Cambrian period.

Petrogenesis

Magmatic evolution

For a basic–ultrabasic rock series resulting from separation crystallization, the projection points on the La/Sm vs. La elemental covariant map form a horizontal line (Allegre and Minster, 1978; Yang and Gu, 1990). In the La/Sm-La diagram (Figure 8A), the horizontal and linear relationship indicates that separation crystallization is the main factor controlling magma evolution rather than partial melting. The general trends of CaO and MgO in the Yushiguo gabbros indicated significant fractionation of olivine and clinopyroxene (Figure 8B). Moreover, the increase in Sr content with increasing Al_2O_3 content (Figure 8C) suggests the removal of plagioclase. However, the Yushigou gabbros do not show a significant negative Eu anomaly, indicating that plagioclase may not have been significantly fractionated during magma evolution.

Temperature is a key variable controlling magmatic phase equilibria (Neave and Putirka, 2017). In addition to composition, crystallinity, and oxygen fugacity, pressure is another primary variable that affects magmatic phase equilibria (Yoder and Tilley, 1962). Understanding the distribution of the magma storage depth within the lithosphere provides information on both

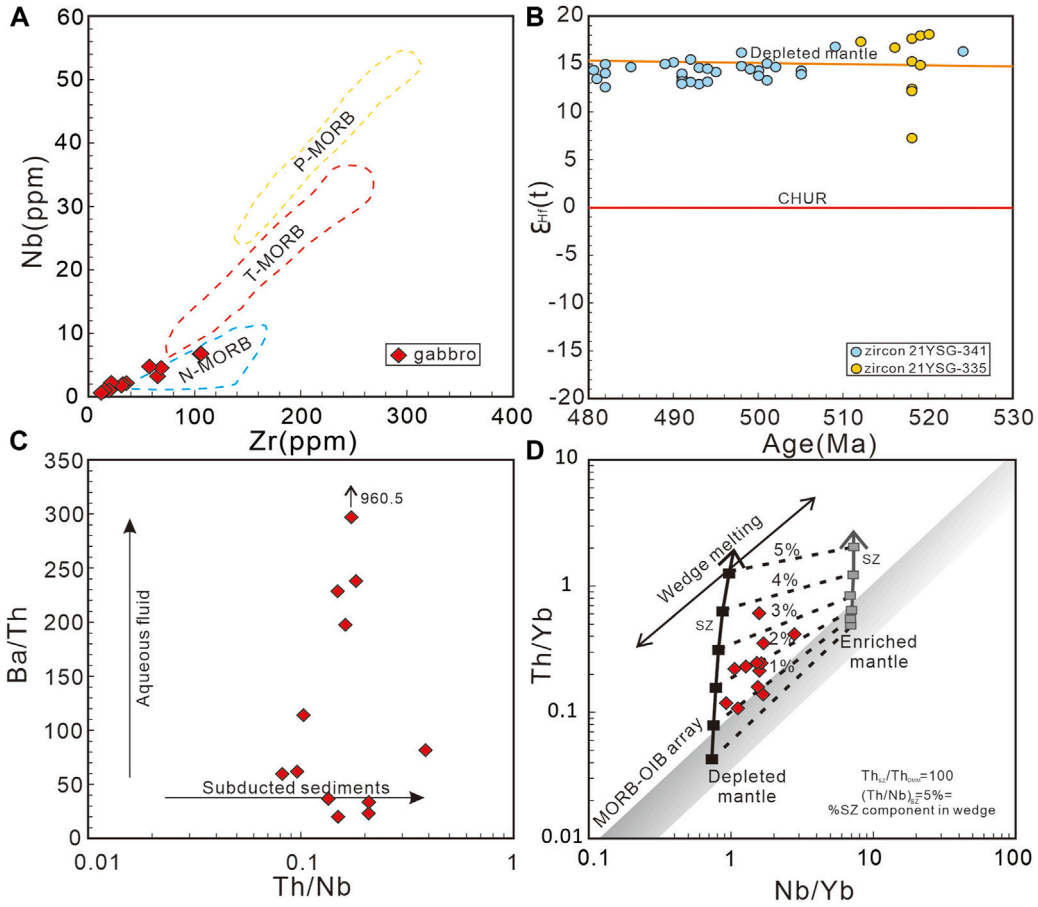

FIGURE 9
(A) Nb vs. Zr diagram (Le Roex et al., 1983); **(B)** $\varepsilon_{Hf}(t)$ vs. Age diagram (Matteini et al., 2010); **(C)** Ba/Th vs. Th/Nb diagram; **(D)** Th/Yb vs. Nb/Yb diagram (after Pearce, 2008); N-MORB, normal or depleted mid-ocean basalt ridge; T-MORB, transitional MORB; P-MORB, plume enriched MORB; CHUR, chondritic uniform reservoir.

oceanic and continental crustal formation mechanisms (Henstock et al., 1993; Kelemen et al., 1997; Annen et al., 2006). Therefore, it is essential to determine magma storage pressures and depths.

In this study, the clinopyroxene thermometer proposed by Putirka (2008) was used to calculate the temperature and pressure of the gabbro in the Yushigou ophiolite. The formation temperature of clinopyroxene is 1,221.3°C–1,376.6°C, and the pressure at this temperature is 4.5–15.0 kbar. The temperature range of the Yushigou ophiolite was 1,174°C–1,402°C, and the mineral phase equilibrium temperature was approximately 1,230°C, which is consistent with the temperature measured in this study. The consolidation equilibrium temperature of mantle magmatic rocks in the Yushigou ophiolite is speculated to be approximately 1,200°C (Yan, 2014). In this study, temperature, pressure, and depth models (Lee et al., 2009) were used to estimate the mantle magmatic depth of the Yushigou ophiolite. The simulation estimated the depth of the clinopyroxene crystals, indicating that the mantle magmatic rocks in the Yushigou ophiolite began to consolidate at approximately 60 km (Figure 8D).

Magma source

The Yushigou gabbro is a magmatic rock of the tholeiitic series, featuring mild large-ion lithophile elements and high-field strength elements, which are typical geochemical characteristics of MORB. The geochemical characteristics of the trace elements show that the gabbro formed in the depleted mantle. The rare Earth distribution curve and trace element multi-element diagram of the Yushigou gabbro are nearly parallel to those of N-MORB (Figure 6), and the Th/Ta, Th/Yb, and Zr/Nb values of trace elements in the Yushigou gabbros are similar to those of the depleted mantle (Th/Ta=2.2, Th/Yb=0.25, Zr/Nb=18, from Condie (1989)). As shown in the Nb vs. Zr diagrams (Figure 9A), the Yushigou gabbros fall near the primitive mantle line, which is close to the depletion type. In addition, the Hf isotopes of the zircons reflect the characteristics of the source area. No inherited or captured zircon was found in the gabbro-zircon CL image or *in situ* micro-survey of the Yushigou ophiolite, indicating that the zircon crystallized in a homogeneous, unmixed magmatic source. The relatively high $\varepsilon_{Hf}(t)$ values of the Yushigou gabbros indicate that they primarily originated from depleted mantle (Figure 9B).

Ba is a fluid-active element (Kessel et al., 2005), which easily enters the mantle *via* fluid migration during subduction (Morris and

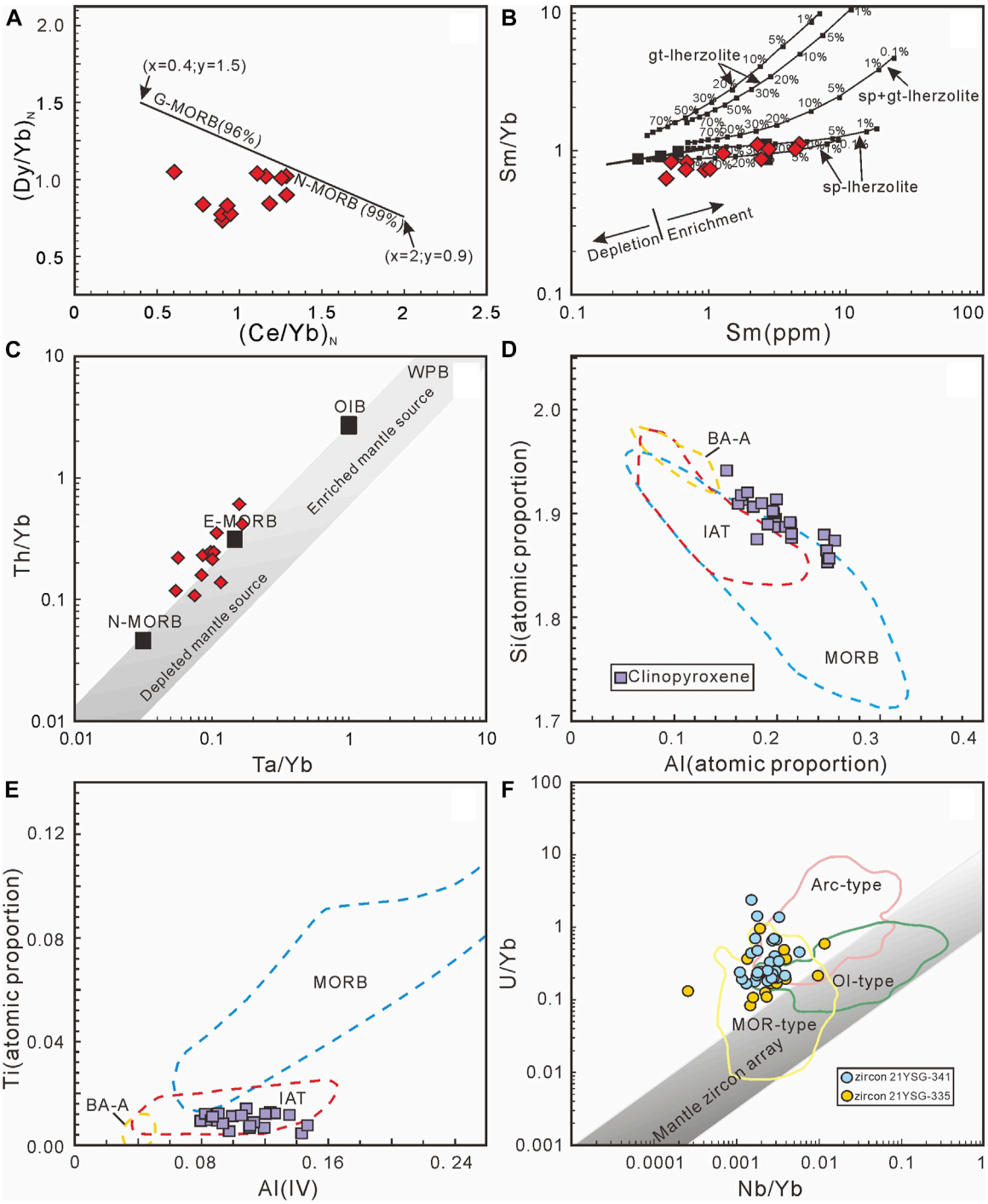

FIGURE 10
(A) $(Dy/Yb)_N$ vs. $(Ce/Yb)_N$ diagram (Saccani, 2015); **(B)** Sm/Yb vs. Sm diagram (Aldanmaz et al., 2000); **(C)** Th/Yb vs. Ta/Yb diagram (Pearce, 1982); **(D)** Si vs. Al diagram; **(E)** Ti vs. Al (IV) diagrams (Beccaluva et al., 1989) of clinopyroxene composition (atomic proportion); and **(F)** Zircon U/Yb vs. Nb/Yb diagram (Grimes et al., 2015);. OI, ocean-island; MOR, mid-ocean ridge; MORB, mid-ocean ridge basalt.; G-MORB, garnet source basalts; N-MORB, normal mid-ocean basalt ridge; Arc, continental arc; BA-A, back-arc andesite; IAT, island-arc tholeiite.

Ryan, 2003). Because of the significant difference in the Ba content between the crust and mantle, Ba can be used to trace the recirculation-related processes of subducting materials (Elliott et al., 1997; Murphy et al., 2002; Pearce and Stern, 2006; Kuritani et al., 2011). A high Ba/Th value indicates aqueous fluid from the dehydrated ocean crust or sediment, and a high Th/Nb value indicates the addition of partially melted material from subducted sediments. The studied samples showed high Ba/Th and Th/Nb values, indicating that they were affected by two subduction components (Figure 9C), and the additional

subduction components comprised 1%–3% of the total composition (Figure 9D).

Recent research has shown that, in contrast to N-MORB, garnet source basalts (G-MORB) exhibit a significant garnet signature (e.g., Montanini et al., 2008; Saccani et al., 2008; 2013). This garnet signature can be highlighted using LREE/HREE and middle rare Earth elements (MREE) to HREE ratios, such as Ce/Yb and Dy/Yb. In the chondrite-standardized $(Ce/Yb)_N$ vs. $(Dy/Yb)_N$ diagram, all sample sites are located on the N-MORB side (Figure 10A), which is significantly different from the G-MORB and depleted of HREE. This indicates that the Yushigou gabbro was derived from a mantle source of non-garnet peridotite (Saccani, 2015). The Ce/Yb values of gabbros ranged from 2.18 to 4.63, which indicates that the gabbros were sourced from the stable zone of spinel less than 70 km deep (Xiao et al., 2003). This is consistent with the formation depth of clinopyroxene in the simulation, where spinel lherzolite partial melts, mantle residues, and melts have similar Sm/Yb values, and Sm values decrease with an increase in the partial melting degree (Aldanmaz et al., 2000). Therefore, the Yushigou gabbro falls within the spinel lherzolite region, and the Sm values vary widely, whereas the Sm/Yb values are relatively constant (Figure 10B).

Geodynamic interpretations

Active elements (Cs, Rb, Sr, and Na) migrate under the influence of alteration and are not effective indicators of tectonic environments; however, most high-field elements (Ta, Nb, Zr, Hf, Ti, Th, and REE) are unaffected (Mullen, 1983). In this study, high-field elements were used to identify the tectonic environment of the Yushigou ophiolite suite gabbro. Studies have demonstrated that both Th and Ta are closely related to subduction. Both are highly incompatible elements, and their elemental ratios remain relatively stable during mantle melting or crystallization differentiation. However, during subduction magmatism, the sediments are rich in Th and depleted in Ta. The addition of a small amount of sediment melt can lead to an increase in the Th content of the magma, and an increase in the Th/Yb value can reflect the contribution of sediment melt in the source region (Elliott et al., 1997; Class et al., 2000; Singer et al., 2007). In contrast, the Ta content is sensitive to subduction fluids. The covariant relationship between the Th/Yb and Ta/Yb values suggests that the components (including sediments and fluids) derived from subduction contributed to the generation of the Yushigou gabbros (Figure 10C).

Tectonic discrimination diagrams of the elemental distributions of Si, Al, and Ti in the clinopyroxene compositions provide a distinct classification of magma types (Beccaluva et al., 1989). In the clinopyroxene Si *versus* Al diagram (Figure 10D), the sample fell into and near the MORB field. However, in the clinopyroxene Ti *versus* Al^{IV} diagram (Figure 10E), the sample falls within the island arc tholeiite (IAT) field. Grimes et al. (2007) used U, Th, Hf, Y, and Yb (as a monitor for HREEs) to discriminate crystallized zircons from the MORB mantle from those formed in continental magmatic settings. During subduction, easily migrated incompatible elements (such as large ion lithophile elements, LREEs, and U) are separated from non-migrated high-field strength elements (such as Nb, Y, and HREEs). These easily migrated incompatible elements are mobilized by plate-derived fluids to increase the U/Yb value in the magma (Grimes et al., 2015). Zircons from the Yushigou gabbros were mostly within the 90% confidence interval of the MORB zircons, as presented in Figure 10F, although several overlapped with primitive magmatic arc zircons. This suggests that zircons from the Yushigou gabbro formed in a subduction-related environment.

Three explanations have been proposed for the tectonic evolution of the North Qilian orogenic belt. The first suggests that the ancient ocean was a part of the Proto-Tethys and that the tectonic evolution of the North Qilian orogenic belt can be regarded as a portion of the Tethyan tectonic domain (Wang and Liu, 1976). The second hypothesis proposes that the ancient ocean represented a limited extensional oceanic basin developed on the southern margin of the North China Craton. The continental margin rifted and expanded to form this basin, which then closed to form an orogenic belt (Feng and He, 1996; Xia et al., 1996; 1998). The final explanation emphasizes that the ancient ocean in the North Qilian orogenic belt was part of the Paleo-Asian Ocean (Zhang et al., 1997). After several years of discussion, most scholars agree with the second hypothesis (Feng and He, 1994; Qian et al., 2001; Du et al., 2006a; 2006b; 2007; Zhu and Du, 2007).

After the division of the Rodinia supercontinent, the Qilian Ocean opened and expanded as part of the Iapetus Ocean from approximately 710–520 Ma (Song et al., 2013b). Basic rocks with mid-ocean ridge or back-arc basin characteristics have been identified in the Yushigou area with ages ranging from 550 to 521 Ma (Xia et al., 1998; Shi et al., 2004; Hou et al., 2006). Initial ocean subduction and infant arc magmatism occurred from 520 to 490 Ma, which caused partial melting of the mantle wedge and formed infant arc basalts from 517 to 505 Ma (Song et al., 2013b). Wu et al. (2010) identified arc volcanic granites with an age of 512 Ma. Song et al. (2013a) reported that the magmatic zircon age of the Chaidanuo intrusion was 516 ± 4 Ma, recording the oldest arc magmatic activity in the North Qilian Orogenic Belt. A report on the Dachadaban boninite (505 Ma) also suggested a pre-arc environment related to the inner oceanic island arc in the North Qilian orogenic belt (Chen et al., 1995; Meng et al., 2010). This implies the formation of back-arc basins (Song et al., 2013b). The study from Hou et al. (2006) of isotope means indicated that the Yushigou ophiolite most likely formed in a mid-ocean ridge or mature back-arc basin. Combined with previous data and this study, the back-arc basin of the North Qilian orogenic belt may have evolved to a relatively mature stage from 519 to 495 Ma.

Conclusion

1) The zircon U-Pb chronology shows that the gabbro in the Yushigou ophiolite from the North Qilian orogenic belt was formed from 519 to 495 Ma as a product of Cambrian magmatism.
2) The gabbro in the Yushigou ophiolite in the North Qilian orogenic belt belongs to the tholeiite series and exhibits typical N-MORB geochemical characteristics. The source area features characteristics of mantle source materials, and 1%–3% of subduction materials were added. When clinopyroxene minerals were formed, the magma temperature ranged from 1,221.3°C to 1,376.6°C, and the pressure ranged from 4.5 to 15 kbar. The

origin of the rocks may include a high degree of partial melting in the spinel lherzolite source area.

3) Whole-rock geochemistry and mineral analysis of gabbro in the Yushigou ophiolite in the North Qilian belt show the dual characteristics of MORB and IAT, suggesting that it may have formed in a back-arc basin environment.

Data availability statement

The original contributions presented in the study are included in the article/Supplementary Material, further inquiries can be directed to the corresponding authors.

Author contributions

HT: Investigation, Conceptualization, Data Curation, Formal analysis, Visualization, Writing–Original Draft, Writing–Review and Editing. XL (2nd author): Investigation, Conceptualization, Formal analysis, Supervision, Writing–Original Draft, Writing–Review and Editing, Funding acquisition, Project administration. HW: Conceptualization, Formal analysis, Visualization, Supervision, Writing–Original Draft, Writing–Review and Editing. DL: Investigation, Conceptualization. XL (5th author): Investigation, Conceptualization, Formal analysis, Writing–Original Draft, Writing–Review and Editing, Funding acquisition, Project administration. QS: Investigation. ZL: Data Curation, Formal analysis. RH: Investigation, Conceptualization. QY: Investigation, Conceptualization.

Funding

This work was financially supported by the National Natural Science Foundation of China (92055208, 42203051), the Guangxi Science Innovation Base Construction Foundation (GuikeZY21195031), Guangxi Natural Science Foundation of China for Young Scholars (2022GXNSFBA035538), and the Fifth Bagui Scholar Innovation Project of Guangxi Province (to Xu Jifeng).

Acknowledgments

We would like to thank the editors and reviewers for their constructive comments, which improved the quality of this paper. We would also like to thank Zhang Zhiguo, Xiao Yao, QS Yujia, Zhang Yinhui, Yu Hongxia, and Liu Yizhi for their help with analyses and fieldwork.

Conflict of interest

The authors declare that the research was conducted in the absence of any commercial or financial relationships that could be construed as a potential conflict of interest.

Publisher's note

All claims expressed in this article are solely those of the authors and do not necessarily represent those of their affiliated organizations, or those of the publisher, the editors and the reviewers. Any product that may be evaluated in this article, or claim that may be made by its manufacturer, is not guaranteed or endorsed by the publisher.

Supplementary material

The Supplementary Material for this article can be found online at: https://www.frontiersin.org/articles/10.3389/feart.2023.1192997/full#supplementary-material

References

Aldanmaz, E., Pearce, J. A., Thirlwall, M. F., and Mitchell, J. G. (2000). Petrogenetic evolution of late Cenozoic, post-collision volcanism in Western Anatolia, Turkey. *J. Volcanol. Geotherm. Res.* 102, 67–95. doi:10.1016/s0377-0273(00)00182-7

Allegre, C. J., and Minster, J. F. (1978). Quantitative models of trace element behavior in magmatic processes. *Earth Planet. Sci. Lett.* 38, 1–25. doi:10.1016/0012-821x(78)90123-1

Annen, C., Blundy, J. D., and Sparks, R. S. J. (2006). The genesis of intermediate and silicic magmas in deep crustal hot zones. *J. Petrology* 47 (3), 505–539. doi:10.1093/petrology/egi084

Beccaluva, L., Macciotta, G., Piccardo, G. B., and Zeda, O. (1989). Clinopyroxene composition of ophiolite basalts as petrogenetic indicator. *Chem. Geol.* 77, 165–182. doi:10.1016/0009-2541(89)90073-9

Buhn, B., Pimentel, M. M., Matteini, M., and Dantas, E. (2009). High spatial resolution analysis of Pb and U isotopes for geochronology by laser ablation multi-collector inductively coupled plasma mass spectrometry (LA-MC-ICP-MS). *Ann. Braz. Acad. Sci.* 81, 99–114. doi:10.1590/s0001-37652009000100011

Chauvel, C., and Blichert-Toft, J. E. (2001). A hafnium isotope and trace element perspective on melting of the depleted mantle. *Earth Planet. Sci. Lett.* 190, 137–151. doi:10.1016/s0012-821x(01)00379-x

Chen, Y., Song, S., Niu, Y., and Wei, C. (2014). Melting of continental crust during subduction initiation: A case study from the Chaidanuo peraluminous granite in the North Qilian suture zone. *Geochimica Cosmochimica Acta* 132, 311–336. doi:10.1016/j.gca.2014.02.011

Chen, Y., Zhou, D. J., and Wang, E. Q. (1995). Discovery and geochemical characteristics of bothite series rocks in dacha daban ophiolite, sunan county, northern qilian. *Acta Petrol. Sin.* 11, 147–153. (in Chinese with English abstract).

Class, C., Miller, D. M., Goldstein, S. L., and Langmuir, C. H. (2000). Distinguishing melt and fluid subduction components in umnak volcanics, aleutian arc: DISTINGUISHING melt and fluid subduction components in umnak volcanics, aleutian ARCfluid subduction components in umnak volcanics, aleutian arc. *Geochem. Geophys. Geosystems* 1. doi:10.1029/1999gc000010

Coleman, R. G. (1977). Ophiolite: Ancient oceanic lithosphere? *Mineral. Mag.* 42 (322).

Condie, K. C. (1989). Geochemical changes in baslts and andesites across the archean-proterozoic boundary: Identification and significance. *Lithos* 23 (1-2), 1–18. doi:10.1016/0024-4937(89)90020-0

Corfu, F., Hanchar, J. M., Hoskin, P., and Kinny, P. (2003). Atlas of zircon textures. *Rev. Mineralogy Geochem.* 16, 469–500. doi:10.2113/0530469

Dilek, Y., and Furnes, H. (2011). Ophiolite Genesis and global tectonics: Geochemical and tectonic fingerprinting of ancient oceanic lithosphere. *Geol. Soc. Am. Bull.* 123 (3-4), 387–411. doi:10.1130/b30446.1

Dilek, Y., Furnes, H., and Shallo, M. (2007). Suprasubduction zone ophiolite formation along the periphery of Mesozoic Gondwana. *Gondwana Res.* 11 (4), 453–475. doi:10.1016/j.gr.2007.01.005

Dilek, Y. (2003). *Ophiolite concept and its evolution*, 373. Special Paper of the Geological Society of America, 1–16.

Du, Y. S., Zhu, J., and Gu, S. L. (2006b). Geochemical characteristics and tectonic significance of ordovician siliceous rocks in shihuigou, yongdeng, North Qilian. *Geol. Rev.* 52 (2), 184–189. (in Chinese with English abstract).

Du, Y. S., Zhu, J., and Gu, S. L. (2007). Sedimentary geochemical characteristics of Cambrian-Ordovician siliceous rocks in North Qilian orogenic belt and their enlightenment to multi-island oceans. *Chin. Sci. Ser. D Earth Sci.* 37 (10), 1314–1329. (in Chinese with English abstract).

Du, Y. S., Zhu, J., and Gu, S. L. (2006a). Sedimentary geochemical characteristics of Ordovician siliceous rocks in Sunan area of North Qilian Mountains and their tectonic significance of multi-island oceans. *Geosciences-Journal China Univ. Geosciences* 31 (1), 101–109. (in Chinese with English abstract).

Elliott, T., Plank, T., Zindler, A., White, W., and Bourdon, B. (1997). Element transport from slab to volcanic front at the Mariana arc. *J. Geophys. Res.* 102, 14991–15019. doi:10.1029/97jb00788

Elthon, D. (1987). Petrology of gabbroic rocks from the mid-cayman rise spreading center. *J. Geophys. Res.* 92, 658–682. doi:10.1029/jb092ib01p00658

Feng, Y. M., and He, S. P. (1996). *Geotectonics and orogenesis of qilian orogenic belt*. Beijing: Geological Publishing House, 37–70. (in Chinese with English abstract).

Feng, Y. M., and He, S. P. (1994). Petrochemical characteristics and formation environment of Cambrian-Ordovician siliceous rocks in North Qilian. *Geol. Sci. northwest China* 15 (1), 17–25. (in Chinese with English abstract).

Feng, Y. M., and He, S. P. (1995). Research for geology and geochemistry of several ophiolites in the North Qilian Mountains, China. *Geol. Rev.* 40, 252–264. (in Chinese with English abstract).

Fu, C. L., Yan, Z., Wang, Z. Q., Buckman, S., Aitchison, J. C., Niu, M., et al. (2018). Lajishankou ophiolite complex: Implications for paleozoic multiple accretionary and collisional events in the South Qilian belt. *Adv. Earth space Sci.* 37 (5), 1321–1346. doi:10.1029/2017tc004740

Griffin, W. L., Pearson, N. J., Belousova, E., Jackson, S., van Achterbergh, E., O'Reilly, S. Y., et al. (2000). The Hf isotope composition of cratonic mantle: LAM-MC-ICPMS analysis of zircon megacrysts in kimberlites. *Geochimica Cosmochimica Acta* 64, 133–147. doi:10.1016/s0016-7037(99)00343-9

Griffin, W. L., Wang, X., Jackson, S. E., Pearson, N., O'Reilly, S. Y., Xu, X., et al. (2002). Zircon chemistry and magma mixing, SE China: *In-situ* analysis of Hf isotopes, tonglu and pingtan igneous complexes. *Lithos* 61, 237–269. doi:10.1016/s0024-4937(02)00082-8

Grimes, C. B., John, B. E., Kelemen, P. B., Mazdab, F., Wooden, J. L., Cheadle, M. J., et al. (2007). Trace element chemistry of zircons from oceanic crust: A method for distinguishing detrital zircon provenance. *Geology* 35, 643–646. doi:10.1130/g23603a.1

Grimes, C. B., Wooden, J. L., Cheadle, M. J., and John, B. E. (2015). Fingerprinting" tectono-magmatic provenance using trace elements in igneous zircon. *Contributions Mineralogy Petrology* 170, 46. doi:10.1007/s00410-015-1199-3

Henstock, T., Woods, A., and White, R. (1993). The accretion of oceanic crust by episodic sill intrusion. *J. Geophys. Res.* 98, 4143–4161. doi:10.1029/92jb02661

Hou, Q. Y., Zhao, Z. D., Zhang, H. F., Zhang, B. R., and Chen, Y. L. (2006). Indian ocean-MORB-type isotopic signature of Yushigou ophiolite in North Qilian mountains and its implications. *Chin. Sci. Ser. D Earth Sci.* 49 (6), 561–572. doi:10.1007/s11430-006-0561-8

Kelemen, P., Koga, K., and Shimizu, N. (1997). Geochemistry of gabbro sills in the crust-mantle transition zone of the Oman ophiolite: Implications for the origin of the oceanic lower crust. *Earth Planet. Sci. Lett.* 146, 475–488. doi:10.1016/s0012-821x(96)00235-x

Kessel, R., Schmidt, W., Ulmer, P., and Pettke, T. (2005). Trace element signature of subduction-zone fluids, melts and supercritical liquids at 120–180 km depth. *Nature* 437 (7059), 724–727. doi:10.1038/nature03971

Kuritani, T., Ohtani, E., and Kimura, J. I. (2011). Intensive hydration of the mantle transition zone beneath China caused by ancient slab stagnation. *Nat. Geosci.* 4 (10), 713–716. doi:10.1038/ngeo1250

Le Bas, M. J. (1962). The role of aluminum in igneous clinopyroxenes with relation to their parentage. *Am. J. Sci.* 260, 267–288. doi:10.2475/ajs.260.4.267

Le Bas, M. J., Le Meaitre, R. W., Streckeisen, A., and Zanettin, B. (1986). A chemical classification of volcanic rocks based on the total alkali-silica diagram. *J. Petrology* 27 (3), 745–750. doi:10.1093/petrology/27.3.745

Le Roex, A. P., Dick, H. J. B., Erlank, A. J., Reid, A. M., Frey, F. A., and Hart, S. R. (1983). Geochemistry, mineralogy and petrogenesis of lavas erupted along the southwest Indian ridge between the bouvet triple junction and 11 degrees east. *J. Petrology* 24, 267–318. doi:10.1093/petrology/24.3.267

Lee, C.-T. A., Luffi, P., Plank, T., Dalton, H., and Leeman, W. P. (2009). Constraints on the depths and temperatures of basal-tic magma generation on Earth and other terrestrial planets using new thermobarometers for mafic magmas. *Earth Planet. Sci. Lett.* 279 (1-2), 20–33. doi:10.1016/j.epsl.2008.12.020

Li, C. Y., Liu, Y. W., Zhu, B. C., Feng, Y. M., and Wu, H. Q. (1978). "Structural evolutions of qinling and qilian," in *Scientific papers on Geology for international exchange* (Beijing: Editorial Office of Chinese Geological Bureau, Geological Publishing House, 174–189. (in Chinese with English abstract).

Lister, G., and Forster, M. (2009). Tectonic mode switches and the nature of orogenesis. *Lithos* 113 (1-2), 274–291. doi:10.1016/j.lithos.2008.10.024

Liu, X. J., Zhang, Z. G., Xu, J. F., Xiao, W. J., Shi, Y., Gong, X. H., et al. (2020). The youngest permian ocean in central asian orogenic belt: Evidence from geochronology and geochemistry of bingdaban ophiolitic melange in central tianshan, northwestern China. *Geol. J.* 55 (3), 2062–2079. doi:10.1002/gj.3698

Liu, Y. S., Hu, Z. C., Gao, S., Günther, D., Xu, J., et al. (2008). *In situ* analysis of major and trace elements of anhydrous minerals by LA- ICP-MS without applying an internal standard. *Chem. Geol.* 257 (1-2), 34–43. doi:10.1016/j.chemgeo.2008.08.004

Ludwig, K. R. (2012). *Isoplot 3.75: A geochronological toolkit for microsoft Excel*. Berkeley geochronology center special Publication, 5.

Mahoney, J. J., Frei, R., Tejada, M. L. G., Mo, X. X., Leat, P. T., and Nägler, T. F. (1998). Tracing the Indian ocean mantle domain through time: Isotopic results from old west Indian, east tethyan, and South pacific seafloor. *J. Petrology* 39, 1285–1306. doi:10.1093/petroj/39.7.1285

Matteini, M., Junges, S. L., Dantas, E. L., Pimentel, M. M., and Bühn, B. (2010). *In situ* zircon U-Pb and Lu-Hf isotope systematic on magmatic rocks: Insights on the crustal evolution of the Neoproterozoic Goiás Magmatic Arc, Brasília belt, Central Brazil. *Gondwana Res.* 17 (1), 1–12. doi:10.1016/j.gr.2009.05.008

Meng, F. C., Zhang, J. X., Guo, M. C., and Li, J. P. (2010). Mor-type and SSZ-type ophiolites from DachaDaban to the North Qilian ocean evolutionary constraints. *Acta Petrologica Mineralogica* 29 (5), 453–466. (in Chinese with English Abstract).

Montanini, A., Tribuzio, R., and Vernia, L. (2008). Petrogenesis of basalts and gabbros from an ancient continent–ocean transition (External Liguride ophiolites, Northern Italy). *Lithos* 101, 453–479. doi:10.1016/j.lithos.2007.09.007

Morris, J. D., and Ryan, J. G. (2003). "Subduction zone processes and implications for changing composition of the upper and lower mantle," in *Treatisse on geochemistry*. Editors H. D. Holland and K. K. Turekian (Oxford: Elsevier), 2, 451–470.

Mullen, E. D. (1983). $MnO/TiO_2/P_20_5$ a minor element discriminant for basaltic rocks of oceanic environments and its implications for petrogenesis. *Earth Planet. Sci. Lett.* 62, 53–62. doi:10.1016/0012-821x(83)90070-5

Murphy, D. T., Collerson, K. D., and Kamber, B. S. (2002). Lamproites from Gaussberg, Antarctica: Possible transition zone melts of Archaean subducted sediments. *J. Petrology* 43 (6), 981–1001. doi:10.1093/petrology/43.6.981

Neave, D, A., and Putirka, K. D. (2017). A new clinopyroxene-liquid barometer, and implications for magma storage pressures under Icelandic rift zones. *Am. Mineralogist* 102 (4), 777–794. doi:10.2138/am-2017-5968

Pearce, J. A. (1996). "A user's guide to basaltic discrimination diagrams," in *Trace element geochemistry of volcanic rocks: Applications for massive sulphide exploration*. Editor D. A. Wyman (Geological Association of Canada Short Course Notes), 12, 79–113.

Pearce, J. A. (2008). Geochemical fingerprinting of oceanic basalts with applications to ophiolite classification and the search for archean oceanic crust. *Lithos* 100, 14–48. doi:10.1016/j.lithos.2007.06.016

Pearce, J. A., and Stern, R. J. (2006). "Origin of back arc basin magmas: Trace element and isotope perspectives," in *Back Arc spreading systems: Geological, biological, chemical, and physical interactions*. Editors D. M. Christie, C. R. Fisher, S. M. Lee, and S. Givens (Washington, D. C: American Geophysical Union), 166, 63–86.

Pearce, J. A. (1982). *Trace element characteristics of lavas from destructive plate boundaries: Andesites, Orogenic Andesites and Related Rocks*. Geology, 528–548.

Pearce, N. J., Perkins, W. T., Westgate, J. A., Gorton, M. P., Jackson, S. E., Neal, C. R., et al. (1997). A compilation of new and published major and trace element data for NIST SRM 610 and NIST SRM 612 glass reference materials. *Geostand. Geoanalytical Res.* 21 (1), 115–144. doi:10.1111/j.1751-908x.1997.tb00538.x

Putirka, K. D. (2008). Thermometers and barometers for volcanic systems. *Rev. Mineralogy Geochem.* 69, 61–120. doi:10.2138/rmg.2008.69.3

Qian, Q., Zhang, Q., and Sun, X. M. (2001). Formation environment and mantle source characteristics of Jiuquan Basalts in Northern Qilian: Constraints of trace elements and Nd isotope Geochemistry. *Acta Petrol. Sin.* 17 (3), 385–394. (in Chinese with English Abstract).

Rao, W. X. (2015). *The study on the mineralization mechanism of Yushigou chromite deposit, Qilianshan belt*. Master's thesis. Lanzhou University. (in Chinese with English Abstract).

Rubatto, D. (2002). Zircon trace element geochemistry: Partitioning with garnet and the link between U-Pb ages and metamorphism. *Chem. Geol.* 184, 123–138. doi:10.1016/s0009-2541(01)00355-2

Saccani, E. (2015). A new method of discriminating different types of post-Archean ophiolitic basalts and their tectonic significance using Th-Nb and Ce-Dy-Yb systematics. *Geosci. Front.* 6 (4), 481–501. doi:10.1016/j.gsf.2014.03.006

Saccani, E., Allahyari, K., Beccaluva, L., and Bianchini, G. (2013). Geochemistry and petrology of the Kermanshah ophiolites (Iran): Implication for the interaction between

passive rifting, oceanic accretion, and OIB-type components in the Southern Neo-Tethys Ocean. *Gondwana Res.* 24, 392–411. doi:10.1016/j.gr.2012.10.009

Saccani, E., Principi, G., Garfagnoli, F., and Menna, F. (2008). Corsica ophiolites: Geochemistry and petrogenesis of basaltic and metabasaltic rocks. *Ofioliti* 33, 187–207.

Shi, R. D., Yang, J. S., and Wu, C. L. (2004). SHRIMP age evidence of Yushigou ophiolite formed in late sinian in North Qilian. *Acta Geol. Sin.* 78 (5), 649–657. (in Chinese with English abstract).

Singer, B. S., Jicha, B. R., Leeman, W. P., Rogers, N. W., Thirlwall, M. F., Ryan, J., et al. (2007). Along-strike trace element and isotopic variation in Aleutian Island arc basalt: Subduction melts sediments and dehydrates serpentine. *J. Geophys. Research-Solid Earth* 112, B06206. doi:10.1029/2006jb004897

Sláma, J., Koler, J., Condon, D. J., Crowley, J. L., Gerdes, A., Hanchar, J. M., et al. (2008). Plešovice zircon — a new natural reference material for U–Pb and Hf isotopic microanalysis. *Chem. Geol.* 249 (1-2), 1–35. doi:10.1016/j.chemgeo.2007.11.005

Song, S. G., Niu, Y. L., Li, S., Zhang, C., and Zhang, L. F. (2014). Continental orogenesis from ocean subduction, continent collision/subduction, to orogen collapse, and orogen recycling: The example of the North Qaidam UHPM belt, NW China. *Earth Sci. Rev.* 129, 59–84. doi:10.1016/j.earscirev.2013.11.010

Song, S. G., Niu, Y. L., Su, L., and Xia, X. H. (2013a). Tectonics of the North Qilian orogen, NW China. *Gondwana Res.* 23 (4), 1378–1401. doi:10.1016/j.gr.2012.02.004

Song, S. G., Wu, Z. Z., Yang, L. M., Su, L., Xia, X. H., Wang, C., et al. (2019). Ophiolite belts and evolution of the proto-tethys ocean in the qilian orogen. *Acta Petrol. Sin.* 35 (10), 2948–2970. (in Chinese with English abstract). doi:10.18654/1000-0569/2019.10.02

Song, S. G., Zhang, G. B., Zhang, C., Zhang, L. F., and Wei, J. C. (2013b). Dynamic processes of oceanic subduction and continental collision: Petrological constraints of high-pressure and ultrahigh-pressure metamorphic belts in the northern qilian-qaidam margin. *Chin. Sci. Bull.* 58 (23), 2240–2245. (in Chinese with English abstract).

Song, S., Su, L., Li, X. H., Zhang, G., Niu, Y., and Zhang, L. (2010). Tracing the 850 Ma continental flood basalts from a piece of subducted continental crust in the North Qaidam UHPM belt, NW China. *Precambrian Res.* 183, 805–816. doi:10.1016/j.precamres.2010.09.008

Song, S., Wang, M. M., Xu, X., Wang, C., Niu, Y., Allen, M. B., et al. (2015). Ophiolites in the Xing'an-Inner Mongolia accretionary belt of the CAOB: Implications for two cycles of seafloor spreading and accretionary orogenic events. *Tectonics* 34 (10), 2221–2248. doi:10.1002/2015tc003948

Song, Z. B., Li, W. Y., Li, H. K., Li, H. M., and Li, Y. Z. (2007). Isotopic age of shijuli gabbro in North Qilian mountain and its geological significance. *Acta Geosci. Sinaca* 28 (1), 7–10. (in Chinese with English abstract).

Sun, S., and McDonough, W. F. (1989). Chemical and isotopic systematics of oceanic basalts: Implications for mantle composition and processes. *Geol. Soc. Lond. Spec. Publ.* 42 (1), 313–345. doi:10.1144/gsl.sp.1989.042.01.19

Tseng, C. Y., Yang, H. J., Yang, H. Y., Liu, D. Y., Tsai, C. L., Wu, H. Q., et al. (2007). The dongcaohe ophiolite from the North Qilian mountains: A fossil oceanic crust of the paleo-qilian ocean. *Chin. Sci. Bull.* 52, 2390–2401. doi:10.1007/s11434-007-0300-3

Wang, Q., and Liu, X. (1976). Paleo-oceanic crust of the Chilienshan region, Western China and its tectonic significance. *Scinetia Geol. Sin.* (1), 42–55. (in Chinese with English abstract).

Williams, I. S. (2001). Response of detrital zircon and monazite, and their U-Pb isotopic systems, to regional metamorphism and host-rock partial melting, Cooma Complex, southeastern Australia. *J. Geol. Soc. Aust.* 48 (4), 557–580. doi:10.1046/j.1440-0952.2001.00883.x

Wu, C. L., Xu, X. Y., Gao, Q. M., Li, X. M., and Lei, M. (2010). Early Paleozoic granitic magmatism and tectonic evolution in Northern Qilian. *Acta Petrol. Sinca* 26 (04), 1027–1044. (in Chinese with English abstract).

Wu, H., Li, C., Yu, Y., and Chen, J. (2018). Age, origin, and geodynamic significance of high-Al plagiogranites in the Labuco area of central Tibet. *Lithosphere* 10 (2), 351–363. doi:10.1130/l711.1

Xia, L. Q., Xia, Z. C., and Xu, X. Y. (1995). Dynamics of tectonic-volcanic magma evolution in North Qilian mountains. *Northwest. Geol.* 1, 1–28. (in Chinese with English abstract).

Xia, L. Q., Xia, Z. C., and Xu, X. Y. (1996). *Petrogenesis on marine volcanic rocks in North Qilian mountains*. Beijing: Geological Publishing House, 5–146. (in Chinese with English abstract).

Xia, L. Q., Xia, Z. C., and Xu, X. Y. (1998). *Volcanism and mineralization in qilian orogenic belt and adjacent areas*. Beijing: Geological Publishing House, 4–55. (in Chinese with English abstract).

Xia, X. H., and Song, S. G. (2010). Forming age and tectono-petrogenises of the jiugequan ophiolite in the North Qilian mountain, NW China. *Chin. Sci. Bull.* 55 (18), 1899–1907. doi:10.1007/s11434-010-3207-3

Xia, X. H., Song, S. S., and Niu, Y. L. (2012). Tholeiite-Boninite terrane in the North Qilian suture zone: Implications for subduction initiation and back-arc basin development. *Chem. Geol.* 328, 259–277. doi:10.1016/j.chemgeo.2011.12.001

Xiang, Z. Q., Lu, S. N., Li, H. K., Li, H. M., Song, B., and Zheng, J. K. (2007). Zircon SHRIMP U-Pb age of Zhuoyougou gabbro in the Western part of North Qilian Mountains and its geological significance. *Geol. Bull. China* 26 (12), 1686–1691. (in Chinese with English abstract).

Xiao, L., Xu, Y. G., Mei, H. J., and Sha, S. L. (2003). Geochemical characteristics of emeishan basalt in binchuan area, yunnan Province: Rock types and evolution law with time. *Chin. J. Geol.* 4, 478–494. (in Chinese with English abstract).

Xiao, X. C., Chen, G. M., and Zhu, Z. Z. (1978). Geological tectonic significance of ancient ophiolite belt in Qilian Mountains. *Acta Geol. Sin.* 4, 281–295+338. (in Chinese with English abstract).

Yan, X. X. (2014). *Petrological chronological characteristics and tectonic significance of Yushigou ophiolite suite in Qinghai Province*. Beijing: China University of Geosciences. (in Chinese with English abstract).

Yan, Z., Fu, C. L., Aitchison, J. C., Niu, M. L., Buckman, S., and Cao, B. (2019). Early cambrian muli arc-ophiolite complex: A relic of the proto-tethys oceanic lithosphere in the qilian orogen, NW China. *Int. J. Earth Sci.* 108 (4), 1147–1164. doi:10.1007/s00531-019-01699-6

Yan, Z., Li, J. L., and Yong, Y. (2008). Tectonic environment for the formation of ordovician carbonate-siliceous rocks in shihuigou, North Qilian. *Acta Petrosinica Sin.* 24 (10), 2384–2394. (in Chinese with English abstract).

Yang, G. X., Li, Y. J., Tong, L. L., Wang, Z. P., Si, G. H., Lindagato, P., et al. (2022). Natural observations of subduction initiation: Implications for the geodynamic evolution of the Paleo-Asian Ocean. *Paleo-Asian Ocean. Geosystems Geoenvironment* 1 (1), 100009. doi:10.1016/j.geogeo.2021.10.004

Yang, H., and Gu, L. X. (1990). Petrogenetic significance of La/Sm-La covariant diagram. *J. Guilin Coll. Geol.* 2, 201–208. (in Chinese with English abstract).

Yang, J. S., Xu, Z. Q., Zhang, J. X., Chu, J. Y., Zhang, R. Y., and Liu, J. G. (2001). "Tectonic significance of caledonian high-pressure rocks in the qilian–qaidam–altun mountains, NW China," in *Paleozoic and mesozoic tectonic evolution of central asia: From continental assembly to intracontinental deformation*. Editors Marc S. Hendrix and Greg A. Davis (Geological Society of America, Memoir), 194, 151–170.

Yoder, H., and Tilley, C. E. (1962). Origin of basalt magmas: An experimental study of natural and synthetic rock systems. *J. Petrology* 3, 342–532. doi:10.1093/petrology/3.3.342

Zeng, J. Y., Yang, H. R., Yang, H. Y., Liu, D. Y., Cai, J. L., Wu, H. Q., et al. (2007). Dongcaohe ophiolite in North Qilian: An early paleozoic oceanic crust fragment. *Chin. Sci. Bull.* 52 (7), 825–835. (in Chinese with English abstract).

Zhang, Q., Chen, Y., Zhou, D. J., Qian, Q., Jia, X. Q., and Han, Q. (1998). Geochemical characteristics and Genesis of dacha osaka ophiolite in North Qilian. *Chin. Sci. Ser. D Earth Sci.* 1, 30–33. (in Chinese with English abstract).

Zhang, Q., Sun, X., and Zhou, D. (1997). The characteristics of North Qilian ophiolites, forming settings and their tectonic significance. *Advence Earth Sci.* 12 (4), 366–393. (in Chinese with English abstract).

Zhang, Z. G., Liu, L., Liu, X. J., Hu, R. G., Gong, X. H., Tang, Z. J., et al. (2019). Geochronology, geochemistry and geological significance of volcanic rocks from Hamutusi area in Western Junggar, Xinjiang. *J. Guilin Univ. Technol.* 39 (2), 258–269. (in Chinese with English abstract).

Zhu, J., and Du, Y. S. (2007). Geochemical characteristics and paleogeographic significance of Ordovician siliceous rocks in Laohushan, North Qilian orogenic belt. *J. Paleogeogr.* 9 (1), 69–76. (in Chinese with English abstract).

frontiers | Frontiers in Earth Science

TYPE Original Research
PUBLISHED 21 August 2023
DOI 10.3389/feart.2023.1237367

OPEN ACCESS

EDITED BY
Meng Wang,
Chang'an University, China

REVIEWED BY
Xijun Liu,
Guilin University of Technology, China
Shi Chen,
China University of Petroleum, China

*CORRESPONDENCE
Hao Yang,
gbwfm3@163.com

†These authors have contributed equally to this work

RECEIVED 09 June 2023
ACCEPTED 07 August 2023
PUBLISHED 21 August 2023

CITATION
Yang F, Li J, Lu S, Bian B, Liu H, Wei Y, Qi X and Yang H (2023), Carboniferous to Early Permian tectono-sedimentary evolution in the western Junggar Basin, NW China: implication for the evolution of Junggar Ocean.
Front. Earth Sci. 11:1237367.
doi: 10.3389/feart.2023.1237367

Carboniferous to Early Permian tectono-sedimentary evolution in the western Junggar Basin, NW China: implication for the evolution of Junggar Ocean

Fan Yang[1†], Jianzhong Li[2], Shan Lu[1], Baoli Bian[3], Hailei Liu[3], Yanzhao Wei[1], Xuefeng Qi[1] and Hao Yang[4†*]

[1]PetroChina Research Institute of Petroleum Exploration and Development, Beijing, China, [2]PetroChina Tuha Oilfield Company, Hami, China, [3]PetroChina Xinjiang Oilfield Company, Karamay, China, [4]School of Energy Resources, China University of Geosciences, Beijing, China

The discovery of Carboniferous hydrocarbon source rocks in the Mahu-Shawan Sag has implied considerable exploration potential in the Carboniferous strata in the western Junggar Basin. However, controversy has long surrounded when and how the Junggar Ocean was eventually closed, leading to a poor understanding of the Carboniferous basin evolution and the continental growth of the Central Asian Orogenic Belt. We performed stratigraphic and geochronologic studies to establish the chronostratigraphic framework of the western Junggar Basin to better understand its tectonic-sedimentary evolution during the Carboniferous-Early Permian. Three tectonostratigraphic units in the southern West Junggar region have been identified as Early Carboniferous shallow-deep marine sequences, Late Carboniferous coast-shallow marine sequences, and Early Permian continental sequences. The Carboniferous strata are similar to forearc and backarc-rift sequences in the Western Fault Belt and the Mahu-Shawan Sag, respectively. The Lower Permian strata in the southern West Junggar region are all continental sequences. Seismic profiles indicate extensional settings in the early stage of Late Carboniferous and Early Permian but a compressional setting at the end of Late Carboniferous. Geochemical data have suggested a Carboniferous continental arc setting and an Early Permian within-plate extensional setting. Meanwhile, calc-alkaline arc magma migrated from the Zhongguai High to the Western Fault Belt at the end of the Late Carboniferous. Collectively, the tectonic-sedimentary evolution in the Carboniferous-Early Permian of the southern West Junggar region can be divided into three stages: 1) Early Carboniferous subduction, 2) Late Carboniferous slab roll-back, and 3) Early Permian intra-continental evolution stage. This model constrains the closure of the Junggar Ocean at the Late Carboniferous.

KEYWORDS

basin evolution, western Junggar Basin, forearc basin, backarc basin, closure time, Junggar Ocean

1 Introduction

The Central Asian Orogenic Belt (CAOB; Jahn et al., 2000; Khain et al., 2003; Jahn et al., 2004; Kovalenko et al., 2004; Windley et al., 2007; Cawood et al., 2009; Wilhem et al., 2012; Kroner et al., 2014; Xiao et al., 2015) or Altaids Tectonic Collage (Şengör et al., 1993; Yakubchuk, 2004; Xiao et al., 2008; Wilhem et al., 2012) is the largest accretionary orogen in the world resulted from a complicated collage of various terranes, including ophiolites, island arcs, accretionary complexes, and possibly some microcontinents during the evolution of the Palaeo-Asian Ocean (PAO; Figure 1A). As an important tectonic unit of the southwestern CAOB (Figure 1B), the southern West Junggar region has become a suitable window for exploring the final closure and evolution of the Junggar Ocean (the final remnants of the PAO in southern West Junggar region, Han and Zhao, 2018). In order to investigate the evolution of this ocean, a large number of studies have been carried out on the margins of the western Junggar Basin. However, the closure time and subduction polarity of this ocean are still under debate. The proposed final closure time of the Jungar Ocean varies a lot from the Devonian (Zhu et al., 2013; Zhu et al., 2015), the Early Carboniferous (Han et al., 2010; Xiang, 2015; Tang et al., 2022), the Late Carboniferous (Xu et al., 2013; Li et al., 2017; Zhang et al., 2018a; Zhang et al., 2018b; Zhang et al., 2021), to the Early Permian (Tang et al., 2010; Xiao et al., 2010). In addition, based on the controversy over the subduction polarity, different models of tectonic evolution have been proposed, including the northwestward subduction model (Zhan et al., 2015; Zhang et al., 2018a; Zheng et al., 2019; Liu et al., 2020; Zhang et al., 2021) and the double-sided divergent subduction model (Yin et al., 2013; Eizenhöfer et al., 2015; Yi et al., 2015; Tang et al., 2022). Some breakthroughs suggest that the Zhongguai High in the western Junggar Basin was a volcanic arc during the Carboniferous, which now has been widely recognized (e.g., Li et al., 2014; Li et al., 2017; Zhang et al., 2018a; Zhang et al., 2021). The above controversies have led to the different understandings of the Carboniferous basin attributes of the Mahu-Shawan Sag, with either being a forearc basin in a double-sided divergent subduction model or a backarc basin if it subducted northwestward. The current vague understanding of the Carboniferous basin attributes has led to the debatable formation and development environment of hydrocarbon source rocks in the Mahu-Shawan Sag.

Previous studies mainly focused on the outcropped southern West Junggar, including ophiolite records (e.g., Zhu and Xu, 2006; Chen et al., 2014; Zhu et al., 2015; Zhang et al., 2018a; Zhang et al., 2018b), volcanic rocks (e.g., Gao et al., 2006; Chen and Zhu, 2015; Liu et al., 2017; Zheng et al., 2019) and granitic intrusions (e.g., Yin et al., 2010; Zhang et al., 2015). Comparatively, the tectonic setting, sedimentology and magmatic activities in the buried western Junggar Basin have not been well-constrained. Therefore, this study obtained rich chronological, stratigraphic, tectonostratigraphic, geochemical data in the western Junggar Basin, and then combined the previous studies on the outcrops over the southern West Junggar to reveal the tectonic-sedimentary evolution of the southern West Junggar region in the Carboniferous-Early Permian. This work is of great significance for understanding the formation background of hydrocarbon source rocks in the Mahu-Shawan Sag and the closing process of the Junggar Ocean.

2 Geological setting

2.1 Regional geological background

The West Junggar region, which is a key component of the southwestern CAOB (Windley et al., 2007; Figures 1A,B), includes the West Junggar (West Junggar terrane) and the western Junggar Basin. Based on previous studies of the magmatic and ophiolitic rocks within this orogen, the West Junggar terrane has been separated into the northern and southern domains, which recorded different subduction-accretion histories (Figure 1; Liu et al., 2017; Xu et al., 2013; Zhang et al., 2018b; Zheng et al., 2019; Zhang et al., 2021). The northern West Junggar is bounded by the Irtysh shear zone and the Altai Mountains to the north and the E-W trending Xiemisitial fault zone to the south (Li et al., 2017). It consists of two E-W trending arcs, namely, the Zharma-Saur arc in the north and the Boshchekul–Chingiz arc (also called Xiemisitial arc) in the south, separated by the pre-Carboniferous Kujibai–Hebukesaier–Hongguleleng ophiolitic mélanges (Zhu and Xu, 2006; Zhang and Guo, 2010). The southern West Junggar, separated from northern West Junggar by the Xiemisitai Fault, consists of successive arcs and accretionary complexes dismembered by several left-lateral strike-slip faults, along which two main Late Paleozoic ophiolitic mélanges (Darbut and Karamay) are present. Recent studies have shown that these two main ophiolitic mélanges were controlled by right-lateral shear zones (Zhang et al., 2018a). In this study, we focus on the southern West Junggar region, including the southern West Junggar and western Junggar Basin (Figure 1B).

Taken the pre-Permian strata as the basement and considering the uplift and depression structures of the basement, the first-order structural units of the Junggar Basin can be divided into five tectonic units, namely, the Wulungu Depression, Luliang Uplift, Central Depression, Western Uplift, and East Uplift (Yang et al., 2004). And the second-order tectonic units are divided based on alteration and differentiation of the late tectonic movement. The first-order tectonic units of the western Junggar Basin, our study area, include the Western Uplift and Central Depression. The second-order tectonic units in the Western Uplift include the Hongche Fault Belt, Kebai Fault Belt, Wuxia Fault Belt, and Zhongguai High, while the second-order tectonic units in the Central Depression include Mahu Sag, Dabasong High, Shawan Sag and Pen1jingxi Sag. To facilitate our research, we divided the research area into three units, namely, the Western Fault Belt (WFB), Zhongguai High (ZGH) and Mahu-Shawan Sag (MSS) (Figure 1B).

2.2 Stratigraphic successions of the southern West Junggar region

The strata in the southern West Junggar include the Early Carboniferous Baogutu and Xibeikulasi Formations (C_1b and

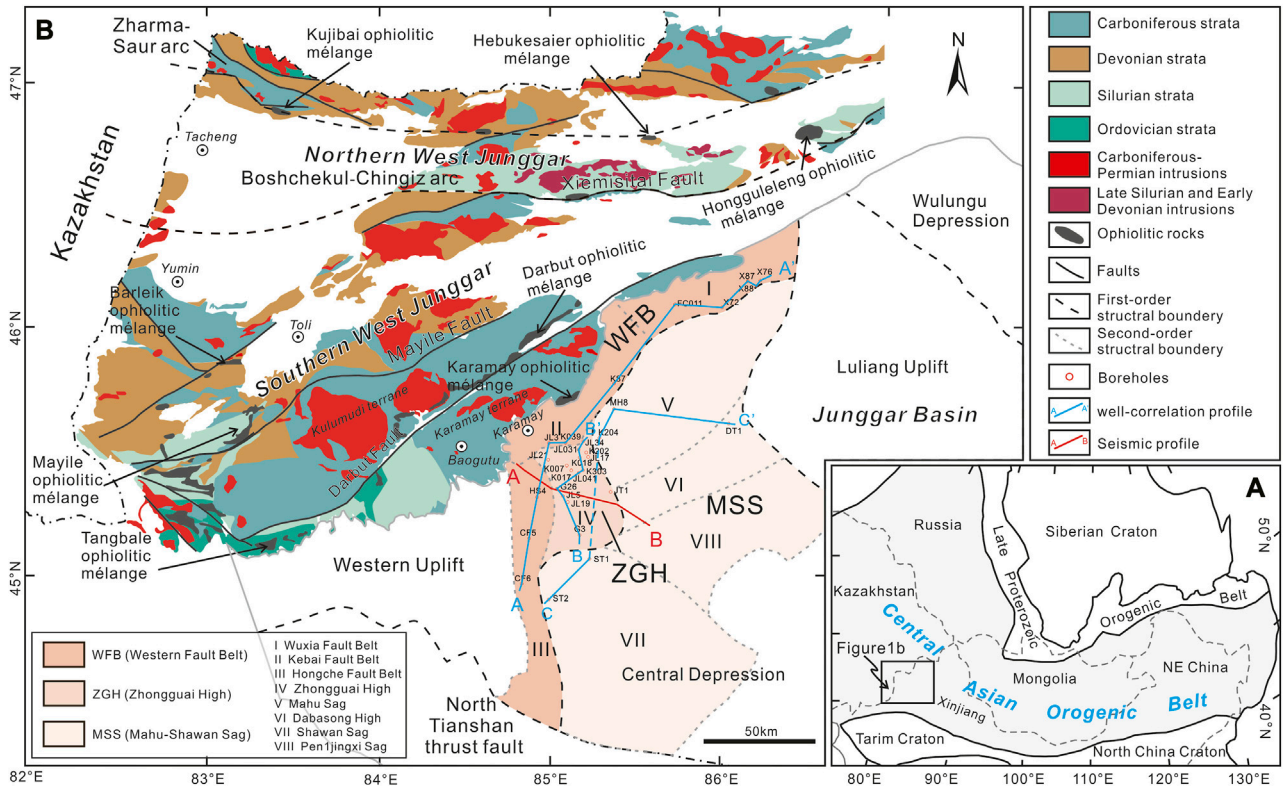

FIGURE 1
Relationship of the study area to the Central Asian Orogenic Belt (modified from Jahn, et al., 2004; Windley, et al., 2007). **(B)** Simplified geological map of the western Junggar Basin and adjacent southern West Junggar showing their tectonic subdivisions and representative wells, seismic reflection profile **(A,B)** location and study areas (modified from Li et al., 2017; Liu et al., 2017; Zhang et al., 2018a; 2021).

C_1x), Late Carboniferous Chengjisihanshan, Hala'alate and Aladeyikesai Formations (C_2c, C_2h and C_2al). The Baogutu and Xibeikulasi Formations are characterized by a set of fine-grained sediments, including siliciclastic rocks, tuffaceous siltstones and volcanic rocks, and mostly developed Bouma sequences (Xiang, 2015). The sedimentary structures and biostratigraphic studies indicate that these Formations formed in a shelf-littoral environment. The Chengjisihanshan Formation (C_2c) unconformably overlying the Baogutu (C_1b) and Xibeikulasi (C_1x) Formations are mainly composed of siltstone and siliciclastic rocks with volcanic rocks interspersed, and their sedimentary structures and biostratigraphic studies indicate a shallow marine environment. The Hala'alate Formation (C_2h) above the Chengjisihanshan Formation mainly contains basalt and andesite, with some continental clastic rocks dominated by sandstone and sand conglomerate, indicating a gradual shallowing of the sea during this period. The Aladeyikesai Formation (C_2al) is overlying the Hala'alate Formation has an increased proportion of continental clastic rocks that mainly include sandstones and siltstones. Their sedimentary structures and biostratigraphic studies indicate this formation formed in a shallow-coastal environment (Figure 4). By contrast, the Lower Permian is characterized by terrestrial deposition.

Three cross-sections were constructed across the western Junggar Basin based on the drilling core data obtained this study (Figure 1B). The WFB is characterized by several foreland thrust belts (He et al., 2004), which formed in the Triassic and early Jurassic (Feng et al., 2008; Feng et al., 2019). The strata in this area include the Lower Carboniferous, Upper Carboniferous, and Lower Permian Jiamuhe Formation and Fengcheng Formation (P_1j and P_1f). The Early Carboniferous strata was only drilled in well K87 of the Kebai fault belt, and the Upper Carboniferous was mainly drilled in the Hongche fault belt. The Lower Permian was distributed in Hongche, Kebai and Wuxia fault belts, and the drilling shows strata in the Wuxia fault belt are thicker with more varied lithologic units than that in the Hongche and Kebai fault belt (Figure 2A). The Early Carboniferous strata are shallow with well-sorted conglomerate and sand conglomerate interbedded with tuff. The GR and SP curves are relatively flat, mainly box-shaped, representing the coastal environment (Figure 4). The Lower Carboniferous can be divided into two parts. The clastic sedimentary rocks in the lower part are mainly tuffaceous siltstones and sandstones, in which the scouring surface and cross-stratification can be seen in the sandstones (Figures 3G,H), the GR value is high, representing shallow-marine environment (Figure 4). The upper part is mainly composed of glutenites, transitioning to tuffaceous mudstones in the southwest direction, representing a shoreface environment (Figure 4). The Early Permian strata, unconformably overlain by the Late Carboniferous strata, are generally rich in continental clastic rocks with horizontal bedding (Figure 3E). The primary

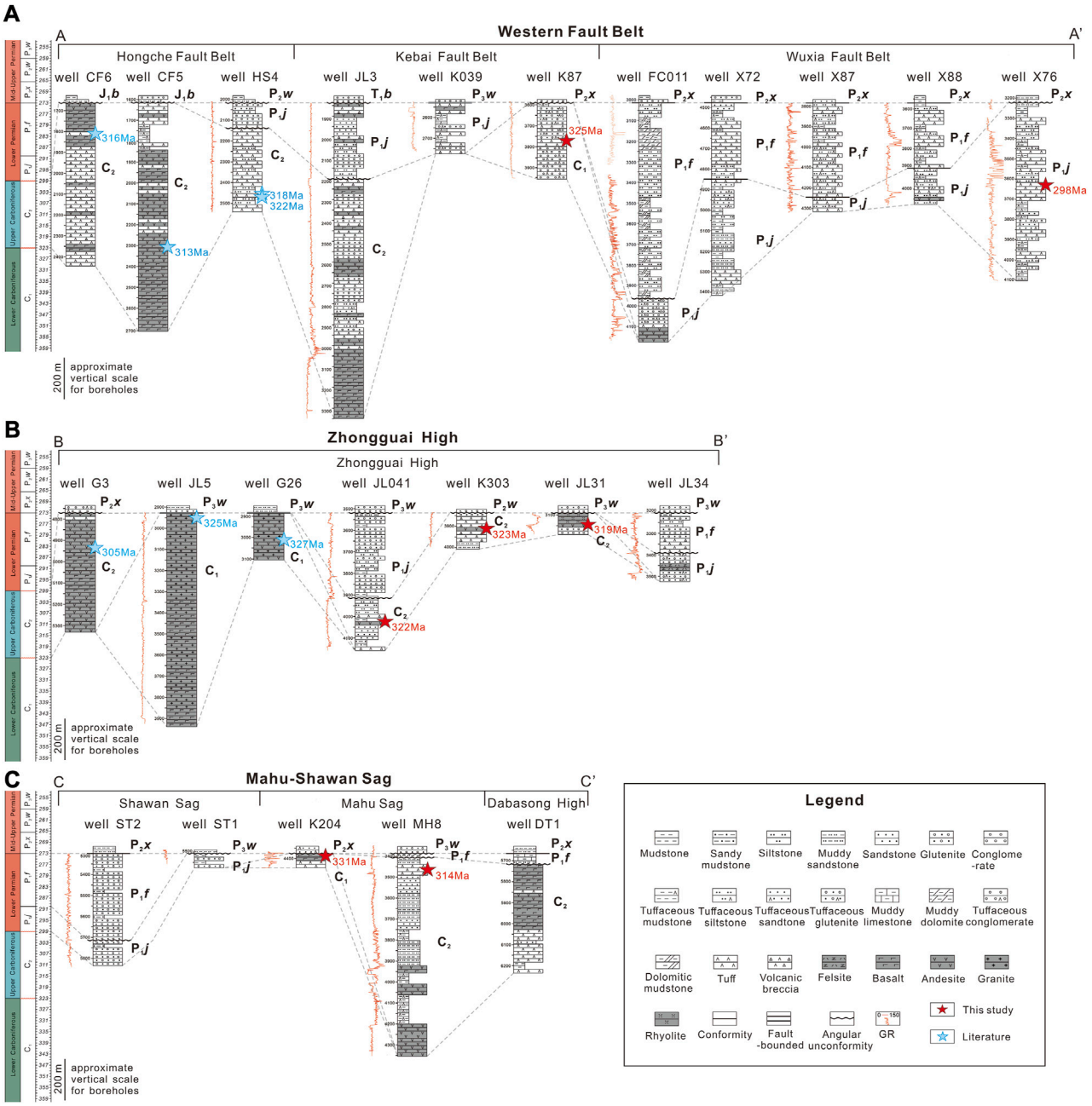

FIGURE 2
Stratigraphic correlation profiles showing the distribution of the Carboniferous-Permian strata in each tectonic unit of the western Junggar Basin.

rock components are tuffaceous mudstones, tuffaceous siltstones layer, tuff, sandstones and andesites. The GR and SP curves are toothed funnel-shaped or bell-shaped, suggesting hydrodynamic variability. They are identified as the lacustrine facies (Figure 4).

The ZGH is characterized by Carboniferous volcanic rocks, while the Early Permian strata were found by drilling in local wells. The Early Carboniferous strata were drilled in wells JL5 and G26 in the center of the ZGH, the Late Carboniferous strata were drilled in wells JL41, K303 and JL31 in the north of the area, and the Early Permian strata were drilled in well JL34 in the north of the area. In general, the Early Permian strata are missing in the southwest of the area but are relatively complete in the northwest part of the ZGH (Figure 2B). The presence of abundant Carboniferous calc-alkaline arc-type volcanic rocks in the ZGH indicates an island arc environment. The overlying Early Permian continental clastic rocks are mainly gray sandy conglomerates, gray siltstones, brown mudstones, gray tuffs and gray volcanic breccias. Load casts and scour surfaces are also identified in the Early and Late Carboniferous strata, respectively (Figures 3I,J). Sawtooth GR and SP curves are box and funnel shaped. These characteristics indicate that the sedimentary facie is fluvial-deltaic facies (Figure 4).

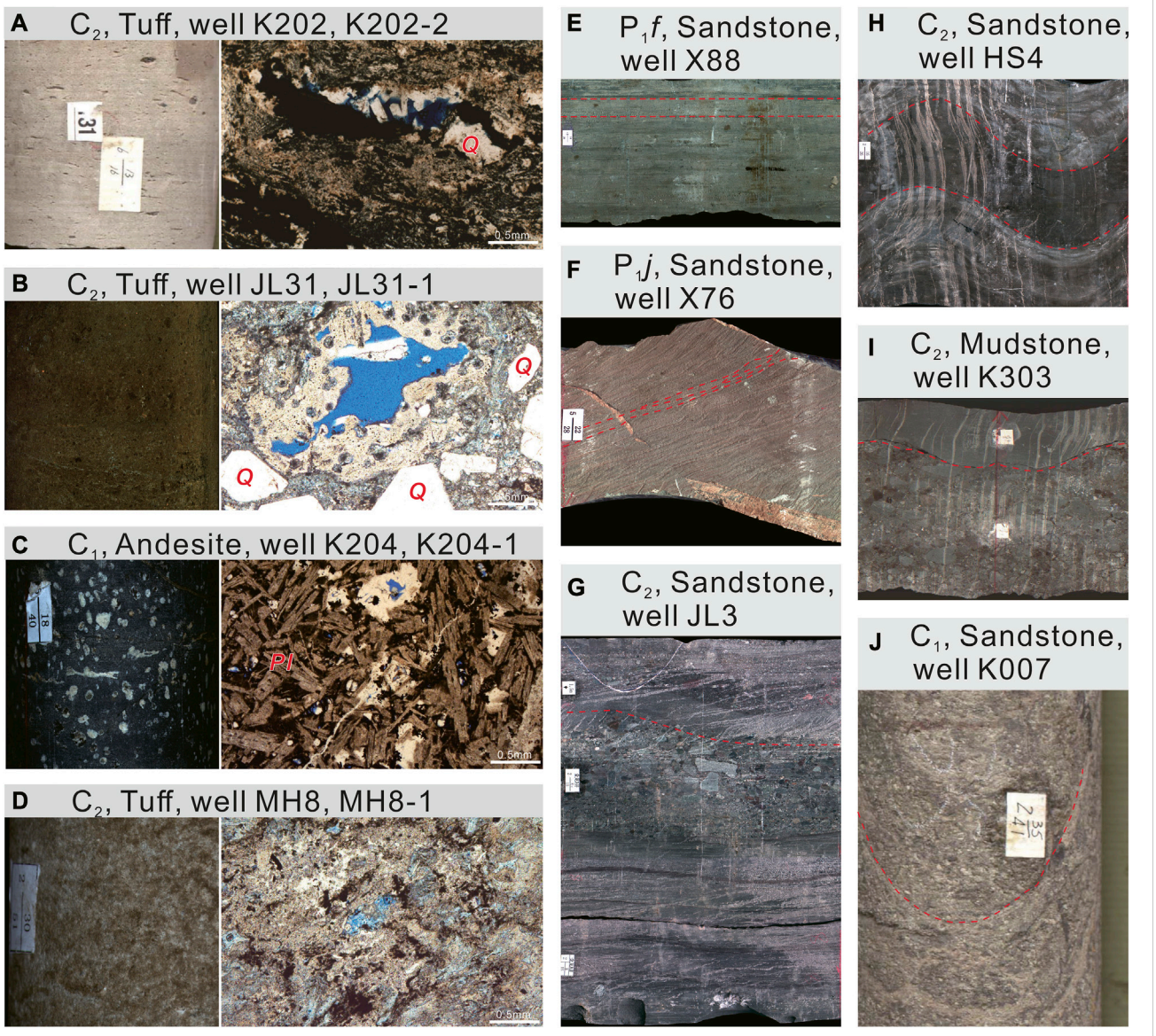

FIGURE 3
Petrological characterisitics and photomicrographs of the Carboniferous-Permian borehole rocks in the western Junggar Basin. **(A)** well K202, 4,169.7 m, C_2, tuff; **(B)** well JL31, 3,148.5 m, C_2, tuff; **(C)** well K204, 4,384.4 m, C_1,andesite; **(D)** well MH8, 3,479.5 m, tuff; **(E)** well X88, 3,830.14–3,830.39 m, P_1j, sandstone, horizontal bedding; **(F)** well X76, P_1j, sandstone, cross-stratification; **(G)** well JL3, 2,132.92–2,133.4 m, C_2, sandstone, scour; **(H)** well HS4, 2,461.30–2,461.64 m, C_2, sandstone and mud, cross-stratification; **(I)** well K303, 3,903.66–3,903.91 m, C_2, mud and glutenite, scour; **(J)** well K007, 3,068.75–3,069.65 m, C_1, sandstone, load cast; Q: quartz; Pl: feldspar.

The distribution of Carboniferous-Early Permian strata in the MSS varies greatly, with the Early Carboniferous strata only drilled in the Mahu Sag' well K204 and Late Carboniferous strata drilled in the Mahu sag and Dabasong high. Strata in the northeast of the Mahu sag and Dabasong high are relatively complete (Figure 2C). The Early Carboniferous strata were drilled in the MSS and mainly consist of dark-gray sandstones, gray basalts, and tuffs, which may represent a coastal environment. The Late Carboniferous strata unconformably overly the Early Carboniferous strata and are mainly composed of fine clastic deposits including tuffaceous mudstones and muddy siltstones, and the GR curve is box-shaped with high value, representing the shallow-marine environment. The Early Permian strata, unconformablly overlying the Late Carboniferous strata, are rich in sandstones and conglomerates, which are considered to be lacustrine facies based on the characteristics of logging curves and previous studies in the MSS (e.g., Tang et al., 2022; Figure 4).

3 Data and methods

This study uses an integrated exploration dataset consisting of geochronological data, wire-line logs, regional seismic profiles and geochemical data, provided by Xinjiang Oilfield, China National Petroleum Corporation (CNPC). Access to many wells and geochronological data allowed us to

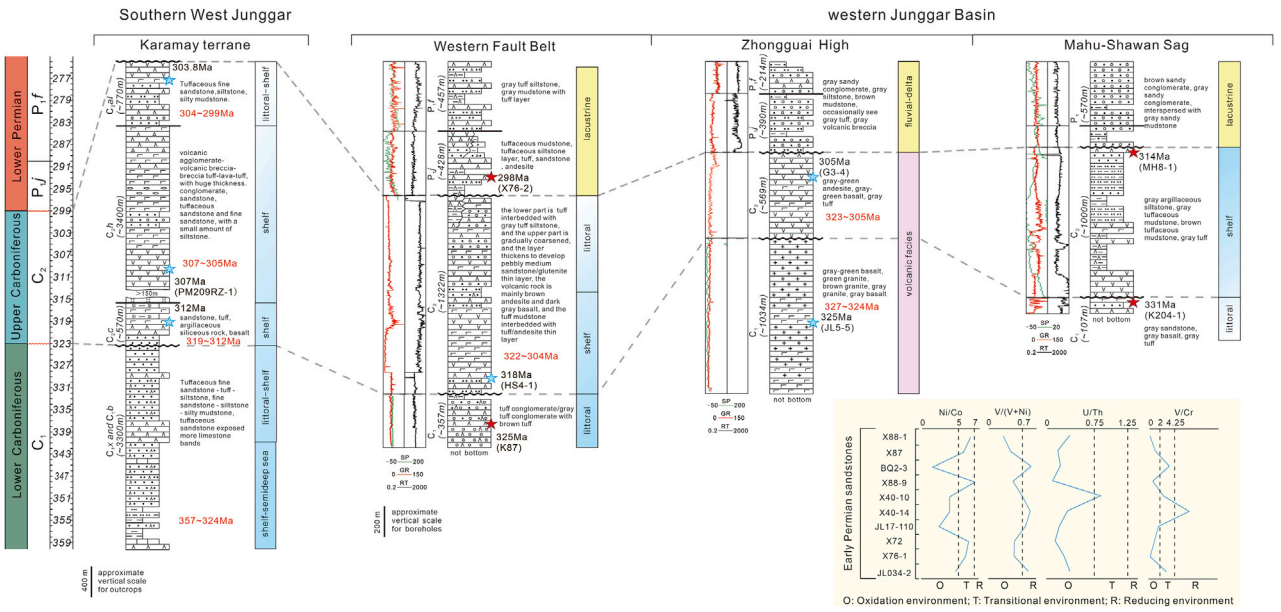

FIGURE 4
Carboniferous to Early Permian stratigraphic columns in the southern West Junggar and in the different tectonic units (WFB, ZGH, MSS) of the western Junggar Basin. Insert diagram shows environments indicated by geochemical data from Early Permian sedimentary rocks.

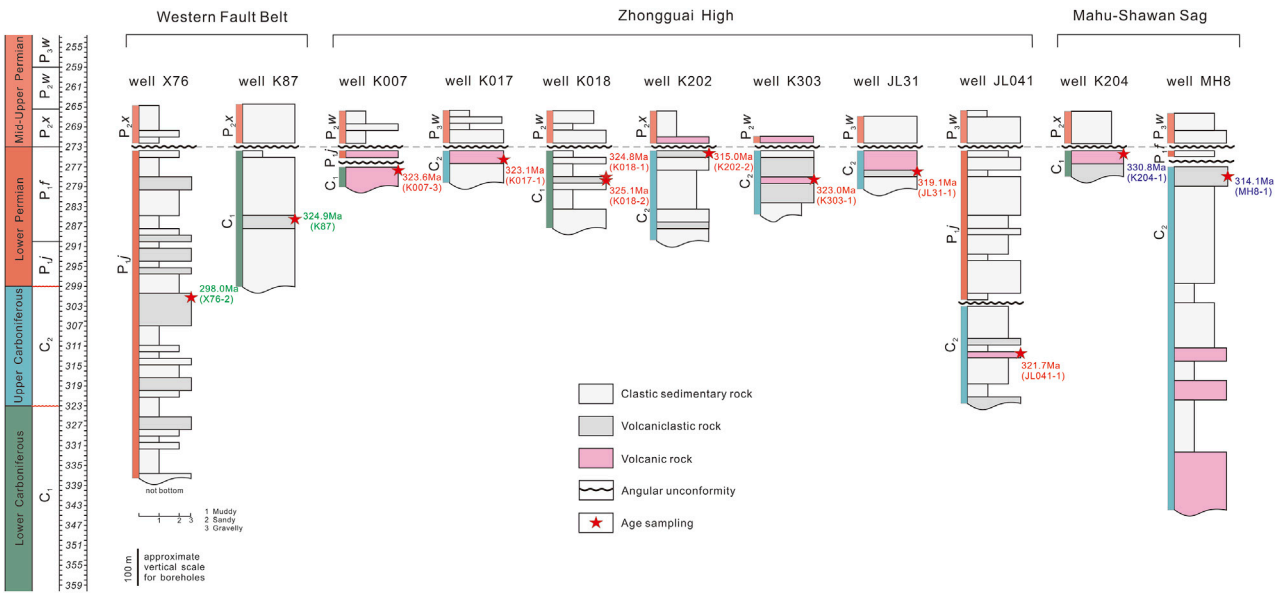

FIGURE 5
Representative stratigraphic column showing the drilled Carboniferous-Permian volcano-sedimentary succession and their sample ages in the western Junggar Basin.

comprehensively reconstruct the stratigraphic sequences of the Carboniferous to Early Permian sedimentary basin in the southern West Junggar region. To determine stratigraphic relationships and to establish the structural framework, we collected seven volcaniclastic and five volcanic rock samples (Figure 5), including two tuff samples from WFB (X76–2 and K87), four tuff samples from ZGH (K018–1, K018–2, K202-2, JL31-1), three andesite samples from ZGH (K017–1, K303-1, JL041-1), one andesitic porphyrite sample from ZGH (K007-3), one tuff sample from MSS (MH8-1), and one andesite sample from MSS (K204-1). Seismic profiles were used to describe the tectonic characteristics and the stratigraphic configuration. In

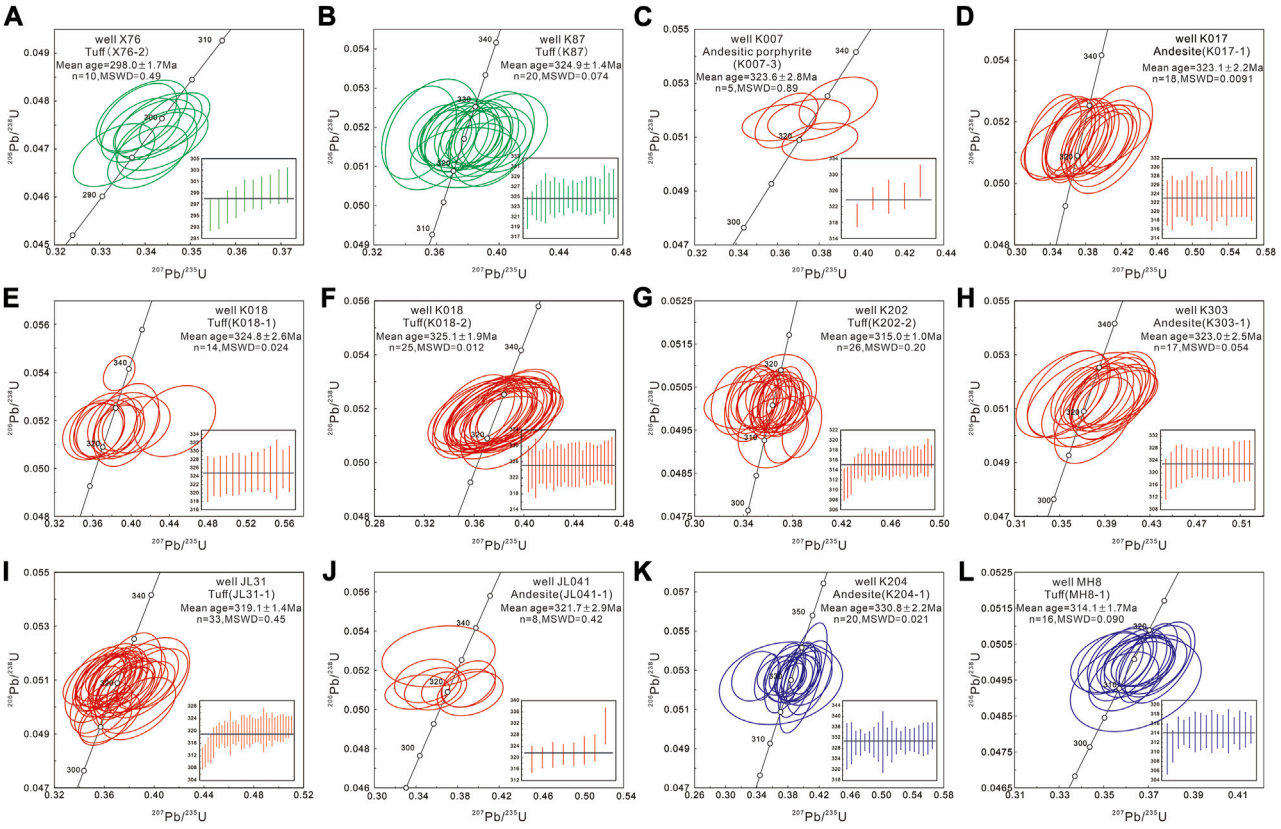

FIGURE 6
Zircon U–Pb concordia diagrams of the borehole volcanic rocks from the Carboniferous-Early Permian strata in the western Junggar Basin.

addition, the large number of whole-rock major and trace element data provide a basis for further investigation of tectonic settings. To summarize, we used geochronological data, analyzed the tectonic deformation characteristics of each period using seismic profiles, and finally used geochemical data to further verify the analysis results. We then established a tectonic-sedimentary evolution model of the Carboniferous-Early Permian in the western Junggar Basin. Taken together, these recent data and geological evidence place critical constraints on the closure history of the Junggar Ocean.

Zircon U-Pb dating were performed by using the laser ablation (multi-collector) inductively coupled plasma mass spectrometer (LA- (MC-) ICP-MS) method at Northwest University in China. Detailed information on sample preparation and analytical procedures is available in the Supporting Material. For U–Pb dating, only one analysis was carried out on each zircon grain.

Major and trace element analyses of the 22 samples were performed at the Analytical Laboratory of the Beijing Research Institute of Uranium Geology, China. Major elements were analyzed by a Philips PW2404 X-ray fluorescence spectrometer. Trace elements of these samples were obtained using a Finnigan MAT high-resolution (HR) inductively coupled plasma mass spectrometer (ICP-MS). The precision and accuracy of the ICP–MS and X-ray fluorescence data were reported by Cullen et al. (2001) and Wu et al. (2010), respectively.

4 Results

4.1 Zircon U–Pb dating

The analyzed zircon grains from all samples show variable U (3-1,294 ppm) and Th (1-1,061 ppm) content with Th/U ratios ranging from 0.26 to 1, indicating a magmatic origin (Williams, 2001; Belousova et al., 2002; Hoskin and Schaltegger, 2003). The U-Pb data are summarized in Figure 6 and Supplementary Table S1.

After excluding the discordant analyses, ten analyses from well X76 tuff (X76-2) from a coherent group define a weighted mean $^{206}Pb/^{238}U$ age of 298.0 ± 1.7 Ma (MSWD = 0.49; Figure 6A). Twenty analyses from well K87 tuff (K87) spread along the concordia in the U-Pb diagram, with $^{206}Pb/^{238}U$ ages clustered from 322 ± 3 Ma to 326 ± 5 Ma, giving a weighted mean age of 324.9 ± 1.4 Ma (MSWD = 0.074) for well K87 tuff (Figure 6B). Five analytical spots from well K007 andesitic porphyrite (K007-3) from a coherent group yield a weight mean $^{206}Pb/^{238}U$ age of 323.6 ± 2.8 Ma (MSWD = 0.89; Figure 6C). Eighteen analytical spots from well K017 andesite (K017-1) are concordant and yield $^{206}Pb/^{238}U$ apparent ages ranging from 322 ± 5 Ma to 324 ± 6 Ma, with a weighted mean age of 323.1 ± 2.2 Ma (MSWD = 0.0091; Figure 6D). Fourteen analytical spots from well K018 tuff (K018-1) have concordant $^{206}Pb/^{238}U$ apparent ages from 323 ± 5 Ma to 326 ± 5 Ma, yielding a weighted mean age of 324.8 ± 2.6 Ma (MSWD = 0.024; Figure 6E). Twenty-five analyses from the well K018 tuff

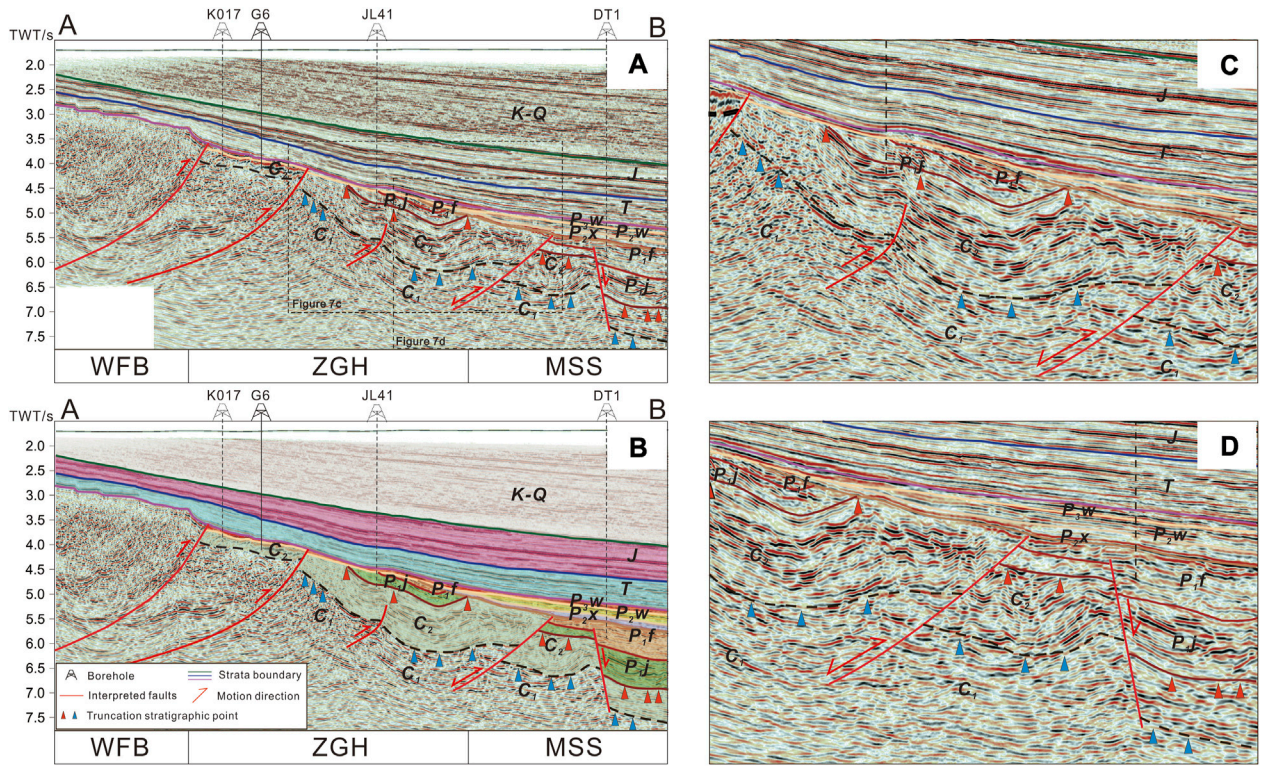

FIGURE 7
(A, B) Seismic profile A-B and their interpretation in the western Junggar Basin. **(C, D)** Enlarged seismic interpretation seismic profile. The primitive seismic profiles were accessed from the Xinjiang oilfield company (CNPC). K-Q, Cenozoic; J, Jurassic; T, Triassic; P_3w, Upper Permian upper-Wuerhe Formation; P_2w, Middle Permian lower-Wuerhe Formation; P_2x, Middle Permian Xiazijie Formation; P_1f, Lower Permian Fengcheng Formation; P_1f, Lower Permian Jiamuhe Formation; C_2, Upper Carboniferous strata; C_1, Lower Carboniferous strata.

(K018-2) cluster on the concordia with concordant $^{206}Pb/^{238}U$ ages ranging from 324 ± 4 Ma to 326 ± 6 Ma, giving a weighted mean age of 325.1 ± 1.9 Ma (MSWD=0.012; Figure 6F). Twenty-six spots from well K202 andesite (K202-2) are concordant and plot on or near the concordia with $^{206}Pb/^{238}U$ apparent ages from 311 ± 3 Ma to 317 ± 2 Ma, giving a weighted mean age of 315 ± 1 Ma (MSWD = 0.20; Figure 4G). Seventeen spots from well K303 andesite (K303-1) have concordant $^{206}Pb/^{238}U$ apparent ages of 318–324 Ma and give a weighted mean age of 323 ± 2.5 Ma (MSWD = 0.054; Figure 6H). Thirty-three spots from well JL31 tuff (JL31-1) have concordant $^{206}Pb/^{238}U$ apparent ages of 311–322 Ma with a weighted mean age of 319.1 ±1.4 Ma (MSWD = 0.45; Figure 6I). Eight analytical spots from well JL041 andesite (JL041-1) are concordant and have $^{206}Pb/^{238}U$ apparent ages of 319–331 Ma, giving a weighted mean age of 321.7 ± 2.9 Ma (MSWD = 0.42; Figure 6J). Twenty analytical spots from well K204 basalt (K204-1) have concordant $^{206}Pb/^{238}U$ apparent ages from 329 to 333 Ma and form a coherent group with a weighted mean $^{206}Pb/^{238}U$ age of 330.8 ± 2.2 Ma (MSWD = 0.021; Figure 4K). Sixteen analytical spots from well MH8 tuff (MH8-1) have concordant $^{206}Pb/^{238}U$ apparent ages of 311–315 Ma and give a weighted mean age of 314.1 ± 1.7 Ma (MSWD = 0.090; Figure 6L). In summary, zircon U-Pb dating suggest the tuffs formed during 325–298 Ma, the andesites formed during 322–323 Ma, one andesitic porphyrite have an age of 323.6 Ma.

4.2 Structural characteristics

Seismic reflection profile A-B (Figure 1B) was employed for understanding the geological structure and structural evolution of the western Junggar Basin. This seismic profile is near NW-SE trending and ~70 km long located within the western Junggar Basin close to the Zaire Mountain. The borehole and log database provide a firm basis for horizon tracing and seismic interpretation as shown in Figure 7. We focus on the interpretation of this seismic section on the Carboniferous and Early Permian strata. The interpretation of the strata after the Early Permian is based on the latest interpretation results of Zhang (2020). For the seismic profile, some truncation stratigraphic points were identified at the interface between the Early Carboniferous and the Late Carboniferous strata, corresponding to the angular unconformity in between. The Late Carboniferous strata are thick near the fault between ZGH and MSS and become thinner toward the west side (Figure 7C). This thrust fault cuts the Late Carboniferous strata and Early Permian strata in the foot wall, and only Late Carboniferous strata remain in the hanging wall. In addition, the seismic profile also reflects more complex deformation in the Late Carboniferous strata compared to in the Early Permian strata in the center of ZGH, indicating a tectonic setting transition from extension to compression at the end of the Late Carboniferous (Figure 7C). In the Early Permian, we identified a southeast normal fault in the MSS and the thickening of the strata

in the foot wall (Figure 7D), indicating they may have formed due to a Permian extension.

4.3 Geochemical characteristics

The analytical geochemical data are listed in Supplementary Table S2. For the following discussion, major elemental data are normalized on an anhydrous basis. Relatively high loss on ignition (LOI = 1.32%–11.20%) indicate that the samples experienced varying degrees of alteration. Therefore, we focus on the immobile and transitional elements (e.g., Zr, Y, Nb, Th, Ti) for rock classification and petrogenetic discussion (Frey et al., 2002).

With exception of sample K204-1, all other Early Carboniferous samples are characterized by their moderate SiO_2 contents (53.92%–65.05%) and relatively low total alkali contents (Na_2O+ K_2O = 3.75%–8.19%), and belong to the andesite/dacite field on the Zr/TiO_2 vs. Nb/Y diagram (Figure 8A). These intermediate-acidic samples have compositions with low $Fe_2O_3^T$ (4.13%–5.33%), MgO (1.14%–2.22%), TiO_2 (0.48%–0.78%), and high Al_2O_3 (13.88%–19.00%). Sample K204-1 exhibits low SiO_2 contents (50.60%), and reatively high $Fe_2O_3^T$ (10.61%), MgO (3.34%), TiO_2 (1.33%). On the Th vs. Co diagram of Hastie et al. (2007) that is affective for altered volcanic rocks, all of these samples are plotted in the calc-alkaline field (Figure 8B). The Late Carboniferous samples can be divided into two groups based on their respective composition characteristics. Group 1 have intermediate-basic compositions with a wide range of SiO_2 (45.14%–68.29%) and low total alkali contents (Na_2O+ K_2O = 2.50–6.87%). The samples have relatively low Al_2O_3 (13.12%–16.18%) and high $Fe_2O_3^T$ (5.01%–7.69%), TiO_2 (0.71%–1.34%), P_2O_5 (0.18%–0.48%) and varying MgO (1.11%–7.20%) and CaO contents (2.95%–9.65%). On the Zr/TiO_2 vs. Nb/Y diagram, the samples plot in the andesite/basalt fields (Figure 8A). Group 2 have intermediate-basic compositions with a narrow range of SiO_2 (66.40%–76.80%) and relatively high total alkali contents (Na_2O+ K_2O = 6.02–7.97%). The samples also have low Al_2O_3 (10.45%–12.04%) and varying Cao contents (0.32%–5.56%), but relatively low $Fe_2O_3^T$ (1.68%–1.86%), TiO_2 (0.09%–0.16%), P_2O_5 (0.03%–0.05%) and MgO contents (0.09%–0.53%). On the Zr/TiO_2 vs. Nb/Y diagram, the samples plot in the rhyolite/comendite fields (Figure 8A). However, the samples both plot in the calc-alkaline field on the Th vs. Co diagram (Figure 8B). With exception of sample X76-2, all other Early Permain samples are characterized by their low SiO_2 contents (55.52%–57.75%) and relatively low total alkali contents (Na_2O+ K_2O = 5.47%–7.69%), and belong to the andesite/dacite field on the Zr/TiO_2 vs. Nb/Y diagram. Sample X76-2 have moderate SiO_2 (58.35%) and total alkali contents (Na_2O+ K_2O = 7.14%), and plot in the rhyolite field on the Zr/TiO_2 vs. Nb/Y diagram (Figure 8A). It also have compositions with relatively high Al_2O_3 (18.83%), MgO (3.35%) and low $Fe_2O_3^T$ (2.83%), TiO_2 (0.18%), and belong to calc-alkaline rhyolite on the Th vs. Co diagram (Figure 8B).

In addition, there are five sedimentary rock samples in this study (X88-1, X87, X72, X76-1, and JL034-2). These rocks show a relatively wide variation in SiO_2 contents (38.31%–74.96%), with an average of 57.64%. The samples have wide ranges of Na_2O (2.06%–4.68%, av. 3.16%) and K_2O (1.36%–4.11%, av. 2.74%). In comparison with the Post-Archean Australian average shale (PAAS) (Taylor and McLennan, 1985), the samples yield lower Al_2O_3 (av. 14.22%) and $Fe_2O_3^T$ (av. 3.67%) and higher MgO contents (2.66%).

5 Discussion

5.1 Carboniferous to Early Permian chronostratigraphic framework in the southern West Junggar region

The rich geochronological data from this study provide firm constraints on the Carboniferous to Early Permian chronostratigraphic framework in the southern West Junggar region. Palaeontological as well as geochronological studies in the Karamay terrane show that the ages of intrusive rocks in the Baogutu Formation are 327–316.9 Ma (Gao et al., 2006; Han et al., 2006; Chen and Zhu, 2015). The geological periods of the fossil assemblage are mainly from the Late Visean to the Bashkirian (e.g., *Pugilis* sp., *Semicostella* sp., *Linoproductus praelongatus*, Xiang, 2015). The volcanic rocks or tuff samples of the Baogutu formation are from 357.5 Ma to 328 Ma (An and Zhu, 2009; Tong et al., 2009; Guo et al., 2010). In addition, the ages of intrusive rocks in the Xibeikulasi Formation are 327–313.7 Ma (Han et al., 2006; Xiang, 2015), and most fossils are in the Early Carboniferous Visean. Although the order of these two formations remain uncertain, the timing of the two formations are well-constrained to the Early Carboniferous within a reasonable range (357–324 Ma, Figure 4). In this study, several borehole volcanic rocks from the western Junggar Basin also gave similar ages of 330.7–324 Ma.

The Upper Carboniferous in the Karamay terrane includes the Chengjisihanshan Formation, the Hala'alate Formation, and the Aladeyikesai Formation, with deposition ages of 319–312 Ma, 307–305 Ma and 304–299 Ma, respectively (Xiang et al., 2013; Xiang et al., 2015; Li et al., 2016; Peng et al., 2016). In the WFB, our chronological data of volcanic rocks suggest depositional ages of 322–304 Ma. In the ZGH, the deposition age are in 323–305 Ma. In MSS, only one volcanic sample gives an age of 314.5 Ma.

The Early Permian strata include the Jiamuhe Formation and Fengcheng Formation, and their ages are 292–273 Ma (Liu, 2015; Lu, 2018; Tang et al., 2021; Tang et al., 2022). In this study, a Permian volcanic rock sample from the well X76 gives an age of 298 Ma.

5.2 Carboniferous arc-basin system of the western Junggar Basin

The southern West Junggar region is a key area to study the Late Paleozoic evolution of the subduction-collision processes of Junggar Ocean (e.g., Xiao et al., 2015; Li et al., 2017; Liu et al., 2017). Combining our detailed stratigrapic and sedimentologic data with seismic reflection features (Figures 4, 7), Carboniferous volcano-sedimentary succession in this region was punctuated by unconformities into aforementioned three main tectonostratigraphic units involving C_1, C_2, and P_1. The ZGH is dominated by Early Carboniferous calc-alkaline arc magmatic

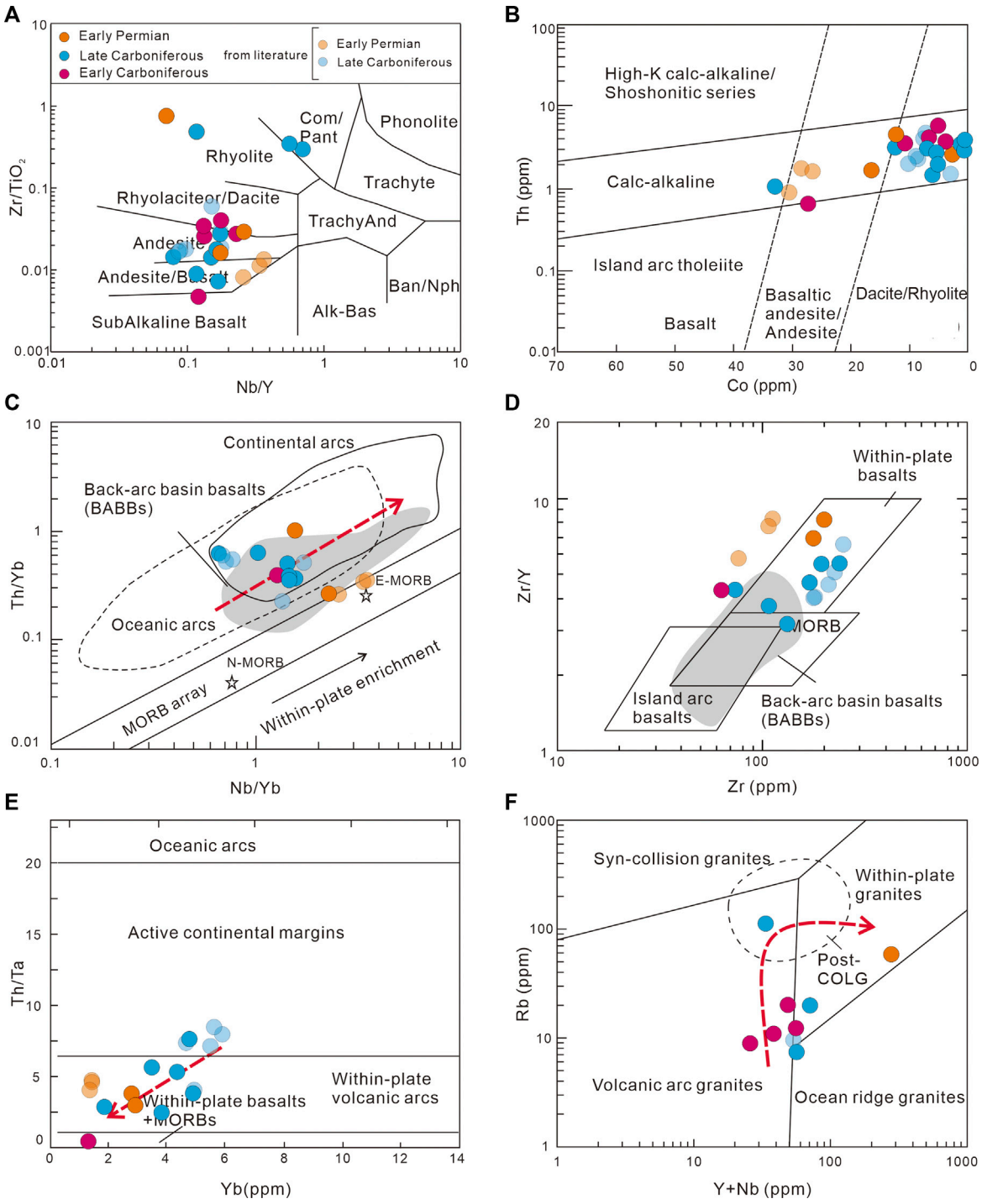

FIGURE 8
Tectonic diacrimination diagrams with trace element plots of the Carboniferous-Early Permian volcanic rocks in western Junggar basin and adjacent areas. **(A)** Zr/SiO_2-Nb/Y diagram (Winchester and Floyd, 1977); **(B)** Th-Co diagram (Hastie et al., 2007); **(C)** Th/Yb-Nb/Yb diagram (Pearce and Peate, 1995; Zhu et al., 2012); **(D)** Zr/Y-Zr diagram (Pearce and Norry, 1979; Zhu et al., 2012); **(E)** Th/Ta-Yb diagram (Gorton and Schandl, 2000); **(F)** Rb-(Y+Nb) diagram (Pearce et al., 1984; Wang et al., 2017). Literature data of the Carboniferous–Early Permian magmatic rocks in the study area are from Yin et al. (2013), Li et al. (2014), and Lu. (2018).

records (Figures 8A,B) and a series of southeastward-vergent thrust faults (Li et al., 2017). Previous studies also have determined the ZGH as an Early Carboniferous island arc (Li et al., 2014; Li et al., 2017; Zhang et al., 2018a; Zhang et al., 2021; Tang et al., 2022), but whether the WFB or MSS is a forearc basin in the Carboniferous remains a key question.

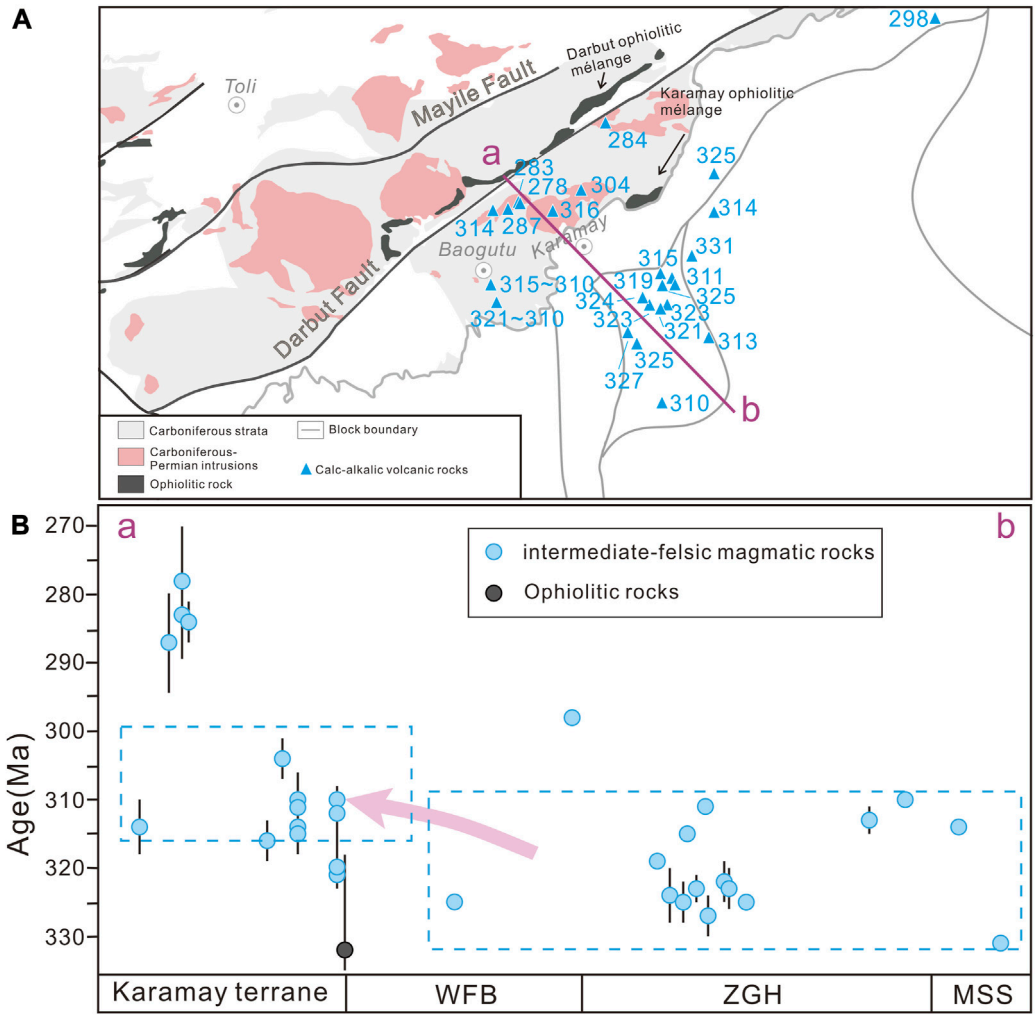

FIGURE 9
Age and distribution **(A)** and migration characteristics **(B)** of the Carboniferous to Early Permian magmatic rocks in the western Junggar Basin and adjacent areas. Literature data of magmatic rocks are from Li et al. (2014), Lu (2018), Cao et al. (2016), Tang et al. (2010), Tang et al., 2021, Yin et al. (2013), and Zhan et al. (2015).

Forearc basins were proposed as sedimentary basins that develop lie between the accretionary prisms and the magmatic arc or superimposed on the accretionary prisms. (Dickinson, 1974; Karig and Sharman, 1975; Dickinson and Seely, 1979; Dickinson, 1995; Noda, 2016). Studies have shown that most of the siliciclastic strata in the forearc basin are derived from igneous rocks produced by arc magmatism and deposited in submarine slope and fan depositional environments (Ingersoll, 1982; Ingersoll and Schweickert, 1986). Typical forearc basin fills shoal upward into shallow-marine or nonmarine strata but is dominated by deep marine strata (e.g., Dickinson, 1995; Busby et al., 1998; Fildani et al., 2008). However, the sedimentary characteristics of modern oceanic arc-related forearc basins have shown that these basins have a massively thick marine sequence, including large sections of pelagic sediments interspersed with thin layers of sandstone or volcanic ash, or large sections of pelagic carbonate rocks (e.g., Kumano basin; Tofino basin). The Carboniferous strata of the WFB was strong affected by tectonic activity after the Middle Permian (Figure 7). Only a relatively coarse-grained set of sediments from Serpukhovian (−324.9 Ma) was drilled in well K87 (Figure 2). However, the similarity between the Late Carboniferous strata of the WFB and the Late Carboniferous strata of the Karamay terrane is obvious (Figure 4). Therefore, the Early Carboniferous stratigraphic information of the Karamay terrane can compensate for the lack of early Carboniferous stratigraphic information in the WFB to a certain extent. The Carboniferous strata of the WFB generally exhibit a sequence of gradually shallowing upward, which conforms to the vertical sedimentary characteristics of forearc basins. The Carboniferous strata under investigation deserve attention because they do not have the same characteristics as the typical forearc basins found in modern oceanic island arcs. Specifically, the strata is lacking in large amounts of mudstone, indicating that they are more likely to be sediments related to a continental island arc forearc basin. Geochemical data also indicate a continental arc attribute during the Carboniferous (Figures 8C,E). In addition, previous studies in the area have found detrital zircons from the ancient crystalline

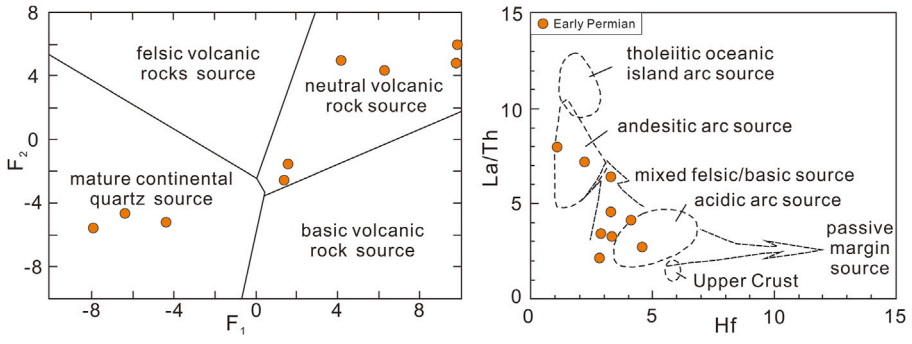

FIGURE 10
Geochemical diagrams showing source variation and composition for the Early Permian sedimentary rocks (Roser and Korsch, 1988). F_1= −1.773*TiO_2+ 0.607*Al_2O_3+ 0.760*Fe_2O_3 − 1.500*MgO + 0.616*CaO + 0.509*Na_2O − 1.224*K_2O − 9.090; F_2= −0.445*TiO_2+ 0.070*Al_2O_3− 0.250*Fe_2O_3− 1.142*MgO+ 0.438*CaO + 1.475*Na_2O + 1.426*K_2O − 6. 861.

basement of the Junggar Basin, suggesting a possible continental island arc (e.g., Li, 2011).

Dickinson (1974) described the sedimentary basins that behind an active volcanic arc as a "retro-arc" basin. Today, the term of "retro-arc basin" refers generally to the compressional regime of the backarc basin, while the extensional or neutral regime of this basin is more often referred to as a "backarc basin." Many backarc basins are extensional in origin, forming by rifting and seafloor spreading (Marsaglia and Ingersoll, 1992). Back-arc rifting is an important process in the evolution of Earth's crust and has been observed in several regions of the world, including the western Pacific Ocean, the South Pacific, and the Andes mountain range in South America. Typically, the sedimentary deposits in backarc basins can be divided into three stages, which reflect changes in the depositional environment and the nature of the sedimentary deposits. These stages are: Initial Rifting Stage: During this stage, the backarc basin is forming as a result of tectonic extension and thinning of the Earth's crust. Sediment is primarily derived from erosion of the surrounding volcanic arc, and is characterized by volcaniclastic deposits, such as ash fall and pyroclastic flow deposits. Transitional Stage: During this stage, the basin continues to evolve and fill with sediment, and the depositional environment becomes more mature and stable. Sediments can include a mixture of volcanic and sedimentary deposits, including volcaniclastics, coarse-grained volcaniclastic sandstones, and shale. Late Stage: During this stage, the backarc basin has reached its maximum size and the rate of sedimentation decreases. The depositional environment becomes dominated by fine-grained sedimentary deposits, such as mudstone, shale, and turbidite sandstone, which are formed by the accumulation of sediment transported by turbidity currents (e.g., Izu-Bonin-Mariana arc; Iizasa et al., 1999; Fiske et al., 2001). Therefore, the filling sequences of the backarc rift basin have many volcanic and volcaniclastic records in the initial rifting stage. As the continue of rifting, the sediment particle size becomes finer during the expansion period and transitioned to deep marine deposition. In the MSS, except that only a thin layer of the Early Carboniferous strata was drilled in well K204, little information is available on the Early Carboniferous strata, limiting the basin study in this area. The Late Carboniferous strata are fine-grained rifting sediments controlled by normal faults (Figures 4, 7). On the Nb/Yb vs. Th/Yb diagram, the vast majority of samples fall in the continental arc field (Figure 8C). Meanwhile, to explore the basin attributes, we delineated the basaltic zone of the backarc basin based on Zhu et al. (2012), and samples from this region falling in the backarc basin basalt (BABB) zone (Figures 8C,D).

In conclusion, the sedimentary characteristics of the Carboniferous show that the WFB area is a gradually shallower sequence, the ZGH area is dominated by calc-alkaline arc magma, and the MSS area is a relatively fine-grained deposit (Figure 4). Based on the above results of sedimentray records, structural features and geochemical characteristics, the southern West Junggar region was a continental arc-basin system during the Carboniferous. At this period, the ZGH was a continental volcanic arc, the WFB was a forearc basin and the MSS was a backarc basin. Combined with the presence of Devonian-Early Carboniferous ophiolites (e.g., Zhang and Huang, 1992; Xu et al., 2006; Yang et al., 2012; Chen et al., 2014; Zhu et al., 2015), we consider that the formation of the arc-basin system in the western Junggar Basin resulted from southward subduction of the Junggar oceanic lithosphere, and the subduction context continued at least to the Late Carboniferous. The temporal and spatial evolution of arc magma reveal a migration pattern from the Zhongguai arc to its forearc area (e.g., WFB and Karamay terrane) at ca. 315–310 Ma (Figure 9), indicating that slab rollback may take place at that time, which is responsible for the Late Carboniferous rifting in the western Junggar Basin and the development of Mahu-Shawan backarc basin.

5.3 Constraint on the closure time of the Junggar Ocean

Given similar occurance of accretionary system in the Kulumudi terrane, our determined southward subduction polarity of the Junggar Ocean provide further support for a divergent double subduction model (Yin et al., 2013). However, the closure time of this oceanic basin is still poorly constrained, with proposals ranging from the Carboniferous to Permian (Han et al., 2006; Tang et al., 2010; Li et al., 2017). The angular

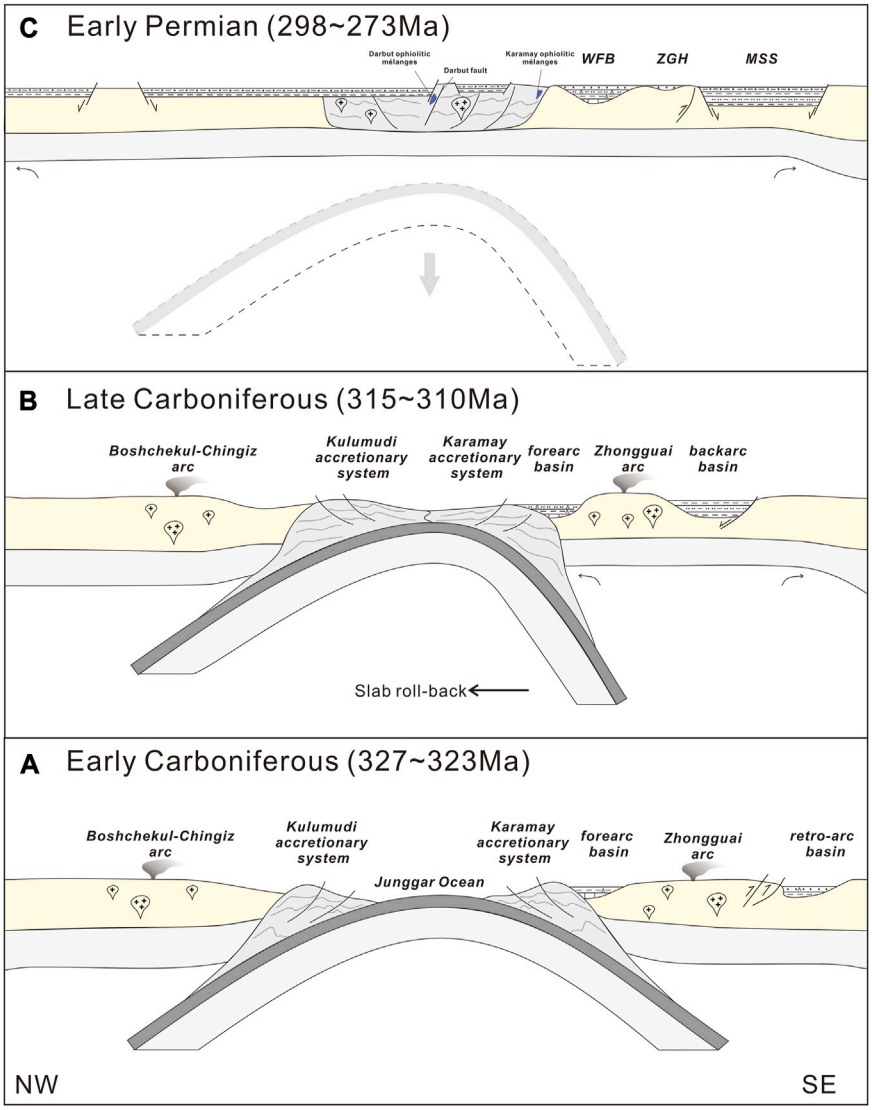

FIGURE 11
Schematic diagram showing the Carboniferous to Early Permian subduction–accretion processes and related basin evolution in the southern West Junggar region.

uncomformity between Carboniferous and Permian strata indicate that the southern West Junggar region may have evolved to a intraplate rift setting in the Early Permian (Figures 8C,E). Several lines of evidence support such inference. Firstly, the acidic volcanic rock samples show a clockwise trend from the Early Carboniferous through the Late Carboniferous to the Early Permian on the Rb vs. Y+Nb diagram (Figure 8F), indicating an evolutionary pattern from volcanic arc, through collision to post-collision (Wang et al., 2017). In addition, the Lower Permian deposition was mainly controlled by normal faults revealed by seismic reflection data and their sedimentary components are derived from the mixed source with mature continental continental quartz source signature (Figure 10). Moreover, the Early Permian strata was deposited in a terrestrial environment in contrast to those Carboniferous marine deposition. Another striking phenomenon is widespread distribution of the Early Permian A-type granites in the southern West Junggar region (Han and Zhao, 2018). These features point to a Carboniferous to Permian tectonic transition from subduction to post-collision, and together with the initial time of slab rollback and post-collisional granites, allow us to consider that the closure of the Junggar Ocean and resultant arc-arc collision occurred in the Late Carbonifeous (ca. 315–300 Ma), corresponding to a soft collision.

Based on the above discussions on tectonic-sedimentary evolution of the western Junggar Basin and magmatic distribution characteristics, an updated geodynamic evolutional model can be set up for the late Paleozoic subduction-collision processes in the southern West Junggar region. In the Early Carboniferous, double subduction of the Junggar Ocean resulted in the development of the Boshchekul-Chingiz and Zhongguai arcs. A forearc basin developed in the WFB in front of ZGH, and a series of thrust faults and related retro-arc basin were formed behind the Zhongguai arc (Li et al., 2017) (Figure 11A). During the Late Carboniferous, the rollback of southward subducted slab caused the lithosphere extension of the Zhongguai arc domain and

thus resulted in the development of the Mahu-Shawan backarc basin with upward fine-grained marine sediments, accompanied by massive rift-related structures and magmatism (Figure 11B). The Karamay and Kulumudi accretionary system may be amalgamated at this time and the Junggar Ocean began to be closed at ca. 315 Ma, which may last to latest Carboniferous. In the Early Permian, slab detachment induced asthenospheric upwelling and led to regional extension and rifting in the southern West Junggar region. This scenario is responsible for the generation of widespread 298-273 Ma A-type granites in this region and the Early Permian extensional structures recorded in the western Junggar Basin (Figure 11C), marking that the western Junggar Basin entered the intracontinental evolutionary stage.

6 Conclusion

(1) Three late Paleozoic tectono-stratigraphic units in the western Junggar Basin are identified, including Lower Carboniferous shallow-deep marine sequences, Upper Carboniferous coast-shallow marine sequences and Lower Permian terrestrial sequences.
(2) The southern West Junggar arc-basin system experienced the evolutionary history from Early Carboniferous retroarc basin to Late Carboniferous backarc basin to Early Permian intraplate rift basin, in response to the subduction-collision processes.
(3) The divergent double subduction resulted in the closure of the Junggar Ocean and the collision between Boshchekul-Chingiz arc and Zhongguai arc, and the oceanic basin was probably closed in the late Carboniferous.

Data availability statement

The original contributions presented in the study are included in the article/Supplementary Material, further inquiries can be directed to the corresponding author.

Author contributions

FY and HY: Conceptualization, Investigation, Methodology, Writing–original draft. JL: Conceptualization, Investigation, Writing–review and edit, Supervision. BB and HL: Funding acquisition. YW and XQ: Writing–review and edit; SL: Investigation. All authors contributed to the article and approved the submitted version.

Funding

This work was funded by the China Petroleum Major Science and Technology Project (2022DJ0507).

Acknowledgments

We appreciate the Editor and reviewers for their critical insight and constructive comments.

Conflict of interest

Authors FY, SL, YW, and XQ were employed by PetroChina Research Institute of Petroleum Exploration and Development; Author JL was employed by the PetroChina Tuha Oilfield Company; Authors BB and HL were employed by the PetroChina Xinjiang Oilfield Company.

The remaining author declares that the research was conducted in the absence of any commercial or financial relationships that could be construed as a potential conflict of interest.

Publisher's note

Supplementary material

The Supplementary Material for this article can be found online at: https://www.frontiersin.org/articles/10.3389/feart.2023.1237367/full#supplementary-material

References

An, F., and Zhu, Y. F. (2009). SHRIMP U-Pb zircon ages of tuff in Baogutu Formation and their geological significances. *Acta Petrol. Sin.* 25 (6), 1437–1445.

Belousova, E. A., Griffin, W. L., O'Reilly, S. Y., and Fisher, N. I. (2002). Igneous zircon: trace element composition as an indicator of source rock type. *Contributions Mineralogy Petrology* 143 (5), 602–622. doi:10.1007/s00410-002-0364-7

Busby, C. J., Smith, D., Morris, W., and Fackler-Adams, B. N. (1998). Evolutionary model for convergent margins facing large ocean basins; Mesozoic Baja California, Mexico. *Geology* 26, 227–230. doi:10.1130/0091-7613(1998)026<0227:EMFCMF>2.3.CO;2

Cawood, P. A., Kroener, A., Collins, W. J., Kusky, T. M., Mooney, W. D., and Windley, B. F. (2009). Accretionary orogens through Earth history. *Earth Accretionary Syst. Space Time* 318, 1–36. doi:10.1144/sp318.1

Cao, M., Qin, K., Li, G., Evans, N. J., Hollings, P., Jin, L., et al. (2016). Genesis of ilmenite-series I-type granitoids at the Baogutu reduced porphyry Cu deposit, western Junggar, NW-China. *Lithos* 246–247, 13–30. doi:10.1016/j.lithos.2015.12.019

Chen, B., and Zhu, Y. (2015). The origin of high-An plagioclase in diorite from Baikouquan, Xinjiang and its petrogenetic significance. *Acta Petrol. Sin.* 31 (2), 479–490. doi:10.00-0569/2009/025(06)-1437-45

Chen, S., Pe-Piper, G., Piper, D. J. W., and Guo, Z. (2014). Ophiolitic melanges in crustal-scale fault zones: implications for the Late Palaeozoic tectonic evolution in West Junggar, China. *Tectonics* 33 (12), 2419–2443. doi:10.1002/2013TC003488

Cullen, J. T., Field, M. P., and Sherrell, R. M. (2001). Determination of trace elements in filtered suspended marine particulate material by sector field HR–ICP–MS. *J. Anal. Atomic Spectrom.* 16, 1307–1312. doi:10.1039/b104398f

Dickinson, W. R. (1995). *Forearc basins*. Cambridge: Blackwell Science, 221–262.

Dickinson, W. R. (1974). Plate tectonics and sedimentation. *Soc. Econ. Paleontologists Mineralogists (SEPM) Special Publ.* 22, 1–27. doi:10.2110/pec.74.22.0001

Dickinson, W. R., and Seely, D. R. (1979). Structure and stratigraphy of forearc regions. *Am. Assoc. Petroleum Geol. Bull.* 63, 2–31. doi:10.1306/C1EA55AD-16C9-11D7-8645000102C1865D

Eizenhöfer, P. R., Zhao, G., Sun, M., Zhang, J., Han, Y., and Hou, W. (2015). Geochronological and hf isotopic variability of detrital zircons in paleozoic strata across the accretionary collision zone between the north China craton and Mongolian arcs and tectonic implications. *Bull. Geol. Soc. Am.* 127 (9-10), 1422–1436. doi:10.1130/b31175.1

Feng, J., Dai, J., and Ge, S. (2008). Structural evolution and pool-forming in Wuxia fault belt of Junggar Basin. *J. China Univ. Petroleum. Ed. Natrual Sci.* 32 (3), 23–29.

Feng, J., Dai, J., Qing, F., and Song, Y. (2019). Subsidence and sedimentary response of Wuxia foreland thrust belt in the northwestern margin of Junggar basin. *Acta Geol. Sin.* 93 (11), 2729–2741. doi:10.19762/j.cnki.dizhixuebao.2019096

Fildani, A., Hessler, A. M., and Graham, S. A. (2008). Trench-forearc interactions reflected in the sedimentary fill of Talara basin, northwest Peru. *Basin Res.* 30, 305–331. doi:10.1111/j.1365-2117.2007.00346.x

Fiske, R. S., Naka, J., Iizasa, K., Yuasa, M., and Klaus, A. (2001). Submarine silicic caldera at the front of the izu-bonin arc, Japan: voluminous seafloor eruptions of rhyolite pumice. *Geol. Soc. Am. Bull.* 113, 813–824. doi:10.1130/0016-7606(2001)113<0813:SSCATF>2.0.CO;2

Frey, F. A., Weis, D., Borisova, A. Y. U., and Xu, G. (2002). Involvement of continental crust in the formation of the cretaceous kerguelen plateau: new perspectives from ODP leg 120 sites. *J. Petrology* 43, 1207–1239. doi:10.1093/petrology/43.7.1207

Gao, S., He, Z., and Zhou, Z. (2006). Geochemical charcteristics of the Karamay granitoids and their significance in West Junggar, Xingjiang. *Xinjiang Geol.* 24 (2), 125–130.

Gorton, M. P., and Schandl, E. S. (2000). From continents to island arcs: A geochemical index of tectonic setting for arc-related and within-plate felsic to intermediate volcanic rocks. *Can. Mineral.* 38, 1065–1073. doi:10.2113/gscanmin.38.5.1065

Guo, L., Liu, Y., Wang, Z., Song, D., Xu, F., and Su, L. (2010). Anticancer activity and molecular mechanism of resveratrol-bovine serum albumin nanoparticles on subcutaneously implanted human primary ovarian carcinoma cells in nude mice. *Acta Petrol. Sin.* 26 (2), 471–477. doi:10.1089/cbr.2009.0724

Han, B., Guo, Z., Zhang, Z., Zhang, L., Chen, J., and Song, B. (2010). Age, geochemistry, and tectonic implications of a late Paleozoic stitching pluton in the North Tian Shan suture zone, western China. *Geol. Soc. Am. Bull.* 122 (3-4), 627–640. doi:10.1130/B26491.1

Han, B., Ji, J., Song, B., Chen, L., and Zhang, L. (2006). Late Paleozoic vertical growth of continental crust around the Junggar Basin, Xinjiang, China (Part I): timing of post-collisional plutonism. *Acta Petrol. Sin.* 22 (5), 1077–1086. doi:10.00-0569/2006/022(05)-1077-86

Han, Y., and Zhao, G. (2018). Final amalgamation of the tianshan and junggar orogenic collage in the southwestern central asian orogenic belt: constraints on the closure of the paleo-asian ocean. *Earth-Science Rev.* 186, 129–152. doi:10.1016/j.earscirev.2017.09.012

Hastie, A. R., Kerr, A. C., Pearce, J. A., and Mitchell, S. F. (2007). Classification of altered volcanic island arc rocks using immobile trace elements: development of the Th–Co discrimination diagram. *J. Petrology* 48, 2341–2357. doi:10.1093/petrology/egm062

He, D., Yin, C., Du, S., Shi, X., and Ma, H. (2004). Characteristics of structural segmentation of foreland thrust belts--A case study of the fault belts in the northwestern margin of Junggar Basin. *Earth Sci. Front.* 11 (3), 91–101.

Hoskin, P. W. O., and Schaltegger, U. (2003). The composition of zircon and igneous and metamorphic petrogenesis. *Zircon* 53, 27–62. doi:10.2113/0530027

Iizasa, K., Fiske, R. S., Ishizuka, O., Yuasa, M., Hashimoto, J., Ishibashi, J., et al. (1999). A Kuroko-type polymetallic sulfide deposit in a submarine silicic caldera. *Science* 283, 975–977. doi:10.1126/science.283.5404.975

Ingersoll, R. V. (1982). Initiation and evolution of the Great Valley forearc basin of northern and central California, U.S.A. *Geol. Soc. Lond. Spec. Publ.* 10 (1), 459–467. doi:10.1144/GSL.SP.1982.010.01.31

Ingersoll, R. V., and Schweickert, R. A. (1986). A plate-tectonic model for Late Jurassic ophiolite genesis, Nevadan Orogeny and fore-arc initiation, northern California. *Tectonics* 5 (6), 901–912. doi:10.1029/TC005i006p00901

Jahn, B. M., Wu, F. Y., and Chen, B. (2000). Granitoids of the Central Asian Orogenic Belt and continental growth in the Phanerozoic. *Trans. R. Soc. Edinburgh-Earth Sci.* 91, 181–193. doi:10.1017/s0263593300007367

Jahn, B., Windley, B., and Dobretsov, N. (2004). Phanerozoic continental growth in central Asia - Preface. *J. Asian Earth Sci.*, 23 (5), 599–603. doi:10.1016/S1367-9120(03)00124-x

Karig, D. E., and Sharman, G. F. (1975). Subduction and accretion in trenches. *Geol. Soc. Am. Bull.* 86 (3), 377–389. doi:10.1130/0016-7606(1975)86<377:SAAIT>2.0.CO;2

Khain, E. V., Bibikova, E. V., Salnikova, E. B., Kröner, A., Gibsher, A. S., Didenko, A. N., et al. (2003). The Palaeo-Asian ocean in the Neoproterozoic and early Palaeozoic: new geochronologic data and palaeotectonic reconstructions. *Precambrian Res.* 122 (1), 329–358. doi:10.1016/S0301-9268(02)00218-8

Kovalenko, V. I., Yarmolyuk, V. V., Kovach, V. P., Kotovet, A. B., Kozakov, I. K., Salnikova, E. B., et al. (2004). Isotope provinces, mechanisms of generation and sources of the continental crust in the Central Asian mobile belt: geological and isotopic evidence. *J. Asian Earth Sci.* 23 (5), 605–627. doi:10.1016/s1367-9120(03)00130-5

Kroner, A., Kovach, V., Belousova, E., Hegner, E., Armstrong, R., Dolgopolova, A., et al. (2014). Reassessment of continental growth during the accretionary history of the Central Asian Orogenic Belt. *Gondwana Res.* 25 (1), 103–125. doi:10.1016/j.gr.2012.12.023

Li, D. (2011). Geochemical Characteristics and Tectonic Settings of Carboniferous Volcanic Rocks from Junggar Basin, China. [Master thesis]. Beijing: China University of Geosciences.

Li, D., He, D., Lian, Y., Lu, Y., and Yi, Z. (2017). Structural evolution and late Carboniferous magmatism of the Zhongguai arc in the western Junggar Basin, Northwest China: implications for tectonic evolution of the Junggar Ocean. *Int. Geol. Rev.* 59 (10), 1234–1255. doi:10.1080/00206814.2016.1160801

Li, D., He, D., Yang, Y., and Lian, Y. (2014). Petrogenesis of mid-Carboniferous volcanics and granitic intrusions from western Junggar Basin boreholes: geodynamic implications for the Central Asian Orogenic Belt in Northwest China. *Int. Geol. Rev.* 56 (13), 1668–1690. doi:10.1080/00206814.2014.958766

Li, G., Li, Y., Xiang, K., Wang, R., Liu, J., Li, Z., et al. (2016). Sheep grazing causes shift in sex ratio and cohort structure of Brandt's vole: implication of their adaptation to food shortage. *J. Stratigr.* 40 (1), 76–84. doi:10.1111/1749-4877.12163

Liu, B., Han, B., Chen, J., Ren, R., Zheng, B., Wang, Z., et al. (2017). Closure Time of the Junggar-Balkhash Ocean: constraints From Late Paleozoic Volcano-Sedimentary Sequences in the Barleik Mountains, West Junggar, NW China. *Tectonics* 36 (12), 2823–2845. doi:10.1002/2017TC004606

Liu, B., Han, B., Xu, Z., Ren, R., and Chen, J. (2020). The Ediacaran to Early Palaeozoic evolution of the Junggar-Balkhash Ocean: a synthesis of the ophiolitic melanges in the southern West Junggar terrane, NW China. *Geol. J.* 55 (3), 1689–1707. doi:10.1002/gj.3475

Liu, J. (2015). Research on Permian in the Hala'alate Mountain, West Junggar. [Master thesis]. Beijing: Chang'an University.

Lu, Y. (2018). Permian Chronostratigraphic Framework and Sedimentary Filling Evolution in Mahu-shawan and Adjacent Area, Junggar Basin. [Master thesis]. Beijing: China University of Geosciences.

Marsaglia, K. M., and Ingersoll, R. V. (1992). Compositional trends in arc-related, deep-marine sand and sandstone: a reassessment of magmatic-arc provenance. *Geol. Soc. Am. Bull.* 104, 1637–1649. doi:10.1130/0016-7606(1992)104<1637:CTIARD>2.3.CO;2

Noda, A. (2016). Forearc basins: types, geometries, and relationships to subduction zone Dynamics. *Geol. Soc. Am. Bull.* 128 (5-6), 879–895. doi:10.1130/B31345.1

Pearce, J. A., and Peate, D. W. (1995). Tectonic implications of the composition of volcanic arc magmas. *Annu. Rev. Earth Planet Sci.* 23, 251–343. doi:10.1146/annurev.ea.23.050195.001343

Pearce, J. A., and Norry, M. J. (1979). Petrogenetic implications of Ti, Zr, Y and Nb variations in volcanic rocks. *Contrib. to Mineral. Petrol.* 69, 33–47. doi:10.1007/BF00375192

Pearce, J. A., Harris, N. B. W., and Tindle, A. G. (1984). Trace element discrimination diagrams for the tectonic interpretation of granitic rocks. *J. Petrol.* 25, 956–983. doi:10.1093/petrology/25.4.956

Peng, X., Li, Y., Li, W., Xiang, K., Li, G., and Li, Z. (2016). The Stratigraphic Sequence, Fossil Assemblage and Sedimentary Environment of Aladeyikesai Formation in Hala alate Mountain,West Junggar. *Xinjiang Geol.* 34 (3), 297–301.

Roser, B. P., and Korsch, R. J. (1988). Provenance signatures of sandstone-mudstone suites determined using discriminant function analysis of major-element data. *Chem. Geol.* 67 (1-2), 119–139. doi:10.1016/0009-2541(88)90010-1

Şengör, A., Natalin, B., and Burtman, V. (1993). Evolution of the Altaid tectonic collage and Palaeozoic crustal growth in Eurasia. *Nature* 364 (6435), 299–307. doi:10.1038/364299a0

Tang, G., Wang, Q., Wyman, D. A., Li, Z., Zhao, Z., Jia, X., et al. (2010). Ridge subduction and crustal growth in the Central Asian Orogenic Belt: evidence from Late Carboniferous adakites and high-Mg diorites in the western Junggar region, northern Xinjiang (west China). *Chem. Geol.* 277 (3), 281–300. doi:10.1016/j.chemgeo.2010.08.012

Tang, W., Wang, X., Guo, X., He, W., Tang, Y., Pe-Piper, G., et al. (2022). Late Carboniferous back-arc rifting in Junggar Basin, NW China: implication for the rapid continental growth in accretionary orogens. *Int. J. Earth Sci.* 111 (08), 2493–2518. doi:10.1007/s00531-022-02163-8

Tang, W., Zhang, Y., Pe-Piper, G., Piper, D. J. W., Guo, Z., and Li, W. (2021). Permian to early Triassic tectono-sedimentary evolution of the Mahu sag, Junggar Basin, western China: sedimentological implications of the transition from rifting to tectonic inversion. *Mar. Petroleum Geol.* 98, 104730–105124. doi:10.1016/j.marpetgeo.2020.104730

Taylor, S. R., and McLennan, S. M. (1985). *The continental crust: Its Composition and Evolution*. Oxford, UK: Blackwell Scientific Publications, 312.

Tong, L., Li, Y., Zhang, B., Liu, J., Pang, Z., and Wang, J. (2009). Zircon LA-ICP-MS U-Pb dating and geologic age of the Baogutu formation and andesite in the south of Daerbute faulted zone,western junggar. *Xinjiang Geol.* 27 (3), 226–230.

Wang, T., Wang, X., Guo, L., Zhang, L., Tong, Y., Li, S., et al. (2017). Granitoid and tectonics. *Acta Petrol. Sin.* 33 (5), 1459–1478. doi:10.00-0569/2017/033(05)-1459-78

Wilhem, C., Windley, B. F., and Stampfli, G. M. (2012). The Altaids of Central Asia: a tectonic and evolutionary innovative review. *Earth-Science Rev.* 113 (3-4), 303–341. doi:10.1016/j.earscirev.2012.04.001

Williams, I. S. (2001). Response of detrital zircon and monazite, and their U-Pb isotopic systems, to regional metamorphism and host-rock partial melting, Cooma Complex, southeastern Australia. *Aust. J. Earth Sci.* 48 (4), 557–580. doi:10.1046/j.1440-0952.2001.00883.x

Windley, B. F., Alexeiev, D., Xiao, W., Kroner, A., and Badarch, G. (2007). Tectonic models for accretion of the Central Asian Orogenic Belt. *J. Geol. Soc.* 164 (1), 31–47. doi:10.1144/0016-76492006-022

Winchester, J. A., and Floyd, P. A. (1977). Geochemical discrimination of different magma series and their differentiation products using immobile elements. *Chemical Geology* 20, 325–343. doi:10.1016/0009-2541(77)90057-2

Wu, F., Yang, Y., Mitchell, R. H., Bellatreccia, F., Li, Q., and Zhao, Z. (2010). *In situ* U–Pb and Nd–Hf–(Sr) isotopic investigations of zirconolite and calzirtite. *Chem. Geol.* 277, 178–195. doi:10.1016/j.chemgeo.2010.08.007

Xiang, K. (2015). Carboniferous Sedimentary Basin Analysis And Tectonic Significance in The Baogutu-Halaalate Mountain, Western Junggar. [Doctoral dissertation]. Xinjiang: Chang'an University.

Xiang, K., Li, Y., Li, Z., Wang, R., Yang, G., Duan, F., et al. (2015). LA ICP-MS Zircon Age and Geochemistry of the Aladeyikesai Formation Volcanic Rocks in the Halaalate Mountain of West Junggar, Xinjiang, and Their Tectonic Significance. *Acta Geol. Sin.* 89 (5), 843–855.

Xiang, K., Li, Y., Xu, L., Zhang, H., and Tong, L. (2013). The Definition of Chengjisihanshan Formation and Its Significances in Baijiantan Region, West Junggar, Xinjiang. *Northwest. Geol.* 46 (2), 63–68.

Xiao, W., Han, C., Yuan, C., Sun, M., Lin, S., Chen, H., et al. (2008). Middle Cambrian to Permian subduction-related accretionary orogenesis of Northern Xinjiang, NW China: implications for the tectonic evolution of central Asia. *J. Asian Earth Sci.* 32 (2-4), 102–117. doi:10.1016/j.jseaes.2007.10.008

Xiao, W., Huang, B., Han, C., Sun, S., and Li, J. (2010). A review of the western part of the Altaids: a key to understanding the architecture of accretionary orogens. *Gondwana Res.* 18 (2-3), 253–273. doi:10.1016/j.gr.2010.01.007

Xiao, W., Windley, B. F., Sun, S., Li, J., Huang, B., Han, C., et al. (2015). A Tale of Amalgamation of Three Permo-Triassic Collage Systems in Central Asia: oroclines, Sutures, and Terminal Accretion. *Annu. Rev. Earth Planet. Sci.* 43, 477–507. doi:10.1146/annurev-earth-060614-105254

Xu, X., He, G., Li, H., Ding, T., Liu, X., and Mei, S. (2006). Basic characteristics of the Karamay ophiolitic mélange, Xinjiang, and its zircon SHRIMP dating. *Geol. China* 33, 470–475.

Xu, Z., Han, B., Ren, R., Zhou, Y., and Su, L. (2013). Palaeozoic multiphase magmatism at Barleik Mountain, southern West Junggar, Northwest China: implications for tectonic evolution of the West Junggar. *Int. Geol. Rev.* 55 (5), 633–656. doi:10.1080/00206814.2012.741315

Yakubchuk, A. (2004). Architecture and mineral deposit settings of the Altaid orogenic collage: a revised model. *J. Asian Earth Sci.* 23 (5), 761–779. doi:10.1016/j.jseaes.2004.01.006

Yang, G., Li, Y., Gu, P., Yang, B., Tong, L., and Zhang, H. (2012). Geochronological and geochemical study of the Darbut Ophiolitic Complex in the West Junggar (NW China): implications for petrogenesis and tectonic evolution. *Gondwana Res.* 21, 1037–1049. doi:10.1016/j.gr.2011.07.029

Yang, H., Chen, L., and Kong, Y. (2004). A novel classification of structural units in Junggar Basin, Xinjiang. *Pet. Geol.* 25, 686–688.

Yi, Z., Huang, B., Xiao, W., Yang, L., and Qiao, Q. (2015). Paleomagnetic study of Late Paleozoic rocks in the Tacheng Basin of West Junggar (NW China): implications for the tectonic evolution of the western Altaids. *Gondwana Res.* 27 (2), 862–877. doi:10.1016/j.gr.2013.11.006

Yin, J., Long, X., Yuan, C., Sun, M., Zhao, G., and Geng, H. (2013). A Late Carboniferous-Early Permian slab window in the West Junggar of NW China: geochronological and geochemical evidence from mafic to intermediate dikes. *Lithos* 175, 146–162. doi:10.1016/j.lithos.2013.04.005

Yin, J., Yuan, C., Sun, M., Long, X., Zhao, G., Wong, K., et al. (2010). Late Carboniferous high-Mg dioritic dikes in Western Junggar, NW China: geochemical features, petrogenesis and tectonic implications. *Gondwana Res.* 17, 145–152. doi:10.1016/j.gr.2009.05.011

Zhan, Y., Hou, G., Hari, K. R., and Shu, W. (2015). Geochemical and isotopic constraints on the evolution of Late Paleozoic dyke swarms in West Junggar, Xinjiang, China. *J. Asian Earth Sci.* 113, 126–136. doi:10.1016/j.jseaes.2014.07.012

Zhang, C., and Huang, X. (1992). The ages and tectonic settings of ophiolites in West Junggar, Xinjiang. *Geol. Rev.* 38, 509–524. doi:10.16509/j.georeview.1992.06.007

Zhang, L. (2020). Geological Architecture, Sedimentary Filling, Formation and Mechanism of the Carboniferous Basin in the Junggar Area, NW China. [Doctoral dissertation]. Beijing: China University of Geosciences.

Zhang, L., Wang, G., Gao, R., Shen, T., Zong, R., and Yan, W. (2015). U-Pb Chronology of Detrital Zircons from the Carboniferous Sequences and its Geological Implications in West Junggar. *Geotect. Metallogenia* 39 (4), 704–717. doi:10.16539/j.ddgzyckx.2015.04.013

Zhang, P., Wang, G., Polat, A., Shen, T., Chen, Y., Zhu, C., et al. (2018a). Geochemistry of mafic rocks and cherts in the Darbut and Karamay ophiolitic melanges in West Junggar, northwestern China: evidence for a Late Silurian to Devonian back-arc basin system. *Tectonophysics* 745, 395–411. doi:10.1016/j.tecto.2018.08.018

Zhang, P., Wang, G., Polat, A., Zhu, C., Shen, T., Chen, Y., et al. (2018b). Emplacement of the ophiolitic melanges in the west Karamay area: implications for the Late Paleozoic tectonic evolution of West Junggar, northwestern China. *Tectonophysics* 747, 259–280. doi:10.1016/j.tecto.2018.08.019

Zhang, P., Wang, G., Shen, T., Polat, A., and Zhu, C. (2021). Paleozoic convergence processes in the southwestern Central Asian Orogenic Belt: insights from U-Pb dating of detrital zircons from West Junggar, northwestern China. *Geosci. Front.* 12 (2), 531–548. doi:10.1016/j.gsf.2020.07.015

Zhang, Y., and Guo, Z. (2010). New constraints on formation ages of ophiolites in northern Junggar and comparative study on their connection. *Acta Petrol. Sin.* 26 (2), 421–430. doi:10.00-0569/2010/026(02)-0421-30

Zheng, B., Han, B., Liu, B., and Wang, Z. (2019). Ediacaran to Paleozoic magmatism in West Junggar Orogenic Belt, NW China, and implications for evolution of Central Asian Orogenic Belt. *Lithos* 338, 111–127. doi:10.1016/j.lithos.2019.04.017

Zhu, D., Zhao, Z., Niu, Y., Dilek, Y., Wang, Q., Ji, W., et al. (2012). Cambrian bimodal volcanism in the Lhasa Terrane, southern Tibet: record of an early Paleozoic Andean-type magmatic arc in the Australian proto-Tethyan margin. *Chem. Geol.* 328, 290–308. doi:10.1016/j.chemgeo.2011.12.024

Zhu, Y., Chen, B., and Qiu, T. (2015). Geology and geochemistry of the Baijiantan-Baikouquan ophiolitic melanges: implications for geological evolution of west Junggar, Xinjiang, NW China. *Geol. Mag.* 152 (1), 41–69. doi:10.1017/S0016756814000168

Zhu, Y., Chen, B., Xu, X., Qiu, T., and An, F. (2013). A new geological map of the western Junggar, north Xinjiang (NW China): implications for Paleoenvironmental reconstruction. *Episodes* 36 (3), 205–220. doi:10.18814/epiiugs/2013/v36i3/003

Zhu, Y., and Xu, X. (2006). The discovery of Early Ordovician ophiolite melange in Taerbahatai Mts., Xinjiang, NW China. *Acta Petrol. Sin.* 22 (12), 2833–2842. doi:10.00-0569/2006/022(12)-2833-42

Frontiers in Earth Science

Investigates the processes operating within the major spheres of our planet

Advances our understanding across the earth sciences, providing a theoretical background for better use of our planet's resources and equipping us to face major environmental challenges.

Discover the latest Research Topics

See more →

Frontiers

Avenue du Tribunal-Fédéral 34
1005 Lausanne, Switzerland
frontiersin.org

Contact us

+41 (0)21 510 17 00
frontiersin.org/about/contact